UNIVERSITAT DE BARCELONA

DEPARTAMENT D'ASTRONOMIA I METEOROLOGIA

New observational techniques and analysis tools for wide field CCD surveys and high resolution astrometry

Memòria presentada per
Octavi Fors Aldrich
per optar al grau de
Doctor per la Universitat de Barcelona
Barcelona, desembre de 2005

PROGRAMA DE DOCTORAT D'ASTRONOMIA I METEOROLOGIA

BIENNI 1996–1998

Memòria presentada per **Octavi Fors Aldrich** per optar al grau de
Doctor per la Universitat de Barcelona

DIRECTOR DE LA TESI

Dr. Jorge Núñez de Murga

Maite, vull agrair-te tant
temps que fa que t'estimo

Agraïments

Agraïments / Agradecimientos / Acknowledgements

Tota llista d'agraïments és incompleta, i més quan l'espai de temps és tan dilatat. Conscient d'això, correré el risc de deixar-me algú i, en aquest cas, confio que se'm disculpi, ja que haurà estat per oblit:

Primerament vull donar les gràcies al meu director de tesi, en Jorge Núñez de Murga. Vas donar-me acollida en el teu grup i em consta que has posat a disposició meva els elements necessaris (científics, tècnics, etc.) per a que aquesta tesi tirés endavant. Més enllà del suport científic, el que queda és la relació personal, la qual considero ha estat excel.lent. Ha anat madurant lentament, com el bon vi. Per tot això i més, gràcies Jorge.

Vull agrair profundament a l'Albert Prades tot el que he après d'ell, tant en el camp científic com en el personal. En el primer, he gaudit llargues i enriquidores converses que, entre d'altres, han servit per incrementar el meu nivell d'autoexigència en la feina feta. En el segon, la teva manera d'entendre la vida i la possibilitat de parlar-ne obertament m'ha permés tirar endavant en moments que em calien referents i consells de company i amic.

Esctic molt agraït a en Xavi Otazu, amb qui he tingut la sort de compartir durant tots aquests anys el seu entusiasme per la ciència i el seu tarannà de treballador incansable, el qual admiro. A en Xavi li dec la maduració d'algunes de les idees en el camp de la deconvolució astronòmica d'imatges que s'exposen en aquesta tesi, així com la utilització del codi de deconvolució basat en wavelets. També vull expressar la meva gratitut per tot allò que he après de tu en el camp informàtic, en el que recordo molt poques ocasions en que no m'hagis satisfet un dubte.

Moltes gràcies a la Maite Merino, qui en la darrera etapa de la tesi ha col.laborat intensament en diversos aspectes de la tesi, com ara les observacions d'ocultacions lunars a Calar Alto, l'obtenció de les dades de la càmera Baker-Nunn de Calgary i la sistemàtica i enriquidora revisió d'aquesta tesi. A més a més, li agraeixo especialment el seu esperit altruïsta en tasques de logística de grup sense les quals la finalizació d'aquesta tesi hauria estat més perllongada.

Vull fer un agraïment especial al Dr. Codina, director de l'Observatori Fabra. Ha estat tot un honor col.laborar amb l'Observatori i poder compartir aquests anys de treball amb el qui ha estat un excel.lent cap, docent, però sobretot un *senyor* com en queden pocs. Amb el temps, els seus consells en moments importants han resultat sempre encertats. Finalment, vull agrair-li que hagi fet seu el projecte de robotització de la càmera Baker-Nunn de San Fernando, que juntament amb en Jorge Núñez, vam imaginar per primera vegada un dia de novembre de 2000. Aquest gran esforç ha estat essencial per a superar tots els alts i baixos d'un projecte que, tot just ara, albira un horitzó de futur immediat.

També vull donar les gràcies a tot el personal de l'Observatori Fabra durant aquest anys: en Nicolau Torras, l'Antonio Gàzquez, en Jaume Pérez, en Dionís Escámez, en Marc Prohom, l'Alfons Puertas, la Teresa Susagna, la Marta González i en Ramon Secanell. Gràcies a ells m'he sentit com a casa i han fet possible que la tasca realitzada a l'Observatori fos encara més realitzant. Finalment, un record especial per als companys de l'Observatori que ja no romanen entre nosaltres: en Joan Pardo, l'Enric Santamaria i la Maria Campo. De tots ells, però en especial d'en Joan, vaig sentir innumerables relats sobre l'Observatori d'un valor, almenys simbòlic, incalculable i que algú hauria d'afanyar-se a recollir per escrit ja que formen part de la memòria col.lectiva de la ciutat de Barcelona i del país.

Al meu company de despatx i amic Marc Ribó mai li prodré estar prou agraït. Possiblement, ell sigui qui millor conegui els detalls cotidians del camí que he hagut de fer per arribar fins aquí. Sempre que m'ha calgut ajuda de qualsevol tipus (científica, informàtica, personal), un consell, en definitiva, un amic, en Marc era allí. La seva gran vàlua com a científic rivalitza amb la qualitat humana que transmet als altres.

Gràcies a la colla d'amics de la Facultat. Molt especialment, gràcies al David Nofre i el seu germà Jordi i al Nèstor i l'Àstrid. Amb tots quatre he passat estones inolvidables que m'han donat aire per seguir amb la tesi. Cinemes, sopars,

excursions, viatges d'estiu, tot plegat quelcom que he grabat per sempre en la retina vital.

També vull tenir un agraïment per en Valentí Bosch, qui ha ocupat el lloc d'en Marc en aquests darrers anys. Has estat un excel.lent company de despatx, amb el qui he pogut compartir coneixement i idees de tot tipus: científiques, informàtiques, fins i tot polítiques. Gràcies també a en Pol Bordas, que s'ha afegit a la colla de la galera 756 en aquest darrer any i amb qui he mantingut tambe converses interessants i m'ha assistit amb el meu italià elemental.

Moltes gràcies als doctorands (bé, la majoria ja sou il.lustres doctors) del Departament d'Astronomia i Meteorologia per deixar-me compartir dinars, sopars de festa, sortides d'observació, excursions, etc. M'ho he passat molt bé i mirant enrere considero que som uns privilegiats quan hem pogut fer recerca en un ambient de companyonia com el del *poble*. Moltes gràcies Marc, Xavi, David, Montse, Maite Beltrán, Ricard, Marta, Lola, Ignasi, Albert Domingo, Eduard, Mercé, Òscar, Imma, Teresa, Josep Miquel, Pep, Andreu Raig, Àngels, Ada i un llarg etcètera.

A en José Ramón Rodríguez (per tots conegut com a JR) li resto profundament agraït principalment per dues coses. En primer lloc per la seva extraordinària professionalitat i eficiència en la Secretaria del Departament d'Astronomia i Meteorologia. Davant de la meva manifesta incompetència a l'hora de gestionar paperassa, has estat el meu *àngel de la guarda* sense el qual no sé què hauria passat. En segon lloc, gràcies per ajudar-me a comprendre la complexitat que comporta un departament universitari com el DAM. Certament, ha estat un exercici de Psicologia de grups interessant.

I would like to express my gratitude to Bill van Altena for the constant support and assistance received while my three research stays at Yale. What I learned about astrometry at those meetings in your group has turned out to be of crucial value for the development of this thesis. The same gratitude applies for all members of your group: Terry Girard, Imants and Vera Platais, Dana Dinescu, Reed Meyer and John Lee. I enjoyed a fruitful scientific experience among all of you. In the personal side, I discovered you all are wonderful people and I often miss you. Voldria també agrair a la Carme Gallart tota la hospitalitat que em va demostrar durant el temps que vam coincidir a Yale.

I would like to acknowledge here my gratitude to Andrea Richichi. His great

scientific enthusiasm encouraged me to pursue the Calar Alto Lunar Occultation Program and their different data analysis derivatives, both projects being essential parts of this thesis. I am also in debt to you for all the assistance and guidance you offered me in the field of lunar occultations. On the personal side, I have always felt like having a close and sincere relationship with you. I also thank you and ESO Director General Discretionary Funding Program (DGDF) for making possible the numerous visits both of us have made to Barcelona and Garching.

También mi más sincera gratitud a todos los observadores que han participado en los numerosos períodos de observación del programa de ocultaciones lunares de Calar Alto, y al que tanto debe esta tesis. Muchas gracias a Maite Merino, Javier Montojo, Jorge Núñez, Xavier Otazu, Dolores Pérez, Albert Prades y Andrea Richichi. Vuestro esfuerzo vale su peso en oro, más teniendo en cuenta que en ningún momento os venció el desánimo incluso en las repetidas noches *en blanco* que cosechamos debido al mal tiempo en Calar Alto. Coordinar este equipo humano ha sido todo un placer para mí.

A deep thanks to Elliott Horch, whose expertise in the field of speckle interferometry helped me to develop a substantial part of this thesis. I greatly enjoyed sharing exciting discussions about instrumental aspects of CCD speckle and bispectral analysis while your visit to Barcelona. Thanks for making understandable what is not obvious for others. I guess you learnt this gift from Bill van Altena.

I am deeply grateful for the assistance of Kenneth Mighell, who shared his great expertise about PSF fitting and centering algorithms during the last months of this thesis. Although by email, the outstanding level of his dissertations allowed my to madurated some of the fundamental concepts exposed in this thesis.

I am indebted to Christoph Flohr, for attending my request of adapting his drift-scanning program SCAN for lunar occultations and speckle interferometry observations. His expertise in the knowledge of CCD adquisition software has been enlightening for the proper course of this thesis.

Thanks also to Craig Markwardt, who kindly provided the IDL subroutines which I adapted for centering stars by means of the Levenberg-Marquardt technique for non-linear least squares curve fitting.

Although we never have met in person, thanks to Michael Richmond from Roc-

Contents

Resum de la tesi: Noves tècniques observacionals i eines d'anàlisi per a observacions CCD de gran camp i astrometria d'alta resolució

1. Introducció

Aquesta tesi es divideix en dues parts diferenciades. La primera part versa sobre l'aplicació de la deconvolució a imatges CCD de gran camp i els beneficis que se n'obtenen. La segona es centra en el desenvolupament de noves tècniques observacionals i d'anàlisi de dades en els camps de les ocultacions lunars i la interferometria speckle.

1.1 Deconvolució d'imatges

La deconvolució d'imatges pretén substraure d'una imatge tots aquells efectes distorsionadors que en el seu procés de formació ha incorporat. Els principals són la funció de distorsió puntual (PSF) i el soroll. La primera està causada per la turbulència atmosfèrica, l'òptica del telescopi i el procés de mostreig. El segon, en els cas dels detectors CCDs, es composa del soroll de conteig Poisson i el sorroll de lectura del mateix detector.

La tasca d'eliminar aquests efectes condueix a una equació inversa mal condicionada, la solució de la qual no té assegurada l'estabilitat ni la unicitat. S'han

proposat una gran varietat d'algoritmes en la literatura per assegurar l'anterior. Les diferències entre ells poden raure en quatre punts: la hipòtesis de formació de la imatge, les restriccions de regularització emprades per assegurar la unicitat i estabilitat de la solució, les tècniques numèriques considerades per cercar la convegència i els tests de validació per avaluar el grau de convergència. En aquesta tesi utilitzarem dos d'aquests algorismes: el Richardson-Lucy (Lucy 1974) o la seva variant per a soroll Poissonià i Gaussià (MLE) (Núñez & Llacer 1993), i el Mètode Adaptatiu de Màxima Versemblança basat en Wavelets (AWMLE) (Otazu 2001). Aquest darrer destaca per mostrar una convergència assimptòtica i un bon control d'amplificació de soroll amb el nombre d'iteracions.

Les aplicacions dels algorismes de deconvolució en el camp de l'Astronomia ha estat molt variades. Aquestes es distribueixen al llarg d'un ampli rang de longitud d'ona, relació-senyal-soroll (SNR), resolució, context astrofísic, etc. Per enumerar-ne només unes quantes, anant de longituds d'ona mes llargues a més curtes:

- primer survey optic-VLA (Haarsma et al. 2005),

- deconvolució del perfil radial HI en superfície de galàxies espirals (Noordermeer et al. 2005),

- millora de la resolució espacial d'observacions submil.limètriques SCUBA d'objectes estel.lars joves (Krause et al. 2003),

- millora de resolució en imatges d'òptica adaptativa ESO 3.6 m/ADONIS del volcanisme de Io en el infraroig mitjà (Marchis et al. 2000),

- millora de resolució de cloves de pols a l'entorn d'estrelles de carboni (Bontekoe et al. 1994),

- increment de la detecció de quasars lensats en el infraroig amb VLT/ISAAC (Faure et al. 2003),

- Anàlisi de lens gravitacionals febles a l'entorn de galàxies properes amb dades HST/ACS (Jee et al. 2005),

- estudi de l'estructura de jet i disc de l'objecte jove triple HV Tauri (Stapelfeldt et al. 2003),

- eliminació de les distorsion d'astigmatisme i coma de l'arxiu de plaques fotogràfiques de l'Observatori de Sonneberg (Hiltner et al. 2003)

- millora de la detecció d'estructures nebulars i jets òptics en objectes BL Lac objects a OJ 287 Benitez et al. (1996),

- guany en la detecció d'un outburst de la estrella Mira A en rajos X *Chandra* (Karovska et al. 2005),

- detecció de hypernoves en spectres γ amb dades INTEGRAL (Schanne & et al. 2004).

Com s'observa, els propòsits de l'aplicació de la deconvolució rauen típicament en la millora de la resolució, la detectabilitat d'objectes febles, la supressió de distorsions de la imatge original.

Una característica comú a totes aquestes aplicacions és que s'han dut a terme amb telescopis grans, camps de visió reduïts i detectors de la més alta qualitat, on sovint la relació SNR de les dades és alta i la PSF i el soroll es poden caracteritzar molt acuradament. A més a més, quasi totes elles són observacions puntuals relatives a l'estudi d'un objecte i no són sistemàtiques, és a dir, no cobreixen grans àrees de cel durant un temps continuat (tipus *survey*). Hi ha diverses raons que justifiquen aquesta aplicació selectiva. En primer lloc, l'esforç necessari per a la deconvolució sistemàtica d'un joc de dades *survey* és més complexe i requereix la utilització d'eines d'anàlisi especialitzades. Segon, el rendiment científic en aplicacions selectives de gran qualitat està assegurat en la majoria dels casos mentre que en el cas *survey* no sempre. Finalment, el cost computacional de la deconvolució és elevat i requereix un esforç addicional quan el volum de dades a reduïr és gran.

1.2 Ocultacions lunars

Una ocultació lunar s'esdevé quan la Lluna s'interposa en la línia visual entre una estrella i l'observador. Degut que la naturalesa ondulatòria de la llum, la intensitat de la estrella no minva instantàniament, sino que ho fa en uns ~ 0.1s. La distribució d'intensitat de l'estrella durant aquest interval de temps es pot aproximar a la predita per la difracció de Fresnel d'una font puntual monocromàtica ocultada per una pantalla rectilínia. La modelització del fenomen pot ser completada amb la inclusió de la policromia de la font, fonts resoltes o multiples i d'altres efectes instrumentals com ara el soroll de centelleig i la influència del diametre del telescopi, el filtre o el mostreig temporal.

D'entre totes les aplicacions que se'ls ha donat a les ocultacions lunars (LO), les dues següents són les que actualment són vigents en l'Astronomia moderna:

- determinació de diàmetres estelars de fins 1 mil.lisegon d'arc (mas) amb una incertesa típica del $\sim 5\%$. Aquestes mesures, que es duen a terme en el visible i IR, són possibles si la SNR de les dades és prou alta (>10). Els diàmetres obtinguts són de gran utilitat per a validar models d'evolució estelar a partir d'incerteses en les temperatures efectives < 50 K. També s'utilitzen per l'estudi estructural de fonts no esfèricament simètriques com ara estrelles pulsants i estudi d'envolcalls circumstelars (Mondal & Chandrasekhar 2005; Ragland et al. 1997; Richichi et al. 1988), fonts Mira (Mondal & Chandrasekhar 2004), etc. La calibració de teperatures efectives per a les estrelles més fredes del diagrama H-R, tipus espectral K, M i de carboni, també s'han beneficiat de les mesures de diàmetres proporcionades per les LO (Richichi et al. 1999).

- detecció de binaries de separació projectada fins a 1 mas i relacions de brillantor de 1:1 a 1:150. Les aplicacions en aquest camp d'estudi són, apart de la detecció en sí, la determinació de l'òrbita i les masses del sistema binari. En aquest darrer camp, Evans (1983); Richichi et al. (2000) han desenvolupat una intensa activitat observadora amb milers d'ocultacions enregistrades i una probabilitat de detecció d'una binària del $\sim 10\%$. Una darrera línia d'aplicació ha estat l'estudi de la freqüència de binaritat d'objectes joves T Tauri. A partir de mesures LO (Chen & Simon 1997; Leinert et al. 1991; Simon et al. 1995, 1996, 1999) han mostrat que aquest escenari de formació estelar està dominat per la presència de sistemes múltiples.

Les LO presenten avantatges i inconvenients respecte altres tècniques d'alta resolució espacial:

Per una banda, els interferòmetres òptics de llarga base que entraran a ple rendiment en breu (VLTI, Keck) requereixen per a la seva calibració d'un cataleg de fonts resoltes per les quals es conegui prèviament el seu diàmeter. Les LO són actualment la única tècnica que pot subministrar aquestes mesures amb suficient nombre i precisió. Un altre avantatge de les LO és que no són fenomens limitats per la difracció del telescopi. Finalment, és una tècnica instrumentalment barata ja que precisa telescopis de $1 - 2$ metres amb instrumentació convencional (fotòmetres o càmeres IR).

Per altra banda, les LO són esdeveniments fixats en el temps i que estan restringits a la franja zodiacal del cel (un 10% del total) on la Lluna projecta la seva òrbita. També cal afegir que els paràmetres mesurats per a una estrela binària no són els reals, sino els projectats al llarg de la direcció d'escombrat de la Lluna.

1.3 Interferometria speckle

La interferometria speckle és una tècnica observacional que permet extraure informació espacial de l'objecte observat per sota el límit de difracció del telescopi. Això s'aconsegueix per mitjà de l'enregistrament ràpid (mostreig ~ 10 ms) i successiu d'exposicions del objecte en questió. Així, la turbulència atmosfèrica fracciona el front d'ona en diverses regions (o *speckles*). En aquestes condicions de mostreig, aquestes es poden considerar coherents i estacionaries per cadascun dels *fotogrames* mostrejats.

Les resolucions que típicament s'aconsegueixen oscilen entre 0."01 i 1."0. Aquest rang se situa enmig del que altres tècniques d'alta resolució venen subministrant (observacions visuals amb micròmetre i els més moderns interferòmetres òptics, respectivament).

El camp principal d'estudi de les mesures speckle han estat les estrelles binaries i el càlcul de les seves òrbites, que constitueixen un primer pas per a l'establiment de la Relació Massa–Lluminositat i la Funció Initial de Massa. Aquesta tasca s'ha realitzat gràcies a la observació sistemàtica d'aquestes per part de nombrosos grups durant més de 25 anys (Balega et al. 2004; Docobo et al. 2004; Hartkopf et al. 2000; Horch et al. 2004; Mason et al. 2004; Saha et al. 2002; Scardia et al. 2005).

Els requeriments instrumentals de la interferometria speckle són: mostreig ràpid, baix soroll de lectura, alta eficiència quàntica i linearitat. La majoria de les observacions anteriorment citades han estat dutes a terme amb detectors CCD intensificats (ICCD), que combinen característiques del fotòmetres i les càmeres CCD. Els ICCDs satisfan la majoria dels anteriors requeriments tècnics. Han mostrat deficiències en la linelitat, cosa que ha conduit a una pèrdua en la precisió fotomètrica.

Paralelament, els CCDs no intesificats han anat incrementant la seva rapidesa, eficiència quàntica i linealitat i reduint el seu soroll de lectura. Com a resultat, noves tècniques d'adquisició amb CCD han estat proposades amb éxit Horch et al. (1997,

2001); Zadnik (1993).

1.4 Motivació de la tesi

Pel que fa a la deconvolució:

Per una banda, com hem vist els *surveys* mai han estat motiu d'aplicació de les tècniques de deconvolució. Per altra banda, la computació distribuida està assolint rendiments de càlcul cada cop més grans. També val a dir que el problema de la deconvolució d'imatges és fàcilment escalable. A més a més, cal tenir en compte que no totes i cadascuna de les imatges captades per un d'aquests projectes hauria de ser subceptible de ser deconvolucionada. Estratègies de selecció de camps més petits basats en informació prèvia poder ajudar i molt al rendiment del mètode de deconvolució en programes de cerca d'objectes específics com ara *macrolensing*, GRBs, NEOs, etc.

Tot plegat ens duu a pensar que la deconvolució d'un banc de dades provinent d'un projecte tipus *survey* podria ser factible i objecte d'estudi en aquesta part de la tesi, la qual pretén assolir els següents objectius:

1. definir i implementar una metodologia general que permeti deconvolucionar imatges CCD genèriques de tipus *survey*.

2. mostrar que la aplicació de la deconvolució amb l'algorisme AWMLE millora l'eficiència observacional, concretament la magnitud limit i la resolució limit de les imatges. Per exemple, una millora en la magnitud límit de $\Delta m_{\lim} \sim 0.6$ mag equivaldria a incrementar el diàmetre del telescopi (D) en un 30%. Tenint en compte que el cost d'un telescopi es proporcional a $D^{2.7}$ (Andersen & Christensen 2000; Meinel & Meinel 1980; Schmidt-Kaler & Rucks 1997; Sebring et al. 2000), queda clar que la deconvolució pot ser altament efectiva des del punt de vista econòmic.

3. clarificar quina incidència sobre la presició astromètrica introdueix la deconvolució.

El punt 2 és especialment pertinent per aquells *surveys* que degut a les seves particularitats en el mètode d'adquisició o sistema òptic, han vist rebaixades les

seves magnitud i resolucion límit.

Pel que fa a les ocultacions lunars:

El panorama descrit en l'apartat anterior és susceptible de canviar en un futur proper degut a les següents consideracions:

En primer lloc, els catàlegs actuals en IR han incrementat en diversos ordres de magnitud el seu nombre d'objectes. Per exemple, mentre que el catàleg Two Micron Sky Survey (TMSS) (Neugebauer & Leighton 1969) només era complet fins a magnitud $K \lesssim 3$, el nou 2MASS (Cutri et al. 2003) ha extés la seva mostra fins a $K_{\mathrm{lim}} \sim 14.3$, amb prop de 500 milions d'objectes. Consequentment, el nombre d'ocultacions potencials en una nit amb un telescopi de $1.5\,\mathrm{m}$ ha passat de 20-30 a més de 100.

En segon lloc, els detectors CCD i càmeres infrarojes han millorat les seves prestacions en termes d'eficiència quàntica, soroll de lectura i freqüència de mostreig. Tot i oferir més avantatges que el fotòmetres unidimensionals, aquest dos tipus de detectors no han estat emprats regularment per observar LO.

Ateses aquestes consideracions, hem cregut oportú fixar els següents objectius:

1. desenvolupar, implementar i validar una nova tècnica d'observació de LO per CCDs. Apart de la consideració anterior respecte la millor constant en aquests detectors, cal tenir en compte que els CCDs són presents a la majoria dels observatoris. El seu interés és, per tant, justificat.

2. disenyar i implementar un nou algorisme de reducció automàtic de LO, que permeti reduir grans nombres d'ocultacions en poc temps i de manera no supervisada. Aquest punt es fa essencial atés el gran increment d'ocultacions potencials que els nous catàlegs han aportat.

3. impulsar i portar a terme un programa d'observació de LO intensiu centrat en la detecció de noves binaries.

Pel que fa a la interferometria speckle:

Ateses les consideracions descrites en l'anterior apartat, hem establert els següents objectius en aquest apartat de la tesi:

1. desenvolupar una nova tècnica observacional basada en CCD no intensificat que permeti realitzar observacions speckle de precisió.

2. validar l'anterior tècnica amb l'observació d'estrelles binaries que tinguin una òrbita ben coneguda.

3. proposar i desenvolupar un nou mètode de calibració per a les dades speckle que permeti observacions més eficients.

2. Aplicació de la deconvolució d'imatges a observacions CCD de gran camp

2.1 Algorismes emprats, dades i procediment

Com hem esmentat en la instroducció, hem treballat amb dos tipus d'algorismes de deconvolució: el MLE i el AWMLE.

El MLE presentat per Núñez & Llacer (1993) pren en consideració una modelització correcta del soroll en la imatge CCD. A partir d'aquí construeix una funció de versemblança que maximitza per mitjà de la tècnica de les substitucions successives. Es tracta, per tant, d'un algorisme iteratiu no lineal. Això comporta problemes de convergència cap a la solució físicament desitjada, ja que si deixem iterar el MLe suficientment aquest amplifica el soroll present en la imatge original. Com a solució parcial, s'acostuma a aturar la convergència a un nombre d'iteracions prudent.

El AWMLE representa l'evolució del MLE (fa servir el mateix estimador estadístic) per a solucionar d'una manera natural l'amplificació del soroll. Això s'aconsegueix amb la descomposició de la imatge original en una base de funcions anomenades *wavelets*. Aquestes permeten obtenir una bona localització espacial dels diferents detalls freqüencials de la imatge (també anomenats plànols wavelet). D'aquesta manera, la deconvolució pot operar de manera selectiva en segons quins plànols i regions estadísticament significatives (no relatives a soroll). Es tracta, doncs, d'un algorisme adaptatiu que no amplifica el soroll i presenta una convergència assimptòtica (elimina la necessitat d'aturar arbitràriament).

Una característica comuna d'ambdós algorismes és l'evolució del mostreig en

la imatge deconvolucionada. S'ha mostrat que aquest tendeix a empitjorar amb el nombre d'iteracions (Prades & Núñez 1997; Prades et al. 1997). Aquest efecte ve acompanyat de l'aparició d'un artifacte anomenat *ringing* i que consisteix en oscil.lacions d'intesitat al voltant de les estrelles més brillants. El *ringing* pot ser eliminat en ambdós algorismes si l'usuari és capaç de modelar amb precisió l'emissió de fons (*background*) de la imatge original.

Per tal de mostrar els beneficis de la deconvolució d'imatges a observacions CCD de gran camp, hem disposat de tres jocs de dades, provinent de tres *surveys*: el Flagstaff Transit Telescope (FASTT), el QUasar Equatorial Survey Team (QUEST) i el Near-Earth Space Surveillance Terrestrial (NESS-T).

FASTT és un telescopi meridià de l'Observatori Naval d'Estats Units que realitza observacions astromètriques de gran precisió, per tal de densificar catàlegs com ara HIPPARCOS i Tycho. Es tracta, doncs, d'un instrument extraordinàriament calibrat i precís des del punt de vista astromètric. És per aquesta raó que hem escollit el FASTT per a avaluar l'impacte de la deconvolució sobre la precisió astromètrica.

QUEST és un telescopi tipus Schmidt situat a Venezuela amb una càmera CCD mosaic de gran format, i coordinat per la Universitat de Yale, el Centro de Investigaciones de Astronomía (CIDA), la Universidad de Los Andes (ULA) i la Universitat d'Indiana. Centra el seu estudi a elaborar un cens de quasars complet fins magnitud $m_B \sim 21$. A resultes d'aquest catàleg, s'espera obtenir una fracció significativa de lents gravitatòries que permeti verificar qüestions fonamentals de la teoria de Relativitat General. L'estratègia d'observació consisteix en obtenir una mostra de candidats a quasars per mitjà del criteri de variabilitat fotomètrica. Aquests candidats són posteriorment confirmats o desmentits amb observacions de suport (*follow-up*), espectroscòpiques i d'imatge, en un telescopi de diàmetre major (WIYN). Gràcies al gran camp i la magnitud profunda de QUEST, el conjunt de candidats pot ser molt nombrós ($> 10^4$). Es fa necessari, per tant, un mètode complementari que permeti refinar la llista de candidats, retenint aquells que podrien ser susceptibles de ser lensats. Aquesta és la tasca que hem dut a terme aplicant la deconvolució AWMLE a dos camps QUEST-WIYN.

NESS-T és un projecte dedicat al cens de NEOs operat pel Rothney Astrophysical Observatory i la Universitat de Calgary. L'instrument emprat és una càmera Baker-Nunn de gran camp ($4°4x4°4$). La relació focal extraordinàriament curta d'aquest instrument fa que el mostreig de la imatge estigui dominat per la figura de

mèrit del sistema òptic (no pel *seeing*). Com a resultat, les dades NESS-T presenten un elevat *deblending* entre estrelles properes, que fa pertinent l'aplicació de la deconvolució AWMLE.

Mentre que FASTT i QUEST han seguit el mode d'observació anomenat *drift-scanning*, NESS-T ho ha fet per mitjà de l'standard o *stare*. El mode *drift-scanning* consisteix en aturar el seguiment del telescopi, alinear l'eix de transferència de càrrega del CCD amb l'equador celest i acomodar el ritme d' aquesta amb el sideri, que és amb el què la imatge de les estrelles es trasllada sobre el detector. Aquest mode presenta diversos avantatges i inconvenients. Per una banda, és més eficient en termes d'àrea observada per unitat de temps, ja que eliminat el temps mort dedicat al reapuntat del telescopi i la lectura de la càmera CCD. Per altra banda, la magnitud límit de les observacions està limitada al ritme sideri d'escombrat. També introdueix una sèrie de distorsions en la PSF de les estrelles que impliquen una pèrdua significativa de SNR i resolució. Hem aplicat la deconvolució AWMLE per tal de compersar aquests darreres restriccions inherents al *drift-scanning*.

Una de les aportacions d'aquesta part de la tesi és la definició d'una metodologia general que permet aplicar l'aplicació de la deconvolució d'imatges (MLE, AWMLE o qualsevol altre algorisme) a un joc de dades de característiques genèriques (tipus *stare* o *drift scanning*). El procediment proposat es divideix en dues fases: la prèvia i la posterior a la deconvolució.

La fase prèvia a la deconvolució pretén aconseguir una caracterització precisa de les dades originals. En altres paraules, volem obtenir una estimació realista de la PSF, el *background*, el guany i el soroll de lectura de la imatge original. Totes aquests valors s'han obtingut per mitjà d'un conjunt d'eines d'anàlisi ben establertes que s'utilitzen pel mateix propòsit en altres camps de l'Astronomia.

La fase posterior a la deconvolució es centra en l'anàlisi dels resultats per mitjà de tres descriptors: el guany en magnitud límit, el guany en resolució i l'impacte sobre l'error astromètric. Pels tres subprocediments cal efectuar una validació dels objectes detectats tant en la imatge original com deconvolucionada. Aquest es realitza amb una imatge d'alta resolució de referència o un catàleg astromètric més complet.

2.2 Resultats

Magnitud límit

Aquest estudi s'ha realitzat aplicant els algorismes AWMLE i MLE a les dades QUEST i NESS-T. Es tracta de calcular quin és la magnitud límit abans i després de deconvolucionar, tot emprant la metodologia proposada en l'apartat anterior.

S'han trobat valors de $\Delta R_{\text{lim}} \sim 0.64$ i $\Delta R_{\text{lim}} \sim 0.46$ per les dades QUEST i NESS-T, respectivament. Il.lustrem el guany obtingut per les dades QUEST en la Fig. 1, on es mostra l'histograma de magnitud pels objectes detectats en la imatge original i deconvolucionada amb AWMLE després de 750 iteracions. Val a dir que aquest guany equival a un increment d'un 81% en el nombre d'objectes nous recuperats que poden ser mesurats i que no estaven disponibles en la imatge original. En termes d'increment d'àrea col.lectora el guany es tradueix en un augment del 32% en diàmetre del telescopi, que suposa multiplicar el cost del mateix per 2.3.
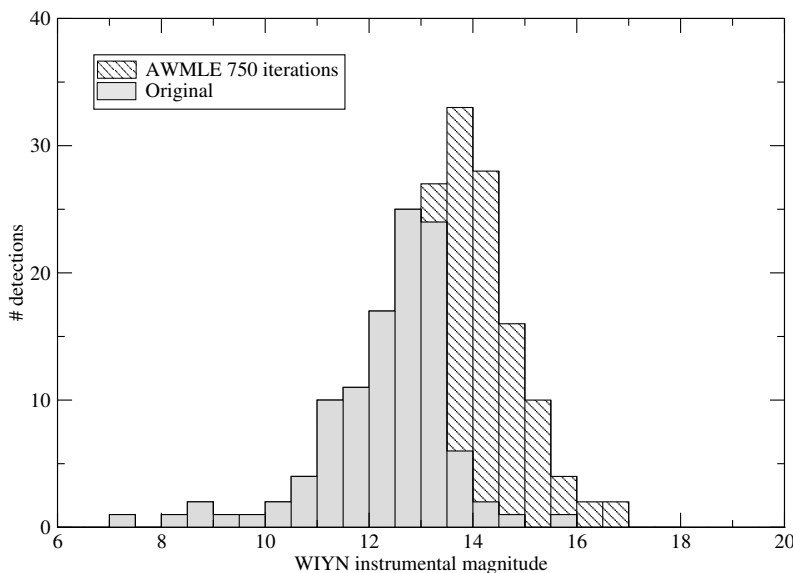
Figura 1: Histograma de magnitud de deteccions per la imatge QUEST original i la deconvolucionada amb 750 iteracions AWMLE.

Com a resultat paral.lel de l'anterior guany, s'ha pogut investigar l'existència d'algun objecte amb interés astrofísic entre les deteccions noves aportades per la deconvolució AWMLE. Efectivament, tal com mostra la Fig. 2 s'ha trobat un possible esdeveniment de magnitud transitòria (*transient*) de magnitud en les dades QUEST. Hem discutit la possible associació d'aquest fenomen amb una estrella binària de

rajos X de l'Halo Galàctic.
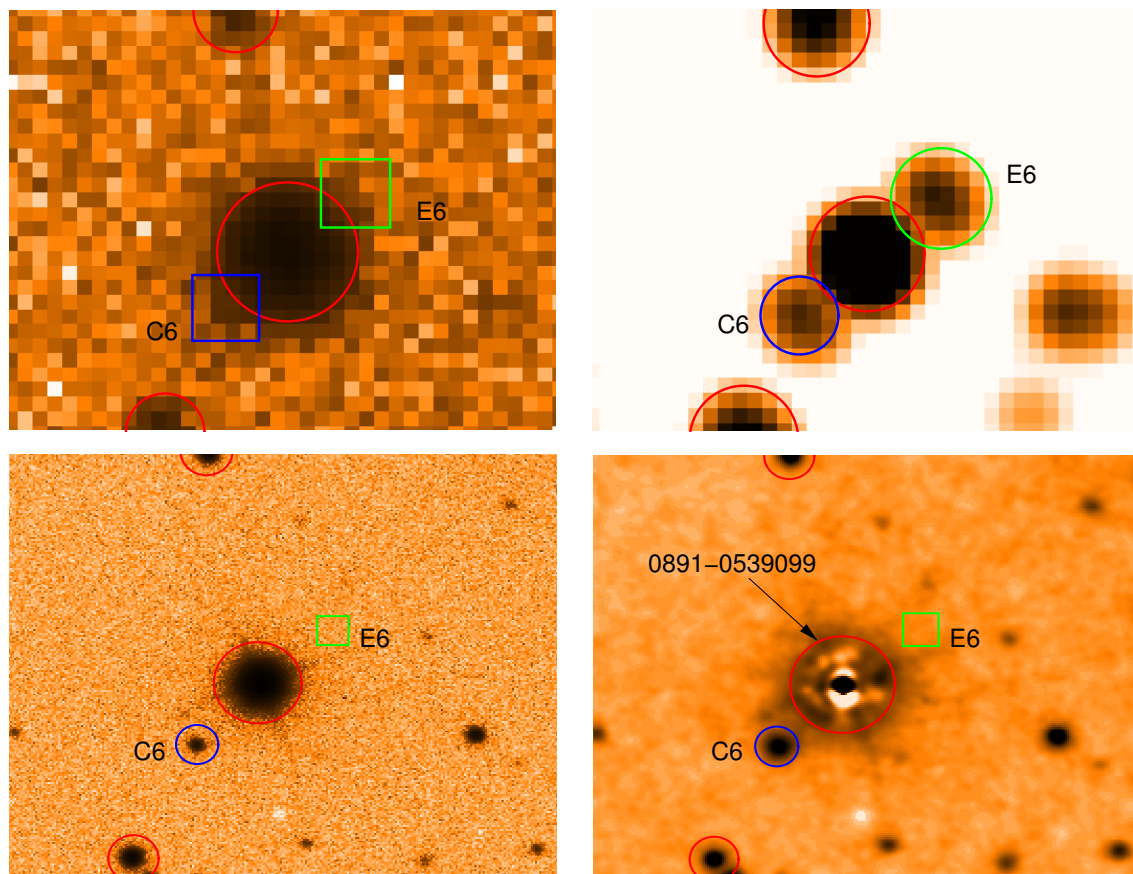
Figura 2: E6, la més brillant de les noves deteccions sense parella trobades en la imatge de referència (WIYN), gràcies a la deconvolució AWMLE. Superior esquerra: Imatge original QUEST. Superior dreta: Deconvolució AWMLE QUEST 750 iteracions. Inferior esquerra: Imatge WIYN del mateix camp. Inferior dreta: Deconvolució AWMLE WIYN 150 iteracions. L'objecte central en vermell correspon a l'estrella $V = 14.7$ USNO-B1.0 0891-0539099. El cercle verd correspon a la nova detecció desaparellada en la imatge QUEST deconvolucionada: els quadrats verds en la resta de panells indiquen la no-detecció en la posició hipotètica de E6 en cada imatge. En blau, una estrella de comaparació C6 amb una separació angular respecte USNO-B1.0 0891-0539099 molt semblant a la d'E6. Noteu que en la imatge QUEST original tant E6 com C6 es poden intuir marginalment sota les ales de l'objecte brillant central. Les magnituds estimades per E6 i C6 són $V \sim 19.9$ i $V \sim 20.4$, respectivament. Val a dir que, malgrat la molt més feble magnitud límit en la imatge WIYN ($V_{\text{lim}} \sim 23.6$), E6 no és detecta allí. Apuntem la possible associació d'aquest fenomen transitori de més de 3 magnituds com una estrella binària de rajos X de l'Halo Galàctic.

La convergència assimptòtica del mètode AWMLE ha propiciat una eficiència excepcional en la detecció de nous objectes. Concretament, s'ha vist que el mètode de deconvolució no introdueix pràcticament cap detecció falsa i que s'arriba a aquesta solució independentment del nombre d'iteracions i el dintell de detecció emprat. Aquest resultat confirma allò apuntat en la presentació del mètode i que la teoria de funcions *wavelet* indicava.

Resolució límit

Aquest estudi pretén quantificar la resolució ($\Delta\phi_{\mathrm{lim}}$) que l'algorisme AWMLE ha estat capaç d'injectar (o recuperar) en relació a la imatge original. Altre cop la metodologia introduïda en l'apartat anterior detalla com hem procedit en aquest estudi.

S'han calculat idèntics valors de $\Delta\phi_{\mathrm{lim}} \sim 1$ pixel per les dades QUEST i NESS-T, o equivalentment a $\Delta\phi_{\mathrm{lim}}^{\mathrm{QUEST}} \sim 1''0$ i $\Delta\phi_{\mathrm{lim}}^{\mathrm{NESS-T}} \sim 3''9$, respectivament. Aquests valors es deriven de la separació angular mínima entre dos objectes resolts en ambdues imatge, l'original i la deconvolucionada. La Fig. 3 ens mostra la distribució
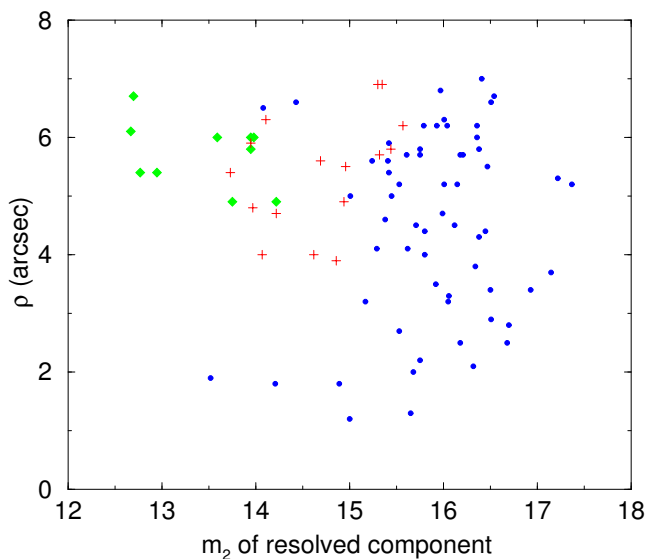
Figura 3: Separació angular de les components resoltes al camps QUEST graficada en funció de la magnitud WIYN. El punts verds indiquen que l'objecte és present a les tres imatges, els vermells els que són a la imatge WYIN de referència i la QUEST deconvolucionada, però no a la QUEST original i els blaus els que només són a la WIYN.

d'aquestes separacions mínimes en funció de la magnitud de l'objecte més feble (o

secundari). Com s'observa, la deconvolució AWMLE (punts vermells) permet resol-
dre objectes més propers i amb una magnitud més feble que no pas la imatge original
(punts verds). S'ha comprobat que aquest guany depén fortament del mostreig de
la imatge original i molt lleument de altres factors com ara els errors sistemàtics
deguts al mode d'adquisició *drift scanning* or el coneixement limitat en el modelatge
de la PSF.
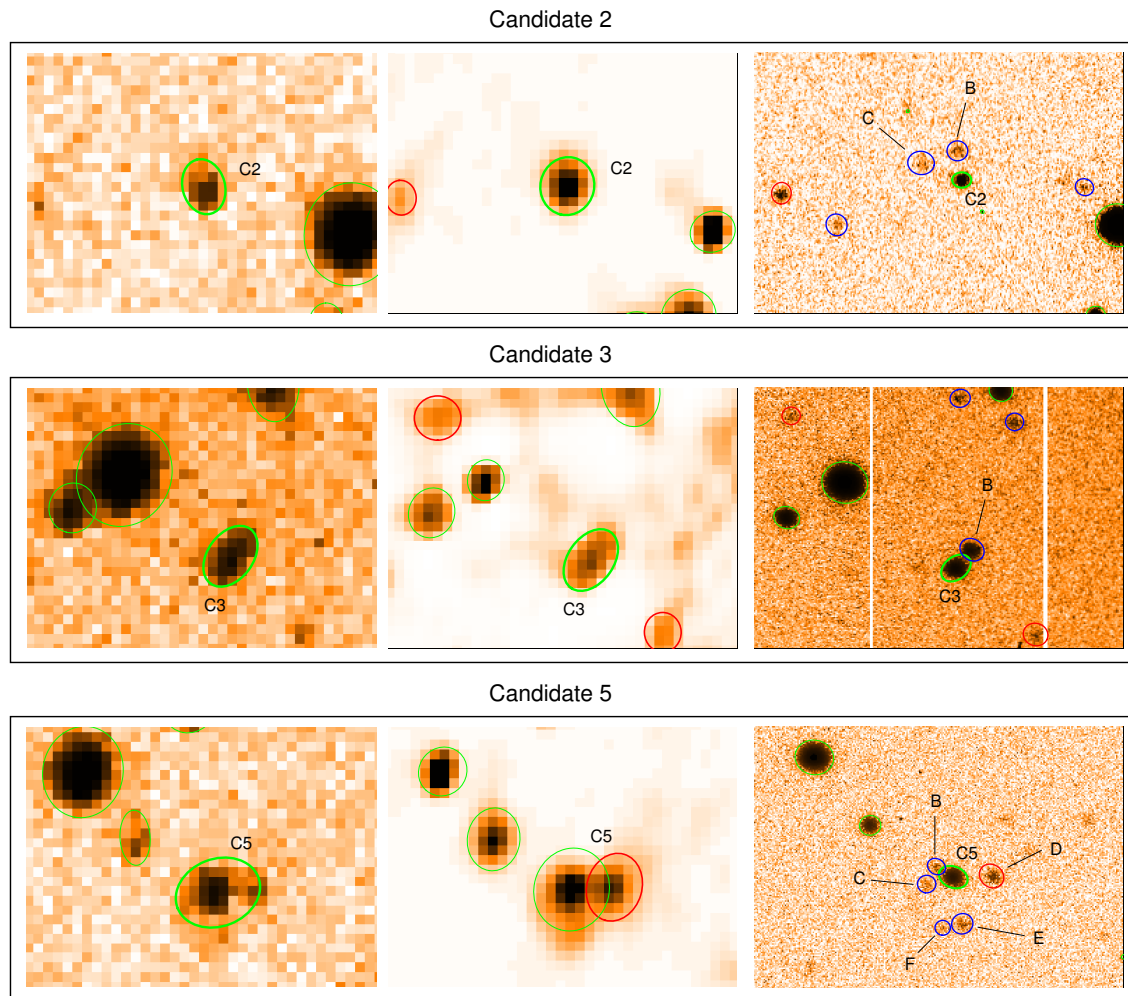
Figura 4: Tres candidats a quasars amb diferents estats de resolució. Per a cada panell,
esquerra: imatge QUEST original, centre: QUEST deconvolucionada, dreta: WIYN de
referència. C2 representa un exemple de candidat no resolt en cap de les tres imatges.
C3 és un cas d'objecte críticament no resolt en la imatge QUEST deconvolucionada. C5
ha estat resolt en la QUEST deconvolucionada però no en la QUEST original.

Com en el cas de l'estudi de magnitud límit, hem considerat un cas particular
d'objectes en les imatges QUEST i NESS-T que poguessin beneficiar-se de l'anterior

guany en resolució. En el cas del QUEST, ho hem aplicat a uns col.lecció de 44 candidats a quasars detectats pel criteri de variabilitat fotomètrica. La deconvolució ens ha permés resoldre per primer cop alguns d'aquests candidats, tot confirmant-los amb la imatge d'alta resolució i amb més magnitud límit WIYN. La Fig. 4 ilustra tres casos típics de candidats deconvolucionats: C2 no resolt, C3 críticament resolt (l'elongació augmenta) i C5 resolt. Aquest darrer podria ser susceptible de ser observat amb un telescopi major i amb espectroscòpia, per tal de confirmar o no si es tracta d'un quasar lensat.

Precisió astromètrica

Diversos autors han mostrat resultats apuntant que la deconvolució d'imatges podria empitjorar l'error astromètric o introduir un biaix posicional cap al centre del pixel (Girard 1995). Hem utilizat les dades FASTT per reproduir aquest experiments amb l'aplicació de l'algorisme MLE (el mateix emprat en l'anterior estudi).

Les dispersions dels residus a la imatge original i deconvolucionada han estat:

- $\sigma_x^{\mathrm{orig}}, \sigma_y^{\mathrm{orig}}$=(0.057,0.041) pixels per les imatges originals,

- $\sigma_x^{\mathrm{deconv}}, \sigma_y^{\mathrm{deconv}}$=(0.059,0.046) pixels per les imatges deconvolucionades.

El lleuger increment per la segona no es pot considerar significatiu, sobretot perquè el biaix assimètric que existia en el núvol original ha estat efectivament eliminat per la deconvolució. A més a més, no s'ha observat biax posicional cap al centre del pixel.

Com a punt decisiu d'aquest resultat destaquem que hem utilitzat una nova eina de centrat d'objectes basada en el mètode de Levenberg-Marquardt. Aquesta ha demostrat ser menys sensible al submostreig que les tècniques convencionals. Com a exemple d'aquesta robustesa, aquest ha pogut ajustar correctament perfils estelars de FWHM fins a 0.8 pixels mentre que la resta d'algorisme divergien a FWHM$\sim$ 1.5 pixels.

3. Noves tècniques observacionals i d'analisi de dades per l'astrometria d'alta resolució

3.1 Nou mètode d'observació *fast drift scanning*

Tant pel que fa a les observacions de LO com d'interferometria speckle, hem coincidit a assenyalar que un ràpid mostreig temporal és essencial per a una correcta representació del fenomen. En ambdós casos aquest ha de ser de l'ordre d'uns pocs mil.lisegons.

Per tal de complaure aquestes necessitats, s'ha ideat, implementat i avaluat una nova tècnica d'observació CCD anomenada *fast drift scanning*. En termes generals, aquesta consisteix en reduir la quantitat de pixels que han de ser transferits en cada mostra i accelerar el ritme de lectura tant com el mòdul digitalizador de la càmera CCD permeti. Com a resultat, el ritme de mostreig augmenta, que és el que preteniem.

Aquest nou mètode d'adquisició no implica cap modificació òptica ni mecànica adicional en el telescopi. Per tant, és molt indicada per a observatoris professionals de baix pressupost i aficionats de perfil alt que vulguin iniciar programes d'observació en LO i interferometria speckle.

3.2 Observacions d'ocultacions lunars

En el cas particular de les LO, el *fast drift scanning* ens ha permés mostrejar cada 2 ms, que és l'òptim per un telescopi del rang 1–2 m.

En paral.lel al desenvolupament d'aquesta nova tècnica, es va endegar un nou programa d'ocultacions a llarg termini (4 anys). Aquest va ser dut a terme a l'Observatori de Calar Alto (Almería) en els telescopis OAN 1.5 m i CAHA 2.2 m, tant en la banda visible com en la infraroja (IR), i rep el nom de CALOP. En el primer cas, es va utilitzar la tècnica *fast drift scanning* amb una càmera CCD comercial. En el segon cas, s'emprà la càmera IR MAGIC (Herbst et al. 1993) en el mode de lectura *subarray*, que era conegut amb anterioritat. Aquest esforç observacional es perllongà durant 71.5 nits produint 388 ocultacions enregistrades.

Els resultats incdouen la detecció d'un sistema triple (IRC-30319) i 14 binaries noves i 1 de coneguda en l'IR proper, i una binària nova en el visible. Les seves separacions projectades estan compreses entre 0″.09 i 0″.002, amb relacions de brillantor fins a 1:35 en la banda K. També s'ha mesurat els següents diàmetres angulars:

- 30 Psc ($\phi_{\rm UD} = 6.78 \pm 0.07$ mas) en el visible,

- V349 Gem ($\phi_{\rm UD} = 5.10 \pm 0.08$ mas) en l'IR,

- RZ Ari ($\phi_{\rm UD} = 10.6 \pm 0.2$ mas) en l'IR. La Fig. 5 il.lustra l'ajust realitzat per obtenir l'anterior diàmetre amb l'algorisme `ALOR` (Richichi 1989).

La Taula 1 inclou un sumari més compet dels resultats obtinguts en el programa CALOP.

Taula 1: Sumari dels resultats obtinguts de les observacions del programa CALOP.

(1) Source	(2) $|V|$ (m/ms)	(3) $V/V_{\rm t}-1$	(4) $\psi(°)$	(5) PA(°)	(6) CA(°)	(7) SNR	(8) Sep. (mas)	(9) Br. Ratio	(10) $\phi_{\rm UD}$ (mas)
SAO 164567	0.6443	3%	−	(74)	(11)	14.3	2.0 ± 0.1	1.7 ± 0.1	
30 Psc	0.2473	−44%	20	122	69	46.1			6.78 ± 0.07
SAO 78119	0.5387	−3%	2	129	41	52.7	13.1 ± 1.1	34.2 ± 2.5	
V349 Gem	0.9462	−2%	8	106	11	65.9			5.10 ± 0.08
SAO 78258	0.6307	2%	1	45	−50	9.4	47.3 ± 1.5	8.6 ± 0.7	
AG+24 788	0.6910	3%	6	75	−13	16.9	28.8 ± 0.7	4.9 ± 0.2	
SAO 79251	0.7215	−1%	−1	85	−15	20.2	26.9 ± 1.1	17.6 ± 1.5	
SAO 80764	0.6568	−3%	−2	73	−45	26.3	42.5 ± 0.3	14.9 ± 0.3	
SAO 185661	0.3287	−5%	−2	155	60	23.7	37.9 ± 1.1	19.3 ± 0.7	
IRC -30319 A-B	0.5647	3%	2	136	44	52.6	15.0 ± 0.1	8.74 ± 0.04	
IRC -30319 B-C						16.1	21.8 ± 0.1	2.98 ± 0.01	
17454891-2809333	0.7720	4%	3	98	6	25.0	39.3 ± 0.7	17.3 ± 0.9	
SAO 165154	0.5870	24%	14	117	62	6.2	43.0 ± 1.9	4.7 ± 0.4	
RZ Ari	0.6520	−2%	10	73	11	41.3			10.6 ± 0.2
SAO 76214 A-C	0.3500	−5%	−2	131	56	7.8	13.0 ± 0.7	2.4 ± 0.1	
IRAS 04395+2521	0.6301	11%	8	135	49	21.4	6.5 ± 0.2	2.9 ± 0.1	
04440885+2540333	0.8013	−0%	−0	77	−10	3.9	15.6 ± 0.8	1.4 ± 0.1	
05415664+2707323	0.9208	−2%	−3	108	12	17.4	24.8 ± 0.3	7.8 ± 0.3	
HD 283610	0.5244	−5%	−3	121	38	9.1	19.4 ± 0.7	6.1 ± 0.3	
04264187+2500314	(0.8900)	−	−	(86)	(0)	3.8	89.5 ± 1.0	2.5 ± 0.1	
SAO 77000	0.4995	2%	−2	109	37	16.0	12.6 ± 0.3	1.49 ± 0.03	

També es va mesurar l'eficiencia de CALOP en termes de magnitud límit i resolució límit. Ambdós paràmetres són claus per a conéixer les limitacions que el programa té amb la instrumentació actualment utilitzada. Com a resultat s'ha obtingut unes magnituds límit $K_{lim} \sim 8.0$ i ≈ 9.0, pels telescopis OAN 1.5 m i CAHA

2.2 m. Pel que fa a les resolucions límit, es van estimar ϕ_{lim} entre 1-3 mas, respectivament.
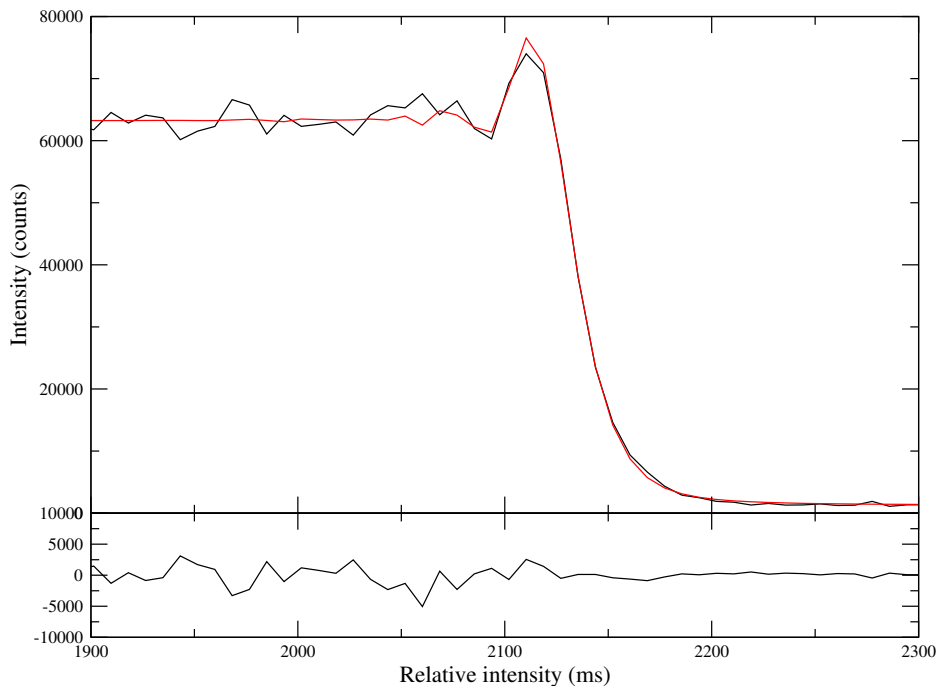
Figura 5:   Superior: Corba de llum de RZ Ari (negre) i ajust amb algorisme ALOR (vermell) corresponent a un diametre de $\phi_{\text{UD}} = 10.6 \pm 0.2$ mas. Inferior: Residus.

La probabilitat de detecció de binaries ha estat calculada a l'entorn del $\approx 4\%$. Aquest valor és significavament menor que l'obtingut en altres programes d'observació similars (Richichi et al. 1996). Atribuïm aquest defecte de binaries al fet que hem utilitzat un catàleg (2MASS) amb una densitat d'estrelles molt major als anteriors estudis per a elaborar les prediccions.

Com una altra contribució desenvolupada en aquest apartat de la tesi, i davant del gran nombre d'ocultacions mesurades, ens vam veure en la necessitat de desenvolupar una nova eina de reducció automàtica basada en la transformada *wavelet* de la corba de llum de l'ocultació. En aquest cas unidimensional, aquesta base de funcions ens permet localitzar molt eficientment el canvi d'intensitat degut a l'ocultació, destriant-lo de manera molt robusta de les oscil.lacions degudes al soroll de la càmera o al centelleig atmosfèric. Una bona mostra de la robustesa d'aquesta nova eina queda il.lustrada en la Fig. 6.

Finalment, dins del programa CALOP s'inclou una nova sèrie d'ocultacions per pasos de la Lluna per Centre Galàctic. Aquesta s'inicià amb l'observació el dia 28
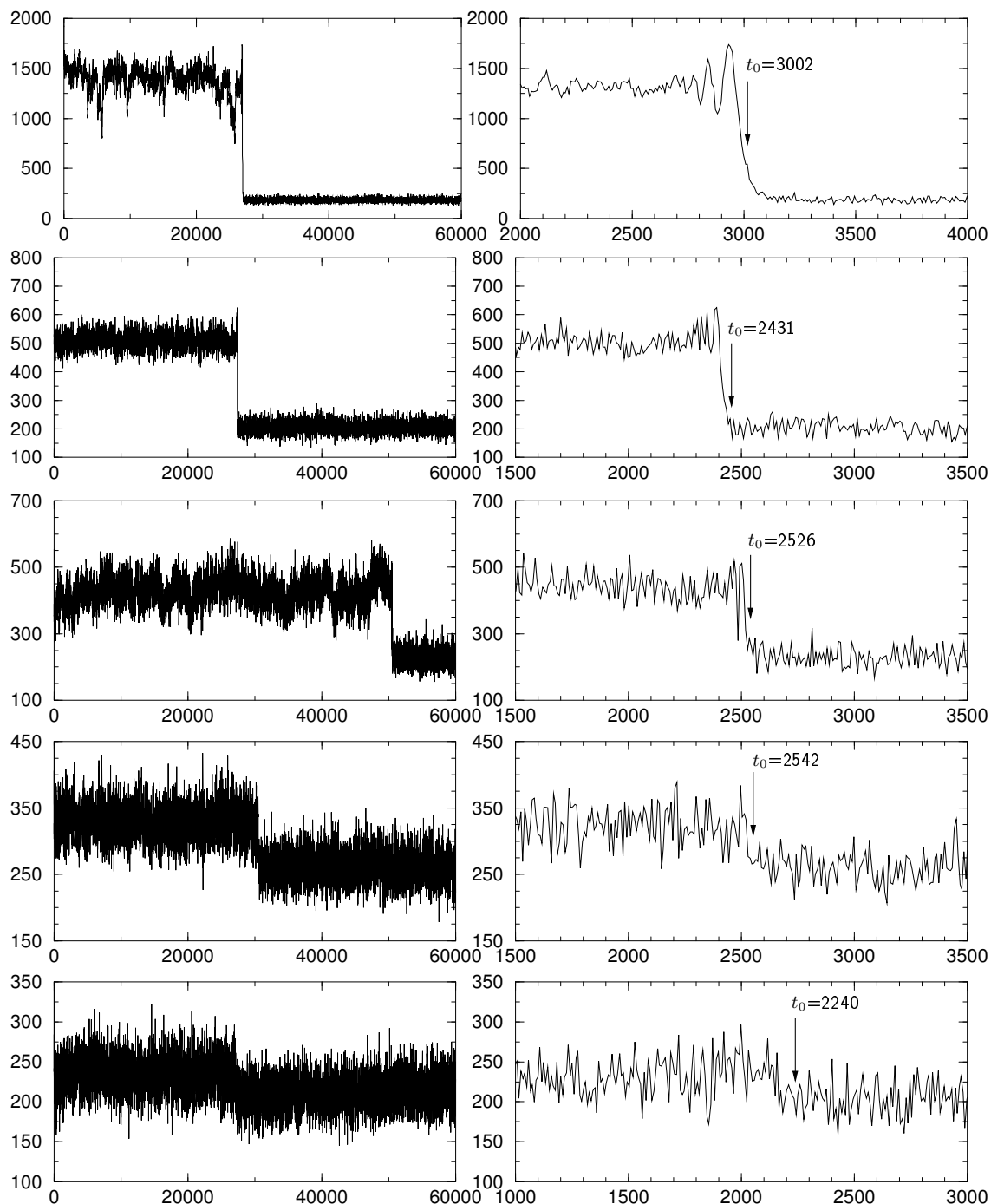
Figura 6: Aplicació d'un criteri basat en wavelets per trobar l'instant d'ocultació t_0 per a 5 corbes de llum amb diferents valors de SNR (de dalt a baix: 20, 10, 5, 2 i 1). Panells de l'esquerra representen la totalitat de les corbes de llum (d diversos segons de durada). Els panells drets representen la porció de la corba de llum a l'entorn del t_0 trobat automàticament. Noteu que fins i tot en el cas de SNR=1, t_0 és localitzat correctament.

de Juliol de 2004. Vam obtenir 54 ocultacions en 3.4h (1.5h de temps efectiu), gran part de les quals són fonts infraroges sense contrapartida òptica, i de les quals s'ha derivat multiplicitat per primer cop (veure IRC -30319 en la Taula 1). Aquest tipus d'esdeveniments dónen l'oportunitat d'extraure informació del millisegon d'arc en regions poc estudiades.

3.3 Observacions d'interferometria speckle

En el cas particular de la interferometia speckle, s'ha adaptar la tècnica d'observació CCD *drift scanning* per assolir els ritmes de mostreigs requerits (poques desenes de mil.lisegonds per fotograma speckle).

De manera similar al que es va fer amb les ocultacions lunars, es va dur a terme un període d'observació a l'Observatori de Calar Alto per a validar aquesta nova tècnica. El telescopi escollir va ser l'OAN 1.5 m amb la mateixa càmera CCD emprada per les campanyes d'ocultacions. Es van observar 4 binaries d'òrbita coneguda. En la Fig. 7 il.lustrem una seqüencia de fotogrames speckle obtinguts en aquelles condicions pel sistema doble ADS 755.
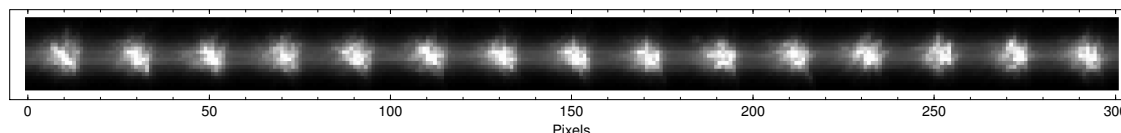
Figura 7: Tira de fotogrames speckle enregistrats per mitjà de la tècnica *drift scanning* per la estrella binària ADS755. Els fotogrames són de 20x20 pixels i el temps d'exposició de 39ms.

Es va seguir el mètode d'anàlisi d'autocorrelació i subplànols bispectrals de ordre inferior descrit a Horch et al. (1997). Com a novetat en aquest mètode d'analisi que s'introdueix en aquesta tesi s'ha proposat utilitzar el mateix sistema doble observat per a obtenir una calibració de la funció de responsa de l'instrument. Habitualment, aquesta s'aconsegueix observant una font puntual i que es coneix que no té companyes. Això implica una pèrdua en l'eficiencia observacional, important sobretot en telescopis grans. La nostra propostra d'autocalibració allibera aquest lligam, i no ha mostrat biaixos per distàncies raonables ($< 60°$).

El resultats de separació angular, angle de posició i diferència de magnitud (ρ, θ, Δm) per les 4 fonts observades estàn d'acord amb els valors publicats i les òrbites

calculades. La Fig. 8 ens ho il.lustra. Estimacions d'error d'aquests parametres són $\sigma_\rho = 0\rlap{.}''017$, $\sigma_\theta = 1\rlap{.}°5$, $\sigma_{\Delta m} = 0.34$ mag, els quals estan dins dels standards d'altres autors.
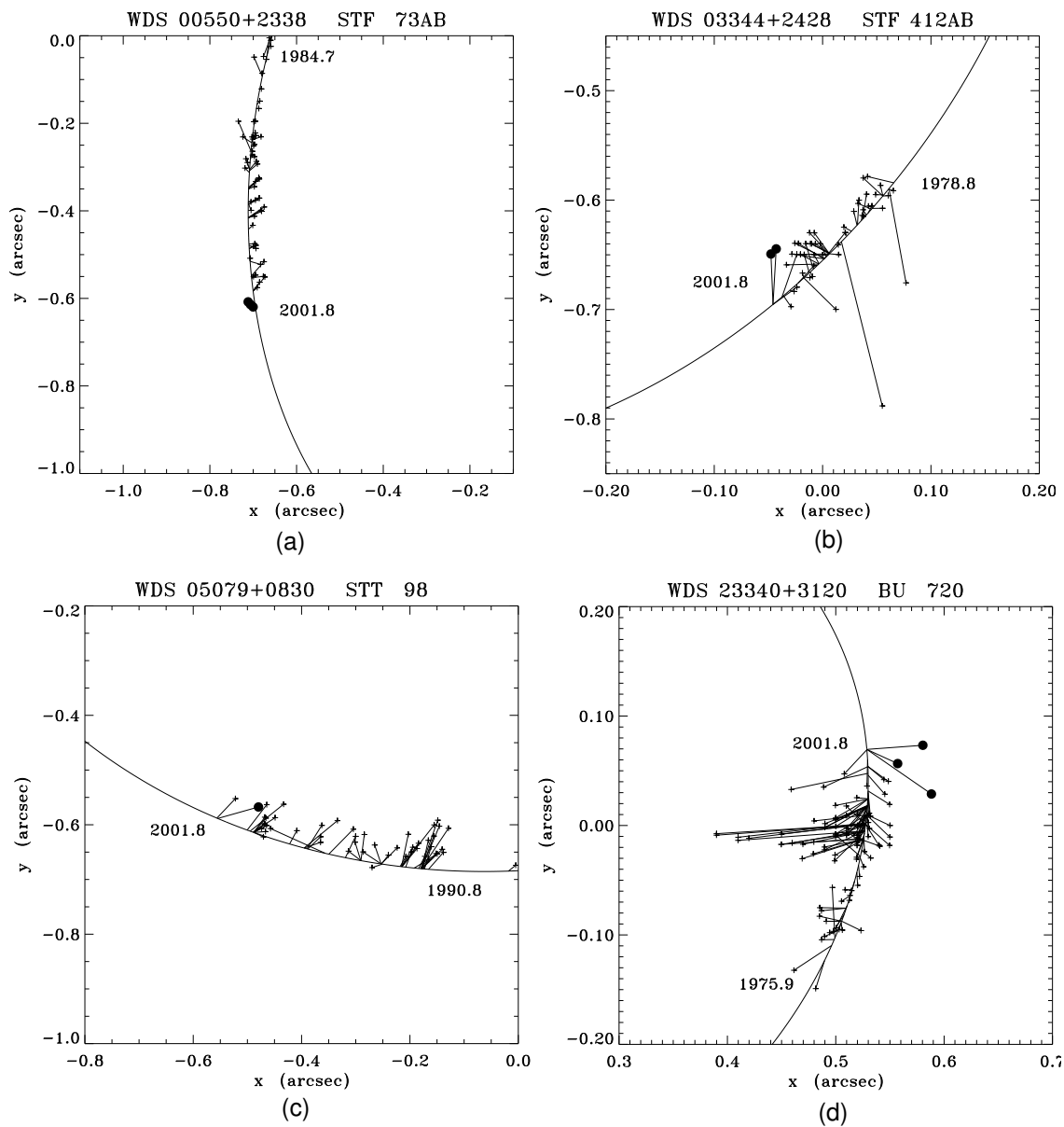
Figura 8: Comapació entre les mesures de separació i angle de posició obtingudes (cercles negres) i les mesurades per altres autors (creus petites) i les òrbites establertes per cada sistema binari.

4. Sumari de conclusions generals

A continuació resumim les conclusions a les quals hem arribat en aquesta tesi:

Part I:

1. Hem aplicat el de deconvolució AWMLE a dos jocs de dades de tipus *survey*: QUEST i NESS-T, les quals havien estat adquirides en mode *drift scanning* i *stare*, respectivament.

   El mètode de deconvolució Richardson-Lucy ha estat aplicat al joc de dades FASTT, que havia estat adquirit en mode *drift scanning*.

2. Una nova metodologia per a aplicar la deconvolució a imatges tipus *survey* has estat proposada. El caràcter general de la mateixa fa possible que els resultats que s'en deriven siguin homogenis i comparables entre diferents jocs de dades. Anticipem que aquesta metodologia pot ser d'interés per a aquells projectes de tipus *survey* que considering implementar la deconvolució en el seu procés automàtic de reducció.

3. El rendiment del l'algorisme AWMLE en termes de guany en magnitud límit ha estat avaluat. S'han trobat valors de $\Delta R_{\lim} \sim 0.64$ i $\Delta R_{\lim} \sim 0.46$ per les dades QUEST i NESS-T, respectivament. Aquest guany de magnitud s'ha aplicat a la detecció d'objectes d'interés astronòmic, com ara les lents gravitatòries (QUEST), NEOs (NESS-T) i altres.

4. El rendiment del l'algorisme AWMLE en termes de guany en resolució límit ha produït idèntics valors de $\Delta \phi_{\lim} \sim 1$ pixel per les dades QUEST i NESS-T, o equivalentment a $\Delta \phi_{\lim}^{\mathrm{QUEST}} \sim 1''0$ i $\Delta \phi_{\lim}^{\mathrm{NESS-T}} \sim 3''9$, respectivament. S'ha aplicat aquest guany a un cas pràctic de resolució de candidats a quasars lensats.

5. S'ha avaluat la incidència de la deconvolució MLE sobre la precisió astromètrica de la imatge ha estat avaluada. El biaix astrometric present en les imatges FASTT degut a un defecte de transferència de càrea en el chip CCD ha estat eliminat per la deconvolució MLE. L'algorisme MLE no ha modificat significativament la precisió astromètrica de centrat repsecte la de les dades original FASTT. S'ha comprobat que l'algorisme MLE no introdueix cap biaix posicional cap al centre del pixel.

Part II:

Pel que fa a les ocultacions lunars:

1. Una nova tècnica observacional basada en CCD *drift scanning* ha estat proposada, implementada i avaluada per l'observació de LO. S'ha mesurat binaries de separació fins a 2.0 ± 0.1 mas i diàmeters angular en el rang dels $\phi \sim 7$ mas.

2. Un nou programa de LO (CALOP) i 4 anys de durada s'ha dut a terme a l'Observatori de Calar Alto (Almería) ha permés fer una aportació notable en el camp de la detecció d'estrelles binàries (15), triples (1) i la mesura d'alguns (3) diàmetres estelars.

3. Una nova eina de reducció i anàlisi de corbes de llum de LO basada en wavelets ha estat disenyada i implementada. Permet la caracterització completa de la corba de llum, per a la seva posterior reducció automàtica.

Pel que fa a la interferometria speckle:

1. Una nova tècnica observacional basada en CCD *drift scanning* ha estat proposada i implementada per a l'observació d'interferometria speckle. S'ha validat amb la mesura de 4 binaries d'òrbita coneguda.

2. El resultats de separació angular, angle de posició i diferència de magnitud i els seus errors estàn d'acord amb els valors publicats i les òrbites publicades i els standards d'altres autors.

3. La tècnica CCD *drift scanning* és extensible a pràcticament tots els CCDs full-frame en el mercat actual, tant professional com amateur. Per tant, permet que qualsevol observatori pugui dur a terme observacions speckle precises.

4. Una nou mètode de calibració del espectre de potències ha estat introduït per les dades speckle. Aquest permet estavial temps d'observació efectiu, cosa important sobretot en telescopis grans.

Bibliografia

Andersen T., Christensen P.H., Aug. 2000, In: Proc. SPIE Vol. 4004, Telescope Structures, Enclosures, Controls, Assembly/Integration/Validation, and Commissioning, Thomas A. Sebring; Torben Andersen; Eds., 373–381

Balega I., Balega Y.Y., Maksimov A.F., et al., Aug. 2004, A&A, 422, 627

Benitez E., Dultzin-Hacyan D., Heidt J., et al., Jun. 1996, ApJ Letter, 464, L47+

Bontekoe T.R., Koper E., Kester D.J.M., Apr. 1994, A&A, 284, 1037

Chen W.P., Simon M., Feb. 1997, AJ, 113, 752

Cutri R.M., Skrutskie M.F., van Dyk S., et al., Jun. 2003, VizieR Online Data Catalog, 2246, 0

Docobo J.A., Andrade M., Ling J.F., et al., Feb. 2004, AJ, 127, 1181

Evans D.S., 1983, Lowell Observatory Bulletin, 167, 73

Faure C., Alloin D., Gras S., et al., Jul. 2003, A&A, 405, 415

Girard T.M., Dec. 1995, International Journal of Imaging Systems and Technology, 6, 395

Haarsma D.B., Winn J.N., Falco E.E., et al., Nov. 2005, AJ, 130, 1977

Hartkopf W.I., Mason B.D., McAlister H.A., et al., Jun. 2000, AJ, 119, 3084

Herbst T.M., Beckwith S.V., Birk C., et al., Oct. 1993, In: Proc. SPIE Vol. 1946, Infrared Detectors and Instrumentation, Albert M. Fowler; Ed., 605–609

Hiltner P.R., Kroll P., Nestler R., Franke K.H., 2003, In: ASP Conf. Ser. 295: Astronomical Data Analysis Software and Systems XII, 407–+

Horch E.P., Ninkov Z., Slawson R.W., Nov. 1997, AJ, 114, 2117

Horch E.P., Ninkov Z., Meyer R.D., van Altena W.F., May 2001, Bulletin of the American Astronomical Society, 33, 790

Horch E.P., Meyer R.D., van Altena W.F., Mar. 2004, AJ, 127, 1727

Jee M.J., White R.L., Benítez N., et al., Jan. 2005, ApJ, 618, 46

Karovska M., Schlegel E., Hack W., Raymond J.C., Wood B.E., Apr. 2005, ApJ Letter, 623, L137

Krause O., Lemke D., Tóth L.V., et al., Feb. 2003, A&A, 398, 1007

Leinert C., Haas M., Mundt R., Richichi A., Zinnecker H., Oct. 1991, A&A, 250, 407

Lucy L.B., Jun. 1974, AJ, 79, 745

Marchis F., Prangé R., Christou J., Dec. 2000, Icarus, 148, 384

Mason B.D., Hartkopf W.I., Wycoff G.L., et al., Dec. 2004, AJ, 128, 3012

Meinel A., Meinel M., 1980, In: Optical and Infrared Telescopes for the 1990's, 1027–+

Mondal S., Chandrasekhar T., Mar. 2004, MNRAS, 348, 1332

Mondal S., Chandrasekhar T., Aug. 2005, AJ, 130, 842

Núñez J., Llacer J., Oct. 1993, PASP, 105, 1192

Neugebauer G., Leighton R.B., 1969, Two-micron sky survey. A preliminary catalogue, NASA SP, Washington: NASA, 1969

Noordermeer E., van der Hulst J.M., Sancisi R., Swaters R.A., van Albada T.S., Oct. 2005, A&A, 442, 137

Otazu X., 2001, Algunes aplicacions de les Wavelets al procés de dades en astronomia i teledetecció, Ph.D. thesis

Prades A., Núñez J., 1997, In: ASSL Vol. 223: Visual Double Stars : Formation, Dynamics and Evolutionary Tracks, 15–+

Prades A., Fors O., Núñez J., Ollé A., 1997, In: Reference systems and frames in the space era : present and future astrometric programmes. Journees 1997 Systemes de Reference Spatio-Temporels., 199–201

Ragland S., Chandrasekhar T., Ashok N.M., Mar. 1997, A&A, 319, 260

Richichi A., 1989, Occultazioni Lunari di Sorgenti Stellari nel Vicino Infrarosso, Ph.D. thesis, Università degli Studi di Firenze

Richichi A., Salinari P., Lisi F., Mar. 1988, ApJ, 326, 791

Richichi A., Baffa C., Calamai G., Lisi F., Dec. 1996, AJ, 112, 2786

Richichi A., Fabbroni L., Ragland S., Scholz M., Apr. 1999, A&A, 344, 511

Richichi A., Ragland S., Calamai G., Richter S., Stecklum B., Sep. 2000, A&A, 361, 594

Saha S.K., Chinnappan V., Yeswanth L., Anbazhagan P., 2002, Bulletin of the Astronomical Society of India, 30, 677

Scardia M., Prieur J.L., Sala M., et al., Mar. 2005, MNRAS, 357, 1255

Schanne S., et al., Oct. 2004, In: ESA SP-552: 5th INTEGRAL Workshop on the INTEGRAL Universe, 73–+

Schmidt-Kaler T., Rucks P., Mar. 1997, In: Proc. SPIE Vol. 2871, Optical Telescopes of Today and Tomorrow, Arne L. Ardeberg; Ed., 635–640

Sebring T.A., Moretto G., Bash F.N., Ray F.B., Ramsey L.W., 2000, In: Proceedings of the Backaskog workshop on extremely large telescopes, 53–+

Simon M., Ghez A.M., Leinert C., et al., Apr. 1995, ApJ, 443, 625

Simon M., Longmore A.J., Shure M.A., Smillie A., Jan. 1996, ApJ Letter, 456, L41+

Simon M., Beck T.L., Greene T.P., et al., Mar. 1999, AJ, 117, 1594

Stapelfeldt K.R., Ménard F., Watson A.M., et al., May 2003, ApJ, 589, 410

Zadnik J.A., 1993, Ph.D. Thesis

Chapter 1

Introduction and background

This thesis is divided into two well separated parts. Part I investigates the benefits of applying image deconvolution to wide field CCD surveys. Part II presents innovative observational techniques and analysis tools in the field of high resolution astrometry, in particular in lunar occultations and speckle imaging frameworks. Accordingly, both parts are introduced in the next two subsections.

1.1   Deconvolution in astronomy

In this section we will just introduce a phenomenological description of deconvolution, and postpone to Chapt. 2 a more detailed and mathematical definition of this concept.

The concept of image deconvolution is related to the understanding of image formation process. In the particular context of astronomy, telescope images are distorted by a number of factors which limits their quality. These can be modeled by two separated and crucial concepts in the overall imaging process: point-spread function (PSF) and noise.

On one hand, PSF can be understood as the blurred image of a point-like source. Apart from the unavoidable diffraction pattern always present in a finite telescope, the PSF spot has its origin in a number of contributory factors of different nature. This topic has been recursively addressed in the literature, sometimes with brilliant

studies as the ones from King (1971) for photographic plates and Racine (1996) for CCDs. In brief, they conclude that the main contributors to PSF are:

1. in the case of ground-based astronomy, atmospheric turbulence spreads the incoming light across the detector. In accordance to Kolmogorov theory of seeing, this stochastic process broads the PSF core in a shape which closely resembles a Gaussian profile. As a result, the image resolution is degraded well above the diffraction limit and the signal-to-noise ratio is decreased. Both effects translate into a lower efficiency of the observations.

2. telescope optics are not perfect and show aberrations which deviates the image from its original point shape. The variety of possible anomalies in optical system is large. They generally contribute in the outer wings of the PSF. While in ground-based imaging they take the form of an aureole or halo approximated by a decreasing exponential function, space-based wings can adopt more complex and extended structures. A well-known example of the latter was the discovery of the spherical aberration in the Hubble Space Telescope (HST) in 1990. This triggered a renewed interest in deconvolution by the astronomical community and a considerable effort was dedicated to design algorithms for overcoming this problem. See Hanisch & White (1994); White & Allen (1991) for two dedicated proceedings specifically held to this topic.

3. effects as light diffusion and reflection within the detector assembly (very common in fast systems as Schmidt cameras), or scattering by atmospheric aerosols, scratches or dust on telescope optics also contribute to the outer structure of the PSF.

4. the fact that the detector is composed by finite pixels introduces an additional distorsion in the PSF when this is sampled in the detection process.

On the other hand, astronomical images are not noise free. First, the photon detection process naturally incorporates an uncertainty in the measured intensity value. As will be detailed in Sect. 2.1.3, this noise follows a Poisson distribution and is always present in data, regardless the type of detector employed. Second, in the case of CCDs, the amplifier converts the collected charge into digital units introducing a Gaussian distributed noise.

All in all, image deconvolution methods have been conceived with the aim of

mitigating all these observational limitations and improving the quality of the image. This task involves finding a solution of an inverse equation. The presence of noise complicates the uniqueness and stability of this solution, and turns image deconvolution to be an inverse problem of ill-posed nature. In this way, several algorithms have been proposed in the literature. They mainly differ in the way they deal with the noise for seeking an stable solution. We will focus our discussion in the family of algorithms based in the Maximum Likelihood Estimator (MLE) which can handle data in presence of Poissonian noise (Lucy 1974; Richardson 1972) and Poissonian+Gaussian noise (Núñez & Llacer 1993; Snyder et al. 1993). In particular, we will carry all the study of Part I with an improved variant of this method, called Adaptive Wavelet-based Maximum Likelihood Estimator (AWMLE) (Otazu 2001). AWMLE takes advantage of the multiresolution support concept (Starck & Murtagh 1994) supplied by the wavelet decomposition to adaptively separate signal features from noise fluctuations, and thus to obtain a more reliable solution. A more detailed description of all these concepts will be held in Chapt. 2.

1.1.1 Applications of deconvolution

In general, deconvolution provides the following outcome:

1. better looking image for visual inspection,

2. higher SNR, resulting in improved detection of faint objects which were hidden below the background noise in the original image.

3. higher resolution, which translates into an enhanced deblending capability since the overlap between close objects becomes reduced.

4. if the PSF of the original image showed artifacts in the image, these can be removed.

Note that even the most spectacular and pristine images from the largest telescopes are blurred by PSF. Deconvolution equally offers a general tool for further improving the data, and enables the access to information which otherwise would had remained hidden or banned.

Indeed, the different approaches in the literature have proved to be decisive for extracting scientific content from a broad range of data. In the next paragraphs we overview some applications of deconvolution to astronomical purposes along the last decades.

Image deconvolution was already applied in the early days of space exploration. In particular, inverse filtering technique was considered for Ranger, Surveyor and Mariner planetary missions (Nathan 1966). Parallely, Harris (1966); McGlamery (1967) deconvolved atmospheric blurring in ground-based astronomical images.

Apart from these pioneering efforts, deconvolution has been widely applied to a good number of data sets, each one in its own wavelength, SNR and resolution domain, and belonging to a specific astrophysical context. A few representative examples are included in Table 1.1. They do not aim to be an exhaustive and complete relation. For more in-dept reviews we refer the reader to Molina et al. (2001); Puetter et al. (2005); Starck et al. (2002). The following comments arise from the inspection of the Table 1.1.

The concept of image deconvolution, based on image formation comprehension, is so general that is applicable to images and spectra from all wavelength domains. The particularities of each case are taken into account in the PSF, the noise characterization and, occasionally, in the optimization technique employed, but does not change the common inversion approach.

As can be seen, the variety of used methods is large. In general, two main aspects are distinctive among the different algorithms. First, the numerical approach considered for seeking the solution. Second, the regularization constraints which are considered to confer stability and uniqueness to the solution: positivity, flux preservation and cutoff frequency for the PSF.

Some deconvolution methods have become essential part of particular standard reduction packages. The case of CLEAN in radio aperture synthesis interferometric maps is a paradigmatic example. EMC2 is also specifically designed for the particular case of X-ray detectors, which show low count statistics data. The rest of algorithms are less data specific, and can be applied to data from mid-infrared to optical bands.

As regard as the astrophysical context of applications, this is seen to be quite diverse, ranging from Solar System objects (Io, Titan) to Seyfert or early-type galaxies. Most of listed applications aim to increase the resolution of original image. An inferior number benefit from the improvement in SNR for detecting new faint objects or structures. Note that a majority of applications are conducted in top-of-the-line facilities, which by themselves already provide high resolution and SNR data. Remarkable examples of this are HST and adaptive optics systems as VLT/NACO. The former has continued to be a unique environment for getting unprecedented imaging resolution, even after the COSTAR fixing. This interest has been boosted with the incorporation of ACS and NICMOS cameras. The latter, despite original AO images already overpass seeing barrier, deconvolution is equally used to gain additional resolution.

The versatility of deconvolution is demonstrated by the fact that it can also be applied to other fields such as speckle imaging and photographic plates, which are not strictly digital imaging. However, the benefits that can be achieved are equally rewarding.

Nearly all the entries in Table 1.1 share one feature: they are restricted to narrow field of view selected observations obtained in a particular and well controlled PSF+seeing+noise configuration. This, plus the fact that the data usually are inherently of high-quality (high SNR, good detector performance, etc.), describes an ideal benchmark for deconvolution. However, few deconvolution experiences with systematic wide field surveys (where data are far more inhomogeneous and PSF and noise cannot be modelled to the same degree of accuracy) have been found in the literature. The exhaustive study of early-type galaxies of (Lauer et al. 1995) might be one of the exceptions, but it is still of limited field of view (FOV). Moreover, its execution was justified because data were affected by pre-COSTAR HST aberration.

This scenario of selected applications is multifold justified:

1. while it is worth to invest additional effort in interactively analyzing a few images which can be well characterized, it is more time consuming and complex to establish a consistent methodology for introducing deconvolution in an unattended reduction pipeline of a survey.

2. the scientific throughput in these selected applications is usually guaranteed in a short-term basis, while in the survey-type imagery is not.

Table 1.1: Overview of applications of image deconvolution.

Spectral band	Detector	Description	Application Algorithm used	Reference
Radio	VLA	First optical-VLA survey for lensed radio lobes	CLEAN	Haarsma et al. (2005)
	Westerbork SRT	Deconvolution of radial profiles of HI surface density survey of spiral and irregular galaxies	RL	Noordermeer et al. (2005)
Submillimeter	SCUBA	High resolution imaging of a very young star forming region ISOSS J 20298+3559	CLEAN	Krause et al. (2003)
Mid-infrared	ESO 3.6 m/ADONIS	Adaptive Optics mapping of Io's volcanism	IDAC	Marchis et al. (2000)
	CFHT/CAMIRAS	High resolution of inner structure of high extincted AGN in NGC 1068	MMEM	Alloin et al. (2000)
	CFHT/CAMIRAS	Sub-arcsecond structure of the young stellar cluster AFGL 4029	MMEM	Zavagno et al. (1999)
	IRAS	Resolution of extended dust shells around carbon stars	PME	Bontekoe et al. (1994)
Infrared	VLT/ISAAC	Detection of binary quasar LBQS 1429-0053	MEM & MCS	Faure et al. (2003)
	ESO/MPI IRAC2b and Keck/NIRC	Lensing galaxy detection in the vicinity of the radio source PKS 1830-211	MCS	Courbin et al. (1998)
Optical	HST/ACS	Weak-lensing analysis of low redshift galaxy clusters	MBD	Jee et al. (2005)
	VLT/NACO	Astrometry of brown dwarf GSC 08047-00232 companion	VR98	Chauvin et al. (2005); Lagrange et al. (2004)
	VLT/NACO	Adaptive optics imaging of Titan	MCS	Gendron et al. (2004)
	HST/WFPC2	Disk and jet structure in HV Tauri young triple system	MEM	Stapelfeldt et al. (2003)
	Photographic plates	Removal of astigmatism/coma distortion and SNR increase of Sonneberg photographic plate archive	PRM	Hiltner et al. (2003)
	Pic Midi PISCO speckle camera	Detection and astrometry of Mira-type binary stars	Custom	Prieur et al. (2002)
	Various 2 m class with IR arrays	Putative detection of underlying nebulosity and a possible optical jet in BL Lac objects in OJ 287	RL	Benitez et al. (1996)
	HST/WFPC	Enhancing resolution of pre-COSTAR survey of early-type galaxies	RL	Lauer et al. (1995)
	Various 1-4 m class	Deconvolution of nuclear and components in Seyfert galaxies stellar	RL	Kotilainen et al. (1993)
X-ray	*Chandra*	Large X-ray Outburst in Mira A	EMC2	Karovska et al. (2005)
	Chandra	Detection of low-mass companion in Orion Nebula Cluster	RL	Grosso et al. (2005)
γ-ray	INTEGRAL	Hypernovae possible detection through spectra	RL	Schanne & et al. (2004)

RL: Richardson-Lucy (Lucy 1974, 1994; Richardson 1972).

MEM: Maximum Entropy Method (Cornwell & Evans 1985; Frieden 1978).

CLEAN: CLEAN (Högbom 1974; Keel 1991).

IDAC: Myopic deconvolution adapted from (Jefferies & Christou 1993).

PME: Pyramid Maximum Entropy method (Izumiura et al. 1994).

MMEM: Multiscale Maximum Entropy Method (Pantin & Starck 1996).

VR98: Based on minimization in the Fourier domain of a regularized least square objective function using the Levenberg-Marquardt method (Veran & Rigaut 1998).

MCS: Magain-Courbin-Sohy (Magain et al. 1998).

PRM: Pixon Restoration Method (Eke 2001; Pina & Puetter 1993; Puetter & Yahil 1999).

MBD: Moment-Based Deconvolution (Bernstein & Jarvis 2002; Refregier 2003).

EMC2: Expectation through Markov Chain Monte Carlo. (Esch et al. 2004; Karovska et al. 2001, 2003).

3. deconvolved images are usually undersampled. Consequently, they require specialized analysis tools for overcoming possible biases which standard reduction packages would suffer.

4. deconvolution is a computationaly slow process and its cost per Mb of original image is demanding. Currently ground-based astronomy is entering in a new era of surveys with panoramic multi-hundred CCDs cameras as QUEST-Palomar at Palomar Oschin (Rabinowitz et al. 2003), Megacam at CFHT (Boulade et al. 2003), Omegacam at ESO (Deul et al. 2002). As a result, the data throughput is increasing above the computational resources needed for deconvolving the whole data set.

5. traditionally, it has been preferable to build larger telescopes and more sensitive detectors than dedicating an small part of the same effort to explore new data analysis as deconvolution for getting additional SNR and resolution from survey images.

1.1.2 Motivations and scope of Part I

The panorama described above is likely to change in near future. A number of factors and alternative strategies can be considered for overcoming the above items and extending the application of deconvolution to wide field surveys:

First, distributed computing is obtaining remarkable achievements in handling very large data sets of the order involved in current surveys. The highly scalable architecture and the easily parallelizable nature of most deconvolution algorithms appear to guarantee reasonable execution times, even in the more demanding situations. However, the situation is not so clear yet because of the near future venue of new CMOS imagers (up to 100 million-pixel chips) in the context of astronomical observations could increase the data rate by several orders of magnitude.

Second, fast PCs and storage devices are becoming cheap these days. In addition, most Linux distributions come with built-in multiprocessor kernels, easily to install and administrate.

Third, adaptive wavelet-based methods as AWMLE do not need stopping criteria as MLE because they asymptotically converge to stable solutions provided data is

well characterized. This removes the dependence on the number of iterations and makes their integration in a reduction pipeline more feasible. In addition, both AWMLE and MLE can be run with an acceleration parameter which speeds up the convergence of the algorithm.

Finally, not every byte recorded by these CCDs is susceptible of bearing meaningful information. In a multitude of astrophysical contexts, the location of the target object is a priori known. If not, sometimes this can be guessed by alternative indirect methods (characteristic photometric variability, mobile objects, follow-up observations, etc.) which might not require the benefits that deconvolution provides. Consequently, deconvolution could focus on a small subset of image patches where science objects stand. This strategy, which is totally general and extrapolable to all surveys, saves a lot of machine time and extends the number of science targets. Note these deep wide field surveys are addressing research areas (macro and microlensing, GRBs coverage, NEOs census, etc.) with unprecedented completeness and depth which cannot be covered only with selective observations at narrow FOV facilities. Therefore, the efficiency gain provided by deconvolution would be very rewarding in terms of scientific throughput.

In view of this, we were motivated to pursue the investigation of Part I of this thesis. This study will attempt to accomplish the following aims in the context of wide field CCD surveys:

1. to define a general analysis methodology, covering both the pre and post-deconvolution stages, which allows to reveal the benefits provided by image deconvolution. This task will be fully described in Chapt. 4.

2. to improve the observational efficiency in terms of SNR or, equivalently, fainter limiting magnitude. Consequently, the number of detectable objects would also be enlarged, allowing new findings which otherwise would had remained hidden within the background noise of the original image.

   Note that a gain in limiting magnitude (Δm_{lim}) can be translated into an enlargement of the effective telescope diameter (D). For example, a gain of $\Delta m_{\mathrm{lim}} \sim 0.6$ mag is equivalent to increase a 30% D or a 80% the collecting area. Considering the relationship between telescope size and cost is estimated to be proportional to $D^{2.7}$ (Andersen & Christensen 2000; Meinel & Meinel 1980; Schmidt-Kaler & Rucks 1997; Sebring et al. 2000), deconvolution is also

a very cost-effective technique, at least in terms of photon gathering power.

3. to increase the limiting resolution. Equivalently, this translates into a smaller physical blur. Preceding studies have yielded promising results. Puetter et al. (2005) reports resolution gains up to 2.5 pixels with simulated well-sampled data. Despite of the non-ideal PSF characterization conditions in wide field surveys, there are evidences to think that a yet rewarding increase of resolution can be achieved.

   Note that, as in the case of limiting magnitude gain, an equivalent increase in resolution can be achieved by other much more expensive ways. Namely, to locate the telescope in a better seeing site, to improve optics in telescope (stronger magnification) or to have a finer focal plane array, which degrades SNR and forces to enlarge telescope diameter.

4. to clarify how deconvolution influence astrometric error. As outlined before, deconvolved images are usually undersampled. It is well-known that might mean a loss in astrometric accuracy. However, several authors (Howell et al. 1996; Mighell 2005) have shown that this can be overcome if adequate centering techniques are considered. In this way, a robust centering technique based in Levenberg-Marquardt Method optimization method will be employed.

Items 2. and 3. are specially pertinent for the two scenarios we will study in Part I. Firstly, for the case of drift scanning surveys where the exposure time is limited by sidereal rate (thus, shortening limiting magnitude) and the image resolution is degraded as a result of PSF smearing intrinsic to this acquisition scheme. Secondly, for wide field surveys with very short focal ratio which are focused in transient objects detection. These telescopes usually have coarse pixel scales and operate in undersampled conditions. As a result, their images are hampered with severe object blending.

1.2 New observational techniques and analysis tools in high resolution astrometry

Part II of this thesis will be devoted to the development of new observational methods and analysis tools in the general context of high resolution astrometry. In

particular, this effort will be focused to Lunar Occultations and Speckle Imaging techniques. A very large number of occultations and one speckle observing run were conducted in order to systematically test new proposed procedures. The former data set by itself already represents a considerable contribution in the field of detection of close binaries.

Although both subparts share some basic characteristics, a separate treatment of these studies was chosen in this introduction and along the whole Part II.

1.2.1   Lunar occultations

Lunar occultations (hereafter LO) are, together with eclipses, the oldest astronomical phenomena ever recorded. They occur when the Moon limb interposes itself between the star and observer line of sight. Because of the wave nature of light this disappearance or reappearance is not instantaneous. During a short but mensurable time interval ($\sim$0.1 s), the variation of the source intensity is described by a characteristic Fresnel diffraction pattern of fringes and a decreasing light profile. This phenomenon can be assimilated to the well-known optical problem of a monochromatic point source occulted by an infinite straight edge. More realistically, non-monochromatic light and resolved and binary or multiple sources, can be numerically incorporated to the former model.

MacMahon (1908) firstly pointed that LO, still inside the geometric optics simplification, could be used to derive spatial information of the occulted source. It was not until Whitford (1939) that ondulatory optics was considered to describe the LO phenomenon and high resolution information was derived from diffraction pattern. With the establishment of fast photoelectric devices, millisecond sampled lightcurves have been feasible for observers. As a result, LO have become one of the highest angular resolution techniques available in visible and infrared astronomy, providing information up to 1 mas scale.

The purpose of observing such events has changed over the centuries. A few of them are enumerated in chronological order:

- geographical longitude calculation. Observations of the same event made at two different places supply precise information of longitude difference between

observers. This was firstly pointed out by J.J.L. de Lalande in 1749, and later sophisticated by O'Keefe (1956).

- measurement of Earth's equatorial radius and distance to the Moon (O'Keefe & Anderson 1952). The latter can be derived with accuracies of the order of centimeters. van Flandern (1981) indirectly determined $\dot{g}$ or a limit to $\dot{g}$ from these measurements.

- precise timing of occultation events. These measurements, firstly visual and then photoelectric, led to centimetric knowledge of the Moon position with respect to the background stars. However, this application was superseded by laser ranging since the mid 1970s.

- information of local relief of lunar limb. For every recorded event, the slope of the lunar limb is fitted with the rest of parameters which play into the shape of lightcurve. Before planetary mission, LO were the only technique providing information of such unexplored areas (Evans 1955, 1970), and helped to disregard the previous belief of lunar limb was in general steep.

- astrometry of radio and X-ray sources. Paradigmatic examples of this class of events were the number of occultations of the Crab Nebula pulsar (Maloney & Gottesman 1979; Weisenberger et al. 1987; Weisskopf et al. 1978) and the first identification of an extragalactic radio source (3C 273) by LO means (Hazard et al. 1963, 1966).

- assistance for guidance systems of early 1990s space-based telescopes, such as HST and HIPPARCOS (Evans 1986).

- stellar angular diameters measurements. Until the recent appearance of long-baseline interferometry (LBI) in visible and near-IR ranges, LO was the only direct method of measuring stellar angular diameters. Williams (1939) was the first in noticing that this fundamental parameter could be deduced from its influence on the diffraction pattern. Indeed, as seen in Fig. 1.1, the diameter modulates the lightcurve so that an small diameter source produces more contrasted fringes than a large diameter source, which shows smoother transition even without any fringes in the limit of geometric optics ($> 10 - 40$ mas depending the wavelength).

  Typically, diameters can be derived by model-dependent least-squares fitting (Nather & McCants 1970; Richichi et al. 1992b) up to the level of 1 mas and
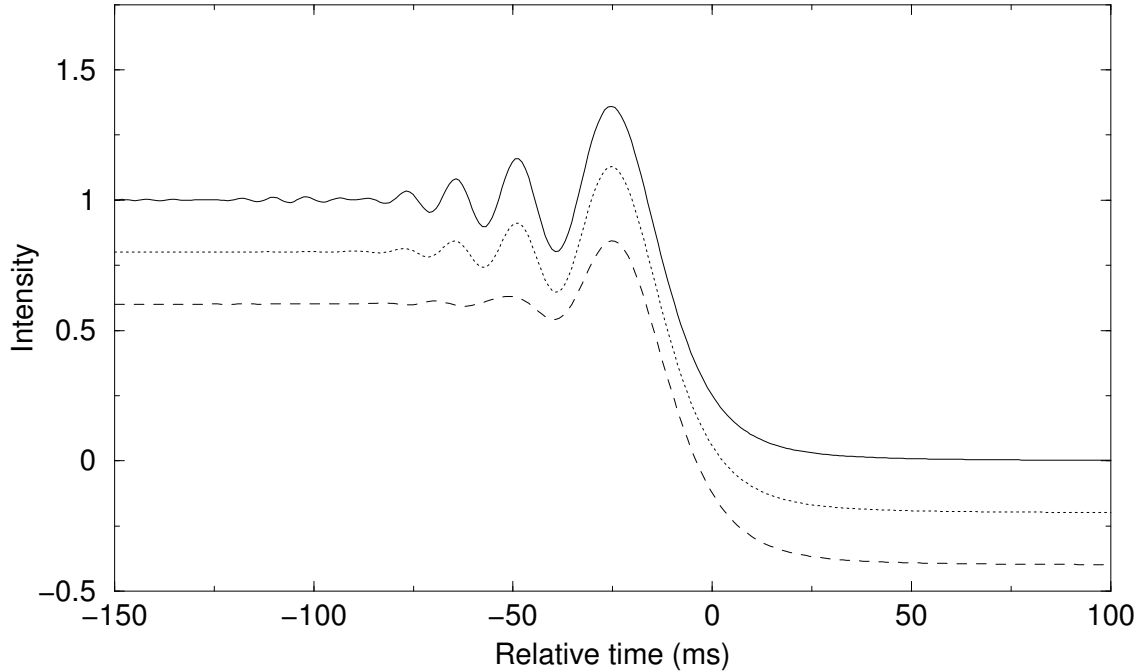
Figure 1.1: Noiseless simulated lightcurves in K band of three sources with diameters
10.0 mas (dashed), 5.0 mas (dotted) and practically unresolved 0.1 mas (solid). Fringe
pattern is smoothed as diameter increases. All three lightcurves are normalized to the
same intensity level but have been shifted in this axis for the sake of comparison.

an average accuracy of $\sim 5\%$. This uncertainty results from the combination
of several factors as the stellar magnitude, scintillation noise, filter bandwidth,
telescope diameter and detector sampling. The diameter distribution shown
in left panels of Fig. 1.2 is justified by a number of observational constraints,
e.g., IR filter mostly used, bias towards late-type sources with larger diameter,
etc.

That precise determination of stellar diameters by LO benefits a number of
astrophysical scenarios. The most important is to obtain a direct estimation of
effective temperatures for testing stellar atmosphere models, sometimes with
accuracies $< 50\ K$ (Richichi et al. 1998b). Most prolific series of observations
in this context have been the ones at KPNO[1] by Ridgway et al. (1977, 1979,
1980, 1982a,b,c); Schmidtke et al. (1986) and at TIRGO[2], Calar Alto[3] and

---

[1]Kitt Peak National Observatory, National Optical Astronomy Observatory, which is operated
by the Association of Universities for Research in Astronomy, Inc. (AURA) under cooperative
agreement with the National Science Foundation.

[2]Telescopio Infrarosso del Gornergrat (TIRGO) is operated by CNR – CAISMI Arcetri, Italy.

[3]Centro Astronómico Hispano Alemán (CAHA) at Calar Alto, operated jointly by the Max-
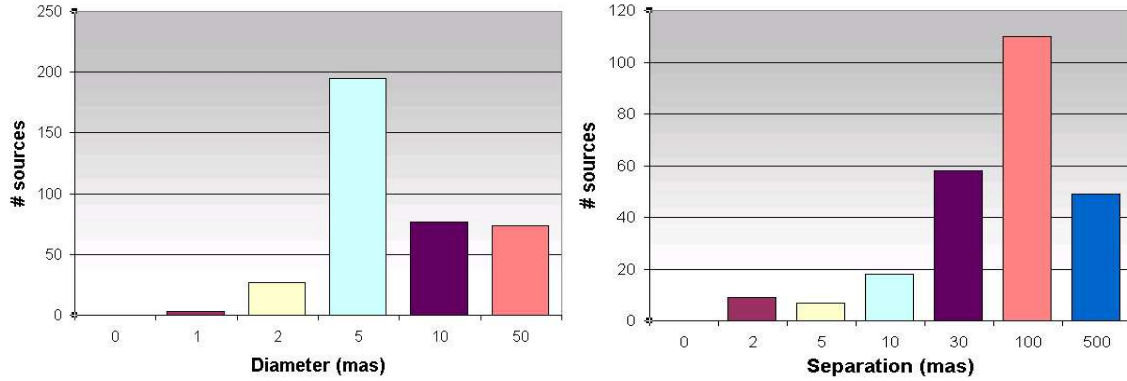
Figure 1.2: Left: Diameters histogram measured by LO. Right: Separation histograms of binaries measured by LO. Both extracted from CHARM2 catalogue (Richichi et al. 2005).

ESO-La Silla by Richichi & Calamai (2001); Richichi et al. (1992a,b, 1998a,b). As a by product of these and other observations, parallel studies of stellar structure can be approached. For example, pulsation in late-type variables and presence of circumstellar shells (Mondal & Chandrasekhar 2005; Ragland et al. 1997; Richichi et al. 1988) and surface assymmetries in Mira variables (Mondal & Chandrasekhar 2004) have been detected. Finally, effective and color temperatures calibrations of cold-end of main sequence stars (K and M types and carbon stars) also benefit from LO diameter measurements (Richichi et al. 1999a).

- investigation of binaries. Since the first occultation of the binary star γ-Virginis observed by Jacques Cassini on April 21, 1720, LO have largely evolved up to becoming one of the most important contributors in this field.

  As an example, Fig. 1.3 illustrates how a binary lightcurve deviates from the single source shape of either of its components. Fringe pattern can adopt different appearance depending the separation and brightness ratio of the components. As in the case of diameters, these two latter parameters can be retrieved by model-dependent least-squares fitting. Other model-independent methods (Richichi 1989) have been found to be more suited for detecting very close companions. LO provide positive detections under very diverse conditions: separations up to 1.4 mas and brightness ratios from 1:1 to 1:150. Right panel of Fig. 1.2 illustrates the former separation limit and that the distribution peaks around 100 mas. This broad range of measurements opens the possibil-
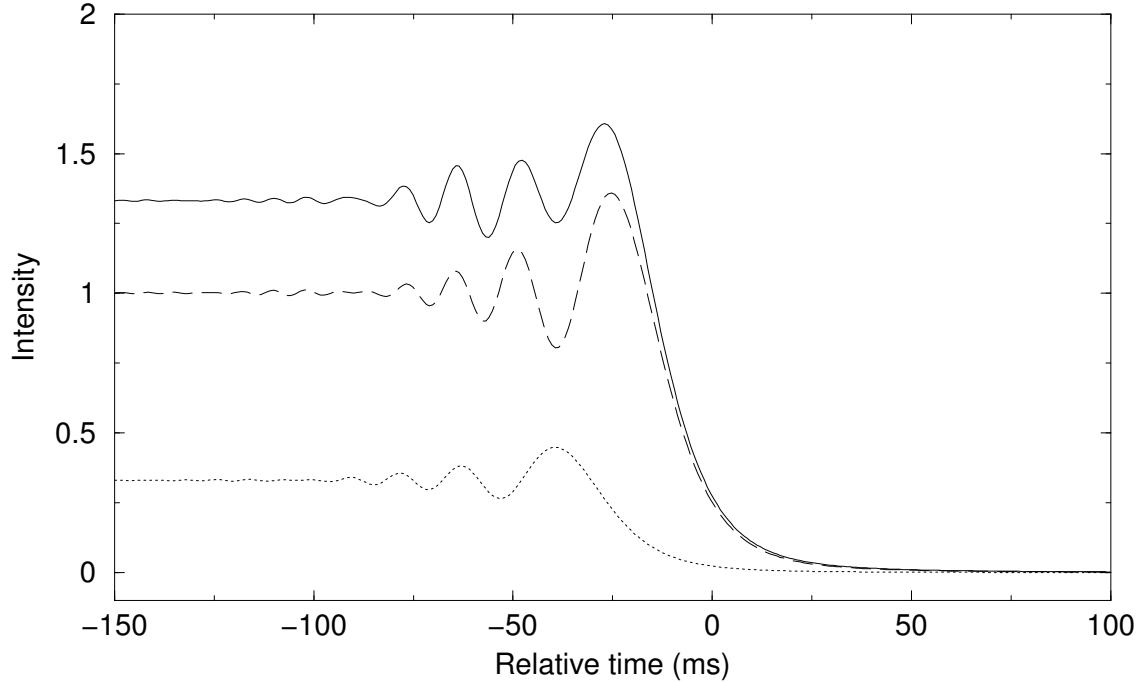
Figure 1.3: Noiseless simulated lightcurve in K band of an unresolved binary (solid). Primary (dashed) and secondary (dotted) components are separated 7.4 mas in the direction of lunar motion with a brightness ratio of $1:3$.

ity to study accurate orbital motions, the determination of stellar masses and, of course, the detection of close companions.

A detailed literature query shows a remarkable activity in this area and the broad type of astrophysical scenarios which can be approached in this context. First, regular campaigns of field stars have been conducted yielding several series of papers: the ones at McDonald Observatory by Africano et al. (1975, 1976, 1977, 1978); Blow et al. (1982); Dunham et al. (1973); Edwards et al. (1980); Evans (1971); Evans & Edwards (1981, 1983); Evans et al. (1985, 1986) in optical wavelengths and at TIRGO by Richichi et al. (1994, 1996b, 1997, 1999b, 2000, 2002) in near-IR. Second, infrared sources with no optical counterpart (Richichi & Calamai 2001) are also relevant. Finally, surveys of multiplicity of young stellar objects as T Tauri stars (Chen & Simon 1997; Leinert et al. 1991; Simon et al. 1995, 1996, 1999) have been crucial for understanding that the dominant mode of star formation is represented by binaries.

More in detail, a few descriptive statistics of the two regular binary programs are given below. As seen in Table 1.2, the series at McDonald Observatory

is a valuable database given the large number of observed objects. This was recently recompiled by Mason (1994) and made electronically available at Evans (1995). The program at TIRGO comprises a shorter sample but shows higher binarity probability, probably because the better SNR conditions in the near-IR and the fact that the program partly focused to observe binary candidates. Needless to say that both probabilities are biased by a number of observational factors and other type constraints.

Table 1.2: Overview of main LO programs dedicated to detection of field binary stars.

Observatory	Band	Total number of occulted field stars	Number of detected binaries	Binarity probability	Reference
McDonald	Visible	>7000	224	7%	Evans (1983)
TIRGO	IR	454	62	14%	Richichi et al. (2000)

In view of this, we can conclude that LO still play of an important role in the direct establishment of fundamental stellar quantities and maintain a considerable activity in the two latter fields of research (diameters and binaries measurements).

Looking to the immediate future, LO measurements are being used in the calibration of modern long-baseline interferometers such as the VLTI, Keck and CHARA. Davis et al. (2005); Richichi & Percheron (2005) represent the first succesful efforts in these calibration tasks for the case of VLTI. In this way, a new Catalog of High Angular Resolution Measurements (CHARM) (Richichi & Percheron 2002; Richichi et al. 2005) has been compiled incorporating several hundreds of LO measurements (both of binaries and stellar diameters) besides the ones from LBI and spectrophotometric techniques.

Another application of LO have been proposed by Absil et al. (2005) who points out that LO measurements could also be used to determine the diameters of the brightest targets ($K \sim 3$) of the *Darwin* space-based IR interferometer mission catalogue with a limiting resolution of 1 mas.

Advantages and disadvantages of LO

As introduced above, LO technique presents a number of advantages with respect to other high resolution techniques:

1. since the occultation is a diffraction phenomenon produced at the lunar limb rather than in the telescope, these observations are characterized by several properties which are significantly different from the ones typically encountered in other high resolution techniques such as adaptive optics (AO), speckle or LBI. For example, the limiting angular resolution is not fixed by either the size of the telescope or the wavelength of observation (diffraction limit), at least to a first approximation. Also, it is not directly influenced by the quality of the seeing.

2. LO turn to be an inexpensive observational technique, only requiring high speed electronics and do not necessarily need large telescopes.

3. the data analysis part is simple and well established and possible biases and limitations are well-known and understood.

While these properties make the LO technique attractive, a number of short-comings considerably limit its application:

1. occultations can be observed only for sources which lie on the apparent orbit of the Moon. This restricts the candidates to a narrow belt around the Zodiac, covering approximately 10% of the celestial sphere.

2. LO are fixed-time events, which need careful planning and the successful combination of technical and meteorological readiness.

3. each LO event only provides a one-dimensional scan of the source, along a direction which is determined by the lunar motion and the source position. Depending on the conditions, a given source can be occulted only once or several times over a period of a few months or very few years. In this case, some limited two-dimensional information can be obtained.

Other lesser observational constraints affect to the outcome of LO measurements. In Fig. 1.4 we represent the V and K magnitudes histograms for the LO entries

in CHARM2 with diameter (top panels) and binary separation (bottom panels) information available.
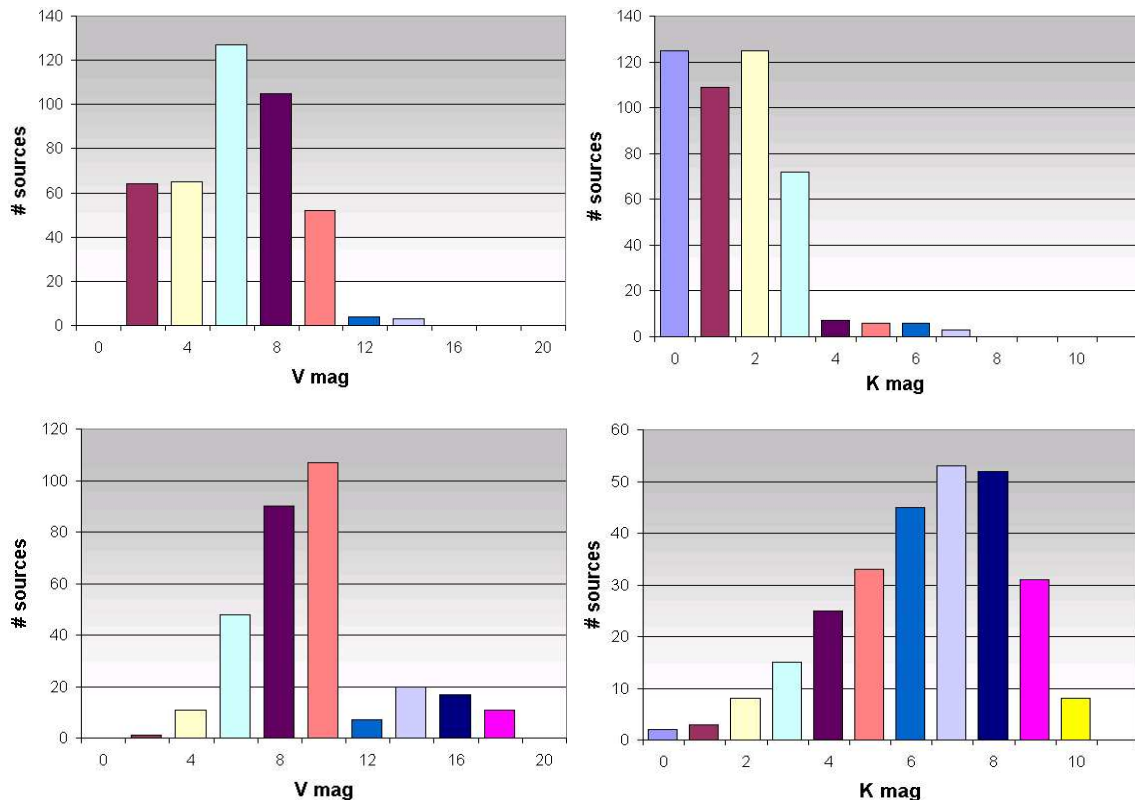
Figure 1.4: V and K magnitude distribution of diameters (top panels) and binaries (bottom panels) measured by LO. Extracted from CHARM2 catalogue (Richichi et al. 2005).

As regard as diameters measurements, the cut-off magnitude is around $K \sim 4$. This bias is motivated by the relatively high SNR (> 10) required by the fitting procedure to yield a minimaly accurate estimation of this parameter.

As regard as LO binaries, the bulk of this sample comes from numerous TIRGO campaigns which employed a near-IR photometer. Note that the magnitude range for binaries detections is much broader than for diameters. The cut-off value in the lower right histogram matches well with the limiting magnitude of $K \sim 7$ (SNR=1) for binaries detection as determined by Richichi et al. (1996a). This limit was twofold caused. On one hand, the sensitivity of the instrument drops at that magnitude due to the strong influence of background variability which degrades SNR in the case of a near-IR photometer. On the other hand, predictions of infrared sources

were not complete up to $K > 7$. Note that the Two Micron Sky Survey (TMSS) (Neugebauer & Leighton 1969) was incomplete in declination and only extended to $K \lesssim 3$. Therefore, LO predictions had to be compiled from a variety of other catalogues. Even a very rich run would consist of about 10-20 sources per night at most.

1.2.2 Speckle interferometry

Speckle interferometry is an observational technique which allows to retrieve diffraction-limited information from a sequence of very-short exposure frames under the assumption they are a time-independent representation of the wavefront phase content. For decades it has been one of the mainstream techniques in the field of binary stars, since it yields direct measurements of separation, position angle and magnitude difference. Speckle imaging is an extension of the latter technique, when the reconstruction of the true diffraction-limited image is aimed. Note that, despite this conceptual difference between speckle interferometry and speckle imaging, the former is usually employed in a broader sense to refer either of them. We will follow this convention along this part of thesis, although in some cases the latter term will be used.

Extensive and long term observational speckle campaigns have been a fundamental tool to determine binary star orbits and stellar masses, and a first step to establish the Mass-Luminosity Relation and Initial Mass Function. In a way, the current role of speckle interferometry is filling the $0\rlap{.}{''}01 - 1\rlap{.}{''}0$ resolution gap between the large database of measurements obtained during decades by visual micrometer and the milliarcsecond observations which more modern and complex facilities such as optical interferometers (VLTI, Keck, CHARA) will soon retrieve in a regular basis.

For the immediate future, the case of the few thousands of objects which HIPPARCOS identified as new doubles turns to be a paradigmatic field of study for speckle interferometry. With their distances already known, an accurate determination of the orbit and component magnitudes and colors would allow to identify which are gravitationally bound and attempt to derive masses in those cases.

The field benefits from a number of active and well established groups which

have filled a baseline of more than 25 years of observations: Balega et al. (2004); Docobo et al. (2004); Horch et al. (2004); Mason et al. (2004); Saha et al. (2002); Scardia et al. (2005) focused in regular binary stars campaigns in the visible and Ghez et al. (1995); Leinert et al. (1991) in the near-IR focused in the study of young stellar objects. Some of them have accumulated a few thousands of observations over more than a decade (see the cases of the series of 23 papers of Hartkopf et al. (2000) and 7 by Mason et al. (2001)). As in other areas of astronomy, the Southern Hemisphere is poorer in the number of studied binary systems by speckle. This gap is being filled by more recent programs (Horch et al. 2001, 1996).

During the last decade, Intensified CCDs have turned to be the detector most commonly used in speckle programs with excellent performance. These systems consist in a combination of photoelectric and CCD technologies, namely an image intensifier which is coupled in front of a frame-transfer CCD sensor. One of the advantages of these systems is that the impact of CCD readout noise over SNR of speckle pattern image is reduced by the intensifier. However, it suffers from several drawbacks. First, because of the limited time and non punctual response of intensifier system, a fraction of photon events become scattered in time and space in the detected image. Second, because of the intensifier saturation ICCDs usually offer unaccurate diffraction-limited photometric information, which translates into unreliable estimates of Δm of binary stars. Typical errors of 0.5 mag are habitual (Hartkopf et al. 1996). As a result, ICCD speckle measurements, which are valuable because of its astrometric content, are not optimal for determining luminosities of the components of binary systems.

1.2.3   Motivations of Part II

Lunar occultations

The situation of LO binaries search exposed above is near to change allowing to extend the study to fainter magnitudes. The following motivations trigger the development of this part of the thesis:

First, the recent availability of all-sky near-infrared surveys, such as 2MASS (Cutri et al. 2003) and DENIS (Paturel et al. 2003) would increase by almost an order of magnitude the number of predictions for IR events observable with 1 m-class

telescopes and above. A typical night of observation in a 1.5 m telescope would offer more than 100 sources close to maximum lunar phase. This increase would be even more dramatic for special events, e.g., on the occasions of passages of the Moon over crowded regions near the Galactic Center, where a thousand of events would be easily accessible to a medium-sized telescope over few hours.

With this foreseeable increase in the number of occultations, new automatic data analysis technique should be required, removing at least in a first stage the need of interactive reduction by the astronomer.

Second, new developments in CCDs and IR arrays could extend the magnitude range of available objects beyond the limit shown in lower right panel of Fig. 1.4. The usual detectors for LO programs have been high-speed photometers, with different photomultiplier technology depending on observing frequency (GaAs for visible and InSb for near-IR). However, neither CCDs nor IR arrays have been intensively used for LO programs.

Regarding CCDs, their technical specifications have constantly been improved during the last two decades. Despite this rapid development, most current research-grade cameras are still not able to meet the millisecond frame rate which LO demand while keeping a low readout noise and high digitization resolution mode.

Regarding IR arrays, thanks to the possibility of implementing fast readout schemes on subarray sections, they have been used for LO observations although at the expense of a reduced sampling. An example is the MAGIC camera (Herbst et al. 1993) at the Calar Alto Observatory (Richichi et al. 1996a).

The advantages offered by both imaging devices are their higher quantum efficiency and the possibility of removing background variation signature. These could increase the efficiency of the LO observations with respect to photometers. In addition, because they are not so specific as photometers, they are broadly available in nearly all the observatories and their cost and maintenance is comparatively cheaper.

In view of this, we foresee that LO can still offer a significant scientific contribution with relatively small effort, and attempts to continue and improve throughput of routine LO observations should be encouraged. In particular, our study is focused in the following topics:

1. to develop, implement and evaluate a new observational technique which enable CCDs for LO observations. This acquisition scheme should allow to obtain millisecond sampled lightcurves without loss of spatial resolution information.

2. to design and implement a new reduction pipeline which allows to automatically analyse large number of occultations in an unattended fashion, only leaving to the skilled user a final interactive analysis of most promising events.

3. to conduct a systematic LO program operated at optical and near-IR wavelengths. The program will be focused in the detection of new binaries because diameters determination would have required a less likely routine access to larger telescopes.

The observational effort in 3. will benefit from the new observing technique and analysis tools aimed in the two former points. Equally, the recent advances in infrared catalogues coverage and detectors sensitivity explained above will be decisive for filling the LO binaries reservoir which is far from being exhausted.

Speckle interferometry

Parallely to the extensive usage of ICCDs explained above, CCDs have also been employed for speckle imaging with increasing frequency. This started more than a decade ago with the work of Zadnik (1993), and has been extended more recently by Horch et al. (1999, 1997) and Kluckers et al. (1997).

There are three main reasons for this change.

1. CCDs have dramatically improved in terms of their frame rate and readout and dark current noise.

2. Second, it has been realized that changing the readout pattern allows to use large-format CCDs effectively for speckle imaging.

3. Finally, there has been the hope that CCDs would allow for reliable diffraction-limited photometric information in a way that intensified cameras have not been able to do up to the present.

In view of all this panorama, we decided to pursue the following research topics:

1. to develop and implement a new observational technique based on CCD which enable most observatories, professionals and high-end amateurs, for conducting speckle measurements.

2. to validate the former new observational technique with the observation of binaries well-known binaries.

3. to propose new calibration methods in the context of speckle data analysis for saving telescope time in the observation of unresolved sources. This development would be specially of interest in large telescope regime.

Bibliography

Absil O., den Hartog R., Gondoin P., et al., Nov. 2005, ArXiv Astrophysics e-prints

Africano J.L., Cobb C.L., Dunham D.W., et al., Sep. 1975, AJ, 80, 689

Africano J.L., Evans D.S., Fekel F.C., Ferland G.J., Aug. 1976, AJ, 81, 650

Africano J.L., Evans D.S., Fekel F.C., Montemayor T., Aug. 1977, AJ, 82, 631

Africano J.L., Evans D.S., Fekel F.C., Smith B.W., Morgan C.A., Sep. 1978, AJ, 83, 1100

Alloin D., Pantin E., Lagage P.O., Granato G.L., Nov. 2000, A&A, 363, 926

Andersen T., Christensen P.H., Aug. 2000, In: Proc. SPIE Vol. 4004, Telescope Structures, Enclosures, Controls, Assembly/Integration/Validation, and Commissioning, Thomas A. Sebring; Torben Andersen; Eds., 373–381

Balega I., Balega Y.Y., Maksimov A.F., et al., Aug. 2004, A&A, 422, 627

Benitez E., Dultzin-Hacyan D., Heidt J., et al., Jun. 1996, ApJ Letter, 464, L47+

Bernstein G.M., Jarvis M., Feb. 2002, AJ, 123, 583

Blow G.L., Chen P.C., Edwards D.A., Evans D.S., Frueh M., Nov. 1982, AJ, 87, 1571

Bontekoe T.R., Koper E., Kester D.J.M., Apr. 1994, A&A, 284, 1037

Boulade O., Charlot X., Abbon P., et al., Mar. 2003, In: Instrument Design and Performance for Optical/Infrared Ground-based Telescopes. Edited by Iye, Masanori; Moorwood, Alan F. M. Proceedings of the SPIE, Volume 4841, 72–81

Chauvin G., Lagrange A.M., Lacombe F., et al., Feb. 2005, A&A, 430, 1027

Chen W.P., Simon M., Feb. 1997, AJ, 113, 752

Cornwell T.J., Evans K.F., Feb. 1985, A&A, 143, 77

Courbin F., Lidman C., Frye B.L., et al., Jun. 1998, ApJ Letter, 499, L119+

Cutri R.M., Skrutskie M.F., van Dyk S., et al., Jun. 2003, VizieR Online Data Catalog, 2246, 0

Davis J., Richichi A., Ballester P., et al., Jan. 2005, Astronomische Nachrichten, 326, 25

Deul E., Kuijken K., Valentijn E.A., Dec. 2002, In: Survey and Other Telescope Technologies and Discoveries. Edited by Tyson, J. Anthony; Wolff, Sidney. Proceedings of the SPIE, Volume 4836, pp. 189-198, 189–198

Docobo J.A., Andrade M., Ling J.F., et al., Feb. 2004, AJ, 127, 1181

Dunham D.W., Evans D.S., McGraw J.T., Sandmann W.H., Wells D.C., Aug. 1973, AJ, 78, 482

Edwards D.A., Evans D.S., Fekel F.C., Smith B.W., Apr. 1980, AJ, 85, 478

Eke V., Jun. 2001, MNRAS, 324, 108

Esch D.N., Connors A., Karovska M., van Dyk D.A., Aug. 2004, ApJ, 610, 1213

Evans D.S., Dec. 1955, AJ, 60, 432

Evans D.S., Jun. 1970, AJ, 75, 589

Evans D.S., Dec. 1971, AJ, 76, 1107

Evans D.S., 1983, Lowell Observatory Bulletin, 167, 73

Evans D.S., 1986, In: IAU Symp. 118: Instrumentation and Research Programmes for Small Telescopes, 187–198

Evans D.S., Nov. 1995, VizieR Online Data Catalog, 1110, 0

Evans D.S., Edwards D.A., Aug. 1981, AJ, 86, 1277

Evans D.S., Edwards D.A., Dec. 1983, AJ, 88, 1845

Evans D.S., Edwards D.A., Frueh M., McWilliam A., Sandmann W.H., Nov. 1985, AJ, 90, 2360

Evans D.S., McWilliam A., Sandmann W.H., Frueh M., Nov. 1986, AJ, 92, 1210

Faure C., Alloin D., Gras S., et al., Jul. 2003, A&A, 405, 415

Frieden B.R., 1978, Optical Society of America Journal A, 68, 1375

Gendron E., Coustenis A., Drossart P., et al., Apr. 2004, A&A, 417, L21

Ghez A.M., Weinberger A.J., Neugebauer G., Matthews K., McCarthy D.W., Aug. 1995, AJ, 110, 753

Grosso N., Feigelson E.D., Getman K.V., et al., Oct. 2005, ApJSS, 160, 530

Haarsma D.B., Winn J.N., Falco E.E., et al., Nov. 2005, AJ, 130, 1977

Hanisch R.J., White R.L. (eds.), 1994, The restoration of HST images and spectra - II

Harris J.L., May 1966, Journal of the Optical Society of America (1917-1983), 56, 569

Hartkopf W.I., Mason B.D., McAlister H.A., et al., Feb. 1996, AJ, 111, 936

Hartkopf W.I., Mason B.D., McAlister H.A., et al., Jun. 2000, AJ, 119, 3084

Hazard C., Mackey M.B., Shimmins A.J., 1963, Nature, 197, 1037

Hazard C., Gulkis S., Bray A.D., 1966, Nature, 210, 888

Herbst T.M., Beckwith S.V., Birk C., et al., Oct. 1993, In: Proc. SPIE Vol. 1946, Infrared Detectors and Instrumentation, Albert M. Fowler; Ed., 605–609

Hiltner P.R., Kroll P., Nestler R., Franke K.H., 2003, In: ASP Conf. Ser. 295: Astronomical Data Analysis Software and Systems XII, 407–+

Högbom J.A., Jun. 1974, A&ASS, 15, 417

Horch E., Ninkov Z., van Altena W.F., et al., Jan. 1999, AJ, 117, 548

Horch E., van Altena W.F., Girard T.M., et al., Mar. 2001, AJ, 121, 1597

Horch E.P., Dinescu D.I., Girard T.M., et al., Apr. 1996, AJ, 111, 1681

Horch E.P., Ninkov Z., Slawson R.W., Nov. 1997, AJ, 114, 2117

Horch E.P., Meyer R.D., van Altena W.F., Mar. 2004, AJ, 127, 1727

Howell S.B., Koehn B., Bowell E., Hoffman M., Sep. 1996, AJ, 112, 1302

Izumiura H., Kester D.J.M., Dejong T., et al., 1994, Nobeyema Solar Radio Observatory, Nobeyama Radio Observatory Report, No. 379 2 p (SEE N95-29836 10-90)

Jee M.J., White R.L., Benítez N., et al., Jan. 2005, ApJ, 618, 46

Jefferies S.M., Christou J.C., Oct. 1993, ApJ, 415, 862

Karovska M., Aldcroft T., Elvis M.S., et al., Jan. 2001, In: IAU Symposium, 66–+

Karovska M., Esch D., van Dyk D., Mar. 2003, AAS/High Energy Astrophysics Division, 7,

Karovska M., Schlegel E., Hack W., Raymond J.C., Wood B.E., Apr. 2005, ApJ Letter, 623, L137

Keel W.C., Jul. 1991, PASP, 103, 723

King I.R., Apr. 1971, PASP, 83, 199

Kluckers V.A., Edmunds M.G., Morris R.H., Wooder N., Jan. 1997, MNRAS, 284, 711

Kotilainen J.K., Ward M.J., Williger G.M., Aug. 1993, MNRAS, 263, 655

Krause O., Lemke D., Tóth L.V., et al., Feb. 2003, A&A, 398, 1007

Lagrange A.M., Chauvin G., Rouan D., et al., Apr. 2004, A&A, 417, L11

Lauer T.R., Ajhar E.A., Byun Y.I., et al., Dec. 1995, AJ, 110, 2622

Leinert C., Haas M., Mundt R., Richichi A., Zinnecker H., Oct. 1991, A&A, 250, 407

Lucy L.B., Jun. 1974, AJ, 79, 745

Lucy L.B., 1994, In: The Restoration of HST Images and Spectra - II, 79–+

MacMahon P.A., Dec. 1908, MNRAS, 69, 126

Magain P., Courbin F., Sohy S., Feb. 1998, ApJ, 494, 472

Maloney F.P., Gottesman S.T., Dec. 1979, ApJ, 234, 485

Marchis F., Prangé R., Christou J., Dec. 2000, Icarus, 148, 384

Mason B.D., 1994, Ph.D. Thesis

Mason B.D., Hartkopf W.I., Wycoff G.L., et al., Sep. 2001, AJ, 122, 1586

Mason B.D., Hartkopf W.I., Wycoff G.L., et al., Dec. 2004, AJ, 128, 3012

McGlamery B.L., Mar. 1967, Journal of the Optical Society of America (1917-1983), 57, 293

Meinel A., Meinel M., 1980, In: Optical and Infrared Telescopes for the 1990's, 1027–+

Mighell K.J., Aug. 2005, MNRAS, 361, 861

Molina R., Núñez J., Cortijo F.J., Mateos J., Mar. 2001, IEEE Signal Processing Magazine, 18, 11

Mondal S., Chandrasekhar T., Mar. 2004, MNRAS, 348, 1332

Mondal S., Chandrasekhar T., Aug. 2005, AJ, 130, 842

Núñez J., Llacer J., Oct. 1993, PASP, 105, 1192

Nathan R., 1966, Digital Video Handling, Tech. Rep. 32-877, Jet Propulsion Laboratory

Nather R.E., McCants M.M., Oct. 1970, AJ, 75, 963

Neugebauer G., Leighton R.B., 1969, Two-micron sky survey. A preliminary catalogue, NASA SP, Washington: NASA, 1969

Noordermeer E., van der Hulst J.M., Sancisi R., Swaters R.A., van Albada T.S., Oct. 2005, A&A, 442, 137

O'Keefe J.A., 1956, Smithsonian Contributions to Astrophysics, 1, 75

O'Keefe J.A., Anderson J.P., Aug. 1952, AJ, 57, 108

Otazu X., 2001, Algunes aplicacions de les Wavelets al procés de dades en astronomia i teledetecció, Ph.D. thesis

Pantin E., Starck J.L., Sep. 1996, A&ASS, 118, 575

Paturel G., Petit C., Rousseau J., Vauglin I., Jul. 2003, A&A, 405, 1

Pina R.K., Puetter R.C., Jun. 1993, PASP, 105, 630

Prieur J.L., Aristidi E., Lopez B., et al., Mar. 2002, ApJSS, 139, 249

Puetter R.C., Yahil A., 1999, In: ASP Conf. Ser. 172: Astronomical Data Analysis Software and Systems VIII, 307–+

Puetter R.C., Gosnell T.R., Yahil A., Sep. 2005, ARA&A, 43, 139

Rabinowitz D., Baltay C., Emmet W., et al., Dec. 2003, American Astronomical Society Meeting Abstracts, 203,

Racine R., Aug. 1996, PASP, 108, 699

Ragland S., Chandrasekhar T., Ashok N.M., Mar. 1997, A&A, 319, 260

Refregier A., Jan. 2003, MNRAS, 338, 35

Richardson W.H., 1972, Optical Society of America Journal A, 62, 55

Richichi A., Dec. 1989, A&A, 226, 366

Richichi A., Calamai G., Dec. 2001, A&A, 380, 526

Richichi A., Percheron I., May 2002, A&A, 386, 492

Richichi A., Percheron I., May 2005, A&A, 434, 1201

Richichi A., Salinari P., Lisi F., Mar. 1988, ApJ, 326, 791

Richichi A., di Giacomo A., Lisi F., Calamai G., Nov. 1992a, A&A, 265, 535

Richichi A., Lisi F., di Giacomo A., Feb. 1992b, A&A, 254, 149

Richichi A., Calamai G., Leinert C., Jun. 1994, A&A, 286, 829

Richichi A., Baffa C., Calamai G., Lisi F., Dec. 1996a, AJ, 112, 2786

Richichi A., Calamai G., Leinert C., Stecklum B., Trunkovsky E.M., May 1996b, A&A, 309, 163

Richichi A., Calamai G., Leinert C., Stecklum B., Jun. 1997, A&A, 322, 202

Richichi A., Ragland S., Fabbroni L., Feb. 1998a, A&A, 330, 578

Richichi A., Ragland S., Stecklum B., Leinert C., Oct. 1998b, A&A, 338, 527

Richichi A., Fabbroni L., Ragland S., Scholz M., Apr. 1999a, A&A, 344, 511

Richichi A., Ragland S., Calamai G., et al., Oct. 1999b, A&A, 350, 491

Richichi A., Ragland S., Calamai G., Richter S., Stecklum B., Sep. 2000, A&A, 361, 594

Richichi A., Calamai G., Stecklum B., Jan. 2002, A&A, 382, 178

Richichi A., Percheron I., Khristoforova M., Feb. 2005, A&A, 431, 773

Ridgway S.T., Wells D.C., Joyce R.R., Jun. 1977, AJ, 82, 414

Ridgway S.T., Wells D.C., Joyce R.R., Allen R.G., Feb. 1979, AJ, 84, 247

Ridgway S.T., Jacoby G.H., Joyce R.R., Wells D.C., Nov. 1980, AJ, 85, 1496

Ridgway S.T., Jacoby G.H., Joyce R.R., Siegel M.J., Wells D.C., Apr. 1982a, AJ, 87, 680

Ridgway S.T., Jacoby G.H., Joyce R.R., Siegel M.J., Wells D.C., May 1982b, AJ, 87, 808

Ridgway S.T., Jacoby G.H., Joyce R.R., Siegel M.J., Wells D.C., Jul. 1982c, AJ, 87, 1044

Saha S.K., Chinnappan V., Yeswanth L., Anbazhagan P., 2002, Bulletin of the Astronomical Society of India, 30, 677

Scardia M., Prieur J.L., Sala M., et al., Mar. 2005, MNRAS, 357, 1255

Schanne S., et al., Oct. 2004, In: ESA SP-552: 5th INTEGRAL Workshop on the INTEGRAL Universe, 73–+

Schmidt-Kaler T., Rucks P., Mar. 1997, In: Proc. SPIE Vol. 2871, Optical Telescopes of Today and Tomorrow, Arne L. Ardeberg; Ed., 635–640

Schmidtke P.C., Africano J.L., Jacoby G.H., Joyce R.R., Ridgway S.T., Apr. 1986, AJ, 91, 961

Sebring T.A., Moretto G., Bash F.N., Ray F.B., Ramsey L.W., 2000, In: Proceedings of the Backaskog workshop on extremely large telescopes, 53–+

Simon M., Ghez A.M., Leinert C., et al., Apr. 1995, ApJ, 443, 625

Simon M., Longmore A.J., Shure M.A., Smillie A., Jan. 1996, ApJ Letter, 456, L41+

Simon M., Beck T.L., Greene T.P., et al., Mar. 1999, AJ, 117, 1594

Snyder D.L., Hammoud A.M., White R.L., May 1993, Optical Society of America Journal A, 10, 1014

Stapelfeldt K.R., Ménard F., Watson A.M., et al., May 2003, ApJ, 589, 410

Starck J., Murtagh F., Aug. 1994, A&A, 288, 342

Starck J.L., Pantin E., Murtagh F., Oct. 2002, PASP, 114, 1051

van Flandern T.C., Sep. 1981, ApJ, 248, 813

Veran J.P., Rigaut F.J., Sep. 1998, In: Proc. SPIE Vol. 3353, Adaptive Optical System Technologies, Domenico Bonaccini; Robert K. Tyson; Eds., 426–437

Weisenberger A.G., Phillips J.A., Gottesman S.T., Carr T.D., May 1987, PASP, 99, 387

Weisskopf M.C., Silver E.H., Kestenbaum H.L., Long K.S., Novick R., Mar. 1978, ApJ Letter, 220, L117

White R.L., Allen R.J. (eds.), 1991, The restoration of HST images and spectra

Whitford A.E., May 1939, ApJ, 89, 472

Williams J.D., May 1939, ApJ, 89, 467

Zadnik J.A., 1993, Ph.D. Thesis

Zavagno A., Lagage P.O., Cabrit S., Apr. 1999, A&A, 344, 499

Part I

Application of image deconvolution to wide field CCD surveys

Chapter 2

Image deconvolution

In this chapter we introduce the concept of image deconvolution and present the details of the algorithm applied in this part of the thesis. As stated in Sect. 1.1.2, our aim is to explore the benefits of this technique applied to wide field CCD imagery, through an in-depth analysis with different data sets. The definition and implementation of a new deconvolution algorithm is beyond the scope of this study.

First, the basis of the image formation, point-spread function, noise and deconvolution concepts will be exposed. Second, the Maximum Likelihood Estimator (MLE) and Adaptive Wavelet-based MLE (AWMLE) deconvolution algorithms will be introduced. Both approaches will be used in this part of the thesis. Finally, particular attention will be paid to the relation between deconvolution and image sampling.

As a terminological note, it is worth noting that in the world of signal processing the problem of image deblurring and denoising has been traditionally denominated as *restoration* or, in a more general context, *reconstruction*. The term *deconvolution* is more restricted to the case of linear and shift-invariant imaging systems, which applies for most situations in astronomy. Therefore, we will adopt the latter term along this thesis.

2.1   Basis

Castleman (1996) defines an image as *a representation of something else*, and in particular, a digital image as *a numerical representation of an scene, sampled in an equally spaced rectangular grid pattern and quantized in equal intervals of amplitude.*

Apart from these general definitions, the process of image formation must be overviewed for a proper understanding of the deconvolution concept.

2.1.1   Image formation and representation

The process of an image formation can be modelled as illustrated in Fig. 2.1.
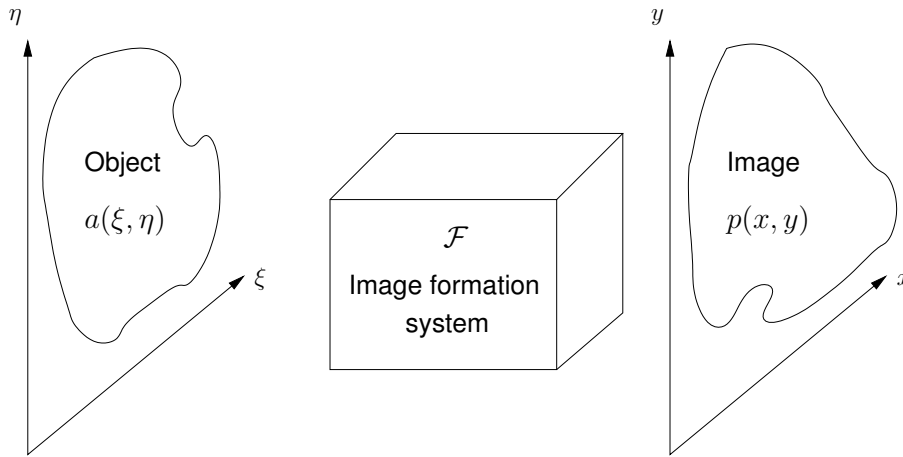
Figure 2.1: Image formation model. The object a is represented as the image p through the imaging system $\mathcal{F}$. (ξ, η) and (x, y) are often referred as object and image spaces, respectively.

$a(\xi, \eta)$ is a continuous function representing the spatial distribution of the intensity emitted by an object. This is projected through an image formation system $\mathcal{F}$ leading to the measured data in the detector $p(x, y)$. $\mathcal{F}$ comprises a number of instrumental effects, namely[1]:

1. the light is focused by the optical system onto a detector array. The response of the overall system can be characterized by f_{ji}, called the point-spread function

---

[1]Note all the commented items are in discrete form, as we assume the image p_j is sampled onto the CCD pixel array. The same applies for the object a_i. Image sampling concept is addressed in Sect. 2.1.2.

(PSF). This can be understood as the probability that an emission from the pixel i in the source be detected on the pixel j at the detector.

2. In the case of a CCD, each pixel has a different quantum efficiency characterized by a gain correction distribution C_j (flatfield).

3. In addition to a_i, some background radiation b_j from the sky or stray internal reflected light is also recorded by the detector.

4. Detection and digitization processes in the CCD imply the appearance of Poisson and Gauss distributed noises. While the former is implicit in p_j, the latter is modelled to be additive as n_j.

All in all, considering discrete notation for accommodating to sampling and assuming $\mathcal{F}$ is linear[2], the image model can be expressed as follows:

$$\sum_{i=1}^{B} \frac{f_{ji}}{C_j} \, a_i + b_j + n_j = p_j \quad j = 1, \cdots, D \tag{2.1}$$

where D and B are the number of pixels in the projected (measured) image and sampled version of object, respectively. Mathematically, the first term of the left side is a convolution between the object a_i and the corrected PSF $f'_{ji} = \frac{f_{ji}}{C_j}$. This first term plus the background b_j, noted h_j, can be understood as a forward projection through $\mathcal{F}$, or more physically, a blurred version of a_i.

In the next two subsections, the concepts of PSF (f_{ji}) and noise are further explained in the context of astronomical imaging.

2.1.2   Point-spread function and sampling

The point-spread function f_{ji} is the result of several contributions of different nature. In brief, PSF is produced by atmospheric turbulence, telescope optics, aerosol and dust scattering, diffusion and reflection of secondary light within the detector assembly and telescope vibrations and tracking errors. All these factors spread the light from the object $a(\xi, \eta)$, either randomly or systematically, onto the detector. As a result, a point-like object is imaged in a more or less diluted profile. We address

---

[2]This is the case of most imaging systems in astronomy.

the reader to Sect. 4.2 for a deeper study of these PSF contributors and how they influence its shape.

Sampling

Another image property which plays a key role in the PSF definition is the sampling. Projected photons over the detector plane are collected and counted in a finite number of pixels with nonzero size. They are usually disposed in an array shape, equally sized and spaced. This sampling process itself impress its own signatures on the image recorded in CCD frame. In particular, as will be seen in Sect 3.1.1, this solely process introduces a significant blur into the measured PSF due to the pixel response function. Equivalently, the posterior analysis (astrometry, photometry, etc.) performed over the image may be handicapped if this is not properly sampled. The sampling theorem (Shannon 1948) establishes a first quantitative limit for that situation, stating that a continuous function $f(x)$ sampled to an interval τ can be completely recovered from its sampled representation $g(x)$, provided that

$$\tau \leq \frac{1}{2s_0} \tag{2.2}$$

where s_0 is the folding frequency of the band-limited spectrum $F(s) = FT\{f(x)\}$. In Fig. 2.2 we illustrate how $f(x)$ is reconstructed from $g(x)$ in two different sampling regimes:

First, when Eq. 2.2 meets an equality (case of critical sampling), $G(s)$ and $F(s)$ can be related via the Fourier Transform of pixel function $\Pi(s)$ as follows

$$F(s) = G(s)\Pi(\frac{s}{2s_1}) \iff f(x) = g(x) \otimes 2s_1\frac{\sin(2\pi s_1 x)}{2\pi s_1 x} \quad ; \quad s_0 \leq s_1 \leq \frac{1}{\tau} - s_0 \tag{2.3}$$

which by inverse Fourier transforming leads to recover $f(x)$ from $g(x)$ via interpolating with the $sinc(x)$ function without theoretical error.

Second, if folding frequency s_0 exceeds sampling frequency, Eq. 2.2 is not met and we are in the case of undersampled data. As seen in lower right corner of Fig. 2.2, higher frequencies from the contiguous replicas are aliased and incorporated to the spectrum G_u. This situation disables Eq. 2.3 and, as a result, $f(x)$ can not be completely recovered.

Critically sampled

Undersampled
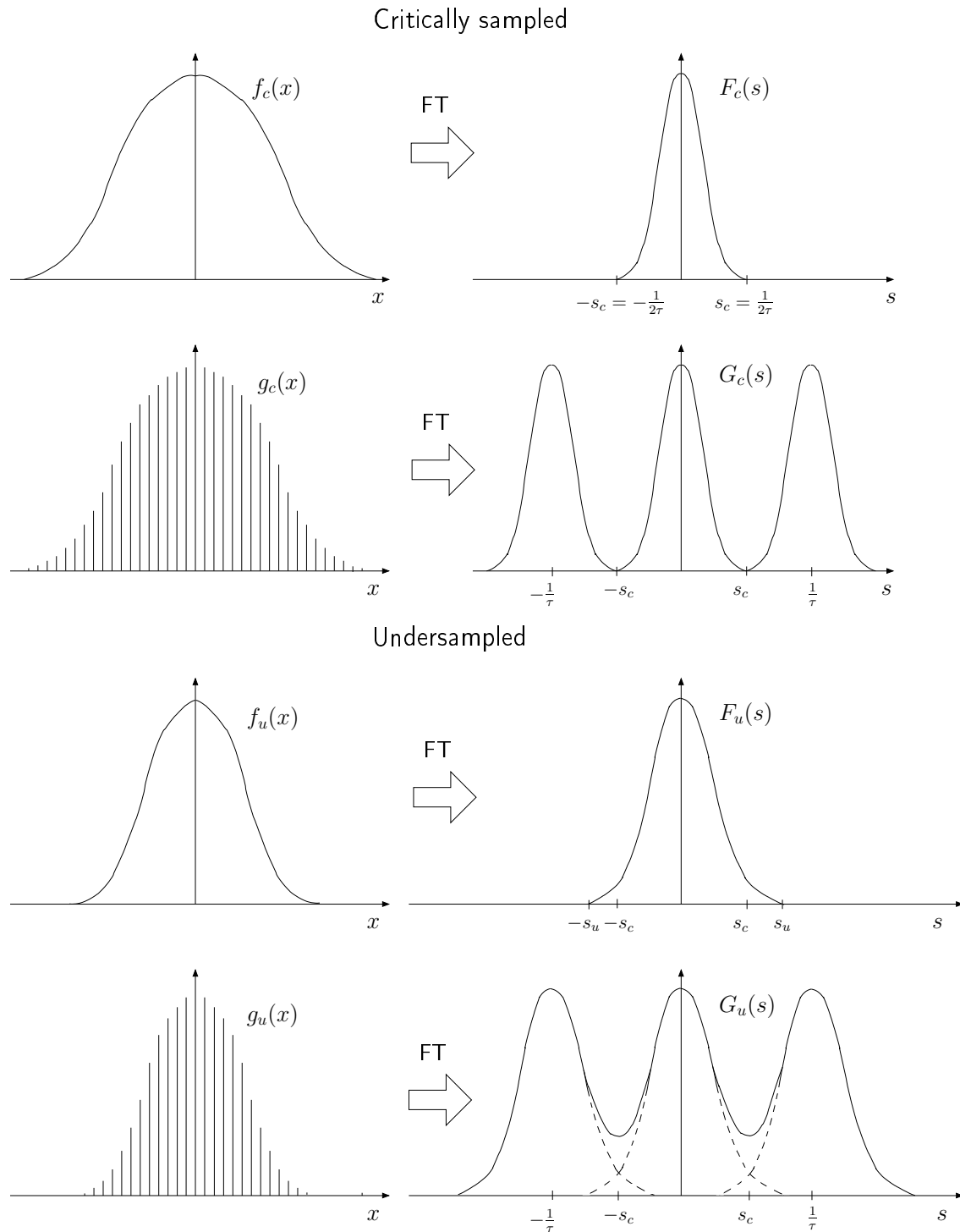
Figure 2.2: Two functions, f_c and f_u, are band-limited at folding frequencies s_c and s_u, respectively. f_c and f_u are sampled into g_c and g_u, with an interval size τ. Note this sampling process adds a series of replicas in their spectra G_c and G_u. g_c is critically sampled since $s_c = \frac{1}{2\tau}$: no overlap between replicas exists. However, g_u is undersampled because $s_u > \frac{1}{2\tau}$. As a result of the replicas overlap, aliasing occurs, i.e., frequencies above s_c are folded back below s_c and added to the spectrum.

When dealing with astronomical CCD images the above folding frequency s_0 can be related with the FWHM[3] of the seeing disk. If this is modeled by a 2D-Gaussian function, the following sampling regimes can be distinguished (Howell et al. 1996; Mighell 2005):

1. oversampled data when FWHM> 2.0 pixels.

2. critically sampled data when FWHM∼ 2.0 pixels.

3. marginally sampled data when 2.0 <FWHM≤ 1.5 pixels.

4. undersampled data when FWHM< 1.5 pixels.

Note that Eq. 2.2 is only met in regimes 1. and 2. However, this does not mean that marginally sampled or undersampled images *do not contain* useful information. On the contrary, despite the violation of sampling theorem and its associated aliasing, accurate photometric and astrometric measurements can be derived if adequate analysis techniques are employed. For example, in the case of astrometric studies Girard et al. (1994, 1995) centroided HST WF/PC 1 data using 2D-Gaussian fits with a precision up to 0.014 pixels. Also, the Lowell Observatory Near-Earth Object Search (LONEOS) project, which operates with a sampling parameter of FWHM= 0.7 pixels, is obtaining centroiding errors up to $\sigma = 0.03$ pixels with the use of a variable-size pixel mask profile fitting technique (Howell et al. 1996). Finally, Mighell (2005) has achieved $\sigma = 0.01$ pixel accurate astrometry for midly exposed stars by using a discrete PSF fitting technique over simulated NGST data, whose PSF concentrates 90% of the light within $0\rlap{.}''01$ with a pixel size of $0\rlap{.}''0064$. Actually, these are not exceptional cases but there is a number of telescopes operating in these marginal and undersampling regimes. They are facilities dedicated to surveys focused to the detection of new objects, where the main concern is to have a large-area coverage. In addition, undersampling is advantageous for these projects because it enables the detection of low SNR objects as most of their light is contained within a few pixels.

In summary, the key point in the analysis of undersampled data is to make use of specialized tools which assess this particular sampling situation. If standard analysis techniques are employed for that kind of data, large errors will appear because they were designed for well-sampled and high SNR data. It is one of the aims of this

---

[3]Full Width Half Maximum. This can also be understood as a sampling parameter.

thesis to apply for the first time a centering technique which becomes more robust and accurate in the particular undersampled regime of deconvolved images. The description of this specialized technique will be addressed in Sect. 4.6.

Of course, in the limiting case where FWHM is beyond 0.5 pixels limit, the real PSF is likely to be much smaller than the pixel size, and consequently the loss of photometric and astrometric accuracy would be unavoidable regardless the analysis technique used.

2.1.3   Noise

As was introduced around Eq.2.1, h_j is the projected (blurred) version of the object a_i. This term incorporates two noise sources: photon and readout noises.

As photon noise, this is inherent to the fundamental property of the quantum nature of light. The collected charge in CCD exhibits the Poisson distributed statistics, so that the probability of obtaining a realization of intensity k coming from a source of mean flux h_j is given by the probability:

$$\mathbf{P}(k|h_j) = e^{-h_j} \; \frac{(h_j)^k}{k!} \tag{2.4}$$

The uncertainty over every realization is $\sigma = \sqrt{h_j}$. Therefore, from the practical point of view, photon noise turns to be multiplicative and can be fully characterized by simply knowing the intensity (in ADUs[4]) in every pixel.

As readout noise, this is introduced in the analog-to-digital conversion by the CCD amplifier. It is zero mean distributed with with a dispersion $\sigma(e^-)$, so that the probability of obtaining a particular realization p_j from k is:

$$\mathbf{P}(p_j|k) = \frac{1}{\sqrt{2\pi}\sigma} \exp\left[-\frac{(k-p_j)^2}{2\sigma^2}\right] \tag{2.5}$$

Practically, the calculation of the readout noise measured in electrons requires the estimation of $\sigma(\text{ADU})$ and gain of the amplifier $g(e^-/\text{ADU})$. These can be empirically derived from calibration frames (bias, dark and flatfield frames).

---

[4]Analog-to-Digital Unit

The compound probability from Eqs. 2.4 and 2.5 can be understood as the probability of obtaining a realization p_j given the mean h_j and all its possible Poissonian realizations k. This can be expressed as (Núñez & Llacer 1993):

$$\mathbf{P}(p_j|h_j) = \sum_{k=0}^{\infty} \frac{1}{\sqrt{2\pi}\sigma} \exp\left[-\frac{(k-p_j)^2}{2\sigma^2}\right] e^{-h_j} \; \frac{(h_j)^k}{k!} \tag{2.6}$$

2.1.4 Image deconvolution: an ill-conditioned inverse problem

We stated the image model in Eq. 2.1. For convenience, we reformulate this in terms of operators as:

$$\mathcal{F}[a] \to p \tag{2.7}$$

The deconvolution problem consists in estimating the object emissions a_i from a set of measurements p_j, assuming that the PSF f_{ji}, the background b_j, the gain corrections C_j and the uncertainty σ of the readout noise n_j are known. In other words, we aim to find $\mathcal{F}^{-1}$ so that:

$$\mathcal{F}^{-1}[p] \to a \tag{2.8}$$

In most astronomical images, the existence of $\mathcal{F}^{-1}$ is assured. However, it might not be unique and stable. The latter means that an small perturbation ϵ in p can largely deviate our solution from a, i.e.:

$$\mathcal{F}^{-1}[p + \epsilon] = a + \delta \tag{2.9}$$

with $\delta \gg \epsilon$.

In the case of a noiseless image, $\mathcal{F}^{-1}$ is unique and stable, and can be obtained via linear restoration methods, such as Fourier-quotient Method, Constrained Least Squares (Hunt 1973), Wiener filter (Helstrom 1967) or its derivatives (Katsaggelos 1991; Tikhonov et al. 1987).

However, if noise is present the solution is very sensitive to this and not unique. In other words, the inversion problem is ill-conditioned as Eq. 2.9 describes. Consequently, the solution a should be sought by deconvolution algorithms which make assumptions about the statistical properties of the noise distribution.

A number of different approaches has been proposed in the literature. Just to mention the most classic ones: CLEAN (Högbom 1974), Maximum Entropy Method (MEM) (Cornwell & Evans 1985; Frieden 1978), Maximum Likelihood Estimator (MLE) method (Lucy 1974; Richardson 1972) and Bayesian-based algorithms (Núñez & Llacer 1993; Snyder et al. 1993). All can be classified attending four basic characteristics, namely: additional hypothesis in image formation model, regularization constraints for conferring uniqueness and stability to the solution, numerical techniques for seeking convergence and validation tests for assessing convergence level. As the scope of this section is not to extensively review all these approaches, we refer the reader to Molina et al. (2001); Puetter et al. (2005); Starck et al. (2002) for three in-depth reviews where most proposed algorithms are fully detailed. We will focus our study over the family of MLE methods.

2.2   Maximum Likelihood Estimator

This deconvolution algorithm takes into account a correct statistical description of the noise present in the data. It aims the maximization of the likelihood function. The resulting image is the one with the measurements of highest probability.

Lucy (1974); Richardson (1972); Shepp & Vardi (1982) first introduced this method for data with Poissonian noise. This is commonly known as Richarson-Lucy algorithm. Later, this was extended to the typical situation of CCD images where Poissonian and Gaussian noises are combined (Núñez & Llacer 1993; Snyder et al. 1993). Below we introduce this latter variant of the algorithm.

First, we consider the combined Poisson and Gauss noise distribution as deduced in Eq. 2.6. The likelihood of that expression is:

$$\mathbf{L} = \mathbf{P}(\mathbf{p}|\mathbf{h}) = \prod_{j=1}^{D}\sum_{k=0}^{\infty} \frac{1}{\sqrt{2\pi}\sigma}\ e^{-\frac{(k-p_j)^2}{2\sigma^2}} e^{-h_j}\ \frac{(h_j)^k}{k!}\ , \qquad (2.10)$$

and its logarithm:

$$\log\mathbf{L} = \sum_{j=1}^{D}\left[-\log(\sqrt{2\pi}\sigma) - h_j + \log\sum_{k=0}^{\infty}\left(e^{-\frac{(k-p_j)^2}{2\sigma^2}}\ \frac{(h_j)^k}{k!}\right)\right]\ . \qquad (2.11)$$

Second, by imposing conversation of energy (with μ as a Lagrange multiplier) from Eq. 2.1 and compressing notation with $q_i = \sum_j \frac{f_{ji}}{C_j}$, we consider the following

functional:

$$
\begin{cases}
F_{MLE} &= \displaystyle\sum_{j=1}^{D} \left[-\log \sqrt{2\pi}\sigma - \frac{(p_j - \sum_{l=1}^{B} f'_{jl}\, a_l\, b_j)^2}{2\sigma^2} \right] - \\[2mm]
& \mu \left(\displaystyle\sum_{i=1}^{B} q_i\, a_i \;-\; \sum_{j=1}^{D} p_j \;+\; \sum_{j=1}^{D} b_j \right)
\end{cases}
\tag{2.12}
$$

Eq. 2.12 is clearly nonlinear. A number of minimization techniques for F_{MLE} are available in the literature: Steepest Ascent, Conjugate Gradient, Expectation Maximization (Dempster et al. 1977; Shepp & Vardi 1982) and Successive Substitutions (Hildebrand 1987; Meinel 1986). The latter, which consists in a series of equations of the type $a^{(k+1)} = F_{MLE}(\{a^{(k)}\})$, was chosen due to greater flexibility and fast convergence.

Finally, by setting $\frac{\partial F}{\partial a_i} = 0$ and some algebraic intermediate steps (see Núñez & Llacer (1993)) the following expression for the Maximum Likelihood Estimator algorithm is obtained:

$$
a_i^{(k+1)} = K a_i^{(k)} \left[\frac{1}{q_i} \sum_{j=1}^{D} \frac{f_{ji}\, p'_j}{\sum_{l=1}^{B} f_{jl}\, a_l^{(k)} + C_j b_j} \right]^n \quad i = 1, \cdots, B
\tag{2.13}
$$

where the auxiliary variable p'_j was defined for notation convenience as:

$$
p'_j = \frac{\displaystyle\sum_{k=0}^{\infty} k\, e^{\frac{-(k - p_j)^2}{2\sigma^2}} \left[\frac{(h_j)^k}{k!} \right]}{\displaystyle\sum_{k=0}^{\infty} e^{\frac{-(k - p_j)^2}{2\sigma^2}} \left[\frac{(h_j)^k}{k!} \right]}
\tag{2.14}
$$

p'_j can be understood as an always positive representation of the data which depends on the projection h_j and σ. K is the normalization constant to conserve the energy (Eq. 2.12), n is an acceleration parameter.

The term inside brackets in Eq. 2.13 is called projection-backprojection, since it can be understood as the blurring projection (denominator) from object to image space and deblurring backprojection from image to object space.

$a^{(k)}$ is successively modified by being multiplied by the factor inside brackets as it approaches the point of maximum likelihood. In most astronomical images, MLE solution approaches to the real object during the first range of iterations, but after a certain point it departs from it until it reaches an $a^{(k)}$ which mathematically matches

the noise distribution. The fact that mathematical and physical convergences do not coincide is a drawback of MLE, since it forces to stop the process at an arbitrary number of iterations $n_{\text{it}}^{\text{max}}$ for preventing noise amplification. This is fixed by the user attending the specific features of the data. In that sense, $n_{\text{it}}^{\text{max}}$ can be understood as a regularization parameter. Other constraints incorporated in this deconvolution algorithm are the positivity of the solution, the flux preservation and cutoff frequency for the PSF.

The particular implementation of Richarson-Lucy algorithm used along this thesis is the one included in `lucy` task (Snyder 1991) of the `STSDAS` package inside `IRAF`[5] reduction facility, which turns to be a maximum likelihood estimator under Poissonian and Gaussian noise.

2.3 AWMLE: Adaptive Wavelet-based Maximum Likelihood Estimator

The concept of multiresolution was firstly introduced in deconvolution by Wakker & Schwarz (1988) when defining the CLEAN algorithm for interferometric images. But it was not until the appearance of wavelets that astronomers have applied this transform to classical deconvolution methods. In the particular case of MLE, its different variants based in wavelets have shown an outstanding performance for solving the noise amplification with number of iterations.

In this section we introduce the wavelet transform concept and present the wavelet-based algorithm employed in this part of the thesis.

2.3.1 Wavelets overview

Astronomical images contain features which span all over the spatial domain (stars, galaxies, nebula, planets). Fourier decomposition cannot optimally represent this variety of signal content, thus a multiscale approach is better suited for this situation.

---

[5]IRAF is distributed by the National Optical Astronomy Observatories, which are operated by the Association of Universities for Research in Astronomy, Inc., under cooperative agreement with the National Science Foundation.

The concept of multiresolution has been widely used in image processing. The main idea behind is to transform the data so that an efficient localization of spatial and frequential contents is simultaneously available. The wavelet transform is one of the mathematical tools which best responses to this aim (Mallat 1989).

It is beyond the scope of this section to give a detailed mathematical overview of the wavelet theory. We refer the reader to Otazu (2001); Starck et al. (1998) and references therein, for deeper description of this topic. We focus our discussion in highlighting a list of the most interesting properties of wavelet transform:

1. A multiscale decomposition of the data is provided, keeping spatial and frequential contents effectively decoupled for posterior processing.

2. In comparison to Fourier transform, wavelet offers better noise vs signal discrimination, since the former is uniformly distributed over all coefficients and the latter is concentrated in a few coefficients.

3. Usual noise distributions (Poissonian, Gaussian) have well defined propagation expressions into the wavelet transform space.

The *à trous* decomposition algorithm

There are different wavelet decomposition algorithms in the literature. Each one differs in a number of properties (employed basis or scaling function, isotropy, redundancy, decimation, etc.) which may be appropriate depending on the data context. In the specific case of image deconvolution, the so-called *à trous* algorithm has been widely used. In addition, it has also been successfully applied to remote sensing image fusion, which is one of the mainstream research areas in our group (González-Audícana et al. 2005, 2006; Núñez et al. 1997, 1998, 1999a,b; Otazu et al. 2005).

The *à trous* algorithm is isotropic, shift invariant, redundant, undecimated and with a cubic B_3-spline as scaling function. All these aspects result very convenient for astronomical images. First, most objects in these images are isotropic. Second, the number of coefficients in the decomposition is equal to the number of samples in the data multiplied by the number of scales. And third, the shape of B_3-spline function resembles a 2D-Gaussian function, which fits very well a stellar profile.

More in detail, given a 2D image $\mathbf{p}$, the *à trous* algorithm constructs a sequence $F_m[\mathbf{p}], m = 1, \cdots M$ of approximations of $\mathbf{p}$. In this multiresolution representation, $F_m[\mathbf{p}]$ is the closest approximation of $\mathbf{p}$ with resolution 2^m. The difference between two consecutive scales m and $m + 1$ is designed as the wavelet or *detail* plane ω_m^p at resolution 2^m, which has the same number of pixels than $\mathbf{p}$. Another interesting property of this algorithm is that the original image can be straightforward reconstructed from the sum of all the wavelet planes and of the coarsest resolution image, $c_n^p = F_n[\mathbf{p}]$:

$$\mathbf{p} = \omega_1^p + \omega_2^p + \omega_3^p + \cdots + \omega_n^p + c_n^p \ . \tag{2.15}$$

In other words, the proposed wavelet transform can be understood as the expansion of $\mathbf{p}$ in a set of base functions defined by scaling functions ϕ of the B_3-spline family. Hereafter, we will assume that residual image c_n^p is implicit in all the expressions where the sum of all the wavelet planes $\omega_i^p \ \ i = 1, \cdots, n$ appears.

Fig. 2.3 illustrates what is expressed in Eq. 2.15 for the case of a decomposition up to M=4 scale. Note the frequency of the features represented in a given wavelet plane decreases with the scale index. For example, ω_1 contains highest frequency details (noise, cosmic rays and some stars) while in ω_4 the extended low frequency emission of the arms of the galaxy dominates.

Another important property of decomposition as Eq. 2.15, is that the residual plane c_n^p retains all the energy of the original image $\mathbf{p}$. Consequently, all the wavelet planes ω_i^p are zero mean images.

2.3.2 Adaptive algorithm

As commented in Sect. 2.2, noise amplification prevention is a key concern for whatever deconvolution algorithm, specially for MLE. Wavelet transform can help in this situation.

In the next we present the algorithm employed in this part of the thesis. It is called Adaptive Wavelet-based Maximum Likelihood Estimator (AWMLE), and was first presented in Otazu (2001). We refer to that study for a detailed description of the algorithm. The following ideas define the backbone of AWMLE:
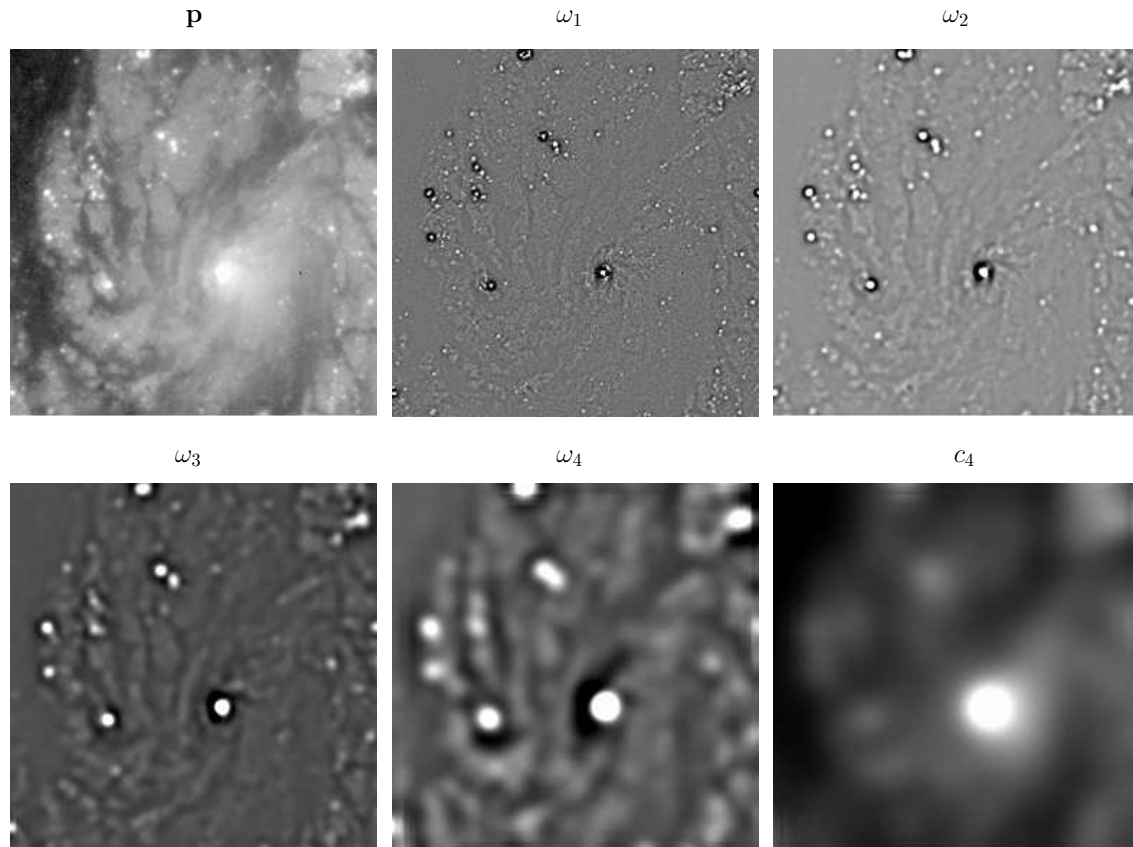
Figure 2.3: Example of effective frequency discrimination of the "*à trous*" wavelet decomposition in separate wavelet (or detail) planes. From left to right and top to bottom: **p** is the original image, ω_1, ω_2, ω_3 and ω_4 the wavelet planes in decreasing order of resolution, and c_4 the residual plane at the scale 4.

1. The effective spatial and frequential localization in different planes of the wavelet transform results in a greater flexibility for MLE to deal with a multichannel deconvolution. Therefore, AWMLE operates over the wavelet planes and not the original image.

2. Noise is mostly concentrated in the few wavelet planes corresponding to the highest frequency range. This allows to selectively deconvolve each plane attending its global SNR characteristics.

3. On one hand, not all the signal features in an image spread its frequential content along the wavelet planes in the same way (see Fig. 2.3). On the other hand, the propagation of Poissonian and Gaussian noise distributions through the wavelet space is well-known (Starck et al. 1998). As a result, well defined significance SNR thresholds can be applied to all the pixels in every wavelet

plane for selectively deconvolving statistically similar regions. This concept is called multiresolution support or probability masks.

The idea behind is, to use this multiresolution support definition, for filtering the residuals in every wavelet plane between consecutive iterations, setting the noise related ones to zero, and leaving only significant structures. In other words, an adaptive regularization in the convergence of the solution is applied. In this way, the minimum elementary unit to be deconvolved is not the wavelet plane but those pixel areas which exhibit similar degrees of resolution and SNR levels.

Below we mathematically formalize those ideas above.

The significance threshold for the pixel i in the wavelet plane ω can be defined as a continuous and normalized probability mask, or multiresolution support, of the form:

$$m_i = \begin{cases} 1 - exp\left\{\frac{-\left(\frac{3}{2}(\sigma_i - \sigma_\omega)\right)^2}{2\,\sigma_\omega^2}\right\} & \text{if } \sigma_i - \sigma_\omega > 0 \\ 0 & \text{if } \sigma_i - \sigma_\omega \leq 0 \end{cases} \quad (2.16)$$

with

$$\sigma_i = \sqrt{\frac{\sum\limits_{j \in \Phi} (\omega_{m,j})^2}{n_f}} \;,$$

where

$$\omega_{m,j} = \omega_{m,j}^p - \omega_{m,j}^h$$

is what remains in the wavelet plane due to noise, being $\omega_{m,j}^p$ is the j-th plane of the data and $\omega_{m,j}^h$ is the j-th plane of the projected data. $\omega_{m,j}$ is also called the residual of the multiresolution support. σ_i is the standard deviation in the subwindow Φ, sized n_f pixels and centered in the pixel i. σ_ω is the standard deviation of the Poissonian+Gaussian noise distribution in the wavelet plane ω.

The concept of multiresolution support applied to deconvolution was first introduced by Donoho & Johnstone (1993); Starck & Murtagh (1994). However, the latter authors proposed a hard thresholding mask ($m_i = 0$ or 1) instead a continuous probability as the one proposed here.

Taking into account the three expressions above and the *à trous* decomposition in Eq. 2.15, the expression for the MLE algorithm (Eq. 2.13) can be rewritten in

the wavelet space as:

$$a_i^{(k+1)} \;=\; K \; a_i^{(k)} \left[\frac{1}{q_i} \sum_{j=1}^{D} \frac{f_{ji} \sum_{i_\omega} \left(\omega_{i_\omega,j}^{h\,(k)} + m_{i_\omega,j}(\omega_{i_\omega,j}^{p'} - \omega_{i_\omega,j}^{h\,(k)}) \right)}{\sum_{l=1}^{B} f_{jl}\, a_l^{(k)} + C_j\, b_j} \right]^n \quad . \qquad (2.17)$$

Note the similarities with Eq. 2.13. Both are based in the Maximum Likelihood Estimator. The structure and the projection term are the same, but there are significant differences. First, the backprojection term incorporates a summation over the wavelet planes. As a result, p' and h have been substituted by $\sum_{i_\omega} \omega_{i_\omega}^{p'}$ and $\sum_{i_\omega} \omega_{i_\omega}^{h}$. This incorporates the first item of gaining in flexibility through multichannel deconvolution stated in Pag 45. Second, the use of multiresolution support (Eqs. 2.16) is included. This addresses the third idea stated in the same page, about including adaptive regularization for those significant structures which show similar degrees of statistical signature.

Note that the use of probability masks in AWMLE avoids large residuals (noise artifacts) which appeared in well-advanced MLE deconvolutions. On the contrary, they asymptotically stabilize the solution until no more significant structures are found in the residual of the multiresolution support. As a result, AWMLE removes the dependence on the number of iterations, and there is no need to stop the deconvolution.

2.3.3 AWMLE computational performance

One important aspect of deconvolution algorithms is their computational cost. MLE requires 2 FFTs per iteration, which implies a cost is of $O(N^2 \log_2 N)$ operations in the case of $N \times N$-pixel images. In comparison, AWMLE requires $4+2N_\omega$ FFTs per iteration and $O(N_\omega N^2 \log_2 N)$ operations, where N_ω is the number of planes considered in the wavelet decomposition. The inclusion of multichannel and probability masks concepts justifies this increase.

The computational performance of AWMLE is illustrated in Tab. 2.1. These tests correspond to a sequential (non parallel) implementation of AWMLE run in a non dedicated desktop Linux PC (Pentium-IV 2.6GHz 1Gb RAM). Two key parameters are included: execution time and RAM usage. Note that while the latter is a bit

less than linear dependent with image size, the former overpasses the linearity. This overhead might be due to a non optimal use of the cache memory which can lead to inappropriate use of slower swap memory.

Table 2.1: Computational performance of the AWMLE algorithm in terms of execution time and RAM usage as a function of input image size. This test was run in sequential mode (non parallel) in a non dedicated desktop Pentium-IV 2.6GHz 1Gb RAM running Linux kernel 2.6.

Input image size (pixels)	Execution time (seconds per iteration)	RAM usage (Mb)
256x256	1.43	11.1
1024x1024	38.58	147.5
2048x2048	189.76	600.3

2.4 Deconvolution and sampling

It is a well-known property of MLE (and also AWMLE) that FWHM of stellar profiles decreases with the number of iterations (Prades & Núñez 1997; Prades et al. 1997). As a result, deconvolved image becomes gradually more and more undersampled. As justified in Sect. 2.1.2, that sole effect does not necessarily translates into a loss of astrometric precision if adequate centering techniques are considered.

However, undersampling does not come alone when deconvolving. In the case of Richardson-Lucy (RL) algorithm, undersampling triggers the appearance of other related artifacts. The most remarkable one is the wavy oscillations which manifest in the surrounding of brightest stars when these are superposed on a non-negligible background. This is usually called *ringing* or, more generally, Gibbs oscillations. A number of papers (Cao & Eggermont 1999; Lagendijk & Biemond 1991; Lucy 1994; Magain et al. 1998) have revised the origin of this artifact. In summary, *ringing* is caused by the undersampling in the solution a_i in presence of a significant background level. In more detail, this artifact can be understood by the following reasoning:

RL attempts to recover stars in p_j as δ-functions in $a(\xi, \eta)$. However, what we finally get from this deconvolution method is the sampled version of $a(\xi, \eta)$, e.g.,

a_i. Those are bound by Eq. 2.3, where the $\frac{\sin(x)}{x}$ function matches the observed *ringing* artifact. In other words, *ringing* is the result of the incorporation of the pixel response function into a well-converged and undersampled solution a_i, where the stars approach to δ-functions. Only in the particular case that p_j does not contain any superposed background, then the positivity constraint will remove the Gibbs oscillations around bright stars, which otherwise would lead to values below the background level.

Note *ringing* prevents from any accurate measurement on the restored image. This is why background term b_j was incorporated into MLE (and AWMLE). These algorithms take into account the background in the image model as a lower bound constraint in the deconvolution convergence. Thus, the deconvolution is banned to take values below b_j. Of course, the key point is to obtain an accurate background map. If the technique employed for obtaining b_j is not appropriate (for example in the vicinity of bright stars), background could be biased and, as a result, *ringing* would again appear in those regions. We postpone this discussion of background map estimation to Chapt. 4.

Chapter 3

Data description

In this section we present the three CCD data sets to be considered for the application of MLE and AWMLE deconvolution algorithms described in Sects. 2.3 and 2.2. Although those CCD images are different in several aspects, all share their wide field of view nature and the fact they belong to survey programs: FASTT, QUEST and NESS-T.

We will start by briefly introducing the conceptual basis of the two acquisition schemes considered in this thesis: stare and drift scanning modes. These will define the data framework in the forthcoming Sections. Special attention to the understanding of the systematics errors involved in drift scanning observation will be devoted.

Next, we will overview the main characteristics of the three considered data sets. A basic data description, an in-depth overview of instrumental aspects concerning the followed acquisition mode and a brief outline of the scientific goals pursued by each survey program will be given.

All in all, it will help us to put into context the discussion of results and conclusions for each particular data set, in Chapts. 5. and 6, respectively.

3.1   Data acquisition schemes

In this subsection the instrumental basis of the data acquisition schemes later considered in Sect. 3.2 and forthcoming chapters will be introduced. We will focus our discussion in how CCD operates in each kind of acquisition scheme, in conjunction to the telescope. A discussion of the systematic errors involved when observing in those modes will be given. Special attention will be devoted to the cases of drift scanning and TDI, where a quantitative estimation of these errors will be exposed.

But before going through the details of different observing modes, we briefly introduce the four stages involved in the formation of a CCD image, as Janesick (2001) states. This will help us to clarify the nomenclature around this topic, which will be intensively used along this thesis:

1. **charge generation**: the physical principle of photoelectric effect states that an incident photon interact with silicon creating one free electron. The effectiveness of this process, known as quantum efficiency (QE), depends on photon wavelength, silicon structure, the addition of special coatings or the thinning of substrate layer to improve blue and UV response, and reflection losses.

   Apart from electrons induced from incident photons, also thermal electrons are spontaneously generated in the silicon. This is also known as dark current noise, which can be minimized by cooling the chip and calibrated and removed in posterior image analysis.

2. **charge collection**: once the photoelectrons have been generated, the following three factors play a key role in the capability of the CCD to reproduce an image: the number of pixels in the CCD array, the charge capacity of a pixel and the charge collection efficiency of every pixel. The first is only limited by cost reasons. The second accounts for the number of electrons a pixel can hold, and is inversely proportional to pixel volume. A larger well capacity translates into an improvement in the magnitude range attainable, without being harmed by either blooming in the bright end, or readout noise in the faint end. Concepts used in further discussions like dynamic range and saturation level are also intrinsically related to charge capacity. The third accounts for the change confination power inside a single pixel, or inversely, the charge diffusion across the neighboring pixels. This has incidence over the final spatial resolution of

the image, i.e. the PSF.

3. **charge transfer**: once the charge is generated and confined, this is transfered from every individual pixel towards a parallel sequence of pixels in a single column, called serial register. This process is done by clocking in the adequate order the voltages of the pixel gates along a given column of pixels. As a result, charge in every column is shifted to its immediate neighbour, and the last column of the chip release its charge to serial register. This is iterated until all the charge in the array has been transfered.

In this process some charge is lost in every column shift. This is accounted by charge transfer efficiency (CTE), which, given the accumulative nature of the loss and the large number of columns in a CCD, turns to be a key parameter for precise measurements. CTE is directly proportional to pixel volume, therefore a trade-off exists between this and well capacity. Finally, CTE can become important at two separate regimes: large format sensors and high pixel rates.

4. **charge measurement**: the final step once the column charge has been transfered to the serial register is to obtain a voltage which is proportional to the input signal. This is achieved by dumping the charge onto a capacitor connected to an amplifier. The sensitivity and linearity of this device becomes important parameters for the proper charge-voltage conversion. But the key parameter here is the noise introduced by the amplifier. This is commonly called readout noise, and its importance become decisive for low light level applications as astronomical imaging. Fortunately, the noise distribution of this noise is known to be Gaussian and its dispersion can be precisely calibrated. The output voltage from amplifier is converted to digital units (known as ADU) by the analog-to-digital converter (ADC).

The whole process of readout and analog-to-digital conversion can be operated at different rates and digitization depths. The first typically ranges from 10kHz to 10MHz and the second from 8 to 16 bits per pixel. A trade-off relation exists between both parameters. Well depth, readout noise, and amplifier gain are determining factors in the balanced election for digitization rate and depth.

Finally, this digital representation of the image is downloaded to the computer through the designed port.

3.1.1   Stare observing mode

This is the most common and classic observing mode in Astronomy. It can be summarized in the following steps:

1. the telescope is pointed to the target position and its tracking system is turned on at sidereal rate,

2. the exposure starts with the opening of the CCD shutter,

3. as the shutter remains open, charge generation and collection starts as previously described, according to the incoming intensity. The target remains over the same position of the CCD: this is why is named *stare* mode.

4. the shutter is closed when the exposure time has been reached,

5. the charge transfer and measurement stages are started until no charge is left in the CCD chip.

6. once all columns have been readout, the whole image is transfered to the computer, and the system is ready to perform another exposure.

How fast this process is executed depends on a number of factors. First, integration time can be fixed arbitrarily long, only being constrained by the accuracy of telescope tracking system and the CCD saturation level. Second, the time spent by the camera to readout and transfer depends basically of two specifications which are fixed for each prototype. On one hand, the digitization rate is fixed by CCD micro-controller design and digitization depth. On the other hand, the data transfer rate is specified by port architecture being used in the way from camera to computer (parallel port, USB, Ethernet, etc.).

The errors involved in stare mode, are well-known. In the following we briefly outline the most important ones and their properties. A very exhaustive discussion of all these errors can be found in Janesick (2001).

For almost all cases, a well defined division between random and systematic noise sources can be established. On the random side, Poissonian photon noise and Gaussian readout noise are the most remarkable errors sources in CCD imagery, as

were fully described in Sect. 2.1.3. On the systematic side, the following are the most common effects which contribute to inaccurate measure of either (or both) astrometry and photometry:

Pixel nonuniformity response

This is an important effect to be taken into account, above all in photometry programs. It is caused by the differential behaviour of each pixel in charge generation and collection stages. This particular response for each pixel typically fluctuates below 1% in current CCD cameras. An accurate modelling of this effect is not a priori possible, but since its systematic nature, it can be removed from dividing the data by flatfield frames taken at the same night. Actually, flatfield correction accounts for other effects unrelated to CCD image formation process, as vignetting, dust and variation of encircled energy across the FOV which may be due to other parts of the imaging system (detector location, optical design, etc.).

Pixel response function

Another systematic error which is present in all CCD images under stare mode is the profile broadening due to pixel response function. As was introduced in Sect. 2.1.2, this is a natural result of sampling the intensity into square pixels. In the following, we quantify the blurring caused by this effect. Let $\Pi(\theta)$ be the pixel response function, defined as:

$$\Pi(\theta) = \begin{cases} 1 & |\theta| \leq 0.5 \\ 0 & |\theta| > 0.5 \end{cases} \tag{3.1}$$

and let $f(\theta)$ be the point spread function (PSF) which is to be sampled by the CCD, to be a Gaussian function, defined as:

$$f(\theta) = \frac{1}{\sqrt{2\pi}\sigma} \exp\left[\frac{-(\theta - \theta_0)^2}{2\sigma^2}\right] \tag{3.2}$$

where θ_0 is the distance between the Gaussian's peak and the centre of the pixel n. Now, if we assume uniform sensitivity throughout the pixel area, the resulting intensity in the pixel n is:

$$I_n = f(\theta) * \Pi(\theta) = \int_{-\infty}^{\infty} \Pi(n - \omega - \theta - \frac{1}{2}) f(\theta) \, d\theta \tag{3.3}$$

where ω measures the distance of $f(\theta)$ from the centre of the pixel n at the time charge is transfered.

A graphical representation of Eq. 3.3 is shown in Fig. 3.3. $\Pi(\theta)$ (solid) can be seen in Fig. 3.3a, and $f(\theta)$ (solid) and $I_n(\theta)$ (dotted) in Fig. 3.3b. As a result of this pixel response convolution, the initial PSF suffers from a symmetrical elongation of the input FWHM of $\sim 9\%$, which translates into a peak decrease of $\sim 7\%$. Of course, that broadening effect depends on the data sampling, σ, as can be seen in Figs. 3.4 and 3.5.

As most CCDs have square pixels, the broadening effect turns out to be identical in both directions x and y, so that the ratio of $\mathrm{FWHM}_x/\mathrm{FWHM}_y$ is preserved.

Focal-plane positional errors

This error is completely independent of the acquisition scheme, but it is included in this enumeration for completeness.

As a result of distorsions in the optics, local irregularities in the pixel locations and mechanical deformation of the CCD, the CCD image turns to be a deformed representation of the FOV to be studied. This distorsion causes that every sky element with undistorted coordinates (x',y') becomes systematically shifted to the imaged coordinates (x,y). Of course, the magnitude and orientation of such shift is coordinate dependent.

This systematic error is present at all the telescopes-CCDs systems and its magnitude and distribution along the focal plane is particular to each case. In Sect. 3.2, a quantitative estimation of this effect will be given for the three data sets analyzed in this part of the thesis.

Clearly, if differential astrometry with respect to a reference catalogue is aimed, this is an error that must be calibrated an removed. Otherwise, the derived astrometry will be biased. However, it is noteworthy that if the stars in the frames to be reduced practically overlap in (x,y) system[1] and only multiframe pixel astrometry is performed[2], the impact of this systematic error is greatly diminished.

---

[1]This is our case in all three data sets.

[2]Without the use of a reference catalogue. That will be our approach, as explained in Sect. 4.7.

Differential Color Refraction

Again, this error is not related with the acquisition scheme, but it is introduced here in order to compare its importance with the rest errors.

As it is well-known, the atmosphere acts as a refracting prism which modifies the zenithal distance of a source, as this approaches to the horizon. This also contributes to the degradation of stellar profiles as a function of spectral type, as shown in Stone (1984). The refraction effect decreases from blue to red stars. Other minor dependences in the overall refraction come from atmospheric and instrumental parameters. Usually, this refraction correction is computed in two separate components: a mean and a differential color dependent refractions. In general, the refraction correction will be different for each observing site.

CTE and magnitude-related errors

The concept of charge transfer efficiency (CTE) was already introduced in Pag. 53. The more CTE value deviates from 1, more and more photoelectrons are left behind and lost from the final readout, as charge is transfered in column-by-column basis towards the serial register. As a result, the stellar profiles become more and more asymmetric in the transfer direction as its x coordinate is further from serial register and the lower is its intensity. In conclusion, the centroids are shifted and astrometry can be distorted. Equally, the same effect can appear in the parallel register direction.

Other errors

Other errors sources like cosmic rays, cosmetic noise, CTE noise at high pixel rates and network decoupling can be of primary importance for the nature of the data which will be managed in this thesis. The first two are self-explanatory and will appear in Chapts. 4 and 5 when discussing how deconvolution and posterior analysis should deal to regions affected by those effects. The last two will be relevant in Part II of this thesis, and will be discussed in Chapts. 7 and 8.

3.1.2 Drift scanning observing mode

This observing mode can described as follows, as shown in Fig. 3.1:
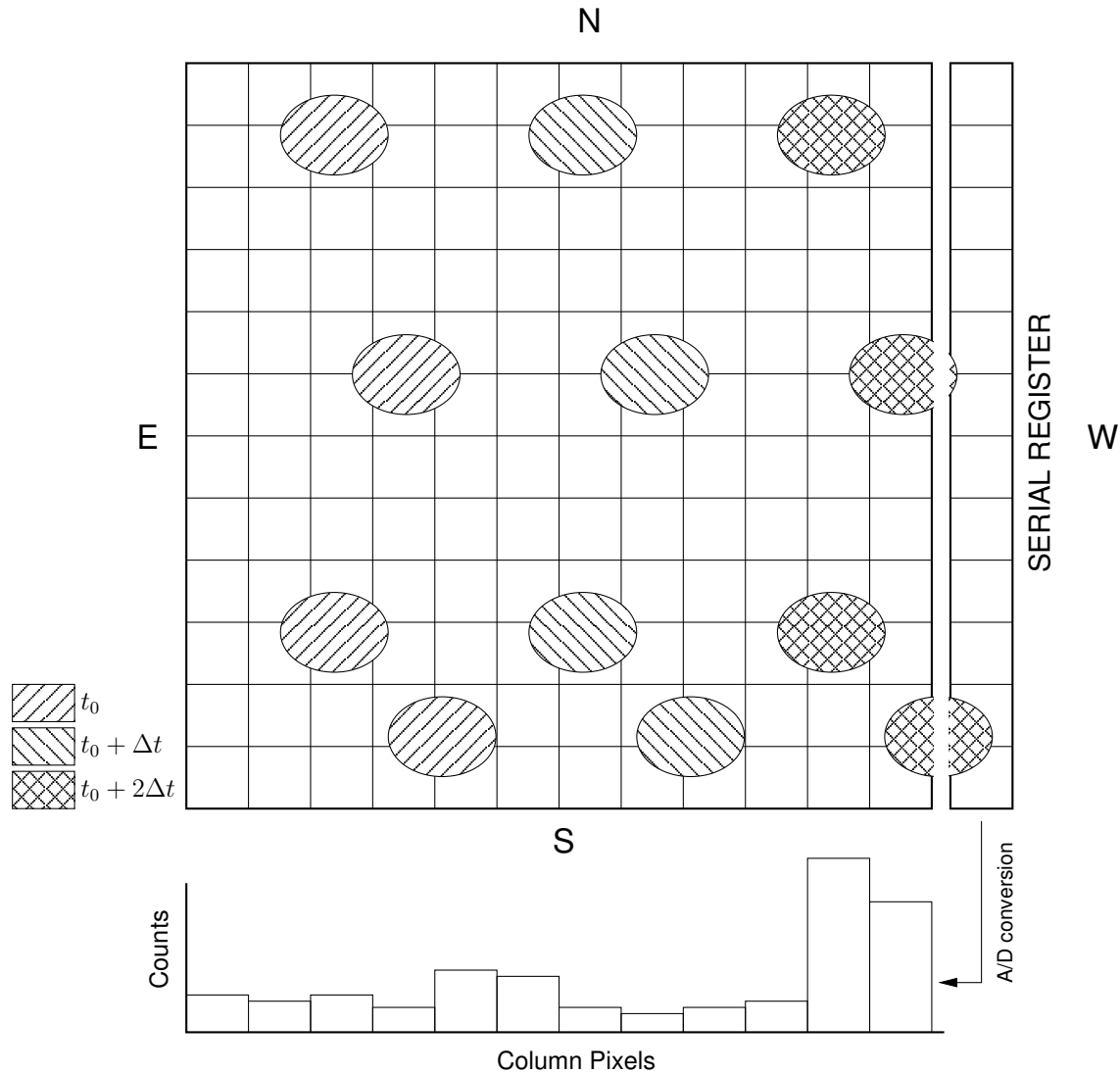
Figure 3.1: Sequence diagram of drift scanning acquisition mode. A four star field is represented by ellipses with changing pattern at each transfer interval. The column charge is transfered along the E-W direction at a sidereal rate, Δt, simultaneously with serial register readout. See Pag. 61 for the justification of the stellar elongation shown. Adapted from McGraw et al. (1982).

1. the CCD camera is oriented so that the axis which is parallel to the column transfer direction is aligned to the E-W direction,

2. the telescope is kept physically fixed (tracking system turned off),

3. the shutter is open,

4. every column of the CCD is transfered and readout at the sidereal rate corresponding to the observed declination,

5. the shutter is closed.

Note that, in contrast to stare mode, the four stages of CCD image formation described in Sect. 3.1 are all executed in sequential order in a column by column basis at each sidereal cycle. Therefore, no dead time exists after the shutter is closed for reading out and downloading the whole array, since these have already been done while the exposure was taking place. Also, it is worth remarking that the equivalent exposure time for each object is only fixed by the angular size of the CCD. The total time with the shutter open can be arbitrarily large, even spanning the whole night.

Another particularity of drift scanning technique (and TDI, too) is that the data is naturally flatfielded by the observing mode itself. This happens because the sky is sampled by every pixel in a row for a fixed amount of time. In other words, this piece of sky is detected with the mean quantum efficiency of all the pixels in the row. This results in a more efficient observation, both in terms of observation time (stare flatfield is not necessary) and minimization of pixel-to-pixel variations, which in most cases are below 0.1% rms, compared to habitual $0.3 - 0.5\%$ rms of stare mode (Gibson & Hickson 1992).

This observing technique was first used by McGraw et al. (1980, 1982, 1986) for accurate relative astrometry of extense areas of sky, and by Gehrels (1981); Gehrels & McMillan (1982); Gehrels et al. (1986) in the framework of Spacewatch project. Since then this mode has been extensively used, above all when maximizing the observing efficiency is demanding (see Table 3.1). Note that most of experiences correspond to transit instruments (meridians or zenithal telescopes) or Schmidt cameras which have been readapted to this observing mode. A variant of drift scanning technique has also has been applied to IR arrays (Bloemhof et al. 1986, 1988; Gorjian et al. 1997), which does not follow the same clocking scheme as CCDs, but each pixel is read out directly by connecting its signal to an output amplifier.

Table 3.1: Surveys operated in drift scanning mode.

Name or Location	Purpose	Reference
Palomar-Prime Focus	Large redshift QSOs search	Schmidt et al. (1986)
Universal Extragalactic Instrument		
Spacewatch Project	Long-term Solar System objects search	Gehrels et al. (1986, 1990)
Crux and Centaurus Cepheids Survey	Cepheids variables search	Caldwell et al. (1991)
CCD/Transit Instrument	Accurate relative astrometry	Benedict et al. (1991)
Swope scanning camera	Multi-band photometry of South Galactic Pole	Caldwell & Schechter (1996)
Flagstaff Transit Telescope	Densification of HIPPARCOS/Tycho Reference Frame	Stone et al. (1996, 2003)
The Great-Circle Camera	Large Magellanic Cloud Survey	Zaritsky et al. (1996)
Bordeaux Meridian Circle	Densification of HIPPARCOS/Tycho Reference Frame	Rapaport et al. (2001)
Venezuela-QUEST Survey	QSOs and gravitational lenses,SNs,GRBs,TNOs	Baltay et al. (2002)
		Rengstorf et al. (2004a)
Large Zenith Telescope Survey	Spectrophotometry of galaxies to $z \sim 1$	Cabanac et al. (2002)
Carlsberg Meridian Telescope Survey	Densification of HIPPARCOS/Tycho Reference Frame	Evans et al. (2002)
		Belizón et al. (2003)
ROA Meridian Circle at Felix	Densification of HIPPARCOS/Tycho Reference	Muiños et al. (2003)
Aguilar Observatory (Argentina)	Frame for Southern declinations	
Palomar-QUEST Survey	QSOs and gravitational lenses,SNs,GRBs,TNOs	Djorgovski et al. (2004a)

We saw in Sect. 3.1.1 how all the presented error sources of stare observing mode were on-chip based, i.e., exclusively originated in the four stages of CCD image formation process. In contrast, we will see in forthcoming lines that drift scanning mode (and TDI too) shows an additional number of off-chip systematic errors due to the observing mode itself. For further reading about these effects see Gibson & Hickson (1992). Note the authors in this article used reversed nomenclature when referring to drift scanning and TDI modes, with respect to the one used in this part of the thesis. Actually Mackay (1982) was the first to use the *drift scan* term referring to what we call now TDI. However, all posterior literature with the only exception of Gibson & Hickson (1992) followed the reversed denomination, so we adopted this terminology.

Ramping effect

As a consequence of steps presented in the beginning of this Section, the first columns to be readout short after the shutter opening have few charge accumulated. As drift operation goes on, columns initially further from the serial register, accumulate more and more charge. As a result, the mean charge along a column linearly raises up to a given value. This is called *ramping* effect. From there, all the sky portions being readout have passed over all columns of the CCD, and that mean value remains stable. The same ramping effect applies for the tail of the scanning strip, which also spans the size of the CCD array.

This effect is represented in Fig. 3.2, a and d correspond to the shutter opening and closing, and b and c delimit the stable part of the strip.

Of course, this ramping represents a loss of efficiency as regards as the data collected. However, if flat part of the strip ($\overline{bc}$) is much longer than ramps ($\overline{ab}$ and $\overline{cd}$), which is the most usual case, such loss is greatly compensated with respect to dead time dedicated to readout in stare mode.

Discrete shifting effect

This effect was early anticipated by McGraw et al. (1982), but it was not until Gibson & Hickson (1992) which was quantitatively analyzed. In the forthcoming lines we summarize what it is further explained in that article.
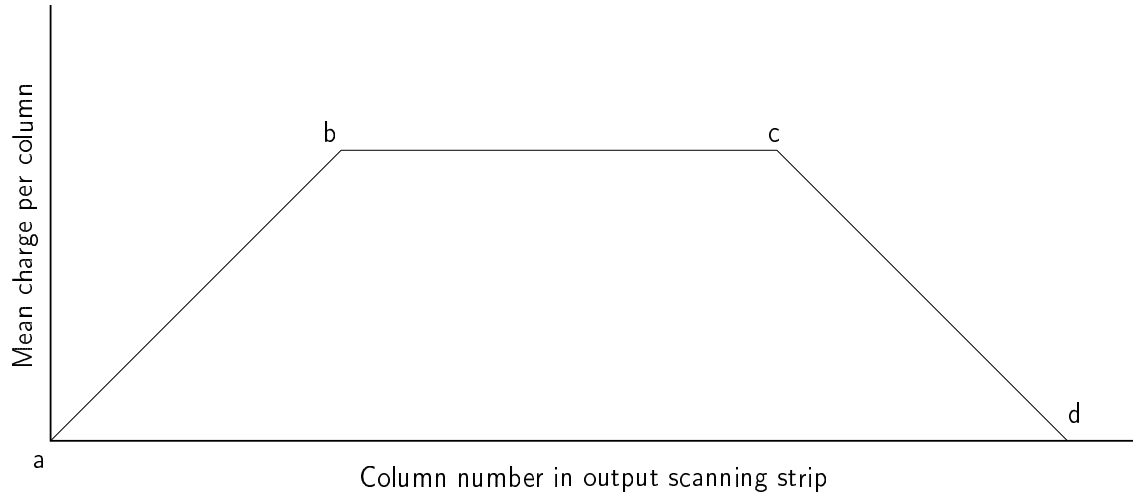
Figure 3.2: Ramping effect in a drift scanning strip.

Discrete shifting effect yields to a symmetric smearing of the image profile along the E-W direction, due to motion of this stellar profile along a CCD row. This can be modeled by the triangle function $\Lambda(\theta)$, defined as:

$$\Lambda(\theta) = \begin{cases} -\theta & -1 \leq \theta \leq 0 \\ \theta & 0 < \theta \leq 1 \end{cases} \tag{3.4}$$

The resulting sampled intensity function will become the convolution of the PSF to be sampled $f(\theta)$ with $\Lambda(\theta)$ and the pixel response function (Π), already defined in Sect. 3.1.1:

$$I_n = f(\theta)*\Lambda(\theta)*\Pi(\theta) = f(\theta)*h(\theta) = \int_{-\infty}^{\infty} h(n - \omega - \theta - \frac{1}{2})f(\theta)\,\mathrm{d}\theta \tag{3.5}$$

where the n and ω are defined in the same way as Eq. 3.3.

As can be seen in Fig. 3.3, the discrete shifting effect causes a broadening in FWHM_x and an intensity peak decrease. This translates into a loss in resolution and a drop in mean SNR, respectively. In other words, an increase of limiting resolution and a decrease of the limiting magnitude which a survey can reach. In the specific case of the Fig. 3.3, the initial PSF suffers from an elongation of the input FWHM of $\sim 25\%$ and a intensity peak decrease of $\sim 19\%$. Of course, this broadening effect depends on the data sampling, σ, as can be seen in Figs. 3.4 and 3.5. From there we deduce that intensity peak (FWHM) suffers a severe decrease (increase) as we consider more and more undersampled data.
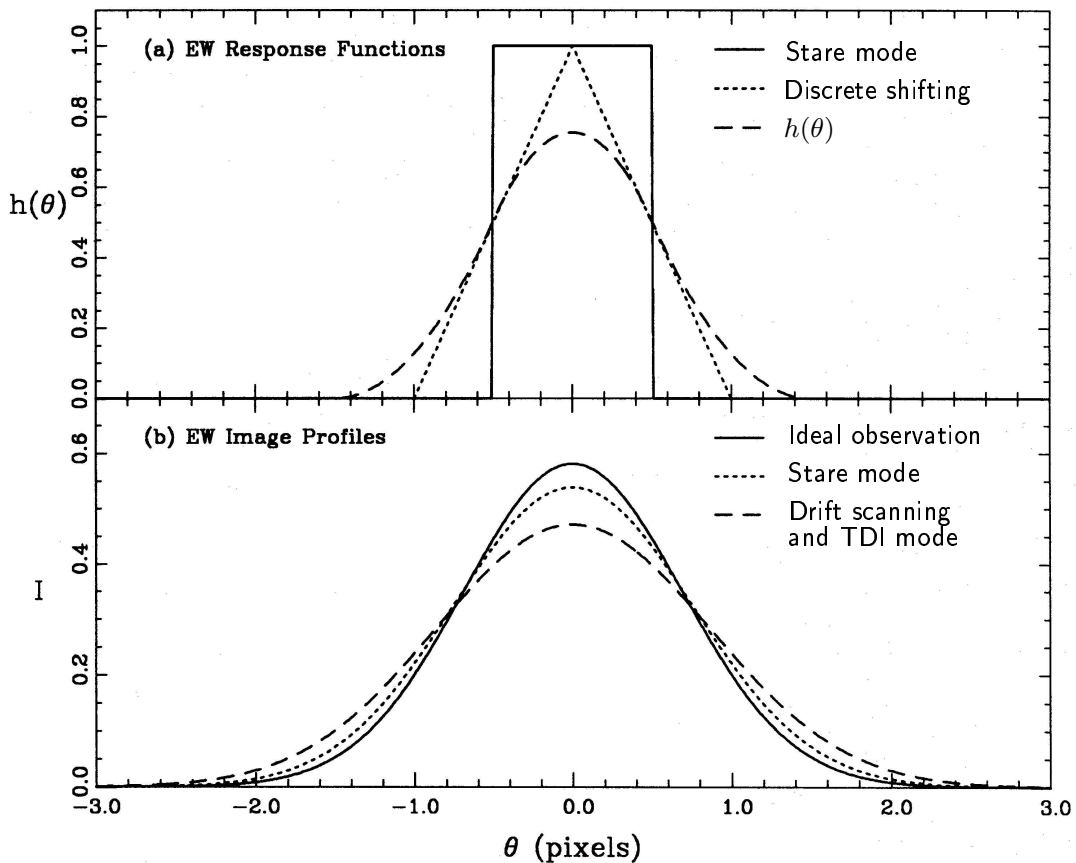
Figure 3.3: Effects of profile broadening due to pixel response function and discrete shifting. Top panel shows E-W (N-S in the case of TDI) profiles of pixel response function (solid), triangle function (dotted) and its convolution $h(\theta)$ (dashed). Bottom panel shows E-W (N-S in the case of TDI) profiles of the input Gaussian stellar profile (solid), which is midly undersampled ($\sigma = 0.686$ pixels), the distorted profile due to pixel response function (dotted) and discrete shifting effect (dashed). See Pag. 55 for explanation of ordinate θ. Adapted from Gibson & Hickson (1992).

Differential trailing

As mentioned in Pag. 59, all the pixels in a column are transfered at the same rate along the whole CCD array. However, this does not accommodates to what really happens with the sky projection over the chip: suppose we park the telescope at a declination δ_0, so that the central point of the CCD overlaps with this position, and we fix the transfer rate to the sidereal rate for δ_0. Of course for that central row the sky elements really scan at the appropriate nominal speed. Nevertheless, as we
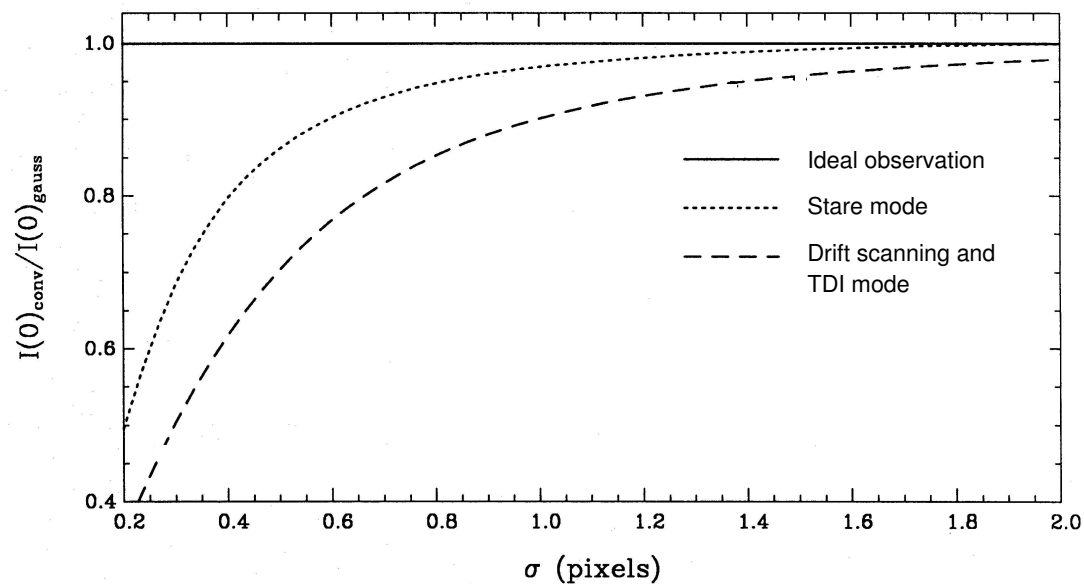
Figure 3.4: Effect of pixel response function and discrete shifting over the intensity peak of the input Gaussian as a function of its sampling, σ. Adapted from Gibson & Hickson (1992).
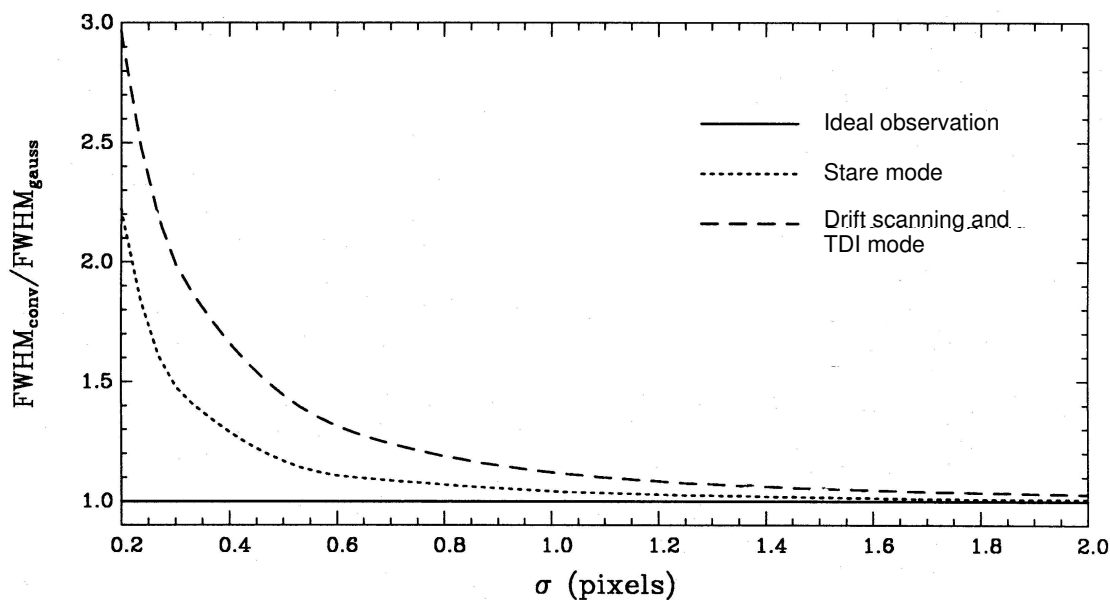
Figure 3.5: Effect of pixel response function and discrete shifting over the FWHM along the E-W (N-S in the case of TDI) direction for the input Gaussian as a function of its sampling, σ. Adapted from Gibson & Hickson (1992).
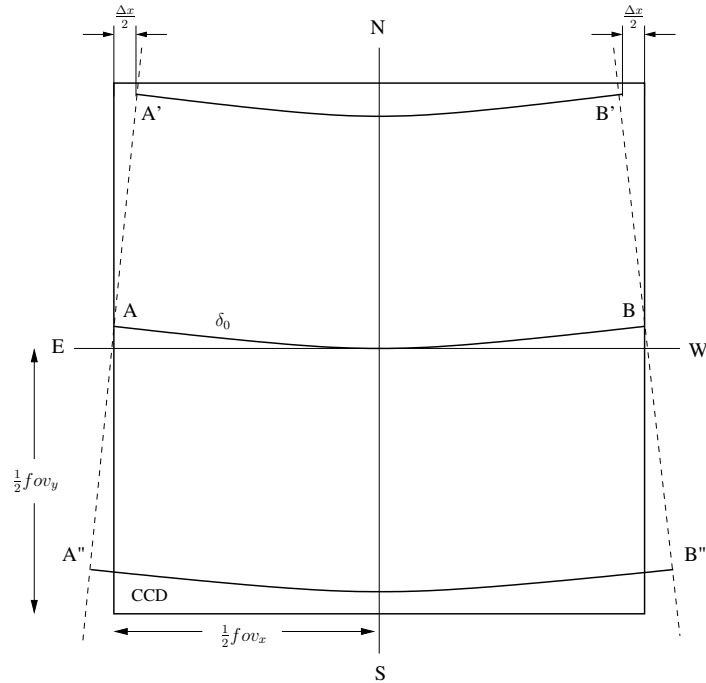
Figure 3.6: Effect of differential trailing. The dashed lines represent the central projection of two consecutive meridians. The angle forming those lines with respect to N-S direction has been exaggerated for the sake of clarity.

consider rows far from δ_0, the actual scanning rate of an sky element deviates from the value we previously fixed. In particular, for $\delta > \delta_0$ the nominal speed is lower than the fixed value and reversing for $\delta < \delta_0$.

As seen in Fig. 3.6, this translates into that sky elements cover in the same time larger $(\overline{A''B''})$ or shorter $(\overline{A'B'})$ arcs than the central one $(\overline{AB})$ at declination δ_0. The deviation Δx, in units of focal distance, introduced by this effect can be accounted by the following expression (Montojo 2004a,b):

$$\Delta x \simeq \frac{1}{2} fov_x fov_y \ \tan \delta_o \tag{3.6}$$

where fov_x and fov_y correspond to the field of view of the CCD, in units of radians, in both coordinates. In Sect. 3.2.1 and 3.2.2 we will evaluate the impact of this effect over the specific data sets which we will work with.

Thus, we have that this systematic effect, called *differential trailing*, introduces an image smearing along the E-W direction which increases at higher declinations and with large format CCDs. Of course, from Eq. 3.6, differential trailing is null for equatorial ($\delta_0 = 0$) scans.

Curvature

As already anticipated in the previous section, the trail described by a sky element in its passage along the CCD array is not rectilinear, but curvilinear coincident with a circle of constant declination. Therefore, this trail does not completely match a single row all along its scan over the CCD chip, but it also contributes to the signal of rows immediately above the nominal one. As can be seen in Fig. 3.7, an sky element of declination $\delta_0 + \Delta\delta$ describes a trail with a deviation from linearity equal to Δy. The distortion introduced by this effect, called *curvature*, can be analytically expressed as (Montojo 2004a,b):

$$\Delta y \simeq \frac{1}{8} fov_x^2 \ \tan(\delta_0 + \Delta\delta) \tag{3.7}$$

where, again, Δy is expressed in units of focal distance and fov_x in radians. This smearing results into an asymmetric elongation of the stellar profile along the N-S direction.
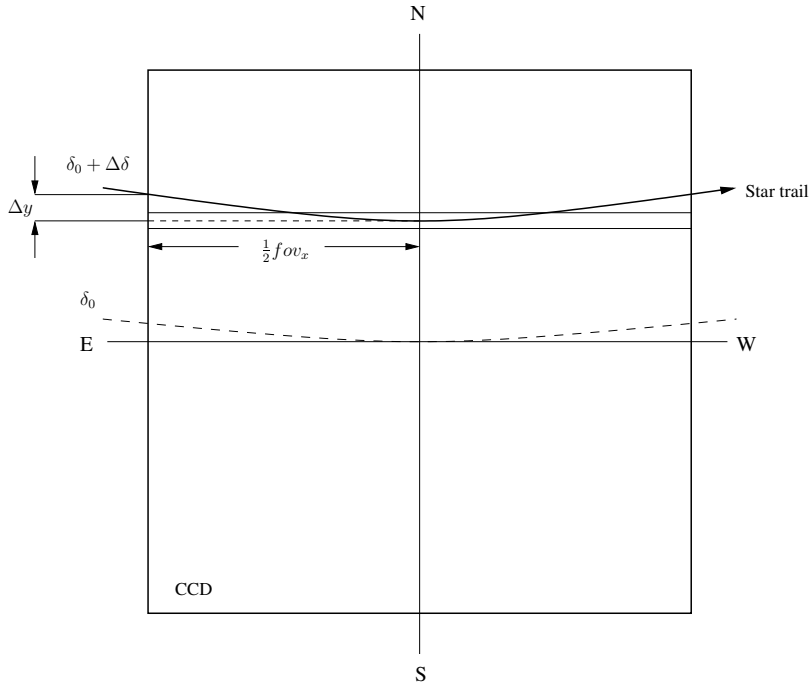
Figure 3.7: Effect of star trail curvature. Δy stands for the maximum deviation of the star trail from the centre of a CCD column at declination $\delta_0 + \Delta\delta$.

In contrast to the two previous systematics, which were symmetric and did not bias astrometry, here the centroid location of the profile is distorted, being pushed to larger values for coordinate y. This can be appreciated in Fig. 3.8: on the top
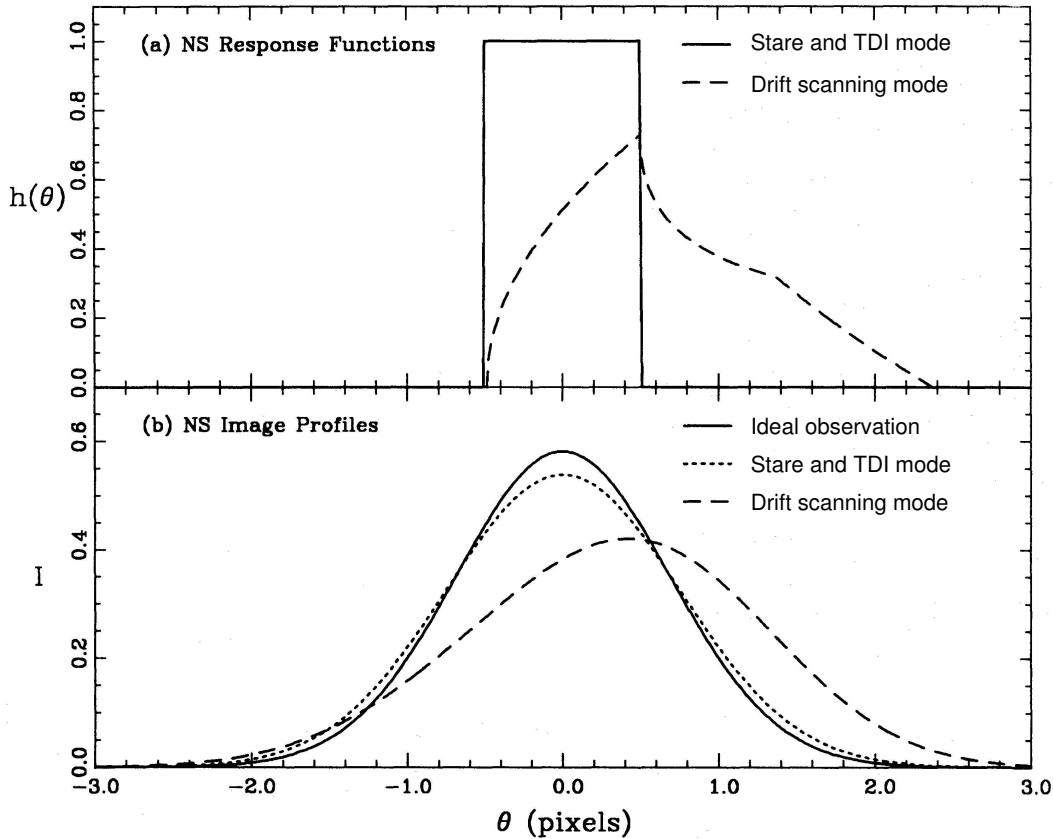
Figure 3.8: Effects of profile broadening due to pixel response function and star trail curvature. Top panel shows the N-S response functions for each effect. Bottom panel shows the N-S profile of an input is marginally sampled ($\sigma = 0.686$ pixels) Gaussian stellar profile (solid), the distorted profile due to pixel response function (dotted) and curvature effects (dashed). See Pag. 55 for explanation of ordinate θ. Adapted from Gibson & Hickson (1992).

panel it can be seen how the response function due to curvature effect is highly non-symmetrical along the N-S direction. On the bottom panel, the dashed curve suffers, with respect to the solid one, from an elongation of the input FWHM of $\sim 38\%$, an intensity peak decrease of $\sim 18\%$ and a significant offset ($\sim 0.26''$) of its original centroid. This particular configuration of fov_x, δ_0 and $\Delta\delta$ yielded a deviation of $\Delta y \sim 1.87$ pixels.

In Figs. 3.9 and 3.10, intensity peak decrease (FWHM) is plotted in dashed curve as a function of the deviation Δy. Note that as we explore regions closer to declination poles, the penalty introduced by curvature effect in the intensity peak

(FWHM) becomes more severe. Actually, for every instrument it exists a limiting declination over which the obtained data is totally useless.
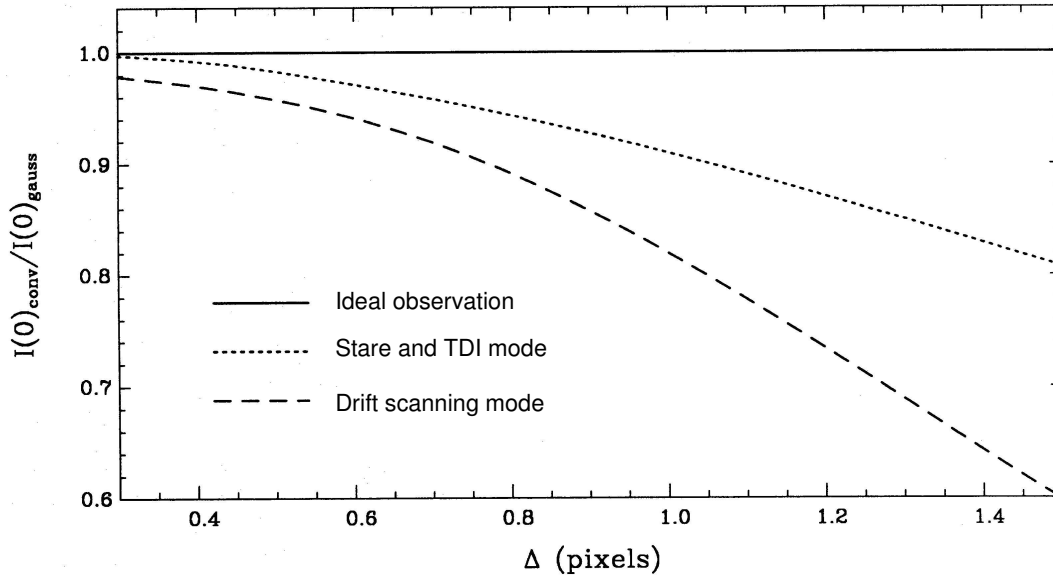
Figure 3.9: Effect of star trail curvature over the intensity peak of the input Gaussian as a function of the maximum deviation of a star trail from the reference CCD column centre Δ. Adapted from Gibson & Hickson (1992).

Seeing fluctuations

Surveys which operate in drift scanning mode and image very wide strips in right ascension (several hours) have exposed an additional problem when trying to perform accurate astrometry over wide areas of sky. Variable sky conditions are recorded spatially in the scanning strip, and are revealed when plotting the residuals in RA and declination as a function of RA, with respect to an accurate reference catalogue as Tycho-2 over a set of multiple nights. The plot comes in a shape of fluctuations with periods ranging from a few to 40 minutes, and a typical amplitude of a few tenths of arcsecond, depending on the zenith distance. Typical examples of this systematic error can be seen in Fig. 17 in Stone et al. (1996) and Figs. 1 and 2 in Evans et al. (2002).

The origin of that effect is more or less understood: Stone et al. (1996) and Naito & Sugawa (1984) claim they are due to anomalous refraction caused by atmosphere motions in lower tropopause.
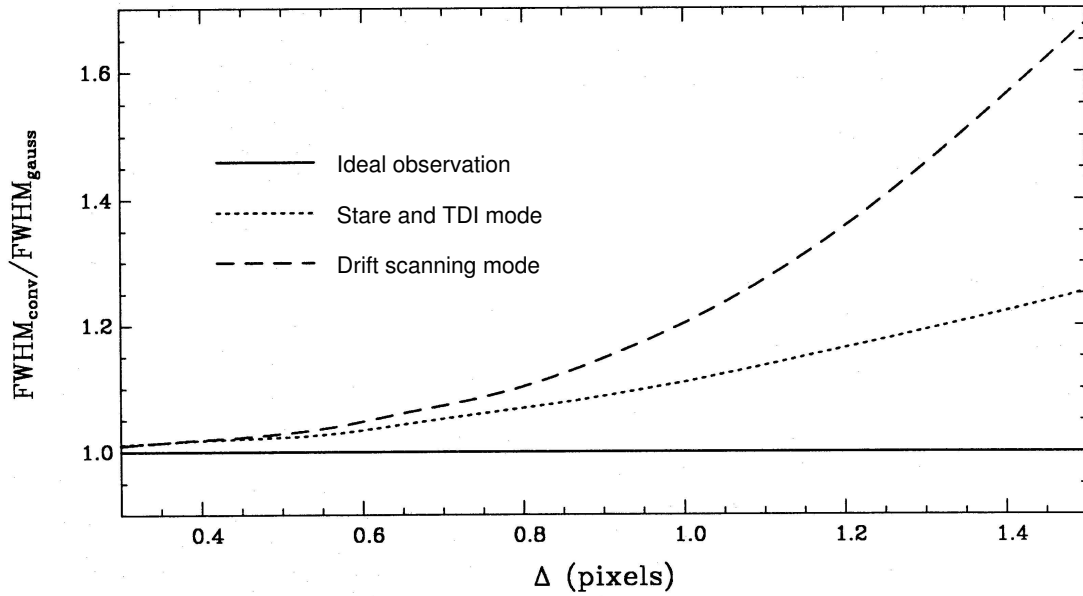
Figure 3.10: Effect of star trail curvature over the FWHM along the N-S direction for the input Gaussian as a function of the maximum deviation of a star trail from the reference CCD column centre, Δ. Adapted from Gibson & Hickson (1992).

It is worth remarking that these fluctuations are not exclusive of drift scanning observations, but also have been reported in other wide field astrometric surveys under stare mode, as is the case of UCAC (Zacharias 1996).

3.1.3   TDI observing mode

This scanning technique is based on the systematic covering of sky areas by following celestial meridians towards the pole while the CCD charge is transferred at the same rate that the telescope is slewed. Schematically, it can described by the following steps, which are represented in Fig. 3.11:

1. the CCD camera is oriented so that the axis which is parallel to the column transfer direction is aligned to the N-S direction,

2. the telescope tracking system is turned on,

3. the shutter is open,
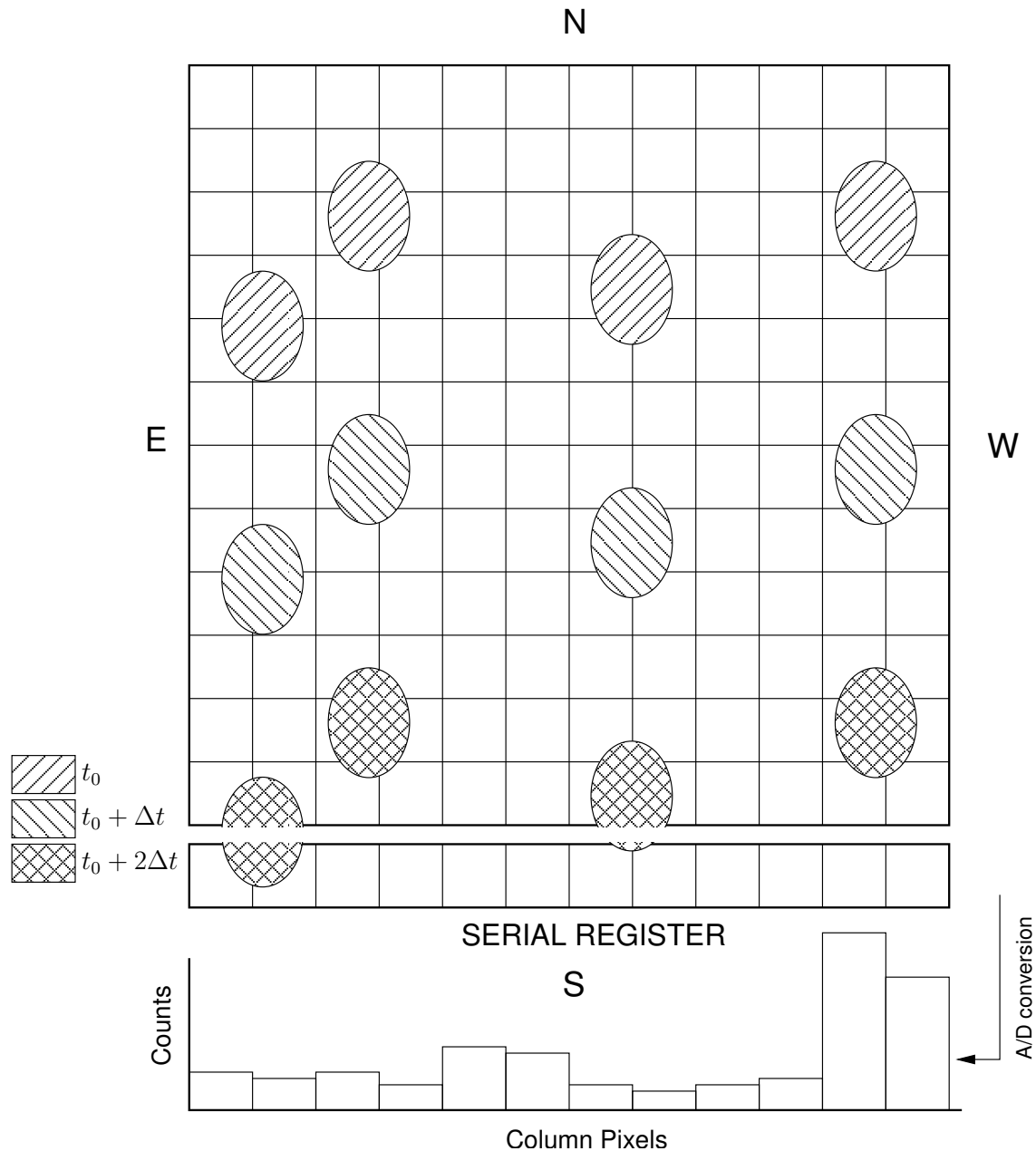
Figure 3.11: Sequence diagram of time delay integration (TDI) acquisition mode. A four star field is represented by ellipses with changing pattern at each transfer interval. The row charge is transfered along the N-S direction at a rate fixed by the user, Δt, simultaneously with serial register readout. See Pag. 72 for the justification of the stellar elongation shown.

4. the telescope declination drive is also turned on, at an arbitrary slow rate, Δt. As a result, the effective exposure time is not fixed to sidereal rate as in the case of drift scanning. Instead, the user can specify an arbitrarily long

exposure time, only being constrained by background level noise and motion accuracy of declination drive under slow rate regime,

5. every row of the CCD is transfered and readout at the same rate Δt,

6. the shutter is closed.

As in the case of drift scanning case, the feature of having intrinsic flat fielding in data itself is also incorporated by TDI mode.

TDI was first proposed and used by Mackay (1982); Wright & Mackay (1981), and has been used in a number of surveys for different purposes, mainly in those which aim to cover large areas of sky at deep magnitude. See Table 3.2 for a brief relation of those observational programs.

Table 3.2: Surveys operated (or to be operated) in TDI mode.

Name or Location	Purpose	Reference
Palomar 1.5m	High precision photometry of early-type galaxies	Boroson et al. (1983)
4-m AAT & 4-m KPNO	Faint galaxy counting and photometry	Hall & Mackay (1984)
4-Shooter at Hale 5-m	Multi-band photometry of the edge-on of a SO galaxy	Silva et al. (1989)
SDSS	Distributions of galaxies	Gunn et al. (1998)
XO project	Extrasolar planets search	McCullough et al. (2004)
8.4-m Large Synoptic Survey Telescope (LSST)	All sky purpose survey program	Claver et al. (2004)
GAIA	Complete astrometric and photometric census of one billion objects	Gai & Busonero (2004)

Note that some of the surveys in Table 3.2 do not strictly operate in what has been defined here as TDI. For example, SDSS follows a more general observing scheme, consisting on slewing the telescope both in RA and declination, and constantly accommodate the CCD orientation to the sky plane axes. Also, note that GAIA being an spaced-based facility will accommodate the charge transfer rate according to its own rotational speed and orbital parameters. Thus, we will hereafter refer to TDI as the specific case of scanning great circles of constant RA.

As in the case of drift scanning, below we overview the off-chip systematic errors which TDI mode introduces over the obtained data. Given that none of the data sets

present in Sect. 3.2 are taken under TDI mode, we will not describe the systematic errors in the same depth as we did for drift scanning in the previous subsections.

For the ease of discussing the systematic errors presented in TDI mode and establishing proper parallelism with the expressions introduced for the case of drift scanning, we outline the following considerations:

- we recall that TDI mode operates slewing the telescope following a great circle of constant RA,

- scanning rate is arbitrary and, of course, can be different from sidereal,

- in terms of spherical geometry, a great circle of constant RA is equivalent to the equator, which is actually a great circle of constant declination. Therefore, the family of curves resulting from the projection of the celestial sphere over the CCD plane are the same taking as a tangent point either along the equator or a great circle of constant RA.

Thus, we can conclude that TDI mode is totally equivalent to equatorial ($\delta_0 = 0$) drift scanning, with the only difference that the transfer rate can be different from the sidereal one. Consequently, we can geometrically represent TDI mode in the same coordinate system used in Figs. 3.6 and 3.7[3], and discuss the TDI systematics in base of Eqs. 3.6 and 3.7.

Ramping effect

The ramping effect behaves exactly in the same way as in drift scanning mode, exposed in Pag. 61.

Discrete shifting effect

As in the case of drift scanning, the pixel response function ($\Pi(\theta)$) introduces a convolution over the input Gaussian profile which elongates and decreases the intensity peak of $f(\theta)$ in the way expressed in Eq. 3.5 and shown in Figs. 3.3, 3.4

---

[3]Note this is not the case of Fig. 3.11.

and 3.5. Note that the only difference with respect to what was stated in Pag. 61 for drift scanning mode, is the change of nomenclature regarding the orientation of the distortion. E-W now should be read as N-S.

Differential trailing

Because TDI is equivalent to equatorial ($\delta_0 = 0$) drift scanning, differential trailing is also null in this case (Eq. 3.6).

Curvature

By direct application of Eq. 3.7 to the case of TDI, consider $\Delta\delta$ to be angular separation between a given RA inside the FOV and the RA of the central great circle. In this way, the same considerations made in Figs. 3.8, 3.9 and 3.10 for the case of drift scanning apply for TDI.

Being TDI a more complex observing scheme in terms telescope operation, some of the groups which operate surveys in this mode have developed innovative approaches for minimizing the curvature effect from TDI data. This is the case of Hickson & Richardson (1998), who designed and built an optical corrector which compensates the curvature distortion and produce high-quality strips. The same concept of corrector is also being implemented in another kind of wide field instrument, which is the Baker-Nunn Camera. This is a joint project between Fabra Observatory and San Fernando Observatory, and aims to refurbish this high-quality optics camera for remote CCD TDI operation. See Appendix A for a full detailed explanation of this project, and specially the Sect. A.3.1 for more information about the optical corrector to be built.

Seeing fluctuations

No past experience about this effect has been found in the literature. However, it is expected that residuals in RA and declination due to temporal changes in seeing will effectively appear under TDI mode in the same way and magnitude as the ones presented in Evans et al. (2002); Stone et al. (1996) with drift scanning mode observations.

3.1.4   Discussion

In this subsection we briefly outline the major advantages and disadvantages of drift scanning mode over stare mode. Note that we discard from this discussion the TDI method, because none of the data sets studied in this part of the thesis (presented in Sect. 3.2) correspond to this mode.

Advantages

- drift scanning turns to be a very efficient observing mode when covering large areas of sky in minimum time at moderate limiting magnitude. With respect to stare mode, we save the time devoted to CCD readout, telescope slew and repointing. The ramping effect appearing in TDI is not significant when very long RA strips are conducted.

- exposure time is not limited by tracking accuracy as it was in stare mode. Since the telescope is kept parked while acquiring under drift scanning mode, most of errors from instrumental motions are removed. The limitation established by the dynamic range of the CCD still applies for both observing modes.

- drift scanning eliminates the need of taking flatfield calibration in the clocking direction frames because the resulting data turns to have been flatfielded naturally by the column-by-column acquisition process itself. An estimate of the flatfield can be calculated a posteriori from the data, by image processing means (see Sect. 4.1).

Disadvantages

All of them come from the systematic errors which are specific of drift scanning mode and not present in stare mode:

- discrete shifting effect is a remarkable handicap for limiting magnitude and shape analysis in the E-W direction, even for marginally sampled images ($\sigma \leq$ 0.85 pixels). For the rest of cases, the introduced distortion is not significant ($< 5\%$).

- differential trailing is another systematic error inherent to drift scanning mode. As discrete shifting, it introduces a symmetrical elongation of the input profile along E-W direction, which translates into a decrease in limiting magnitude and FWHM_x broadening. The magnitude of such distortion exclusively depends on the CCD FOV and the central declination δ_0. Thus, a workaround solution turns to be only observing near equatorial zones for surveys operating in drift scanning.

- curvature effect, in contrast to discrete shifting and differential trailing, introduces an asymmetrical distortion over the input PSF, producing a systematic shift of the centroid towards to Celestial North Pole which depends on how far is the object from the center of the FOV. The impact of this effect is more important as we enlarge CCD FOV and central declination δ_0. Thus, equatorial scanning is again a preferred option.

We recall that seeing fluctuations are not specific of drift scanning, because they also appear into other wide surveys operating under stare mode.

In summary, we realize from the disadvantages stated above that drift scanning and TDI data suffer from an *unavoidable loss in limiting magnitude and spatial resolution*. To overcome these drawbacks with the use of image deconvolution is an important scope of Part I. This will be shown in forthcoming chapters. It is in this context that proceed to present the data sets which will serve as examples for validating this motivation.

3.2 Data sets description

In the next three subsections we present the sets of data we have worked with in this part of the thesis. Generic aspects for each data set will be detailed. In addition, a description of the acquisition scheme used and a quantitative estimation of the involved systematic errors (as described in Sect. 3.1) will be given in each case.

3.2.1   Flagstaff Astrometric Transit Telescope (FASTT)

FASTT is a meridian circle telescope property of USNO which operates in drift
scanning mode in a totally automated and robotic fashion. A general description of
the FASTT features is given in Table 3.3.

Table 3.3: Generic features of FASTT. Adapted from Stone et al. (2003).

Location	
Site	Flagstaff, AZ
Longitude	$111° \, 44' \, 40.''14$ W
Latitude	$+35° \, 11' \, 4.''65$
Elevation	2230 m
Median zenithal seeing	$1.''3$
Telescope	
Type	Meridian circle
Aperture	20 cm
Focal ratio	f/10.4
Scale	$99'' \text{mm}^{-1}$
Filter	F606W ($\lambda\lambda \, 4700 - 7300$ Å)
Detector	
Sensor	Ford-Loral CCD
Format	2Kx2K
Pixel size	15 μm
Gain	$3.69 \, e^- \, \text{DN}^{-1}$
Readout noise	$11 \, e^-$
FOV of single frame	$50.'1 \text{x} 50.'1$
Pixel scale	$1.''486$
Observational facts	
Average data throughput	41,000 CCD frames/year
Effective exposure time ($\delta_0=0$)	202s
Average FWHM[a]	2.8 pixels
Magnitude range	$7.5 < V < 17.7$

[a] Image is defocused on purpose with a smearing screen and broad passband filter to
overcome undersampling (Stone et al. 2003).

Nightly astrometric reductions for this and other contemporary programs were
computed differentially over wide-area strips with respect to the sparse collection
of radio reference sources which defined the ICRF (Johnston et al. 1995). This
non-optimal election was conditioned by the lack of dense and accurate reference-

star catalogues at the time of ACR observation (see Table 3.4). After releases of Tycho (Hög et al. 1997), Tycho-ACT (Urban et al. 1998) and its definitive extension Tycho-2 (Hög et al. 2000) catalogues, enough reference stars exist in FASTT FOV for assuring sufficiently accurate positions ($\sigma \geq \pm 47$mas). Thanks to this differential reduction, systematic errors could be evaluated, calibrated and removed. These will be discussed in the final part of this section.

Table 3.4: Description of reference catalogues used for FASTT astrometric reductions. The list is chronologically ordered as they were used from 1994 to nowadays.

Catalogue	V_{lim}	σ (mas)	Stellar density	
			$1°\mathrm{x}1°$	FASTT single frame FOV
ICRF radio	19.5	1	0.01	0.007
Tycho-ACT	10.5	25	25	18
Tycho-2	11.5	60	62	44

The FASTT data to be studied in this part of the thesis correspond to 11 2K×2K frames from astrometric calibration region D, taken during the end of 1998. This data was kindly supplied by Ronald C. Stone (Stone 1998)[4]. As can be seen in Table 3.5, these frames are completely equatorial. This will have consequence in the systematic errors discussion in this Section.

The filter used for all the frames is a F606W, with a broad band curve similar to the one employed in HST, which allows to increase the limiting magnitude with respect to Johnson family while maintaining tolerable crowding in the regions close to the galactic plane. In the case of our frames in region D, the density amount to 1607 stars deg^{-2} which will not impose us problems of overcrowding in the reduction methodology presented in Chapt. 4. This can also be visually checked in Fig. 3.12.

Systematic errors considerations

Below we review in some more depth all those systematic errors which were introduced in Sect. 3.1.1 and 3.1.2, and which do apply for the currently discussed data.

---

[4]A completely equivalent deconvolution study has been performed with a smaller data set consisting on 3 CCD 1K×1K frames also from FASTT (Stone 1997c). We will not include the description and posterior analysis for this data set, since it yielded very similar results and conclusions to the ones we reached with the 10 ACR frames.

Table 3.5: Specific features of FASTT data.

Frame ID	Date (dd-mm-yy)	α_0	δ_0
F98d287.274	14-10-98	4h 43m $13\overset{s}{.}1$	$0° \ 3' \ 30\overset{''}{.}71$
F98d288.279	15-10-98	4h 43m $13\overset{s}{.}7$	$0° \ 2' \ 51\overset{''}{.}86$
F98d290.281	17-10-98	4h 43m $1\overset{s}{.}5$	$0° \ 3' \ 31\overset{''}{.}66$
F98d291.259	18-10-98	4h 43m $7\overset{s}{.}7$	$0° \ 3' \ 7\overset{''}{.}07$
F98d301.255	28-10-98	4h 43m $16\overset{s}{.}0$	$0° \ 2' \ 1\overset{''}{.}43$
F98d302.241	29-10-98	4h 43m $11\overset{s}{.}6$	$-0° \ 0' \ 9\overset{''}{.}57$
F98D306.251	02-11-98	4h 43m $27\overset{s}{.}2$	$0° \ 1' \ 21\overset{''}{.}49$
F98d317.247	13-11-98	4h 43m $12\overset{s}{.}0$	$0° \ 1' \ 7\overset{''}{.}25$
F98d318.253	14-11-98	4h 42m $55\overset{s}{.}7$	$0° \ 4' \ 18\overset{''}{.}42$
F98d319.248	15-11-98	4h 43m $4\overset{s}{.}5$	$0° \ 4' \ 36\overset{''}{.}41$
F98d321.163	17-11-98	4h 43m $18\overset{s}{.}9$	$0° \ 0' \ 12\overset{''}{.}13$

In Tables 3.6 and 3.7 we anticipate a quantitative estimation of those errors. The first table includes those conventional sources which could be common to most astrometric surveys, and the second table comprises those sources specifically related to drift scanning technique.

Table 3.6: Conventional systematic errors for FASTT data.

Systematic error	Error in RA (mas)	Error in δ (mas)
Differential Color Refraction	0	+33 to -39
Focal-plane positional errors	± 24	± 24
CTE and magnitude-related errors	0	+39
Seeing fluctuations	$\pm 89 - \pm 230^{(a)}$	$\pm 86 - \pm 270^{(a)}$

[a] These are errors for wide-field RA strips. See Pag. 84 for more details.

Table 3.7: Drift scanning specific systematic errors for FASTT equatorial data.

Systematic error	Intensity peak drop (%)	FWHM broadening (%)	Error in RA (mas)	Error in δ (mas)
Discrete shifting	6	10	0	0
Differential trailing	0	0	0	0
Curvature effect	n/a	n/a	50	20

- **Differential Color Refraction**
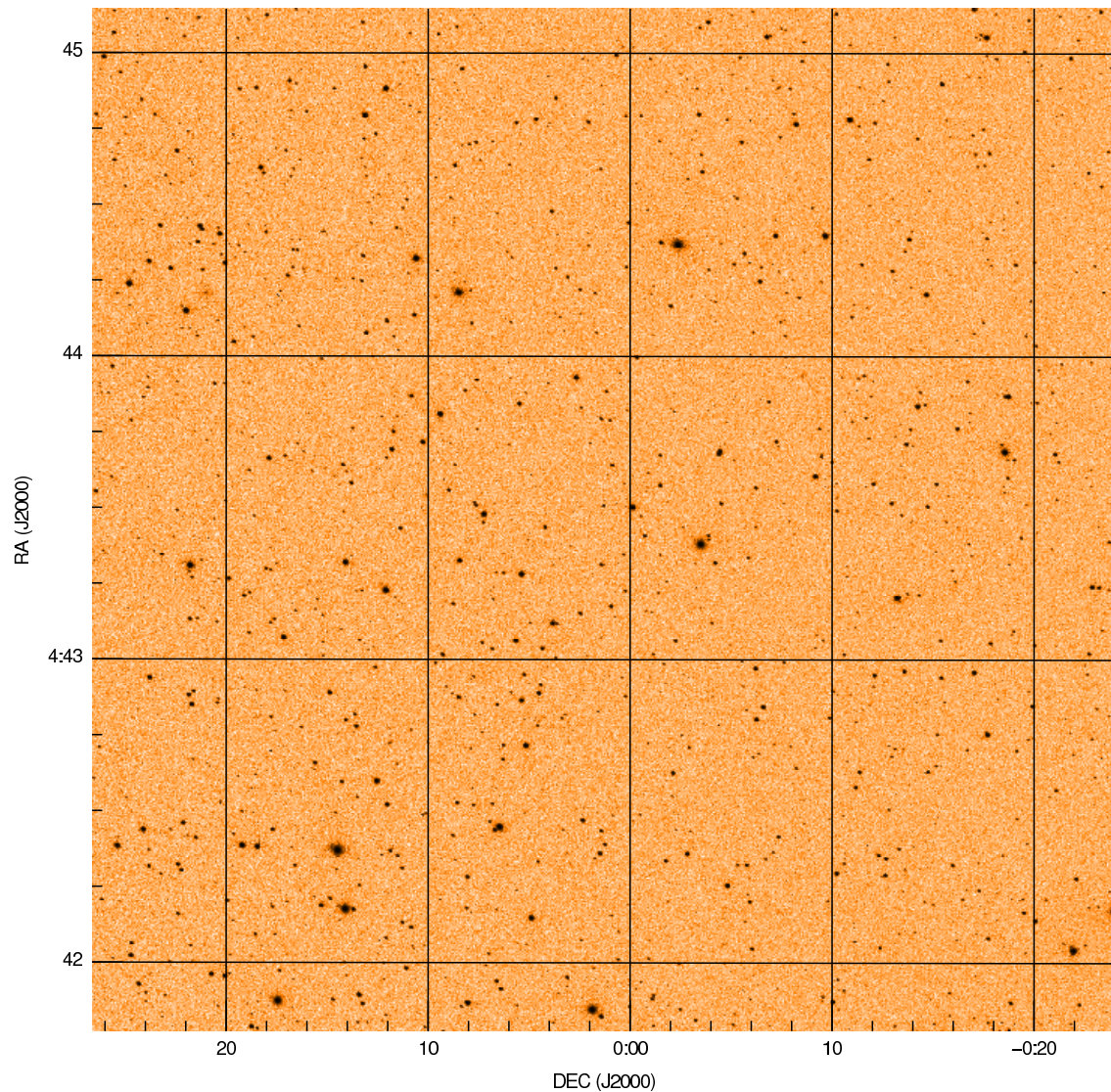
Figure 3.12: One of the 2K×2K CCD frame from USNO FASTT to be studied. The stellar density is large enough for having rich statistics when deriving astrometric constants and sparse enough for avoiding undesirable crowding effects.

In Pag. 57 we introduced the need of correcting positions from differential color refraction. For the case of FASTT, Stone et al. (2003) observed a large number of Tycho-2 stars and obtained the following calibration expression:

$$\Delta\delta(arcsec) = \delta - \delta_{FASTT} = 0.0317[(B-V) - 0.8]\tan ZD \qquad (3.8)$$

where ZD is the zenithal distance. This expression leads to systematics shifts which can exceed $0''05$ for sufficient bluish stars at large zenith distances. However, given the normal observing conditions, the average value of this

error range between 33 mas and −39 mas for O and M5 stars, respectively.

- **Focal-plane positional errors**

  Focal-plane positional errors are mainly caused by misaligments of CCD enclosure, filter and rest of optical elements which originate focal-plane to deviate from its ideal shape. Calibrating these errors is usually a long task which involves many observations. This is because non-linear least-squares techniques can not provide desired performance by fitting a polynomial as a global deformation model across the FOV. Instead, an empirical approach is followed up to achieving a dense enough residual map with respect to an accurate reference catalogue.

  This is what Stone et al. (2003) did for FASTT focal plane, by performing thousands of observations over many nights of Tycho-2 stars and obtaining the residual map of whirls shown in Fig. 3.13. The average error in both coordinates was found to be ±24 mas, although errors with modulus up to 150 mas can be appreciated.
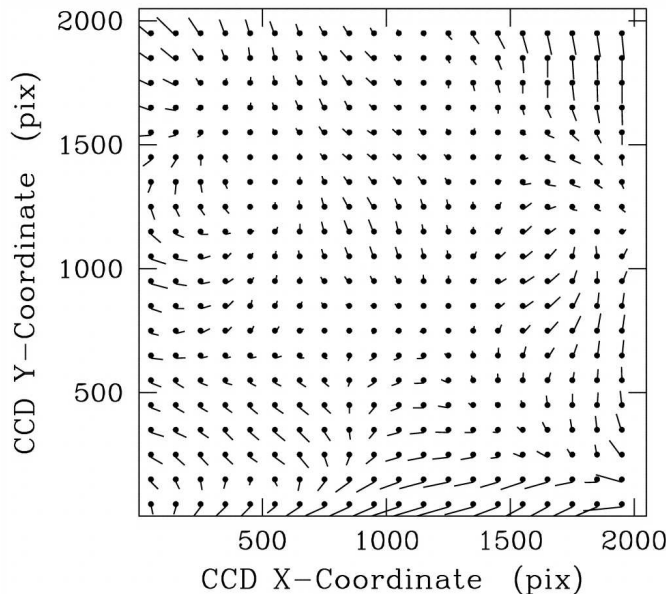
Figure 3.13: Map of focal-plane positional errors for CCD in FASTT telescope (Stone et al. 2003).

- **CTE and magnitude-related errors**

  It is not unusual that large format front-illuminated CCDs suffer from this effect. Initially, this is the case of FASTT 2K×2K CCD which showed asym-

metric profiles in the serial register direction (declination) due to poor CTE. Those were minimized by increasing the cooling temperature. A detailed study was performed by Stone et al. (2003) to check if any residual CTE effect after this fixing remained, and if this could handicap astrometry. The results yielded no evidence of magnitude dependence for RA residuals. However, the faint end of declination residuals had a systematic shift towards lower values. This amounts up to an average of 39 mas for the faintest end of the magnitude range. In addition, this magnitude-related error in declination was found to lack of dependence on the pixel position. All in all, the authors conclude that this marginal of magnitude-related error is due to the charge loss produced in the summing well[5].

In order to check the status of this CTE error over our data, we measured the $\mathrm{FWHM_{RA}}$ and $\mathrm{FWHM_{DEC}}$ by 2D-Gaussian fitting and plotted their histograms in Fig. 3.14. Note that, apart from the habitual seeing variations through different nights, $\mathrm{FWHM_{DEC}}$ are systematically broader than $\mathrm{FWHM_{RA}}$ for all considered frames. In addition, as will be shown in Sect. 5.1.1, this elongation is not exactly parallel to declination axis, but shows a systematic orientation of $\theta \sim 160°$. This angle becomes clearly visible for nearly all star profiles, regardless their pixel coordinates.

The origin of this large asymmetry (ratio of 1 : 1.4) seems to be linked with CTE problem explained above because the semi-major axis (declination) of our measured profiles coincides with the serial register direction reported by Stone et al. (2003). Moreover, the magnitude dependence in that direction appears to be confirmed by Fig. 3.15: red circles ($\mathrm{FWHM_{DEC}}$) show larger scatter for bright sources than black ones ($\mathrm{FWHM_{RA}}$). We are unsure if our data was taken before or after to the cooling temperature fix. Anyway, the stellar profiles are equally not round.

We speculate that the non-perpendicularity of $\theta \sim 160°$ in our images could be due to a secondary (and less important) poor CTE in the parallel register direction.

Finally, other non radially broadening effects such as differential color refraction could also contribute to the observed assymetry. However, we note the

---

[5]This is the DC-biased last gate just before the amplifier which readouts the photogenerated electrons. Summing well serves to decouple the serial clock pulses from the output node coming from the serial register.
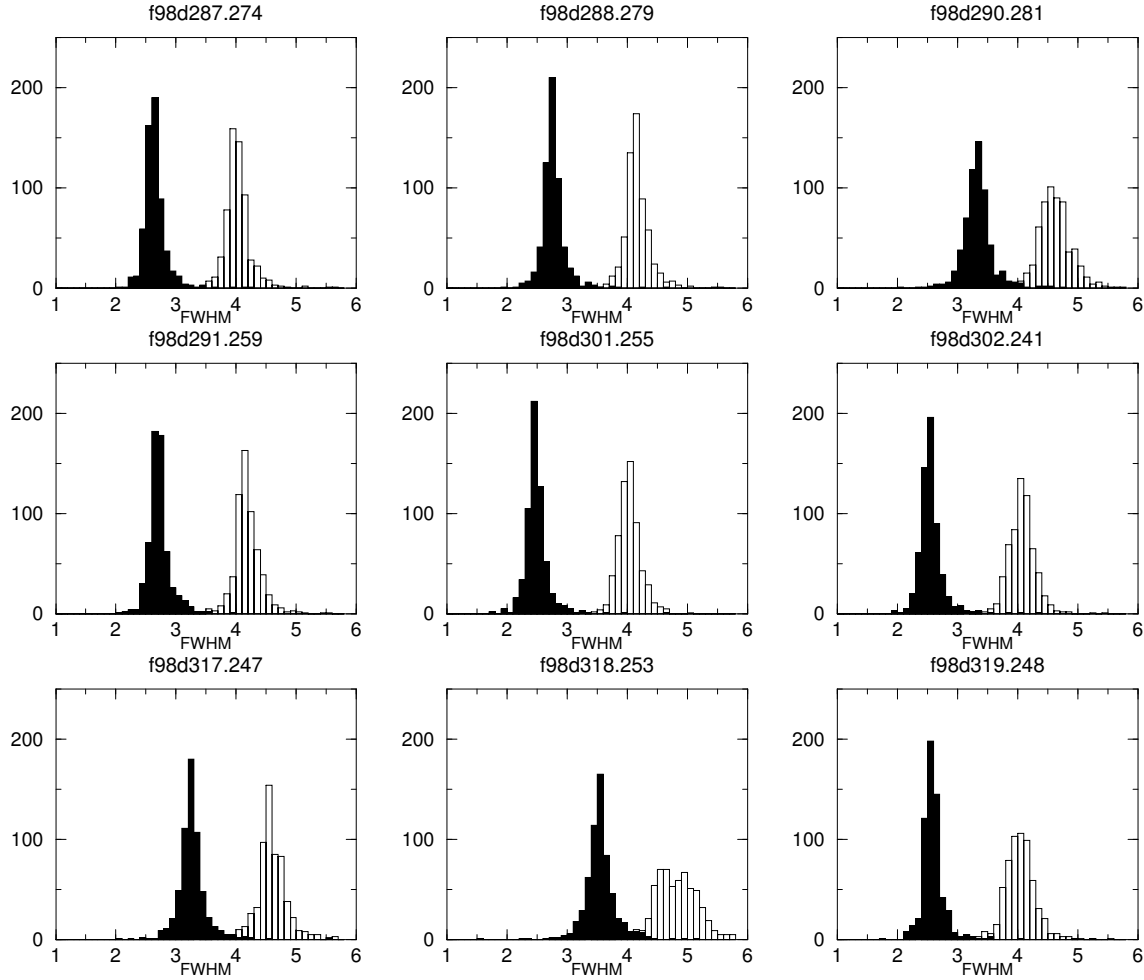
Figure 3.14: Histograms of FWHM$_{\text{RA}}$ (filled) and FWHM$_{\text{DEC}}$ (empty) for nine of the 11 studied FASTT frames. The large asymmetry between both profile widths is likely to be due to CTE defect in the direction of serial register (DEC) of the CCD chip.

mean elevation of our FASTT data is far above the typical one where that effect should begin to be significant.

- **Seeing fluctuations**

  As explained in Pag. 68, this error arises in a wavy pattern when plotting residuals versus RA. In the case of FASTT programs the error ranges its peaks between ± 89 and ± 230 mas in RA and between ± 86 and ± 270 mas in declination for ZD comprised between $0°$ and $70°$, respectively (Stone et al. 2003).

  In principle, if sufficiently dense reference catalogue were available, this sys-
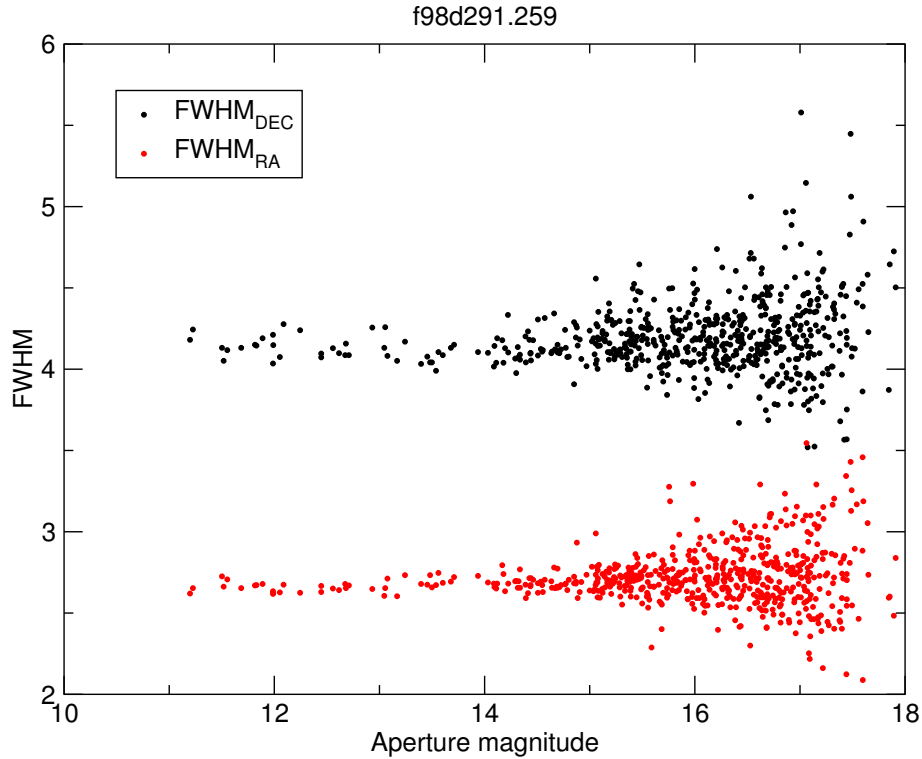
Figure 3.15: FWHM$_{RA}$ (red) and FWHM$_{DEC}$ (black) for nine of the 11 studied FASTT frames. The CTE defect in DEC direction is likely to be the responsible of larger value and scatter in FWHM$_{DEC}$.

tematic error could be removed with the inclusion of higher orders in the polynomial model used when doing differential astrometry. However, given the period of these fluctuations can be as short as 3 min (Stone et al. 1996), even Tycho-2 turns to be too sparse for this purpose. As a workaround solution, and with additional observational effort, either by creating a subcatalogue from multiple observations (Viateau et al. 1999) or by using overlapping frames (Evans et al. 2002; Stone 1997a), the calibration of the fluctuations is possible to achieve.

Although our FASTT frames are not long RA strips, and therefore only comprise the shortest frequency content of these fluctuations, the image PSF does spatially vary accordingly to this effect, in particular along RA direction. We checked this with our FASTT data and the result is illustrated in Fig. 3.16, where the FWHM along declination axis is plotted as a function of RA coordinate along the whole CCD chip. Only three nights (f98d290.281,f98d318.253 and f98d319.248) show appreciable variation of profile width. Note the effec-
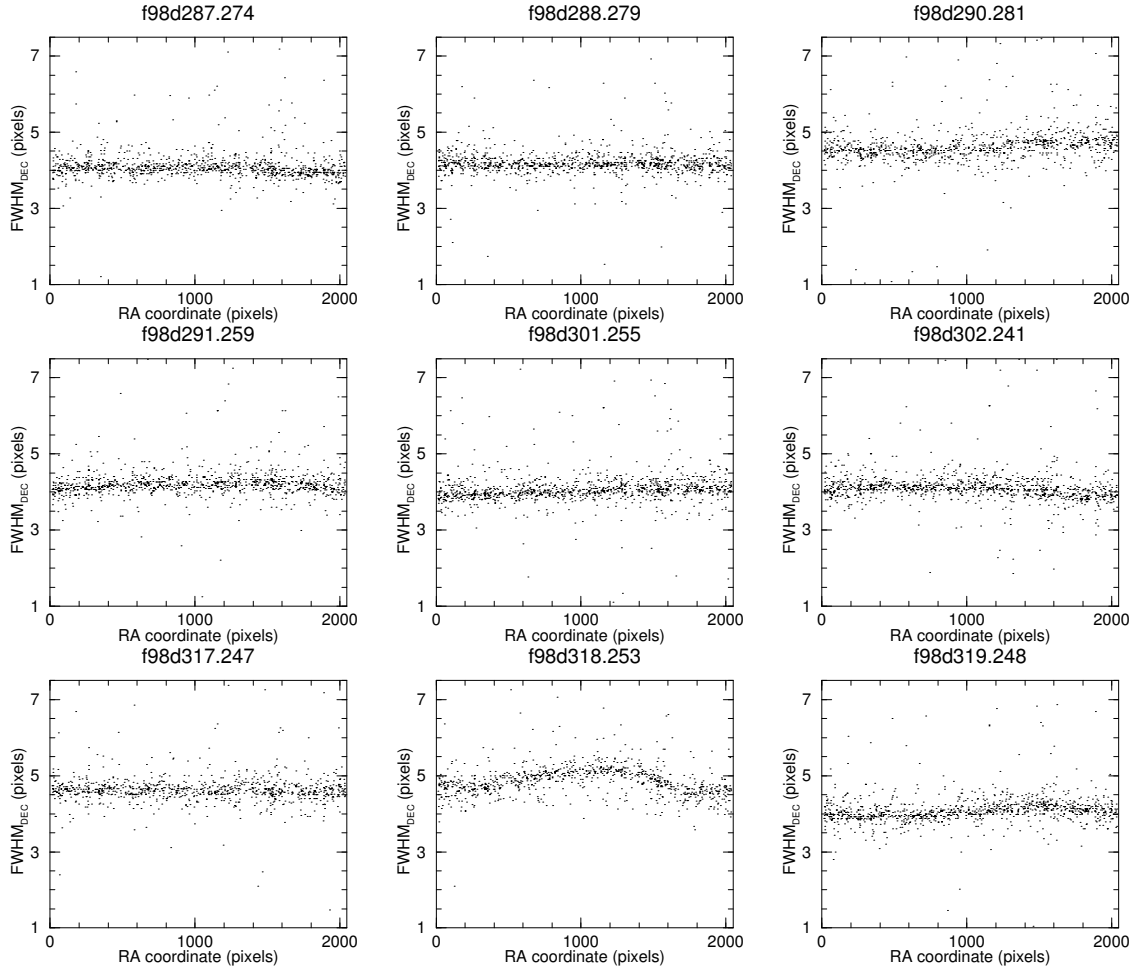
Figure 3.16: FWHM$_{DEC}$ as a function of RA coordinate for nine of the 11 studied FASTT frames, showing the perceptible influence of seeing fluctuations over this PSF parameter. The wavelength of the oscillations in f98d290.281, f98d318.253 and f98d319.248 frames are compatible to the typical quasi-periodic fluctuations due to anomalous refraction according the equivalent exposure time of 202 s for every frame.

tive exposure time of one FASTT frame is 202s, which is slightly larger than the minimum typical period of oscillation (3 min) reported by Stone et al. (1996). When present, the oscillation patterns in Fig. 3.16 match to this timescale. As we will see in Sect. 5.1.1, this effect can be of relevance when obtaining an estimate of the PSF for posterior deconvolution.

Finally, from Tables 3.6 and 3.7, seeing fluctuations are the dominant error source in FASTT data. Note, however, those large errors correspond to wide-field RA strips (several hours) used for habitual survey programs. In contrast,

our 11 frames are only 50$'$1x50$'$1, so it is expected that the incidence of seeing fluctuations over the astrometry we derive for our FASTT data is significantly lower.

- **Discrete shifting**

  We can obtain an estimate of this effect for FASTT data directly from Figs. 3.4 and 3.5, provided a value for σ is given. However, σ can not be extracted from data since this already incorporates all the other distortions included in Tables 3.6 and 3.7. Instead, we indirectly estimated σ from median seeing (1$''$3) reported for NOFS site (Harris & Vrba 1992) and making use of the relation FWHM$\propto(\cos ZD)^{-0.43}$, which is also deduced in the cited paper. Given that in our data $36° < ZD < 46°$, the average sampling value for an input Gaussian profile before being distorted is FWHM$\sim$ 1$''$47 = 0.99 pixels. That would certainly be severely undersampled data, and discrete shifting would seriously penalty the intensity peak in that sampling regime. However, as reported in Stone et al. (2003), the chosen broad passband filter introduces a defocusing which augments sampling up FWHM$\sim$ 2.8 pixels. Therefore, for this value of σ ($\sim$1.2 pixels), Figs. 3.4 and 3.5 supplies a decrease in the intensity peak of 6% and a profile broadening of 10%, as described in Table 3.6. This SNR drop, while not being dramatic, justifies the convenience of the application of image deconvolution to this kind of data. We recall from Pag. 61 that discrete shifting yields to symmetric broadening of FWHM which does not imply any degradation of astrometric accuracy, apart from the one derived from the SNR decrease.

- **Differential trailing**

  As explained in Pag. 63, charge can only be clocked at one single rate in the whole chip. This yields to a broadening of the star profile in the clocking direction (RA), whose magnitude depends on declination in accordance to Eq. 3.6.

  Stone et al. (1996) presents in its Fig. 9 an extreme case of this systematic error for an image at high declination ($\delta_0 = 70°$). The FWHM$_{RA}$ ranges from 4$''$ to 7$''$, with the minimum located at central row, where the clocking rate is the appropriate.

  In our particular case of equatorial images ($\delta_0 = 0$) the expected smearing is null. We confirmed this by plotting in Fig. 3.17 the FWHM along RA axis as
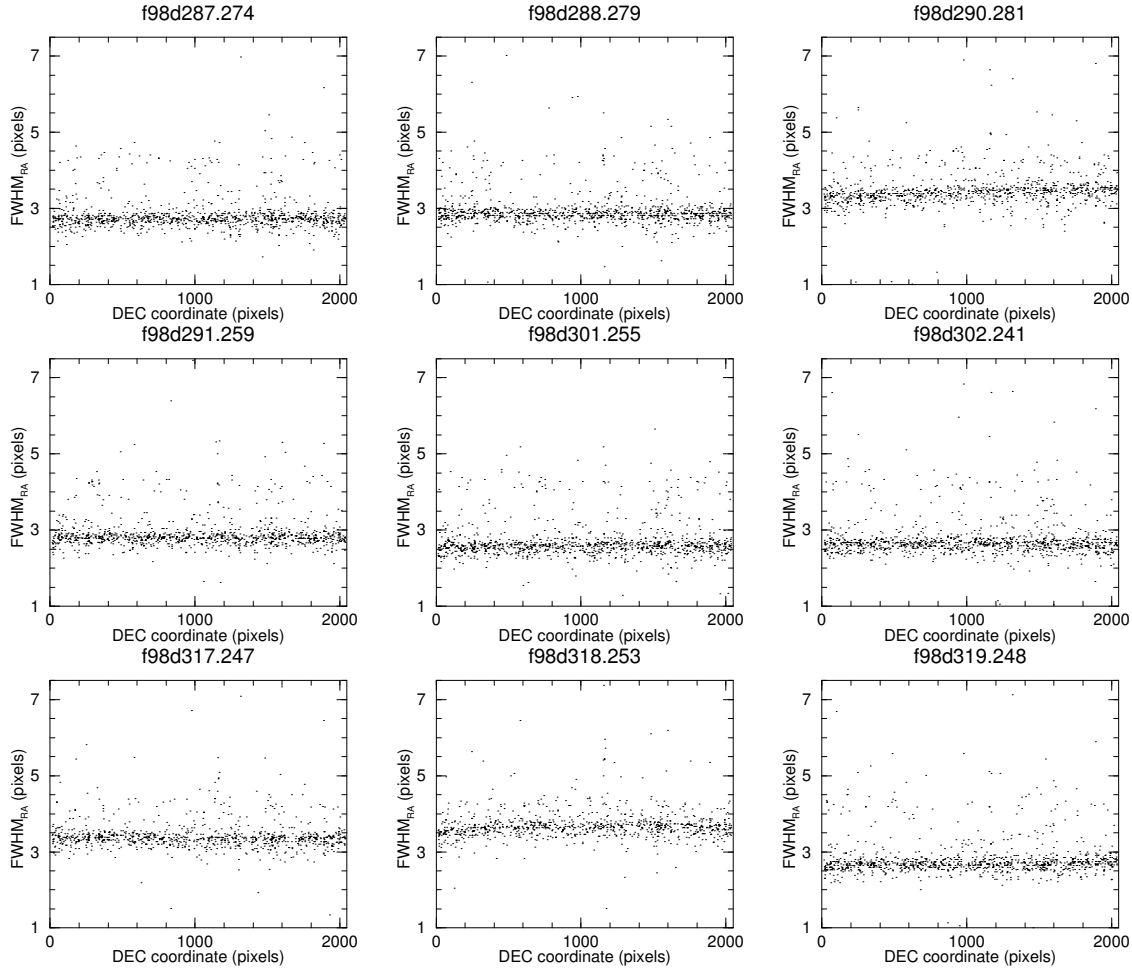
Figure 3.17: FWHM$_{\text{RA}}$ as a function of declination coordinate for nine of the studied FASTT frames.

a function of declination coordinate along the whole CCD chip. As expected, none of the ten night frames show any significant variation of profile width.

- **Curvature effect**

  As discussed in Sect. 3.1.2, the star profile is expected to be asymmetrically distorted by this effect, causing a degradation of the astrometric accuracy. In the case of our FASTT equatorial images, and taking into account Eq. 3.7, this distorsion is greatly reduced. We could not accurately derive the intensity drop the profile broadening for FASTT data, but Stone et al. (1996) supplies the corresponding astrometric errors in RA and DEC (see Tab. 3.7).

In summary, we can extract the following conclusions from our FASTT data set:

1. systematic errors due to drift scanning scheme in our case of equatorial data are far smaller than those originated by other conventional sources.

2. the main error source is the seeing fluctuations.

3. FASTT shows poor CTE resulting in elongated stellar profiles in the N-S direction and slight magnitude dependence of FWHM_{DEC}.

4. unfortunately, we do not have quantitative calibration maps for most of the conventional errors. For example, this is the case of focal-plane errors, CTE or seeing fluctuations. This forced us to disregard differential astrometry with respect to Tycho-2 catalogue (which is the usual catalogue followed in all the meridians) and consider a multi-frame approach based on average pixel coordinates, for obtaining an estimate of internal astrometric error instead. This will be further explained in Sect. 4.7.

3.2.2   QUasar Equatorial Survey Team (QUEST)

The QUEST (QUasar Equatorial Survey Team) project, is a collaboration between Yale University, the Centro de Investigaciones de Astronomía (CIDA), the Universidad de Los Andes (ULA) and Indiana University. They designed and installed a 16×2K×2K CCDs mosaic camera at the focal plane of the 1 m Venezuelan Schmidt Telescope. This facility has been used for surveying equatorial sky in high galactic latitudes ($\sim 4000\ \text{deg}^2$) under drift scanning mode up to $m_B \sim 21$, since November 1998.

The main goal of the collaboration is to discover a large number of quasars ($\sim 10^4$) in an homogeneous and unbiased way, which makes possible to determine cosmological parameters through the study of the distribution of dark matter via gravitationally lensed quasars (also known as macrolensing).

A general description of QUEST features is given in Table 3.8.

Again, as in FASTT case, drift scanning mode was chosen as the best acquisition scheme for surveying equator in a short period of time, allowing to develop variability studies with repeated scans of the same area.

The area of the whole array formed by the 16 2K×2K chips is 2°.4x3°.5. As

Table 3.8: Generic features of QUEST telescope and camera (Baltay et al. 2002).

Location	
Site	Llano del Hato, Venezuela
Longitude	$70° \ 52' \ 0'' \ W$
Latitude	$+8° \ 47'$
Elevation	$3600 \, m$
Median zenithal seeing	$1''5$
Telescope	
Type	Schmidt camera
Aperture	1 m
Mirror diameter	1.52 m
Focal ratio	f/3
Scale	$67'' \text{mm}^{-1}$
Corrector optics	Field flattener lens with barrel-like distorsion
Detector	
Sensor	Ford-Loral CCD
Format	16x2Kx2K
Pixel size	15 μm
Average gain	$1.0 \pm 0.1 \ e^- \ \text{DN}^{-1}$
Average Readout noise	$13 \pm 3 \ e^-$
FOV of single frame	$34'1 \text{x} 34'1$
Total effective FOV of the camera	5.4 deg^2
Pixel scale	$1''033$
Observational facts	
Average data throughput	3.2 Gb hr^{-1}
Effective exposure time (δ_0=0)	143s
Average seeing (FWHM)	2.4 pixels
Limiting magnitude (SNR$\geq$10)	V$\sim$ 19.2

seen in Fig. 3.18, these are grouped in 4 four-CCDs *fingers*, aligned towards the N-S direction. Each finger is covered by a color filter which resemble Johnson color system (U,B,V and R). Therefore, the camera can collect images in each of four colors practically in a simultaneous way.

The QUEST Schmidt telescope has its focal plane in a shape of a convex spherical surface. To allow the CCD camera to be in a flat plane, a new 30 cm field-flattener lens was manufactured to reimage the focal plane. The lens design includes on purpose a barrel-like distorsion, in order to compensate the curvature effect inherent to drift scanning mode. This was optimized for observing at zero declination.
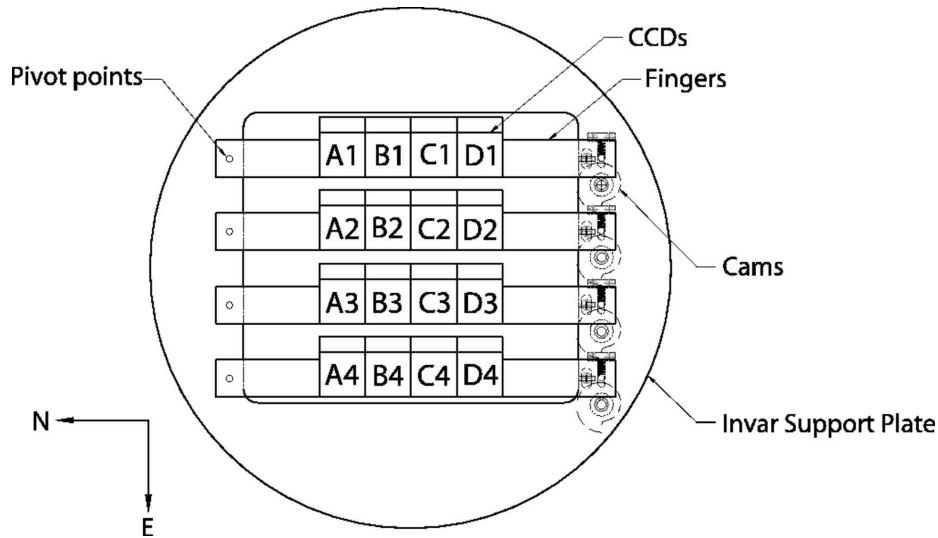
Figure 3.18: Layout of the CCDs on the image plane of QUEST camera. Also shown are the fingers supporting the CCDs, their pivot points, and the finger-rotating cams. Courtesy of Baltay et al. (2002).

With QUEST data, quasar candidates can be identified by the following criteria:

1. $H\alpha$ emission line survey (for $0.2 > z > 0.37$) (Sabbey et al. 2001),

2. U-V vs. B-V color diagram (for $z < 2.2$) (Baltay et al. 2002),

3. long and short term multiband variability[6] (Rengstorf et al. 2004a,b),

4. absolute proper motion.

All four are robust indicators for elaborating candidates lists, which are typically confirmed with a posteriori spectroscopic observations at larger telescopes. In the case of QUEST candidates, those are conducted at the 3.5 m WIYN[7] telescope with the Hydra Multiple Object Spectrograph (MOS).

By now, the variability criteria is the one which have produced larger number of quasar candidates. Rengstorf et al. (2004a) present two preliminary samples of 248 and 203 variable candidates and claims a positive quasar detection efficiency

---

[6]Quasars are known to show intrinsic brightness variability in timescales ranging from few to several years due to their central core nature (Ulrich et al. 1997).

[7]The WIYN Observatory is a joint facility of the University of Wisconsin-Madison, Indiana University, Yale University, and the National Optical Astronomy Observatory.

of $\sim 7\%$ in both cases. As survey progresses in area coverage and time span, the candidate list become more and more populated.

Unfortunately, the access to WIYN or other > 3 m class telescopes is limited and the efficiency (number of observed targets/night) which offers the MOS technique is low compared to the candidates list increase. Therefore, recalling that the main scope of the project is to detect macrolensing events, alternative and less time-consuming observational techniques are required for discriminating those candidates which show multiple components (likely to be the result of the lensed quasar) and/or occasional visible galaxy in the vicinity of the lens. This can be accomplished by a parallel campaign of wide field imaging observations which are being conducted also at WIYN with the MiniMosaic camera. This instrument offers high resolution images $(0.141'' \text{ pixel}^{-1})$ under excellent seeing conditions at deep limiting magnitude $(R \sim 23$ for a 3 min. exposure).

Parallely to the quasar survey, a number of complimentary science results have arisen from QUEST team. These range from discovery of bright TNOs (Ferrin et al. 2001), new supernova detection (Schaefer 2000, 2001; Vicente et al. 2001), discovery of GRBs optical counterparts (Schaefer et al. 1999), survey of young low-mass and T-Tauri stars in Orion OB1 (Briceño et al. 2001) and RR Lyrae survey (Vivas et al. 2001, 2004).

The QUEST data to be studied in this part of the thesis is divided in two sets of nearly equatorial images. The first one corresponds to a single 568x560 pixel subframe, called q100899_F14. The second is composed of 5 256x256 pixel overlapping frames, taken in nearly consecutive nights and which is suffixed by F13. This data was kindly supplied by the team of QUEST collaboration at Departments of Astronomy (van Altena et al. 2000) and Physics (Baltay et al. 2000) at Yale University, during a research stay spent there by the author.

As shown in Table 3.9, F13 and F14 sets result from different chips: B4 and C4, respectively. Following the chip nomenclature in Fig 3.18, B4 and C4 are located in the same finger and follow contiguous declination strips. The V filter was used in all the studied QUEST frames.

Both QUEST sets overlap with two MiniMosaic WIYN fields which, as explained earlier in this section, are part of the parallel campaign devoted for discriminating lensed quasar candidates from those previously culled via variability criteria. Fol-

Table 3.9: Specific features of QUEST-WIYN data pairs for Fields 13 and 14. Since each QUEST set overlaps with its corresponding WIYN pair, the central coordinates (α_0, δ_0) also apply for QUEST sets. Seeing for q120899_F13 is unknown.

QUEST						
Frame ID	Field	Date	Chip	FWHM	Filter	FOV
		(dd-mm-yy)		($''$)		($'$)
q050899_F13	13	05-08-99	B4	2.0	V	4.3x4.3
q100899_F13	13	10-08-99	B4	2.3	V	4.3x4.3
q100899_F14	14	10-08-99	C4	2.4	V	9.5x9.3
q110899_F13	13	11-08-99	B4	2.2	V	4.3x4.3
q120899_F13	13	12-08-99	B4	unknown	V	4.3x4.3
q180899_F13	13	18-08-99	B4	2.2	V	4.3x4.3
WIYN						
Frame ID	Field	Date	α_0	δ_0	Filter	FOV
		(dd-mm-yy)				($'$)
w250700_F13	13	25-07-00	19h 39m 52s	$-0° \, 50' \, 18''$	Harris R	9.7x9.6
w240700_F14	14	24-07-00	19h 45m 42s	$-1° \, 30' \, 24''$	Harris R	2.5x9.6

lowing the same suffix notation for the two fields, these WIYN frames will be called w250700_F13 and w240700_F14, respectively.

The data introduced in former paragraphs are summarized in Table 3.9, and displayed in Figs. 3.19 and 3.20 (only one night frame is shown from QUEST F13 set). WIYN images have been severely unzoomed so that they respectively match the displayed scales of QUEST frames[8]. In addition, note the zoom ratio at Fig. 3.19 was chosen to be a bit smaller than in Fig. 3.20.

Systematic errors considerations

As in the case of FASTT data, we overview, and quantify when possible, those systematic errors introduced in Sect. 3.1.1 and 3.1.2 which do apply for the QUEST data.

A basic difference between QUEST and FASTT has to be commented at this

---

[8]Of course this causes a loss in resolution and makes visually appreciate far less stars than really are detected by a dedicated routine.

point. While FASTT concentrates most of its effort in providing accurate astrometry, QUEST focus its attention in the astrophysical throughput. As a result, some of the systematic errors of QUEST data have not been fully calibrated yet, at least to the same depth as has been done for FASTT. In the considerations below we will constrain our discussion to those systematic errors for which an estimation is directly computable or available in the literature. We anticipate a quantitative estimation of these in Tables 3.10 and 3.11.

In general, the intrinsic smearing to drift scanning restricts QUEST camera to operate in declinations below $\delta \sim 7°$, noticeably less than the $\delta \sim 19°$ for FASTT (see Sect. 3.2.1). This is understandable, because the smaller pixel scale makes it more sensitive to PSF systematic distorsions under similar seeing conditions.

Table 3.10: Conventional systematic errors for QUEST data.

Systematic	Error in RA (arcsec)	Error in DEC (arcsec)
Focal-plane positional errors	< 3	< 3
Magnitude-related errors	(-0.1,+0.6)	(-0.5,+0.4)

• **Focal-plane positional errors**
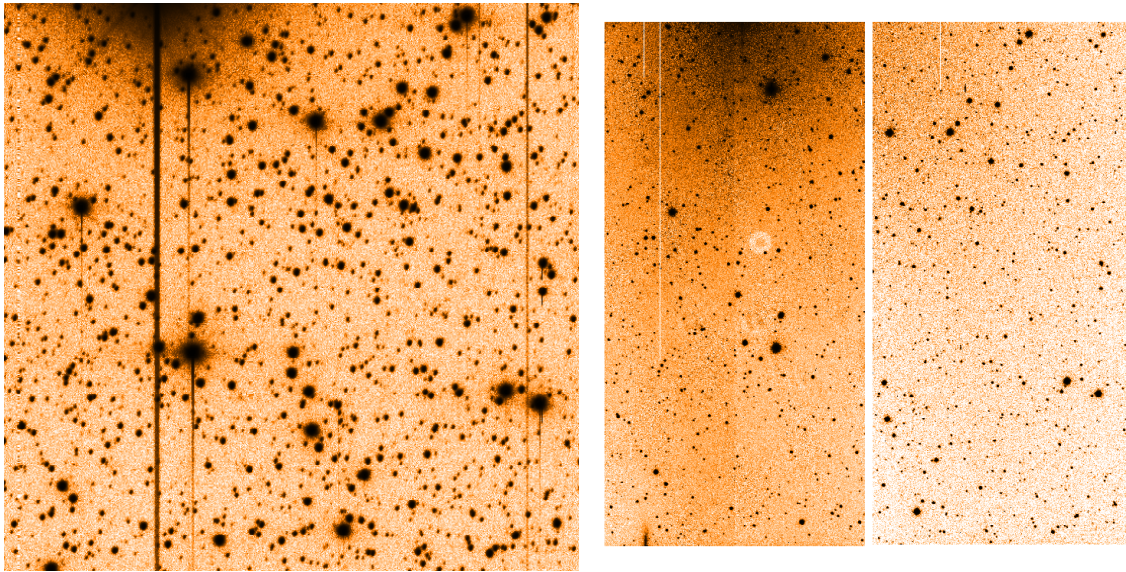
Figure 3.19: Left: QUEST q100899_F14 frame. Right: WIYN w240700_F14 frame. The gap column in the middle corresponds to MiniMosaic division.
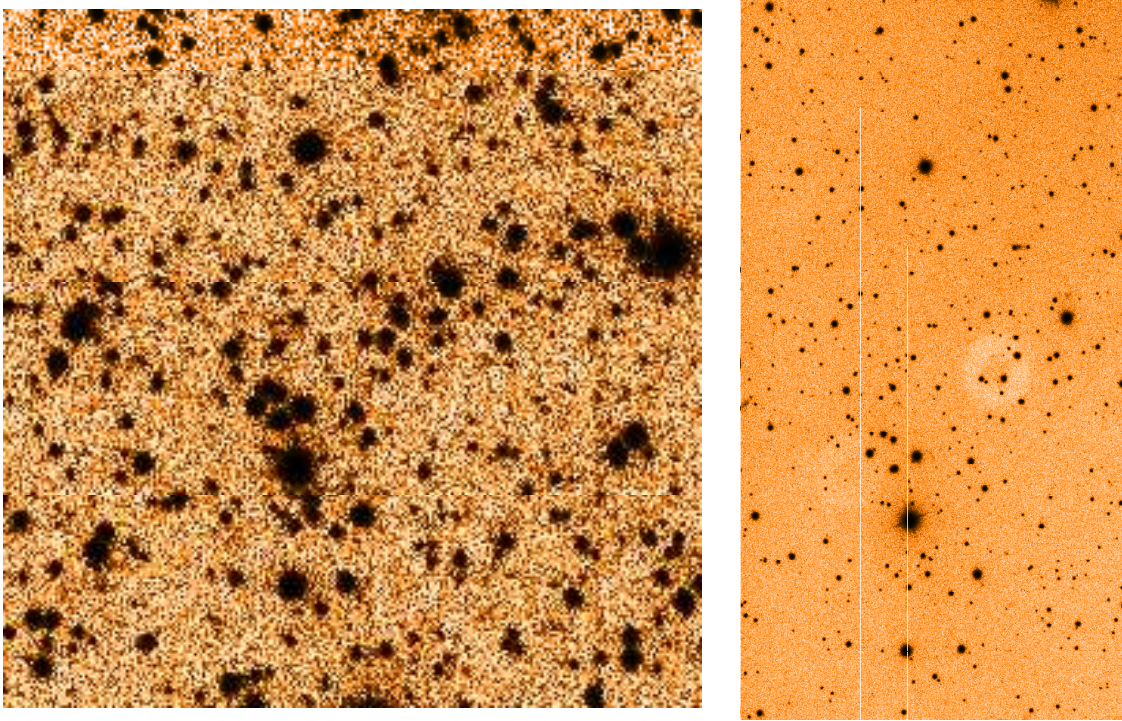
Figure 3.20: Left: QUEST q100899_F13 frame (zoomed twice with respect to q100899_F14 in Fig. 3.19). Right: WIYN w250700_F13 frame.

Table 3.11: Drift scanning specific systematic errors for QUEST data.

Systematic	Intensity peak drop (%)	FWHM broadening (%)	Error in RA (mas)	Error in DEC (mas)
Discrete shifting	12	14	0	0
Differential trailing	(a)	(a)	(a)	(a)
Curvature effect	(b)	(b)	(b)	(b)

[a]: Not quantified, but minimized by nearly equatorial images.

[b]: Smearing below $1''$. Minimized by fingers motion and nearly equatorial images.

As stated in Pag. 88, a corrector lens with an inverse barrel-like distorsion was inserted in front of the camera to flatten the image plane. While this is optimal for purely equatorial observations (Baltay et al. 2002), a noticeable focal-plane systematic error is introduced when the camera is observing at non-zero declinations, as it is the case of our data ($\delta \sim -1°$).

Abad & Vicente (2000) show that this effect is not negligible and has to be calibrated and removed from derived astrometric positions. QUEST positions were transformed to the reference frame defined by the Astrometric Calibration

Regions (ACR) (Stone 1997b) in order to derive a focal-plane positional errors map. Residuals as large as $3''$ for extreme coordinates were found.

- **Magnitude-related errors**

  Abad & Vicente (2000) also investigated magnitude-related errors by plotting the residuals from QUEST vs. ACR magnitude. A severe magnitude equation was detected, both for RA and declination. Depending on the considered coordinate and chip, residuals spread in the bright end ($V \sim 10-12$) from $-0.1''$ to $+0.6''$ for RA, and from $-0.5''$ to $+0.4''$, for declination. Regarding intermediate magnitude range and faint end, few chips showed flat trend around zero, above all in declination.

  However, it is noteworthy that raw (x, y) positions were computed by an early version of QUEST reduction pipeline, which made use of a simple baricentre algorithm. Therefore, this strong systematic error with magnitude is likely to be mostly caused by the use of that inadequate centering algorithm, which can deliver biased positions and magnitudes (Auer & van Altena 1978; Stone 1989).

- **Seeing fluctuations**

  No specific study related to this effect has been found in the literature.

  On one hand, as explained in Pag. 68, the origin of this error is totally general and, therefore, is likely to appear in QUEST, which performs wide-field astrometry over long periods of time. As introduced in Pag. 68, the periods of fluctuations in the declination residuals typically range from 3-4 to 40 minutes of time. On the other hand, the FOV of the F13 and F14 QUEST images (see Table 3.9) is much smaller than this variation range. Therefore, again as in FASTT case, we can assume this systematic effect will not be significant among the rest.

- **Discrete shifting**

  Sabbey et al. (1998) reported QUEST data to be with circularly symmetric PSFs with FHWM$\sim 2''.5$. In a posterior study, Baltay et al. (2002) confirm latter measurement with the median seeing to be around $2''.4$. Both are in accordance with the FWHM values calculated in our two data sets (see Table 3.9). In the same article, the authors also provide $2''.1$ as the median seeing operating in stare mode observed during the same period of time. Therefore

the overall degradation from stare to drift scanning seeings turns to be $0\!\!''3$ (14%).

On the other hand, if we revisit Figs. 3.4 and 3.3 with the above mentioned value of stare mode seeing ($\sigma =$ 0.89 pixels), we obtain a decrease in the intensity peak of 12% and a profile broadening of 14%, as described in Table 3.10.

The fact that both profile broadening values coincide indicates an important point: the rest of systematic effects due to drift scanning (differential trailing and curvature) have been effectively minimized in the way explained in the next two subsections.

Again, the magnitude drop due to this effect, while not being dramatic, will be one of the reasons which justifies the convenience of the application of image deconvolution to this kind of images.

- **Differential trailing**

  There are three features of our data which minimize the incidence of differential trailing over the final PSF and resulting astrometry.

  First, each one of the CCDs in QUEST camera is clocked at slightly different rates in order to compensate for the gradient in sidereal rate across the FOV.

  Second, the data we are going to study belong to a single chip.

  Finally, our data is nearly equatorial. As explained in Pag. 63, this turns the differential trailing effect to be nearly null.

- **Curvature effect**

  Two instrumental engines minimize the curvature effect impact over the QUEST data:

  As commented before in this section, the camera includes a field flattener lens with inverse barrel-like distorsion designed to compensate the curvature effect when observing at zero declination. It is clear that the inclusion of this corrector is to remove the bulk of PSF smearing which the curvature effect would introduce otherwise. However, our data has been observed at $\delta = 1.5°$ instead of at the equator. To our knowledge, the implications of this misalignment over the PSF and astrometry have not been studied in detail.

  Second, as seen in Fig. 3.18 the QUEST camera include the possibility of orientating their 4 fingers in the appropriate configuration which minimizes

the curvature effect. Baltay et al. (2002) reports PSF smearing is kept below $1''$ thanks to this engine.

3.2.3   NESS-T: Baker-Nunn camera at Rothney Astrophysical Observatory

The Rothney Astrophysical Observatory (Canada) is currently operating a wide field Baker Nunn camera (NESS-T BNC), which has been retrofitted for CCD imagery. This is one of wide field cameras built between 1950s and 1970s and coordinated by Smithsonian Astrophysical Observatory for artificial satellite follow-up. Original Baker-Nunn cameras were a modified Schmidt design with a symmetrical close triplet group of 50 cm lenses in the entrance pupil. The focal length was 510 mm at f/1 with a workable FOV of 5°x30° over the curved film field.

The NESS-T BNC was refurbished during the 2001-2003 period for enabling the CCD observing with an automated equatorial mount (Mazur et al. 2005). Optics were upgraded with a field-flattener corrector lens which provides a useful 4°4x4°4 FOV for the 4K×4K chip installed at prime focus.

A general description of the NESS-T BNC features is given in Table 3.12. For a closer understanding of the instrumental aspects of this facility, we refer the reader to Appendix A, where a very similar project, operated by Fabra Observatory and Real Instituto y Observatorio de la Armada en San Fernando, is presented.

One of the main programs developed in this telescope is called Near-Earth Space Surveillance Terrestrial (NESS-T) and aims to provide a new census of NEOs in North pole regions where other instruments located in moderated latitudes cannot access. NESS-T is the facility with widest FOV specifically dedicated to professional asteroid search. Note that NESS-T is optimized for NEOs discovery, and not for accurate astrometry. In this context, the project is fully operative in the detection part, but a complete astrometric calibration is still being held.

The data set considered in this section was kindly supplied by the NESS-T team at Rothney Observatory and Department of Geology and Geophysics at University of Calgary (Hildebrand et al. 2004). This study is inscribed in a wider collaboration for optimizing the scientific return of the two BNCs (NESS-T's and the one in San Fernando), and has been recently complemented with research stay of a member

Table 3.12: Generic features of NESS-T Baker Nunn camera.

Location	
Site	Rothney Observatory, Calgary (Canada)
Longitude	114° 17′ 18″ W
Latitude	+50° 52′
Elevation	1284 m
Telescope	
Type	Modified Schmidt camera
Aperture of corrector triplet lens	0.5 m
Mirror diameter	0.78 m
Focal ratio	f/1
Scale	$410''\mathrm{mm}^{-1}$
Corrector optics	2-element Field flattener lens
Spot size	20 μm
Filters	Light Pollution Removal (LPR) 99% (710 ± 210nm)
Detector	
Sensor	Kodak KAF-168801E
Format	4Kx4K, 9 μm, 36.8mmx36.8mm
QE	67% (peak)
Camera	Finger Lakes Instrumentation IMGX16801E
Average gain	1.73 e^- DN^{-1}
Average Readout noise	14.41 e^-
Pixel scale	$3''\!.9$
CCD FOV	$4°\!.4$x$4°\!.4$
Cooling	Peltier (ΔT $\sim$ 50 ℃)
Support CCD	Spider with low expansion material and
	± 1 μm accurate remote focus
Observational facts	
Acquisition mode	Stare
Typical exposure times	30s-180s
Limiting magnitude (IT=120s and SNR=1.3)	V$\sim$ 19.2

of our group, Maite Merino. The data features of this set do not correspond to habitual near pole NEOs observational strategy, but a test data customized for this deconvolution study.

As shown in Table 3.13, this particular set of NESS-T data comprise 10 overlapping frames taken in the same night. All these 30s exposures were conducted under stare mode during a short interval of time (1 hour). Seeing for that night was

Table 3.13: Description of NESS-T data to be studied.

Night global features	
Seeing	$\sim 3''$
FWHM	2.1 pixels
Filter	LPR
Considered FOV	Central patch of $0°.8 \times 0°.8$
Exposure time	30s
α_0	17h 45m 26s
δ_0	$+39° \; 21' \; 42''$

Frame specific features		
Frame ID	Date	Time
	(dd-mm-yy)	(hh:mm:ss)
NESS-T_01	12-11-04	03:37:49
NESS-T_02	12-11-04	03:44:00
NESS-T_03	12-11-04	03:50:11
NESS-T_04	12-11-04	03:56:23
NESS-T_05	12-11-04	04:02:36
NESS-T_06	12-11-04	04:08:45
NESS-T_07	12-11-04	04:14:57
NESS-T_08	12-11-04	04:21:16
NESS-T_09	12-11-04	04:27:27
NESS-T_10	12-11-04	04:33:37

significantly worse to the average in that site.

By the time the observations and data analysis were conducted, no precise dark and flatfield calibration frames were available. The implications of this oer the results will be discussed in Sects. 5.3.2 and 5.4.2.

Although unsuccesfully, an effort for obtaining realistic flatfield calibration frames was performed. Note that accomplishing this in an f/1 system is not straighforward. The usual techniques employed in slower telescopes are not valid in this case. On one hand, the usual twilight exposures do not suffice because of the significant brightness gradient within the large FOV of the BNC. On the other hand, dome flats suffer from appreciable stray and off-axis light which unvalidate the assumption of a uniformly illuminated source. Finally, with such a fast system as this, very short exposure time are required and, as a result shutter mapping correction becomes appreciable.
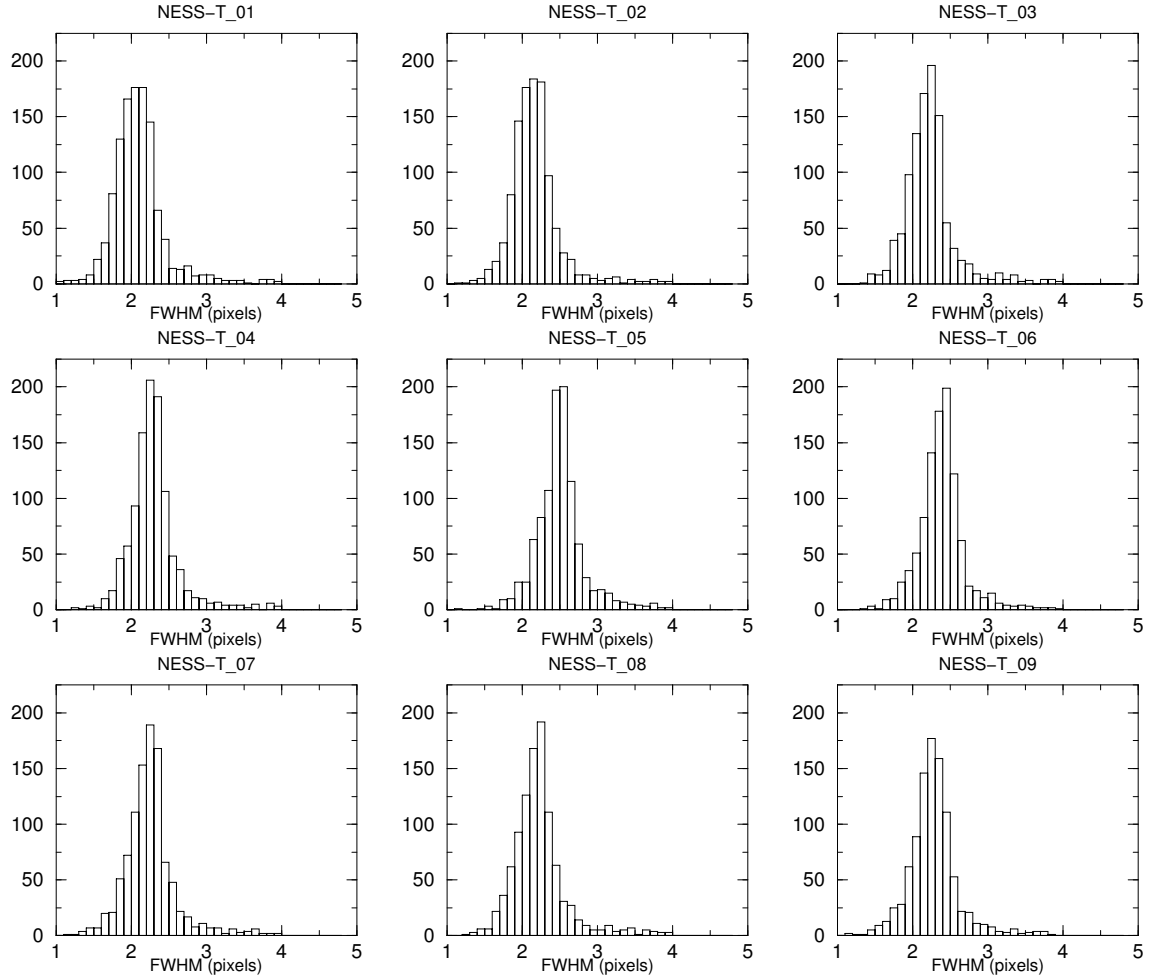
Figure 3.21: Histograms of FWHM for nine of the 11 studied NESS-T frames. FWHM values were obtained by profile 2D Gaussian fitting.

All previous complications were confirmed by observation tests taken by Merino (2004), and it has led us to the convenience of exploring other flatfield techniques, still to be tested. As a result, only the central 1K×1K subframe of 0°8x0°8 FOV was considered (see Fig. 3.22), where the flatfield and vignetting contributions are reasonably negligible. This election will allow us a more direct understanding of the benefits introduced by image deconvolution. With identic purpose a region lacking stellar crowding and very bright stars was chosen. A light pollution removal (LPR) filter was used for skipping sodium lamps emission present in suburban skies like this. As mentioned above, NESS-T is mainly dedicated to NEOs discovery, and not to accurate photometry. Therefore, as to maximize photon gathering is the main concern the choice of LPR filter is fully justified.

As can be seen in Fig. 3.21, sampling of NESS-T frames is comprised between 2.1 and 2.5 pixels. In contrast to most telescopes, the main contributor to FWHM is the spot size of the optical system, which on average accounts for rms$\sim 20\mu$m (~ 2.2 pixels) over the CCD FOV. From the observation logs of that night seeing is known to be about $3''$ due to the presence of thin clouds and moderate wind. In this regime, the seeing contribution ($\sim$0.7 pixels) to final FWHM matches well the second order variations in the histogram peaks in Fig. 3.21. In conclusion, the sampling (FWHM) of stellar profiles in NESS-T images is mostly dominated by the optical spot size and the slight modulation due to atmospheric seeing is only significant with quite bad seeing conditions ($\geq 3''$). Apart from the fact that NESS-T was not taken under drift scanning, three important differences come up when comparing NESS-T to FASTT data. First, NESS-T PSF is slightly correlated with seeing and dominated by optical spot size and its systematic distortions over the FOV. Second, as a result of its coarser pixel scale ($3.9''$pixel^{-1}), NESS-T data are likely to show significantly larger object blending than in FASTT case. Finally, note that NESS-T sampling is closer to the critical sampling limit (FWHM=2.0 pixels) for a Gaussian profile than FASTT's. All three differences will have consequences in the results and analysis of NESS-T deconvolved images, discussed in Sects. 5.3.2 and 5.4.2.

Systematic errors considerations

In contrast to FASTT and QUEST cases, systematic errors only related to stare mode (introduced in Sect. 3.1.1) do apply for NESS-T data.

Being NESS-T an observational program with recent first light, few systematic errors have been definitively calibrated. However, the most important errors (summarized in Table 3.14) have been already identified and are roughly discussed below.

- **Focal-plane positional errors**

  Although no map of focal-plane positional errors is available, several considerations on behalf of this can be addressed.

  First, we recall that in its original design, the focal plane of the BNC was spherical. Thanks to the inclusion of a 2-element lens field flattener corrector and a proper collimation of the system the focal plane has turned out to be practically flat within the CCD FOV.
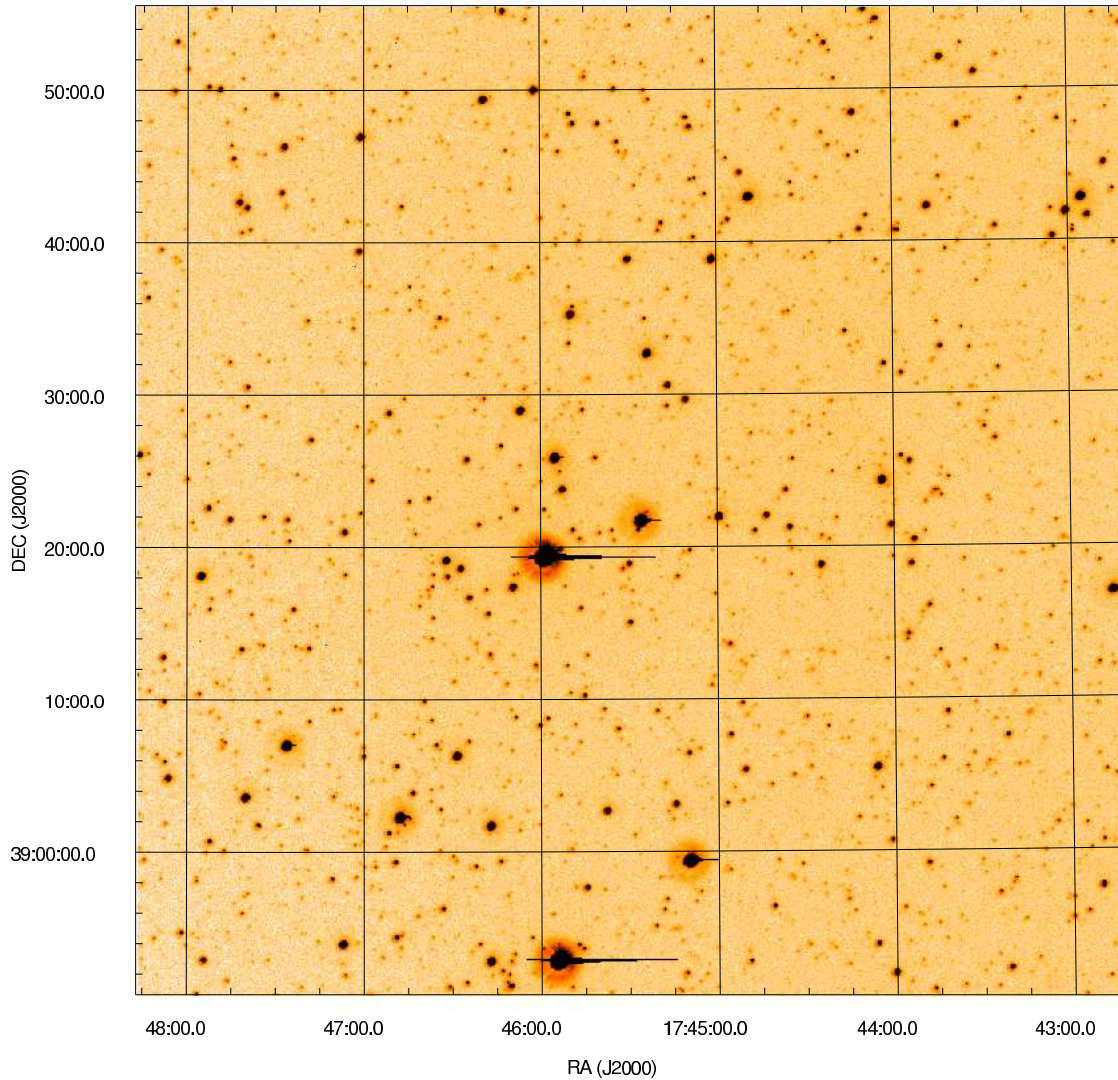
Figure 3.22: One of the 1K×1K ($0\overset{\circ}{.}8$x$0\overset{\circ}{.}8$ FOV) CCD frames from NESS-T Baker Nunn camera to be studied. The stellar density is sparse enough for avoiding undesirable crowding effects. The presence of very bright stars and its associated blooming is also minimized.

Second, and despite the former, when performing plate astrometric solution of our NESS-T frames, high order polynomials have been required to fit the whole FOV to standard astrometric coordinates using USNO-A2.0 (Monet et al. 1998) as reference catalogue. After this plate correction a significant number of star residuals exceeded far more than 3 times the rms of the fit ($0\overset{\prime\prime}{.}25$). Of course, this experiment is not conclusive and should be repeated with more denser grid of reference stars spread all along the CCD array and more accurate

Table 3.14: Most important systematic errors for NESS-T data.

Systematic	Error in RA (arcsec)	Error in δ (arcsec)
Focal-plane positional errors	> 1	> 1

Systematic	Intensity peak drop (%)	FWHM broadening (%)	Error in RA (mas)	Error in δ (mas)
Pixel response function	$\sim 3\%$	$\sim 2\%$	0	0

reference catalogue (for example UCAC2 (Zacharias et al. 2004b)). However, it is already indicative that the systematic focal-plane positional errors do exist in NESS-T camera and they are above the typical astrometric accuracy supplied by the camera.

Finally, it has been observed that the NESS-T PSF does show appreciable variability across the whole $4°.4$x$4°.4$ CCD FOV. However, this effect becomes minimized in the central $0°.8$x$0°.8$ patch considered for this study. In addition, as will be shown in Sect. 5.1.3, NESS-T PSF suffers from coma even in this central patch. It is noteworthy that posterior recollimations of the optical system have been performed in order to improve PSF uniformity.

On the whole, it is noteworthy that, luckily, our data set was acquired in a very homogeneous fashion. In other words, the objects coordinates derived from our 10 frames practically overlap (there are no inter-frame offsets) and, as the astrometric accuracy will derived just by the comparison of pixel coordinates of every frame (see Sect. 4.7), the positional systematic errors do not play a decisive role in our case.

- **Pixel response**

  Despite the relatively coarse scale of NESS-T images, the fact that the sampling is dominated by spot size up to a level always well above FWHM=$2''$ leads to that the broadening of stellar profile due to pixel response function is not as crucial as in drift scanning images as FASTT and QUEST. For a typical sampling value of $\sigma = 1.0$ pixels, which is very close to the FWHMs shown in Fig. 3.21, an intensity drop of 3% and a FWHM broadening of 2% were derived from Figs. 3.4 and 3.5.

- **Seeing fluctuations**

Although we do not have any study of this systematic error in NESS-T data, we do not expect it to be of decisive importance over the derived astrometry. This is because, as we mentioned above, NESS-T PSF is mostly determined by the spot size diagram of the optical system and not by atmospheric and its associated temporal variations.

- **Photon shot noise**

  The number of incoming background photons are proportional to the pixel area. In the case of NESS-T pixel, this is 7 (15) times larger than FASTT's (QUEST's). In addition, NESS-T sky is not as dark as FASTT's or QUEST's. As a result of these two factors, NESS-T background noise is dominated by Poissonian statistics at early exposure times (e.g. 30s)[9]. This translates into a lower SNR for a fixed exposure time, or equivalently, an decrease of the limiting magnitude of the image.

  Attending this, we will show in Sects. 5.3.2 that AWMLE deconvolution can be considered as solution for compensating that loss of limiting magnitude.

- **Vignetting obscuration**

  This particular data set suffers from significant vignetting. This was due to the excessive shutter diafragming which was installed to remove lateral light. As a result, about 6% of flux variation between the centre and the edge of the FOV was observed in our data. That problem was overcome by considering only the central patch of $0°8x0°8$, where such effect is minimized. That shutter diafragming problem was solved after this study was completed.

---

[9]Note that at this high count regime, Poissonian probability distribution can be approximated by a Gaussian with a dispersion of $\sigma = \sqrt{n}$, with n the number of counts.

Chapter 4

Proposed methodology

In this chapter we describe the methodology proposed for applying deconvolution to CCD images of arbitrary properties. Two separate stages in this reduction process are distinguished. First, the one devoted to calibrate and characterize the original data set for preparing the deconvolution. A diagram of the whole procedure is shown in Fig. 4.1. Second, the one dedicated to assess the deconvolution performance in terms of limiting magnitude gain, limiting resolution gain and astrometric precision. Each one is composed of several steps, namely: generic CCD reduction (Sect. 4.1) and PSF fitting (Sect. 4.2) for the first stage, and object detection (Sect. 4.3), limiting magnitude gain calculation (Sect. 4.4), limiting resolution gain calculation (Sect. 4.5), source centering (Sect. 4.6) and astrometric precision estimation (Sect. 4.7) for the second stage.

4.1   Generic CCD reduction

As justified in Chapt. 2, image deconvolution requires an accurate description of all the uncertainties presented in the data.

In CCDs, that begins with the knowledge of fundamental aspects of the data as the amplifier gain, readout and dark current noises and spatial quantum efficiency variations along the detector. This generic calibration turns to be the first step for whatever analysis algorithm. Image deconvolution is not an exception, as the proper removal of all these effects allows to separate the measured image p_j from flatfield
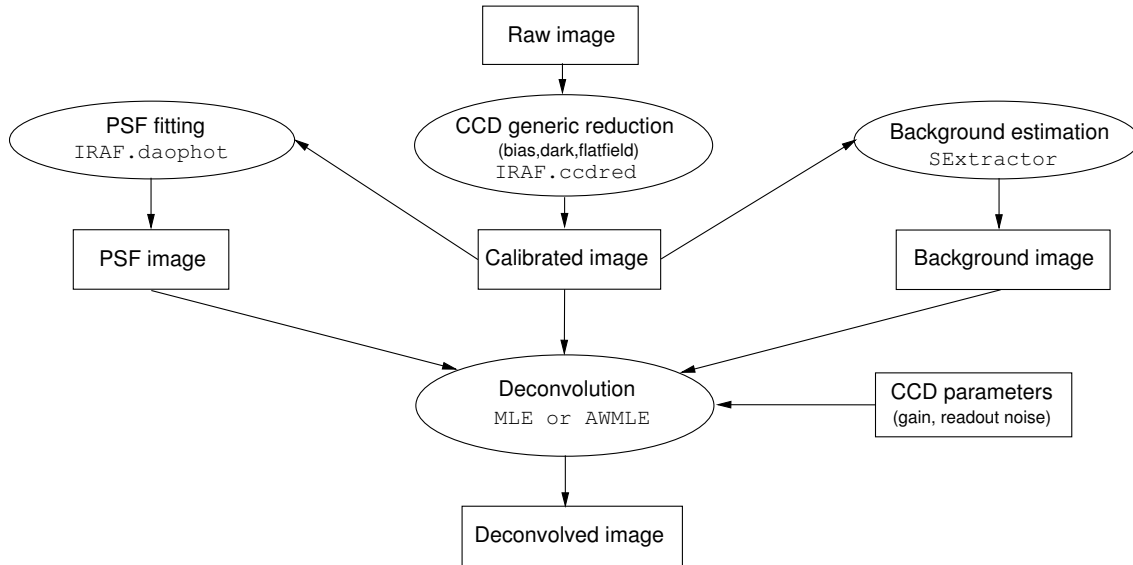
Figure 4.1: Flow-chart of the methodology for pre-deconvolution reduction steps. Background estimation is explained in Sect. 4.3, as part of the object detection process.

C_j and background b_j maps, which are input parameters of MLE and AWMLE deconvolution algorithms.

At this point, an important remark arise from Eq. 2.1. While C_j contributes multiplicatively to the measured data, b_j is an additive term. As a result, the correct assignment of every single signal ADU to either C_j or b_j is crucial for posterior image deconvolution performance, since this aims to keep original statistics and it distinguishes between flatfield (multiplicative) and background (subtractive) contributions. Therefore, both C_j and b_j should be estimated with the best accuracy possible.

For the case of CCD data taken under stare mode this generic reduction needs to have bias, dark and flat calibration frames. The procedure is very well-known and has been implemented in most astronomical reduction packages, as for example `ccdred` package (Valdes 1988) inside `IRAF`.

However, this generic calibration is not so well established for the case of drift scanning data, at least for the flatfield correction. As introduced in Sect. 3.1.2, this acquisition scheme naturally flatfields the resulting image, as each sky elementary region is sampled by every pixel in a row. Consequently, a certain pixel has an spectral response which is the mean quantum efficiency of all the pixels in its row. As a result, pixel-to-pixel noise is diminished. This is why some surveys do not apply

flatfield correction to their scanning strips. Others extract a flatfield vector from object frames themselves by calculating, for all the rows in the image, the mode of all pixels along a given row (Richmond et al. 2000). This special flatfield technique was implemented as a custom script inside `IRAF`.

4.2 PSF fitting

PSF fitting has been one of the mainstream topics in data analysis in astronomy during the last decades. It was originally motivated by the need of performing precise photometry in crowded fields. As a by product of this effort a kernel of the PSF can be obtained and introduced in the methodology we are defining as an input parameter of image deconvolution algorithm (see Fig. 4.1).

The performance of image deconvolution is highly dependent of the accuracy of the PSF modelling. Among other effects, an occasional deviation of the model with respect to the actual PSF can result in the confusion of those faint sources which are disposed around brightest stars. As MLE-family deconvolution algorithms are iterative, this mismatch incorporated in the PSF modelling can yield to undesirable artifacts in the solution image. Ideally, errors caused by uncertainties in the PSF should be well below noise fluctuations.

As anticipated in Sect. 1.1, the shape of telescopic PSF has been the subject of a number of studies. For the case of ground-based astronomy, both in photographic plates (King 1971) and in CCDs (Racine 1996) the authors define two well-separated parts in the PSF profile. These have different origin and localization on radial distance to the center θ:

- a central core caused by atmospheric turbulence. A number of factors, as the changes in wind speed and direction, index refraction and density play a key role in the magnitude of this turbulence. The larger the turbulence the broader this profile is. Note that this part of the PSF (commonly denominated as Kolmogorov profile or simply seeing) is slightly dependent ($\propto \lambda^{\frac{6}{5}}$) on wavelength (in optical and IR) (Racine 1996). As a result of the stochastic nature of this component, its shape cannot exactly be described in analytical means. Two profiles have been proposed in the literature for accounting this distorsion.

First, a Gaussian shape (Lagendijk & Biemond 1991) which is a simple model and convenient because of its particular properties in the Fourier space. (Stetson 1992, 1994) has also proposed 2D elliptical Gaussian model, which adds more flexibility for elongated profiles.

Second, Moffat (1969) first introduced and gave name to a radially symmetric function which can be expressed as:

$$I(\theta) = \frac{I_0}{\left(1 + \frac{\theta^2}{R^2}\right)^\beta} \qquad (4.1)$$

where R is related to FWHM by FWHM $= 2R \sqrt{2^{1/\beta} - 1}$ and β is a parameter which measures the power of the wings at large θ's. This function has been found to fit the Kolmogorov profile better than the Gaussian profile, specially in the outer part up to $\theta \sim 5$ FWHM, where Gaussian profile decays faster than Moffat (Racine 1996).

Eq. 4.1 has also been used for fitting space-based PSFs which showed extended emission in the outer wings, even above the power defined by Moffat function. This was the case of aberrated pre-COSTAR HST PSF, whose best analytical fit responds to that expression with β=1, also called Lorentzian function.

In the limit of $\beta = 0$, the Moffat function of Eq 4.1 becomes a radially symmetric Gaussian.

- an extended external aureole with a decreasing intensity as the inverse square of the radial distance. This component becomes dominant over the central core for $\theta > 5$ FWHM (turbulence limit). It is caused by a combination of atmospheric and instrumental effects. First, the optical system may have aberrations or anomalies. Depending on the their strength, the outer structure might be complex and even show asymmetries (e.g. coma). Second, the light is scattered by atmospheric aerosols, scratches or dust on telescope optics. Finally, the diffused and reflected light in the detector assembly also contributes to this outer halo.

Note that the magnitude difference between the peak of the central core and the region where aureole begins to become dominant ($\theta \sim 5$ FWHM) is about 11-12 mag (Racine 1996). Taking into account that this magnitude range nearly fulfills the whole CCD dynamic range and that background level in wide field surveys is usually high, it can be concluded that aureole will not be really appreciable in bright

non-saturated stars. In the brightest saturated objects some information of this PSF component could be extracted, but only in basis of a reduced sample of elements. Therefore, apart from a few state-of-the-art experiments of PSF characterization or very exotic data which may use saturated stars wings, the rest of ground-based PSF fitting work has been devoted to model the Kolmogorov profile dominated by turbulence. In addition, in the case of undersampled data, an attempt of fitting aureole features from saturated stars could be in danger of recovering part of the high frequency smearing introduced by aliasing. In accordance to this, we will concentrate the subsequent PSF analysis within turbulence limit radial distance ($\theta < 5$ FWHM).

Most of PSF fitting packages have Gaussian and Moffat profile functions as models choices (Buonanno et al. 1983; Mateo & Schechter 1989; Penny & Dickens 1986). This is also the case of the reduction tool considered for our PSF modeling, `DAOPHOT II`[1] (Stetson 1992; Stetson et al. 1990), which has the following ones:

1. a Gaussian function,

2. a Lorentzian function, as defined in Eq. 4.1 with $\beta = 1$,

3. two Moffat functions, as defined in Eq. 4.1 with $\beta = 1.5$ and $\beta = 2.5$.

For all three models `DAOPHOT II` includes additional 2D elliptical parameters which allow to reproduce elongated profiles. An interesting feature which is not available in `DAOPHOT II` would have been to have a PSF model composed by the combination of two Moffat analytical functions. In theory, this is the model (with $\beta = 7$ and $\beta = 2$) which best fits Kolmogorov profile (Racine 1996).

It is not in the scope of this thesis to review the procedure followed by `DAOPHOT II` for fitting the PSF. In brief, it consists in an iterative process which numerically computes the PSF by fitting a list of selected stars to a specified model with weighted least-squares method. Every iteration step includes removal of close neighbours from selected stars sample. This fitting procedure is interrupted when either a satisfactory data-model rms deviation is achieved or the maximum number of allowed iterations is reached. We refer the reader to Davis (1994); Stetson (1987) for a complete description. However, in the following some considerations about `DAOPHOT II` procedure which are pertinent for our deconvolution application are outlined:

---

[1]It is included in standard `IRAF` distribution

1. largely discordant pixels, mostly caused by cosmic rays and overlapping with neighbour stars, are automatically penalized in the fitting process. These are identified by comparing among those pixels located at the same place within the profiles of the other selected stars.

2. in principle, this new version of the package offers the possibility of including saturated stars in the derivation of the final PSF. As stated above, the outer regions of these objects yield information about the aureole component of the PSF. After several tests, we concluded that the inclusion of saturated stars in the PSF model does not lead to significant improvements, at least for the data presented in Chapt. 3. We attribute this to the fact of disposing of a few (sometimes only one) saturated star in the studied FOV.

3. in general, the whole PSF fitting process can be automated. In our specific case, still some visual inspection and catalogue identification of the PSF selected stars was performed by the author, for discarding close blending or extended objects (galaxies). However, this interactive step was found to be irrelevant most times, and could be easily protocolized for its complete automation. Note this is very convenient for the overall integration of the deconvolution algorithm in a unattended reduction pipeline.

4. the purely analytical fitting approach has been found insufficient for completely modeling the PSF. Normally, analytical function can reproduce up to 95% of the intensity variations within a star's profile (Stetson 1992). The remaining 5% residual is mainly distributed in the outer wings before reaching the turbulence limit ($3 < \theta < 5$ FWHM). In response to this, DAOPHOT II offers the possibility of using an empirical look-up table of correcting values in order to mitigate this fitting deviation. As a result, the photometric scatter is significantly improved even for undersampled data.

   Note that this part of the stellar profile is the one more affected by background noise. Therefore, the solely incorporation of this correction table by averaging pixel values of selected targets could imply the undesired introduction of high frequencies features related to noise and aliasing. This problem can be mitigated by sampling residuals at higher spatial resolutions than the observational data. In the case of DAOPHOT II, these are oversampled in grid twice finer by using bicubic interpolation.

As explained in Sect. 2.1.2, the fact that the detector is composed by finite pixels

introduces an additional distorsion in the PSF when this is sampled in the detection process. As the pixel size increases with respect to PSF width (lower FWHM), more and more flux is localized in the few central pixels. Interesting experiments about DAOPHOT II performance in different data sampling regimes have been carried out by Stetson et al. (1990) with real images. Table 4.1 includes a summary of results for the same set of real (non-synthetic) stars, spanning a wide magnitude range, in oversampled and severely undersampled conditions. From the inspection of the table several considerations arise:

Table 4.1: Sampling-induced photometric scatter (Stetson et al. 1990).

PSF Model	σ (mag)
FWHM = 2.54	
Gaussian+LUT[a]	0.0077
Moffat+LUT	0.0081
FWHM = 0.85	
Gaussian	0.0894
Gaussian+LUT	0.0826
Moffat	0.0281
Moffat+LUT	0.0178

[a] Empirical look-up table of correcting values.

- Gaussian and Moffat models seems to be equally preferable for the oversampled case despite the theoretical priority for Moffat justified above.

- σ is in general worse for the undersampled case. This scatter increase is induced by the interpolation method used to encode the PSF.

- the case of Gaussian model is specially hampering in the undersampled case and denotes the poor performance of this model under these sampling conditions. This discrepancy is not only localized in the outer wings, but also in the central pixel of the profile. The latter is justified by the fact that the inclusion of the look-up table (which is mainly defined in outer wings) over the Gaussian model does not lead to a great improvement.

- Moffat model shows a remarkably better performance for undersampled data. Therefore, again as the Kolmogorov profile reasoning, Moffat profile is favoured

in place of Gaussian function because it is less affected by sampling-induced interpolation errors of PSF fitting packages.

- with the addition of a look-up table of corrections, Moffat scatter is slightly improved and approaches to the figure of over-sampled data.

In summary, photometric scatter derived from `DAOPHOT II` seriously degrades with undersampling for Gaussian model, but this is nearly avoided if Moffat model is considered.

Note the discussion above was dealt around photometric, not astrometric, scatter. The latter will be issued in Sect. 4.6.

4.3   Object detection

The object detection process is conducted with `SExtractor` (Bertin & Arnouts 1996). This package is widely used among the astronomical community, and has shown to be a robust tool in a large variety of data features (CCD and photographic response, sampling, SNR, etc.).

The algorithm followed by `SExtractor` can be divided in four separated phases:

1. the sky background (either constant or variable across the field) is modeled by using a combination of $\kappa\sigma$-clipping and mode estimation.

2. the image is background-subtracted, filtered and thresholded. As the filtering process, this is performed via a convolution with an optimal kernel (`FILTER_NAME`) which matches the PSF of the image. This particular choice maximizes the detectability. In our particular case, we chose `FILTER_NAME` to be a Gaussian kernel with FWHM close to the PSF one. One might object that to use the same convolution kernel is not appropriate because PSF is indeed variable across the image. However, detectability has been found to be a rather slow function of the FWHM of employed kernel (Irwin 1985). For example, a mismatch of 50% between the kernel FWHM and that of the PSF, which is far larger than what we expect from typical PSF variations in our data, leads to no more than a 10% loss in SNR peak. A similar test of

this trend was performed for both original and deconvolved QUEST images (Sect. 3.2.2), yielding to even smaller loss of detection efficiency.

Two key parameters play an important role in the thresholding step. First, DETECT_THRESH which is the detection threshold, in units of background rms $(\sigma)^2$. And second, DETECT_MINAREA which is the minimum number of 8-connected[3] pixels above threshold for a positive detection.

Finally, a flag image FLAG_IMAGE can be used to specify those regions in the image likely to trigger false detections due to dark and hot pixels, deferred charge columns, CCD defects, etc. These detections are accordingly flagged for later disregarding.

3. a deblending process is run over the detection list obtained in step 2. The pixels of each thresholded object are filtered in order to obtain occasional overlapping components. This filter is based on a multi-thresholding technique which does not make any assumption about the object profile. Its performance is modulated by DEBLEND_MINCONT parameter. This is the minimum deblending contrast and establishes how sensitive is SExtractor to blended objects. Of course, this parameter is crucial for resolution gain study described in Sect. 4.5.

4. photometry and classification via image segmentation are performed for all the detected objects, before writing to the output catalogue to disk.

Optimal values for the above key parameters were found after some empirical learning in each data set, for both the original and deconvolved images. This parameter tuning does not lead to the same values depending the purpose. For example, narrower FWHM values for FILTER_NAME were found to be more effective in the resolution gain study (Sect. 4.5) than the ones employed in the limiting magnitude study (Sect. 4.4), although that choice imply a slight increase of false detections in the former case.

---

[2]Note that SNR is proportional (not identical) to DETECT_THRESH. For example, Benítez et al. (2004) found in the context of galaxies detection that SNR=3.5 when DETECT_THRESH=1.5.

[3]Two pixels are 8-connected if their edges or corners touch.
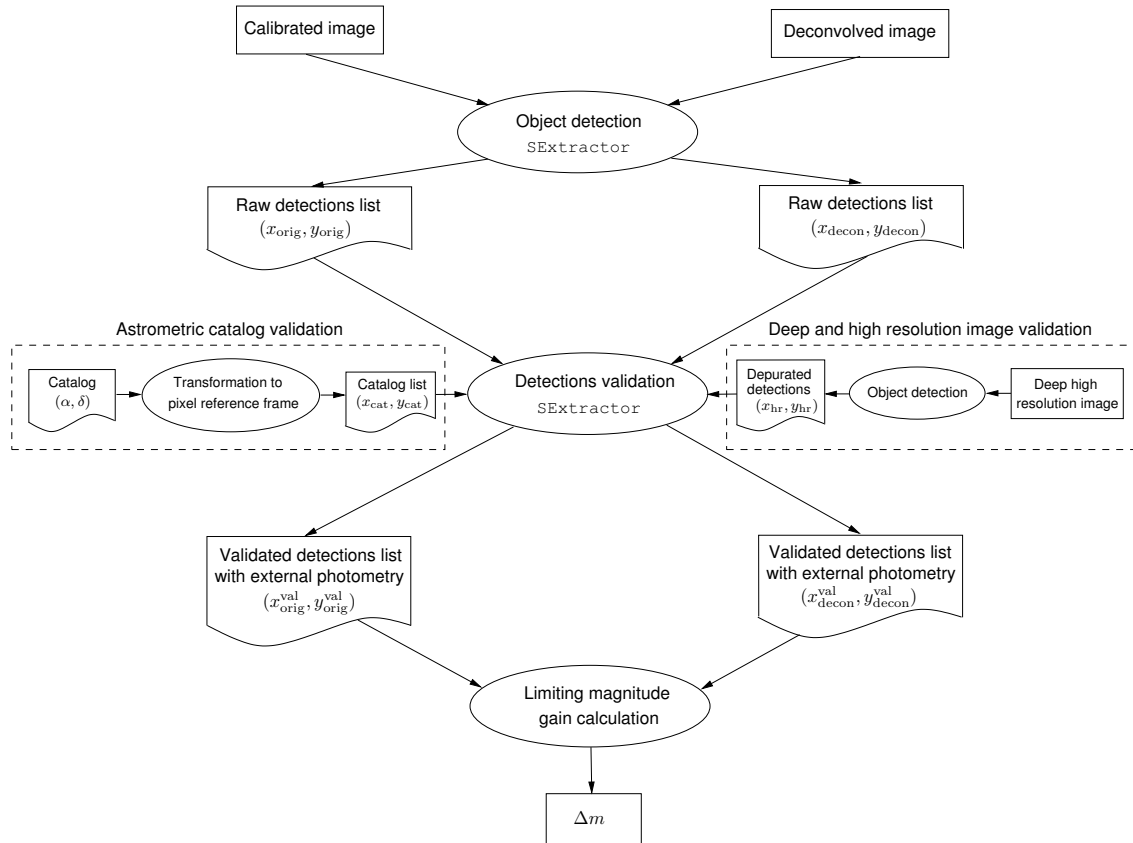
Figure 4.2: Flow-chart of the methodology for post-deconvolution reduction stages. The validation of raw detection lists can be derived from either astrometric catalogue (left) or deeper and higher resolution image (right). Multiframe comparison validation process has not been included as it was not finally used.

4.4   Increase in SNR and limiting magnitude

The aim of this Section is to define a methodology for validating the detections found by SExtractor in the former Section. Once these have been assured to be true with one of the procedure proposed in Sects. 4.4.1, 4.4.2 and 4.4.3, and not due to artifacts, they can be used for calculating the limiting magnitude gain introduced by deconvolution. The diagram shown in Fig. 4.2 summarizes the steps involved in this process.

Typically, for multiframe CCD data sets as the ones described in Sect. 3.2, we propose three alternatives in order of preference which we describe in the following.

4.4.1 Validation with a deeper and higher resolution image

Wide field surveys normally conduct follow-up observations with larger telescopes when confirmation is needed for a number of selected objects. Therefore, a deeper and higher resolution image which overlaps the selected survey image might be available in some cases. In addition, it is preferable that both images have been taken with similar bandpass filters. This should ease the confirmation of faint detections which might not appear in deeper image because of extreme spectral types.

The followed methodology is simple. First, `SExtractor` detection is performed in both survey and deeper images. Next, the latter detection list in pixel coordinates is transformed to the pixel reference frame of the former one, by using `xyxymatch`, `ccmap` and `cctran` tasks inside `IRAF`. Finally, a matching process is performed keeping those objects in common (within a tolerance radius) between the survey and the deep images lists.

4.4.2 Validation with reference catalogue

All-sky deep and accurate astrometric catalogues have become common along the last decade. As seen in Tab. 4.2, in most cases (with the exception of UCAC2) their limiting magnitude is large enough for assuring object completeness for moderately deep images ($V_{\mathrm{lim}} < 20$), as the ones we study in this part of the thesis (see Sect. 3.2). USNO-B1.0 and GSC 2.2 would be the more appropriate choices, since provide high stellar density, acceptable astrometric error and proper motion information. USNO-A2.0, although it shows about half number of objects than USNO-B1.0 and does not provide proper motions, is still a reasonable alternative for the level of accuracy required for our limiting magnitude gain study.

Note that recent efforts for merging best astrometric and photometric catalogues available (HIPPARCOS, Tycho-2, UCAC2, and USNO-B) have led to the release of NOMAD (Zacharias et al. 2004a). Although NOMAD provides the *best* astrometric and photometric data for a given star, our concern to keep homogeneity in the magnitude scale made us to disregard this alternative and keep USNO-B1.0 as the reference catalogue despite its considerable poor photometric error.

Catalogues are queried online with the `scat` program of `WCSTools` package (Mink

2002). Next, (α,δ) coordinates are transformed to the pixel reference frame by using `ccxymatch`, `ccmap` and `cctran` tasks inside `IRAF`. Finally, a matching process is performed keeping only those objects common to the frame detection list and the catalogue within a tolerance radius.

Table 4.2: Overview of some all-sky astrometric catalogues.

Name	Number of objects	Limiting magnitude	Mean error (at J2000)	Reference
UCAC2	48,330,571	$R \sim 16$	$0.''015$–$0.''070$	(Zacharias et al. 2004b)
GSC 2.2	435,457,355	$J \sim 19.5$	$0.''3$–$0.''75$	(Morrison et al. 2001)
USNO-A2.0	526,280,881	$V \gtrsim 20$	$0.''25$	(Monet et al. 1998)
USNO-B1.0	1,045,913,669	$V \sim 21.0$	$0.''2$	(Monet et al. 2003)

4.4.3   Validation with multiframe comparison

One of the survey frames is considered as reference. Next, the rest of detection lists are transformed into this reference system. Finally, a matching process is performed keeping only those objects appearing in all lists, within a tolerance radius.

For the matching process used in all three methodologies described in Sects. 4.4.1, 4.4.2 and 4.4.3 a tolerance radius value needs to fixed. There are several factors which constrain the optimum value of this parameter. On one hand, in the case of Sect. 4.4.2., the mean random error of the reference catalogue can contribute to slightly enlarge the residual between the pixel coordinates of survey and catalogue lists. The impact of high proper motion objects with respect to their position in the reference catalogue has been found non significant for the statistical nature of the limiting magnitude study[4]. On the other hand, if the tolerance radius is too large it could lead to fictitious detections due to neighbouring objects contamination. In conclusion, the value for the tolerance radius will be empirically determined attending the above mentioned constrains for each particular data set. This value will be assigned

---

[4]Note that, given the pixel scales of the data sets in Sect. 3.2 ($1''$–$4''$), even the highest proper motion objects would need epoch difference larger than the ones found in catalogues of Tab. 4.2 for producing wrong validations. Anyway, if present, a very small number of objects would be affected, and would not yield to biased estimations of limiting magnitude gain.

to the `ASSOC_RADIUS` parameter in `SExtractor`, which will accordingly perform the matching process between the survey and reference lists.

Several reasons justify the preference order of the three validation methodologies exposed above:

- First, if the follow-up image in Sect. 4.4.1 is deep enough (2–3 additional magnitudes), this is very likely to include all the objects detected in the survey image. In contrast, the degree of completeness achieved in Sect. 4.4.3. is subordinated to the number of detections offered by the frame with worst seeing. This can yield to an effective underestimation of limiting magnitude gain achieved by deconvolution.

- Second, although the use of a deep reference catalogue as Sect. 4.4.2 (e.g. USNO-B1.0) could offer completeness even for the list of deconvolved images, their performance in front of blended objects is not so optimal as the follow-up image in Sect. 4.4.1, which can have far better resolution[5]. In addition, occasional mismatches due to proper motion in Sect. 4.4.1 would be marginal, given the very short epoch difference between our survey and follow-up images.

- Third, both follow-up images of Sect. 4.4.1 and reference catalogues of Sect. 4.4.2 include false objects. The former due to image artifacts (cosmic rays, deferred charge columns and hot and cold pixels). The latter due to plate internal reflections, emulsion defects, etc. However, while the former can be easily removed by either visual inspection[6] or filtering detection parameters (ellipticity, roundness), the latter are usually undetectable, since catalogues do not provide such kind of morphology information.

- Finally, as commented above, most references catalogues in Tab. 4.2 are photographic plate based. In this situation, missing objects around very bright stars are common.

After one of the three validation methodologies is chosen attending for each data set, this is applied to both the original and deconvolved image. As a result, the values for number of raw (N^{raw}), matched (N^{matched}) and unmatched ($N^{\mathrm{unmatched}}$)

---

[5]Note that all deep catalogue in Tab. 4.2 were compiled from photographic plates with a $0''8$–$1''$ pixel scale.

[6]At least for demostrative examples like the ones of this thesis.

detections are obtained for each image. Raw detections are simply those being output by `SExtractor`. Matched detections are those raw detections (from original and deconvolved images) which are present in the reference list, in accordance to the validation method chosen. On the contrary, unmatched detections are those which are not present in reference list. The latter and their origin will be separately discussed for each data set. For a given deconvolution algorithm, a large increase in N^{matched} is as important as the control of a low $N^{\mathrm{unmatched}}$.

The ratio of $N^{\mathrm{matched}}_{\mathrm{orig}}$ to $N^{\mathrm{matched}}_{\mathrm{deconv}}$ is a direct indicator of the limiting magnitude gain. This can be written as:

$$\Delta m = m_{\mathrm{deconv}} - m_{\mathrm{orig}} = 2.5 \ \log \frac{N^{\mathrm{matched}}_{\mathrm{deconv}}}{N^{\mathrm{matched}}_{\mathrm{orig}}} \tag{4.2}$$

The result led by Eq. 4.2 is similar to that derived from dividing the areas below the magnitude histograms of matched objects for both original and deconvolved images.

Complementary, other descriptors can be considered for understanding the way image deconvolution improves limiting magnitude. They are the number of detections (raw and matched) versus number of iterations, the number of detections (raw and matched) versus detection threshold and the magnitude histogram of matched detections versus number of iterations. They all will be used in Sects. 5.3.1 and 5.3.2 for the considered data sets.

4.5 Increase in limiting resolution

The aim of this Section is to define a methodology for estimating the gain in limiting resolution delivered by image deconvolution.

A simple custom program was developed for pairing all the objects with their closest neighbour and calculating their separation and magnitude difference. The employed algorithm is as follows:

1. choose one of the validation methods described in Sect. 4.4,

2. perform object detection as detailed in Sect. 4.3. DEBLEND_MINCONT parameter is set to its minimum contrast, i.e., SExtractor sensitivity to blended objects is set to its maximum value. DETECT_MINAREA is fixed to the same value for the original and deconvolved image.

3. perform the matching process between object and reference lists,

4. consider the lists of matched detections of original and deconvolved images,

5. for each object, find its closest companion. Store the separation, positions, magnitudes and magnitude difference,

6. exclude pair repetitions[7],

7. sort pairs by increasing separation,

Once the algorithm above is run, two possible approaches for evaluating the results in terms of resolution gain introduced by image deconvolution can be considered. These are presented in the next two subsections.

4.5.1 Qualitative assessment of resolution gain

Most wide field surveys are orientated to the discovery of a particular type of objects. Usually, the efficiency of this process is not complete and the most interesting objects are collected in a list of candidates for posterior follow-up observations.

In this context, a couple of qualitative descriptors are proposed. First, a visual comparison of the closest pairs for both original and deconvolved images. From these, the newly resolved objects are labeled for easing their identification. Second, a table with the computed separation, components magnitudes and magnitude difference of newly resolved companions for the list of candidates objects. Both closest objects figures and table will be further discussed in Sects. 5.4.1 and 5.4.2 for considered data sets.

---

[7]Caused by the fact that $\|\overrightarrow{AB}\| = \|\overrightarrow{BA}\|$.

4.5.2   Quantitative assessment of resolution gain

Two statistical descriptors were used for this aim.

First, the histogram of separations of closest components, $N(\rho)$. The separation distribution for original and deconvolved images is compared. In general, a shift towards smaller separations is observed for deconvolved histogram. In particular, a quantitative estimation of resolution gain ($\Delta\rho_{\mathrm{lim}}$) is derived by simply subtracting the minimum resolved separations (or limiting resolutions ρ_{lim}) of each histogram. That is:

$$\Delta\rho_{\mathrm{lim}} = \rho_{\mathrm{lim}}^{orig} - \rho_{\mathrm{lim}}^{\mathrm{deconv}} \tag{4.3}$$

Note that the value of $\Delta\rho_{\mathrm{lim}}$ is crucial for the applicability of deconvolution to an specific survey project. For example, in the context of data sets described in Sect. 3.2.2 and 3.2.3, if $\rho_{\mathrm{lim}}^{\mathrm{deconv}}$ were below the cut-off value of the separation distribution for binary asteroids or gravitational lenses, the use of deconvolution would be very convenient for the resolving new close components which are inaccessible in the original image. More in general, central crowded regions of globular clusters could be a suitable data set for testing this resolution gain.

Second, other complementary plots such as the magnitude difference (Δm) versus separation (ρ) and the secondary component magnitude (m_2) versus separation (ρ) are considered. In general, both plots illustrate that ρ and m_2 intervals where secondary components are resolved in deconvolved image are larger than in the original image.

4.6   Source centering

In contrast to PSF fitting techniques commented in Sect. 4.2, source centering has been approached by means of the fit of purely analytical models. Thus, this turns out to be a non-linear problem of parameters estimations. In this way, effort in the literature has been mainly focused in the proposal of accurate models and the seek of robust and efficient optimization techniques.

As regard as the models, Auer & van Altena (1978); Lee & van Altena (1983) for photographic plates and (Monet & Dahn 1983; Stone 1989) for CCDs show that 2D

Gaussian is the one providing highest astrometric accuracy. This simple result can seem at first glance surprising, because one would expect that the model offering best astrometric performance should be the one offering best profile fit. On the contrary, Fig.1 in Auer & van Altena (1978) shows that the inclusion of additional parameters (e.g. sloping background) in centroid fitting model does not yield to more reliable positional measurements, although they actually improve the goodness of fit estimator. This was later confirmed for CCDs by Monet & Dahn (1983). This is more formally explicited in Eq. 9 of Lee & van Altena (1983) for photographic plates and in Eq. 13 of Mighell (2005) for CCDs, where positional and photometric parameters of the centering fit can be supposed to be uncorrelated. In particular, the positional standard error σ_x turns to be inversely proportional to the square root of the partial derivative of the intensity distribution model $\frac{\partial F}{\partial \mathcal{X}}$.

Thanks to the positional-photometric uncorrelation, the theoretical astrometric error in the photonic limit can be estimated to be a function of a few basic parameters of the stellar profile, namely: the SNR and sampling. This relation is usually split in bright and faint stars regimes yielding (Irwin 1985; Mighell 2005):

$$\sigma^2_{\mathcal{X}:\,\text{bright-PL}} \approx \frac{\mathcal{L}^2}{\mathcal{E}} \qquad , \qquad \sigma^2_{\mathcal{X}:\,\text{faint-PL}} \approx \frac{8\pi\,\mathcal{B}\,\mathcal{L}^4}{\mathcal{E}^2} \qquad (4.4)$$

where $\mathcal{E}$ is the measured stellar intensity, $\mathcal{B}$ corresponds to observed background level and $\mathcal{L}$ is the *sampling scale length* ($\mathcal{L} > 1$ for oversampled, $\mathcal{L} = 1$ for critically-sampled and $\mathcal{L} < 1$ for undersampled profiles). Note Eq. 4.4 is a Cramér-Rao Lower Bound of the positional estimator (Winick 1986). Thus, it yields the minimum error value for an unbiased position.

A more visual interpretation of the above formalization consists in wondering in which part of the PSF the positional information resides. We recall that $\sigma_{\mathcal{X}} \propto \left[\frac{\partial F}{\partial \mathcal{X}}\right]^{-\frac{1}{2}}$. Let us assume that better localized positional information is equivalent to smaller $\sigma_{\mathcal{X}}$ and the typical intensity distribution of an stellar profile (e.g. Gaussian). As a result, that positional information basically turns out to reside at intermediate radial distances, between the core and wings, where $\frac{\partial F}{\partial x}$ is maximum (van Altena 1998).

Note that positional error in Eq. 4.4 refers to the photonic limit (PL), where the sampling is ignored as infinitely small pixels are supposed. However, in the case of undersampled data as the images described in Sect. 3.2, the $\sigma_{\mathcal{X}}$ expression is much more complicated but in general we should expect larger astrometric errors than

predicted by Eq. 4.4. Apart from this theoretical relation, numerical complications in the centering routine also appear: as stellar profile is sampled below the sampling theorem, $\frac{\partial F}{\partial \mathcal{X}}$ and rest of derivatives are more poorly determined because of the larger interpolation errors. As a result, $\sigma_\mathcal{X}$ becomes degraded below its expected Cramér-Rao Lower Bound. The limiting case when all the stellar light resides in a single pixel constitutes the worst scenario, since any subpixel positional information is lost.

4.6.1   Deconvolution and centering

From the considerations above, it can be concluded that positional accuracy is a trade-off relation between SNR and sampling. It is expected that at some point of intermediate sampling, the sampling contribution might become dominant over the inversely proportional contribution of $\mathcal{E}$.

The role that MLE deconvolution plays in this competition is twofold. On one hand, deconvolution images enhances SNR, both in bright and faint stars regimes. On the other hand, stellar profiles are sharpened. As a result, the sampling of MLE deconvolved image is worse than the one of the original image. In most algorithms this trend is accentuated with the number of iterations, in the majority of cases violating the limit stated by the sampling theorem (FWHM$\sim$ 2.0 pixels).

In view of this, special attention to the use of specialized centering algorithms should be given. Otherwise, the positional information retrieved from deconvolved images could be biased and/or less accurate than what really is. The same idea of seeking specialized tools for the proper analysis of undersampled (non-deconvolved in that case) images have been pointed out by Howell et al. (1996).

4.6.2   Levenberg-Marquardt Method

Centering routines are commonly based on nonlinear least-squares fitting technique, which allows the simultaneous determination of all the parameters of the stellar profile model. The measure of the goodness of fit between the data z_i and the model m_i, called chi square, is defined as:

$$\chi^2(\mathbf{p}) \equiv \sum_{i=1}^{N} \frac{1}{\sigma_i^2} (z_i - m_i)^2 \tag{4.5}$$

where σ_j is the standard error associated with the jth parameter (p_j).

In most cases centering algorithms in the literature have approached the minimization of Eq. 4.5 by using two well studied numerical techniques: steepest-descent (or gradient) and Taylor series method (which assumes local linearity in the $\chi^2(\mathbf{p})$ at each iteration). Both alternatives have been proved to be satisfactory for well-sampled and critically sampled data.

However, their performance in undersampled data, where the structure of $\chi^2(\mathbf{p})$ surface is much complex, has been questioned (Mighell 1989): Taylor series method is not robust because it easily diverges and Steepest-descent is not efficient because it shows very slow convergence. Our global proposed methodology employs a different minimization approach which is characterized by its simultaneous robustness and efficiency in finding the global maximum in the $\chi^2(\mathbf{p})$ space. It is based on Levenberg-Marquardt Method (`LMM`) (Levenberg 1944; Marquardt 1963). It makes use of a damping factor λ for efficiently seeking the global solution across the parameters space and can be understood as a generalization of steepest-descent (case $\lambda \gg 1$) and (case $\lambda \ll 1$) Taylor series methods.

`LMM` was first applied to CCD stellar profiles centering by Mighell (1989) showing it was much more insensitive to undersampling complications than other more conventional approaches.

A custom source centering program called `FITSTAR` and based on `LMM` technique was developed. It makes use of the Curve Fitting and Function Optimization Library (`MPFIT`) (Markwardt 2001), written in `IDL` language. Posterior adaptations and inclusions of alternative stellar profile models (Moffat, Lorentz) were performed by the author.

In contrast to other minimization routines (e.g. `CURVEFIT` in `IDL`, `fitpsf` in `IRAF`), which are based on ordinary least-squares by simple matrix inversion from Numerical Recipes (Press 2002), `MPFIT` makes use of `MINPACK-1` (More 1993), a very robust fitting library. Numerous comparison tests between `CURVEFIT` and `MPFIT` were performed with simulated 2D-Gaussian profiles in presence of Poissonian+Gaussian noise. While the former crashed its convergence for profiles of FWHM< 1.5 pixels, the latter could fit successfully up to FWHM~ 0.8 pixels.

`MPFIT` also exhibits a lot of other desirable features:

1. model parameters can be constrained. For example, upper and lower boundaries can be established or even can be fixed to specified values,

2. formal 1-σ errors in each parameter are supplied by the algorithm,

3. pixel weighting mask based on its Poissonian and Gaussian noise can be introduced in the fit.

4.7 Astrometric assessment

In Sect 3.2 systematic errors affecting our data were quantified in basis of literature and general considerations. As stated in Pag. 86, seeing fluctuations and focal-plane positional errors were found to be the most important systematic errors for FASTT data set. Ideally, in order to perform an astrometric assessment of the AWMLE deconvolution algorithm, these errors should be first calibrated and then corrected by the use of differential astrometry with respect to a reference catalogue. This process requires a far more complete set of observations that we do not have.

However, note that our CCD frames practically overlap in pixel coordinates in all the three considered sets of data and, in the case of drift scanning ones, they are very short scans. Thus, the contribution from focal-plane positional and seeing fluctuations to the global error is greatly minimized.

Consequently, a multiframe pixel astrometric reduction, without the use of a reference catalogue, will be employed to evaluate the incidence of deconvolution over the astrometric error. This procedure is illustrated in Fig. 4.3 as is composed by the following steps:

1. The positions lists centroided as explained in Sect. 4.6 are considered for all the N_{frames} original and deconvolved frames. Note that the number of stars in every original and deconvolved list can be different.

2. A bijective matching process is carried out. This assures all position lists (original and deconvolved) have the same stars (not only the same number N_{mat}).

3. One of the N_{frames} is chosen as reference. This decision can be chosen attending the seeing quality or similar criteria.
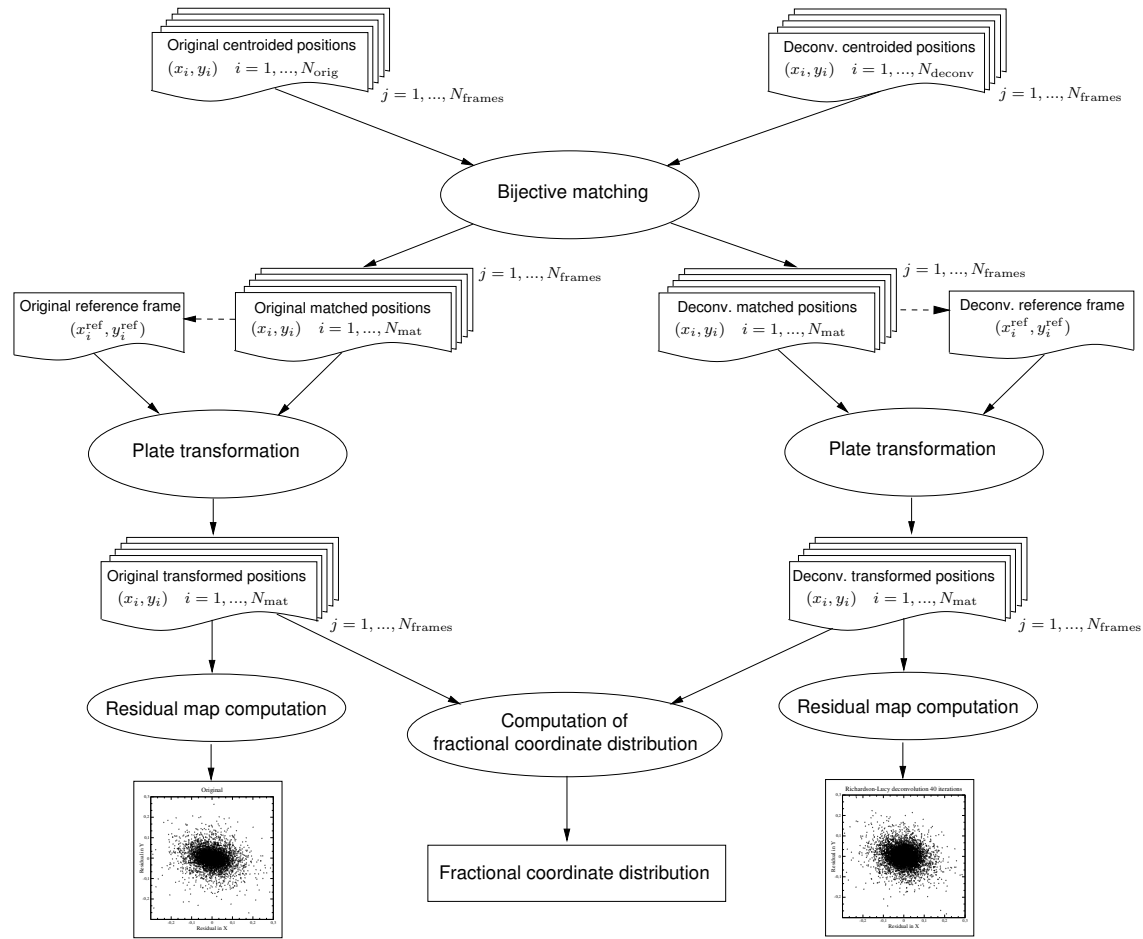
Figure 4.3: Diagram of the methodology followed for evaluating the incidence of deconvolution over the astrometric error.

4. Original and deconvolved matched lists are transformed to the reference frame coordinate system. At this point, residual analysis of the plate solutions is performed to choose the correct polynomial order needed in these transformations.

5. A residual map of all the N_{frames} frames is computed for original and deconvolved transformed lists, respectively. This calculation consists in calculating, for every star, the difference between the average position along the N_{frames} and the transformed position in frame j. This is done for all the N_{mat} stars and N_{frames} frames. The dispersion of both positional residual maps is computed for later comparison.

6. The fractional coordinate distribution is computed. This is done by subtracting to each star position its integer part. This is done for all the N_{mat} stars

and N_{frames} frames. As will be seen in Sect. 5.5.1, the pixel phase is plotted as a function of x and y coordinates.

The justification of the calculation of residual maps and pixel phase distributions will be given in Sect. 5.5.1, but we anticipate they will serve us to study what is the impact of image deconvolution over astrometric accuracy.

Chapter 5

Results

This chapter presents the results of Part I of the thesis. AWMLE and Richarson-Lucy deconvolution was applied to the data sets described in Chapt. 3. This outcome, and its comparison with original data, will be evaluated in several aspects: PSF fitting, deconvolution convergence, limiting magnitude gain (QUEST, NESS-T), limiting resolution gain (QUEST, NESS-T) and astrometric accuracy (FASST). This chapter is structured in 5 sections, one for each of those topics.

5.1 PSF fitting

PSFs for the three data sets (FASTT, QUEST and NESS-T) were fitted with `DAOPHOT II` following the methodology described in Sect. 4.2. Fig. 5.1 illustrates a comparison between the three PSFs.

5.1.1 FASTT

Before PSF fitting, periodic fringes noise was removed from original images. This appeared in the frames and was of low light level (<0.5%). However, note that spatially correlated noise is not white in *à trous* wavelet space, and if not removed that spectral signature could have led AWMLE to inject undesired artifacts.

Left panel in Fig. 5.1 shows the PSF with best fit for the F98d287 FASTT frame.

$\theta = 162°$ 25 pixels
$\mathrm{FWHM_x : FWHM_y} = 4.1 : 2.6$

$\theta = 106°$ 11 pixels
$\mathrm{FWHM_x : FWHM_y} = 2.0 : 2.8$

$\theta = 85°$ 12 pixels
$\mathrm{FWHM_x : FWHM_y} = 2.0 : 2.1$
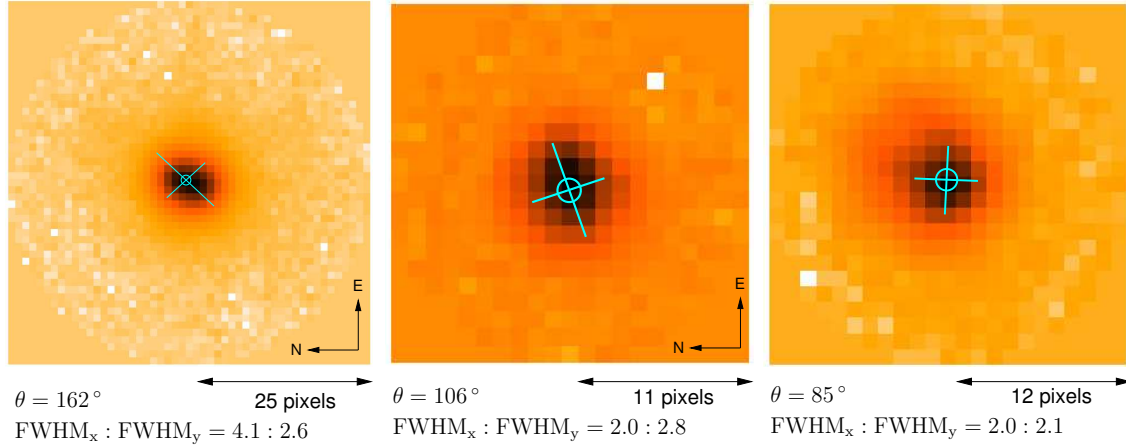
Figure 5.1: Best PSFs for the three considered data sets are compared. Left: Hybrid Moffat25 FASST (see Tab. 5.1). Middle: Hybrid Moffat25 QUEST (see Tab. 5.3). Right: Hybrid Moffat15 NESS-T (see Tab. 5.5). The panels have been rescaled to the same display size. The resulting centroids, FWHMs ratios and orientation angles are shown graphically (see blue crosses and circles) and numerically. For FASTT and QUEST PSFs, which were acquired by drift scanning, E-W and N-S axes are indicated. Further comments for each PSF in Sects. 5.1.1, 5.1.2 and 5.1.3.

As introduced in Pag. 80, FASTT profiles suffer from CTE problem which yield a 1 : 1.4 asymmetry with an average orientation of 160°. This can be appreciated in Fig. 5.1 and in 2nd, 3rd and 4th columns in Table 5.1. As we will see in Sect. 5.5.1, this distorsion in the PSF shape had incidence in the computed astrometric residual map. The rest of columns in Table 5.1 include the number of stars and radius considered in the PSF fit, this latter according to what was explained in Sect. 4.2 and final PSF size.

PSF fitting was performed considering four different profiles, each one with its analytic and hybrid variant. Purely analytical profiles showed systematically inferior fits. The normalized photometric scatter of the four hybrid models is shown in Table 5.2. Moffat25 appears to be the best model which can incorporate the CTE distorsion. Being FASTT a well-sampled data, we speculate that in absence of the CTE effect Gaussian model should have shown similar performance as Moffat one.

Note all hybrid models are space invariant. As we introduced in Pags. 68 and 84, it is known that anomalous atmospheric refraction introduces quasi-periodic oscillations in FASTT PSF profiles as a function of their RA coordinate. Despite `DAOPHOT II` allows to model spatially variant PSFs, we disregarded this because the current

Table 5.1: Input parameters for PSF fitting FASTT data.

Frame	FWHM$_x$ (pixels)	FWHM$_y$ (pixels)	θ (°)	Number of selected stars	PSF radius (pixels)	PSF size (pixels)
F98d287.274	4.06	2.57	162	38	37.9	51x51
F98d288.279	4.15	2.70	163	38	37.9	51x51
F98d290.281	4.60	3.30	159	38	37.9	51x51
F98d291.259	4.20	2.64	163	38	37.9	51x51
F98d301.255	4.06	2.52	159	38	37.9	51x51
F98d302.241	4.10	2.47	162	38	37.9	51x51
F98d317.247	4.61	3.20	159	38	37.9	51x51
F98d318.253	4.92	3.51	162	38	37.9	51x51
F98d319.248	4.11	2.56	162	38	37.9	51x51
F98d321.163	4.33	2.88	162	38	37.9	51x51

implementation of AWMLE does not consider this possibility.

Table 5.2: Performance of different PSF models when fited to FASTT data.

Frame	Normalized scatter			
	Gauss	Moffat15	Moffat25	Lorentz
F98d287.274	0.0856	0.0553	0.0536	0.0728
F98d288.279	0.0723	0.0489	0.0434	0.0734
F98d290.281	0.0592	0.0421	0.0346	0.0661
F98d291.259	0.0763	0.0514	0.0463	0.0689
F98d301.255	0.0967	0.0563	0.0556	0.0742
F98d302.241	0.0860	0.0532	0.0500	0.0734
F98d317.247	0.0602	0.0405	0.0327	0.0626
F98d318.253	0.0565	0.0412	0.0354	0.0589
F98d319.248	0.0949	0.0673	0.0627	0.0700
F98d321.163	0.0669	0.0464	0.0392	0.0633

5.1.2   QUEST

Middle panel in Fig. 5.1 shows the PSF with best fit for the q050899_F13 QUEST frame. An appreciable (although less important than FASTT one) PSF elongation

can be seen in this figure and in Table 5.3. As explained in Pag. 95, this can be attributed to the uncorrected curvature effect when observing at $\delta = 1.5°$ under drift scanning mode.

The rest of columns in Table 5.3 include the number of stars and radius considered in the PSF fit, this latter according to what was explained in Sect. 4.2 and final PSF size. Note that PSF radius and size were smaller than the ones employed in FASTT (Table 5.1) because QUEST data is close to be critically sampled.

Table 5.3: Input parameters for PSF fitted QUEST data.

Frame	$FWHM_x$ (pixels)	$FWHM_y$ (pixels)	θ (°)	Number of selected stars	PSF radius (pixels)	PSF size (pixels)
q050899_F13	2.84	2.04	106	6	10.5	21x21
q100899_F13	2.61	2.02	106	6	10.5	21x21
q110899_F13	2.64	1.84	112	6	10.5	21x21
q120899_F13	2.99	2.39	106	6	10.5	21x21
q180899_F13	2.77	2.02	103	6	10.5	21x21
q100899_F14	3.17	2.18	76	21[a]	21	43x43[a]

[a]: For the sake of comparison with F13 PSFs, PSF radius (and consequently PSF size) was set to twice the value corresponding to the FWHM values.

Table 5.4: Performance of different PSF models when fited to QUEST data.

Frame	Normalized scatter	
	Gauss	Moffat25
q050899_F13	0.0508	0.0276
q100899_F13	0.0397	0.0219
q110899_F13	0.0700	0.0445
q120899_F13	0.0503	0.0290
q180899_F13	0.0489	0.0304
q100899_F14	0.0588	0.0398

PSF fitting was performed with two different profiles (Gaussian and Moffat25), each one with its analytic and hybrid variant. Purely analytical profiles showed systematically inferior fits. The normalized photometric scatter of the four hybrid

models is shown in Table 5.4. Moffat25 was found to be superior to Gaussian model. As explained in Sect. 4.2 this is in agreement with critically sampled nature of QUEST data.

As in FASTT case, all hybrid models are space invariant. Note that q100899_F14 PSF was fitted with a PSF radius double of the one employed for rest of frames. This was made on purpose for checking the possible dependence of the fit with respect this parameter. As seen in Table 5.4, no significant difference can be deduced.

5.1.3 NESS-T

Right panel in Fig. 5.1 shows the PSF with best fit for the NESS-T_02 NESS-T frame. $FWHM_x$ and $FWHM_y$ values do not appear to differ significantly in Table 5.5.

Table 5.5: Input parameters for PSF fitting NESS-T data.

Frame	$FWHM_x$ (pixels)	$FWHM_y$ (pixels)	θ (°)	Number of selected stars	PSF radius (pixels)	PSF size (pixels)
NESS-T_01	2.00	2.01	75	34	11.5	23x23
NESS-T_02	1.97	2.06	85	34	11.5	23x23
NESS-T_03	2.17	2.07	173	34	11.5	23x23
NESS-T_04	2.25	2.16	168	34	11.5	23x23
NESS-T_05	2.51	2.46	163	34	11.5	23x23
NESS-T_06	2.40	2.28	176	34	11.5	23x23
NESS-T_07	2.22	2.10	2	34	11.5	23x23
NESS-T_08	2.15	2.13	31	34	11.5	23x23
NESS-T_09	2.16	2.29	115	34	11.5	23x23
NESS-T_10	2.20	2.23	30	34	11.5	23x23

However, a closer look at the relative position of the PSF with respect to the blue cross reveals an slight asymmetry in the upper left part. This can be better appreciated in Fig. 5.2. This was generated by rotating the fitted Moffat15 PSF 57° clockwise and extracting the central column profile. A clear asymmetry at mid and large radial distances is shown. We attribute this effect to coma of the optical system, which was still in process of collimation at the time of data acquisition.

PSF fitting was performed with five different profiles, each one with its analytic
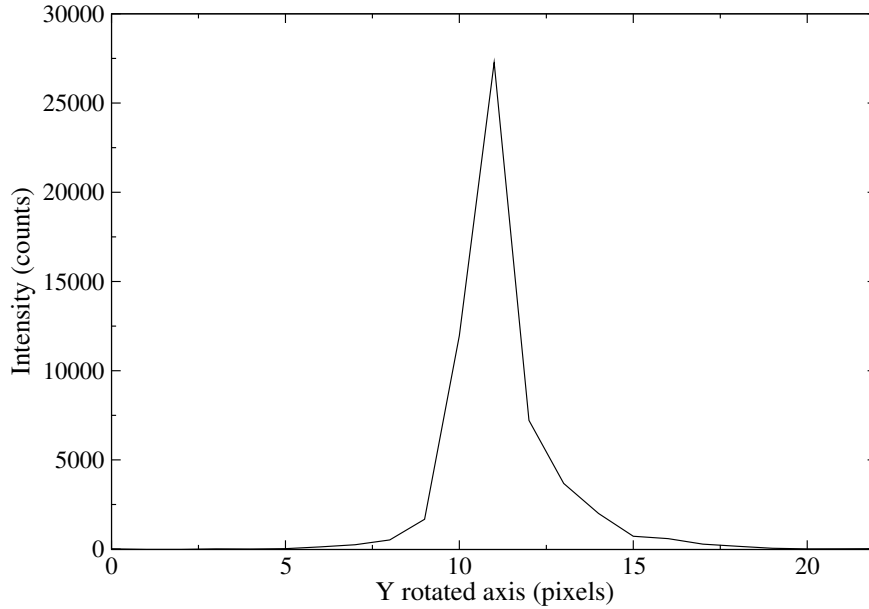
Figure 5.2: Coma in NESS-T Moffat15 PSF.

and hybrid variant (expect Penny that was always analytical). Purely analytical profiles showed systematically inferior fits, Penny included. The normalized photometric scatter of the five hybrid models is shown in Table 5.6. As QUEST case, Lorentz and Moffats are preferable to Gaussian because of the critically sampled nature of NESS-T data. Lorentzian model was found to be superior to Moffat, above all at mid and large radial distances. This is likely due to that NESS-T PSF shows extended wings originated by optical system spot (coma effect mainly) and also diffused and reflected light from the detector assembly (NESS-T is an f/1 system).

5.2   Deconvolution convergence

As introduced in Sect. 2.3.2, one of the most remarkable characteristics of AWMLE algorithm is the use of multiresolution support to stabilize the solution and automatically decide the significant structures in the residual map. This translates into an asymptotic behaviour of the solution which we now illustrate.

One of the QUEST images with a Moffat25 PSF was deconvolved up to 800 iterations. Next, object detection and validation was performed following the methodology detailed in Sect. 4.3. The number of raw and matched detections as a function

Table 5.6: Performance of different PSF models when fitting to NESS-T data.

Frame	Normalized scatter				
	Gauss	Moffat15	Moffat25	Lorentz	Penny
NESS-T_01	0.0656	0.0343	0.0437	0.0302	0.0302
NESS-T_02	0.0623	0.0318	0.0406	0.0292	0.0289
NESS-T_03	0.0584	0.0301	0.0382	0.0278	0.0270
NESS-T_04	0.0610	0.0337	0.0417	0.0302	0.0296
NESS-T_05	0.0501	0.0270	0.0333	0.0270	0.0261
NESS-T_06	0.0533	0.0280	0.0353	0.0272	0.0258
NESS-T_07	0.0619	0.0301	0.0399	0.0262	0.0261
NESS-T_08	0.0603	0.0295	0.0389	0.0258	0.0258
NESS-T_09	0.0591	0.0281	0.0368	0.0269	0.0267
NESS-T_10	0.0621	0.0289	0.0392	0.0248	0.0245

of number of iterations is shown in Fig. 5.3.

After a range of iterations where the number of detections increases steeply, this reaches a maximum. The fact that the number of detections is stabilized around this maximum, denotes that practically the solution has been asymptotically accomplished.

The consideration of either a constant or a variable background level can be relevant in terms of the number of iterations needed to reach an stable maximum of detections. A delay of about 140 iterations can be appreciated for constant background deconvolution.

5.3   Increase in SNR and limiting magnitude

5.3.1   QUEST

In this subsection we proceed to estimate the limiting magnitude gain introduced by AWMLE algorithm to QUEST images. A comparative study with the Richardson-Lucy algorithm will be carried out.

The data set considered for this study was the q050899_F13 QUEST frame and its
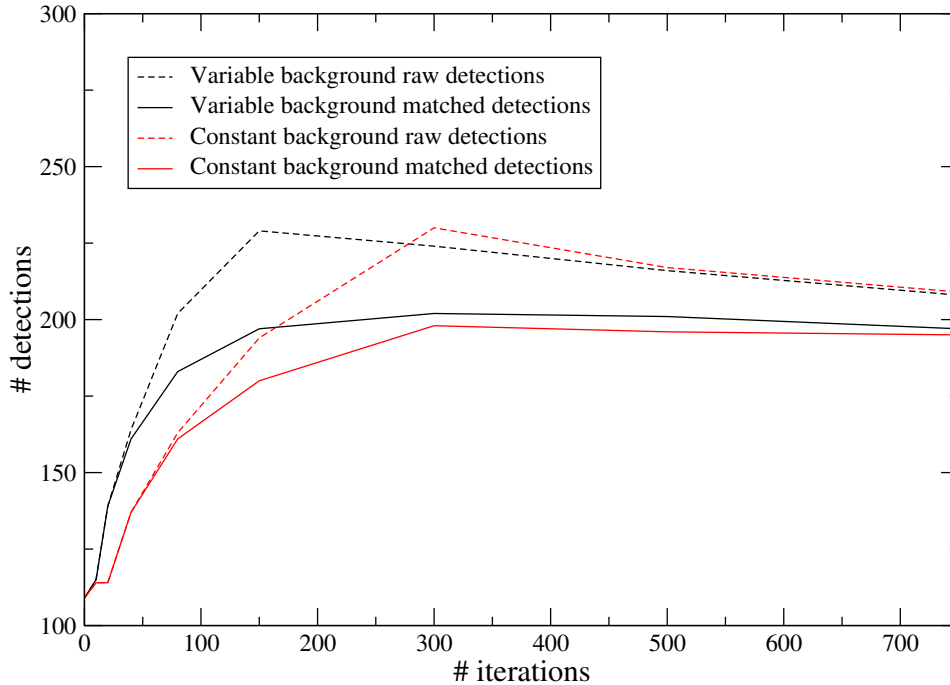
Figure 5.3: Number of raw and true detections as a function of number of iterations for AWMLE deconvolution with variable (black) and constant (red) background.

corresponding w250700_F13 WIYN frame are described in Table 3.9. This field was chosen because it has a moderate number of objects (avoiding excessive crowding) and it lacks bright stars and CCD defects. As a result, we skip undesirable effects from very bright stars like blooming, strong stray light and reflections, which could distort the direct understanding of the results of this Section.

In contrast to the limiting magnitude definition adopted in Table 3.9 (detections with SNR$\geq$ 10), we will perform this study in the regime of marginal detections (SNR$\geq$ 2.0)[1]. As regard as QUEST, the limiting magnitude of q050899_F13 frame, taken under Moon phase around 40%, was calculated to be $V_{lim} \sim 19.9$. As w250700_F13 WIYN frame, we estimated this to be around $V_{lim} \sim 23.0$. Finally, USNO-B1.0 is believed to be complete up to $V_{lim} \sim 21$ (Monet et al. 2003). Attending these numbers and the assessment methodologies exposed in Sect. 4.4, we will consider the w250700_F13 WIYN image for validating QUEST new detections. This is preferable, as it shows far deeper limiting magnitude and higher resolution.

Image deconvolution was applied to q050899_F13 QUEST frame using the imple-

---

[1]This is the definition adopted by most astrometric catalogues.

mentations of Richardson-Lucy (RL) and AWMLE algorithms described in Sects. 2.2 and 2.3, respectively.

In Table 5.7 we summarize the parameters used for running the deconvolutions discussed in the following. In this order, hybrid Moffat25 and Gaussian PSFs were found to fit best to q050899_F13 data as explained in Sect. 5.1.2.

Table 5.7: Parameters used for the deconvolutions of q050899_F13 QUEST frame.

Algorithm	Iterations range	Considered PSFs	Variable background
Richardson-Lucy	0–200	Moffat25,Gauss	Yes
AWMLE	0–2500	Moffat25,Gauss	Yes

A variable background image was obtained from `SExtractor` and considered into both algorithms. As we discussed in Sect. 5.2, the inclusion of either a constant or a variable background level can be relevant in terms of number of effective detections and its subsequent limiting magnitude gain.

Due to the small size of the images and that execution time was not a crucial requirement, both algorithms were executed without acceleration parameter.

All object detections were obtained with `SExtractor` as described in Sect. 4.3. For the validation WIYN image, about 40 false detections due to cosmic hits and cold or hot pixels were manually removed. Given its fine sampling, this cleaning operation is very likely to be efficient[2]. It is remarkable that the optimal `SExtractor` parameters found for original and deconvolved QUEST images were very similar. This confers homogeneity to the results.

In Table 5.8 we summarize the results in terms of number of detections for the three considered sets of QUEST images: original, RL and AWMLE deconvolved. Detections labeled as **Raw** correspond to those directly obtained from `SExtractor`, while those labeled as **Matched** are obtained with the validation methodology in Sect. 4.4.1 using w250700_F13 as referefnce image. Unmatched detections correspond to objects detected in QUEST frame (original or deconvolved) but not in WIYN reference list. Although the figures in Table 5.8 are only for a particular number of iterations in each case, this is large enough to be representative of the

---

[2]The typical width of stellar objects and artifacts is very different.

global performance of each algorithm. The following considerations apply for this table:

Table 5.8: Summary of the number of raw, matched and unmatched detections from the comparison between w250700_F13 WIYN and q050899_F13 QUEST original and deconvolved images. These results are from a 80-iteration Richardson-Lucy and a 750-iteration AWMLE runs. Object detection was carried out with SExtractor with a 2σ threshold and a kernel filter of FWHM=2.0 pixels. In contrast to the Richardson-Lucy performance, AWMLE only introduces an small percentage (5%) of unmatched detections (see text for further details).

Algorithm	Detections		
	Raw	Matched	Unmatched (%)
Original	109	109	0
Richardson-Lucy 80-iteration	419	262	37
AWMLE 750-iteration	208	197	5

1. all the 109 objects detected in the original QUEST image are effectively detected in WIYN image.

2. there is a substantial increase in the number of matched objects for both deconvolution algorithms with respect to original image.

3. in comparison to the original image, AWMLE combines a significant increase of matched detections (81%) with a slight number of unmatched detections (5%). In contrast, RL offers a larger increase in matched detections (140%) but at expense of an unacceptable number of unmatched detections (37%).

4. most of this 5% of fake detections appeared with AWMLE can be explained by means of artifacts not introduced by the deconvolution algorithm itself but due to limited PSF modelling. A residual part of this 5% may be considered as authentic, being their non-detection in deeper WIYN images explained by a suspected moving or transient nature.

   All this will be discussed and justified in the following subsection.

5. an early stage of this study was already performed by the author, in collaboration with X. Otazu. The results were anticipated in the thesis of the latter

(Otazu 2001) and are very similar to the ones in Table 5.8: 36% and 6% of unmatched detections for RL and AWMLE, respectively.

Categorization of unmatched detections from AWMLE: a new Halo X-ray Nova candidate?

We categorize the 11 unmatched detections with AWMLE in three distinctive groups.

First, as illustrated in Fig. 5.4, some unmatched detections are caused by our limited knowledge of the PSF which, in the vicinity of a very bright star, made AWMLE to trigger image artifacts. It is normal these detections are located in the outer wings of the bright star, because it is there where the mismatch between the modelled and true PSF is larger. E1 and E2 correspond to representative examples of these kind of false detections.

A second category of unmatched objects is formed by those momentary appearing in the 750-iteration convolved QUEST image, but not persisting after larger number of iterations. See Fig. 5.5 for a typical example of this group. E3 is marginally detected with a minimal SNR in the 750-iteration image. However, after a number of iterations the adaptive mask approach of AWMLE described in Sect. 2.3 does not consider E3 to be an object-like feature. As a result, its SNR is gradually reduced up to no detection is found by `SExtractor`. This behaviour is a natural consequence of the asymptotic convergence which AWMLE shows (see Sect. 5.2 for a complementary discussion). In this asymptotic regime, those pixels in original image which contain only marginal information at highest wavelet scales (lowest frequencies), and not at all at lowest and intermediate scales (highest and intermediate frequencies), where the main stellar signature is located, are candidates to suffer from momentary unmatched detection. During the first range of iterations some little likelihood is assigned to them, but AWMLE finally discards them as object-like features and vanish into the background level. In other words, E3 signal contributing at stellar-like scales is not enough for maintaining the likelihood above a certain level to get a minimal SNR in the final image.

The third group of detections labeled as unmatched corresponds to three objects with no counterpart in WIYN images, despite their deeper limiting magnitude ($V_{\lim} \sim 23.0$) compared to the $V_{\lim} \sim 19.9$ of original QUEST image. Nonetheless, a 150-iteration AWMLE deconvolution was carried out over original WIYN image.
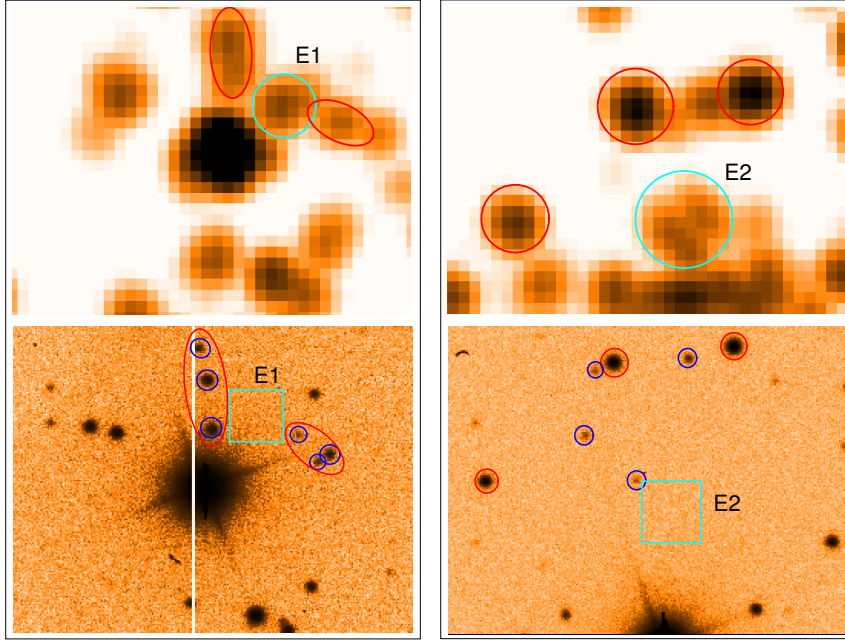
Figure 5.4: Two representative examples of false detection due to the presence of a very bright star in their vicinity. These were found by matching the detections of a 750-iteration AWMLE deconvolution of QUEST image (top in each panel) with the sources in WIYN image (bottom in each panel). Circles in cyan represent false detections, with no match in WIYN images (cyan squares). Circles in red are those nearby objects both detected in deconvolved QUEST and WIYN images, and in blue those nearby objects only resolved in WIYN. Note that the bright star in E2 is at the bottom of the figure. The display scaling in deconvolved QUEST figures were chosen so that it accentuates the dynamic range close to the background level.

This allows to extend the counterpart search in the reference image up to $V_{\lim} \sim 23.3$, which constitutes a gain of about +0.6 magnitudes[3].

These objects, named E4, E5 and E6, are shown in Figs. 5.6 and 5.7, and cannot be assigned to none of the two previous groups of unmatched detections. On one hand, they are not located near very bright stars, and no PSF-related artifacts are visible in their vicinity. On the other hand, the authenticity of the detections in deconvolved QUEST images is fully assured: on the contrary to what happened to the former category of momentary detections, E4, E5 and E6 persist with stable SNRs along a wide range of iterations (up to 2500). Following the same reasoning about asymptotic convergence stated two paragraphs above, we can conclude that

---

[3]This increase attained by AWMLE deconvolution will be derived in the course of this Section.
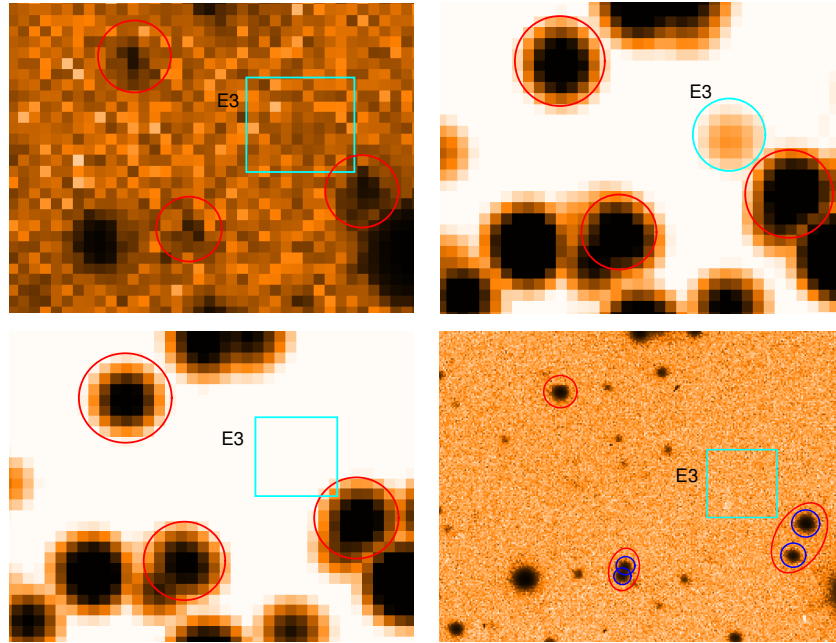
Figure 5.5: A representative example of a momentary unmatched detection. Upper left: original QUEST image. Upper right: 750-iteration AWMLE deconvolution of QUEST image. Lower left: 2500-iteration AWMLE deconvolution of QUEST image. Lower right: WIYN image. Circles in cyan represent unmatched detections, with no match in original or WIYN images (cyan squares). Circles in red those nearby objects detected in all 4 images, and in blue those nearby objects only resolved in WIYN. Note that E3 is not detected in the 2500-iteration deconvolution (see text for further explanation). The display scaling of the figures has been chosen so that it accentuates the dynamic range close to the background level.

AWMLE considered these signal features as potentially real objects, and therefore their detection should have a satisfactory explanation. First, we evaluate possible artificial explanations:

1. The presence of cosmic rays, dark or hot pixels or deferred charge can be safely discarded by simply inspecting the original QUEST images (upper left panels in Figs. 5.6 and 5.7): they lack these features in all cases.

2. the formation of strong stray light or ghost reflections is also a very unlikely cause. The companions of E4, E5 and E6 are not very bright stars (only E6's is moderately bright). In addition, those systematic effects, if present, should also appear in the rest of brightest stars. Finally, the fact that the image
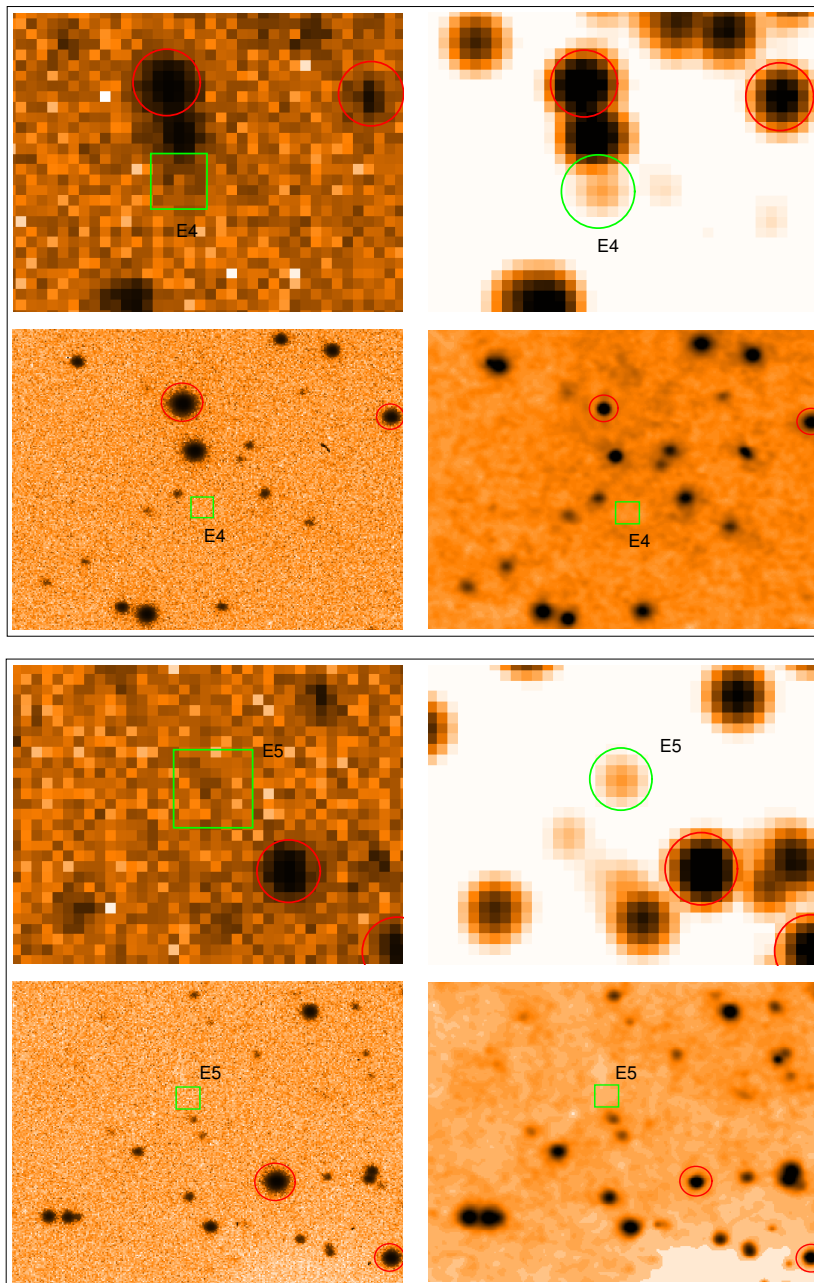
Figure 5.6: Two detections labeled as unmatched which do persist in deconvolved QUEST image after 2500 iterations of AWMLE. For each box, upper left: Original QUEST image. Upper right: 750-iteration AWMLE deconvolution of QUEST image. Lower left: Original WIYN image. Lower right: 150-iteration AWMLE deconvolution of WIYN image. Green circles represent detections with no match in none of the other three images (green squares). In the case of WIYN panels, green squares are scaled to the size of QUEST pixel. The fact that E4 and E5 are not present in much deeper WIYN images (original and deconvolved), in addition to their non-detection in any of the other QUEST frames (original and deconvolved) from the consecutive nights (see Table 3.9) might indicate they are moving objects (minor planets). See text for further discussion. The display scaling of the figures has been chosen so that it accentuates the dynamic range close to the background level.
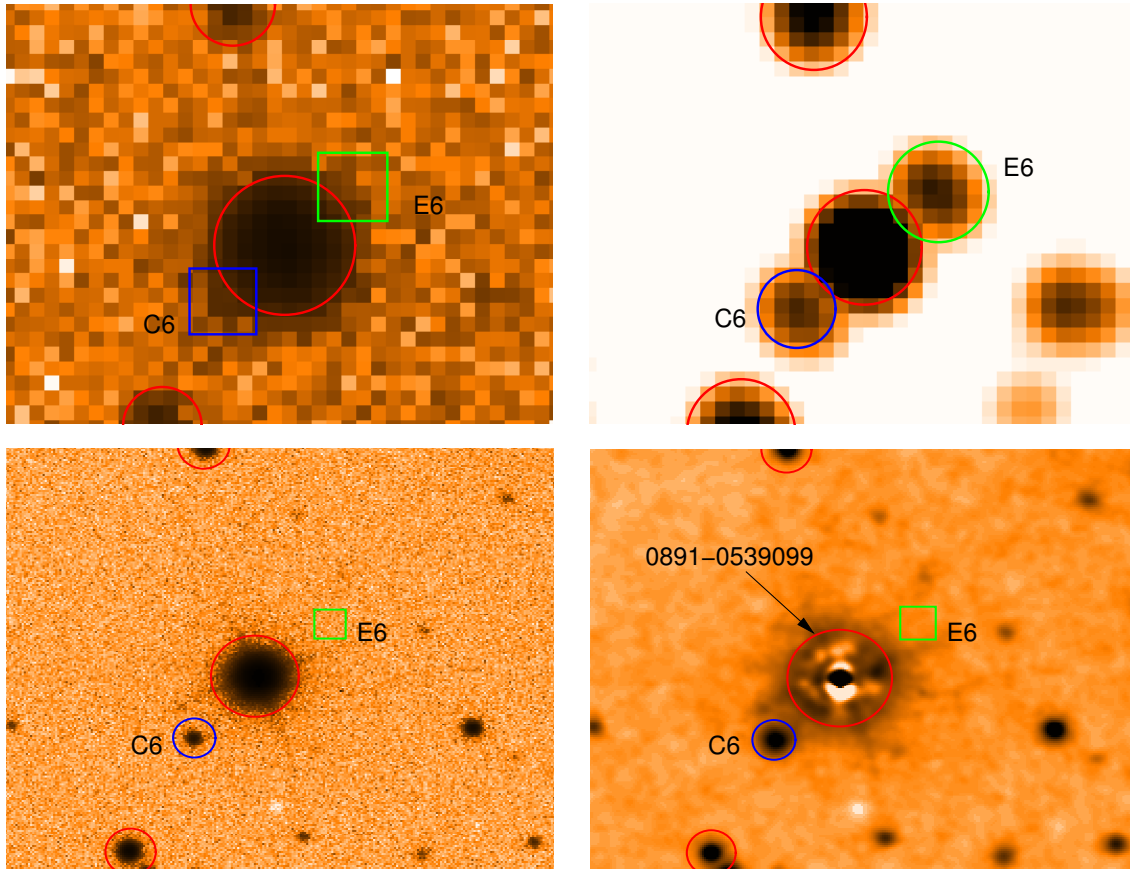
Figure 5.7: E6, the brightest among the detections labeled as unmatched in Table 5.8 for AWMLE algorithm, does persist in deconvolved QUEST image after 2500 iterations. Upper left: Original QUEST image. Upper right: 750-iteration AWMLE deconvolution of QUEST image. Lower left: Original WIYN image. Lower right: 150-iteration AWMLE deconvolution of WIYN image. The $V = 14.7$ USNO-B1.0 0891-0539099 star in the center is labeled. Green circle in deconvolved QUEST image represents detection with no match in none of the three other images (green squares). In the case of WIYN panels, green squares are scaled to the size of QUEST pixel. In blue, C6 is a comparison star with an angular separation with respect USNO-B1.0 0891-0539099 very similar to E6. Note that, in original QUEST image, both E6 and C6 can be marginally intuited as they are veiled by the outer wings of the central star (see green and blue boxes of upper left panel). The magnitudes estimated for E6 and C6 at the QUEST deconvolved panel are $V \sim 19.9$ and $V \sim 20.4$, respectively. Remarkably, despite the much fainter limiting magnitude of deconvolved WIYN image ($V_{\lim} \sim 23.6$), E6 is not detected there. However, although with similar separation and magnitude conditions, C6 is clearly matched already in original WIYN panel. A possible association of this > 3 magnitude transient event with an Halo X-ray Nova is further discussed in the text. For the sake of easing panels comparison, brightest companions are circled in red in all four images. The display scaling of the figures has been chosen so that it accentuates the dynamic range close to the background level.

has been taken under drift scanning technique implies the ghost inducer star moves across the CCD plane, causing even less favourable optical conditions for this systematic effect.

3. As explained in Sect. 4.2, the PSF extraction process can be affected of close neighbour contamination. A PSF suffering from this effect, plus the iterative non-linear nature of AWMLE, could undoubtedly trigger fake detections near moderately bright stars. However, we have followed the iterative neighbour substraction methodology which DAOPHOT II package establishes to avoid this undesired effect. In addition, visual inspection of the resulting PSF reveals no companions around. Finally, if an artifact or neighbour was present in PSF, all moderately bright stars should include a false detection in the same separation and position angle, which is not the case by the inspection of upper right panels in Figs. 5.6 and 5.7.

Once the most likely artificial scenarios have been ruled out, we discuss what kind of astronomical phenomena could lead to these unmatched detections:

The two fainter, E4 and E5, are shown in boxes of Fig. 5.6. Their coordinates are detailed in Table 5.9. On one hand, the detections encircled in green in deconvolved QUEST panel (upper right) have no counterpart in neither of deeper WIYN images, original or deconvolved (green squares in lower panels). On the other hand, E4 and E5 do not show up in neither of the deconvolutions of the four QUEST consecutive night frames (q100899_F13, q110899_F13, q120899_F13 and q180899_F13) described in Table 3.9. In view of this, the most likely explanation for those detections is to be Solar System bodies (minor planets), which exhibit fast enough motion for not being present in second epoch images (WIYN and rest of QUEST nights). No known objects were found for E4 and E5 coordinates in the Minor Planet Center database (Williams 2005a) on the corresponding dates. However, this does not rule out the former explanation, given their relatively faint magnitudes ($V \sim 20.3 - 20.5$) and their relatively high ecliptic latitudes ($\beta \sim 20°$), where most of deep minor planets surveys do not operate (Williams 2005b).

E6 detection is illustrated in Fig. 5.7. This is only present in the deconvolved QUEST image (green circle in upper right panel), while is missing in the two deeper WIYN images, both original and deconvolved (lower panels). By using USNO-B1.0 magnitude scale, V magnitudes for E6 and the comparison star C6 were derived from

Table 5.9: Coordinates of E4 and E5 detections found in deconvolved QUEST image taken on Aug 5th 1999 (upper right panels of Fig. 5.6). C1 and C2 were used for deriving magnitudes according USNO-B1.0 scale.

Object	$\alpha(2000)$	$\delta(2000)$	$\lambda(2000)$	$\beta(2000)$
E4	19h 39m 49.2s	$-0°$ 48′ 51″5	19h 46m 57.2s	$20°$ 20′ 18″3
E5	19h 39m 53.5s	$-0°$ 49′ 08″3	19h 47m 1.5s	$20°$ 19′ 50″2

deconvolved QUEST image, with values of $V \sim 19.9$ and $V \sim 20.4$, respectively. These and astrometry information is included in Table 5.10.

Table 5.10: Coordinates and V magnitudes E6 found in deconvolved QUEST image (upper right panel of Fig. 5.7). The V magnitudes epoch correspond to QUEST (Aug 5th 1999) and WIYN (July 25th 2000) observations. The latter corresponds to the limiting magnitude of deconvolved WIYN image (this gain limiting magnitude is confirmed at the end of this Section).

Object	$\alpha(2000)$	$\delta(2000)$	$\ell(2000)$	$b(2000)$	$V(1999.5917)$	$V(2000.5649)$
E6	19h 39m 49.2s	$-0°$ 48′ 51″5	2h 31m 8.8s	$11°$ 8′ 10″9	19.9	> 23.6

From upper left panel in Fig. 5.7, note that both E6 and C6 can already be intuited in the outer wings of the central star (see green and blue boxes) in original QUEST image. After the 750-iteration AWMLE deconvolution (see upper right panel), the image has increased its limiting magnitude and resolution, allowing the three stars in the centre to be clearly distinguishable.

In contrast to E4 and E5, E6 can be safely discarded as a moving object (Solar System origin) because it is also detected with similar level of significance in two (q100899_F13 and q120899_F13) of the four consecutive nights of QUEST images described in Table 3.9. The non-detection in q110899_F13 and q180899_F13 frames is in accordance with the fact that background level was higher[4] on those nights. In addition, no known minor planet was found in Minor Planet Center database (Williams 2005a) at E6 coordinates included in Table 5.10.

---

[4]Likely due to thin overhead clouds.

If not a minor planet, a transient event could be the most likely explanation for E6. The progenitor of this event should be able to explain a V variation of more than three magnitudes in a period of 0.97 years, which is the timebase between QUEST and WIYN observations.

An X-ray Nova is proposed as a satisfactory scenario for E6. These objects, also known as Soft X-ray Transients, are low-mass accreting X-ray binaries (LMXRBs), usually in quiescent state, which undergo sudden few-month-long X-ray outbursts with typical recurrence periods of many years (Chen et al. 1997). Most of X-ray novae are dynamically proved to host a black hole. The outburst is probably initiated by an instability which suddenly produces the fall of the matter accumulated into the disc during quiescence. The observational facts that are characteristic for this kind of objects are (McClintock & Remillard 2003, 2005):

1. LMXRBs distribution shows a significant population in the Galactic Halo.

2. early stage of transient emission is detected by gamma and X-ray space missions with all-sky monitoring cameras ($SWIFT$, $HETE - 2$, $RXTE$).

3. at IR and optical wavelengths, the counterpart fades from outburst maximum about $\Delta V \sim 5 - 7$ mags to quiescence.

4. the return period from transient to quiescent regimes typically spans a few months.

As seen in Table 5.10, E6 meets all the observational features stated above. An example of these observational properties can be found in the recent detection of SWIFT J1753.5−0127 gamma ray source (Palmer et al. 2005) and its optical counterpart by Halpern (2005); Torres et al. (2005).

An exhaustive search was conducted in all the public databases and archives, in the seek of both known gamma and X-ray quiescent emission and optical counterpart at E6 coordinates. This was done through HEASARC Browse Interface (Pence et al. 2002), which allows to simultaneously interrogate multitude of multiwavelength missions archives and catalogues. Unfortunately, no positive hit was found. As a result, the following conclusions about the E6 transient nature can be drawn:

• no gamma and X-ray mission detected its outburst in Aug 1999.

- now that the outburst is gone, the X-ray emission of E6 is faint below the sensitivity of current missions with all-sky coverage cameras.

- its V magnitude on Aug 1999 was at least 3.7 mags brighter than the magnitude at quiescence, which is known to be $V_{\lim} > 23.6$ on July 2000. This variation is compatible with the typical optical emission of an X-ray nova in a transient episode.

- no current deep image is available to confirm and quantify this quiescence optical magnitude.

A more in-depth study of E6 should be required to confirm the X-ray binary scenario proposed above. This would involve long integration times in the largest optical telescopes available to derive radial velocity curve from its spectrum (Charles & Coe 2003). Alternatively, a selective pointage of recent sensitive X-ray missions ($XMM-Newton$, $Chandra$) with moderately long integration time could also provide the desired confirmation and further information about the thermal properties of compact object (Wijnands 2004). This kind of observation has already been conducted with other quiescent systems (Tomsick et al. 2005). In any case, both follow-up strategies are highly competitive and deserve of further evidences. This, plus to the fact that other similar systems are being studied at brighter magnitudes/X-ray fluxes, make the confirmation of E6 X-ray nova nature not straight-forward to address in near future.

Number of detections versus number of iterations

Complementary to Table 5.8, the number of raw and matched detections as a function of number of iterations for both deconvolution processes is shown in Fig 5.8. We here recall that, as was concluded in Sect. 5.2, the number of iterations is not comparable between different deconvolution algorithms. This explains why the iterations range used for RL algorithm is considerably shorter than the one for AWMLE. From the inspection of Fig 5.8 several conclusions can be drawn:

1. as was already pointed out in Table 5.8, the number of false detections with RL is exponentially boosted with the number of iterations. This is a clear consequence of the noise amplification introduced by the algorithm.

2. on the contrary, AWMLE shows an stable number of matched (and false) detections over a broad range of iterations. A maximum deviation is reached around 150 iterations but this is slowly corrected after a few hundred of additional iterations. This asymptotic behaviour of the AWMLE convergence was already anticipated in Sect. 5.2. It turns to be very convenient for limiting magnitude gain purposes, since it makes the process practically independent of the number of iterations, and therefore the results are homogeneous and more easily comparable from one image to another.

3. the final number of matched detections at the iterations high end is considerably larger in the RL case. However, this is somewhat fictitious because from 80 iterations and above most of these newly incorporated detections are matched just by random chance.
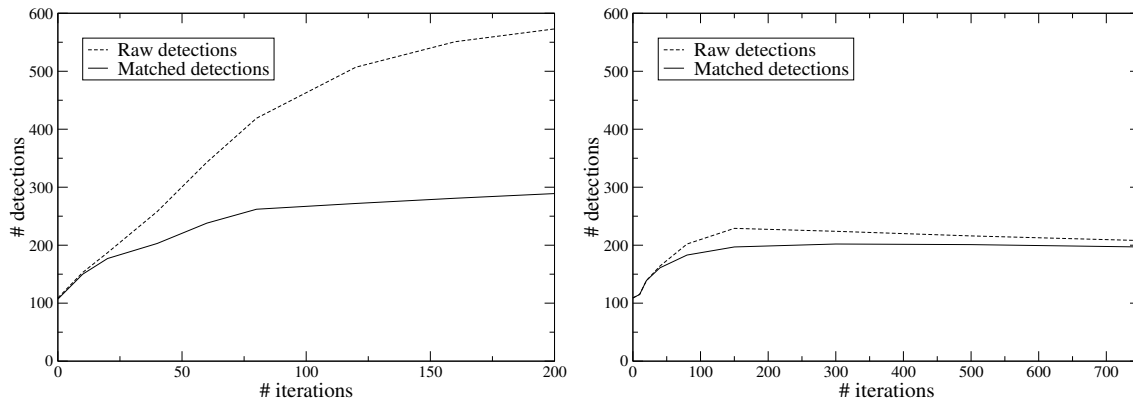
Figure 5.8: Number of raw and matched detections as a function of number of iterations for Richardson-Lucy (left) and AWMLE (right) deconvolution.

Number of detections versus detection threshold

In the following we study the dependence of the number of detections with the detection threshold. In Figs. 5.9 and 5.10 the number of raw and matched detections are plotted as a function of the detection threshold for RL and AWMLE algorithms, respectively. The threshold is expressed in SNR units, i.e., times σ the background rms.

The top-left panel of each figure shows the detections of the QUEST original image. The result corresponding to the deconvolved images with different number of iterations is shown in the 5 remaining panels.
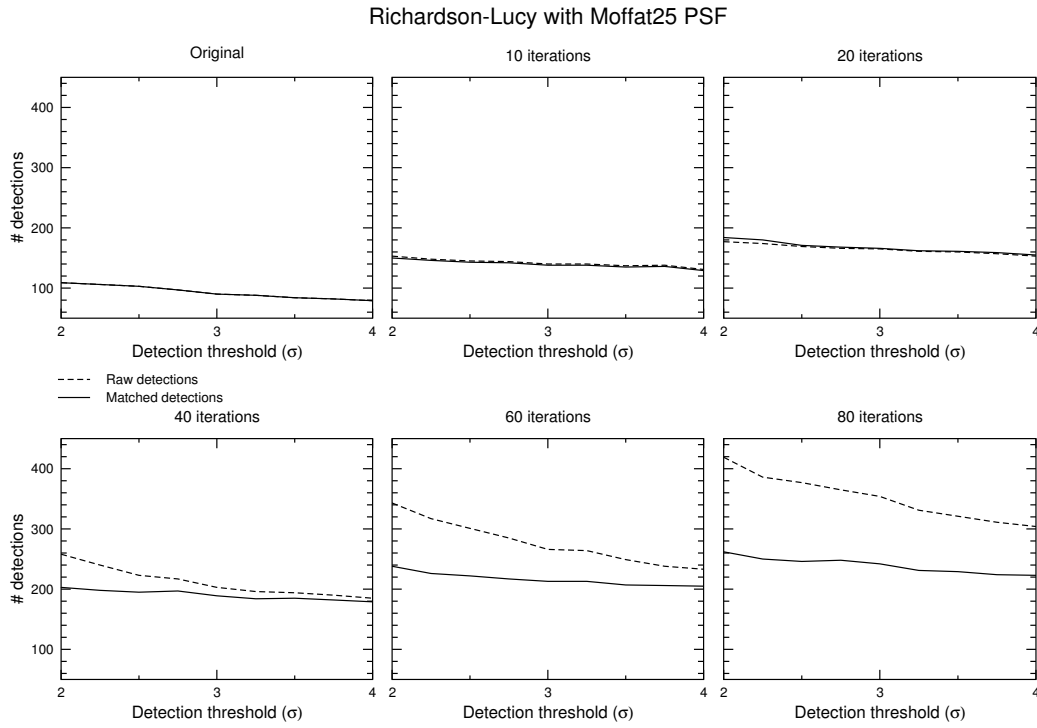
Figure 5.9: Number of raw and matched detections versus the detection threshold for original and Richardson-Lucy deconvolved (10, 20, 40, 60 and 80 iterations) image.
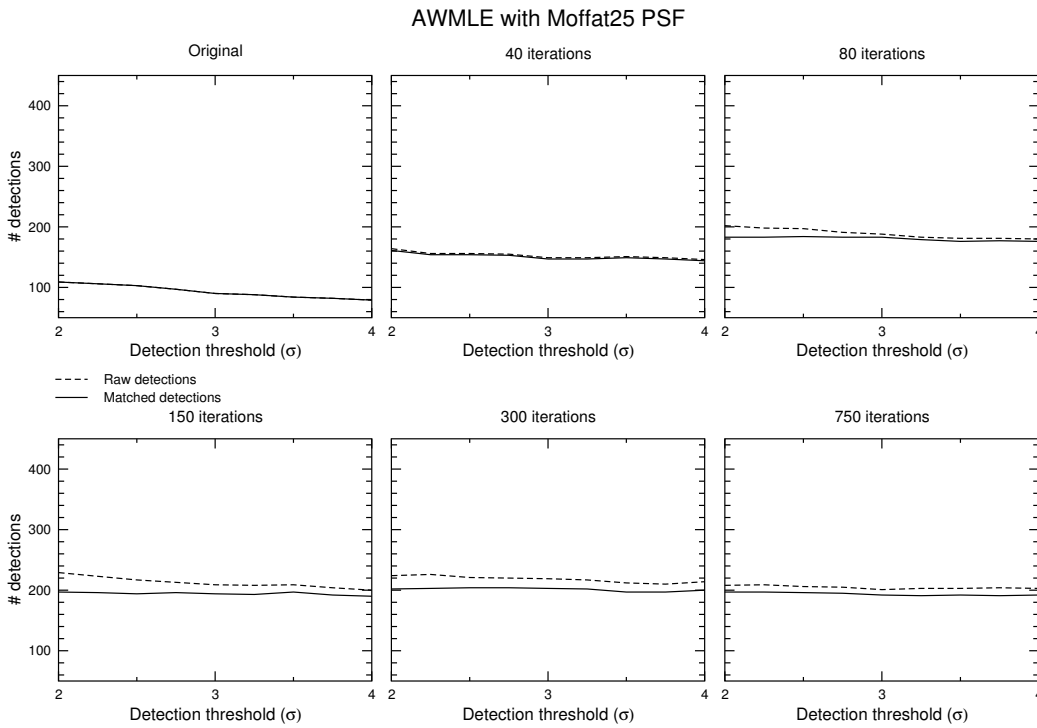
Figure 5.10: Number of raw and matched detections versus the detection threshold for original and AWMLE deconvolved (40, 80, 150, 300 and 750 iterations) image.

Two important remarks can be made from Figs. 5.9 and 5.10.

First, for both deconvolution algorithms, the number of matched detections is larger than in the original image, even for shortest number of iterations.

Second, in the case of AWMLE the number of detections (raw and matched) does not practically depend on the detection threshold. This is a natural consequence of the characteristics of the deconvolved image. We recall that AWMLE asymptotically converges to a collection of sources superimposed over a flat background level practically free of noise. Therefore, it is not surprising that SExtractor detects a constant number of objects regardless the value of detection threshold (which is measured in σ time the background noise). Like in the case of the independence upon the number of iterations seen in Fig. 5.8, this is a very convenient property of the AWMLE algorithm, since it removes an additional parameter from the analysis of the deconvolved images. This latter contrasts to what happens in original image and, above all, in RL deconvolved images, where the number of raw detections shows a clear trend as a function of threshold.

Magnitude histogram of detections versus number of iterations

The dependence of the histogram magnitude of the matched sources as a function of number of iterations has also been investigated in Fig. 5.11. The magnitude was derived from w250700_F13 WIYN image (taken in Harris R filter) by means of aperture photometry. As expected, the histogram shape evolves with the number of iterations by being more populated in the faint end part and keeping brightest detections. Once the algorithm has reached an stable number of detections (above 150 iterations), the histogram only suffers slight variations of a few objects (2 or 3 from one panel to the next) which does not affect its global distribution. Note that the couple of momentary detections (E4 and E5) discussed around Fig. 5.5 has been removed during the last 450 iterations.

Limiting magnitude gain

Finally, an estimate of the limiting magnitude gain was computed. In Fig. 5.12 we overplot the magnitude histogram of the original image (top-left panel in Fig. 5.11) with the one from a 500-iteration AWMLE deconvolution (bottom-right panel in
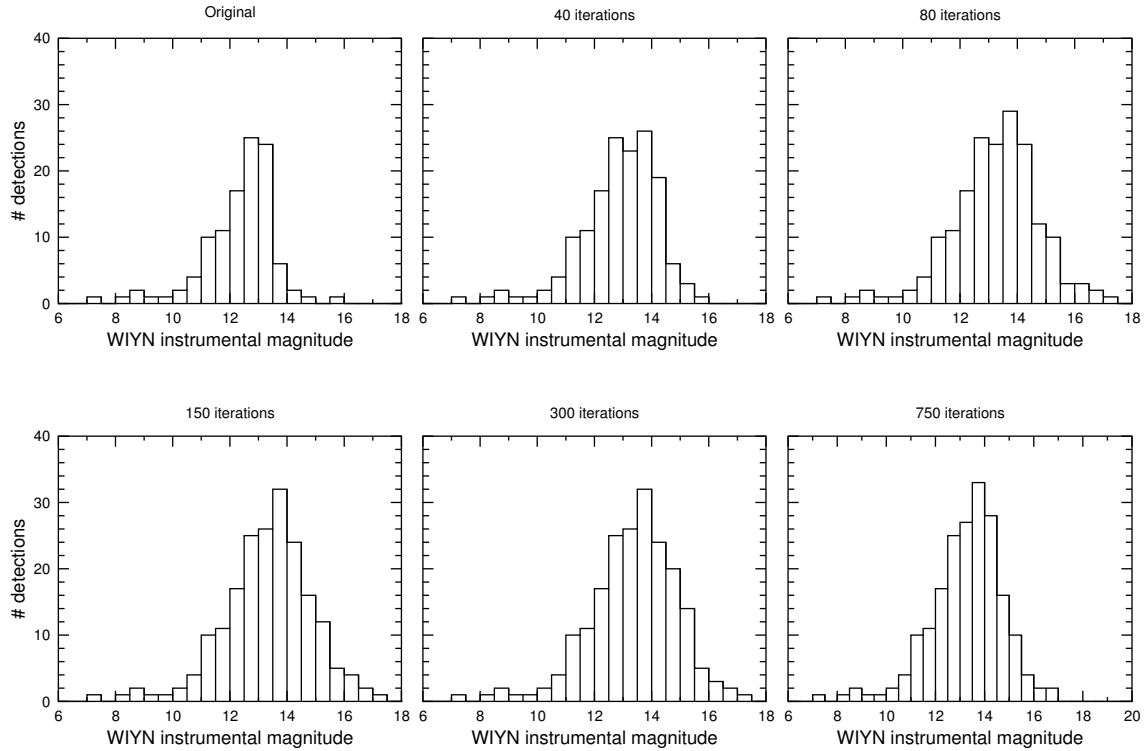
Figure 5.11: Magnitude histogram for matched detections over a range of iterations of the AWMLE algorithm. The magnitude corresponds to the instrumental aperture magnitude derived from w250700_F13 WIYN image, in Harris R filter.

Fig. 5.11). If the area of each histogram (which coincides with the number of matched detections included in Table 5.8) is considered, and these are inserted into Eq. 4.2 as N_2 and N_1, a limiting magnitude gain of $\Delta R \sim 0.64$ is derived.

Conclusions

We have applied Richardson-Lucy and AWMLE deconvolution to the QUEST q050899_F13 frame. The performance of the algorithms has been evaluated and compared in terms of number of true and unmatched detections. The validation of true detections has been carried out with the w250700_F13 WIYN frame. The dependence of those results on the number of iterations and detection threshold was also investigated.

AWMLE shows better performance results in several aspects:

1. The number of false detections with respect to RL algorithm is dramatically
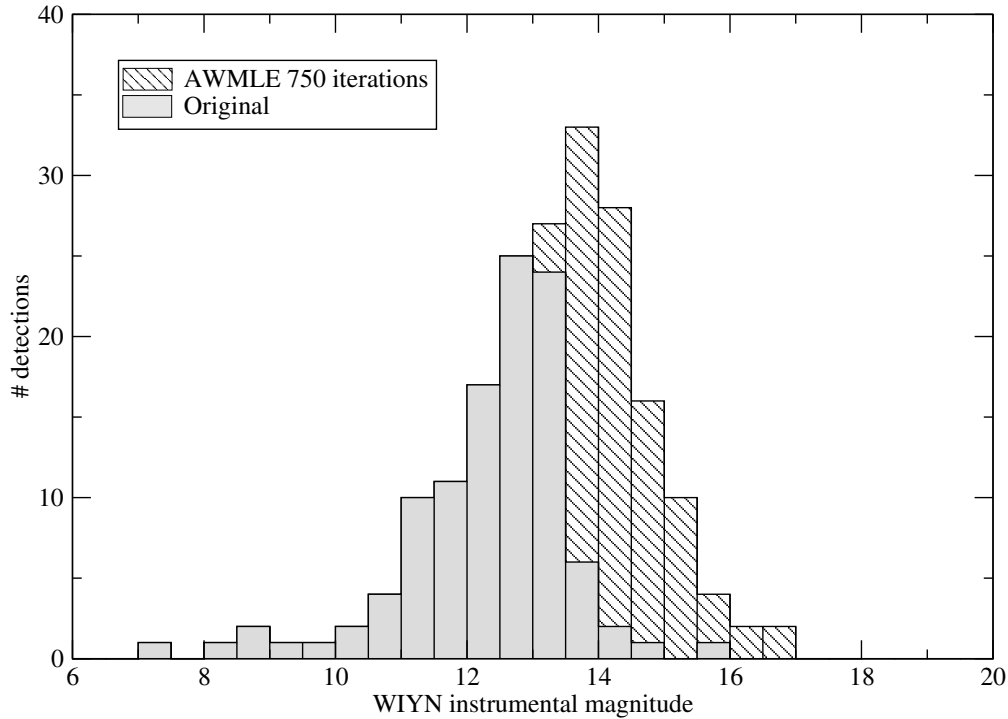
Figure 5.12: Magnitude histograms of matched detections for the original image and a 500-iteration AWMLE deconvolution. The magnitude corresponds to the instrumental aperture magnitude derived from w250700_F13 WIYN image, in Harris R filter.

decreased, typically from $\sim 84\%$ to $\sim 7\%$. This remaining percentage can be fully explained by instrumental or observational reasons or by constrains of the original data, but are not in any case due to artifacts artificially introduced by the algorithm.

2. The number of raw and matched detections found by AWMLE remains very stable above a certain number of iterations (around 150).

3. The same stable behaviour occurs over the whole range of detection threshold (from 2σ to 4σ).

where 2. and 3. are fully justified by the asymptotic convergence of the AWMLE algorithm, which was showed in Sect. 5.2.

Finally, the evolution of the magnitude distribution of the detected objects as a function of number of iterations was studied. A limiting magnitude gain of $\Delta R \sim 0.64$ has been found for a typical AWMLE 500-iteration deconvolution. In

comparison, note that, as was calculated in Table 3.11, the limiting magnitude loss introduced by drift scanning technique is $\Delta R \sim 0.14$. Therefore, it is clear that AWMLE deconvolution by far compensates that unavoidable magnitude loss instrinsic to the data acquisition scheme.

Possible extensions of this work

The increase of the limiting magnitude shown in this section could be of interest for a large number of observational programs, either systematic surveys or punctual observations. As the deconvolution algorithm is totally general, a broad range of data sets could benefit from this result.

Some constrains mentioned in this section, as the incomplete knowledge of the PSF, could be of course minimized in the case of better sampled data sets.

The current execution time and and RAM usage parameters for AWMLE were already discussed in Table 2.1. Of course, if an intensive usage of AWMLE algorithm over a massive amount of data was desired, an additional effort in the algorithm optimization could be dedicated to improve current performance. Two different strategies can be used to do so. On one hand, by pure code optimization (loop optimization, factorization, deleting redundant calculation and other profiling tasks). On the other hand, by parallelizing the algorithm with as many nodes as wavelet planes used in the decomposition of the original image (4 to 6). As a result, roughly speaking, the execution time could be shortened to less than a half of the original, apart from the scalability factor supplied by parallel approach, which highly varies upon the architecture implementation chosen (multiprocessor system, multicomputer system, etc.).

5.3.2 NESS-T

In this section we repeat the former limiting magnitude study with the NESS-T data described in Sect. 3.2.3. The assessment methodology explained in Sect. 4.4 will be followed. Part of the results exposed below have been recently published in Fors et al. (2006) and Merino et al. (2006).

We considered the NESS-T_02 frame for this study as original image. Although

all the frames in Table 3.13 are similar in terms of limiting magnitude, this is the one which shows largest number of true detections. As we anticipated in Pag. 103, the limiting magnitude of original NESS-T data is handicapped due to its large pixel and relatively bright sky conditions. Thus, the application of image deconvolution to this set of images is highly recommended.

As will be seen in the last part of this section, the limiting magnitude of NESS-T_02 frame was calculated to be $R_{\lim} \sim 16$. In Sect. 4.4 we justified that it is preferable to validate the object detections with a deeper and higher resolution image of the same field of view. However, we do not have this one. Therefore, USNO-A2.0 (Monet et al. 1998), whose $R_{\lim}$ is believed to be well above 20, turns to be an appropriate reference catalogue in terms of completeness in this case. Although we are aware that UCAC2 and USNO-B1.0 are more accurate than USNO-A2.0, we don't expect this has relevance for the purpose of this Section: we recall that our aim is to estimate a relative limiting magnitude gain, and therefore the occasional systematic errors in USNO-A2.0 magnitude scale are not a concern.

As regard as image deconvolution applied to NESS-T_02 frame, we only used AWMLE, given the clear incapacity of Richardson-Lucy algorithm for keeping false detections to a reasonable level, as shown in Sect. 5.3.1. In Table 5.11 we summarize the parameters used for running the deconvolutions discussed in the following. Hybrid Lorentzian, Moffat15, Moffat25, Gaussian and pure analytical Penny PSFs were found to fit best in that order, as explained in Sect. 5.1.3.

Due to the small size of the images and that execution time was not a crucial requirement in this study, AWMLE algorithm was executed without acceleration parameter.

Table 5.11: Parameters used for the deconvolutions of NESS-T_02 frame.

Algorithm	Iterations range	Considered PSFs	Variable background
AWMLE	0–600	Lorentz,Moffat15,Moffat25,Penny,Gauss	No

A variable background image was obtained from SExtractor. A noticeable gradient was observed with a relative flux ratio between the brightest and faintest regions of $\sim 5\%$. However, this background image was not finally considered for deconvolv-

ing process because no realistic flatfield calibration frame could be obtained[5]. All in all, we decided to consider a constant background level, which was also estimated by SExtractor. Note that the former discussion of correctly assigning the origin of variable background is crucial for a proper deconvolution: sky emission statistics is additive and flatfield is multiplicative. If one of the contributions is over or underestimated with respect to the other, the deconvolution algorithm will suffer from inappropriate convergence and the solution image is likely to be unreliable. For the sake of comparison, note that, in Sect. 5.3.1, QUEST data had less problems when assigning the origin of variable background. This is because the intrinsic flatfielding process introduced by the drift scanning acquisition scheme.

As we discussed in Sect. 5.2, the inclusion of a constant background level instead of a variable one, can introduce a delay in the convergence of the algorithm. However, we recall that, as seen in Fig. 5.3, the number of true detections (or, equivalently, the limiting magnitude gain) accomplished in both situations is nearly the same after a sufficient number of iterations.

All object detections were obtained with SExtractor. An effort was made for tuning the search parameters of this program (see Sect. 4.3). In particular, special attention was given to find the best value for tolerance radius when matching the NESS-T detections list with USNO-A2.0 catalogue. Attending the considerations made in Pag.116 and the empirical approach shown in Fig. 5.13, a radius of 2.25 pixels was found to be a good compromise.

It was already commented in Sect. 5.3.1 that NESS-T_02 frame is not dark corrected. In order to remove the contribution of this effect to false detections, a complete catalogue of dark pixels was compiled by carefully inspecting the original NESS-T_02 frame. In this process, the other 9 overlapping frames in Table 3.13 were compared for verifying the dark current nature of the excluded pixels. As a result, 196 regions were identified and a binary mask image was created to be input to SExtractor detections. In this way, dark induced detections are cleanly removed from our analysis below, both in original and deconvolved images.

In Table 5.12 we summarize the results in terms of number of detections for the two considered sets of NESS-T images: original and AWMLE deconvolved. Detections labeled as **Raw** correspond to those directly obtained from SExtractor,

---

[5]Several tests indicate that most part of the observed background gradient is due to vignetting
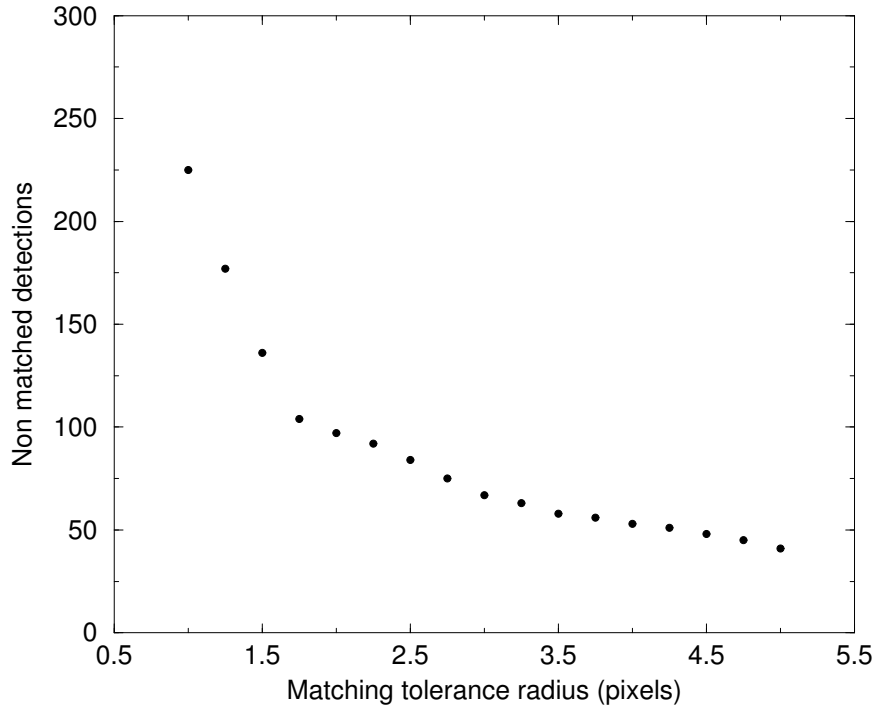
Figure 5.13: Number of unmatched detections of a 40-iteration deconvolved NESS-T image. Object matching is made with USNO-A2.0 and different values of tolerance search radius. A clear cut-off value is observed around 1.9 pixels. A less strict value of 2.25 pixels, was considered large enough for preventing mismatches due to catalogue mean error and proper motion deviations, and small enough for not introducing contamination of fictitious close detections.

while those labeled as **Matched** are obtained by removing saturated and truncated objects from raw detections list, and by matching the remaining with USNO-A2.0. Therefore, they can be considered as true (or validated) detections. Unmatched detections correspond to objects detected in NESS-T frame (original or deconvolved) but not present in USNO-A2.0. Although the figures in Table 5.12 correspond only to a particular a number of iterations, they are representative of the global performance of AWMLE. A graphical illustration of the result in the table is shown in Fig. 5.14. Very similar considerations to those commented in Sect. 5.3.1 for QUEST data apply for this table:

1. there are 7 objects detected in the original NESS-T_02 frame which do not appear in USNO-A2.0. Three of them were effectively found in USNO-B1.0, which claims a higher completeness in all magnitude ranges than USNO-A2.0.

Table 5.12: Summary of the number of raw, matched and unmatched detections from the comparison between NESS-T_02 NESS-T original and deconvolved images with USNO-A2.0 catalogue. Deconvolutions were run until 140-iteration (Moffat15 PSF) and 120-iteration (Lorentz PSF). Object detection was carried out with SExtractor with a 2σ threshold and a kernel filter of FWHM=2.0 and 1.0 pixels for original and deconvolved images, respectively. Detections due to dark pixels were previously discounted from this study. See text for further discussion.

Algorithm	Detections		
	Raw	Matched	Unmatched (%)
Original	1731	1724	0.4
AWMLE 140-iteration Moffat15	2733	2644	3.2
AWMLE 120-iteration Lorentz	2677	2610	2.5
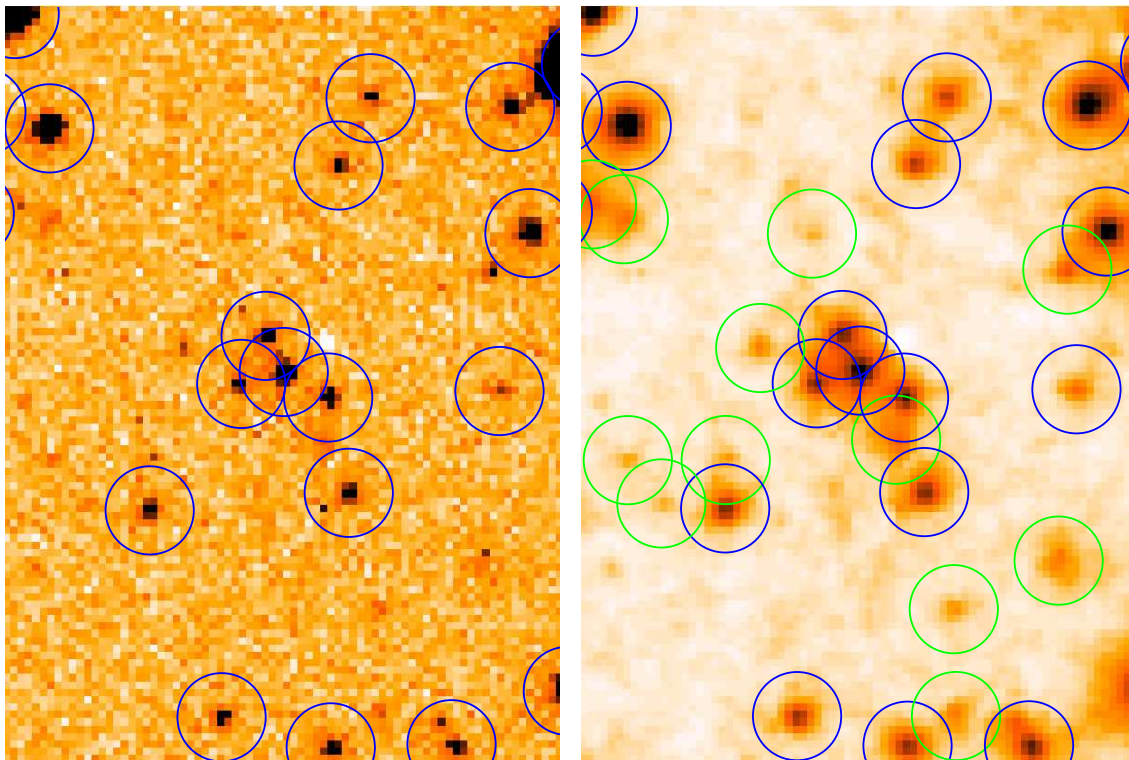
Figure 5.14: Image patch with new matched detections contributed by AWMLE deconvolution. Left: original image with, in blue, the matched detections in USNO-A2.0 catalogue. Right: 140-iteration Moffat15 PSF based deconvolution with, in green, 12 new matched detections not present in original image.

The 4 remaining objects were identified as internal ghost reflections of the brightest stars in the field of view.

2. in comparison to the original NESS-T_02, AWMLE deconvolved frames (Moffat15 and Lorentz) offer a significant increase of matched detections (53% and 51%) with an small number of unmatched detections (3.2% and 2.5%).

3. compared to Moffat15 PSF deconvolution, Lorentz PSF reaches similar number of matched detections with 20 less iterations. In addition, it also accomplishes significantly less unmatched detections (67 versus 89). We will further discuss this in the next subsection.

4. most of these fake detections can be explained by means of artifacts not introduced by the deconvolution algorithm itself but due to limited PSF modelling and very bright stars blooming. Three additional ghost reflections were detected with deconvolution.

Categorization of unmatched detections from AWMLE

A summary of the different categories of unmatched objects in the deconvolved images[6] is anticipated in Table 5.13. In the forthcoming discussion the two deconvolutions included in Table 5.12 will be considered, leading to 89 and 67 unmatched detections, respectively:

Table 5.13: Categorization of 7, 89 and 67 unmatched detections in USNO-A2.0 for the original, AWMLE 140-iteration Moffat15 and 120-iteration Lorentz deconvolved images, respectively.

Image	Category of unmatched detections				
	PSF mismatch and ringing	Bright stars blooming	Reflection ghosts	USNO-A2.0 uncompleteness[a]	Momentary detections
Original	-	-	4	3	-
140-it. Moffat15	56	4	7	4	18
120-it. Lorentz	48	3	5	4	7

[a] These objects are present in USNO-B1.0, though.

---

[6]We recall detections due to dark pixels were cleanly removed in advance to current discussion.

First, as a consequence of our limited knowledge when modelling the PSF, AWMLE deconvolution triggered the appearance of artifacts close to very bright stars. In addition to that, the ringing effect (see Sect. 2.4 added more complication to the recovery of faint souces in the vicinity of bright ones. The latter was powered by two properties of the original image. On one hand, the FWHM ($\sim$ 2.2 pixels) is very close to sampling limit. This was not the case, for example, of FASTT data. On the other hand, as bias and flatfield correction could not applied, the background estimate considered by AWMLE was not as accurate as in QUEST, for example. As a result, it is justified that the impact of ringing became more important in NESS-T than in FASTT and QUEST, making this category be the most numerous of fake detections. All in all, 63% and 72% of the fake objects found in both Moffat15 and Lorentz deconvolutions, respectively, were due to the combined action of the two above mentioned effects.

Second, due to the large pixel scale of NESS-T camera, bright stars experience full well blooming in original image, even at these short exposure times (30s). This causes the signal charge to spill into neighbouring pixels only in the vertical direction. However, this has shown to be a minor category. It only appears in the three brightest stars of the field with 3 or 4 fake detections, in original and deconvolved images.

The third group of unmatched detections corresponds to ghost reflections of the brightest stars in the image. This is a well-known effect in wide field cameras, and can be identified by locating those moving objects along a sequence of consecutive frames whose coordinates are mirrored with respect to the brightest stars in the field. The motion of the ghosts is caused by the change in the attitude of the telescope with time, and as a result, the geometric conditions of the reflections. The ghosts objects found in NEST_02 frame are illustrated in Fig. 5.15. Up to seven ghosts were identified, as included in Table 5.13. G1 to G4 were produced by the four brightest stars in the field and already detected in the original image. G5 was recovered in both 140-iteration Moffat15 and 120-iteration Lorentz deconvolved images. Finally, G6 and G7 were only present in 140-it. Moffat15 deconvolved image. The motion of G6 is shown in upper and right side panels. It is noteworthy that G6 is only detectable in deconvolved images. Although G6 is not an asteroid, its faint and mobile nature is similar to a real asteroid. Therefore, the recovery of G6 shows how AWMLE deconvolution could help to recover true faint asteroids, which would remain undetected in the original image otherwise.
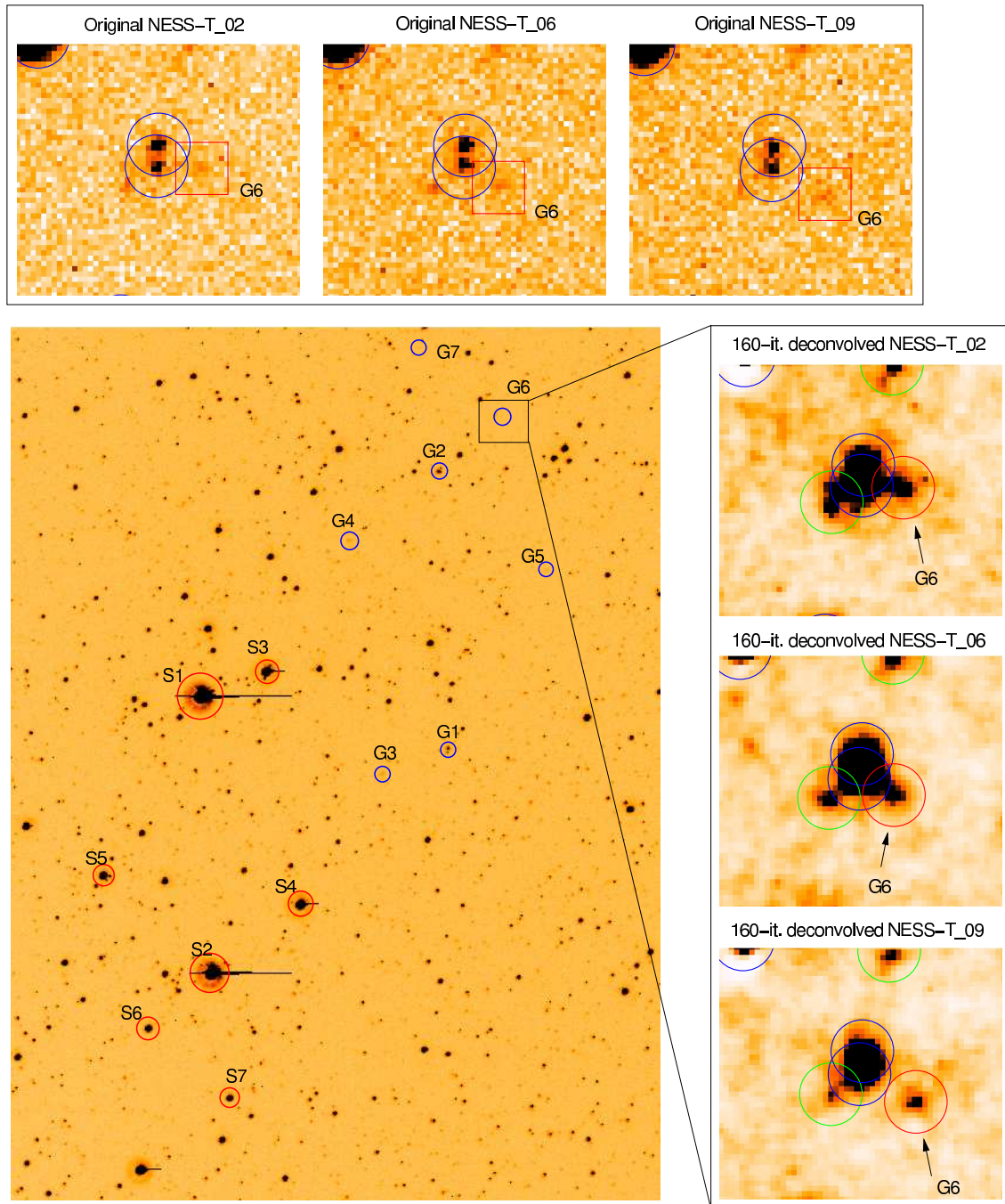
Figure 5.15: Central panel: Ghosts detections (blue) due to internal reflection of light from brightest objects in the image (red). Note the geometry of ghosts is totally inverted with respect to their progenitors. Upper side panel: sequence of three consecutive frames with the moving faint ghost G6 which remains undetected due to low SNR. The motion of ghosts is due to the varying attitude of the telescope within the 50 min between first and third exposures. Right side panel: the same sequence of frames after a 140-iteration deconvolution. G6 is effectively detected in all three frames. Despite its artificial origin, G6 recovery shows the feasibility of deconvolution for accessing to real asteroids, when they are undetectable in the original image.

The fourth category in Table 5.13 corresponds to 3 objects in both original and deconvolved images and 1 only in deconvolved images are not included in USNO-A2.0 catalogue. These have moderate magnitude ($R \sim 13 - 15$). By inspecting the geometry of these objects, we noted all were blended with close companions. Therefore, we suspect these unmatchings are exclusively due to defective deblending in the detection process when compiling USNO-A2.0. This was improved in USNO-B1.0 and all the four mismatches disappeared revealing all of them to be real objects in that catalogue, and not artifacts due to deconvolution.

Finally, there are 18 and 7 remaining unmatched objects in 140-iteration Moffat15 and 120-iteration Lorentz deconvolved images, respectively. They are all marginal detections with faint magnitude which could not be classified in none of the former categories above. They also cannot be assigned to any deblending improvement of the deconvolution because there are no close companions around them. Therefore, they can be considered as momentary detections appearing in these iteration ranges, but not in more converged solutions after a well advanced number of iterations (> 200) have been run. This category was already introduced and justified in Pag. 137. Complementary, this seems to be confirmed by the fact that no positive hits in USNO-B1.0, Minor Planet Center Checker (Williams 2005a), NED and SIMBAD databases were found. In addition, possible high-proper motion stars[7] were also ruled out for being insufficient in all cases.

Number of detections versus number of iterations

Complementary to Table 5.12, the number of raw and matched detections as a function of number of iterations for two AWMLE deconvolutions (with Moffat15 and Lorentz PSFs), is shown in Fig 5.16. From the inspection of this figure several conclusions can be drawn:

1. until the maximum of matched detections is reached (around 140 and 120 iterations, respectively), the number of matched objects increases much faster than the unmatched detections.

2. from these maxima to 600 iterations, the number of raw and matched objects drops to even below the number of original image. This second part is totally

---

[7]available from USNO-B1.0.

discordant with what was seen for QUEST data in Fig. 5.8, where the detections remained stable in a large value along a wide number of iterations after the maxima. What Fig. 5.16 illustrates is that the asymptotic convergence of AWMLE is broken for NESS-T data. The reason for this is the already announced inability of getting an accurate background estimate due to lack of bias, dark and flatfield calibration frames. As a result, the noise (and signal) statistical distribution of the image deviates from the assumptions made in the image model considered by AWMLE. This statistical mismatch specially plays a key role when considering a background estimate for the deconvolution, since the bulk of new detections are a few counts above this background level in the original image.

Despite of this handicap, it is remarkable that AWMLE still reaches an advanced stage of convergence in a wide range of iterations, where it delivers far more detections than in original image, as shown in Table 5.12.

3. Lorentz PSF based deconvolution reaches similar number of matched detections with 20 less iterations than Moffat15. Although being a weak difference, this is a direct result of which part of the PSF fits best to each one of the two models. On one hand, Moffat15 offers minimum residual in the core, as this is typically the best option for undersampled ground-based data. As a result, it is not surprising this model delivers more detections than Lorentz, because these are mainly triggered by the flux in the core. On the other hand, Lorentzian model performs its best at mid and large radial distances, where NESS-T PSF shows extended wings due to the optical system spot and internally reflected light. Consequently, it is normal that Lorentz based deconvolution suffers from less false detections (see Table 5.12) and has better global convergence, because, as seen in Pag. 156, it is in outer wings of bright stars were of these fake artifacts are generated.

Number of detections versus detection threshold

In the following we explore the dependence of the number of detections with the detection threshold, a key parameter in the detection process. In Figs. 5.17 and 5.18 the number of raw and matched detections are plotted as a function of the detection threshold for AWMLE Moffat15 and Lorentz PSFs based deconvolutions, respectively. The threshold is expressed in SNR units, i.e., times σ the background rms.
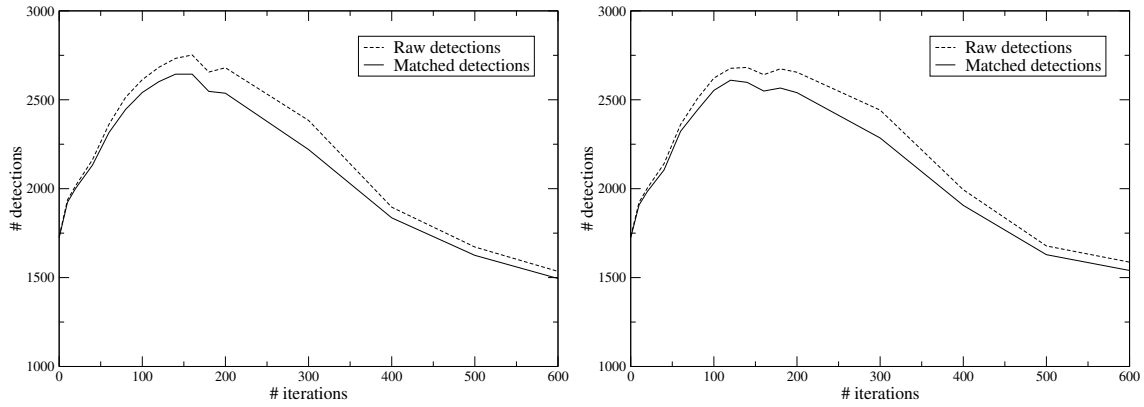
Figure 5.16: Number of raw and matched detections as a function of number of iterations for AWMLE deconvolution with a Moffat15 (left) and Lorentz (right) PSFs.

The top-left panel of each figure deals with the detections of the NESS-T original image. The result corresponding to deconvolved images with different number of iterations is shown in the 5 remaining panels. We limited this study up to 200 iterations, because, as seen in previous subsection, the number of detections above this number of iterations drops considerably. Three remarks can be made from Figs. 5.17 and 5.18.

First, for both PSFs deconvolutions, the number of matched detections is larger than in the original image, even for short number of iterations.

Second, for a fixed number of iterations, the number of false detections does not depend on the detection threshold. This is not surprising if we recall that AWMLE converges to a collection of sources superimposed over a flat background level practically free of noise.

Third, in contrast to what was deduced from Fig. 5.10 for QUEST data, the number of raw and matched detections does depend on the detection threshold. This distinctive behaviour, as the one previously shown in Fig. 5.16, is again caused by the fact we could not calibrate (bias, dark and flat) the raw image properly. In other words, we are considering a less converged solution of AWMLE than the one we ended up with QUEST example, where up to 2,500 iterations were run.
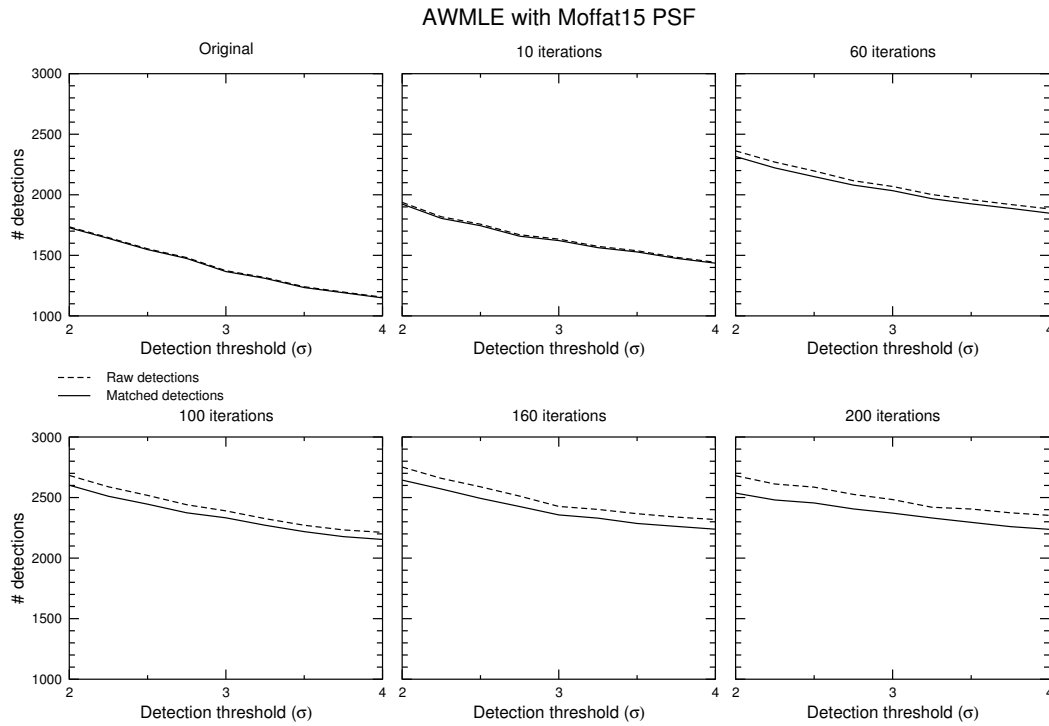
Figure 5.17: Number of raw and matched detections versus detection threshold for original and AWMLE deconvolved (10-200 iterations) image with a Moffat15 PSF.
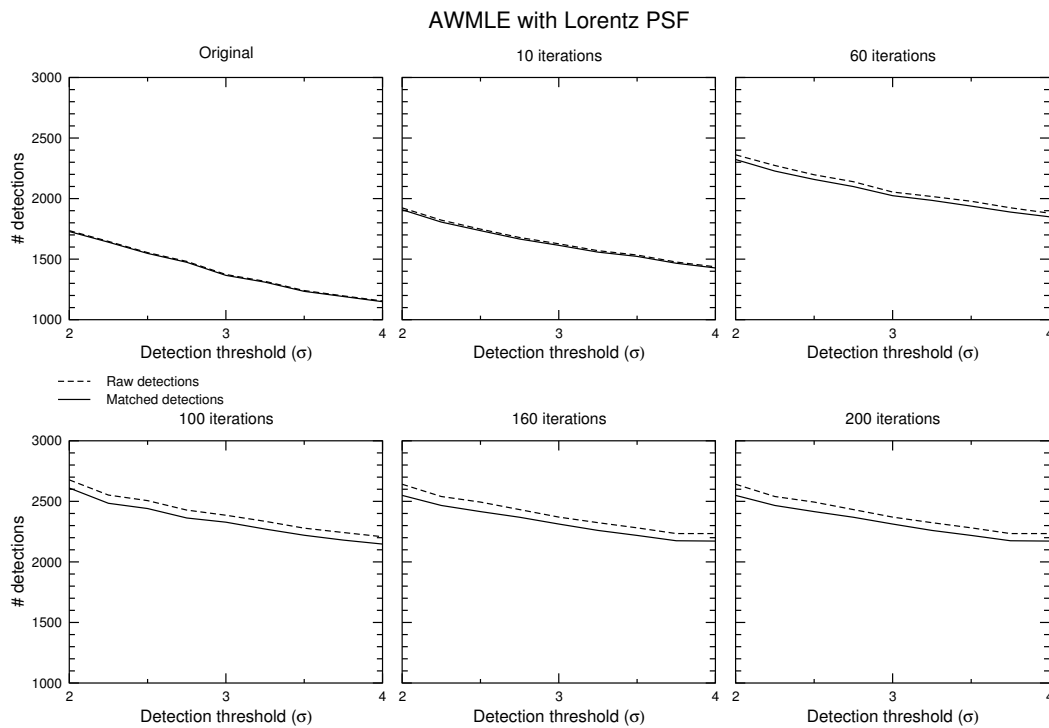
Figure 5.18: Number of raw and matched detections versus detection threshold for original and AWMLE deconvolved (10-200 iterations) image with a Lorentz PSF.

Magnitude histogram of detections versus number of iterations

The dependence of the magnitude histograms of the matched sources as a function of number of iterations was also investigated in Figs. 5.19 and 5.20 for Moffat15 and Lorentz based deconvolutions. All histograms correspond to 2σ thresholded detections. Again, we restricted this study to a maximum number of 200 iterations. The magnitude corresponds to the R in USNO-A2.0. As expected, the histogram is more and more populated in the faint end part as the number of iterations increases, while it keeps brighter objects with respect to the previous deconvolved images with less number of iterations. Once the algorithm has reached an stable number of detections (at 140 and 120 iterations, respectively), the histograms only suffers slight variations of a few faint objects which do not affect their global distribution.

Limiting magnitude gain
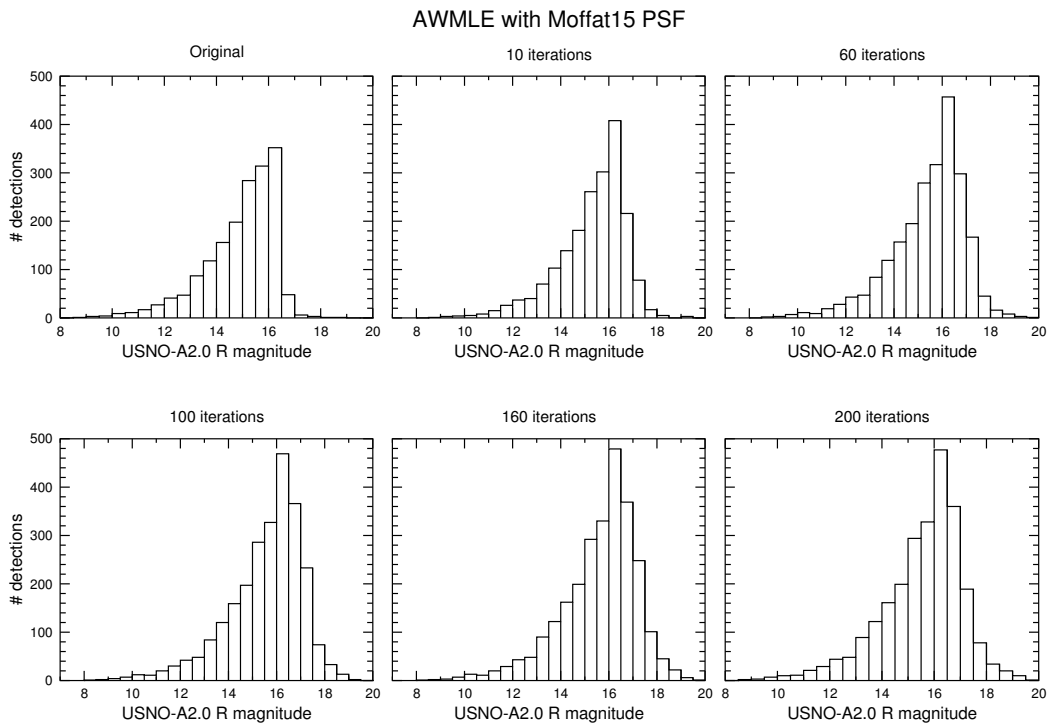
Figure 5.19: USNO-A2.0 R magnitude histogram of matched detections over a range of iterations for original and AWMLE Moffat15 PSF based deconvolved images.

By simply applying Eq. 4.2 to the number of matched detections in Table 5.12, a limiting magnitude gain of $\Delta R \sim 0.46$ is obtained. If a more conservative de-
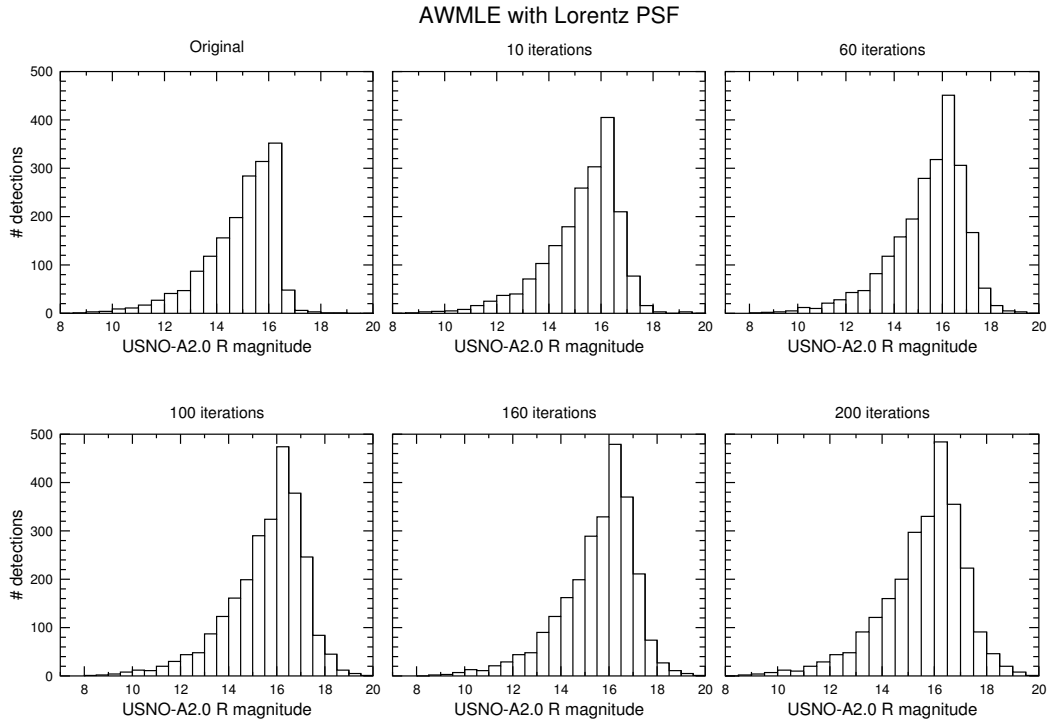
Figure 5.20: USNO-A2.0 R magnitude histogram of matched detections over a range of iterations for original and AWMLE Lorentz PSF based deconvolved images.

tection threshold of 3σ is considered for both original and deconvolved images, this gain turns into a more favourable $\Delta R \sim 0.59$. Of course, although in this latter the relative gain with respect to the original image is larger, the absolute limiting magnitude in the 2σ case is deeper.

Note that gain estimate does not take into account the intrinsic magnitude distribution of the studied FOV, and could be somewhat biased. To check this, an alternative estimate can be derived from the comparison of the original and deconvolved images magnitude histograms with the histogram of USNO-A2.0. This is illustrated in Fig. 5.21, where we overplot the magnitude histogram of the original image with the one from a 140-iteration AWMLE Moffat15 deconvolution, and with the complete histogram from USNO-A2.0. A similar magnitude gain can be derived.

Conclusions

We have applied AWMLE deconvolution to the NESS-T_02 frame. Its performance was evaluated in terms of number of true and unmatched detections. The validation
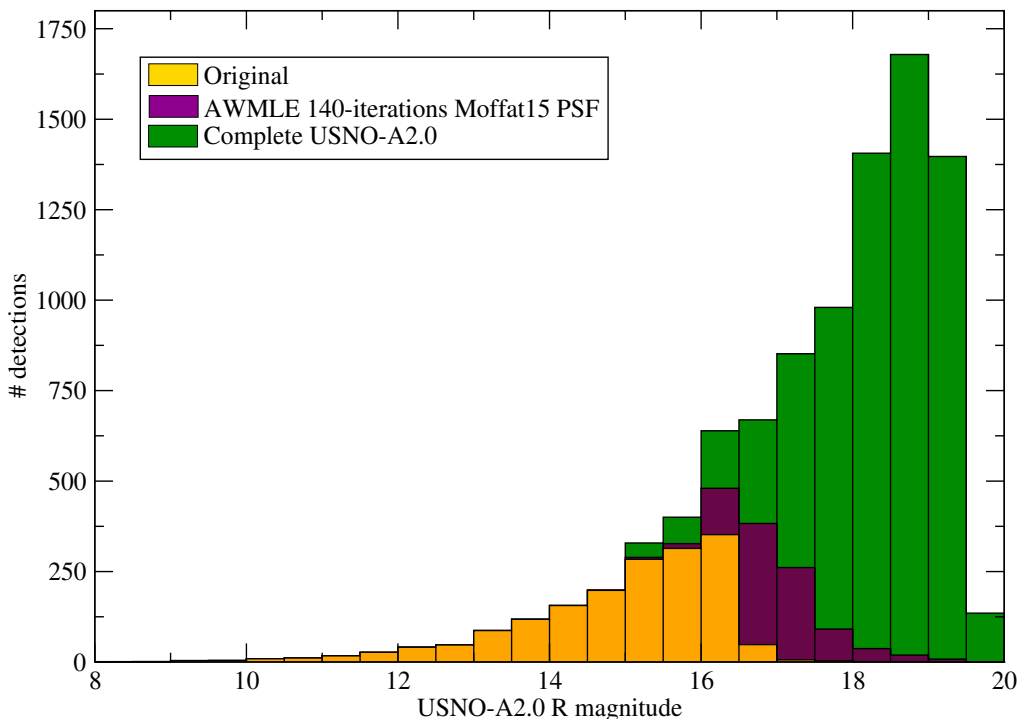
Figure 5.21: USNO-A2.0 R magnitude histograms of matched detections for the original image and a 140-iteration AWMLE deconvolution with a Moffat15 PSF and a 2σ detection threshold.

of true detections was carried out with USNO-A2.0 catalogue. The dependence of those results on the chosen PSF model, the number of iterations and detection threshold were also investigated.

AWMLE shows excellent performance in keeping the unmatched detections to very low percentages (2-3%). It delivers limiting magnitude gains of $\Delta R \sim 0.46$ and $\Delta R \sim 0.59$ for 2σ and 3σ detections thresholds, respectively. This turns AWMLE to be as a powerful technique for increasing the number of useful science objects from the faint part of magnitude distribution.

A detailed analysis of the origin of those few unmatched objects was conducted. The bulk of them were found to be caused by limited PSF knowledge and ringing artifacts, which are accentuated by the severe original undersampling and inaccurate background estimation. As a consequence of these two shortcomings, NESS-T deconvolved images appear to be less converged than QUEST's. This leads to a less homogeneous detection process (this still depends on the chosen threshold), and a smaller limiting magnitude gain (0.18 mag less) for the same detection threshold

as QUEST. However, it is noteworthy that a similar gain is obtained when a 3σ detection threshold is considered.

The asymptotic convergence found for QUEST data in Sect. 5.3.1 was broken by not having the original data properly calibrated (bias, darks and flats). This translated into a non-stability in the number of detections as a function of number of iterations and a real dependence of number of detections with the considered threshold. We emphasize that with these calibration frames, the performance of AWMLE is likely to improve and recover the same level of convergence (and magnitude gain) as QUEST data.

Finally, a comparative study between Moffat15 and Lorentz PSFs was made. On one hand, the former delivered more matched detections. On the other hand, the latter was shown to offer faster convergence (similar level of detections with 20 iterations less). This result is important if a systematic application of AWMLE to NESS-T images is desired, since it saves execution time. In addition, thanks to its better fit of the outer wings of the PSF, Lorentz based deconvolutions offered significantly less false detections than Moffat15.

Possible extensions of this work

Being the Baker-Nunn Camera a wide field instrument, the increase of the limiting magnitude shown in this section could be of interest for a large number of observational programs. In the particular case of NESS-T project, this could lead to an important increase in its efficiency in terms of the number of detectable NEOs.

From the above mentioned constrains which introduce $\sim 2\%$ of false detections, at least the one refering to accurate background estimation could be easily solved in near future when accurate flatfield calibration frames can be routinely obtained. As a result, AWMLE convergence would be improved and false detections reduced to an assumible percentage for a systematic usage in a dedicated NEOs detection pipeline. For that purpose, with a 4K×4K CCD chip, execution time and RAM usage of AWMLE are crucial issues for determining its feasibility. They were already discussed in Table 2.1. As commented in QUEST case, an additional effort in the algorithm optimization could improve the current performance up to shortening the execution time by a 50%. In addition, by parallelizing the algorithm with as many nodes as wavelet planes used in the decomposition of the original image (4 to 6)

the scalability factor could be approximately proportional to the number of nodes depending on the architecture implementation chosen. After all, execution time could be safely reduced to a few seconds per iteration.

The presented results are totally general and are likely to be improved for data sets with finer pixel scale. For example, a project like NOAO Deep Lens Survey (DLS) (Becker et al. 2004; Wittman et al. 2002), would be an potential application of AWMLE deconvolution. It is being operated on the 4 m Blanco and Mayall telescope at the Cerro Tololo Inter-American Observatory (CTIO) and Kitt Peak National Observatory (KPNO) with a 8K×8K CCD mosaic, yielding complete variability census in the optical down to 24th magnitude. Given its fine scale of $0.''26$, the PSF extraction could be largely improved in comparison to NESS-T case. As a result, the performance of AWMLE algorithm would be improved to the level of QUEST data in Sect. 5.3.1 or even better.

5.4 Increase in resolution and object deblending

This section will be devoted to assess the resolution gain obtained by image deconvolution in QUEST and NESS-T data sets described in Chapt. 3.

5.4.1 QUEST: QSO candidates deblending for gravitational lenses detection

In this section we will show how deblending capabilities of image deconvolution can contribute to the detection of gravitational lenses among a list of QSOs[8] candidates culled from QUEST images. First, a brief overview of the current state of macrolensing detection field will be given. Next, the results of the deconvolution for the two data sets described in Table 3.9 will be presented. Finally, we will discuss the limits and future extensions of this work.

A gravitational lens is one of the astrophysical observables predicted by General Relativity. It appears when a very massive object (galaxy, massive black hole, etc.)

---

[8]We will use the terms *QSO* (quasi stellar object) and *quasar* as equivalent terms along this section, although the concept quasar is often used only for radio sources.

deflects light coming from a very distant source, in most cases a quasar, and as a result the observer can record a variety of phenomena such as *Einstein Rings*, the amplification of the apparent intensity of the background source, or the splitting of this source into two or more separated components.

It was early shown that crucial cosmological parameters (dark matter distribution, Hubble's Constant through time delays between lens components and Einstein's Cosmological Constant) could be directly derived if a dense enough census of lenses will be available in the future. Therefore, it was clear that intense and maintained observational effort should be dedicated in this topic. At a first stage, the search was mainly conducted with VLBI observations among a selected sample of already known quasars (8,609 (Veron-Cetty & Veron 1995)). This strategy yielded to relatively scarse lenses discoveries (8 over a thousand of selected quasars by 1995) since the first discovery of QSO 0957+561 by Walsh et al. (1979). In a second stage, the new generation large QSO surveys, such as the SDSS (Loveday et al. 1998) and the 2dF (Lewis et al. 1998), raised the number of catalogued quasars several up to tens of thousands of entries (counting 48,921 in Véron-Cetty & Véron (2003)). This shifted the lens search strategy towards a more exhaustive and unbiased one, based on multi-band photometric variability and/or spectra classification criteria.

It is in this second framework which QUEST is currently working with a QSO detection efficiency of $\sim 7\%$ (Rengstorf et al. 2004a,b) by using a photometric variability criteria. As anticipated in Pag. 90, the strategy for lens searching is to reobserve these QSOs candidates with larger telescopes equiped with high resolution CCDs. That is the case of follow-up campaigns conducted at WIYN telescope with the MiniMosaic camera.

Our aim here is to see how deblending capabilities of image deconvolution could help to resolve potentially lensed QSOs. As explained above, intensive follow-up observations at large telescopes are needed for lens detection, and if a more depurated list of deblended candidates were available, that could be of crucial importance for improving the confirmation efficiency.

Two different data sets were considered for the development of this work. They consist of two different fields, labeled as Field 14 and Field 13, from which we have QUEST (low resolution) and WIYN (high resolution) images, as described in Table 3.9. The analysis procedure in both cases is the following:

1. extract PSF from QUEST images as explained in Sect. 4.2,

2. perform deconvolution of QUEST images with the AWMLE algorithm described in Sect. 2.3,

3. run `SExtractor` object detection (see Sect. 4.3) in all three images: WIYN and original and deconvolved QUEST,

4. follow the methodology in Sect. 4.4.1 for validating detections between original and deconvolved QUEST images, and the corresponding WIYN image,

5. apply the resolution assessment method described in Sect. 4.5.1 to those image patches which comprise QSOs candidates culled by variability criteria and compute image separation, magnitude and magnitude difference of newly resolved companions.

Field 14

QUEST and WIYN images considered in this case are q100899_F14 and w240700_F14, as labeled in Table 3.9. Average seeing for QUEST data that night was around $2.''4$.

In Fig. 5.22 we illustrate the result after a 400-iteration deconvolution of the QUEST image with the AWMLE algorithm. An hybrid Moffat25 PSF was used since it was found to be the best fit to the original data, as explained in Sect. 5.1.2. Attending the variability criteria explained above, up to 6 QSO candidates are included in Field 14 for which we supply their corresponding USNO-B1.0 identificator in Table 5.14. For each canditate panel in Fig. 5.22 we include three zoomed regions: original QUEST, deconvolved QUEST and WIYN[9]. The background level varies from image to image, mostly due to the proximity to bright stars (the most notable case, C3).

---

[9]The zoom ratio for WIYN panels (1:6) is a bit smaller than the one for QUEST (1:7.3).
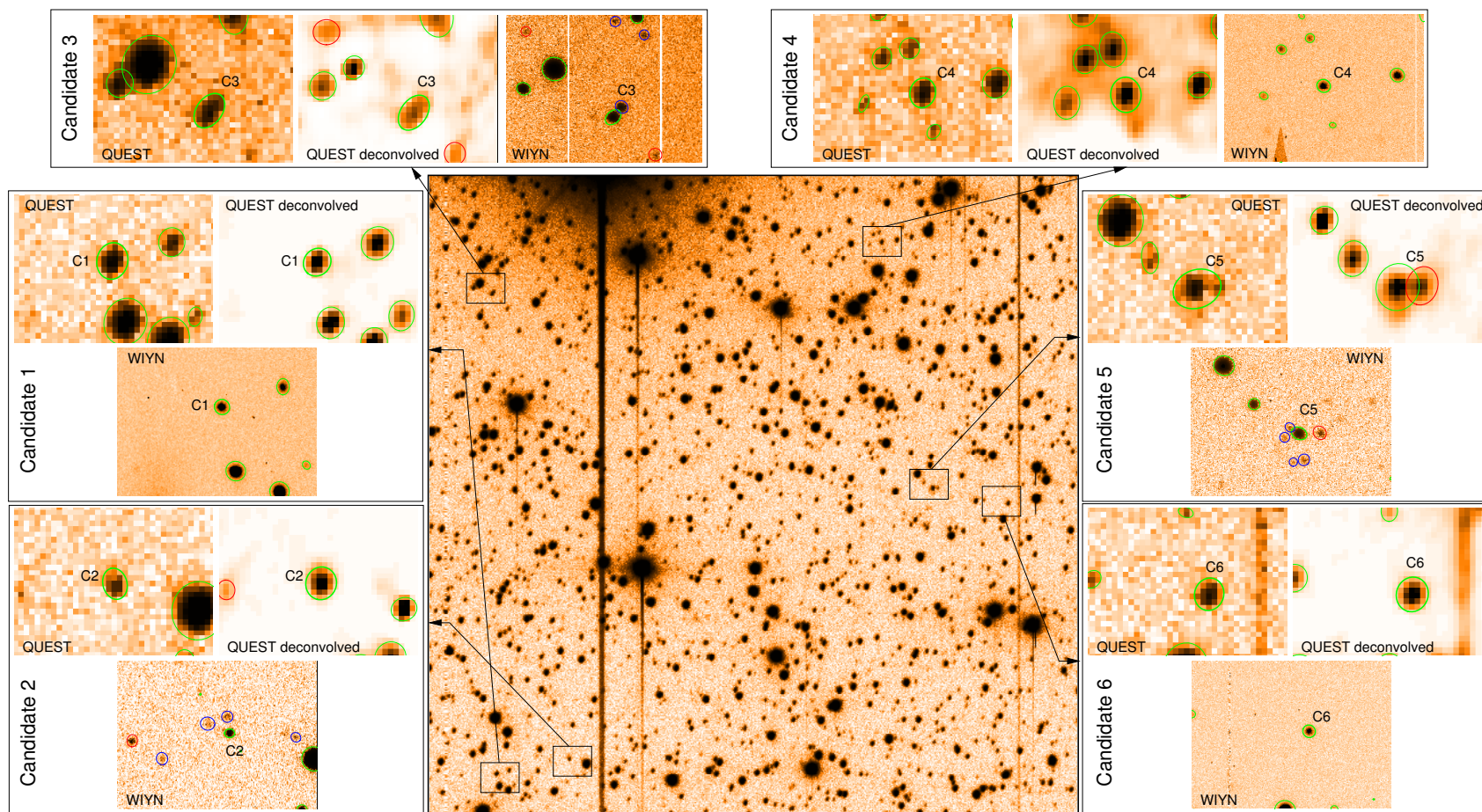
Figure 5.22: Application of image deconvolution to 6 QSO candidates in Field 14 field, described in Table 5.14. The original QUEST frame is displayed in the centre. Each candidate panel includes original QUEST image, deconvolved QUEST image (400 iterations) and high resolution WIYN image, respectively. The QSO candidates are labeled in each case. Ellipses indicate objects detected by SExtractor. Those in green correspond to objects present in all three images, in blue those only resolved in WIYN and in red those resolved both in WIYN and deconvolved QUEST images but not resolved in original QUEST image. This is the case of C5, where deconvolution achieves to resolve the most distant component on the right of the sixtuple system.

The detections labeled in green ellipses correspond to objects present in all three images. Those in blue are objects only detected by WIYN. Finally, those in red are detected both in WIYN and deconvolved QUEST images but not present in original QUEST image.

Qualitatively, we can distinguish two causes which trigger the new detections in the deconvolved QUEST image. On one hand, the increase in limiting magnitude: this is the case of C2 and C3 red ellipses which are far from QSO candidate. On the other hand, the increase of image resolution: this is the case of C5, where deconvolution achieves to resolve the brightest companion of the sixtuple system. Of course, both causes are not exclusive but they both simultaneously contribute to new detections. Their relative importance depends mainly on the candidate-companion separation and magnitude difference.

In Table 5.14 we summarize the results of what is shown in Fig. 5.22. The column format for each candidate is: the second column corresponds to the id number in USNO-B1.0 catalogue (Monet et al. 2003), 3rd to 5th columns indicate the resolving status for all three kind of images, 6th to 9th columns are the parameters computed from WIYN image for each component of the binary or multiple system. We decided to split the resolving status into three separate categories: single, unresolved and resolved. Below we discuss each one of these:

- **Single source candidates**
  This is the case of candidates C1, C4 and C6, where even in high resolution WIYN image they appear as unique components, without any near companion which could be assumed to be a lens event.

  Of course, in these cases image deconvolution cannot contribute to an improvement of resolution, since the companion (if any) is much closer than the limit which the AWMLE algorithm can reach with QUEST original sampling.

- **Resolved candidate**
  this is the case of the D component of C5. This candidate **is not** resolved in original QUEST image. On the contrary, the deconvolved QUEST image yields a new component D at $4''.0$ from the candidate with a magnitude difference of 1.82, as determined from high resolution WIYN image. As seen in Fig. 5.23, the presence of this companion was evident by eyeball already in the original QUEST image. However, this detection procedure is not practical given the

Table 5.14: Summary of image resolution improvement for the 6 QSO candidates (supplied by Andrews (2000)) in Field 14 field after deconvolving QUEST image. Angular separation (ρ), magnitude difference Δm and magnitude of secondary component (m_2) are derived from WIYN image.

Candidate Id	USNO-B1.0 Id	Resolving status[a]			Companions parameters[b]			
		QUEST	QUEST deconvolved	WIYN	Id	ρ ($''$)	Δm	m_2
C1	0885-0528372	S	S	S	-	-	-	-
C2	0885-0528372	UR	UR	R	B	3.2	1.15	15.17
		UR	UR	R	C	4.5	1.70	15.71
C3	0885-0527746	UR	UR	R	B	1.9	0.61	13.52
C4	0884-0529657	S	S	S	-	-	-	-
C5	0884-0529982	UR	UR	R	B	2.0	2.88	15.68
		UR	UR	R	C	2.7	2.73	15.53
		UR	R	R	D	4.0	1.82	14.62
		UR	UR	R	E	5.0	2.21	15.01
		UR	UR	R	F	5.7	3.41	16.21
C6	0883-0548350	S	S	S	-	-	-	-

[a] S: single, UR: unresolved, R: resolved.

[b] A given object in the vicinity of a candidate is considered to be a companion when its separation is smaller than $7''$.

large extension of candidates list, which makes indispensable the use of an automatic detection package as `SExtractor`, which in this case was not able to deblend the companion from the candidate.

After a systematic search in NASA/IPAC Extragalactic Database (`NED`)[10] and `SIMBAD`[11], we found no hit in either QSO catalogue or similar. SDSS database was also queried, but coverage of this zone still remains to be done. Hence, in absence of complementary information and spectroscopic confirmation, few more can be said about the real nature of this candidate.

---

[10]The NASA/IPAC Extragalactic Database (NED) is operated by the Jet Propulsion Laboratory, California Institute of Technology, under contract with the National Aeronautics and Space Administration.

[11]`SIMBAD` database is operated at CDS, Strasbourg, France
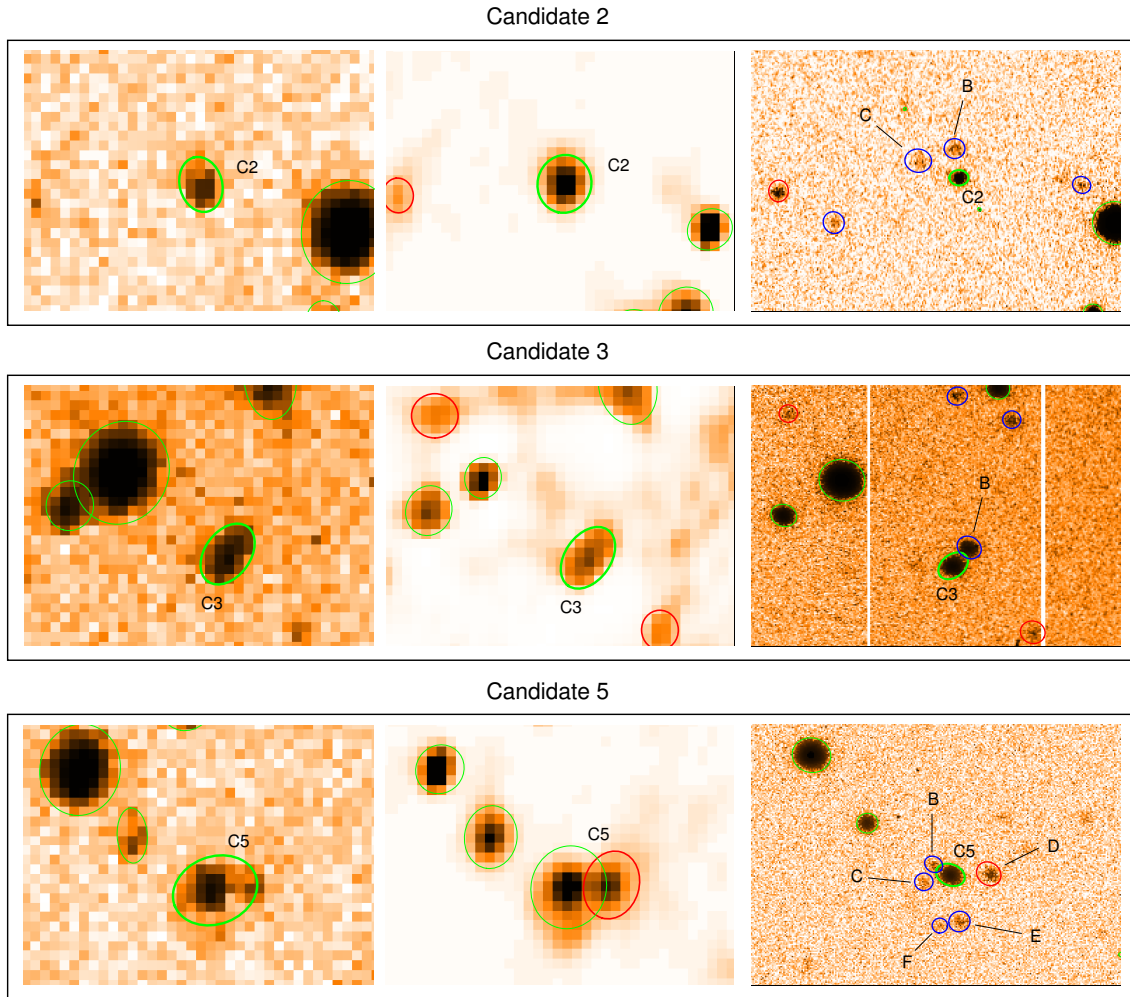
Figure 5.23: A zoomed display of those panels in Fig. 5.22 which show unresolved (C2 and C3, top and middle) and resolved components (C5-D, bottom). The same ellipses, colors and labeling criteria as Fig. 5.22 apply here.

- **Unresolved candidates**

  These are the cases of B and C components of C2, B component of C3 and rest of components (B,C,F and E) of C5, which are only resolved in high resolution WIYN images.

  All 7 components represent a good example of how different values for angular separation and magnitude of the secondary can limit the image resolution of an image. Below we describe them:

  First, C3-B is unresolved despite of having a secondary one magnitude brighter than C5-D, which is actually resolved. This is because its separation ($1''9$) is cleary lower than in C5 case and below the seeing value at QUEST site for

that night (see Table 3.9). In addition, its closer magnitude difference does not help the detection routine to deblend the companion. Although deconvolution is not able to get the secondary detected, it is worth remarking that the object ellipticity[12] was found to be a bit larger (1.485 vs. 1.503) with respect to the original image. That might be an indicator that C3 is a critically resolved object.

Next, C2-B and C2-C are characteristic cases of moderate separation and notably faint magnitude values. They are well above the seeing value ($\rho = 3''2$ and $4''5$, respectively) and fainter ($m_2 = 0.6$ and 1.1, respectively) than C5-D. If one could compute the magnitudes of the companions in original QUEST images, those would be below the corresponding limiting magnitude. Even the $\Delta V_{\mathrm{lim}} \sim 0.6$ gain supplied by deconvolution would not be sufficient in that case.

Finally, an example of well separated but extremely faint components is represented by the C5-E and C5-F.

To sum up, C3-B could be considered as a critically unresolved case limited mostly in terms of its close angular separation. In the other extreme, C5-E and C5-F would be critically unresolved in terms of their faint limiting magnitude. C2-B and C2-C can be considered as intermediate cases.

Field 13

QUEST and WIYN images considered in this case are q100899_F13 and w250700_F13, as labeled in Table 3.9. The average seeing for QUEST data that night was around $2''3$.

Note from Table 3.9, we have 5 QUEST frames of different nights covering the same field Field 13. We chose only the one from Aug 10th 1999 for several reasons:

- in principle all 5 night frames could be coadded to obtain a deeper image, comparable to WIYN limiting magnitude. However, we recall that what we address in this section is the resolution gain introduced by the deconvolution process. This strongly depends on the performance of the PSF extraction

---

[12]As computed by `SExtractor`.

process. If we coadd frames with PSFs of different quality, the resulting image is likely to have a complex PSF and a resolution worse than, at least, the best of the input frames. To study the influence of the coadding process over the PSF used for deconvolving is beyond the scope of this thesis.

Other coadding techniques in the superresolution context, such as *drizzle* algorithm (Fruchter & Hook 2002), in combination with deconvolution, have led promising results for undersampled images. However, this is equally outside of the scope of this thesis.

- this was the night with best seeing. So it will allow us to estimate the maximum absolute resolution attainable we can expect from QUEST data once they have been deconvolved.

- this is the same night as previous q100899_F14 frame of Field 14. Therefore, as seeing values recorded in chips B4 and C4 are pretty similar (see Table. 3.9), we can assume that the results from Fields 14 and 13, in terms of resolution gain, will be directly comparable.

Similarly to Field 14 example, an hybrid Moffat25 PSF was chosen for running a AWMLE 300-iteration deconvolution. Field 13 is richer in QSO candidates, and up to 38 of them have been studied this time.

A zoomed display of the three panels (original and deconvolved QUEST, and WIYN) for each candidate can be seen in Figs. 5.24-5.29. The same labeling and colors criteria as previous example were followed here. Note that in candidates C7, C12, C23, C26, C28 and C29 a grey ellipse is shown, indicating detections of deconvolution artifacts. The cause of this effect was already discussed in Sect. 5.3.1. We briefly recall this is due to the fact that the mismatch in PSF extraction process triggers false detections in the vicinity of bright stars when deconvolution is run to a large number of iterations.

In Table 5.15 we summarize the results of what is shown in Figs. 5.24-5.29. The column format is the same as Table. 5.14.

Table 5.15: Summary of image resolution improvement for the 38 QSO candidates (supplied by Snyder (2001)) in Field 13 after deconvolving QUEST image. Angular separation (ρ), magnitude difference Δm and magnitude of secondary component (m_2) are derived from WIYN image.

Candidate Id	USNO-B1.0 Id	Resolving status[1]			Companions parameters[2]			
		QUEST	QUEST deconvolved	WIYN	Id	ρ (″)	Δm	m_2
C1	0891-0538903	UR	UR	R	B	2.9	4.06	16.51
		UR	UR	R	C	3.4	4.05	16.50
C2	0891-0538916	UR	UR	R	B	3.5	2.24	15.92
		UR	UR	R	C	4.1	1.94	15.62
		UR	R	R	D	4.8	0.28	13.97
		UR	R	R	E	5.8	1.76	15.44
C3	0891-0538962	R	R	R	B	4.9	0.55	13.75
C4	0891-0538959	UR	UR	R	B	5.2	2.75	16.01
		UR	R	R	C	6.2	2.31	15.57
		UR	UR	R	D	6.8	2.71	15.97
C5	0891-0538874	UR	UR	R	B	4.0	5.83	15.80
C6	0891-0538922	UR	R	R	B	4.9	2.99	14.94
		UR	UR	R	C	5.7	3.80	15.75
		UR	UR	R	D	5.7	4.22	16.18
C7	0891-0538934	UR	UR	R	B	2.8	5.18	16.70
		UR	UR	R	C	4.5	4.60	16.12
		UR	UR	R	D	5.0	3.94	15.45
		R	R	R	E	6.0	2.46	13.98
C8	0891-0538827	UR	UR	R	B	3.2	5.31	16.05
C9	0891-0538866	UR	UR	R	B	5.5	3.72	16.47
		R	R	R	C	6.0	0.84	13.59
		UR	UR	R	D	6.2	3.27	16.04
C10	0891-0538869	UR	R	R	B	5.7	2.55	15.32
		UR	UR	R	C	7.0	3.62	16.41

[1] S: single, UR: unresolved, R: resolved.

[2] A given object in the vicinity of a candidate is considered to be a companion when its separation is smaller than 7″.

Table continues on next page.

Candidate Id	USNO-B1.0 Id	Resolving status[1]			Companions parameters[2]			
		QUEST	QUEST deconvolved	WIYN	Id	ρ $('')$	Δm	m_2
C11	0891-0538897	UR	UR	R	B	2.1	3.44	16.32
C12	0891-0538980	UR	R	R	B	5.6	5.80	14.69
C13	0891-0538963	UR	UR	R	B	1.8	0.80	14.21
		UR	UR	R	C	4.6	1.97	15.38
		UR	UR	R	D	6.3	2.60	16.01
C14	0891-0538977	UR	UR	R	B	5.6	3.91	15.24
		UR	UR	R	C	5.8	4.42	15.75
		UR	R	R	D	6.3	2.78	14.11
C15	0892-0535528	UR	UR	R	B	5.9	2.18	15.42
		UR	UR	R	C	6.0	3.13	16.36
C16	0892-0535541	UR	UR	R	B	5.4	1.89	15.42
		UR	UR	R	C	6.2	2.84	16.36
C17	0891-0539018	UR	UR	R	B	5.2	4.64	16.15
C18	0891-0539025	UR	R	R	B	4.0	1.55	14.07
		R	R	R	C	6.0	1.43	13.95
C19	0891-0539033	R	R	R	B	5.8	0.51	13.95
C20	0892-0535569	UR	UR	R	B	1.2	2.09	15.00
C21	0892-0535592	S	S	S	-	-	-	-
C22	0891-0539078	UR	UR	R	B	4.4	2.91	15.80
		UR	UR	R	C	4.4	3.55	16.45
C23	0891-0539083	UR	UR	R	B	1.8	2.16	14.89
		UR	UR	R	C	5.7	2.88	15.61
C24	0891-0539059	R	R	R	B	6.7	0.34	12.70

[1] S: single, UR: unresolved, R: resolved.
[2] A given object in the vicinity of a candidate is considered to be a companion when its separation is smaller than $7''$.

Candidate Id	USNO-B1.0 Id	Resolving status[1]			Companions parameters[2]			
		QUEST	QUEST deconvolved	WIYN	Id	ρ $('')$	Δm	m_2
		UR	R	R	C	6.9	3.00	15.35
		UR	R	R	D	6.9	2.95	15.30
C25	0891-0539071	UR	UR	R	B	2.2	2.35	15.75
C26	0891-0539050	UR	UR	R	B	4.3	2.85	16.38
		UR	UR	R	C	6.6	2.98	16.51
		UR	UR	R	D	6.7	3.02	16.54
C27	0891-0539060	UR	UR	R	B	1.3	2.82	15.65
		UR	UR	R	C	4.1	2.46	15.29
		R	R	R	D	4.9	1.39	14.22
		UR	UR	R	E	5.8	3.55	16.38
C28	0891-0539020	UR	UR	R	B	6.5	5.16	14.08
C29	0891-0538983	R	R	R	B	5.4	0.18	12.95
C30	0891-0538986	R	R	R	B	5.4	-0.18	12.77
C31	0891-0539004	UR	UR	R	B	3.3	3.23	16.06
		UR	UR	R	C	3.4	4.10	16.93
		UR	R	R	D	5.5	2.13	14.96
C32	0891-0539001	UR	R	R	B	3.9	3.51	14.86
		UR	UR	R	C	5.2	6.02	17.37
		R	R	R	D	6.1	1.32	12.67
C33	0891-0539021	UR	UR	R	B	4.7	4.33	15.99
		UR	UR	R	C	6.2	4.13	15.79
C34	0891-0538970	UR	UR	R	B	3.7	5.26	17.15
C35	0891-0538985	UR	UR	R	B	2.5	4.55	16.18
		UR	R	R	C	4.7	2.59	14.22
		UR	UR	R	D	6.6	2.81	14.43

[1] S: single, UR: unresolved, R: resolved.
[2] A given object in the vicinity of a candidate is considered to be a companion when its separation is smaller than $7''$.

Candidate Id	USNO-B1.0 Id	Resolving status[1]			Companions parameters[2]			
		QUEST	QUEST deconvolved	WIYN	Id	ρ ($''$)	Δm	m_2
C36	0891-0538981	UR	UR	R	B	3.8	3.18	16.34
		UR	UR	R	C	5.2	2.37	15.53
C37	0891-0538999	UR	UR	R	B	2.5	4.23	16.68
		UR	UR	R	C	5.3	4.77	17.22
		UR	R	R	D	5.9	1.50	13.95
		UR	UR	R	E	6.2	3.47	15.93
C38	0891-0538980	UR	R	R	B	5.4	1.82	13.73
		UR	UR	R	C	5.6	3.50	15.41

[1] S: single, UR: unresolved, R: resolved.
[2] A given object in the vicinity of a candidate is considered to be a companion when its separation is smaller than $7''$.

As in the Field 14 case, below we discuss the three separate categories: single, unresolved and resolved:

- **Single source candidates**

  This is the case of candidate C21, where even in high resolution WIYN image it appears as a single component, without any companion within $7''$ which could be assumed to be a lens event.

  Of course, in these cases image deconvolution cannot contribute to an improvement of resolution, since the companion (if any) is much closer than the limit that AWMLE can reach with QUEST original sampling.

- **Resolved candidates**

  Among the 38 candidates in Table 5.15, 20 of them show a total of 25 resolved components. 10 of these components were already detected in the original QUEST images. The 15 remaining were resolved only in the deconvolved QUEST and WIYN images. The separation of these newly detected companions ranges from $3\overset{''}{.}9$ to $6\overset{''}{.}9$.

  As seen in Figs. 5.24-5.29, most of the companions triggered by AWMLE could be guessed by visual inspection already in the original QUEST image.

However, `SExtractor`, even with optimized input parameters, was not able to deblend them from the primary.

As in Field 14, a systematic search in `NED` and `SIMBAD` databases was performed with no positive hits which could reveal additional information about the QSO nature of these multiple candidates.

- **Unresolved candidates**

  There are 17 candidates and 54 components in Table 5.15 which could only be resolved by high resolution WIYN images. They cover a wide range of separations, magnitude of secondaries and difference of magnitudes. We discuss some representative cases for each parameter:

  C13-B is unresolved because of its close separation to primary ($1.''9$) and despite of having a secondary a magnitude brighter than other resolved fainter components. Thus, this is a clear example of a critically unresolved candidate mostly because of its close angular separation, which is below the seeing value at QUEST site for that night ($2.''0$).

  C1-C and C14-B are characteristic cases of moderate separation and notably faint magnitude values. They are well above the seeing value ($\rho = 3.''4$ and $5.''6$, respectively) but significantly fainter than other resolved components. In other words, those candidates are critically unresolved because of their faint limiting magnitude.

Quantitative assessment of resolution gain

In Field 14 example we qualitatively anticipated that both the increase in limiting magnitude and the gain image resolution contribute to new components detected in deconvolved QUEST images. We also pointed out that each one of these causes become dominant over the other depending on the particular combination of image separation, secondary magnitude and magnitude difference of every component.

In order to establish a quantitative study of resolution gain, the methodology described in Sect. 4.5.2 was followed. We grouped all the QSOs candidates from Fields 14 and 13 examples (44 in total), and plotted the separation (ρ) of all the resolved components as a function of their magnitude (m_2) in Fig. 5.30, and the magnitude difference (Δm) as a function of (ρ) in Fig. 5.31. As previous figures,
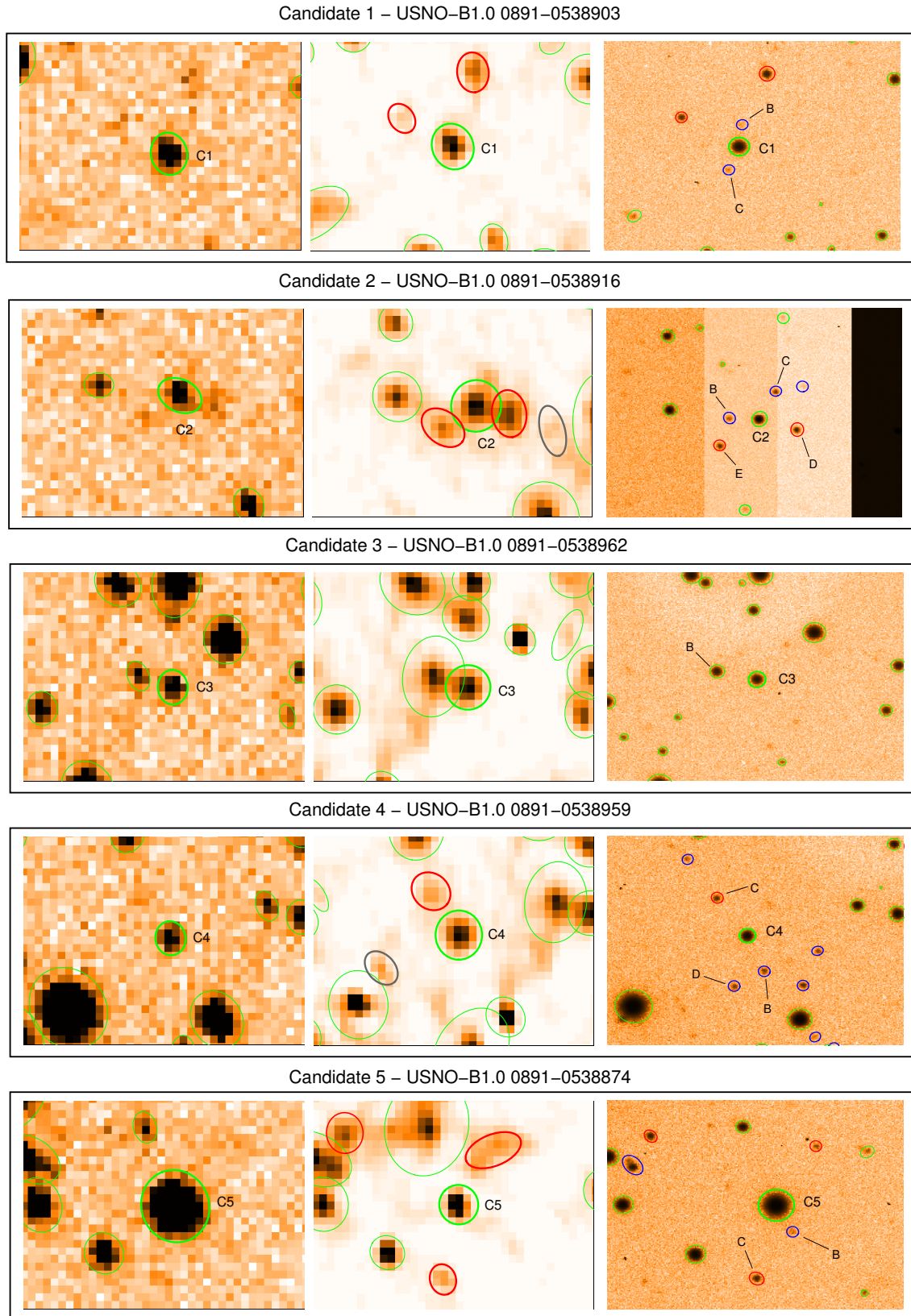
Figure 5.24: QUEST, original and deconvolved, and WIYN panels of QSO candidates included in Table 5.15. Their resolved components are labeled accordingly to the same table. Green ellipses for objects present in all three images, red for those detected both in WIYN and deconvolved QUEST, but not in original QUEST image, and blue for those only detected by WIYN.

Candidate 6 – USNO–B1.0 0891–0538922

Candidate 7 – USNO–B1.0 0891–0538934

Candidate 8 – USNO–B1.0 0891–0538827

Candidate 9 – USNO–B1.0 0891–0538866

Candidate 10 – USNO–B1.0 0891–0538869
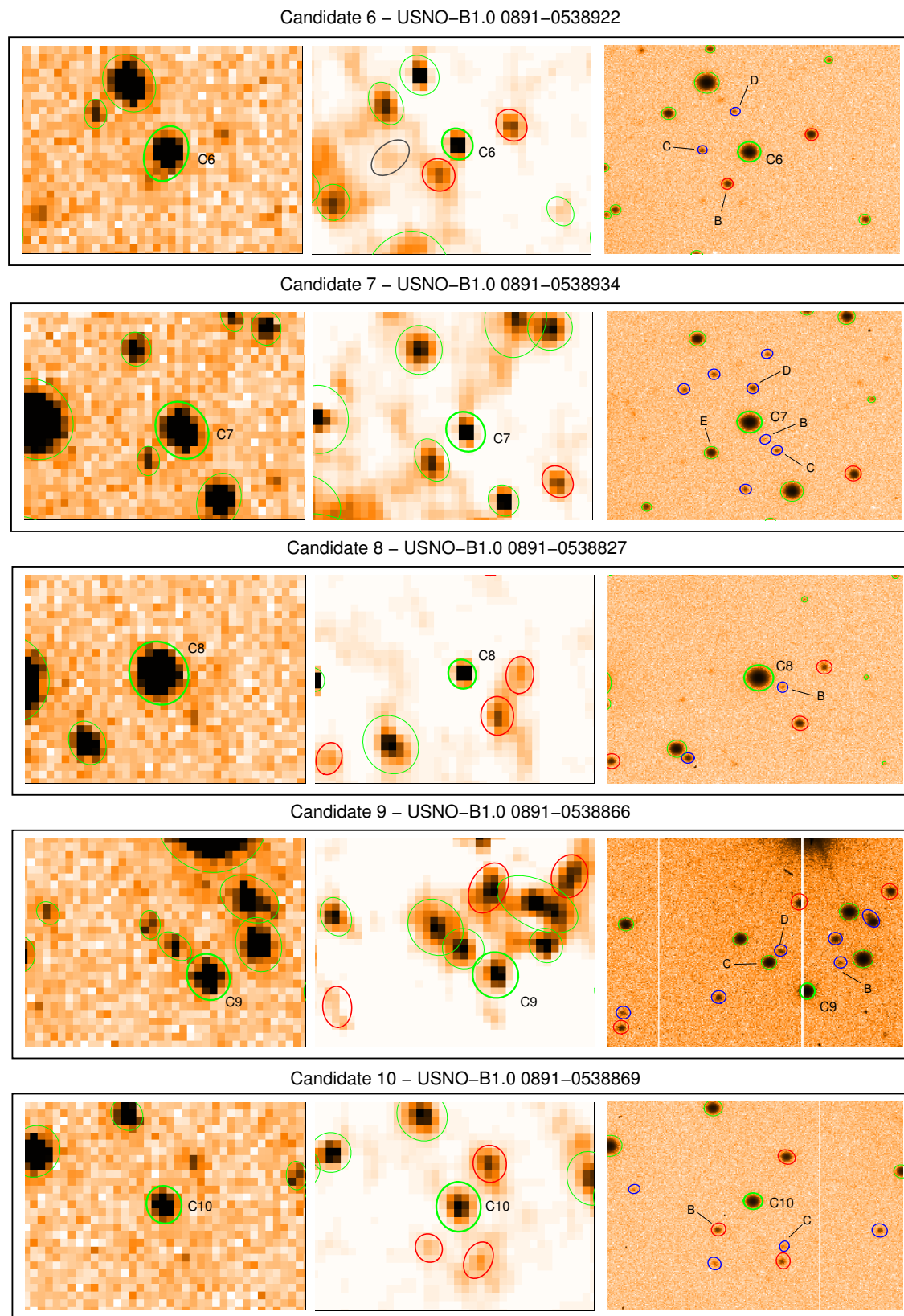
Figure 5.25: QUEST, original and deconvolved, and WIYN panels of QSO candidates included in Table 5.15. Their resolved components are labeled accordingly to the same table. Green ellipses for objects present in all three images, red for those detected both in WIYN and deconvolved QUEST, but not in original QUEST image, and blue for those only detected by WIYN.
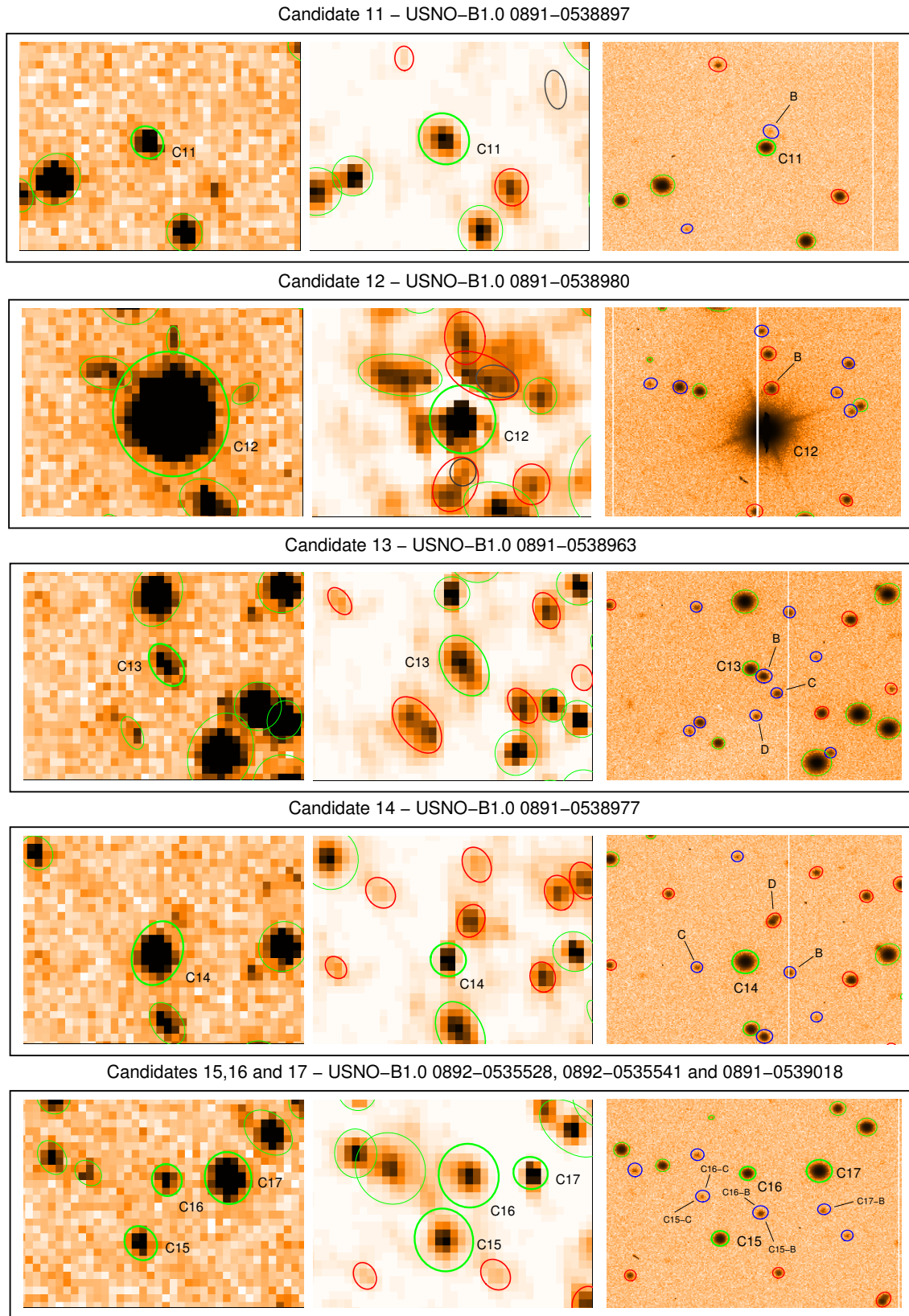
Figure 5.26: QUEST, original and deconvolved, and WIYN panels of QSO candidates included in Table 5.15. Their resolved components are labeled accordingly to the same table. Green ellipses for objects present in all three images, red for those detected both in WIYN and deconvolved QUEST, but not in original QUEST image, and blue for those only detected by WIYN.

Candidates 18 and 19 – USNO–B1.0 0891–0539025 and 0891–0539033

Candidate 20 – USNO–B1.0 0892–0535569

Candidate 21 – USNO–B1.0 0892–0535592

Candidate 22 – USNO–B1.0 0891–0539078

Candidate 23 – USNO–B1.0 0891–0539083
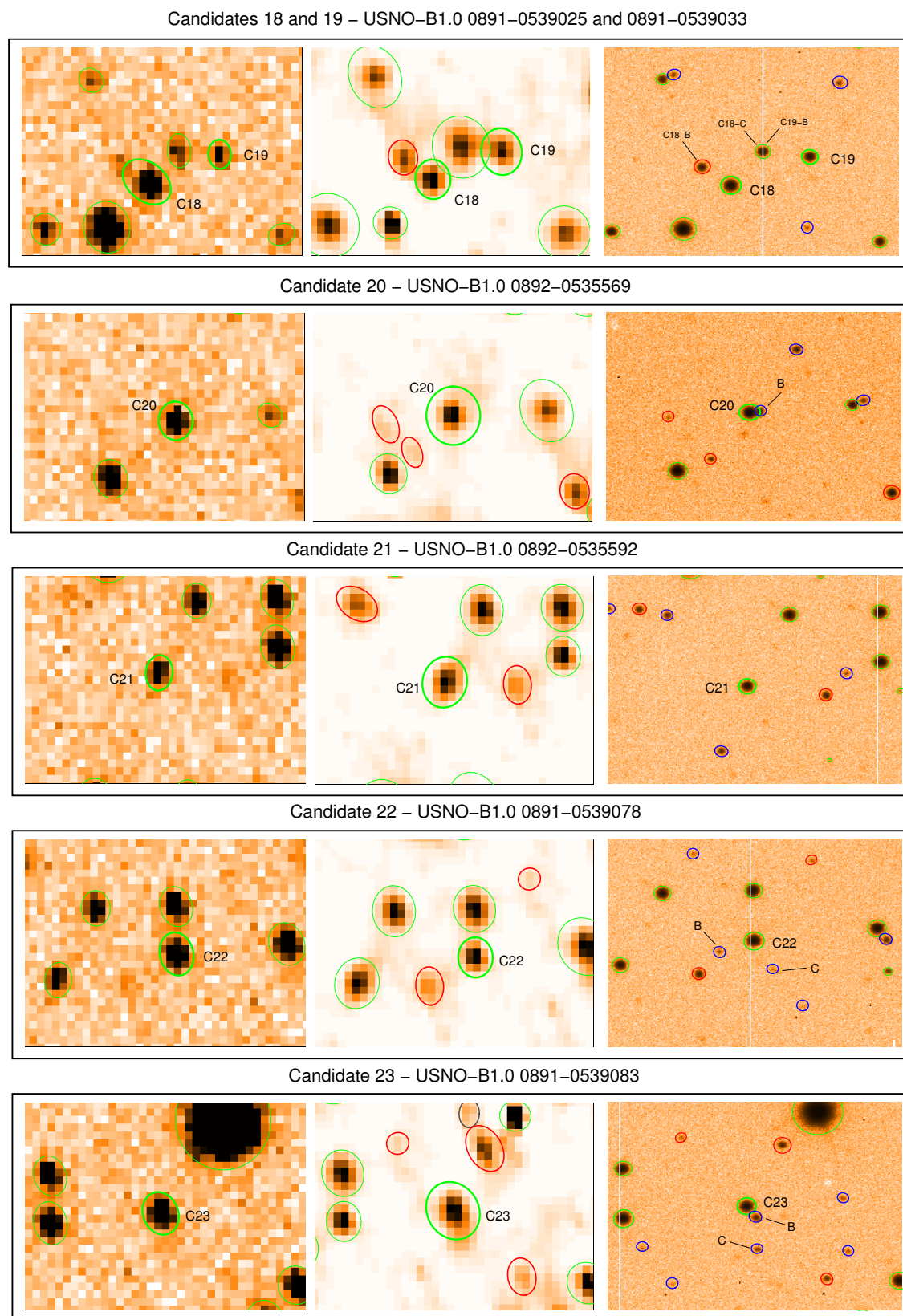
Figure 5.27: QUEST, original and deconvolved, and WIYN panels of QSO candidates included in Table 5.15. Their resolved components are labeled accordingly to the same table. Green ellipses for objects present in all three images, red for those detected both in WIYN and deconvolved QUEST, but not in original QUEST image, and blue for those only detected by WIYN.
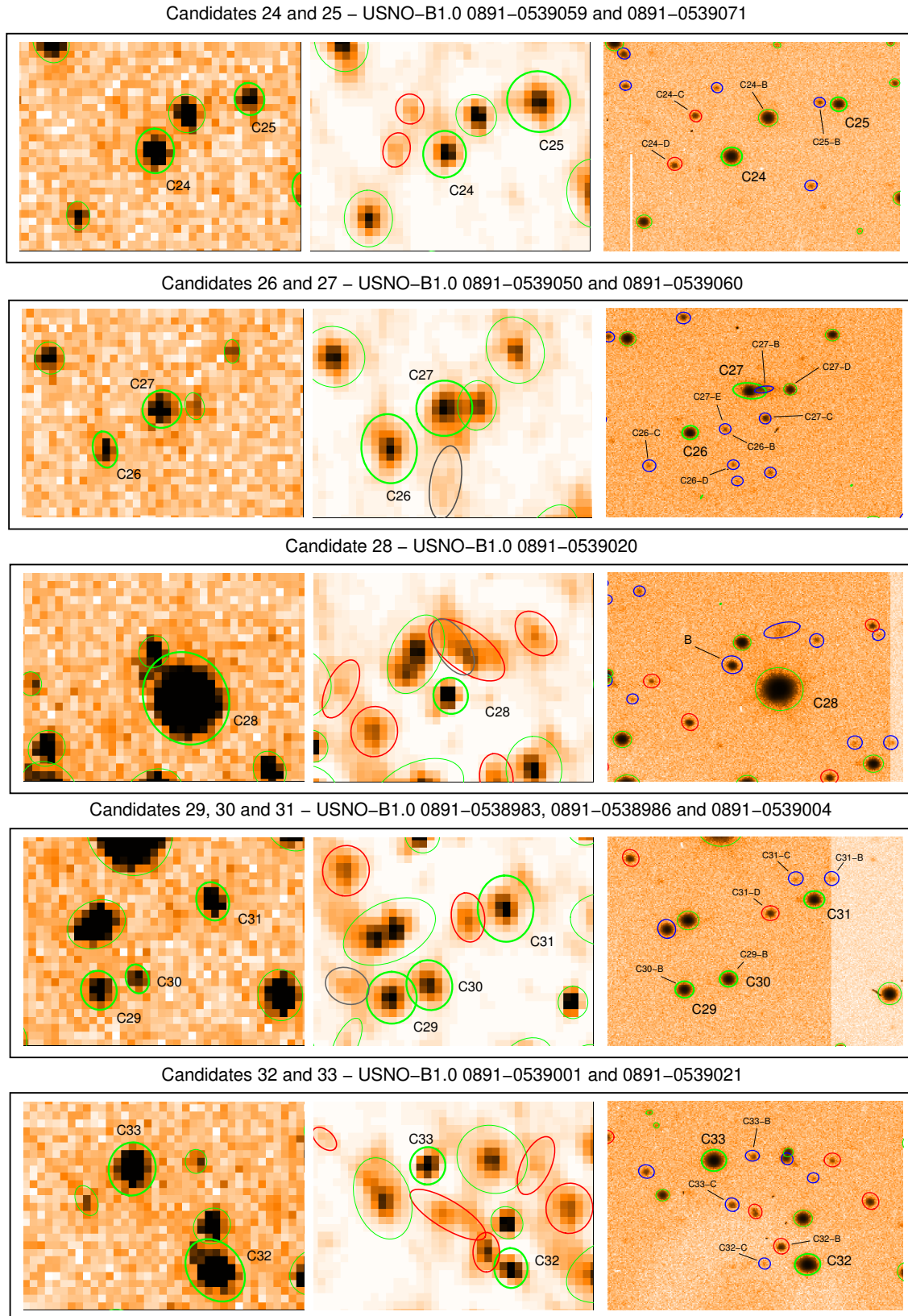
Figure 5.28: QUEST, original and deconvolved, and WIYN panels of QSO candidates included in Table 5.15. Their resolved components are labeled accordingly to the same table. Green ellipses for objects present in all three images, red for those detected both in WIYN and deconvolved QUEST, but not in original QUEST image, and blue for those only detected by WIYN.
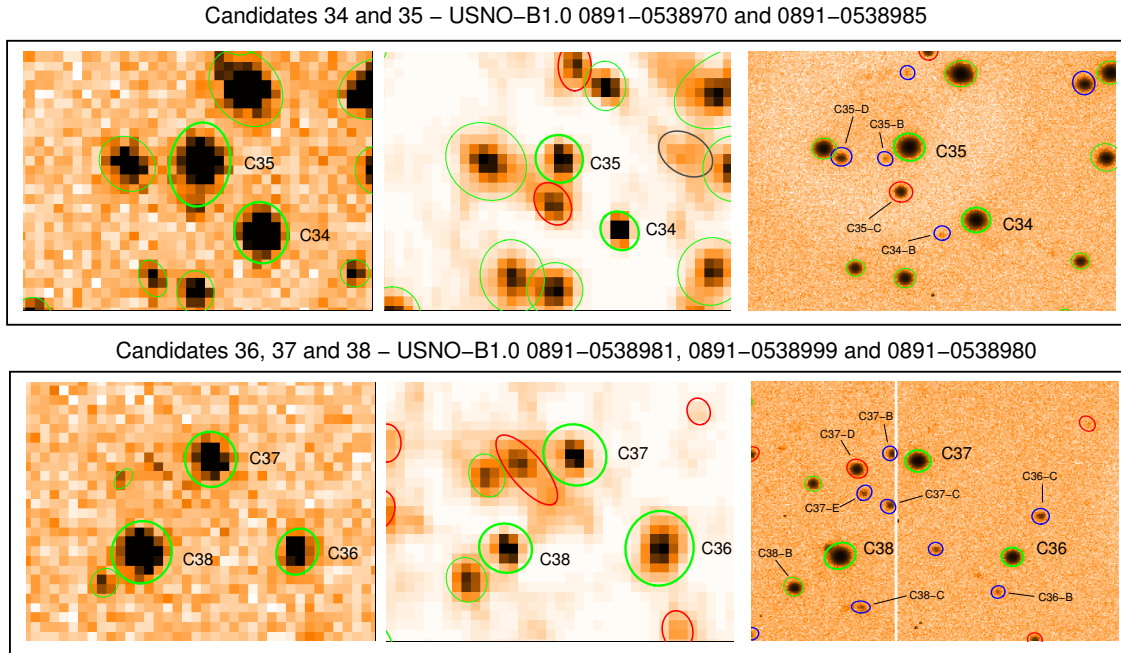
Figure 5.29: QUEST, original and deconvolved, and WIYN panels of QSO candidates included in Table 5.15. Their resolved components are labeled accordingly to the same table. Green ellipses for objects present in all three images, red for those detected both in WIYN and deconvolved QUEST, but not in original QUEST image, and blue for those only detected by WIYN.

green circles indicate those resolved in all three images (original and deconvolved QUEST and WIYN), red those resolved in deconvolved QUEST images and WIYN, and blue those only resolved by WIYN.

In Fig. 5.30, the three categories (colors) of resolving status are disposed in differentiated regions of the (ρ, m_2) space.

As expected, blue circles populate the faint and high resolution ends of the plot. The component C28-B ($m_2 = 14.08$, $\rho = 6\rlap{.}''5$) and the component C35-D ($m_2 = 14.43$, $\rho = 6\rlap{.}''6$), constitute the exception to this rule. Despite of being brighter than other resolved components at less favourable separations (C35-C, for example), they could not be resolved in deconvolved image because of their proximity to other stars in the field (see Figs. 5.28 and 5.29).

The bright and low resolution end is populated, first by red and finally by green circles. The component C32-B, point ($m_2 = 14.86$, $\rho = 3\rlap{.}''9$), corresponds to the closest companion resolved in deconvolved QUEST images, while the component
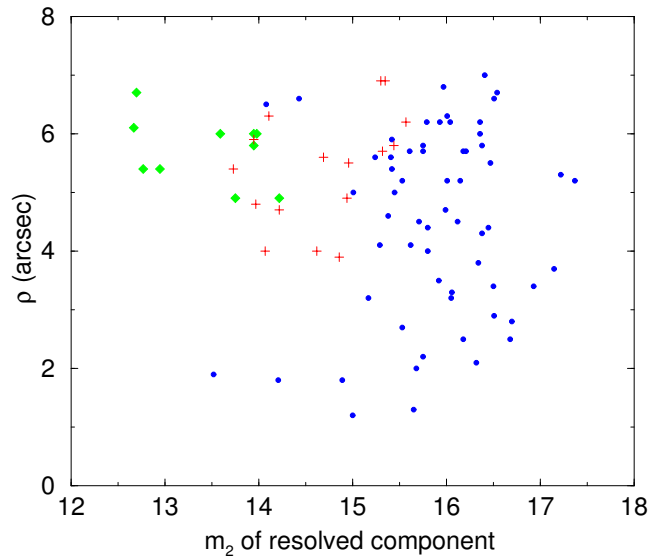
Figure 5.30: The separation of the resolved components in Fields 14 and 13 is plotted as a function of their instrumental magnitude measured in WIYN. Green diamonds indicate objects present in all three images, red pluses those detected both in WIYN and deconvolved QUEST, but not in original QUEST image, and blue circles for those only detected by WIYN.
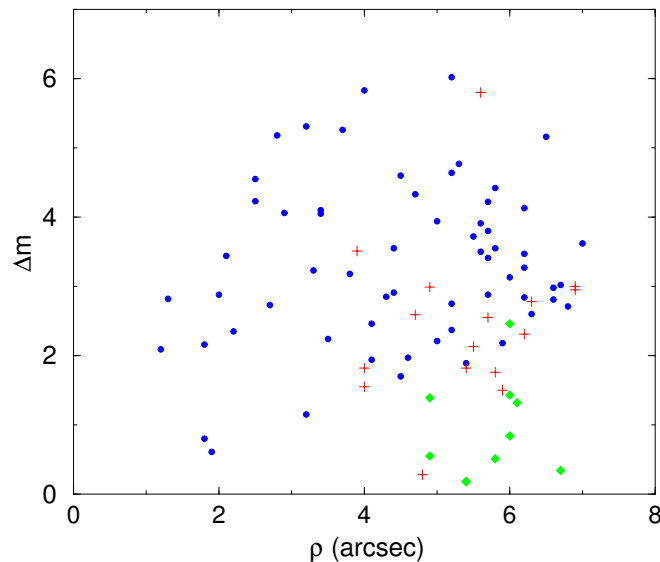
Figure 5.31: The magnitude difference of the resolved components in Fields 14 and 13 is plotted as a function of their separations. Green diamonds indicate objects present in all three images, red pluses those detected both in WIYN and deconvolved QUEST, but not in original QUEST image, and blue circles for those only detected by WIYN.

C27-D, point ($m_2 = 14.22$, $\rho = 4\rlap{.}''9$), turns to be the faintest and closest to be resolved in original QUEST images. From that we can derive that image deconvolution increases the image resolution in about $1''$. This improvement could be even larger with better knowledge of original PSF. Of course, this is only an estimate since the statistics of our candidates sample is not complete in terms of (ρ,m_2) space density.

As regard as Fig. 5.31, we note that newly resolved components by AWMLE deconvolution are distributed along a wider range of Δm. It is remarkable that C32-B, resolved at $\rho = 3\rlap{.}''9$ in the deconvolved image, is 3.51 fainter than its companion. This is a magnitude difference 1.39 mag fainter than C27-D, resolved at $\rho = 4\rlap{.}''9$ in the original image.

We put this result into the context of current state of macrolensing field by making the following remarks. As a result of the recent injection of new QSOs from photometric and spectroscopic surveys, the number of discovered lenses has been constantly increasing and some descriptors as separation distribution can already be considered statistically significant. Fig. 5.32 illustrates the histogram of angular separation between farthest components of known gravitational lenses up to now. This is a 82 object sample catalogued by Kochanek et al. (2005), which spans from widest to closest separation values. It can be seen that the bulk of lenses companions are comprised within $2''$ of separation and they are very rare beyond $4''$. It is noteworthy that the limiting resolution of deconvolved QUEST images ($3\rlap{.}''9$) is within this cutoff value of $4\rlap{.}''0$ in Fig. 5.32. This enables deconvolved QUEST data to directly resolve lenses, at least in a small percentage of the separation distribution, and establish a significant difference with respect to the original images, where the resolution limit of $4\rlap{.}''9$ vanishes the probability of direct resolving.

Of course, lenses will always need to be confirmed with high resolution imagery (WIYN, HST, etc.), but to have a QUEST limiting resolution around the same value where the lens population begins to increase could be useful for obtaining a list of resolved QSO candidates more likely to be really lensed.

Conclusions

At this point, a number of conclusions can be drawn:

- AWMLE deconvolution increases the resolution of the QUEST images by $1''$,
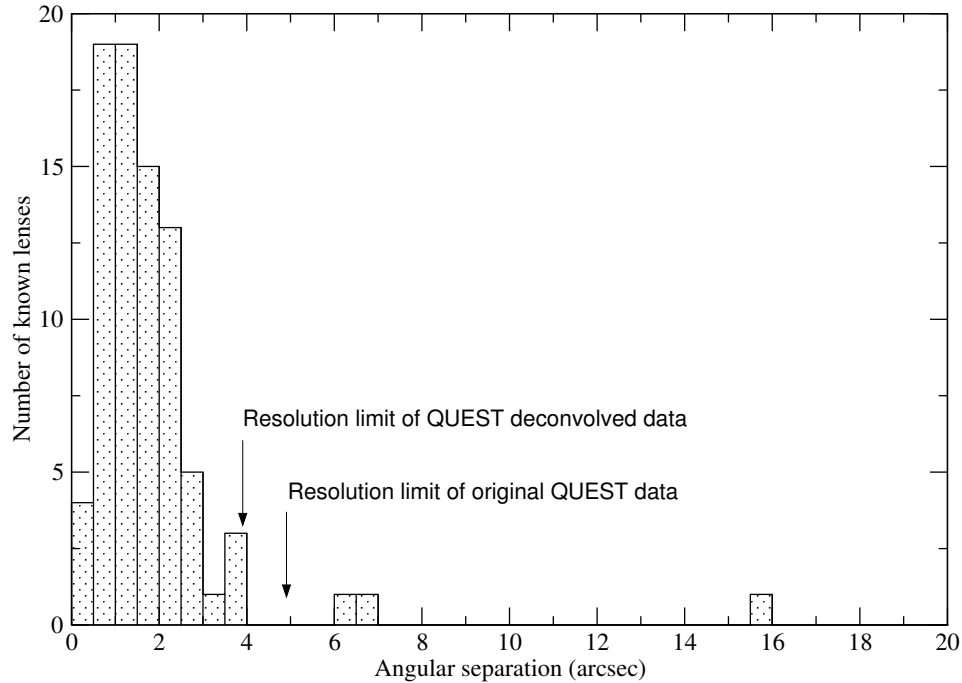
Figure 5.32: Histogram of angular separation for known gravitational lenses (Kochanek et al. 2005). Deconvolution shifts the limiting resolution of QUEST data to $3.''9$, just below the cutoff value at $4.''0$.

from $4.''9$ to $3.''9$. For the sake of comparison, this improvement ($\sim 26\%$) turns to be about twice the smearing introduced by drift scanning, as seen in Table 3.11 and explained in Pag. 94.

• The limiting resolution after deconvolution of QUEST images is $3.''9$, which is within the cutoff value of the separation distribution of the 82 gravitational lenses currently known (Kochanek et al. 2005). This enables QUEST data for potentially resolving lensed QSOs directly from deconvolved data. Of course, high resolution images continue to be necessary for confirming lens geometry.

• The limiting magnitude gain of 0.6 mag derived in Sect. 5.3.1 is parallely confirmed on average in Fig. 5.30. Actually, there are 5 red points which exceed this gain value. However, we note that m_2 is only an instrumental magnitude, which has not been calibrated to be comparable to the study made in Sect. 5.3.1 with catalogued magnitude.

Possible extensions of this work

We have shown that AWMLE deconvolution can deliver a resolution gain of $1''$ for moderately undersampled data like QUEST (FWHM$\sim 2\rlap{.}''3$).

The followed methodology for applying image deconvolution to QSO candidates resolution is totally general, and other ongoing multiband wide field surveys in the seek of new quasars could benefit from the achieved increase in resolution. For example, projects like Palomar-QUEST (Djorgovski et al. 2004a,b) (with pixel scale of $0\rlap{.}''88$) and SDSS (with median PSF FWHM of 3.2 pixels), would be suitable targets for gaining additional resolution through image deconvolution. As resolution gain strongly depends on the adequate modelling and characterization of the PSF, and this depends basically on sampling, we anticipate that the former resolution gain is expected to be better than 1 pixel for these two better sampled surveys.

SDSS Data Release 3 (6TB of images) (Abazajian et al. 2005) and its corresponding Quasar catalogue ($\sim 46,420$ entries) (Schneider et al. 2005) have been recently offered to the community. From the combination of these two products, plus follow-up high resolution observations, up to 12 lensed quasars of 260 candidates have been confirmed (Pindor 2004). This applied candidate selection algorithm is able to resolve components down to separations of $\rho = 0\rlap{.}''6$ with $\Delta m = 0$ and $\rho = 1\rlap{.}''2$ with $\Delta m \sim 3$. Taking into account the resolution gain of 1 pixel deduced from Figs. 5.30 and 5.31, components separations up to $0\rlap{.}''5$ with $\Delta m = 0$ and $0\rlap{.}''75$ with $\Delta m \sim 3.5$ could be attainable for SDSS data after AWMLE deconvolution. This gain could be even better given the finer PSF sampling of SDSS with respect to QUEST. Therefore, we emphasize the convenience of applying AWMLE deconvolution to this data set, in order to consider this improved geometry separation as an additional criteria for lensed quasar candidate selection.

As both surveys, Palomar-QUEST and SDSS, are operated under drift scanning and TDI schemes, respectively, their data throughput rate is extremely high (several Tbs/night). One could object that the application of image deconvolution to this kind of data is not feasible by computational constrains. However, note that this application does not aim to deconvolve the whole image archive. On the contrary, we recall the objective is to resolve QSOs candidates from a list previously culled by variability criteria. Therefore, the computer resources can be focused to deconvolve only small patches (256x256 pixels) containing those objects. As shown in Table 2.1,

the performance of AWMLE algorithm with images of this size is of about 42 iterations per minute (a typical 300 iteration run in just 7.1 minutes) without aceleration parameter in AWMLE. Therefore, although the number of candidates is relatively large (several tens of thousands for SDSS Quasar catalogue Data Release 3), the feasibility of the deconvolution is fully assured.

Other deconvolution algorithms with the same purpose of resolution increase exist in the literature. Just to mention two examples: Eigenbrod et al. (2005a,b,c) have recently applied the 1-D version of their MCS deconvolution algorithm (Magain et al. 1998) to VLT/FORS spectra of lensed quasars for determining H_0 from the time delay method. Also, 'HiRes' software (Velusamy et al. 2004) was being applied for deconvolving SPITZER images, delivering an increase in the angular resolution by a factor of two. This major achievement, shows that image deconvolution can be even more effective in space-based data, where PSF modelling is usually more accurate than in ground-based data.

5.4.2   NESS-T

We here repeat the analysis of resolution gain for NESS-T images. The aim of this study is to estimate how the deblending capabilities of image deconvolution can help to improve NESS-T original resolution. We emphasize that, in the particular case of this data where pixel scale is so coarse ($3''9$ per pixel), whatever increase in resolution is of importance for extending the range of scientific targets, in this case NEOs.

The considered frame was NESS-T_2, which was described in Sect. 3.2.3. The election of this frame is justified because it is one of the best in Table 3.13 in terms of resolution, as can be deduced from FWHM histograms in Fig. 3.21. Therefore, the resulting derived resolution gain (which is a relative quantity) will also give us an upper estimate of the best absolute resolution attainable, at least for the night we are considering.

The PSF extraction was performed in a very similar fashion to the limiting magnitude study. See Sect. 5.1.3 for more details.

As regard as image deconvolution, we only used AWMLE given the clear incapacity of Richardson-Lucy algorithm for keeping false detections to a reasonable

level, as was shown in Sect. 5.3.1. The rest of parameters for the deconvolution runs were identical to the ones in Table 5.11.

As `SExtractor` detections, a different set of parameters was used. In particular, the minimum area for a positive detection was set to 3 pixels. In addition, the convolution kernels widths used for enhancing the detection maps were set to the actual values of FWHM for both original and deconvolved images. Finally, the same process for matching and validating these detections with USNO-A2.0 catalogue described in Pag. 153 was followed.

Both the qualitative and quantitative approaches in Sect. 4.5.1 and 4.5.2 for assessing the resolution gain were considered in this section. This constrasts to the only usage of the qualitative method in Sect.5.4.1, where the individual resolving status for a set of 44 selected QSO candidates was calculated.

Below we present the results from the application of this algorithm.

Qualitative assessment of resolution gain

We first apply the methodology anticipated in Sect. 4.5.1 to the object pairs with minimum separation in original and deconvolved images. For the latter, the two combinations of PSF and number of iterations which offered closest resolved objects were Moffat15 and Lorentz PSFs with 140 and 120 iterations, respectively. These three objects, D0, D1 and D2 are illustrated in Fig. 5.33. For each panel, the original image in the left and its corresponding deconvolved version in the right are shown. Their separation values are stored in Table 5.16. In addition, the corresponding USNO-B1.0 object for each component is included with its catalogued magnitude. Below we separately discuss these three closest resolved objects:

- D0 is the closest pair resolved in the original image. Of course, this object is also deblended in all the deconvolved images (not only in the two we are considering). Moffat15 140-iteration deconvolution is displayed in the right side of top panel.

- D1 is the closest pair resolved in Moffat15 140-iteration deconvolved image, and, actually, in all the deconvolutions along the considered iterations range (10–600) and PSFs. However, because of its faint magnitude it is not detected
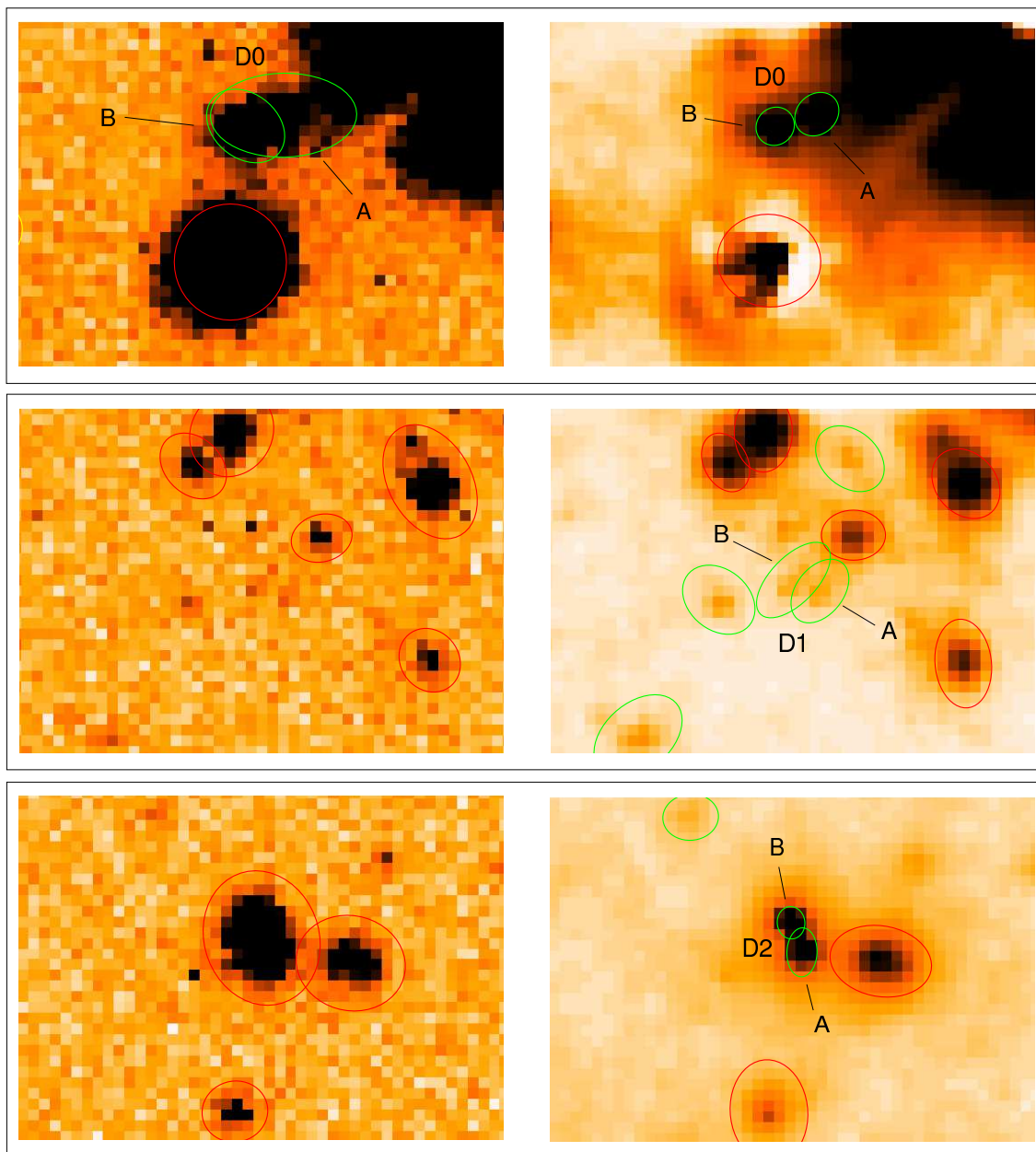
Figure 5.33: D0, D1 and D2 are the three closest objects resolved in NESS-T original, 140-iteration Moffat15 and 120-iteration Lorentz deconvolved images, respectively. Their components separations are 3.69 pixels $(14\rlap{.}''4)$, 2.68 pixels $(10\rlap{.}''4)$ and 2.95 pixels $(11\rlap{.}''5)$, leading to resolution gains of $(4\rlap{.}''0)$ in Moffatt15 case and $(2\rlap{.}''9)$ in the Lorentz case. Left side panels are NESS-T original images: object detection circled in red. Both D1 and D2 are unresolved. Right side panels are AWMLE deconvolved images: 140-iteration Moffat15 for D0 and D1 and 120-iteration Lorentz for D2. The objects already detected on the left are circled in red, and those newly detected are in green. It is noteworthy the different SNR domain in which D1 and D2 are resolved. On one hand, D1 is an example of a couple recovery with very faint components. On the other hand, D2 represents the opposite situation of two bright components of similar magnitude. Note that D1-A, although being detected as single source in deconvolved image, it is really composed by the blending of three USNO-B1.0 faint sources (see Table 5.16).

Table 5.16: Three closest detections in original, 140-iteration Moffat15 and 120-iteration Lorentz deconvolved images. Angular separation is between components A and B in Fig. 5.33. The two columns on the right are USNO-B1.0 stars approximately coincidents with D0, D1 and D2 components. Note the special case of the D1-A detection, which includes three very close catalogue entries.

NESS-T resolved detections			USNO-B1.0 objects	
Id	Component Id	$\rho('')$	Id	R1 mag
D0	A	14.''4	1293-0285550	14.29
	B		1293-0285558	14.40
D1	A	10.''4	1296-0294046	19.19
	A		1296-0294054	17.96
	A		1296-0294058	19.06
	B		1296-0294064	19.08
D2	A	11.''5	1292-0282993	14.56
	B		1292-0282995	14.22

in the original image. With respect to D0, D1 represents a resolution gain of 1.01 pixels (4.''0).

As was pointed out in Sect. 5.4.1, both the increase in limiting magnitude and the resolution gain contribute to newly detected close components. D1 contitutes a paradigmatic example of this synergy: without the SNR increase, it would have not been detected and, consequently, resolved.

Although D1 is resolved as to be double in NESS-T deconvolved image, note that D1-A component is really composed by three USNO stars: USNO-B1.0 1296-0294046, USNO-B1.0 1296-0294054 and USNO-B1.0 1296-0294058. As seen in Table 5.16, the main part of the flux is supplied by USNO-B1.0 1296-0294054, which is more than a magnitude brigther than the other two companions. Despite USNO-B1.0 1296-0294046 and USNO-B1.0 1296-0294058 being as faint as D1-B component, they could not be resolved because their even closer separations.

- D2 is the closest pair resolved in Lorentz 120-iteration deconvolution. With respect to D0, D2 represents a resolution gain of 0.74 pixels (2.''9). Note in lower left panel of Fig. 5.33 that D2, in contrast to D1, is actually detected in the original image, although as a single object. Only in the deconvolved image

the resolution is high enough to deblend the two components, A and B.

With respect to D1, D2 represents the opposite situation as magnitude of their components. Both are bright objects well above the limiting magnitude of NESS-T original image. Therefore, in this case the resolving of D2 can be exclusively attibuted to the deblending capabilities of AWMLE deconvolution.

Note that the aim of this subsection was to provide a first estimate of the resolution gain introduced by AWMLE deconvolution. A more complete and quantitative study in the style of Sect. 4.5.1 is detailed below.

Quantitative assessment of resolution gain

A direct indicator of the resolution gain between original and deconvolved images is to compare the corresponding histograms of separations for closest resolved objects. These can be seen in Fig. 5.34, for 140-iteration Moffat15 and 120-iteration Lorentz PSF based deconvolutions, respectively. For the sake of comparison, the histogram from original image was superposed in both cases.

Due to the increase in SNR introduced by AWMLE deconvolution described in Sect. 5.3.1, the histograms of deconvolved images show larger number of events. Note that most part of these new objects are incorporated in short end of the histogram ($\rho < 10$ pixels).

We define the limiting resolution of a given image ρ_{lim} as the shortest separation detected in it. This minimum separation corresponds to D0, D1 and D2 objects displayed in Fig. 5.33 and discussed in previous subsection. ρ_{lim} has been computed and labeled for every histogram in Fig. 5.34. ρ_{lim} was found to be 3.69 pixels (14$''$4), 2.68 pixels (10$''$4) and 2.95 pixels (11$''$5) in the original, AWMLE 140-iteration Moffat15 and AWMLE 120-iteration Lorentz deconvolved images, respectively. This translates into a resolution gain of (3$''$9) in Moffatt15 case, and (2$''$9) in the Lorentz case. It is noteworthy that, at least for the former, the gain is well larger than the seeing that night.

Four comments are worth emphasizing from Fig. 5.33:

1. the two considered deconvolution runs were the ones showing the maximum

resolution gain over all the rest of performed deconvolutions (from 10 to 200 iterations).

2. the resolution gains from these images differ slightly, only a $\sim 9\%$.

3. the derived resolution gains were accomplished at the same number of iterations which a maximum of limiting magnitude gain was found in Sect. 5.3.2 (140-it. and 120-it.).

4. at least for the 140-it. Moffat15 deconvolution, the resolution gain in terms of pixel units is nearly identical to the one obtained with QUEST data in Sect. 5.4.1. This fact indicates that, at the level of the constrains (sampling and limited PSF modeling) appearing in NESS-T and QUEST data, AWMLE deconvolution achieves similar resolution performance in a similar number of iterations. In other words, for two independent data sets (QUEST and NESS-T), AWMLE appears to inject the same bulk of resolution after an intermediate range of iterations (200–400) is run.

Next we consider the relation between the object separation of all the resolved components as a function of their magnitude difference (ΔR), as illustrated in Fig. 5.35. In general, the objects distribution is more concentrated around $\Delta R \sim 0$. In detail, they are *cone-like* distributed with its vertex in abscisa ρ_{lim}. This is due to the fact that the fainter is a component with respect to its companion, the harder is to deblend them as we approach one to each other. `SExtractor` tries to overcome this by using a deblending method based on multi-thresholding scheme, which is tuned by `DEBLEND_MINCON` and `DETECT_MINAREA` parameters. However, its performance is limited, and normally excludes to separate objects with a difference in magnitude greater than ~ 8 mag (Bertin & Arnouts 1996).

From the inspection of Fig. 5.35, two differences can be appreciated between the distribution of objects from original and deconvolved images. On one hand, the vertex of the distribution is shifted towards closer separations in the case of deconvolved image. This is equivalent to the limiting resolution gain (ρ_{lim}) derived above. On the other hand, the opening angle of the *cone-like* distribution is larger for deconvolved image. As a result, fainter companions can be resolved at separations which remained inaccessible in the original image.

Note also that the larger separation end lacks objects from deconvolved image (red pluses). This is a natural consequence of the fact that those objects with far
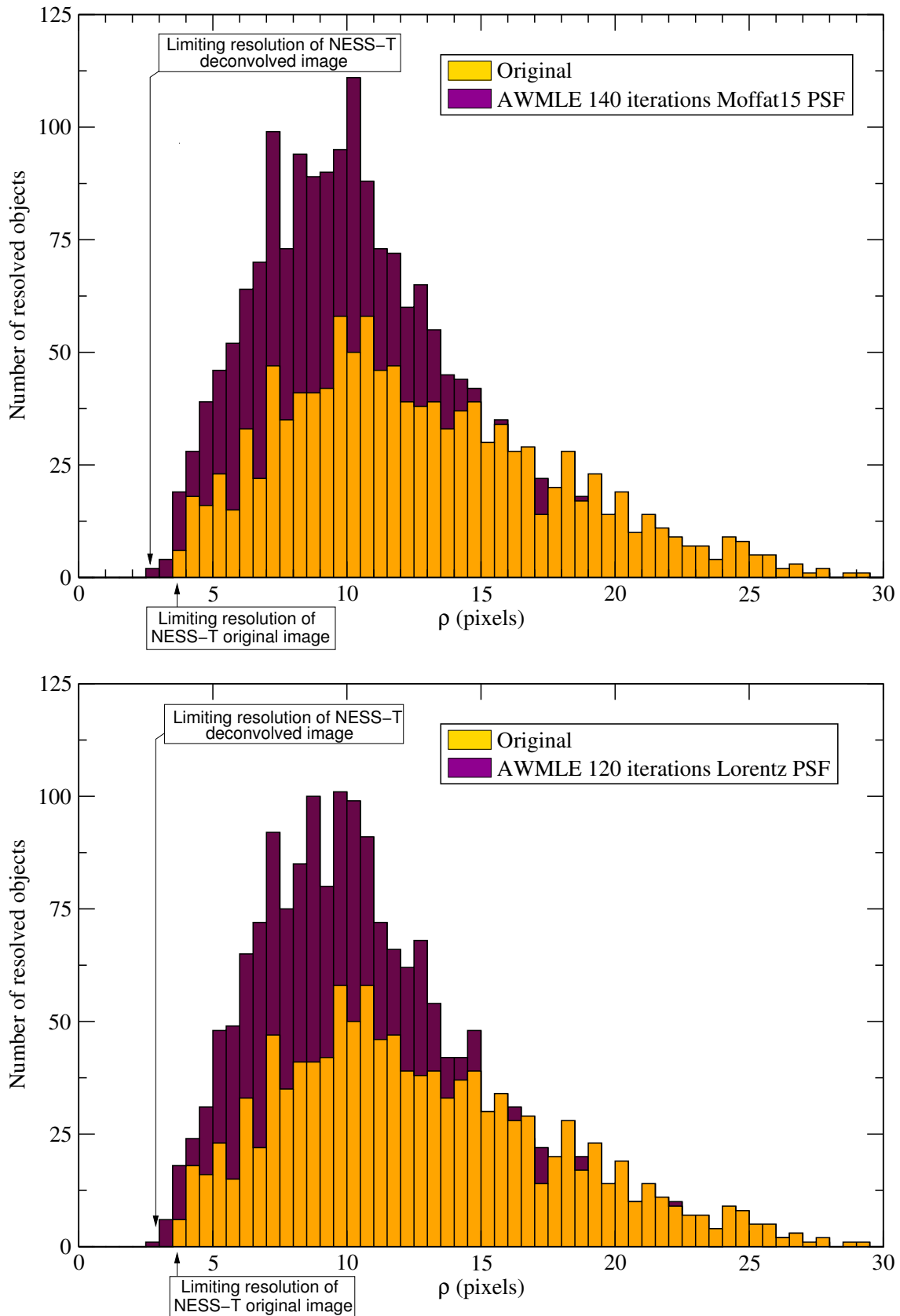
Figure 5.34: Histogram of separation of closest resolved objects up to $30''$. Limiting resolution is 3.69 pixels ($14''4$), 2.68 pixels ($10''4$) and 2.95 pixels ($11''5$) for the original, AWMLE 140-iteration Moffat15 (top) and AWMLE 120-iteration Lorentz (bottom) deconvolved images, respectively.
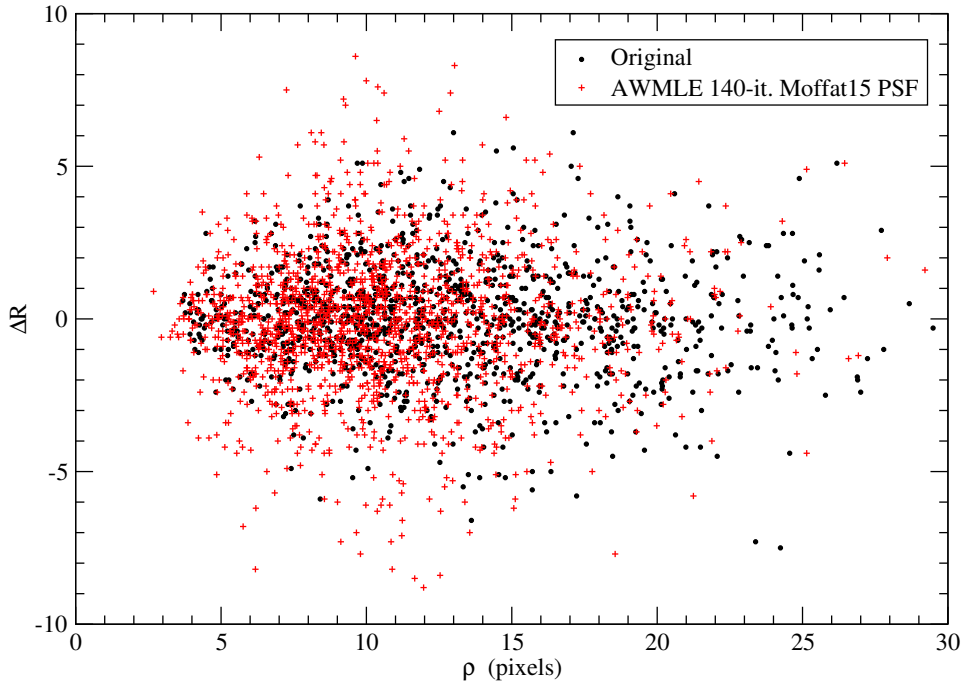
Figure 5.35: Magnitude difference of closest resolved objects versus their separation, for original (circles in black) and AWMLE 140-iteration Moffat15 deconvolved (pluses in red) images, respectively.

companions in the original image have been repaired to new closer companions after AWMLE deconvolution. As a result, the plot of red pluses is more compressed towards lower separations.

The equivalent of Fig. 5.35 for 120-iteration Lorentz PSF deconvolution was not included because the results are totally equivalent.

Conclusions

A qualitative and quantitative study of the resolution gain introduced by AWMLE deconvolution in NESS-T images was carried out. A number of conclusions can be drawn:

1. AWMLE deconvolution increases the resolution of the NESS-T data by 3″9. For the sake of comparison, this improvement is well larger than the seeing for that night ($\lesssim 3''$) and about 14 times the smearing introduced by pixel response function, as seen in Table 3.14 and explained in Pag. 102.

2. In terms of pixel units, this resolution gain corresponds to ~ 1.0 pixels. This is nearly the same gain obtained for QUEST data in Sect. 5.4.1. This is remarkable, and it addresses an interesting point: although the pixel scales of both data sets differ significantly ($1''$ to $3''.9$), their sampling (FWHM) is nearly identical. Consequently, we can conclude that the resolution gain mainly depends on sampling, and is only sightly modulated by other constrains (drift scanning systematics, correct flatfield calibration and limited PSF modeling).

3. The derived resolution gain shows slight dependence over the PSF chosen in the deconvolution process. At maximum, differences between Moffat15 and Lorentz PSFs of only $\sim 9\%$ are observed.

4. The maximum resolution gain is accomplished around 140 and 120 iterations, for Moffat15 and Lorentz PSF based deconvolutions, respectively. These are the same iteration numbers where limiting magnitude gain was also maximized in Sect. 5.3.2. This coincidence is indicating that optimal convergences for magnitude and resolution studies are simultaneously reached.

5. As deduced from Fig. 5.35, deconvolution enables the detection of companions comprised at a range of separation and magnitude difference which was totally forbbiden in the original image.

Possible extensions of this work

We have shown how AWMLE deconvolution can improve significantly the resolution of a wide field facility with coarse pixel scale as NESS-T.

Of course, as pointed out in Sect. 5.3.2, AWMLE deconvolution could be inserted in the reduction pipeline of NESS-T data. Once the flatfield calibration and computation time constrains are solved, this is an option to be seriously considered for increasing the detection efficiency of NEOs survey.

Apart from NESS-T, there are a number of similar observational projects which could benefit of this resolution gain. Just as an example, we briefly justify the potential of applying deconvolution for resolving binary asteroids:

Up to the present, the discovery of binary asteroids, specially NEOs, has been conducted by time-resolved photometric observations (lightcurves) (Pravec et al.

2004, 2005). A period analysis by Fourier series (Harris et al. 1989; Pravec et al. 2000) can provide indirect evidence of binarity (Pravec et al. 2002), which is posteriorly confirmed by space based imaging (HST) or radar observations (Busch et al. 2005). Apart from being indirect, the detection by lightcurves is time consuming. As a result, this turns to be a relatively low efficiency technique, and the binarity of only a very small percentage of known asteroids has been studied.

Only recent advances in adaptive optics (AO) imagers as VLT/NACO have enabled the direct detection of binary asteroids. For example, the case of the triple main-belt asteroid 87 Sylvia (Marchis et al. 2005) led to components separation up to $0.''17$ and $0.''84$, with $\Delta m < 3.8$ and $\Delta m < 4.2$. Of course these AO systems are very competitive facilities and cannot be dedicated to intensive search of binary asteroids.

However, the application of AWMLE deconvolution to medium resolution all-sky surveys could be decisive in the aim of directly resolving binary asteroids. For example, projects like SDSS (already active), PAN-STARR[13] and LSST[14] (Claver et al. 2004) have well sampled FWHMs in the $0.''8$–$0.''5$ range. In these conditions, better than those exhibited by QUEST and NESS-T, AWMLE deconvolution is expected to accomplish even better resolution gain (1–1.5 pixel). In that case, asteroid components separated within $0.''4$–$0.''25$ could be resolvable, and this would open the possibility of massively detecting binary asteroids. As the existence of most of the imaged asteroids would be a priori known, the inclusion of AWMLE in a pipeline reduction process would not involve special computational requirements, since the deconvolution would be run only over a small patch of a few pixels (256x256).

5.5   Astrometric assessment

In this section the incidence of image deconvolution over astrometry of the original image is evaluated. The methodology presented in Sect. 4.7 was applied to FASST data, described in Sect. 3.2.1. This choice is justified because this is the only data set from a telescope specifically dedicated to precise astrometric measurements, which

---

[13]Panoramic Survey Telescope and Rapid Response System, is being developed by the University of Hawaii's Institute for Astronomy. First prototype operational by early 2006.

[14]Large Synoptic Survey Telescope, is being developed by LSST Corporation, Tucson (AZ). First light scheduled by 2008.

has fully calibrated its systematic errors (see Tables 3.6 and 3.7).

5.5.1   FASTT

40-iteration Richardson-Lucy image deconvolution was applied to the 11 FASTT frames included in Table 3.5 by making use of the PSFs derived in Sect. 5.1. This algorithm was chosen in favour of AWMLE because a complete implementation of the latter was not available at the time this study was conducted.

Object detection process as described in Sect. 4.3 was performed over these 11 original and deconvolved frames.

Next, these detected sources were centered by means of Levenberg-Marquardt Method-based `FITSTAR` program, described in Sect. 4.6.2. Centering tests with 2D Gaussian, Moffat15, Moffat25 and Lorentz models were conducted in both original and deconvolved images. 2D Gaussian offered best performance in terms of robustness: very few stars ($\sim 1\%$) could not be fitted due to `FITSTAR` non-convergence. Moffat15, Moffat25 and Lorentz profiles had a little more convergence incidences (3%, 5% and 7% respectively).

Finally, the astrometric assessment methodology in Sect. 4.7 was applied to those centered stars. This resulted in 11 lists of 597 stars for both original and deconvolved sets of frames. The resulting maps of astrometric residuals are shown in Fig. 5.36. The following considerations around this figure can be made:

1. the map for original images (left) is elongated.

   We are unsure about the complete explanation of this effect, but it is noteworthy that the axis ratio and orientation of the map resembles the asymmetry caused by a charge transfer efficiency problem. Note that PSF elongation was computed to be 1 : 1.4 with an average orientation of 160° (see Sect. 5.1.1), which is very approximately the observed shape in the residual map on the left.

2. the former elongation has been greatly removed in the residuals map of deconvolved images (right). This is an important point because deconvolution is able to remove the elongated signature from all the sources in the original

images, and distribute their positions in such a way that the map of residuals is isotropic.

3. the dispersion of both maps of residuals was computed yielding to:

$\sigma_x^{\mathrm{orig}}, \sigma_y^{\mathrm{orig}}$=(0.057,0.041) pixels,
$\sigma_x^{\mathrm{deconv}}, \sigma_y^{\mathrm{deconv}}$=(0.059,0.046) pixels.

This non-significant increase for the latter might seem contradictory attending the apparently larger expansion in Fig. 5.36 for deconvolved map. However, we note that the initial asymmetry may bias the visual interpretation towards smaller *apparent* dispersion values.

This practically null incidence of deconvolution over astrometric centering error is in agreement to the results yielded by Prades & Núñez (1997) with the same deconvolution algorithm applied to CCD simulated data. Actually, authors in that paper showed that astrometric error after deconvolution was slightly smaller than the original. The fact that this is not reproduced in our case of real FASTT data can be safely attributed to the limited modeling of the PSF which in this case is highly elongated by the CTE problem.

Note this test over the astrometric precision has been conducted with FASTT data, which is oversampled. The same study with critically sampled data (as QUEST or NESS-T) could not be completed. At least, the high robustness shown by FITSTAR for synthetic 2D Gaussian profiles guarantees the application of our methodology to images with moderate stage of undersampling.

Finally, in Fig. 5.36 the fractional pixel coordinate for deconvolved images are plotted as a function of its corresponding pixel coordinate. The idea behind is to evaluate if deconvolution could introduce a positional bias towards the center of the pixel. This effect was first noticed by Girard (1995) when deconvolving HST WF/PC 1 data with a very similar deconvolution algorithm to the one employed here (Núñez & Llacer 1990). As seen in Fig. 5.36, none part of the pixel is privileged and the pixel phase is randomly distributed. In this way, we confirm the results Prades & Núñez (1997) where also no bias was observed for the deconvolution of CCD simulated deconvolved data. Consequently, we speculate that the bias proved with WF/PC 1 data was likely due to an incomplete characterization of the PSF or other instrumental issues, but not because of the deconvolution algorithm itself.
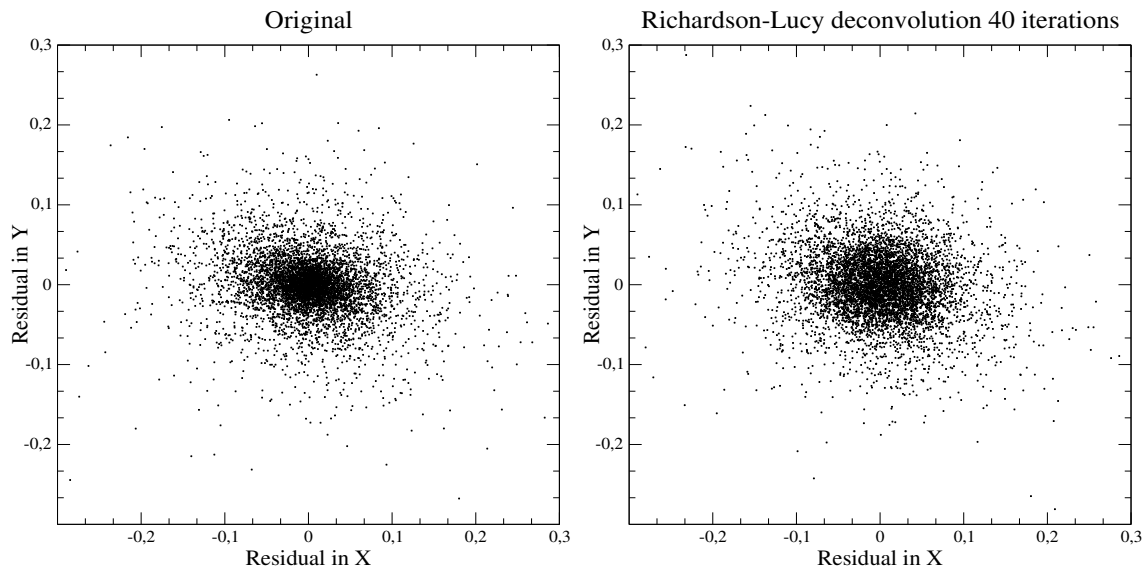
Figure 5.36: Maps of astrometric residuals for 597 stars centered in each of the 11 FASTT frames. Left: original images. Right: 40-iteration Richardson-Lucy deconvolved images. Therefore each residual map contains 11×597 points.
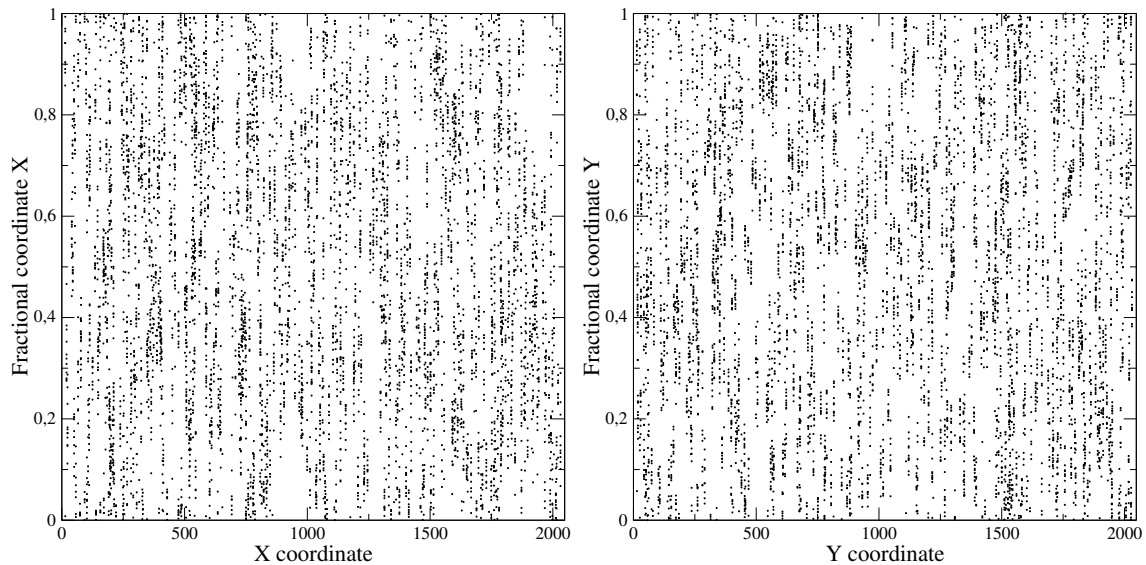
Figure 5.37: Fractional pixel coordinate X (left) and Y (right) as a function of pixel coordinate X (left) and Y (right).

Chapter 6

Conclusions

In this Part. I, an exhaustive study of the benefits that image deconvolution can introduce to CCD wide field surveys has been carried out. The following conclusions can be drawn:

1. Three sets of survey-type data have been considered. FASTT and QUEST had been acquired by means of drift scanning mode. NESS-T had been taken by stare mode. Because of different reasons, all three sets suffered from limiting magnitude and limiting resolution losses. Therefore, we conclude that the application of image deconvolution is specially indicated.

2. A wavelet-based adaptive image deconvolution algorithm (AWMLE) has been applied to two of the data sets: QUEST and NESS-T.

   Richardson-Lucy (RL) image deconvolution algorithm has been applied to FASTT data set.

3. A complete methodology for applying deconvolution to generic CCD survey-type images has been proposed for the first time. This includes all the required steps, namely: calibration and characterization of original data, object detection, evaluation of limiting magnitude and limiting resolution performance, source centering and assessment of astrometric incidence.

   This proposed procedure has given homogeneity to the obtained results and we anticipate that could be of importance for survey programs which attempt to insert deconvolution in their pipeline reduction facilities.

4. PSF characterization for the three data sets has been carried out. In QUEST and NESS-T, Moffat and Lorentzian profiles offered better fits than Gaussian in agreement to the ground-based undersampled nature of the data. Only in FASTT case, where data is oversampled, Moffat and Gaussian showed similar goodness of fit.

5. The performance of AWMLE has been evaluated in terms of the gain in limiting magnitude. Values of $\Delta R_{\mathrm{lim}} \sim 0.64$ for QUEST and $\Delta R_{\mathrm{lim}} \sim 0.46$ for NESS-T were found for 2σ thresholded detections in both original and deconvolved images. That discrepancy was justified by the incomplete generic calibration of NESS-T data. Note this magnitude gain is equivalent to an increase of 81% in the number of objects which can be measured and were not available in the original image. Therefore, we conclude that deconvolution is a very useful technique for increasing telescope efficiency.

   The asymptotic convergence of AWMLE has resulted in an outstanding detection reliability. First, only $\sim 5\%$ of new detections are false and practically all of them can be attributed to the limited characterization of the PSF. In contrast, RL algorithm performs a much intolerable 37% of false detections. Second, the number true detections remains very stable above a certain number of iterations (around 150–200). Third, the AWMLE solution image turns to be insensitive to detection threshold value. In conclusion, the outcome of AWMLE deconvolution in terms of new detected objects is not subject to the number of iterations chosen.

   Finally, the feasibility of this magnitude gain has been evaluated in the context of projects which are used for QSOs lensing search (QUEST) or new NEOs discovery (NESS-T). As a by product of our study, the possible detection of a transient event in QUEST data set has been discussed: the scenario of a Halo X-ray Nova has been proposed.

   In conclusion, AWMLE turns to be a powerful technique for increasing the number of useful science objects from the faint part of magnitude distribution. Note that magnitude gain fulfills by far the magnitude loss due to drift scanning ($\Delta R_{\mathrm{lim}} \sim 0.1$) and it is equivalent to increasing in 80% the telescope collecting area (or a 32% its diameter), which would translate into multiplying its cost by 2.3. Therefore, this gain could be of interest for many projects which we have discussed.

6. The performance of AWMLE has been assessed in terms of the gain in lim-

iting resolution. Identical values of $\Delta\phi_{\lim} \sim 1$ pixel are obtained for QUEST and NESS-T data, corresponding to $\Delta\phi_{\lim}^{\text{QUEST}} \sim 1\rlap{.}''0$ and $\Delta\phi_{\lim}^{\text{NESS}-\text{T}} \sim 3\rlap{.}''9$, respectively.

Those resolution gains has been found to depend only on this parameter, and only slightly modulated by other factors as drift scanning systematics or limited knowledge of PSF modeling.

Finally, the feasibility of that resolution gain has been evaluated in the context of images which are used for QSOs lensing search (QUEST) or new NEOs discovery (NESS-T). For example, after AWMLE deconvolution $\phi_{\lim}^{\text{QUEST}} \sim 3\rlap{.}''9$, which is for the first time below the cutoff value of the separation distribution of the 82 gravitational lenses currently known.

In conclusion, AWMLE has showed its powerful deblending capabilities, which could be of interest for many projects which have been discussed.

7. RL deconvolution algorithm has been applied to FASTT images in order to evaluate its possible incidence over astrometric accuracy.

A centering algorithm based on Levenberg-Marquardt Method specially indicated for undersampled data was employed for this astrometric evaluation. This method has been found to be more robust than conventional techniques based on steepest-descent and Taylor series methods. In particular, stellar profiles of FWHM up to 0.8 pixels were successfully centered. Therefore, we conclude this is a technique well suited for centering deconvolved images, where undersampling is common.

FASTT original images has showed an astrometric bias caused by a defect of charge transfer efficiency in the CCD chip. This systematic error has appeared in the map of residuals and has been effectively removed by deconvolution.

The comparison of map of residuals for original and deconvolved images has led us to conclude that deconvolution has not significantly modified the centering error with respect to the one for original FASTT images.

No positional bias towards the centre of pixel has been observed for deconvolved positions, to the contrary of was shown in former studies of deconvolution applied to HST WF/PC 1 images. Therefore, we conclude that deconvolution algorithm was not the cause of such distorsion in that case.

The two former statements allow us to conclude that deconvolution studies in the context of astrometric programs could be revisited.

Bibliography

Abad C., Vicente B., Dec. 2000, Astrometric quality of the QUEST camera for drift-scan observations

Abazajian K., Adelman-McCarthy J.K., Agüeros M.A., et al., Mar. 2005, AJ, 129, 1755

Andrews P., Nov. 2000, private communication

Auer L.H., van Altena W.F., May 1978, AJ, 83, 531

Baltay C., Snyder J.A., Andrews P., Nov. 2000, private communication

Baltay C., Snyder J.A., Andrews P., et al., Jul. 2002, PASP, 114, 780

Becker A.C., Wittman D.M., Boeshaar P.C., et al., Aug. 2004, ApJ, 611, 418

Belizón F., Muiños J.L., Vallejo M., et al., Nov. 2003, In: Astronomy in Latin America, 61–68

Benedict G.F., McGraw J.T., Hess T.R., Cawson M.G.M., Keane M.J., Jan. 1991, AJ, 101, 279

Benítez N., Ford H., Bouwens R., et al., Jan. 2004, ApJSS, 150, 1

Bertin E., Arnouts S., Jun. 1996, A&ASS, 117, 393

Bloemhof E.E., Townes C.H., Vanderwyck A.H.B., 1986, In: Instrumentation in astronomy VI; Proceedings of the Meeting, Tucson, AZ, Mar. 4-8, 1986. Part 2 (A87-36376 15-35). Bellingham, WA, Society of Photo-Optical Instrumentation Engineers, 1986, p. 473-478., 473–478

Bloemhof E.E., Danchi W.C., Townes C.H., McLaren R.A., Oct. 1988, ApJ, 333, 300

Boroson T.A., Thompson I.B., Shectman S.A., Dec. 1983, AJ, 88, 1707

Briceño C., Vivas A.K., Calvet N., et al., Jan. 2001, Science, 291, 93

Buonanno R., Buscema G., Corsi C.E., Ferraro I., Iannicola G., Oct. 1983, A&A, 126, 278

Busch M.W., Benner L.A.M., Ostro S.J., et al., Aug. 2005, AAS/Division for Planetary Sciences Meeting Abstracts, 37,

Cabanac R.A., Hickson P., de Lapparent V., 2002, In: ASP Conf. Ser. 283: A New Era in Cosmology, 129–+

Caldwell J.A.R., Schechter P.L., Aug. 1996, AJ, 112, 772

Caldwell J.A.R., Keane M.J., Schechter P.L., May 1991, AJ, 101, 1763

Cao Y., Eggermont P.P.B., 1999, IEEE Trans. Image Processing, 8, 286

Castleman K.R., 1996, Digital Image Processing, Prentice Hall, Upper Saddle River, NJ 07458

Charles P.A., Coe M.J., Aug. 2003, ArXiv Astrophysics e-prints

Chen W., Shrader C.R., Livio M., Dec. 1997, ApJ, 491, 312

Claver C.F., Sweeney D.W., Tyson J.A., et al., Oct. 2004, In: Proceedings of the SPIE, Volume 5489, pp. 705-716 (2004)., 705–716

Cornwell T.J., Evans K.F., Feb. 1985, A&A, 143, 77

Davis L.E., Jan. 1994, A Reference Guide to the IRAF/DAOPHOT Package

Dempster A.D., Laird N.M., Rubin D.B., 1977, J. Royal Statistical Soc. Ser. B, 39, 1

Djorgovski S.G., Baltay C., Mahabal A., et al., Dec. 2004a, American Astronomical Society Meeting Abstracts, 205,

Djorgovski S.G., Mahabal A., Graham M., et al., May 2004b, American Astronomical Society Meeting Abstracts, 204,

Donoho D.L., Johnstone I.K., 1993, Adapting to unknown smoothness via wavelet shrinkage, Tech. rep., Stanford University

Eigenbrod A., Courbin F., Dye S., et al., Oct. 2005a, ArXiv Astrophysics e-prints

Eigenbrod A., Courbin F., Meylan G., et al., Nov. 2005b, ArXiv Astrophysics e-prints

Eigenbrod A., Courbin F., Vuissoz C., et al., Jun. 2005c, A&A, 436, 25

Evans D.W., Irwin M.J., Helmer L., Nov. 2002, A&A, 395, 347

Ferrin I., Rabinowitz D., Schaefer B., et al., Feb. 2001, ApJ Letter, 548, L243

Fors O., Merino M., Otazu X., et al., 2006, In: Revista Mexicana de Astronomía y Astrofísica Conference Series (in press)

Frieden B.R., 1978, Optical Society of America Journal A, 68, 1375

Fruchter A.S., Hook R.N., Feb. 2002, PASP, 114, 144

Gai M., Busonero D., 2004, In: Scientific Detectors for Astronomy, The Beginning of a New Era, 565–572

Gehrels T., Sep. 1981, Icarus, 47, 518

Gehrels T., McMillan R.S., 1982, In: ASSL Vol. 96: Sun and Planetary System, 279–+

Gehrels T., Marsden B.G., McMillan R.S., Scotti J.V., May 1986, AJ, 91, 1242

Gehrels T., McMillan R.S., Scotti J.V., Perry M.L., 1990, In: ASP Conf. Ser. 8: CCDs in astronomy, 51–+

Gibson B.K., Hickson P., Oct. 1992, MNRAS, 258, 543

Girard T.M., Dec. 1995, International Journal of Imaging Systems and Technology, 6, 395

Girard T.M., Li Y., van Altena W.F., et al., May 1994, Bulletin of the American Astronomical Society, 26, 860

Girard T.M., Li Y., van Altena W.F., et al., 1995, In: IAU Symp. 166: Astronomical and Astrophysical Objectives of Sub-Milliarcsecond Optical Astrometry, 101–+

González-Audícana M., Otazu X., Fors O., Seco A., Feb. 2005, International Journal of Remote Sensing, 26, 595

González-Audícana M., Otazu X., Fors O., Alvarez-Mozos J., 2006, IEEE Transactions Geoscience Remote Sensing (in press)

Gorjian V., Wright E.L., McLean I.S., Jul. 1997, PASP, 109, 821

Gunn J.E., Carr M., Rockosi C., et al., Dec. 1998, AJ, 116, 3040

Hall P., Mackay C.D., Oct. 1984, MNRAS, 210, 979

Halpern J.P., Jul. 2005, The Astronomer's Telegram, 549, 1

Harris A.W., Young J.W., Bowell E., et al., Jan. 1989, Icarus, 77, 171

Harris H.C., Vrba F.J., Feb. 1992, PASP, 104, 140

Helstrom C.W., Mar. 1967, Journal of the Optical Society of America (1917-1983), 57, 297

Hickson P., Richardson E.H., Sep. 1998, PASP, 110, 1081

Hildebrand A., Cardinal R., Mazur M., Nov. 2004, private communication

Hildebrand B.F., 1987, Introduction to numerical analysis: 2nd edition, Dover Publications, Inc., New York, NY, USA

Hög E., Bässgen G., Bastian U., et al., Jul. 1997, A&A, 323, L57

Hög E., Fabricius C., Makarov V.V., et al., Jan. 2000, VizieR Online Data Catalog, 1259, 0

Högbom J.A., Jun. 1974, A&ASS, 15, 417

Howell S.B., Koehn B., Bowell E., Hoffman M., Sep. 1996, AJ, 112, 1302

Hunt B.R., Sep. 1973, IEEE Trans. Computers, 22, 805

Irwin M.J., Jun. 1985, MNRAS, 214, 575

Janesick J.R., 2001, Scientific charge-coupled devices, Scientific charge-coupled devices, Bellingham, WA: SPIE Optical Engineering Press, 2001, xvi, 906 p. SPIE Press monograph, PM 83. ISBN 0819436984

Johnston K.J., Fey A.L., Zacharias N., et al., Aug. 1995, AJ, 110, 880

Katsaggelos A.K., 1991, Digital image restoration, Springer Series in Information Science, Berlin: Springer, 1991, edited by Katsaggelos, Aggelos K.

King I.R., Apr. 1971, PASP, 83, 199

Kochanek C., Falco E.E., Impey C., et al., 2005, CASTLES Survey - Gravitational Lens Data Base, available at
`http://cfa-www.harvard.edu/castles`

Lagendijk R.L., Biemond J., 1991, Iterative identification and restoration of images, The Kluwer International Series in Engineering and Computer Science, Boston: Kluwer, 1991

Lee J.F., van Altena W., Nov. 1983, AJ, 88, 1683

Levenberg K., 1944, Quart. Appl. Math., 2, 164

Lewis I.J., Glazebrook K., Taylor K., Jul. 1998, In: Proc. SPIE Vol. 3355, Optical Astronomical Instrumentation, Sandro D'Odorico; Ed., 828–833

Loveday J., Pier J., The SDSS Collaboration, 1998, In: Wide Field Surveys in Cosmology, 14th IAP meeting held May 26-30, 1998, Paris. Publisher: Editions Frontieres. ISBN: 2-8 6332-241-9, p. 317., 317–+

Lucy L.B., Jun. 1974, AJ, 79, 745

Lucy L.B., 1994, In: The Restoration of HST Images and Spectra - II, 79–+

Mackay C.D., 1982, In: Instrumentation in Astronomy IV: Tucson: SPIE331 p.146, 1982, 146–+

Magain P., Courbin F., Sohy S., Feb. 1998, ApJ, 494, 472

Mallat S.G., Jul. 1989, IEEE Pattern Analysis on Machine Intelligence, 7, 674

Marchis F., Descamps P., Hestroffer D., Berthier J., Aug. 2005, Nature, 436, 822

Markwardt C.B., 2001, MPFIT - Robust non-linear least squares curve fitting. IDL Curve Fitting and Function Optimization, available at
`http://cow.physics.wisc.edu/ craigm/idl/fitting.html`,

Marquardt D., 1963, SIAM J. Appl. Math., 11, 431

Mateo M., Schechter P.L., 1989, In: 1st. ESO/ST-ECF Data Analysis Workshop, Proceedings, held in Garching, F.R.G., April 17-19, 1989. Editors, P.J. Grosbol, F. Murtagh, R.H. Warmels; Publisher, European Southern Observatory, Garching bei Munchen, F.R.G., 1989. ISBN # 3-923524-32-3. LC # QB51.3. E43 E86. P. 69, 1989, 69–+

Mazur M.J., Cardinal R., Hildebrand A.R., 2005, Final Report for Baker Nunn Telescope Retrofit, Tech. Rep. CR 2005-040, Defence Research and Development Canada

McClintock J.E., Remillard R.A., Jun. 2003, ArXiv Astrophysics e-prints

McClintock J.E., Remillard R.A., 2005, Black Hole Binaries, in Compact Stellar X-ray Sources, Walter Lewin Ed.: Cambridge University Press

McCullough P.R., Stys J., Valenti J., et al., Dec. 2004, American Astronomical Society Meeting Abstracts, 205,

McGraw J.T., Angel J.R.P., Sargent T.A., 1980, In: Conference on Applications of Digital Image Processing to Astronomy, Pasadena, Calif., August 20-22, 1980, Proceedings. (A81-25962 10-35) Bellingham, Wash., Society of Photo-Optical Instrumentation Engineers, 1980, p. 20-28., 20–22

McGraw J.T., Stockman H.S., Angel J.R.P., Epps H., Williams J.T., 1982, In: Instrumentation in Astronomy IV: Tucson: SPIE331 p.137, 1982, 137–+

McGraw J.T., Cawson M.G.M., Keane M.J., Sep. 1986, BAAS, 18, 1013

Meinel E.S., Jun. 1986, Optical Society of America Journal A, 3, 787

Merino M., Dec. 2004, private communication

Merino M., Fors O., Otazu X., et al., 2006, In: ASP Conf. Ser. : Astronomical Data Analysis Software and Systems (ADASS) XV (in press)

Mighell K.J., May 1989, MNRAS, 238, 807

Mighell K.J., Aug. 2005, MNRAS, 361, 861

Mink D.J., 2002, In: ASP Conf. Ser. 281: Astronomical Data Analysis Software and Systems XI, 169–+

Moffat A.F.J., Dec. 1969, A&A, 3, 455

Molina R., Núñez J., Cortijo F.J., Mateos J., Mar. 2001, IEEE Signal Processing Magazine, 18, 11

Monet D.B.A., Canzian B., Dahn C., et al., Oct. 1998, VizieR Online Data Catalog, 1252, 0

Monet D.G., Dahn C.C., Oct. 1983, AJ, 88, 1489

Monet D.G., Levine S.E., Canzian B., et al., Feb. 2003, AJ, 125, 984

Montojo F.J., May 2004a, Boletín del Real Observatorio de la Armada, 5, 1

Montojo F.J., 2004b, Optimización de la Estrategia Observacional para el Recubrimiento Rápido del Cielo por TDI, Master's thesis, Universitat de Barcelona

More J.J., 1993, MINPACK-1, available at http://www.netlib.org,

Morrison J.E., McLean B., GSC-Catalog Construction Team I., Nov. 2001, Bulletin of the American Astronomical Society, 33, 1194

Muiños J.L., Belizón F., Vallejo M., Mallamaci C., Pérez J.A., 2003, In: Journées 2002 - systèmes de référence spatio-temporels. Astrometry from ground and from space, Bucharest, 25 - 28 September 2002, edited by N. Capitaine and M. Stavinschi, Bucharest: Astronomical Institute of the Romanian Academy, Paris: Observatoire de Paris, ISBN 2-901057-48-9, ISBN 973-558-108-6, 2003, p. 180 - 184, 180–184

Núñez J., Llacer J., Sep. 1990, A&SS, 171, 341

Núñez J., Llacer J., Oct. 1993, PASP, 105, 1192

Núñez J., Otazu X., Fors O., Prades A., 1997, Vistas in Astronomy, 41, 351

Núñez J., Otazu X., Fors O., et al., Dec. 1998, In: Proc. SPIE Vol. 3500, Image and Signal Processing for Remote Sensing IV, Sebastiano B. Serpico; Ed., 202–213

Núñez J., Otazu X., Fors O., et al., May 1999a, IEEE Transactions Geoscience Remote Sensing, 37, 1204

Núñez J., Otazu X., Fors O., et al., Mar. 1999b, Optical Society of America Journal A, 16, 467

Naito I., Sugawa C., 1984, Geodetic Refraction, F. K. Brunner Ed.: Springer, Berlin

Otazu X., 2001, Algunes aplicacions de les Wavelets al procés de dades en astronomia i teledetecció, available at `http://www.tdcat.cesca.es/`, Ph.D. thesis, Universitat de Barcelona

Otazu X., González-Audícana M., Fors O., Núñez J., May 2005, IEEE Transactions Geoscience Remote Sensing, 37, 1204

Palmer D.M., Barthelmey S.D., Cummings J.R., et al., Jul. 2005, The Astronomer's Telegram, 546, 1

Pence W.D., McGlynn T., Chai P., Heikkila C., Dec. 2002, In: Virtual Observatories. Edited by Szalay, Alexander S. Proceedings of the SPIE, Volume 4846, pp. 77-80 (2002)., 77–80

Penny A.J., Dickens R.J., Jun. 1986, MNRAS, 220, 845

Pindor B.J., Apr. 2004, A search for strongly-lensed quasars in the Sloan Digital Sky Survey, Ph.D. thesis, Princeton University

Prades A., Núñez J., 1997, In: ASSL Vol. 223: Visual Double Stars : Formation, Dynamics and Evolutionary Tracks, 15–+

Prades A., Núñez J., Fors O., Ollé A., 1997, In: Reference systems and frames in the space era : present and future astrometric programmes. Journees 1997 Systemes de Reference Spatio-Temporels., 199–201

Pravec P., Šarounová L., Rabinowitz D.L., et al., Jul. 2000, Icarus, 146, 190

Pravec P., Šarounová L., Hicks M.D., et al., Jul. 2002, Icarus, 158, 276

Pravec P., Scheirich P., Kušnirák P., et al., Nov. 2004, AAS/Division for Planetary Sciences Meeting Abstracts, 36,

Pravec P., Harris A.W., Scheirich P., et al., Jan. 2005, Icarus, 173, 108

Press W.H., 2002, Numerical Recipes in C++ : the art of scientific computing, Numerical Recipes in C++ : the art of scientific computing by William H. Press. xxviii, 1,002 p. : ill. ; 26 cm. Includes bibliographical references and index. ISBN : 0521750334

Puetter R.C., Gosnell T.R., Yahil A., Sep. 2005, ARA&A, 43, 139

Racine R., Aug. 1996, PASP, 108, 699

Rapaport M., Le Campion J.F., Soubiran C., et al., Sep. 2001, A&A, 376, 325

Rengstorf A.W., Mufson S.L., Abad C., et al., May 2004a, ApJ, 606, 741

Rengstorf A.W., Mufson S.L., Andrews P., et al., Dec. 2004b, ApJ, 617, 184

Richardson W.H., 1972, Optical Society of America Journal A, 62, 55

Richmond M.W., Droege T.F., Gombert G., et al., Mar. 2000, PASP, 112, 397

Sabbey C.N., Coppi P., Oemler A., Sep. 1998, PASP, 110, 1067

Sabbey C.N., Oemler A., Coppi P., et al., Feb. 2001, ApJ, 548, 585

Schaefer B.E., Mar. 2000, IAU Circ., 7387, 1

Schaefer B.E., May 2001, IAU Circ., 7635, 1

Schaefer B.E., Snyder J.A., Hernandez J., et al., Oct. 1999, ApJ Letter, 524, L103

Schmidt M., Schneider D.P., Gunn J.E., Jul. 1986, ApJ, 306, 411

Schneider D.P., Hall P.B., Richards G.T., et al., Aug. 2005, AJ, 130, 367

Shannon C., 1948, Bell System Technical Journal, 27, 379

Shepp L., Vardi Y., Oct. 1982, IEEE Transactions on Medical Imaging, 1, 113

Silva D.R., Boroson T.A., Thompson I.B., Jedrzejewski R.I., Jul. 1989, AJ, 98, 131

Snyder D.L., 1991, In: The Restoration of HST Images and Spectra, 56–+

Snyder D.L., Hammoud A.M., White R.L., May 1993, Optical Society of America Journal A, 10, 1014

Snyder J.A., Mar. 2001, private communication

Starck J., Murtagh F., Aug. 1994, A&A, 288, 342

Starck J.L., Murtagh F., Bijaoui A., 1998, Image processing and data analysis. The multiscale approach, Image processing and data analysis. The multiscale approach, Publisher: Cambridge, UK: Cambridge University Press, 1998, ISBN: 0521590841

Starck J.L., Pantin E., Murtagh F., Oct. 2002, PASP, 114, 1051

Stetson P.B., Mar. 1987, PASP, 99, 191

Stetson P.B., 1992, In: ASP Conf. Ser. 25: Astronomical Data Analysis Software and Systems I, 297–+

Stetson P.B., 1994, In: Calibrating Hubble Space Telescope, 89–+

Stetson P.B., Davis L.E., Crabtree D.R., 1990, In: ASP Conf. Ser. 8: CCDs in astronomy, 289–304

Stone R.C., Sep. 1984, A&A, 138, 275

Stone R.C., Apr. 1989, AJ, 97, 1227

Stone R.C., Aug. 1997a, AJ, 114, 850

Stone R.C., Dec. 1997b, AJ, 114, 2811

Stone R.C., Jun. 1997c, private communication

Stone R.C., Nov. 1998, private communication

Stone R.C., Monet D.G., Monet A.K.B., Walker R.L., Ables H.D., Apr. 1996, AJ, 111, 1721

Stone R.C., Monet D.G., Monet A.K.B., et al., Oct. 2003, AJ, 126, 2060

Tikhonov A.N., Goncharskii A.V., Stepanov V.V., Kochikov I.V., 1987, Akademia Nauk SSSR Doklady, 294, 832

Tomsick J.A., Gelino D.M., Kaaret P., Sep. 2005, ArXiv Astrophysics e-prints

Torres M.A.P., Steeghs D., Blake C., et al., Jul. 2005, The Astronomer's Telegram, 566, 1

Ulrich M., Maraschi L., Urry C.M., 1997, ARA&A, 35, 445

Urban S.E., Corbin T.E., Wycoff G.L., May 1998, AJ, 115, 2161

Véron-Cetty M.P., Véron P., Dec. 2003, A&A, 412, 399

Valdes F., 1988, In: Instrumentation for Ground-Based Optical Astronomy, Present and Future. The Ninth Santa Cruz Summer Workshop in Astronomy and Astrophysics, July 13- 24, 1987, Lick Observatory. Editor, L.B. Robinson; Publisher, Springer-Verlag, New York, NY, 1988. LC # QB856 .S26 1987. ISBN # 0-387-96730-3. P.417, 1988, 417–+

van Altena W.F., Jul. 1998, private communication

van Altena W.F., Girard T., Vicente B., Nov. 2000, private communication

Velusamy T., Beichman C.A., Backus C.R., Marsh K.A., Thompson T.J., May 2004, American Astronomical Society Meeting Abstracts, 204,

Veron-Cetty M.P., Veron P., Oct. 1995, VizieR Online Data Catalog, 7188, 0

Viateau B., Réquième Y., Le Campion J.F., et al., Jan. 1999, A&ASS, 134, 173

Vicente B., Vieira K., Cova J., et al., May 2001, IAU Circ., 7624, 2

Vivas A.K., Zinn R., Andrews P., et al., Jun. 2001, ApJ Letter, 554, L33

Vivas A.K., Zinn R., Abad C., et al., Feb. 2004, AJ, 127, 1158

Wakker B.P., Schwarz U.J., Jul. 1988, A&A, 200, 312

Walsh D., Carswell R.F., Weymann R.J., May 1979, Nature, 279, 381

Wijnands R., May 2004, ArXiv Astrophysics e-prints

Williams G.V., Sep. 2005a, mPChecker: Minor Planet Checker, available at http://scully.harvard.edu/ cgi/CheckMP

Williams G.V., Sep. 2005b, sky Coverage Plots, available at http://cfa-www.harvard.edu/iau/lists/Supernovae.html

Winick K.A., Nov. 1986, Optical Society of America Journal A, 3, 1809

Wittman D.M., Tyson J.A., Dell'Antonio I.P., et al., Dec. 2002, In: Survey and Other Telescope Technologies and Discoveries. Edited by Tyson, J. Anthony; Wolff, Sidney. Proceedings of the SPIE, Volume 4836, pp. 73-82 (2002)., 73–82

Wright J.F., Mackay C.D., 1981, In: Solid State Imagers for Astronomy: SPIE#290 1981 p.160, 1981, 160–+

Zacharias N., Dec. 1996, PASP, 108, 1135

Zacharias N., Monet D.G., Levine S.E., et al., Dec. 2004a, American Astronomical Society Meeting Abstracts, 205,

Zacharias N., Urban S.E., Zacharias M.I., et al., May 2004b, AJ, 127, 3043

Zaritsky D., Harris J., Hodge P., et al., May 1996, Bulletin of the American Astronomical Society, 28, 930

Part II

New observational techniques and analysis tools for high resolution astrometry

Chapter 7

Lunar occultations

What is presented in this chapter has been partially published in Fors et al. (2001a, 2004b); Richichi et al. (2006) and presented in numerous symposiums (Fors & Núñez 2000a,b, 2001; Fors et al. 2001b, 2006; Núñez & Fors 2001).

7.1   Phenomenon description

In this section a brief overview of the lunar occultation phenomenon will be given along the most important mathematical expressions needed in the forthcoming sections.

Fig. 7.1 graphically illustrates a lunar occultation and all the quantities involved in it. Two events for the same star are described, the disappearance S_D and the reappearance S_R, each one occurring on the dark and bright limb, respectively[1]. The lunar speed V_M is typically $\approx 0''\!.4$ s^{-1} (0.75 m ms^{-1}). The module and orientation of the speed V_P in which the source is scanned by the limb is determined by the contact angle (CA) and position angle (PA), respectively. Depending on the particular area of the limb where the occultation takes place, a local slope correction ψ (most times smaller than 10%) slightly modifies both CA and PA.

As introduced in Sect. 1.2.1, LO can be precisely described in the ondulatory

---

[1]This is a simplification. In some rare cases both S_D and S_R occur on the dark limb. Hereafter, only the disappearance event will be considered.
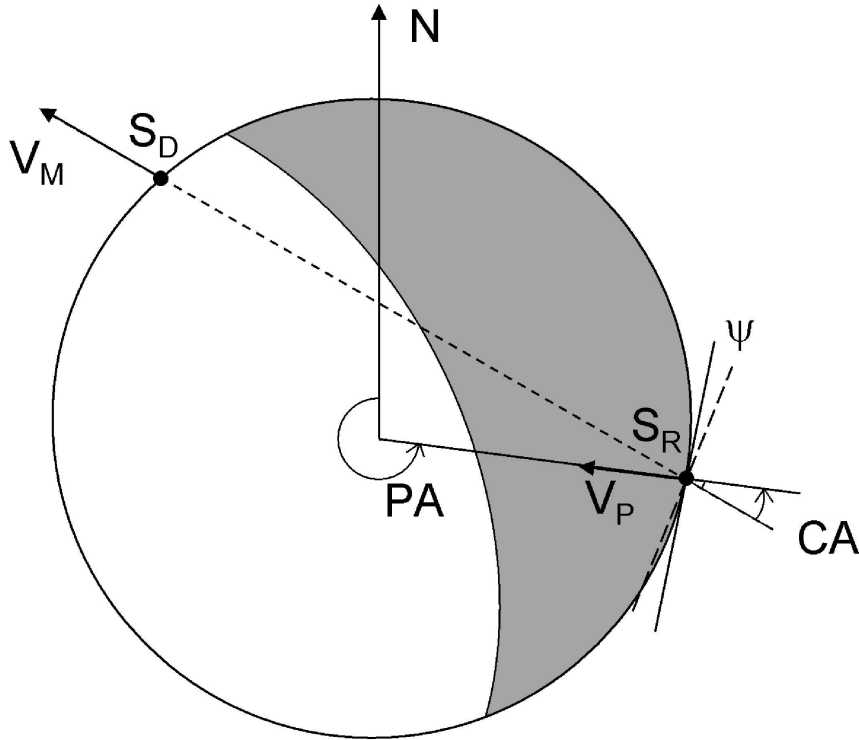
Figure 7.1: Descriptive layout of a lunar occultation. See text for explanation of the quantities.

optics framework. Only in the limit of resolved sources with diameters $\phi \sim 10 - 20$ mas the approximation of the geometric optics is valid. In the following lines, the mathematical description of LO event is briefly outlined. For a more detailed description see Richichi (1989b).

Given an extended source with a brightness profile $S(\phi)$, when this is occulted by a straight edge the projected intensity distribution over the ground can be expressed in first approximation as:

$$I(t) = \int F(\omega(t))S(\phi)d\phi \tag{7.1}$$

where $F(\omega)$ is the Fresnel diffraction pattern of a monochromatic point source covered by a straight edge expressed as:

$$F(\omega) = \frac{1}{2}\left\{ \left[\frac{1}{2} + C(\omega)\right]^2 + \left[\frac{1}{2} + S(\omega)\right]^2 \right\} \tag{7.2}$$

with

$$C(\omega) = \int_0^\omega \cos\frac{\pi}{2}z^2\, dz \qquad , \qquad S(\omega) = \int_0^\omega \sin\frac{\pi}{2}z^2\, dz$$

being the Fresnel integrals. ω can be expressed in terms of physical quantities of the observation as:

$$\omega = \sqrt{\frac{2}{d_{\mathbb{C}}\,\lambda}}(x_0 - V_{\mathrm{P}}t - d_{\mathbb{C}}\,\phi) \tag{7.3}$$

where $d_{\mathbb{C}}$ is the distance to the Moon, λ the observing wavelength and x_0 the position of the edge of the geometric shadow of the Moon's limb.

The next step in completing Eq. 7.1 is to consider polychromatic light passing through a filter of $\Delta\lambda = \lambda_2 - \lambda_1$ bandpass. This yields to following expression:

$$I(t) = \int_{-\frac{\phi}{2}}^{\frac{\phi}{2}} d\phi \int_{\lambda_1}^{\lambda_2} d\lambda \int F(\omega(t))S(\phi) \tag{7.4}$$

where the integration limits of $S(\phi)$ have been considered.

At this point the different instrumental effects playing in the final lightcurve formation can be addressed.

7.1.1 Observational constraints

When recording stellar interference fringes of an occulted star, the limiting resolution, i.e. the minimum resolvable angle, ϕ_m, is fixed by several instrumental constraints. In the nearly point-like source domain, three of them apply among others: aperture of the telescope D, filter bandwidth, $\Delta\lambda$, and integration time, τ. The dependence of ϕ_m on these can be expressed as (Sturmann 1997):

$$\phi_{\mathrm{m}} \cong 0.54(D + V_{\mathrm{P}}\tau) \tag{7.5}$$
$$\phi_{\mathrm{m}} \cong 0.158(\Delta\lambda)^{1/2}, \tag{7.6}$$

where ϕ_m, V_{P}, D, $\Delta\lambda$ and τ are expressed in mas, $\mathrm{m\,ms^{-1}}$, m, Å and ms, respectively.

In addition, SNR is a key parameter for limiting resolution. If this is high enough it is possible to deconvolve for the other three deterministic effects on the lightcurve, and achieve much higher angular resolution than the formal limits of Eqs. 7.5 and 7.6.

From Eq. 7.5 we see that large telescopes and long integration times, in spite of increasing SNR, blur high frequency information. This is one of the few cases

in which the size of the telescope plays against the observer. On the other hand, with smaller D and shorter τ the resolution is preserved, but the SNR is decreased, making more difficult the *a posteriori* removal of instrumental distortions, and restricting observations only to bright stars. For $m_V \leq 5$ stars, this trade-off relation balances to optimal SNR for about 1 m telescope and 1 ms integration time in visible wavelengths. For a typical value of V_P of $0.5 \mathrm{m\, ms^{-1}}$, the above relation yields $\phi_m = 0.8 \mathrm{mas}$.

In Eq. 7.4 we introduced polychromatic light. Since diffraction is a wavelength-dependent phenomenon, polychromatic observations introduce an additional distortion in the lightcurve, in particular affecting the contrast and the frequency of the fringes. As seen in Eq. 7.6, the magnitude of that smearing depends on filter bandwidth. Again, we find a trade-off between $\Delta\lambda$ and recorded SNR, which must be properly balanced.

Another key constraint when observing LO is scintillation noise, which is caused by atmospheric turbulence at rapid timescales. The lightcurve is affected in several ways:

- temporal random fluctuations in the stellar intensity. Scintillation makes intensity to fluctuate as a log-normal distribution with a dispersion proportional to the intensity value itself. In certain conditions of turbulence and intensity range (specially for bright sources) this noise can overpass Poisson noise.

- spatial random fluctuations in the stellar position, also known as image *wandering*. The frequency of these fluctuations are again proportional to the stellar intensity.

- variation in the atmospheric transmission. This is a low frequency variation of the intensity which is specially important in IR wavelengths and is caused by the fluctuations in the percentage of water vapour.

- the occasional presence of clouds during the event can dramatically modify the atmospheric extinction and, as a result, introduce notable variations in the recorded intensity.

As a result of all these scintillation components, it has been observed that lightcurve intensity can vary significantly in the range from a few tens to a few

hundreds of milliseconds. Knoechel & von der Heide (1978) numerically showed that the non-inclusion of scintillation noise into the lightcurve model can introduce biases in the derived stellar diameters. Richichi et al. (1992) adopted this idea and introduced scintillation into the classical least-squares fitting procedure as a low-frequency component modeled by a set of Legendre polynomials.

Finally, the acquisition system occasionally introduces in the lightcurve data high-frequency noise due to several causes: long cable impedance, electrical interferences, telescope vibrations, cooling system, power supply, etc. This is usually named as pick-up noise. Fortunately, the spectral signature of this noise is very monochromatic and can be effectively removed *a posteriori* in the data analysis. This can be done either by simply removing the corresponding frequencies in the Fourier space or by accounting this noise contribution in the lightcurve model.

7.1.2 LO lightcurve model

All these instrumentals effects (telescope, filter bandwidth and sampling smearings, scintillation and pick-up noise) can be incorporated in the lightcurve model (Eq. 7.4) yielding the following expression (Richichi 1989b):

$$
I'(t) = F(t) + \left[[1 + \xi(t)] \int_{-\frac{\phi}{2}}^{\frac{\phi}{2}} d\phi \int_{-\frac{D}{2}}^{\frac{D}{2}} d\alpha \int_{\lambda_1}^{\lambda_2} d\lambda \int_{-\Delta t}^{0} d\tau F(\omega) S(\phi) O(\alpha) \Lambda(\lambda) T(\tau) + \beta(t) \right]
$$

(7.7)

where the following terms have been introduced to account for the instrumental effects described above:

- $\xi(t)$ accounting for low-frequency fluctuation caused by atmospheric scintillation.

- $O(\alpha) = O(x, y)$ is the projection of the telescope aperture in the direction perpendicular to the lunar limb,

- $\Lambda(\lambda)$ is the total spectral distribution of the measured signal. It is the convolution between the stellar spectra and the spectral transmission of the telescope, filter and detector,

- $T(\tau)$ is the temporal responsivity of the acquisition system to an impulsive signal. This accounts the non-instantaneous response of a non-ideal detector,

- $\beta(t)$ is the background level which is superposed to the stellar source signal. This term can be notable in presence of thin cirrus and lunar halo,

- $F(t)$ is the term including the pick-up noise.

Note that the variables (α and τ) of those new instrumental effects have been incorporated to the argument ω of the Fresnel diffraction pattern as:

$$\omega = \sqrt{\frac{2}{d_{\mathbb{C}}\,\lambda}(x_0 + \alpha - V_{\mathrm{P}}(t + \tau) - d_{\mathbb{C}}\,\phi)} \tag{7.8}$$

The source brightness profile distribution $S(\phi)$ can be arbitrarily modeled. The two most common alternatives are a uniformly illuminated disk of diameter ϕ_{UD} or a limb-darkened disk of diameter ϕ_{LD}. The latter is a more realistic assumption, specially for red giants which have been observed to show this feature. Typically, the limb-darkening law is chosen to be analytical as a function of a coefficient κ (see for example Diercks & Hunger (1952)), in a way that ϕ_{UD} and ϕ_{LD} can be linked by a simple function of this parameter.

7.2 Data acquisition techniques

LO are very fast events. The whole set of fringes passes over the observer in only a couple of tenths of second[2]. Human eye or video frame rate cannot sample the occultation efficiently. Therefore, millisecond sampling devices are required for a proper representation of the event.

In the next two subsections, two acquisition techniques based on panoramic detectors are presented. Among others, this 2D representation turns to be a very convenient property because the background level can be subtracted from stellar signal and, as a result, the effective SNR is not degraded as it was in visual and near-IR photometers.

---

[2]In the case of a grazing occultation this can be considerably larger.

7.2.1   CCD fast drift scanning

As introduced in Sect. 1.2.1, most LO work has been conducted with high speed photometers which use different photomultiplier technology depending on the observing wavelength, visible or near-IR. In the former case, such systems are called photoelectric photometers (PEP) (Henden & Kaitchuck 1990).

In the following we state the main advantages and disadvantages of PEPs compared to CCDs. Among the advantages:

1. photometers are faster than CCDs and can normally achieve millisecond sampling.

2. they lack read out noise because they are nearly pure photon counting devices.

Among the disadvantages:

1. PEPs show lower quantum efficiency. In Appendix B a quantitative comparison of the SNR performance between PEPs and CCDs has been derived, resulting in the following expression:

$$\eta = \frac{SNR_{\mathrm{CCD}}}{SNR_{\mathrm{PEP}}} \sim 2.2 \tag{7.9}$$

for the regime of moderately bright stars. Eq. 7.9 is less true as we approach fainter stars, where readout noise becomes dominant with respect to Poisson noise. However, well before reaching this point the lightcurve SNR becomes so low that it is in any case impossible to deconvolve for instrumental effects (D, $\Delta\lambda$ and τ) described in Sect. 7.1.

2. their field of view must be small enough to include as less sky background as possible. This is one of the main limitations of photoelectric LO observations (even in the IR), because the background level noise cannot be subtracted from stellar signal and, as a result, the effective SNR is degraded.

3. the use of PEPs for habitual photometry programs is currently dropping in favour of CCDs. As a result, they are becoming specialized instruments and in most observatories are not available as post-focus detectors anymore.

In view of this, a new CCD acquisition mode for LO observations is proposed for extending this technique to practically all the observatories.

Proposed acquisition technique

As detailed in Sect. 3.1.1, the conventional use of a CCD device is the operation in stare mode in which the CCD chip is read out at the end of the exposure. Once the shutter is closed, the charge generated by the incident light on the surface of the CCD is converted into digital numbers, in a column-by-column basis, as the clocked charge moves through the serial register. However, other modes can be considered since the clocking rate Δ can normally be specified by the user. Typically, one has three options: $\Delta = \Delta_0$, $\Delta < \Delta_0$ or $\Delta > \Delta_0$, where Δ_0 is the sidereal rate.

In the first case, the acquired data appear as point-like sources. The clocking direction coincides with star motion over the chip and the telescope tracking system is disconnected.

In the second case, in order to record point-like images it is necessary to have the camera properly aligned and to slow down telescope tracking. These two variants, denominated as drift scanning and time delay integration (TDI), were introduced in Sects. 3.1.2 and 3.1.3 and analyzed in the context of image deconvolution along the Part I of this thesis.

The third case is the one we propose for observing LOs. Δ can be chosen according to the rate and magnitude of the event to be recorded. The detector does not need to have an specific orientation since telescope tracking is on. Thus, the stellar image remains stationary over the chip while photo-generated charge is clocked through the serial register at the desired rate Δ, or equivalently, with a sampling interval $\Delta t = \frac{1}{\Delta}$. This idea is illustrated in Fig. 7.2. For the sake of simplicity, lunar limb speed V_P was exaggeratedly increased in comparison to sampling rate Δt. Normally, in a LO observation $V_P \sim 0.5'' s^{-1}$ and $\Delta \sim 1$ ms, so much more panels in the figure would be required to describe the whole event.

It is interesting to note that our technique is, in a way, based on the same principle originally proposed by MacMahon (1908) to observe lunar occultations. In that case, a photographic plate on a revolving cylinder had been considered. Such observation was later performed by Arnulf (1936).

Practically, a measure of the star flux is obtained every time a column is read out. In standard full-frame CCDs this can be done typically at frequencies of 10 to 500 kHz, which is fast enough for LO work. The fact that these CCDs can only

readout one column at a time might introduce some smearing in the LO lightcurve because a stellar profile usually spans a subwindow of a significant number of pixels. However, this can be overcome by compressing the image scale in order to image the star over only a few pixels. In our technique this is achieved by using a focal reducer.

The following instrumental considerations about the new acquisition technique apply:

1. CCD dead time. The integration time τ and the sampling time Δt do not have to be necessarily coincident. In every interval the CCD employs a certain amount of dead time τ_d in shifting and digitizing the column charge and transferring the obtained values to the computer. τ_d can be a significant percentage of Δt. However, after all, it will be fixed by each CCD specifications and very little can be done to improve it.

2. accurate timing. Although it is convenient to have a low value of τ_d, what is most important is that its dispersion becomes minimized. This is equivalent to have an stable value of sampling interval Δt, which is crucial for deriving a reliable value of a binary separation or an stellar diameter. In summary, fast drift scanning technique demands an accurate relative[3] timing method while reading out columns. As the sampling interval required for LO is about $1\,\mathrm{ms}$, the timing accuracy should be far below this figure. Accuracies of $\sim 1\,\mu\mathrm{s}$ are usually achieved by using specifically dedicated PC-boards, which are connected to a GPS receiver. However, this turns to be an expensive solution. Alternatively, the CPU of the acquisition computer can be used as precise emisor of time ticks. By properly interrupting the CPU internal clock cycle counter, similar accuracies of a few $\mu\mathrm{s}$ can be obtained. This timing subroutine, if properly programed, can also work at the microsecond precision under non-real-time operative systems such as `DOS` or even `Windows`, although the system timers of them are much more unprecise (~ 50 ms).

---

[3]Note that the absolute time reference is not strictly necessary for stellar diameter determination and binaries detection.
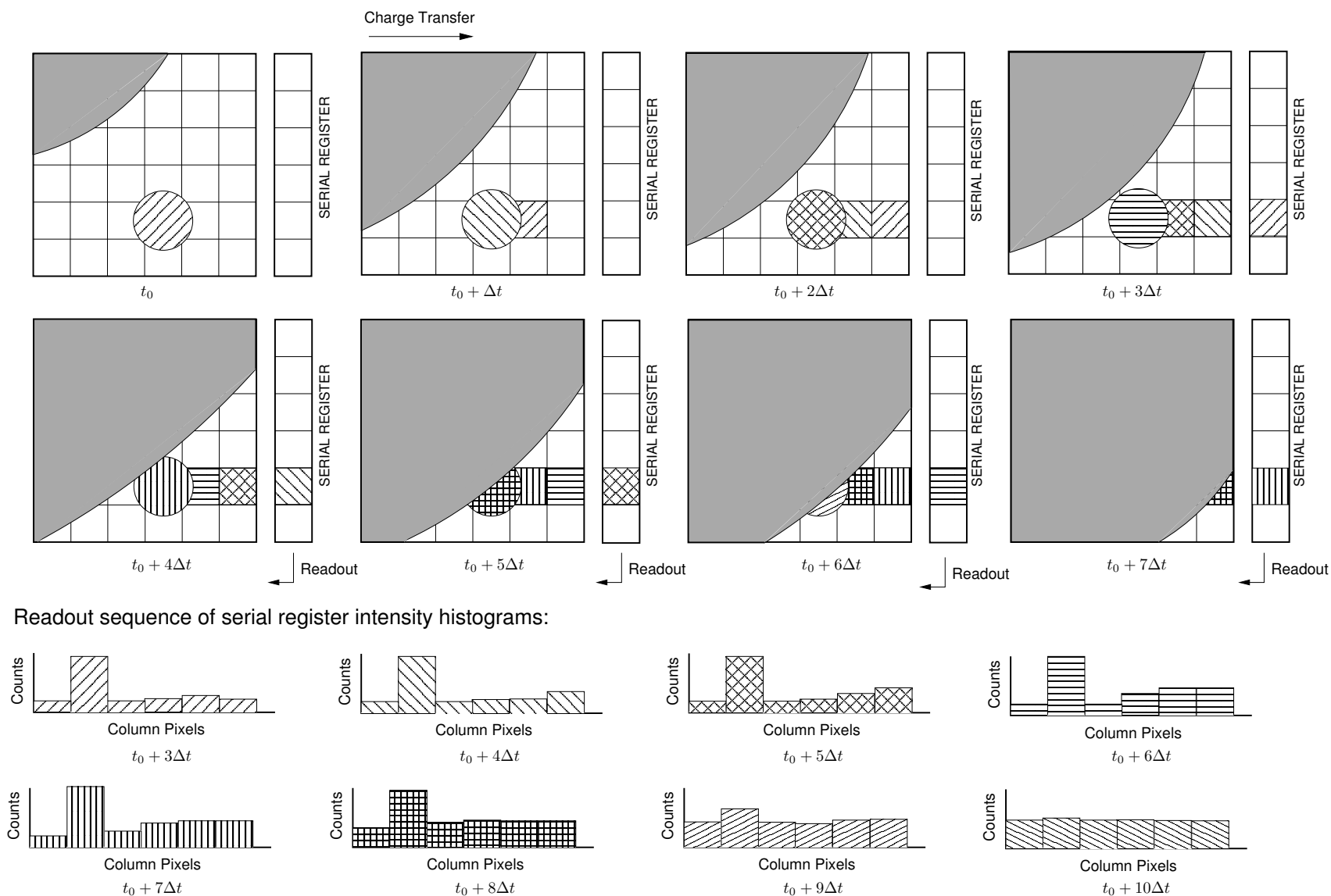
Figure 7.2: Sequence diagram of fast drift scanning acquisition mode applied to a LO observation. Top: each picture corresponds to a sampling interval, Δt. Note that telescope is tracking the star (represented by circle with changing pattern) which, as a result, remains steady over the same region of the CCD. Lunar limb speed has been exaggerated in comparison to sampling interval. Bottom: intensity histograms resulting from reading out serial register. Note that as the star approaches the limb, the lunar background contribution increases.

3. CTE noise. In Pag. 53 we mentioned that CTE noise may be significant when operating at high pixel rates. However, we note this is not the case of that technique: the pixel rate in full frame CCDs is usually fixed by digitization rate and transfer speed. Fast drift scanning does not require to operate on a CCD with selectable pixel rate. Thanks to its slim data throughput, it can be used in most full frame CCDs, even through the slow parallel port. Therefore, CTE noise is not a problem that is increased because of this new acquisition method.

4. pick-up noise. As explained in Sect. 7.1.1, this kind of monochromatic noise might be incorporated to the lightcurve because of diverse reasons. In the case of CCDs this high-frequency noise might be due to residual periodic components in the CCD power supply and cooler. In any case, this noise is considered by the model in Eq. 7.7, with the term $F(t)$.

5. synthetic aperture. The proposed technique allows to adjust *a posteriori* the size of the integrating aperture. In the data reduction stage, the user could adapt this size to obtain the optimum SNR depending on the actual image motion and on the brightness of the source. In the case of PEPs, the integrating aperture is *a priori* fixed and in general this has the disadvantage, especially for faint sources and in the visual range, of introducing a large noise contribution from the background.

6. optimal pixel size. There are two competing factors which fix the optimal size of pixel. On one hand, as stated above, stellar profile is compressed in order to fit most of its flux in a few pixels. Ideally, this image compression should be done only in the scanning direction. For example, Ghedina et al. (1998) applied this idea to monitor the seeing by making use of a anamorphic relay of the same kind used in `Cinemascope` projection systems. On the other hand, excessive scale compression precludes from adequate synthetic aperture analysis (SNR would be decreased). A limiting case would be all the light concentrated in a single pixel, where CCD would be employed as a PEP system.

To sum up, as SNR plays a key role in LO analysis, the choice of a detector with both high QE and low readout noise is crucial for data quality. From this point of view, CCDs look very attractive in terms of QE compared to PEPs. Therefore, with the proposed fast drift scanning technique we see how a low cost full-frame CCD could be used for recording fast photometry events as LO. This detector,

far from being a specialized one, is very common among instrumentation available in all astronomical observatories. Even it turns out to be a low-cost satisfactory solution for sub-meter class telescopes at small professional and high-end amateur observatories.

7.2.2   IR arrays subarray

IR arrays do not follow the CCD clocking scheme described in Sect. 3.1. Instead, the photo-generated charge in each pixel is read out directly by connecting its signal to an output amplifier. Therefore, alternative readout techniques have to be addressed for increasing the time resolution of resulting IR lightcurves. The most commonly used mode for general IR observing is named Reset-Read-Read, or Double-Correlated Sampling. For further details about these we refer the reader to Bizenberger (1993); Herbst et al. (1993). What is important for our LO observations is that Reset-Read-Read mode can be operated over an specified subarray, allowing a high-speed sampling (few milliseconds) of that area of the array.

In addition, several reasons make near-IR domain preferable for LO work in front of other wavelengths as the visible and mid-infrared:

- LO observations are greatly affected by lunar background emission. As this light is reflected solar light, it shows an intensity maximum in visible wavelengths. In addition, because of the atmospheric Rayleigh scattering ($\propto \lambda^{-4}$), the lunar background level greatly decreases as we approach the near-IR. Consequently, SNR in near-IR is improved.

- in mid-infrared wavelengths ($10\mu m - 20\mu m$) the thermal emission of Earth atmosphere and Moon surface introduces again a high background level which degrades SNR.

- as predicted by Kolmogorov turbulence theory, seeing in visible and near-IR domains is slightly dependent ($\propto \lambda^{\frac{6}{5}}$) on wavelength. As a result, seeing is more favourable near-IR.

- finally, as deduced in Sect. 7.1, the speed of diffraction fringes in front of the telescope is proportional to $\lambda^{\frac{1}{2}}$. Therefore, for two LO observations with the

same sampling, the one conducted in IR will obtain higher spatial resolution information than the one in the visible.

- at least in the field of stellar diameters, a larger number of stellar sources can be resolved in IR than in visible. This is because at equal conditions of magnitude, cold late-type stars are more easily available from IR.

7.3 Events prediction: inclusion of 2MASS Point Source Catalogue

Predicting LO events is a well-defined problem. In brief, it consists in matching the coordinates of a sample of stars normally compiled in a number of catalogues with apparent position of the Moon in a given interval of time as seen from a given location. In our case the prediction computations were performed with the Arcetri Lunar Occultation Prediction (ALOP) program (Richichi 1989b). This software provides not only the predicted occultation time, but a number of parameters which will become necessary in the reduction analysis of the lightcurve: for example, the limb linear velocity and the distance to the Moon.

ALOP is fed with ~ 30 catalogues listed in Table 7.1. They are of diverse nature: astrometric in the visible (SAO, AGK3), astrometric in the IR (IRAS, CPIRSS, TMSS), variable stars (GCVSB), close binaries (CHARM, A1110, SB8), YSO (LEITAU, OPH, NTAU), etc. Given the low stellar density defined by these catalogues, even a very rich run in a 1.5 m telescope would consist of 10-20 sources per night at most.

However, this situation changed dramatically with the release of catalogues associated to all-sky near-infrared surveys, such as 2MASS (Cutri et al. 2003) and DENIS (Paturel et al. 2003). Coverage completeness and limiting magnitude of these databases overpassed by several orders of magnitude the ones from mentioned above. For example, The Two Micron Sky Survey (TMSS) (Neugebauer & Leighton 1969) was incomplete in declination and only extended to $K < 3$, while 2MASS is complete up to $K_{\mathrm{lim}} \sim 14.3$. Consequently, the number of predicted observable events has jumped up by very large factors. For example, a typical night in a 1.5 m telescope would offer in excess of 100 sources close to maximum lunar phase. This increase is even more dramatic when the Moon scans specially populated areas of the

sky, e.g., crowded regions near the Galactic Center. In this environment, thousands of events would be easily accessible to a medium-sized telescope over few hours.

In view of this, the author collaborated with Andrea Richichi for incorporating 2MASS catalogue into `ALOP` (Richichi & Fors 2003). A working release of this `ALOP` update was made available on January 2004. A few considerations about LO predictions are worth mentioning:

1. it might be objected that lunar limb irregularities could unvalidate the assumption of perfect straight edge made in Sect. 7.1. In that case, the predictions and, most important, the high resolution information derived from the diffraction pattern would be totally biased and useless. This was the common belief for many years, yielding to confronted discussions between Thomas Gold and David Evans in the Royal Astronomical Society. Unfortunately, the wrong arguments of the former convinced the astronomical community and LO were discouraged up to final 1960s (Evans 1977). The correct justification of Evans is as follows:

   First, it is true that lunar limb is not a perfect straight line. However, this has a small curvature: in a typical ~ 3 mas angular separation where the corresponding scale in the Moon limb is $\lesssim 5.5$ m, the assumption of nearly perfect straight line is valid. Only when measuring separations of a few tens of arcsec (Richichi et al. 1994), errors arising from lunar surface curvature become non-negligible. However, that separation regime is far larger than the typical binaries and diameters by LO.

   Second, even the smallest scale structures in the lunar limb such as rocks and cliffs are known to be very smooth (Abell et al. 1993; Evans 1970), below the meter scale involved in LO phenomena.

   Third, and most important, even if limb irregulatities were larger than Fresnel scale, these would have to be integrated over all the Fresnel diffraction zones, which greatly reduces their effect.

2. accuracy of the predictions ranges from $\sim$10s to a few tenths of a second, depending on the astrometric error of the catalogue and the lunar limb region.

Table 7.1: Catalogues employed for LO predictions.

Code	Name	Number of sources	Reference
2MASS	2MASS All-Sky Catalogue of Point Sources	470,992,970	Cutri et al. (2003)
SAO1990	SAO Star Catalog J2000	25,711	SAO Staff (1995)
AGK3	AGK3 Catalogue	19,576	Heckmann (1975)
IRASPSC3	IRAS catalogue of Point Sources, Version 2.0 ($F(12\mu m) > 1\ Jy$ and $F(12)/F(25) > 1.5$)	4,381	Joint IRAS SWG (1988)
CPIRSS	Catalog of Positions of IR Stellar Sources (CPIRSS)	3,470	Hindsley & Harrington (1994)
DO	Dearborn Catalogue of faint red stars	2,867	Lee et al. (1997)
GCVSB	Combined General Catalogue of Variable Stars	1,999	Kholopov et al. (1998)
NLTT	New Luyten Catalog of Stars with Large Proper Motion	1,013	
IRASPSC2	IRAS catalogue of Point Sources, Version 2.0 ($F(12\mu m) > 10\ Jy$)	905	Joint IRAS SWG (1988)
TMIND	Two-Micron Sky Survey (TMSS)	889	Neugebauer & Leighton (1969, 1997)
CUCCATE	Sources in the Arcetri archive (as 21 mar 2000)	668	
CHARM	List of binaries from CHARM	429	Richichi & Percheron (2002)
CNS3	Catalogue of Nearby stars, 3rd Ed.	409	Gliese & Jahreiss (1995)
CARBON	General catalog of cool galactic carbon stars, Second edition.	347	VVAA (1989)
STAR25PC	Catalogue of stars within 25 parsecs of the Sun	254	Woolley (1970)
LEITAU	YSOs in Taurus, 3rd version	245	Leinert (1991)
OPH	YSOs in Ophiucus	214	Leinert (1992)
A1110	Catalog of occultation binaries (only SAO entries)	212	Mason (1995)
SB8	8th Catalogue of the orbital elements of spectroscopic binary systems	182	Batten et al. (1989)
IRASPSC1	IRAS catalogue of Point Sources, Version 2.0 ($F(12\mu m) > 40\ Jy$)	166	Joint IRAS SWG (1988)
MASH2O	H2O masers in HII regions	68	Codella et al. (1994)
WICHMANN	ROSAT identification of new T Tauri stars in Taurus	64	Wichmann (1994)
SSTARS	General Catalog of S Stars	56	Stephenson (1976)
HAEBE	Herbig Ae/Be	39	The et al. (1993)
NTAU	New T Tauri stars from CIDA Schmidt survey	31	Briceno et al. (1993)
GALCEN	Sources in the proximity of the galactic centre	28	
MASSTAR	Stellar Masers	27	Palagi et al. (1993)
KENYON	IRAS survey of the Taurus-Auriga molecular cloud	19	Kenyon et al. (1990)
SHELLS	Stars with circumstellar shells	10	
WR	Sixth Catalogue of Galactic Wolf-Rayet Stars	10	van der Hucht et al. (1997)
WW	Cool circumstellar matter around nearby main-sequence stars	4	Walker & Wolstencroft (1988)

3. with the introduction of large, deep IR catalogues such as 2MASS in `ALOP` predictions, the magnitude distribution of observable targets has shifted its peak beyond the LO limiting sensitivity (even with largest telescopes) in constrast to previous campaigns (Evans et al. 1986; Richichi et al. 2002). Therefore, it can be expected that most of the LO lightcurves will have on average lower SNR than in the previous observational efforts. As a result, this extended sample is likely to become less efficient in binaries detection, especially those with brightness ratios larger than unity. We will further clarify this in Sect. 7.7.1.

7.4   Data description

As a result of considerations stated in above sections, LO observations were started in a regular basis, mainly aiming two purposes:

- to test the proposed CCD fast drift scanning technique under realistic conditions.

- to contribute with a systematic program of LO, specially in the field of new binaries detection.

- to have a large data bank of occultations for developing new analysis algorithms in this field, which will be explained in Sect. 7.5.

In the next subsections we describe the data obtained from each one of these observational efforts. Data sets are separated by the observing site where they were acquired.

7.4.1   Fabra Observatory

First tests of CCD fast drift scanning technique were conducted under the small-telescope regime. In particular, a Celestron 14 inches Schmidt-Cassegrain telescope (hereafter C14) was used to observe the occultation events reported below. The C14 tube was mounted parallel to the Mailhat double 38cm-astrograph at Fabra Observatory, Barcelona, Spain (see Docobo (1989); Núñez et al. (1992) for a more

Table 7.2: Summary of observing runs at Fabra Observatory.

Run	Date (dd-mm-yy)	Telescope	Detector	Events description	Number of occultations
F1	11-01-00	C14	CCD	Test	0
F2	16-02-00	C14	CCD	Test	0
F3	13-03-00	C14	CCD	BS	1
F4	14-03-00	C14	CCD	BS	1
F5	11-04-00	C14	CCD	Test	0
F6	12-04-00	C14	CCD	Test	0
F7	15-04-00	C14	CCD	Test	0

C14: Celestron 14 inches Schmidt-Cassegrain telescope.

Test: Testing of CCD fast drift scanning technique.

BS: Occultation of bright source.

specific description of the astrograph). In Sect. 7.2.1 we expressed the convenience of compressing the pixel scale only in the scanning direction. Unfortunately, we had to compress scale in both directions, because we did not have an anamorphic relay as the one employed in Ghedina et al. (1998).

Regarding the detector, we employed a Texas Instruments TC-211 CCD set inside an SBIG ST8 camera as the tracking chip. This is a full-frame front-illuminated CCD with 13.75×16 μm pixels and a 192×164 pixel format. Being read out through a parallel port, its electronic module can operate at 30 kHz with 12 electrons rms readout noise. With these technical specifications and its high quantum efficiency (QE peak reaches 70% at both 650nm and 730nm), the TC-211 appears to be suitable for fast imaging purposes, such as tracking and millisecond photometry.

LO data has been acquired by the drift scanning scheme described in Sect. 7.2.1. As justified, this technique demands an accurate relative timing method while reading out on a column by column basis. In our case, both the CPU-interrupted timing and read out procedures were carried out by a DOS-based program called SCAN (Flohr 1999).

Table 7.2 summarizes the tests conducted with that instrumental setting, including five testing sessions and two successfully observed occultations of one binary and one triple systems. Complete prediction information of events F3 and F4 is given in Table 7.3.

Table 7.3: Summary of observed occultation events. Columns (10), (11) and (12) are predicted values.

(1) Source	(2) Date (dd-mm-yy)	(3) Filter	(4) $\lambda_0 \pm \Delta\lambda$ (nm)	(5) τ (ms)	(6) m_V	(7) CA (°)	(8) PA (°)	(9) Limb vel. ($''/s$)	(10) System magnitudes	(11) Sep. ($''$)	(12) PA (deg)
SAO 77911	13-03-00	R	641±58	2.344	4.6	34S	146	0.242	5.5	-	-
									6.3	0.02^a	178^a
									6.3^a	1.0^a	335^a
SAO 79031	14-03-00	R	641±58	2.067	4.0	63S	123	0.350	4.5	-	-
									4.5^a	0.10^a	90^a

[a]: Uncertain values. See text in Sect. 7.6.
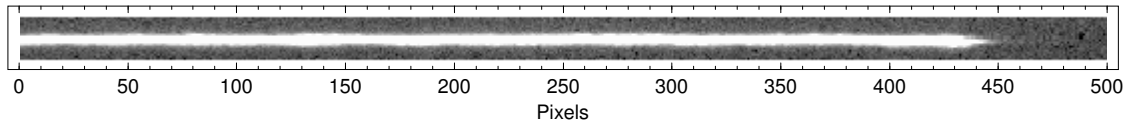
Figure 7.3: Raw image of SAO 79031 occultation at Fabra Observatory. Strip patch spans for 1 second of data record, where every 20-pixel column corresponds to 2.067 ms.

Columns (1) and (2) report source name and observation date. Columns (3) to (5) correspond to filter name, central wavelength and bandwidth and integration time. The responsivity function of the CCD was not characterized. Consequently, no conclusive statements can be done regarding the CCD dead time and the actual difference between integration time (τ) and sampling interval (Δt). At this time we assumed them to be identical. Visual magnitude is detailed at column (6), while columns (7) to (9) report position angle, contact angle and angular rate of the event, respectively. The last three columns are predicted values. Columns (10) to (12) show the binary system description: magnitudes of the components, angular separation and position angle. We have split the components into different lines.

As an example of a strip obtained by the technique described in Sect. 7.2.1, we show in Fig. 7.3 the final part of the SAO 79031 occultation. In that case, a 20-pixel column is stored every 2.067 ms on average. It is important to note that the proposed drift scanning scheme allows the recording of arbitrarily long lightcurves. Thus, observation can be started well before the predicted occultation time, providing much more flexibility in the case of eventual prediction errors or tracking problems.

7.4.2   CALOP: Calar Alto Lunar Occultation Program

The combination of the advantages and limitations described in Sect. 1.2.1, makes the LO technique particularly appealing, specially for small and medium-sized telescopes where a routine program of observations can be established. The availability of relatively cheap detectors for visual and near-IR fast photometry is bringing this method within the budget of most observatories. In this way, we note the benefits of commercial, relatively cheap CCDs developed for amateur astronomers on one side, and previous-generation near-IR arrays of small format on the other side. In their respective wavelength ranges, both kinds of detector offer sufficient quality for the purpose of LO observations, where noise is essentially set by the lunar background.

As a result, the author was motivated for starting a long-term LO program focused in the field of detection of new binaries. This effort has been developed in collaboration with Andrea Richichi (ESO), one of the principal experts in this area. Calar Alto Observatory was chosen because of the long experience accumulated there in LOs conducted in the past Richichi et al. (1996b, 1997, 1999, 2000a, 2002). Consequently, the program was denominated Calar Alto Lunar Occultation Program (CALOP).

Because of the SNR considerations stated in Sect. 7.2.2, most part of CALOP was developed in near-IR domain. Despite this preference, part of the program was also conducted in the visible by using a CCD. This is because a confirmation in a larger telescope regime of the first successful tests of fast drift scanning technique described in Sect. 7.4.1 was aimed.

The visual and near-IR observations were carried out with the 1.5 m telescope of the Observatorio Astronomico Nacional (hereafter OAN 1.5 m) in Calar Alto Observatory. On two occasions, we used the 3.5 m and 2.2 m telescopes of the Centro Astronómico Hispano-Alemán (hereafter CAHA 2.2 m and CAHA 3.5 m, respectively), located at the same site.

For the visual occultations we employed the same CCD and fast drift scanning technique described in Sect. 7.4.1. Again, that allowed us to sample the LO lightcurves at millisecond rates.

For the near-IR observations, we made use of the IR NICMOS3 array based MAGIC camera (Herbst et al. 1993), operated in fast subarray mode with a window

Table 7.4: Summary of observing runs at Calar Alto Observatory

Run	Date (dd-mm-yy)	Telescope	Detector	Events description	Number of nights	Number of occultations
A	Mar-01	OAN 1.5m	CCD	Bin	8	0[a]
B	Oct-01	OAN 1.5m	CCD	Bin	6	13
C	02-Feb-02	CAHA 2.2m	MAGIC	Tau	1	0[a]
D	Feb-02	OAN 1.5m	MAGIC	Bin	4	27
E	Feb-03	OAN 1.5m	MAGIC	Bin	5	0[a]
F	Nov-03	OAN 1.5m	MAGIC	Bin	5	9
G	Dec-03	OAN 1.5m	MAGIC	Bin	5	0[a]
H	Feb-04	OAN 1.5m	MAGIC	Bin	6	29
I	Mar-04	OAN 1.5m	MAGIC	Bin	7	3
J	28-Jul-04	CAHA 2.2m	MAGIC	GC	0.5	54
K	30-Oct-04	CAHA 3.5m	OMEGA-CASS	Tau	1	0[a]
L	Nov-04	OAN 1.5m	MAGIC	Bin	6	45
M	Dec-04	OAN 1.5m	MAGIC	Bin	5	7
N	Jan-05	OAN 1.5m	MAGIC	Bin[b]	6	105
O	Feb-05	OAN 1.5m	MAGIC	Bin	6	96
				Total	71.5	388

Bin: Binaries search.

TTau: Passage over Tauri star-forming region.

GC: Galactic Center passage.

[a]: Devoid due to bad weather conditions.

[b]: Includes a single night with a passage through Taurus star-forming region.

size of 8x8 pixels. This size was found to provide a good compromise between a sufficiently fast sampling rate (typically $8.5\,\mathrm{ms}$ with an integration time of $3\,\mathrm{ms}$) and a robust estimation of the background level around the stellar image.

Observations were carried out during fifteen observing runs over a period of four years including 71.5 nights of observation, as detailed in Table 7.4. All in all, the 388 recorded occultations represent one of the very few large-scale efforts in LO active at present. The author would like to express here his gratitude to all the observers who contributed in this long-term effort: Maite Merino, Javier Montojo, Jorge Núñez, Xavier Otazu, Dolores Pérez, Albert Prades and Andrea Richichi.

Runs A,B,D-I and L-O spanned 69 nights dedicated to binaries search. On average, they consisted of a few nights per run allocated in periods of crescent Moon close to full phase, in order to maximize the number of occultations of field stars and observe disappearances rather than reappearances. The disparity in the number of

recorded occultations between runs of this category is due to two reasons. First, bad weather conditions. Note that three of the 12 runs were completely devoid of results due to this reason. The average percentage of success for the other 9 was around 40%. In global, a success rate around 30% was found for all the 12 runs of binaries search. This is in part understandable because all these runs were conducted during the first and last quarter of the year, which are the worst seasons in Calar Alto weather statistics. Second, the incorporation of 2MASS catalogue in the prediction program since Jan 2004 (see Sect. 7.3) increased the number of potential events to be occulted. Runs N and O are representative examples of the outcome which can be attained in a binaries search run, because they were conducted under fine weather conditions (success around $\sim 85\%$) and this prediction catalogue extension.

Run J was designed to follow up the passage of the Moon over a minimum distance of $0°59$ from the Galactic Center, on July 28th, 2004. With the incorporation of 2MASS catalogue in predictions about 3700 objects were occulted during the 3.4 hours which the Moon scanned that region of the sky. Despite of the low elevation of the Moon during the whole event (below $35°$ at any time) we could manage to record 54 useful events during a total of 1.5 hours of productive observing time. In these conditions, the maximum number of recordable occultation was exclusively limited by telescope pointing and tracking accuracy and detector readout overheads. In this crowded, heavily obscured region the majority (50) of the recorded objects has no counterpart in optical catalogues. Spectral types on the other hand are known for about half the sample, thanks mostly to the work of Raharto et al. (1984). With very few exceptions, the stars are all of M spectral type. From the photometry available in the 2MASS catalogue, it can be observed that about half of the stars have a color $J - K > 1$, indicating significant reddening. This is presumably due to interstellar dust in the direction of the Galactic Center. However in some cases colors as red as $J - K = 3.5$-5.0 are present, possibly pointing to additional circumstellar extinction. Two distinctive observing strategies were considered with respect to the rest of binaries search runs. First, LO events were priorized by, apart from their magnitude, their $J - K$ color. Second, for the events most close in time (separated a few tens of a second) continuous lightcurve recordings where performed without saving in the computer after each source was occulted. In other words, the telescope was repointed to the next source while MAGIC was still integrating in subarray mode. That special observing mode introduce some additional complexity in the automatic reduction pipeline presented in Sect. 7.5.3.

Finally, runs C and K were allocated to follow up a passage of the Moon over the Taurus star-forming region. These are relatively frequent, and have been used in the past especially to derive important insights on the frequency of binaries in the early stages of stellar evolution (see Simon et al. (1995), and references therein). However, both runs were completely devoid of results due to weather. The case of J was specially unfortunate, because it was the run with the largest telescope (CAHA 3.5 m) and with the detector (OMEGA-CASS) with highest sensitivity, finer pixel scale and, above all, best temporal sampling interval ($\Delta t \sim 1$ ms). In addition, on 20th January 2005, during a regular binaries search run, a passage of the Moon over a Taurus star-forming region was also recorded with OAN 1.5 m telescope.

Detailed information of all the recorded events and the characteristics of the corresponding objects can be found in Table C.1 of Appendix C. A subset of the 38 sources which yielded positive results or pertinent coments is included in Table 7.5. The column format of both tables is identical. Columns (1) through (3) list the source identification, the date of the event and the telescope+detector configuration used. Note that 2MASS prefix in the longest identificators has been omitted. The code CA refers to observations with the CCD, and the code CB to observations with MAGIC at OAN 1.5 m, while the code CC corresponds to observations with MAGIC at CAHA 2.2 m. Broad band R (641 ± 58nm) and K ($2.2 \pm 0.4 \mu$m) filters were used in CA and CB, CC cases, respectively. Concerning the K filter an accurate transmission curve at operating temperature was determined. For this purpose we have used the same MAGIC camera in the laboratory, taking exposures with and without the filter, using the same resin-replica grism used for astronomical observations at liquid nitrogen temperature. As a light source we employed a source without significant emission in the J band, thus avoiding contamination of short-wavelength light from a different order. For the observation of the very bright star RZ Ari we employed a narrow band filter, with $\lambda_0 = 2.26 \mu$m and $\Delta\lambda = 0.06 \mu$m.

Column (4) lists the field of view set either by the diaphragm aperture or by the array subwindow. Columns (5) and (6) list the sampling time of the lightcurves and the integration time for each data point.

Columns (7) and (8) list the total magnitude of the star in the V and K filters. The V magnitudes are taken from the literature. In principle, photometric information could be extracted directly from the LO data. However, the lack of an accurate instrument calibration and the hetereogenous and non photometric condi-

Table 7.5: List of occultation events with positive results and their circumstances of observation.

(1)	(2)	(3)	(4)	(5)	(6)	(7)	(8)	(9)	(10)	(11)
Source	Date	Telescope	Filter	D	Δt	τ	V	K	Sp.	Dist.
	UT	+detector		($''$)	(ms)	(ms)	(mag)	(mag)		(pc)
SAO 164553	25-10-01	CA	R	7	5.0	5.0	8.5		F0III/IV	
SAO 164567	25-10-01	CA	R	8	1.8	1.8	7.4		K5III	
SAO 165578	27-10-01	CA	R	6	2.1	2.1	6.1		K5III	256
30 Psc	28-10-01	CA	R	6	1.5	1.5	4.4		M3III	127
SAO 78119	22-02-02	CB	K	7	8.7	3.0	8.1	4.9	K0	
SAO 78122	22-02-02	CB	K	7	8.4	3.0	7.9	5.7	G5	217
SAO 78168	22-02-02	CB	K	7	8.4	3.0	6.1	3.9	G8III	134
SAO 78197	23-02-02	CB	K	7	8.6	3.0	8.2	5.3	K0	
V349 Gem	23-02-02	CB	K	7	8.3	3.0	12.2	4.1		
SAO 78258	23-02-02	CB	K	7	8.5	3.0	8.2	6.9	G0	198
AG+24 788	23-02-02	CB	K	7	8.4	3.0	10.3	6.4	K0	
SAO 79251	23-02-02	CB	K	7	8.5	3.0	8.7	6.3	K0	
SAO 79257	23-02-02	CB	K	7	8.5	3.0	8.4	7.4	F5	167
SAO 80310	03-03-04	CB	K	7	8.5	3.0	6.9	5.6	F8	35
SAO 80764	01-04-04	CB	K	7	8.4	3.0	7.8	4.0	K2	1429
SAO 185661	28-07-04	CC	K	5	8.4	3.0	9.9	5.9	K5	
IRC -30319	28-07-04	CC	K	5	8.4	3.0	8.8	1.8	K2	
17454891-2809333[a]	28-07-04	CC	K	5	8.3	3.0		6.1		
SAO 164601	18-11-04	CB	K	7	8.6	3.0	6.2	5.7	A0m...	110
SAO 165154	19-11-04	CB	K	7	8.4	3.0	9.0	6.2	K1III	
SAO 109617	22-11-04	CB	K	7	8.4	3.0	8.2	5.5	K2	21
SAO 110089	23-11-04	CB	K	7	8.4	3.0	8.5	6.7	K0	47
SAO 92659	23-11-04	CB	K	7	8.5	3.0	5.9	5.1	F2Vw	43
RZ Ari	18-01-05	CB	K	7	8.4	3.0	5.8	-0.9	M6III	124
SAO 76214	19-01-05	CB	K	7	8.5	3.0	8.2	5.4	K0	
LH 98-106	19-01-05	CB	K	7	8.5	3.0	7.3	6.0	F5	37
DL Tau	20-01-05	CB	K	7	8.4	3.0	13.6	8.0	GV:e...	
GN Tau	20-01-05	CB	K	7	8.5	3.0	15.1	8.1	M2.5	
Elias 3-18	20-01-05	CB	K	7	8.5	3.0			B5	
ITG 31	20-01-05	CB	K	7	8.5	3.0	9.1	5.2	K0	565
LkHA 332	21-01-05	CB	K	7	8.4	3.0	14.7	7.9	K5	
IRAS 04395+2521	21-01-05	CB	K	7	8.5	3.0		5.5		
04440885+2540333[a]	21-01-05	CB	K	7	8.6	3.0		6.9		
05415664+2707323[a]	22-01-05	CB	K	7	8.5	3.0				
SAO 78540	23-01-05	CB	K	7	8.6	3.0	6.9	5.3	G0	36
HD 283610	16-02-05	CB	K	7	8.5	3.0	9.6	5.4	K5III	
04264187+2500314[a]	17-02-05	CB	K	7	8.4	3.0		6.7		
SAO 77000	17-02-05	CB	K	7	8.4	3.0	9.1	5.4	G5	244

[a] 2MASS prefix in the longest identificators has been omitted.

tions of some nights of the program made us to collect the R and K magnitudes from the USNO-B1.0 and 2MASS catalogues, respectively. In addition, note that the source does not effectively fit within the single column when this is recorded by drift scanning technique. This might introduce a possible systematic bias in the

global magnitude of the object which has not been investigated. Of course we realize
that some of the brightest sources of CB an CC runs have K magnitudes above the
saturation limit of 2MASS. Although this has been accounted for in the catalogue,
systematic errors might still be present. We will further discuss the consequences of
this in Sect. 7.7.3.

In column (10) we report the spectral types, again extracted when available from
the literature; in the case of multiple determinations, the most frequent or most
recent was used. Finally, column (11) lists the distances based on HIPPARCOS
parallaxes, when available. Those values affected by a large uncertainty ($> 10\%$)
have been omitted.

7.5   Data reduction and analysis

Data described above was analyzed by means of two reduction programs (`ALOR` and
`CAL`) which will be presented in Sects. 7.5.1 and 7.5.2. The introduction of those
methods will be brief and we refer the reader to Richichi (1989a,b) for a detailed
explanation. Sect. 7.5.3 comprises most of the effort dedicated to LO data analysis
in this part of the thesis. It consists on a new automatic reduction technique based
on wavelets for extracting and characterizing lightcurves.

7.5.1   ALOR

Arcetri Lunar Occultation Reduction software (`ALOR`) (Richichi 1989b) is an im-
plementation of the model-dependent lightcurve fitting algorithm described around
Eq. 7.7, which of a non-linear least squares method (LSM) estimator. Two groups
of parameters can be considered in the `ALOR` fit. First, the ones related to the geom-
etry of the event: the stellar intensity (I_0), the occultation time (t_0), the rate of the
event (V_P), the intensity of the background (B_0) and its time drift ($\beta(t)$). The coef-
ficients of a series of Legendre polynomials can also be included in the fit in case of
significant stellar intensity fluctuations due to image motion and scintillation noise
(Richichi et al. 1992). Second, the ones related to physical quantities of the source:
the angular diameter and additionally for binary (or multiple) stars the projected
separation and the brightness ratio of the components.

In general, the first set of parameters can be fitted in a good accordance by only considering as initial values the ones derived in the prediction. However, diameters and binary parameters fitting requires to be performed interactively for understanding each particular lightcurve nature and the possible correlation with other parameters. In this latter step, `ALOR` allows to fix whatever parameters combination in order to help the algorithm to converge to the global solution.

`ALOR` convergence is reached when one of the following criteria is met: the residual of the fit does not significantly change from one iteration to another or a maximum number of iterations has been run. In general, this happens in a few (< 15) iterations even in the LO with low SNR.

Note that the only instrumental effect from Eq. 7.7 which was not taken into account in the data analysis with `ALOR` is the temporal responsivity of the acquisition system, $T(\tau)$. Richichi (1989b) establishes a method for calibrating $T(\tau)$ consisting in the `ALOR` reduction of a set of unresolved sources with a the value of $T(\tau)$ being changed incrementally and diameter parameter kept free. As a result, a plot of diameter versus $T(\tau)$ is available. At the end, the correct $T(\tau)$ is found by extrapolating to null diameter. However, note that a precise knowledge of $T(\tau)$ is only required for diameter determination. Since this is not the main field of study of CALOP data, we did not carry out this calibration exercise.

7.5.2 CAL

We recall that `ALOR` is a model-dependent algorithm, i.e., the user must specify an analytic expression of the brightness profile $S(\phi)$. Limb darkening model is adequate for most situations. However, in a couple of situations the lightcurve cannot be optimally fitted by a simple model of $S(\phi)$. This is the case of sources with extended circumstellar emission and the detection or confirmation of companions at very small separations.

In both cases, the distribution of $S(\phi)$ is not *a priori* known, and the adoption of a given analytic model could bias the derived diameter or separation. As a solution, Richichi (1989a) proposed a model-independent method, named *Composite Algorithm* (`CAL`), which does not make any assumption about $S(\phi)$ shape. The idea behind `CAL` is to separate the calculation of $S(\phi)$ from the fit of the rest of parameters

$(I_0, t_0, V_P, B_0, \beta(t))$. To do this, first the latter are calculated by `ALOR` with a fixed value of $S(\phi)$. Second, with new values of $I_0, t_0, V_P, B_0, \beta(t)$ a corresponding matrix of instrumental effects $\Pi(t, \phi)$ is computed. Third, a new profile $S(\phi)$ is computed from the expression:

$$I(t) = \int S(\phi)\Pi(t, \phi)d\phi + \beta(t) \tag{7.10}$$

by making use of the 1D version of Richardson-Lucy deconvolution algorithm (Lucy 1974). Finally, convergence test based on residuals is performed. In case this is not accomplished, the process is iterated.

Note that in the case of very close binaries, the use of `CAL` is very convenient for confirming possible companions. More in depth, the brightness profile provided by `CAL` is used to decide the existence and to obtain an estimate of the separation and brigthness ratio of two components. The binary is finally detected only if `ALOR` converges with the secondary indicated by `CAL` as initial values. This procedure has been found to be very robust and not biased over the large number of LO inspected in CALOP database.

7.5.3   Automatic reduction with wavelet analysis

As pointed out in 7.3, the inclusion of 2MASS catalogue in the prediction program yielded out a great increase in the number of recorded occultations per run. As a result, it was soon evident that the data reduction process with `ALOR`, described in Sect. 7.5.1 should have been automatized if a a regular flow of results was desired.

For this purpose, a new reduction pipeline was designed. This is graphically illustrated in Fig. 7.4 and comprises the following steps:

Object files archiving

Some basic archiving for every occultation is done. First, a subdirectory for each event is created. Second, the FITS cube image file which was recorded at telescope is copied to that directory. Its keywords `OBJECT`, `TELESCOPE` and `FILTER` are edited to their corresponding values. Finally, the predicted values for limb linear velocity and Moon distance are also copied to the object directory.
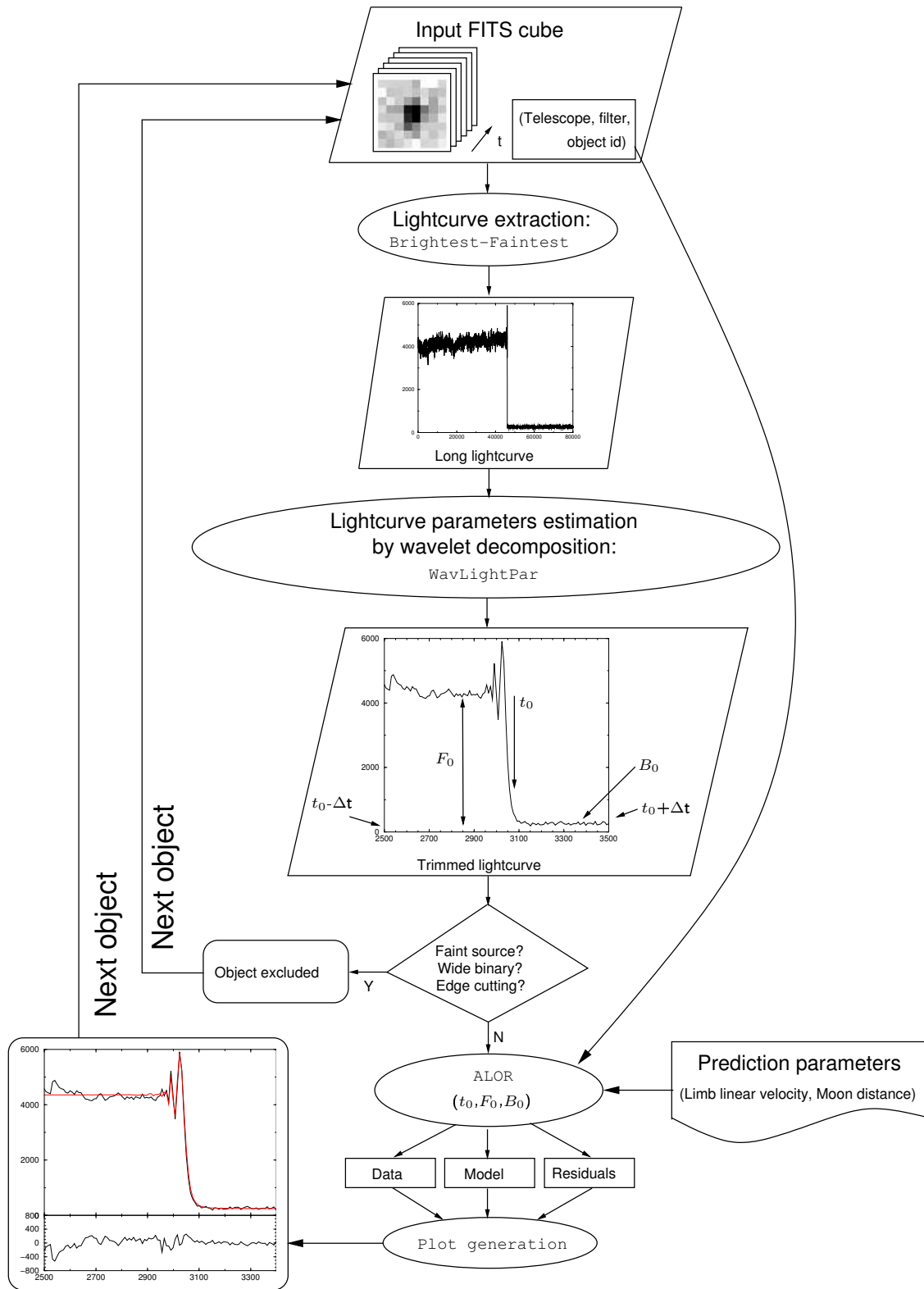
Figure 7.4: Flow-chart describing the steps followed in the automatic LO reduction pipeline.

`Brightest-Faintest` **and** `3D-SExtractor`**: lightcurve extraction**

This step creates an `ASCII` lightcurve file from the above mentioned binary FITS cube, providing an estimate of the source flux for all planes in the cube, which are uniformly sampled in time.

As there is not a unique way of getting the flux from an object in a subframe, some effort was dedicated into investigating which algorithm performed best in our specific case.

Shortly after some tests, it was learnt that classic aperture and profile photometry algorithms should be discarded. This was because of the notable object motion present along the few seconds recorded in the FITS cube and the large profile variations present in short timescales below the atmospheric coherence time.

A much simpler and faster approach consisting in the subtraction of the M faintest pixels of the frame to the N brightest pixels was considered. This algorithm, hereafter noted as `Brightest-Faintest`, demonstrated to be really flexible and reliable for flux estimation over a wide range of SNR situations. One of the advantages of this approach is that the flux estimation does not require a localized knowledge of the source. Therefore, the algorithm is not affected by the temporal source motion. On the other hand, it is assumed that the ratio of number of source pixels to the number of background pixels is the same along the whole lightcurve. Intuitively, this can be considered to be approximately true while the source intensity remains roughly constant within a given range. However, one could wonder if this assumption is valid in the presence of scintillation and electronic noise or when the most prominent diffraction fringes occur. In such situations, it could happen that the flux of the fringes could be underestimated. However, we anticipate that the correctness of this assumption will be confirmed with an independent extraction algorithm explained in the next paragraphs and Figs. 7.5 and 7.6, at least to the significance level required for avoiding the triggering of an spurious binary detection.

In order to tune the M and N parameters of `Brightest-Faintest`, we extracted a set of lightcurves with different values for N and M and for a number of unresolved single sources with very different SNRs. `ALOR` fit was computed for all of them. As a result, (N=15,M=30) was found to be the combination which offered best compromise between maintaining high SNR and minimizing the residuals of the fit.

Finally, another attempt for extracting the lightcurves was conducted by designing and implementing a new algorithm. This consists in a customization of SExtractor object detection package (Bertin & Arnouts 1996) for the use of 3D FITS cubes of fast photometry observations. The algorithm, hereafter referred as 3D-SExtractor, invokes the usual SExtractor for every frame, and handles the output to decide if the object has been effectively detected and obtain the flux estimate accordingly. A segmentation map is computed for every positive detection. When occultation occurs and detection turns to negative, those *object* pixels in the segmentation map are used for computing the mean background intensity. In addition, the algorithm also provides, as a by product result, a value for t_0, B_0 and F_0, computed when detected-to-undetected source change occurs.

A comparison between the two extraction algorithms is shown in Fig. 7.5. Both approaches were run for two distinct cases, a moderately bright (SNR=21.9) and faint (SNR=7.6) source. Three comments apply at this point.

First, it is clear that 3D-SExtractor lightcurves are noisier than Brightest-Faintest ones, both in bright and faint cases. This might be due to the temporal profile variations. In order to demonstrate this, an study of the distribution of the number of segmented pixels assigned to the detected source has been plotted in Fig. 7.6. The sample used for this study comprises all the planes of SAO 78128 lightcurve displayed in Fig. 7.5 which correspond to positive detection. In this case, that occurs for all planes previous to the occultation time (t=2500 ms). On the left, the histogram of the number of pixels contributing to the source flux is broadly distributed, confirming that 3D-SExtractor is highly sensitive to the temporal profile variations. The right panel illustrates that the same distribution as a function of time. Apart from the previously mentioned scatter, it can be seen that there is no evident dependence with time. In other words, although some correlation with fringes located in Fig. 7.5 is noticeable for the few last points, the value of number of pixels remains within the same range as other pre-fringe samples. This partly confirms what was anticipated in Pag. 250, where a possible flux underestimation in the fringes by Brightest-Faintest was early discarded.

Second, when comparing the two bright lightcurves in Fig. 7.5, an smaller amplitude in the fringes can be seen in the case of Brightest-Faintest algorithm. Far from indicating this the above mentioned flux underestimation, we stress that
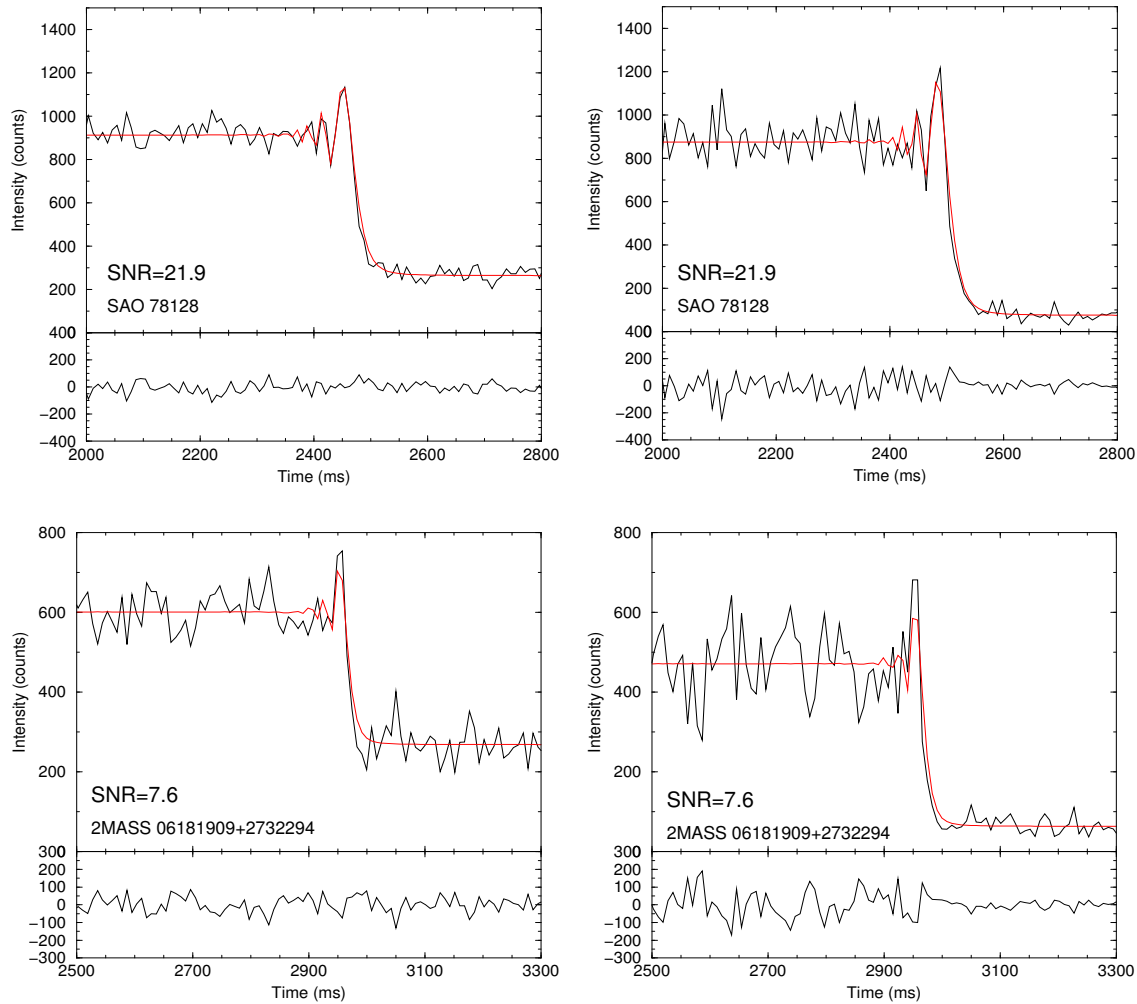
Figure 7.5: Comparison of lightcurve extraction with `Brightest-Faintest` and `SExtractor`-based algorithms. Two typical cases, a moderately bright (upper panels) and faint (bottom panels) source are considered, both of them unresolved and single. Left panels have been extracted with `Brightest-Faintest` algorithm with (N=15,M=30), while right panels by `3D-SExtractor`. In all the cases `ALOR` has been fitted to the lightcurve with a fixed value of the limb linear velocity equal to the predicted one. Note that `3D-SExtractor` provides noisier lightcurves in both cases. The apparent, but well-known and non-significant, flux underestimation at first and second fringe when `Brightest-Faintest` is used in the brighter source case is further explained in the text.

the amplitude proportion between the first minimum and first and second maxima[4] is the same as the one shown in the `3D-SExtractor` lightcurve. In addition, the

---

[4]That proportion is one of the factors which matters for a proper fit (single or binary) of the curve with `ALOR`.
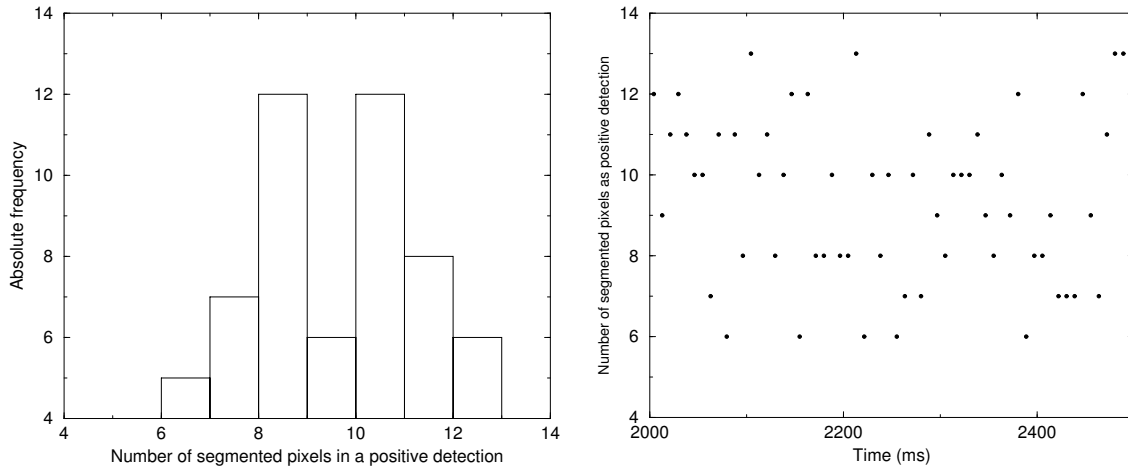
Figure 7.6: Consequences of temporal profile variation over the segmentation map resulting from the application of 3D–SExtractor algorithm in the SAO 78128 lightcurve, displayed in Fig. 7.5. Only those samples with positive detection, i.e., below the occultation time (t=2500 ms), were accounted for the completion of both figures. Left: histogram of number of segmented pixels assigned to belong to the detected source at each cube plane. Right: the same but plotted as a function of time.

noise approximately follows this proportional decrease, too. Therefore, again the flux underestimation is ruled out for Brightest-faintest algorithm.

Finally, we extended our comparison to the faint end (SNR<7) of our lightcurves repository. A batch lightcurve extraction for more than a hundred events was run with both Brightest-Faintest and 3D-SExtractor algorithms. The former showed identical flexibility and robustness as when it was run with brighter sources, apart from the unavoidable increase of noise due to the lower SNR. In contrast, 3D-SExtractor failed to provide useful lightcurves in most of the faint cases. For example, several spurious detections were accounted along a single lightcurve. This disfunction is understandable when noting that the approach of kernel convolution and segmentation phylosophy used by SExtractor was designed for a very different situation as the one we have now: the faint sources show very few pixels above the background level, a feature that, in terms of spatial frequency, cannot be effectively discriminated from single noisy pixels.

In the end, taking into account the problems of 3D-SExtractor with faint objects, and having confirmed the robustness and unbiased behaviour of Brightest-Faintest algorithm, it was decided to keep this latter as the default to be used in

our pipeline process.

WavLightPar: estimation of lightcurve parameters with wavelet analysis

Once a long lightcurve spanning several seconds has been extracted with Brightest-Faintest algorithm, the next step is to determine the values for occultation time (t_0), background level after occultation (B_0) and object source intensity (F_0). We recall these will be input parameters in ALOR as first iteration guesses. Therefore, their accurate determination is a key requisite for a proper ALOR convergence.

The problem we have in hands corresponds to detect an slope of certain frequency range along a noisy equally sampled 1D data series. The key idea here is to note that the first fringe magnitude drop is always characterized by a signature of a given spatial frequency. Of course, that frequency depends on the data sampling, but once this is fixed the algorithm we look for should be able to detect whatever first fringe magnitude drop, no matter its SNR is. Once t_0 is known, the other two parameters $(B_0$ and $F_0)$ are straightforward to estimate.

This problem description calls for a data transformation which is capable of isolating that frequential signature while keeping the temporal information untouch at the same time. Undoubtedly, wavelet transform is very convenient for this purpose, since, as was extensively explained in Sect. 2.3.1, it meets both above requirements.

The same *á trous* decomposition algorithm (Starck & Murtagh 1994) employed in Part I for deconvolution purposes was used in this occasion, with the only difference that it was adapted to the input of 1D data (Otazu 2004). A Mexican hat function was again chosen as the mother wavelet base function. This election was motivated by the convenience of already having the implementation done for the 2D case discussed in Part I.

The program, called dwd, performs a discrete wavelet decomposition of the lightcurve into n_{wav} wavelet planes. n_{wav} is the only input parameter fixed by the user, and $n_{wav} = 7$ was empirically found to be a suitable value for the particular first fringe frequency range and sampling (~ 8 ms) of our LO data. Each wavelet plane can be understood as a localized frequential representation at a given scale[5].

---

[5]According to the scaling function derived from the chosen mother wavelet base function. In the case of Mexican hat function, the scaling function corresponds to a B_3 spline.

The scale is represented by a power series of 2^n ($n = 1, ..., n_{wav}$). The 2th to 7th wavelet planes of the lightcurve of SAO 190556, a very bright star (SNR=43), are represented in Fig. 7.7. The 1st plane was excluded as it nearly exclusively contains noise features, not relevant for this discussion.

The algorithm, called `WavLightPar`, followed for estimating t_0, B_0 and F_0 from the previously created wavelet planes, operates in two steps:

First, it was determined empirically that the 7th plane serves as an invariant indicator, regardless the SNR, of the occultation time (t_0). In particular, t_0 coincides very approximately with the zero located between the absolute minimum (t_0^{min}) and maximum (t_0^{max}) of the plane (see upper right panel in Fig. 7.7). The good localization of t_0 in this plane is justified because the first fringe magnitude drop is mostly frequentially represented at this wavelet scale. In addition, the presence of noise is greatly diminished in this plane. This is because noise sources (electronic or scintillation) contribute only at higher frequencies, and therefore are better represented at lower wavelet scales (planes). In other words, this criteria for estimating t_0 is highly insensitive to noise and was found to be very efficient even for the lowest SNR cases. An example of this robustness is shown in Fig. 7.8, where even in the lightcurves at the limit of detection (SNRs=1 to 2) the value of t_0 is correctly estimated (additional check with predicted values of t_0 was performed).

Second, estimation of B_0 and F_0 can be obtained by considering the 5th wavelet plane. It was found that plane can indicate those values with fairly good approximation. The procedure is illustrated in Fig. 7.7 and described as follows:

1. the abscissa which defines t_0 at the 7th plane is practically the same as the one in 5th plane. Therefore, we consider t_0 at 5th plane,

2. from t_0, we search for the immediate previous and posterior zeroes in the 5th plane, which we call t_{before} and t_{after}, respectively.

3. we estimate B_0 by averaging the lightcurve values around t_{after} within an specified time range. We empirically fixed this to [-67,67] milliseconds, because it provided a good compromise between improving noise attenuation and suffering from occasional background slopes.
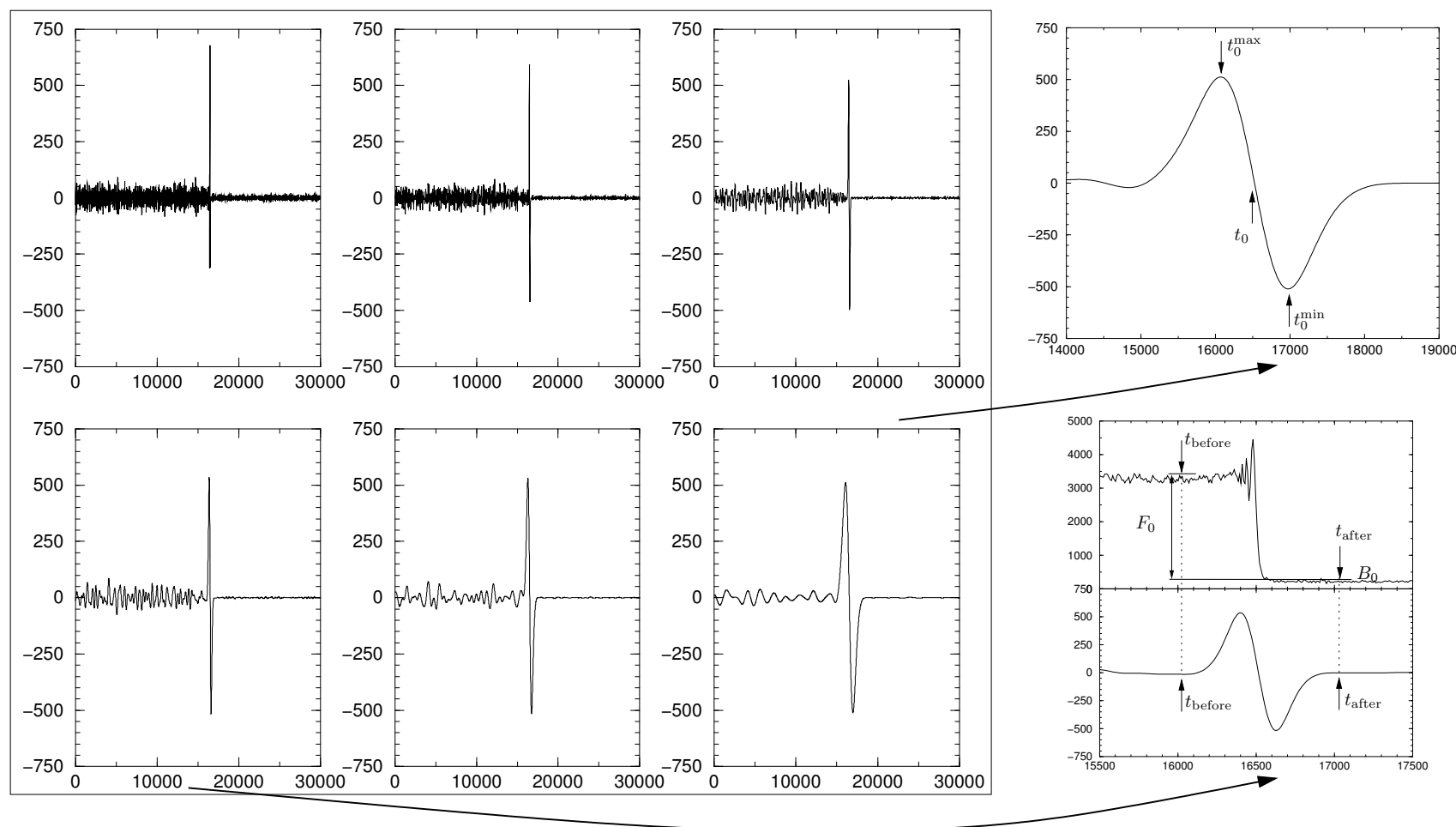
Figure 7.7: Schematic of the wavelet-based algorithm followed for automatically estimating t_0, F_0 and B_0 of the original lightcurve. Left: box with 2nd to 7th wavelet planes resulting from decomposition of original lightcurve by the *á trous* algorithm. Upper right: 7th plane was found to be a good indicator of t_0. Bottom right: 5th plane (bottom part of this panel) provides the abscissas where to compute F_0 and B_0 in the original lightcurve (upper part of the same panel). See text for further details.

4. the same window average is computed around t_{before}. The obtained value (I_{plateau}) represents a mean value of the intensity at the *plateau* region previous to the diffraction fringes. It is noteworthy that the 5th wavelet plane was chosen because its zero at t_{before} is safely before the fringes region, where the intensity is not constant.

5. F_0 is computed by subtracting B_0 to I_{plateau}.

As in the case of 7th plane, the contribution in the 5th plane is dominated by signal features represented at this scale, while noise, even the scintillation component, has a minor presence. Therefore, again, the estimation criteria for B_0 and F_0 turns to be very well behaved and robust in presence of high noise (low values of SNR).

`ALOR` and plot generation

Once `WavLightPar` provides the lightcurve parameters and the limb rate (V_{P}) and Moon distance are extracted from prediction file, `ALOR` is ready to fit a single unresolved source model to the data in the same way it is described at Sect. 7.5.1. We stress that is an automatic and unsupervised fit with the only purpose of generating a quick look plot. Therefore, V_{P} is kept fixed to the predicted value which, in most of the cases turns to be accurate enough for having a reasonable fit.

Once the pipeline process has automatically generated all the single source fit plots (data, model and residual files), it is time for the analyst to perform a quick visual inspection of them. The objective of this first evaluation is to separate those promising events which could bear positive binary detection or resolved diameter from the bulk of other objects which, either because of their low SNR or unresolved nature, do not have the same interest.

Afterwards, a more detailed and complete analysis is started for each one of the selected sources. This is done by following the methodology explained in Sects. 7.5.1 and 7.5.2.

The pipeline was coded entirely in `Perl` programming language, which turns to be a powerful and flexible tool for concatenating the I/O streams of independent programs like `dwd` and `ALOR`.
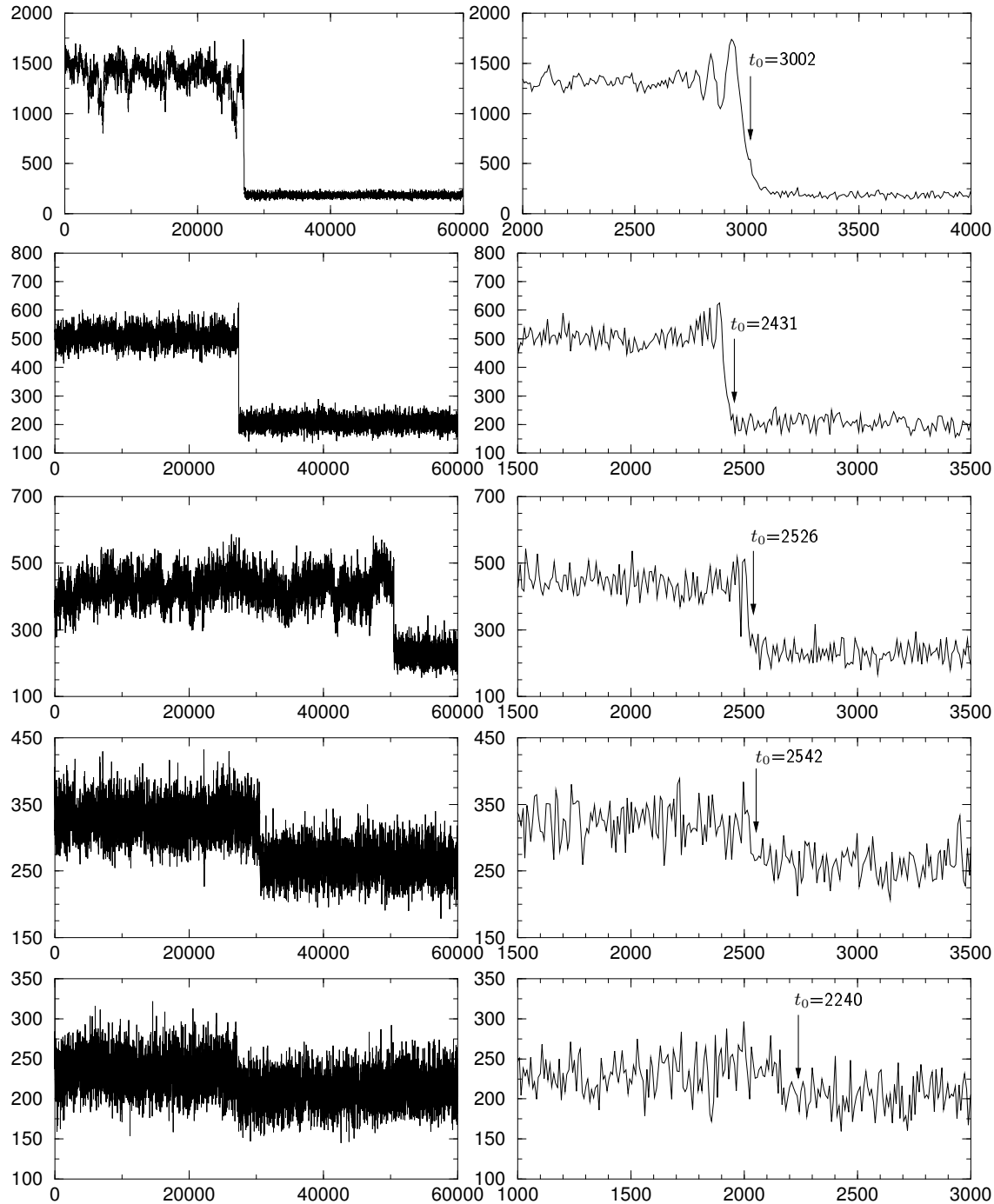
Figure 7.8: Application of the wavelet-based t_0 estimation criteria for lightcurves of different SNR (from upper to bottom: 20, 10, 5, 2 and 1). Left side panels represent the whole event lightcurve recorded by the camera (typically spanning for 60 seconds) and extracted by `Brightest-Faintest` algorithm. Right side panels illustrate the trimmed lightcurves (spanning for 2 seconds) around the estimated value of t_0. Note that even in the faintest cases, the occultation time is effectively detected.

Note this automatic pipeline frees us from the most tedious and error-prone part of `ALOR` reduction. On average, the pipeline spends no more than 10 seconds per occultation to complete the whole process described in Fig. 7.4. Comparatively, an experienced analyst took about 10 minutes per event for manually reaching the same stage of the reduction pipeline, and of course, with non negligible chances of committing errors.

Limitations of the automatic reduction pipeline

The presented pipeline works well for about 98% of the recorded events. There are, however, a few special situations where the algorithm of Fig. 7.4 fails. Those can be classified in three distinctive groups:

1. the current version of `WavLightPar` does not support wide binaries. In other words, it cannot simultaneously determine the values for $(t_0^A, B_0^A$ and $F_0^A)$ and $(t_0^B, B_0^B$ and $F_0^B)$. Certainly, with the appropriate sophistication, `WavLightPar` could derive those parameters for wide enough binaries. However, since these represent a few percent of the overall bulk of data, an effort to accomplish this feature has not been done yet. See upper panel of Fig. 7.9 for a illustration of this situation.

2. sometimes, for observational constraints reasons, large prediction O-C error or simply by observer mistake, the recording of an event is started few seconds before the actual occultation time. This is the situation shown in central panel of Fig. 7.9. The performance of the discrete wavelet decomposition is unavoidably affected by this: since the scaling function (B_3 spline) has a given size at each wavelet scale, there is a filter ramp effect which makes useless whatever analysis of the first R_n milliseconds. In our particular case this happens up to 4000 milliseconds from the beginning of the lightcurve, since this is the size of the scaling function at the scale of 7th plane.

3. on one hand, the size of the subarray where the object is continuously imaged is finite. On the other hand, the object has a given size over the array. As a result, if a large enough image motion occurs, part of the object profile can be displaced outside the subarray and the estimated flux will decrease accordingly. This can happen under extremely bad seeing conditions (strong wind) or when
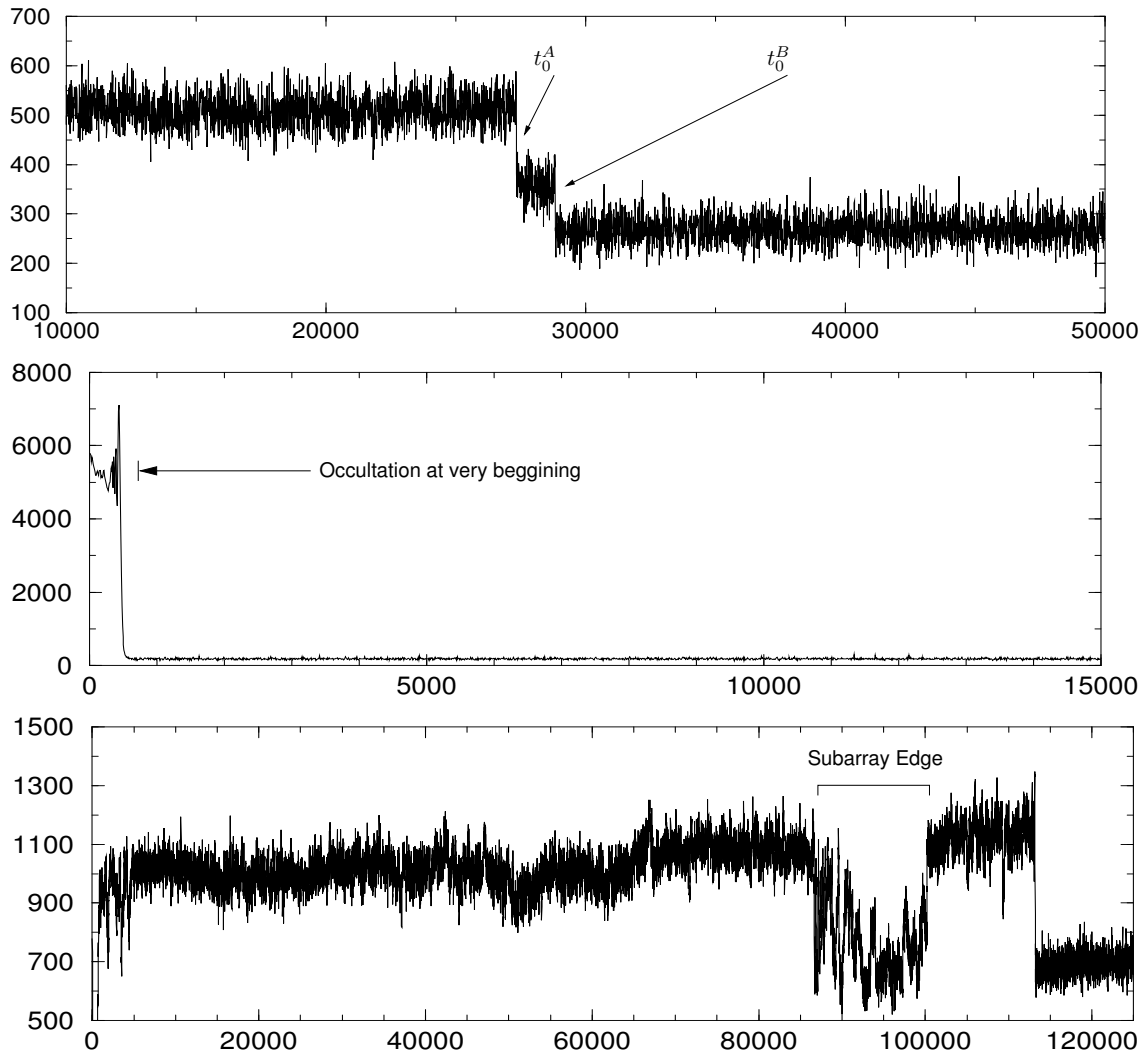
Figure 7.9: Three paradigmatic cases where automatic LO pipeline fails. Upper: a wide binary (SAO 110099; sep=623 mas). Middle: a bright star (2MASS 17425741-2813508) was recorded few milliseconds before its occultation, making useless the wavelet analysis. Bottom: the flux of 2MASS 17420326-2821070 star during the [85000,100000] ms interval was diminished due to subarray edge cutting. This was caused by defective telescope tracking.

observing at very low elevation, like in the case of Galactic Center passages seen from observatories at Northern Hemisphere as Calar Alto. The bottom panel of Fig. 7.9 shows an example of subarray edge cutting effect. Note that depending on how fast the object entirely returns to the subarray, the resulting slope is more or less steeper.

7.6 Fabra results

The two lightcurves were analyzed using `ALOR`, including a low-frequency term due to atmospheric turbulence and a high-frequency term due to pick-up noise. The latter is likely caused by telescope vibrations and electrical network interference. We computed lightcurves from raw strip images (see Fig. 7.3) by averaging central pixels of every column and subtracting the background estimated from the outer pixels. This represents an advantage of the proposed technique with respect to lightcurves derived from PEP systems, since it distinguises between source and background level in the recorded signal. In this way, $\beta(t)$ can be discarded from Eq. 7.7.

7.6.1 SAO 77911

χ^2 Ori (HR 2135, BD+20 1233) is a B2 Ia emission line star. Its angular diameter has been determined by indirect methods three times, with all values smaller than 1 mas (Pasinetti Fracassini et al. 2001). As stated in Table 7.3, this is suspected to be a close binary system, discovered by grazing LO (Reynolds & Povenmire 1975). There is great uncertainty in the separation of the components derived from that graze, since there were only two rather widely spaced stations. In addition, a tertiary component is catalogued. However, serious doubts about its actual existence have been cast of, since if it were really 1″0 apart, it would have been resolved by HIPPARCOS (Dunham & Bulder 2001).

The observation was conducted under partially cloudy conditions, and we are confident that the SNR of the resulting lightcurve could have been slightly higher under clear skies. Nevertheless, a visual inspection denotes a clear magnitude drop at the moment of occultation, and reveals at least the first diffraction fringe. The same occultation event was also observed few minutes before by TIRGO telescope with an IR photometer (λ_0=2.2μm).

A binary fit of both Fabra and TIRGO lightcurves was performed, and no evidence of binarity was found in either of them. Thus, we have assumed a single source model. In order to check the good degree of accordance of SAO 77911 Fabra lightcurve data with single point source model in Eq. 7.7, we show this in Fig. 7.10, along lightcurve data, the fit and residuals as calculated by `ALOR`.
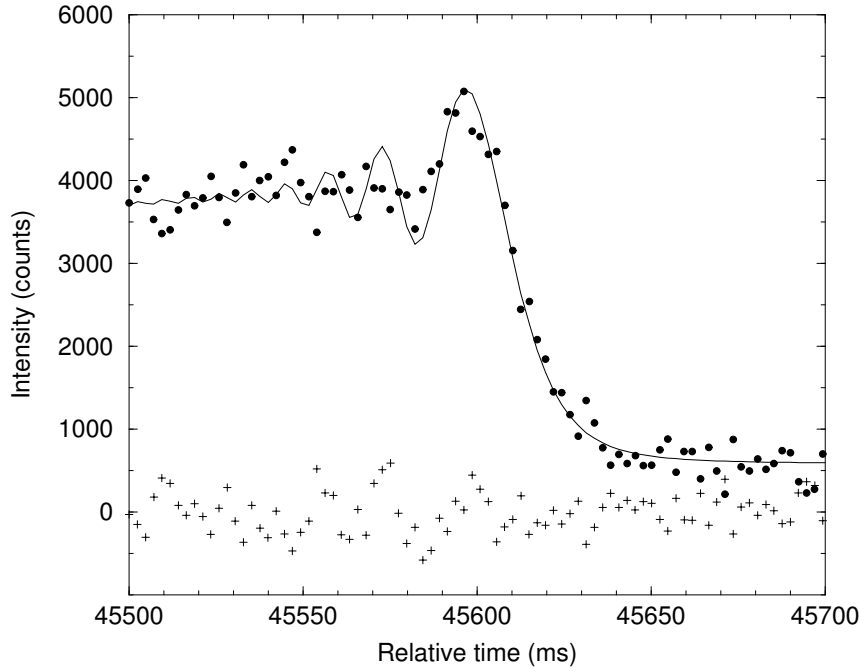
Figure 7.10: SAO 77911 occultation on March 13th, 2000 at Fabra Observatory under CCD fast drift scanning technique (see Table 7.3 for full description of the event). Data shown as dots, best point-like source fit as solid line, residuals as crosses.

7.6.2   SAO 79031

Mekbuda (HR 2650, ζ Gem, BD+20 1687) is a Cepheid variable whose fundamental properties (angular diameter, absolute radius, etc.) have been studied by several authors (see Table 7.6). Dunham & Warren (1995) catalogued this object as a multiple system, with the brightest component separated by $0.''10$. That was derived from a single visual observation made with a nearly full Moon (Dunham 2001). However, recent observations performed by modern optical interferometers clearly discard such duplicity (Nordgren et al. 2000). Therefore, hereafter we will consider SAO 79031 as a single object.

The recorded occultation is shown in Fig. 7.11: at least two first diffraction fringes can be clearly seen. The lightcurve is significantly affected by both scintillation and pick-up noise. Data analysis with ALOR accounted for both effects. On the other hand, in this particular case with small telescope, stellar diameters could be confidently derived only for very bright and large stars. As shown in Table 7.6, SAO 79031 appears to have an angular diameter smaller than the limiting angular
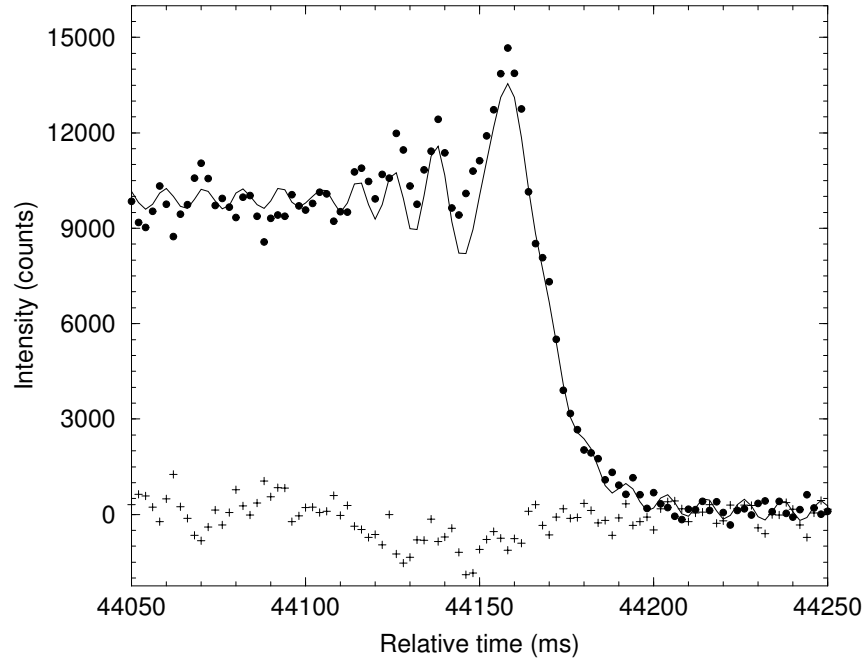
Figure 7.11: SAO 79031 occultation on March 14th, 2000 at Fabra Observatory under CCD fast drift scanning technique (see Table 7.3 for full description of the event). Data shown as dots, best point-like source fit with periodic pick-up noise term as solid line, residuals as crosses.

resolution imposed by our instrumentation (ϕ_m=4.0 mas with R filter bandwidth as Eq. 7.6). The lightcurve SNR appears to be insufficient to remove such smearing effect.

Table 7.6: Measurements of stellar diameter for SAO 79031

λ_0 (nm)	ϕ_{UD} (mas)	Observational technique	Reference
2200	1.6±0.5	Lunar occultation (1m telescope)	Ashok et al. (1994)
2170	1.81±0.31	Lunar occultation (4m telescope)	Ridgway et al. (1982)
2170	1.66±0.16	Optical interferometry (38m baseline)	Kervella et al. (2001)
1670	1.88±0.86	Lunar occultation (4m telescope)	Ridgway et al. (1982)
1650	1.65±0.30	Optical interferometry (104m baseline)	Lane et al. (2000)
800	1.60±0.05	Optical interferometry (8-31m baseline)	Mozurkewich et al. (1991)
735	1.48±0.08	Optical interferometry (37.5m baseline)	Nordgren et al. (2000)
450	1.66±0.05	Optical interferometry (8-31m baseline)	Mozurkewich et al. (1991)

Thus, as shown in Fig. 7.11, we have fitted the lightcurve using a single point-

source model. Superimposed over the theoretical diffraction curve we have included the a 90Hz pick-up noise. At the bottom, residuals give idea of the behaviour of scintillation component of noise. All in all, considering the modest equipment being used, the fit is in good accordance with the data points, showing that the proposed acquisition technique does not introduce any apparent bias or distorsion in the expected lightcurve diffraction pattern.

7.7 CALOP results

CALOP data was analyzed by means of `ALOR` and `CAL` as was described in Sect. 7.5. The automatic pipeline described in Sect. 7.5.3 was employed for preliminary reduction of all the lightcurves of runs E to O dedicated to binaries search.

The stars for which a positive result could be obtained are listed in Table 7.7.

Table 7.7: Summary of CALOP results. Line separates CCD from IR observations.

(1) Source	(2) $|V|$ (m/ms)	(3) V/V_t-1	(4) $\psi(°)$	(5) PA($°$)	(6) CA($°$)	(7) SNR	(8) Sep. (mas)	(9) Br. Ratio	(10) ϕ_{UD} (mas)
SAO 164567	0.6443	3%	−	(74)	(11)	14.3	2.0 ± 0.1	1.7 ± 0.1	
30 Psc	0.2473	−44%	20	122	69	46.1			6.78 ± 0.07
SAO 78119	0.5387	−3%	2	129	41	52.7	13.1 ± 1.1	34.2 ± 2.5	
V349 Gem	0.9462	−2%	8	106	11	65.9			5.10 ± 0.08
SAO 78258	0.6307	2%	1	45	−50	9.4	47.3 ± 1.5	8.6 ± 0.7	
AG+24 788	0.6910	3%	6	75	−13	16.9	28.8 ± 0.7	4.9 ± 0.2	
SAO 79251	0.7215	−1%	−1	85	−15	20.2	26.9 ± 1.1	17.6 ± 1.5	
SAO 80764	0.6568	−3%	−2	73	−45	26.3	42.5 ± 0.3	14.9 ± 0.3	
SAO 185661	0.3287	−5%	−2	155	60	23.7	37.9 ± 1.1	19.3 ± 0.7	
IRC -30319 A-B	0.5647	3%	2	136	44	52.6	15.0 ± 0.1	8.74 ± 0.04	
IRC -30319 B-C						16.1	21.8 ± 0.1	2.98 ± 0.01	
17454891-2809333	0.7720	4%	3	98	6	25.0	39.3 ± 0.7	17.3 ± 0.9	
SAO 165154	0.5870	24%	14	117	62	6.2	43.0 ± 1.9	4.7 ± 0.4	
RZ Ari	0.6520	−2%	10	73	11	41.3			10.6 ± 0.2
SAO 76214 A-C	0.3500	−5%	−2	131	56	7.8	13.0 ± 0.7	2.4 ± 0.1	
IRAS 04395+2521	0.6301	11%	8	135	49	21.4	6.5 ± 0.2	2.9 ± 0.1	
04440885+2540333	0.8013	−0%	−0	77	−10	3.9	15.6 ± 0.8	1.4 ± 0.1	
05415664+2707323	0.9208	−2%	−3	108	12	17.4	24.8 ± 0.3	7.8 ± 0.3	
HD 283610	0.5244	−5%	−3	121	38	9.1	19.4 ± 0.7	6.1 ± 0.3	
04264187+2500314	(0.8900)	−	−	(86)	(0)	3.8	89.5 ± 1.0	2.5 ± 0.1	
SAO 77000	0.4995	2%	−2	109	37	16.0	12.6 ± 0.3	1.49 ± 0.03	

The columns list the absolute value of the fitted linear rate of the event V, its deviation from the predicted rate V_t, the local lunar limb slope ψ, the position and

contact angles and the signal–to–noise ratio (SNR). For binary detections, the projected separation and the brightness ratio are given, while for RZ Ari the angular diameter ϕ_{UD} is reported, under the assumption of a uniform stellar disc. All angular quantities are computed from the fitted rate of the event. The only two exceptions are SAO 164567 and 2MASS 04264187+2500314. In the former the predicted contact angle was sufficiently close to zero that even a small difference of 3% between predicted and measured rate results in an imaginary value of the limb slope. In the latter, we were not able to reliably fit a rate, due to the low SNR. In both cases, the predicted, rather than measured, PA and CA values are listed in parentheses. Note that in the tables of this chapter the 2MASS prefix is omitted.

7.7.1 Binaries

CALOP results in the field of binaries are shown in this section. First, 1 new triple, 15 new binaries and 1 known binaries (see Table 7.7) are discussed separately. Their corresponding lightcurves and `ALOR` fits are shown in Figs. 7.12, 7.13 and 7.14. A second group of 3 wide binaries detected but not included in Table 7.7 will be commented. Finally, the non-detection of 9 known or suspected binaries will be discussed.

SAO 164567

This star was observed both by the HIPPARCOS satellite and radial velocity measurements (Duflot et al. 1995; Moore & Paddock 1950), but it was never reported as binary.

Apart from the CALOP positive detection, the same source was observed the same night from TIRGO, also yielding positive detection. Table 7.8 includes a comparison of binary parameters derived from both observations. Note that it is difficult to extract a true position angle from the combination of CALOP and TIRGO values. This is partly due to the relatively small difference in position angle predicted for the two sites (only 3°), and partly to the fact that the Calar Alto event was fitted with a speed that, in spite of just 2.9% excess over the predicted value, does not allow to compute unambiguously the exact position angle. This happens occasionally when a LO event has a very small contact angle.
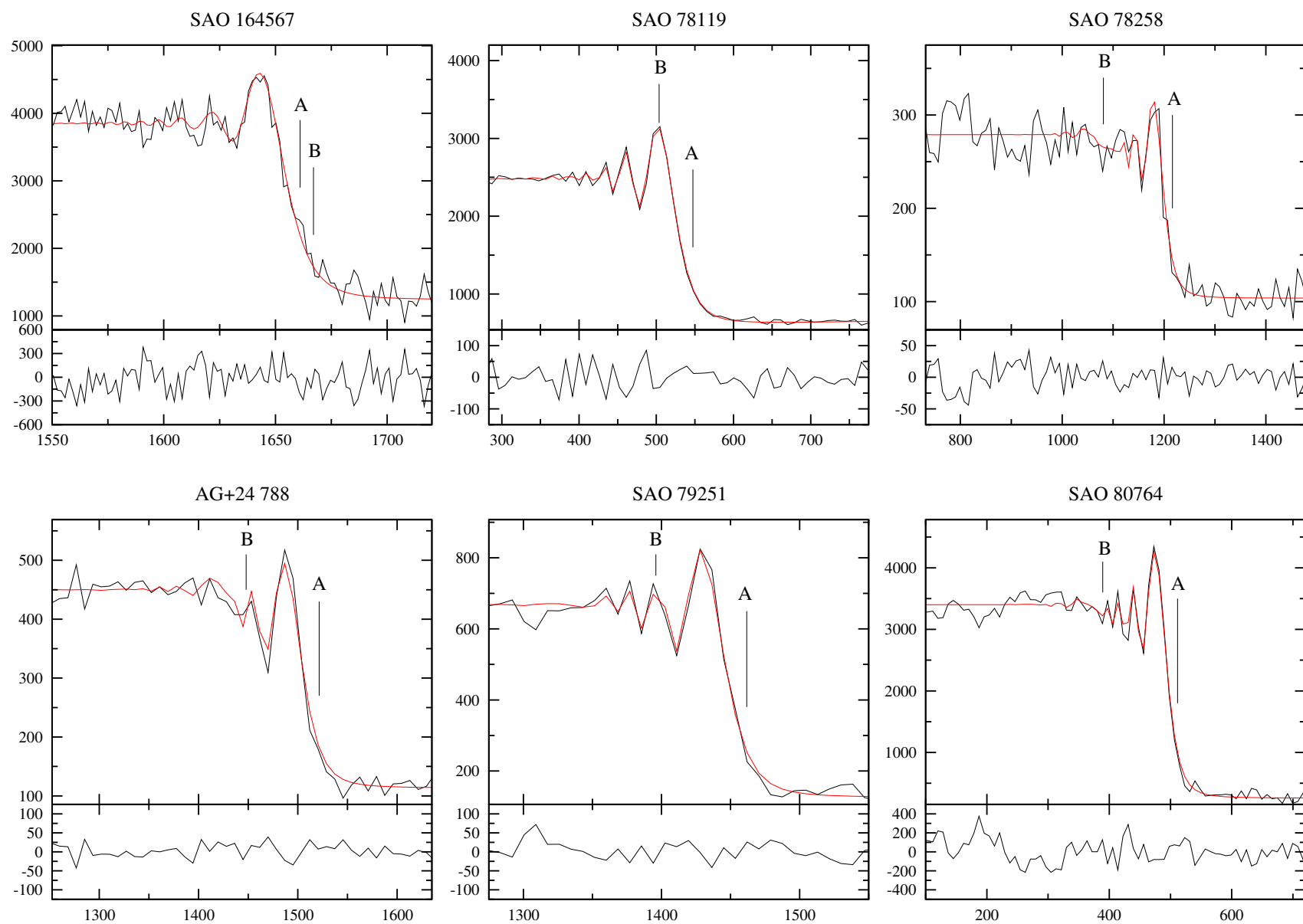
Figure 7.12: CALOP lightcurves with positive binary detection. ALOR fit are in red and residuals at the bottom. Position of the components are marked with letters.
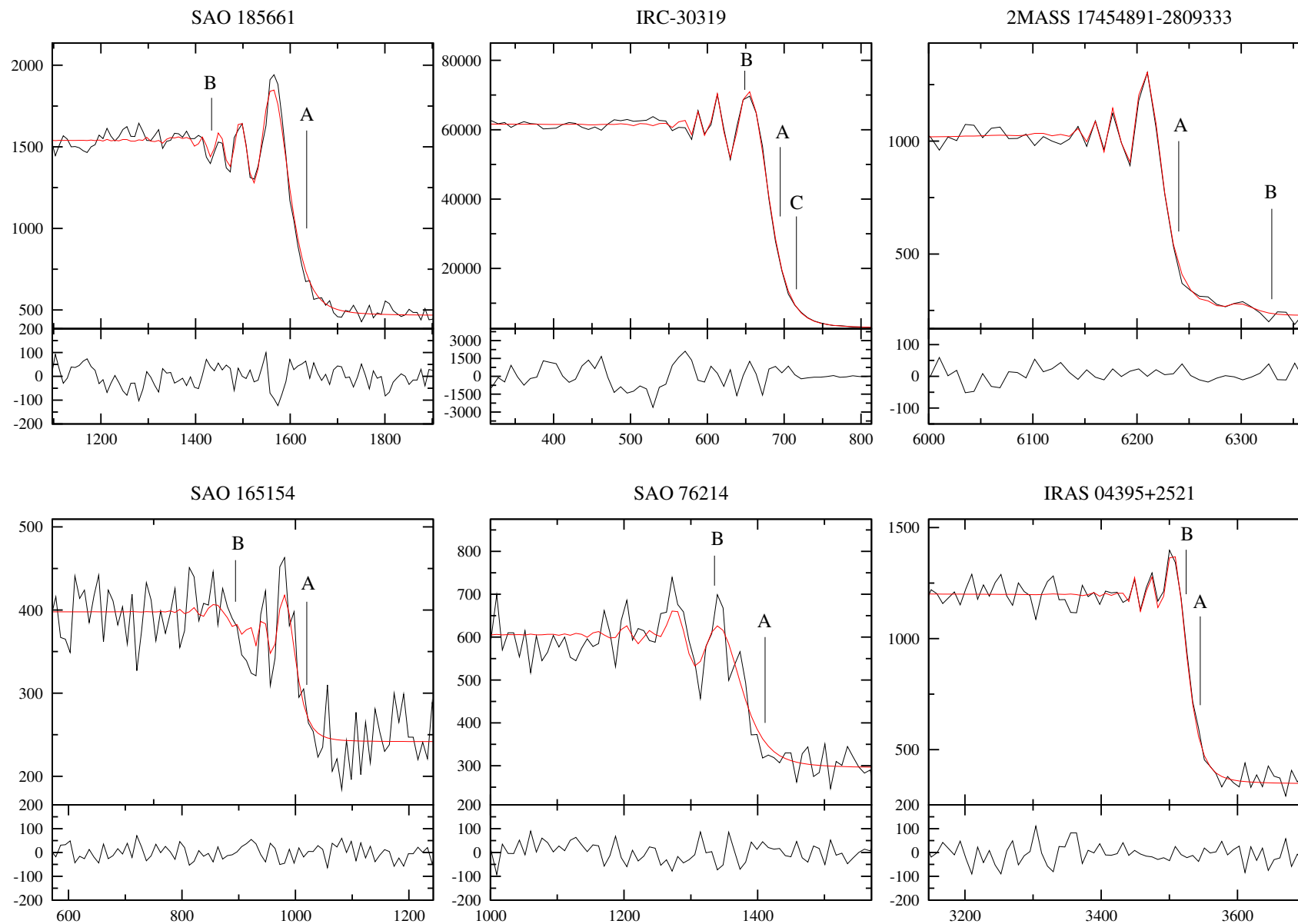
Figure 7.13: CALOP lightcurves with positive binary detection. `ALOR` fit are in red and residuals at the bottom. Position of the components are marked with letters.
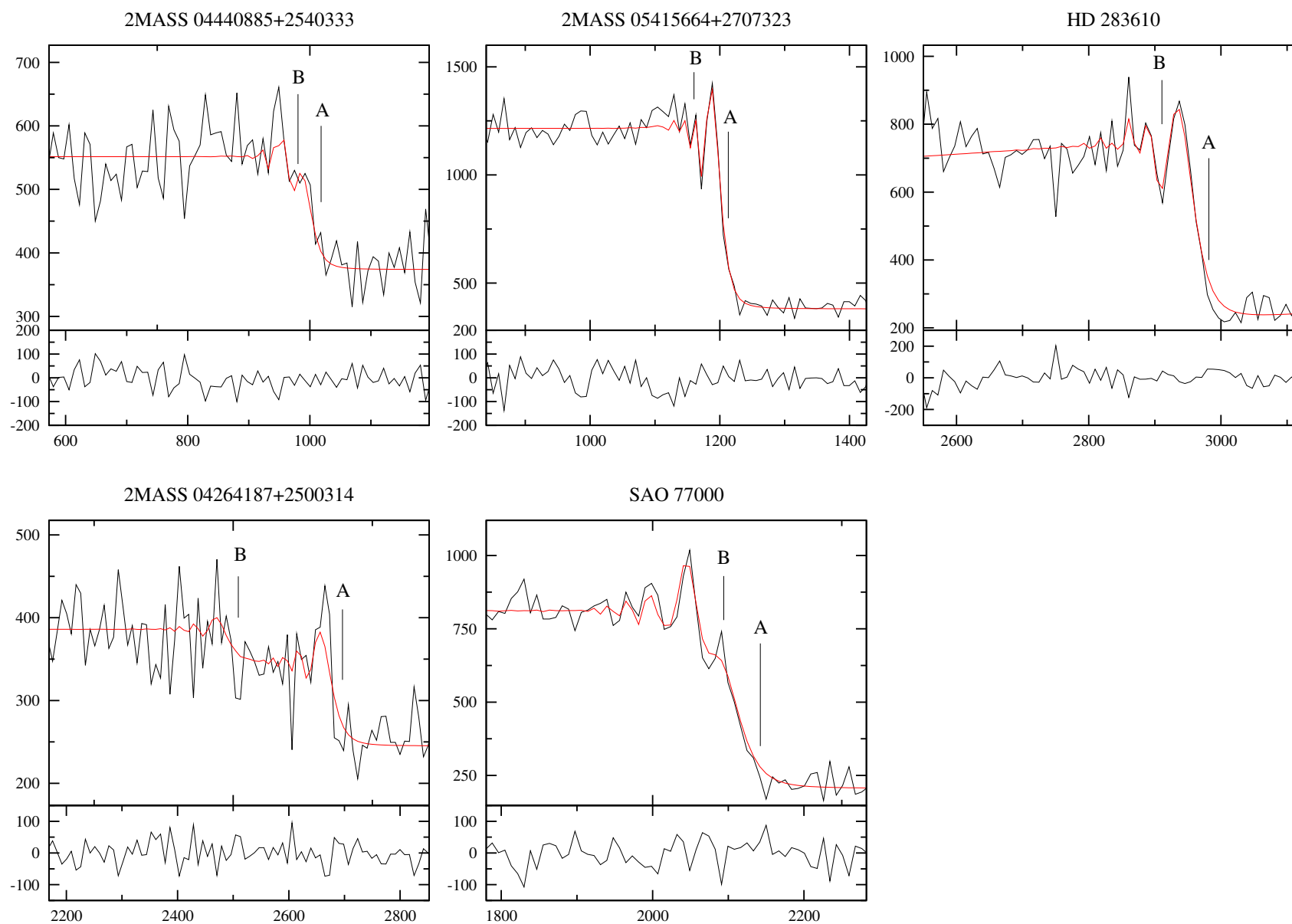
Figure 7.14: CALOP lightcurves with positive binary detection. `ALOR` fit are in red and residuals at the bottom. Position of the components are marked with letters.

Table 7.8: Results from nearly simultaneous occultation of SAO 164567 from TIRGO and Calar Alto observatories.

Observatory	$|V|$ (m/ms)	V/V_t-1	$\psi(°)$	PA(°)	CA(°)	SNR	Sep. (mas)	Br. Ratio	ϕ_{UD} (mas)
TIRGO	0.7325	3%	7	78	14	49.2	8.4 ± 0.2	6.8 ± 0.2	
Calar Alto	0.6443	3%	–	(74)	(11)	14.3	2.0 ± 0.1	1.7 ± 0.1	

We can only conclude that the companion is generally oriented towards the North, at a separation that could be significantly larger than the projected value of Table 7.7, up to ≈ 50 mas. Attempts to confirm the true position angle by techniques such as speckle interferometry are planned to be conducted, as will commented in Sect. 7.9.1. From the two events we have reliable magnitude differences both in the R and the K bands. This permits us to infer that the secondary is bluer, by $R - K \approx 1.5$ mag, than the primary. The primary is classified as a K5 giant (Houk & Smith-Moore 1988), therefore we estimate that the secondary should have $R - K \approx 0.9$, which would be consistent with a late A or early F star.

SAO 165154

A LO event for this star was reported by Evans et al. (1985), who did not find evidence of binarity. We note that the star is relatively faint in the visual and the secondary might not have been detected at that time for reasons of dynamic range.

SAO 76214

Although this star is a known binary (Mason et al. 2001b), our detection corresponds to a new component, with the characteristics listed in Table 7.7. We also detect the previously known component in our LO event record, with a separation consistent with PA=270° and separation 0″.5 listed by Mason et al. (2001b), but it is outside the scope of our observations to deal with such wide components. Moreover, the quantitative evaluation of the trace for SAO 76214 is hampered, especially on long time scales, by significant scintillation. We estimate the brightness ratio between the B and the A-C components to be 0.56 ± 0.10 in the K band. It is interesting to note that the Tycho Double Star Catalogue (Fabricius et al. 2002) examined this

pair and found a ΔV=2.59. However, LO (Africano et al. 1975) and visual estimates (most recently, Worley (1989)) found a much smaller value, $\Delta V \approx 0.3$.

Rest of newly detected binaries

The remaining newly detected binary stars listed in Table 7.7 have no previous report of binary detection.

Among these, the following objects have at least one bibliographical entry present in the SIMBAD database: SAO 78119, SAO 78258, AG+24 788, SAO 79251, SAO 80764, SAO 185661, the triple star IRC-30319, IRAS 04395+2521 and HD 283610. However these publications are on subjects not related to high angular resolution observations. There are no known either SIMBAD entry or previous publications associated with the four 2MASS objects 17454891-2809333, 04440885+2540333, 05415664+2707323 and 04264187+2500314.

Fig. 7.15 illustrates the confirmation of a tertiary component (left peak) in IRC-30319 system by means of the brightness profile obtained with CAL. Note that the pick around -46 mas is an artifact of the reconstruction due to noise. Also, the ratio of the peaks in this figure are only orientating and may not correspond to the measured values included in Table 7.7.

SAO 78258 was listed in the HIPPARCOS catalogue as single star.

Known binaries: SAO 77000

This star has been repeatedly observed by filar micrometry (Couteau 1972, 1975, 1979, 1987, 1989; Heintz 1980) as well as by HIPPARCOS. Orbital motion is apparent over the period of 20 years spanned by the observations, however no clear orbital trend can be deduced yet. Due also to the intrinsically larger errors associated with visual observations, it is hard to extrapolate a possible position of the component for the epoch of our LO event (2005.13). Nevertheless we note a general consistency of quadrant and magnitude of the separation. Our measurement provides a significant constraint, since it follows about 14 years after the most recent available measurement. Assuming to a first approximation that the magnitude difference observed by HIPPARCOS (ΔHp=0.58 mag) is similar to that in the V band, the compari-
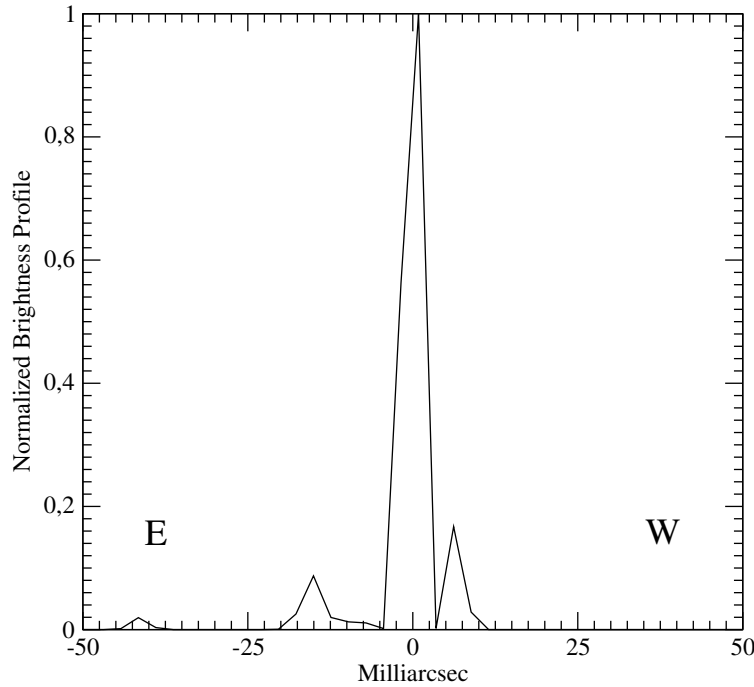
Figure 7.15: Brightness profile of IRC-30319 reconstructed by CAL.

son with the K band brightness ratio provided in Table 7.7 indicates that the two components have almost the same color, i.e. similar spectral types.

Wide binaries

We also mention that we have detected binarity in three further stars from Table 7.5, namely SAO 109617, SAO 110089 and SAO 78540. These are relatively wide systems, with separations in the of order $0''\!.5$, and therefore easily accessible to standard observations. For this reason, and also because LO are not very accurate for such large separations due to possible differences in local limb slope for the two components, we have not included these results in Table 7.7. However, we consider useful to report the brightness ratios in the K band. The values are 1.26 ± 0.02, 1.70 ± 0.03 and 0.5 ± 0.1, in the above order. It is noteworthy that all three stars have been measured at visual wavelengths by speckle interferometry and/or by HIPPARCOS. We quote, among others, Δm values of 1.66 mag (G band, Balega et al. (2004) and 1.87 mag (Hp band, Fabricius & Makarov (2000) for SAO 109617, and ΔHp values of 0.49 mag and 1.73 mag for SAO 110089 and SAO 78540, respectively (Fabricius & Makarov 2000). We note that these latter authors provide also Tycho B and V

magnitude differences. We do not speculate at this point on the combination of all these values with our K-band determination, in view of the diversity of spectral bandpasses used in the visual.

A number of stars from Table C.1 are additionally wide binaries with separations of several arcseconds, and we do not concern ourselves with them here.

Stars with negative binary detection

Among the stars for which we did not detect any binarity, a few are worth commenting either because of their known binary nature or because of previous attempts by high angular resolution techniques. After a close examination of the characteristics of the stars and a comparison with the circumstances and achieved performance of our observations, we conclude that there are no significant discrepancies (see Table 7.9 for a brief explanation of each non-detection). In the following, we provide a discussion of the individual cases which deserve special attention.

Table 7.9: Summary of negative detection results.

(1)	(2)	(3)	(4)	(5)
Source	ψ	PA	SNR	Notes
SAO 164553	-4	122	2.9	Outside field of view
SAO 165578/B	3	22	5.9	Too faint
SAO 165578/C				Outside field of view
SAO 78122	6	87	26.6	Large separation
SAO 78168	0	73	78.9	No details known
SAO 78197	12	110	31.8	Outside field of view
SAO 79257	10	74	6.0	Consistent with projection
SAO 80310	30	86	11.8	Previous non-detection with speckle
SAO 92659		(50)	25.0	Previous non-detection with speckle
SAO 164601		(110)	18.7	Not fine enough sampling

SAO 78168 was reported to be a double from visual occultation (Zhitetski 1977). However, this observation was catalogued as doubtful in XZ80 catalog (Dunham & Warren 1995) as the event was recorded to show gradual disappearance (Dunham & Herald 2004). In addition, no binarity is reported in the HIPPARCOS catalogue. Finally, we note that the occultation trace of this star could be recorded at a very

good SNR, permitting us to cover a dynamic range of almost five magnitudes from the primary.

SAO 79257 is known to be a subarcsecond binary, reported in the Washington double star (WDS J07181+2405) as well as in the HIPPARCOS (HIP 35344) catalogues. However, the entries are not entirely consistent for what concerns the position angles. WDS reports PA of 153° and 132° for epochs 1971 and 1991 respectively, with a separation of 0.″4 in both cases and a magnitude difference of about unity. HIPPARCOS reports a PA of 158° in 1991, with a separation of 0.″393. Given that the scan angle of our LO event (74°) was almost orthogonal to the PA reported above, the differences between HIPPARCOS and WDS are significant. We have used a binary star model to fit our occultation data of SAO 79257. The result was that the data are consistent with a binary separation of about 20 mas and a brightness ratio of about 2 mag (i.e., at the limit of the sensitivity permitted by the SNR). The resulting χ^2 was improved by only 4% with respect to the case of a single star model, and we cannot claim a positive detection. Our derived projected separation can be reconciled with the true separation, if the LO scan direction was about 87° from the PA of the binary. This would imply PA close to 161°, which is very close to the value measured by HIPPARCOS in 1991. We conclude that our data is not inconsistent with the presence of the known companion, and indicate that it would have to be significantly redder than the F5 primary. However, further conclusions are not possible given the uncertainties in the actual PA of the binary.

SAO 80310 was investigated by Mason et al. (2001a) by speckle interferometry, with negative conclusions. The same result with the same technique was reported by Hartkopf & McAlister (1984) for SAO 92659. Both these stars were also found unresolved by HIPPARCOS.

SAO 164601 is a spectroscopic binary, which was previously observed as double by Evans et al. (1986). These authors reported a separation close to 1 mas, although without information on the brightness ratio. We have analyzed our trace (SNR=18.7) with both the `ALOR` and `CAL` methods, without finding evidence of binarity. In any case, due to the near-IR wavelength and the relatively slow sampling, we are insensitive to separations of less than about 3.5 mas on this trace. We notice that the position angle of our event (110°) was almost orthogonal with that of the event observed by Evans and collaborators.

Passage over Tauri star-forming region

On 20th January 2005 a passage of the Moon over a Taurus star-forming region was recorded in the course of a CALOP regular binaries search run. The occultations of the following known young stellar objects were recorded: LH 98-106, DL Tau, GN Tau, Elias 3-18, ITG 31, LkHA 332. Unfortunately, the sensitivity offered by the OAN 1.5 m telescope was not sufficient to obtain quantitative results. Details on this sample of occulted objects can be found in Table 7.5.

7.7.2 Diameters

For sampling reasons of MAGIC camera CALOP data cannot be dedicated to diameters studies. However, we were able to resolve three sources on the whole program, one with CCD and two with MAGIC.

30 Psc

This long period variable is classified as an oxygen-rich AGB MIII giant without dust emission (Sloan & Price 1998). It has been catalogued by HIPPARCOS as suspected non–single. One speckle observation with a limiting resolution of $0\rlap{.}''054$ was inconclusive in this respect (Mason et al. 1999). Two interferometric observations in the K band by Dyck et al. (1998) led to an angular diameter of 7.2 ± 0.5 mas. This is in agreement, within the error bars, with our estimation given in Table 7.7. Further observations would be useful to assess whether there is a measurable dependence of the angular diameter with wavelength. Neither the interferometric measurements nor our LO indicate evidence of binarity.

V349 Gem

No previous high-angular resolution measurements are listed for this carbon star in the literature. Epchtein et al. (1987) have classified it as having a temperature below 2500 K, and a circumstellar dust shell of 400-1500 K. Our value for the angular diameter of this star seems to be consistent with its general properties. However, the
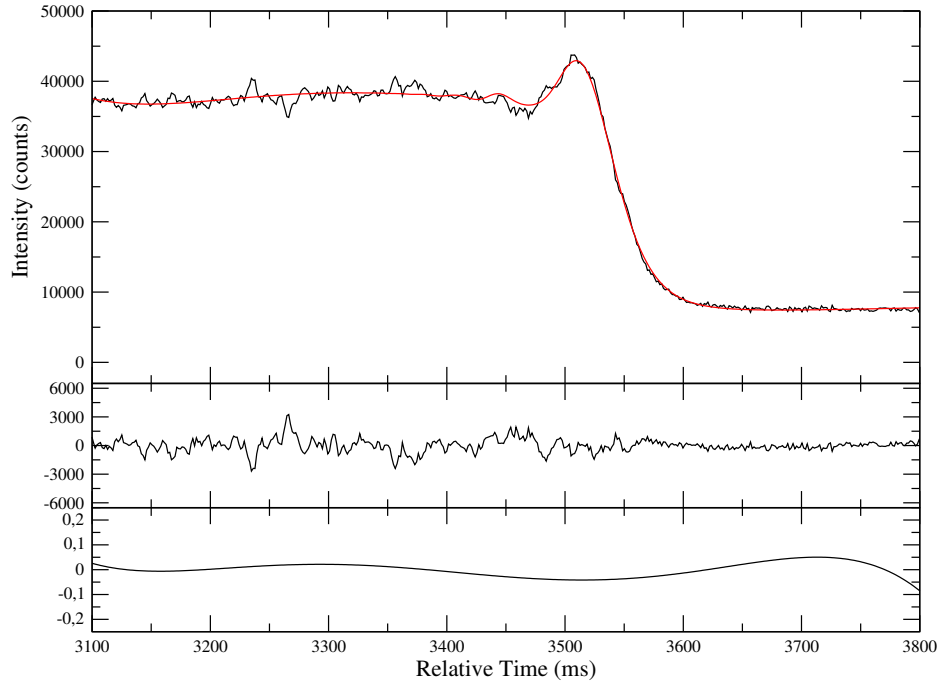
Figure 7.16: Top: 30 Psc lightcurve (black) and `ALOR` fit (red) corresponding to a diameter of $\phi_{UD} = 6.78 \pm 0.07$ mas. Middle: Residuals. Bottom: Low-frequency fluctuations due to scintillation modeled by Legendre polynomials.
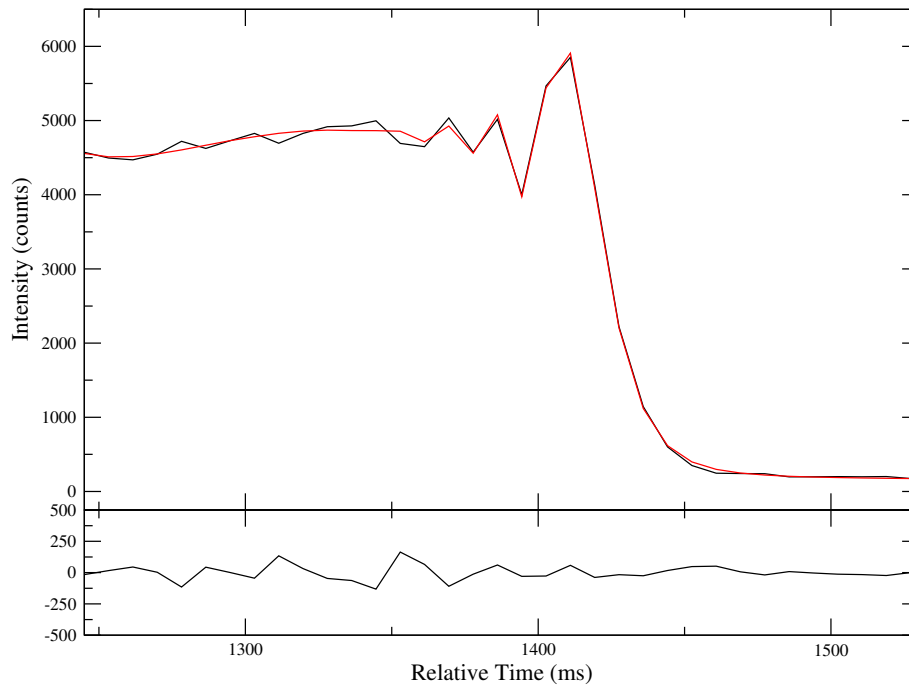
Figure 7.17: Top: V349 Gem lightcurve (black) and `ALOR` fit (red) corresponding to a diameter of $\phi_{UD} = 5.10 \pm 0.08$ mas. Bottom: Residuals.

spectral energy distribution of this source is poorly known, also considering its variability and that it is not possible to constrain significantly the effective temperature. Further photometric monitoring is desirable.

RZ Ari
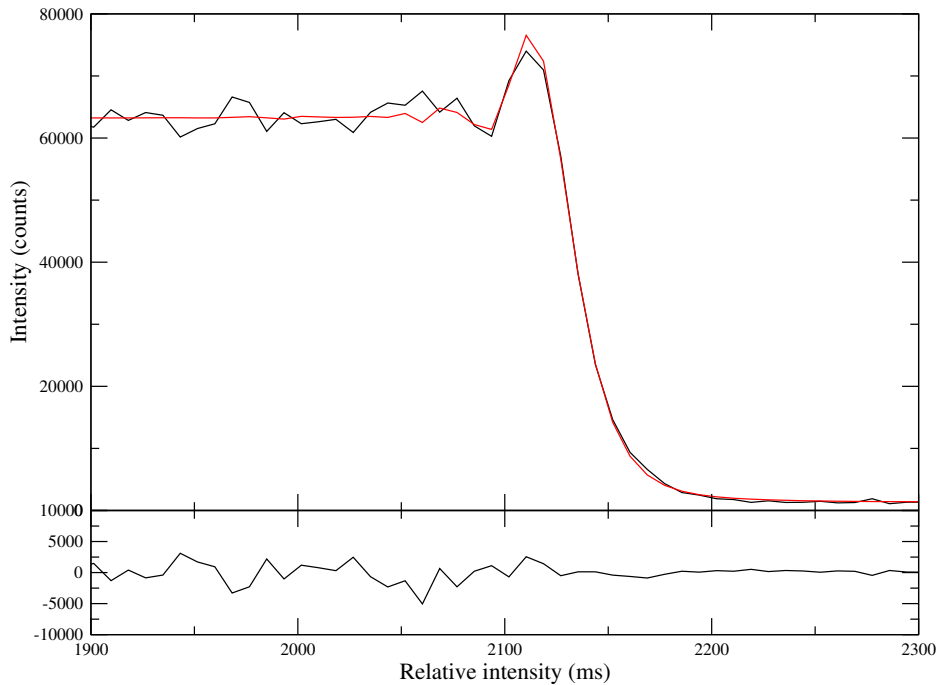
Figure 7.18: Top: RZ Ari lightcurve (black) and ALOR fit (red) corresponding to a diameter of $\phi_{\mathrm{UD}} = 10.6 \pm 0.2$ mas. Bottom: Residuals.

The bright, O-rich M6 star RZ Ari (45 Ari, ρ_2 Ari, HR 867) has been the subject of several investigations by high angular resolution methods. Five previously available angular diameter determinations are listed in the CHARM2 catalogue (Richichi et al. 2005). The results are somehow heterogeneous, including observations at various wavelengths in the optical and near-IR by LO and LBI, and referring to either uniform, partially or fully limb-darkened disk diameters (UD, LD, FD respectively).

The star is an irregular long-period variable, although the amplitude is relatively small (0.6 mag in Kukarkin et al. (1971)). In the near-IR the amplitude of variability is not well documented, and it can be assumed to be even smaller. An examination of the data available from the AAVSO shows a slight trend of increasing luminosity in about 0.5 mag over the past 30 years in which diameter measurements are avail-

able. Neglecting in a first approximation significant changes of angular diameter due to variability, we plot all available determinations in Fig. 7.19, using UD values. The conversion from LD and FD to UD has been done by using guidelines and conversion factors provided in the original references. The uncertainties in this conversion can be considered smaller than the error bars on the diameter determinations. It can be noted that there is a general agreement among the various determinations. A weighted mean yields the UD value 10.22 ± 0.12 mas. No definite trend of the char-
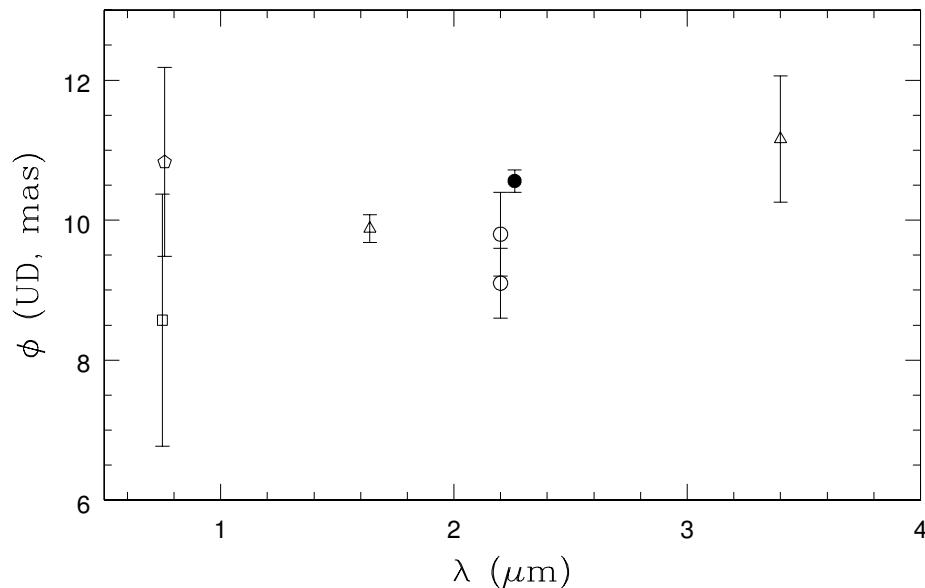
Figure 7.19: Angular diameter determinations for RZ Ari. The filled circle is our result, while the open symbols are: square Africano et al. (1975), pentagon Beavers et al. (1981), triangles Ridgway et al. (1980), circles Dyck et al. (1998).

acteristic size with wavelength seems to be present, as would have been expected in the presence of circumstellar matter, due to scattering at shorter wavelengths and thermal emission at longer ones. Therefore we can conclude that circumstellar matter is not dominant. This is independently confirmed by mid-infrared spectra, that show a featureless continuum around 10μm (Speck et al. 2000). Also, there seems to be no evidence of binarity, a possibility which had initially been postulated on the basis of HIPPARCOS results. (Percy & Hosick 2002) have discussed the origin of the problem with the HIPPARCOS data. Also speckle interferometry investigations by Mason et al. (1999) did not find companions. From our LO result, we can put an upper limit of $\approx$1:40 on the brightness ratio of a hypothetical companion with a projected separation in the range $\pm$70 mas.

RZ Ari has been used as a building block in several empirical T_{eff} calibrations, such as those by Barnes & Evans (1976); Barnes et al. (1978); di Benedetto (1993); Ridgway et al. (1980). Dyck et al. (1998) provided a revised value of the bolometric flux, and using their own LBI diameter derived $T_{eff} = 3442 \pm 148$ K. Of course, diameter variations must exist in this star, and therefore it seems of secondary importance at this point to discuss the accuracy of the various determinations and to refine the T_{eff} value. It would be more important to follow diameter and temperature variations with a dedicate monitoring, a possibility which is made available by several of the current interferometers.

7.7.3 Limiting magnitude

By plotting SNR as a function of the magnitude of the occulted stars, we can estimate an empirical relation for the limiting magnitude that can be achieved by CALOP observations both with CCD and MAGIC. This is shown in Figs. 7.20 and 7.21.
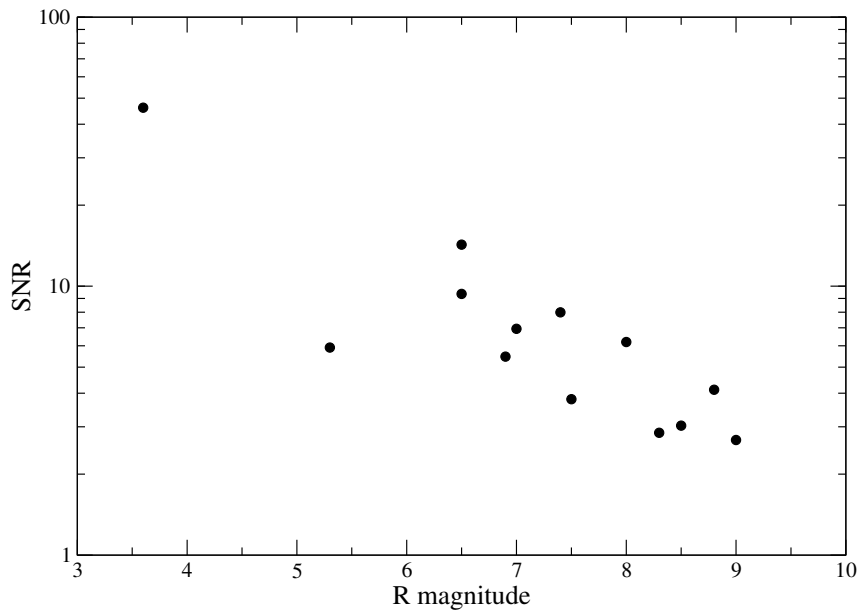
Figure 7.20: Relation between SNR and R magnitude, for CALOP measurements with CCD in run B.

It can be noted that in both cases the data indicate that the logarithm of the SNR of a LO lightcurve is approximately in inverse linear relation to the R and K
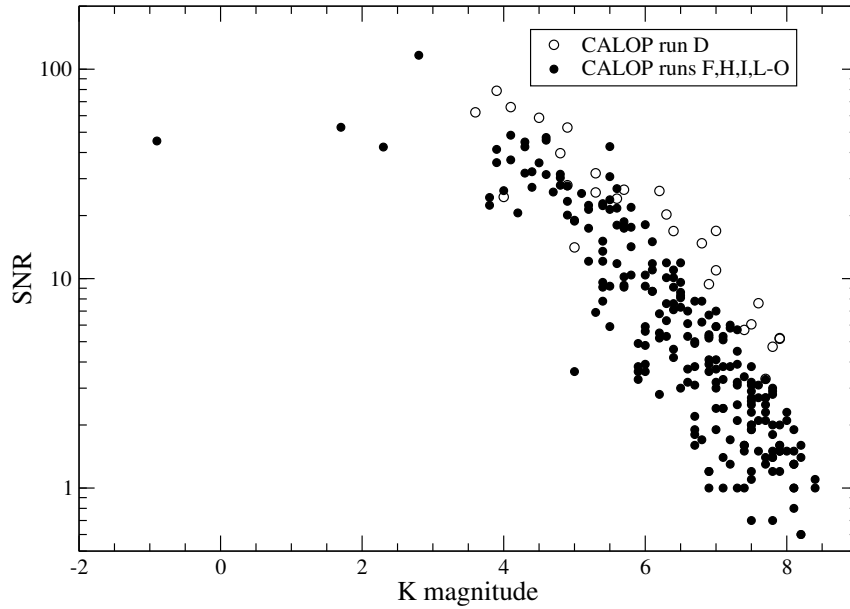
Figure 7.21: Relation between SNR and K magnitude, for CALOP measurements with IR MAGIC camera. Solid dots and open circles correspond to sources observed in runs F,H,I,L-O and D, respectively. Occultations of run J at CAHA 2.2 m have been excluded.

magnitudes. For studies of binary stars, companions with a brightness ratio close to unity can be detected already when the SNR is relatively small, in the range 1-3.

On CCD data, Fig. 7.20 shows that LO observations at OAN 1.5 m can be used for investigations of binary systems down to magnitudes R≈9.

However, the SNR-K relationship in Fig. 7.21 is not straightforward to interpret. For this analysis, we excluded the sources observed with the CAHA 2.2 m because they showed a trend which is offset from the main relationship by the expected factor of mirror area, a number of sources which were deemed too faint and plainly not binary and RZ Ari which was observed with a narrow-band filter. At the end, the sample contained 258 events. From these, two subsets were considered: 27 sources from run D and 232 sources from runs F,H,I,L-O. Comparing the SNR performance of both subsamples, the following considerations can be made:

1. On average, sample from run D shows a SNR about ×1.5 larger than the other subsample from runs F,H,I,L-O.

   About 2/3 of the events among the runs F,H,I,L-O were carried out with a wrong position of the pupil wheel which holds the cold stop. This had no effect

on the stellar signal, but produced a large increase in thermal background, resulting in higher noise and lower SNR than expected for a given stellar magnitude.

2. The SNR scatter in runs F,H,I,L-O is larger. This can be a consequence of a combination of two effects. On one hand, the noisier background stated above. On the other hand, a much larger database of LO observations implies a wider range of observing conditions (lunar phases, background levels, etc.). All in all, these constraints made the F,H,I,L-O subsample more inhomogeneous than that of the run D.

3. A second order effect contributing to the global dispersion of F,H,I,L-O subsample may be the intra-run dispersion. In other words, among these runs, the SNR dispersion between sources inside the same run is occasionally higher than the one in run D. However, note this only happens in some runs, not in all of them.

   All in all, part of the dispersion of this subsample seems to be related to star-to-star conditions of centering and/or possible biases in lightcurve extraction. Although we have not performed a quantitative calibration of this effect, it is likely to be less significant than to the two stated in 1 and 2.

4. The deviation of sources in bright end ($K < 2.5$) can be explained in terms of two independent factors. First, 2MASS catalogue guarantees a photometric bias of $< 2\%$ in its saturation limit $K \sim 4.0$. Thus, larger bias are expected for brighter sources as the ones on the left side of Fig. 7.21. Second, we note that size of the MAGIC subarray is limited. As a result, the lightcurve extraction algorithm (see Pag. 250) might also introduce a photometric bias when the star is very bright and very few pixels are due to background emission.

5. The outlier source around ($K = 5.0, SNR = 3.6$) was recorded at low elevation ($\sim 24°$) and in presence of intermitent clouds.

Despite of these considerations, the general characteristics of the same relationship are present in both subsamples. All in all, and taking into account all the sources in Fig. 7.21, we can state that LO observations at OAN 1.5 m, with the typical integration and sampling times of 3 and ≈ 8 ms respectively, can be used for investigations of binary systems (SNR$\gtrsim 3$) down to magnitudes K≈ 8.0. At the CAHA 2.2 m, used only for the very crowded passage near the Galactic Center, we

had a sufficient number of bright sources and the real limiting magnitude was not reached, but we estimate this to be $K \approx 9.0$.

It is interesting to compare this result of Fig. 7.21 with Fig. 3 of Richichi et al. (1996a), which showed a similar plot for LO data obtained also with a 1.5 m telescope (TIRGO) in the K band, but using a fast photometer. The IR array shows better SNR for the range K≈4-7 mag, probably thanks to the ability to reject more background signal and thus reduce significantly the photon noise in the data. Below K≈7 mag the advantage is less clear, due also to the scarcity and scatter of the data available for a comparison. One possible reason could be that LO events at TIRGO for such faint sources were recorded under conditions systematically better than average in terms of background (for example, at low lunar phases). In addition, we stress that MAGIC performance in this faint domain can be significantly improved, and therefore slightly beat TIRGO figures. This was shown to be possible for run D, when the correct pupil wheel which holds the cold stop was used. Regarding the bright end, very few sources with $K > 3.5$ were recorded in Fig. 7.21. However, as comented above, the limited size of MAGIC subarray may affect the SNR performance, which is inferior to the one showed in TIRGO figure.

The SNR scatter in both figures is similar. Both are programs with comparable number of events, collected over a wide range of lunar phases and background conditions. Again, we claim that MAGIC scatter had been smaller than the shown in Fig. 7.21 if the noisier thermal background when cold stop pupil was set to wrong position would have not been present.

7.7.4 Limiting resolution

An analysis of the limiting angular resolution achieved by CALOP observations was performed. The same definition of resolution and estimation approach described at Richichi et al. (1996a) was adopted. In brief, this consists in:

1. to consider a subsample of unresolved sources with enough SNR.

2. for every source, run `ALOR` over a wide range of fixed diameter values.

3. for every source, pick the diameter ϕ_R and SNR values from the fit which showed best residuals.
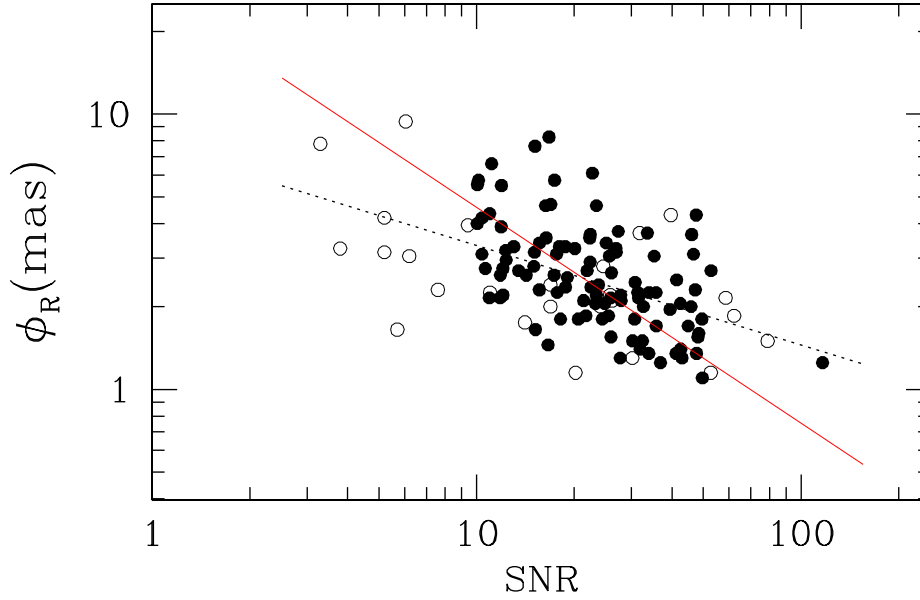
Figure 7.22: Limiting resolution ϕ_R for the unresolved sources in CALOP sample as a function of SNR. Open circles and solid dots correspond to sources observed in runs F,H,I,L-O with SNR>10 and B and D with SNR>3, respectively. The dotted line in black is a log-log fit through all points. The solid line in red is the trend shown in Fig. 5 of Richichi et al. (1996a).

4. plot this diameter value (which should be understod as limiting resolution) as a function of SNR.

ϕ_R was computed from two separate CALOP subsamples of unresolved sorces. First, 25 sources from runs B and D with SNR>3. Second, 103 sources from runs F,H,I,L-O with SNR>10. This higher threshold in the latter aims to avoid the SNR faint end inhomogeneity caused by the noisier thermal background when cold stop pupil was set to wrong position, and which was discussed in Sect. 7.7.4. The resulting limiting resolution is in Fig. 7.22. The figure shows, as expected, an improvement in the limiting angular resolution for increasing SNR. In particular, diameters below 2 mas are expected to be resolved for SNR values approaching 100.

It can be noted that the both CALOP subsamples have an almost identical distribution of limiting resolution against SNR, and can be fitted by the same log-log relationship. This is reassuring, since the behaviour be independent of the source, and be determined by the instrumental characteristics and in particular by the integration time. The large spread in the relationship can be understood in

terms of large variations of SNR from one LO lightcurve to another due to different situations of background and also to the specific conditions of signal extraction from the discrete pixels of the detector. Broadly speaking, the average relationship is such that SNR=10 ensures a limiting resolution of about 3 mas.

However, the slope of this function is significantly different from that of LO measurements obtained with an IR photometer. Fig. 7.22 shows the linear approximation (by least-squares fits) of our data (dotted line), and the same from Fig. 5 of Richichi et al. (1996a) for the TIRGO telescope (red solid line). It can be appreciated how the data obtained with CCDs and IR arrays (CALOP) provide a better performance in terms of limiting angular resolution in the low SNR regime. This is due to the better performance on faint sources, as already discussed in Sect. 7.7.3. However, the data obtained with the TIRGO photometer provide better angular resolution for SNR values above 20-30. This is probably due to the fact that in the bright source regime the advantages of arrays are less decisive, and the improved time sampling offered by photometers becomes important. Indeed, the sampling time achieved with our instruments (see column 5 of Tables 7.5 and C.1) is 2 to 4 times slower than what can be achieved by a fast photometer.

7.7.5   Binary detection probability

A final consideration can be addressed about statistics of binary detections in our sample. We have observed a total of 17 binaries (counting as such also the triple star IRC -30319), out of a total sample size of 388 stars. This points to a fraction of 4.4%, or more than two times smaller than what observed by Richichi et al. (1996a) and Fors et al. (2004b), this latter with a shorter and more homogeneous subsample of CALOP observations.

This result seemed puzzling at first, since all the samples considered have a broad sky distribution and should have similar characteristics. It is not excluded that the targets that we observed in the direction of the Galactic Center have an actual deficit of binaries, due to the fact extinction introduced a bias towards stars that for a given apparent magnitude are more distant than in the previous samples. Therefore, hypothetical companions would have smaller angular separations for the same statistics of semi-major axis. However, only 20% of the stars in our sample were observed in the direction of the Galactic Center, and another explanation must

exist for the lower binary fraction that we observe in the present work.

In fact we note that with the introduction of large, deep IR catalogues such as 2MASS in our predictions, we have effectively shifted the distribution of K magnitudes in CALOP sample much closer to the limiting sensitivity of the technique. Therefore, we can expect that most of the LO lightcurves will have on average lower SNR than in the previous samples. As a result, it will become effectively more difficult to detect companions, especially those with brightness ratios larger than unity. Although we have not performed a detailed computation of this effect, its magnitude could easily explain the observed apparent deficit of binary detections. We conclude that the introduction of large catalogues, while increasing the number of predictions and correspondingly of observed LO, does not automatically produce a higher rate of results.

7.7.6   Upcoming improvements in detectors technologies

We foresee that LO programs based on IR arrays as CALOP are likely to improve the former stated limitations in magnitude and resolution in the near future thanks to two aspects:

1. The technologies involved in both CCD and IR array manufacturing are under continuous improvement, thus producing detectors with better performance.

   For what concerns CCDs, three important achievements have recently occurred. Firstly, subelectron readout noise is being achieved at Megapixel rate thanks to L3CCD low–light chip technology (Jerram et al. 2001). This has been a major step forward for low signal applications, e.g., adaptive optics wavefront sensors (Downing 2005). Indeed, LO could benefit from this.

   Secondly, and in a less restricted and not so state-of-the-art market, on-board SDRAM memory has been recently implemented in commercial cameras (Apogee 2003b), enabling to store fast frame sequences without being limited by the data transfer interface throughput (USB, Ethernet).

   Thirdly, drift scanning readout modes have been natively implemented in the camera electronics with an accurate 25Mhz time base (Apogee 2005). Thus, our CPU-interrupt based time tick control approach would be no more needed. The manufacturer claims row shifts as fast as 5.12μs can be achieved.

All these improvements are of crucial importance for LO observations in the visual, since it opens the possibility of recording occultations at millisecond rates on the basis of real subframe mode (∼10-30 pixels wide), as opposed to the drift scanning technique which only records the flux of a few pixels. As a result, pixel scale reduction would not be needed and optimal resolution information could be obtained.

As IR arrays, and catering to the needs of adaptive optics, new prototypes with subelectron readout noise are also presently being introduced. In addition, faster on-board image storage memory will allow next-generation arrays to increase the time sampling of the occultation to 1 or 2 milliseconds, yielding an improvement in limiting resolution.

As a result, a significant improvement in SNR and resolution is to be expected in the near future. In particular, it is hoped that such technological achievements will be transferred to a wide range of detectors, and become available also to relatively low-budget programs such as the one described in this part of the thesis. In particular, access to fast, sensitive detectors at affordable cost could be the key to promote LO observations not only at professional large observatories, but also at smaller facilities. In turn, this could partially overcome some of the intrinsic limitations of LO, such as the lack of repeated observations at various wavelengths, epochs and position angles.

2. The increasing trend in allocating time availability in larger telescopes holds promises of increased LO performance in the near future. While LO have the advantage of providing an angular resolution which is not limited by the diffraction limit of the telescope, the technique is of course not insensitive to benefits of observing with large facilities. In particular for the case of binary stars, the increase in SNR achieved by moving to a large telescope is reflected directly in the range of brightness ratios of possible companions that can be explored, and also extends dramatically the number of stars that can be studied.

The extrapolation of LO observations to larger telescopes can be split into two diameter regimes. On one hand, telescopes in the 3-4 m class offer growing availability due to the increasing number of 8-10 m telescopes. The forthcoming 30-100 m facilities will accentuate this trend even more. By making use of flexible time allocation schemes, routine LO observations could be implemented with this class of telescope. Typically, a 3.5 m telescope would offer

a limiting magnitude gain of about 1.5 units in K with respect to the facility used in CALOP (Richichi 1994). On the other hand, telescopes in the 8-10 m class could be used for special opportunities, and achieve a performance of the utmost quality. An example of this is the Moon passage over a region close to the Galactic Center on March 2006, already scheduled at the VLT-UT1 (see Sect. 7.9.4). In addition, Richichi (2003) has investigated the possibility to use LO at very large telescopes to perform detailed studies of stars with exoplanet candidates. In the years 2004 to 2008, up to 14 events could be observed from the largest observatories.

7.8 Conclusions

A number of conclusions can be drawn:

1. A new CCD observational technique for LO has been proposed, implemented and validated. We demonstrated with two independent sets of data (with different telescopes) that CCD fast drift scanning at millisecond rate turns to be a viable alternative for LO observations.

   In particular, the detection of the very close companion of SAO 164567 (sep=2.0± 0.1 mas) with the OAN 1.5 m telescope is illustrative of the level of spatial information that can be extracted in this field of binaries detection.

   The diameter of 30 Psc was also measured to be $\phi_{\mathrm{UD}} = 6.78 \pm 0.07$ mas. Thus, when enough SNR is available, scanning technique can also be dedicated to diameter measurements. However, this could only be conducted in a regular basis with 3-4 m class telescopes.

   We remark that the proposed technique implies no optical and mechanical additional adjustments and can be applied to any CCD which supports charge shifting at a tunable rate. This applies for nearly all full frame CCDs of professional profile and in a large number on the amateur market. The use of an anamorphic relay lens for compressing pixel scale only in scanning direction could improve the derived spatial resolution.

   The recent CCD advances in terms of speed and sensitivity suggest that the performance of fast drift scanning could be even better than the one accomplished in our results.

2. A successful and prolific four-year LO program has been conducted at Calar Alto Observatory spanning 71.5 nights of observation and including a total of 388 recorded lunar occultation events. This constitutes the largest set of LO observed with an IR array. OAN 1.5 m and CAHA 2.2 m telescopes in combination to CCD and MAGIC IR array cameras were employed. The achieved lightcurve sampling was 2 and 8 milliseconds for CCD and IR array, respectively.

The results include the detection of one triple system (IRC-30319) and 15 binaries in the near-IR, and one binary in the visible. For all but one star (SAO 77000), these represent first time detections. Projected separations range from $0''.09$ to $0''.002$, and brightness ratios reach up to 1:35 in the K band.

Angular diameters of 30 Psc in the visible and V349 Gem and M6 RZ Ari in the near-IR were determined. They have been discussed in comparison with previous determinations.

The performance achieved in CALOP observations in terms of limiting magnitude and angular resolution have been calibrated. Limiting magnitude for binary detection was found to be $K_{lim} \sim 8.0$ and ≈ 9.0, for the OAN 1.5 m and the CAHA 2.2 m, respectively. Limiting resolution study yielded a value of $\phi_{\lim}$ ranging 1-3 mas.

The rate of binary detection in random observations of field stars that emerges from the present work is $\approx 4\%$, considerably lower than established earlier by similar studies (Richichi et al. 1996a) and (Fors et al. 2004b). We attribute this effect largely to the fact that the use of catalogues such as 2MASS has increased dramatically the number of occultations observable per night, but this increase is injected mostly at the faint magnitude end, where the dynamic range available is much smaller than for brighter stars.

3. CALOP observations have also included a passage of the Moon over a crowded region in the vicinity of the Galactic Center (resulting in 54 events observed in 1.5 effective hours), and a passage in the Taurus star-forming region. Passages of the Moon close to the Galactic center are taking place in these years. A list of exciting observations planed in near future such as the one at the VLT on March 21st 2006 is detailed in Sect. 7.9.4. These events provide a unique opportunity to extract milliarcsecond resolution information on a large number of objects in obscured, crowded and relatively unstudied regions, and can be

adequately observed with large telescopes.

4. A new wavelet-based method of lightcurve extraction and characterization, suitable to perform in an automated fashion the preliminary analysis of large volumes of LO events was developed and extensively used and tested with CALOP data. Typically, a few hundreds of occultations were reduced in matter of a few minutes, including the preparation of auxiliary batch files.

   This pipeline has been made necessary by the availability of large, deep near-IR catalogues such as 2MASS and DENIS, which permit the prediction and observation of a much increased number of occultation events.

7.9   Work in progress and future plans

This section is dedicated to describe these ongoing projects which have not been culminated before the completion of this thesis.

The first four subsections are in the observational stage and are continuations or extensions of the ones exposed in former subsections. The last one in Sect. 7.9.5 introduces an ongoing effort in applying wavelet decomposition for enhancing close binaries detection, overall in situations of low SNR.

7.9.1   Speckle follow-up observations

LO provide projected separations for detected binaries. A classical approach to confirm and obtain coomplete 2D information of these systems consists in conducting speckle interferometry observations.

A coordinated effort of follow-up campaigns was started in collaboration with two experienced teams of observers: E. Horch with the WIYN 3.5 m telescope and RYTSI CCD camera (Horch et al. 2004) and J.A. Docobo with CAHA 3.5 m telescope and ICCD speckle camera (Docobo et al. 2004).

The sample of LO binaries considered for being followed up is not restricted to the detected systems in CALOP. A more numerous set of LO binaries was extracted from latest version of CHARM (Richichi et al. 2005) which comprises LO measurements

from the compbination of several telescopes (TIRGO, Calar Alto, WHT, etc.) and detectors (IR photometer, IR array, etc.). This sample was selected according the observational limititations which visual speckle technique in a 3-4 m class telescope imposes: $V_{\mathrm{lim}}^{ICCD} \lesssim 13$ and $V_{\mathrm{lim}}^{\mathrm{CCD}} \lesssim 11.5$, $\rho_{\mathrm{lim}} \sim 40$ mas (diffracted limited) and $\Delta V \lesssim 3$. In the end, the candidates list comprises a total of 111 targets.

Table 7.10 shows the speckle follow-up campaings conducted so far.

To date, all these observations are being analyzed and preliminary results are not available yet. Thus, no conclusive results can be anticipated for neither of the binaries.

7.9.2 CALOP-II: extension to a long-term remotely operated program

As concluded in Sect. 7.8, a LO program in the CALOP style can delivers significant contribution in the field of close binaries. Despite these positive results, note that CALOP efficiency was considerably decreased by weather incidence (success rate around 30% along 69 nights of observation) and the limited number of observers.

Recently CAHA Executive Committee decided to open a call for proposals at the 1.23 m telescope for specific long-term programs. This telescope has a twin prototype of the MAGIC employed in CALOP along this part of the thesis. Therefore, the performance and limitations of the instrument for LO observations are very well-known. Also, and most important, this facility is being refurbished and automatized for enabling remote operational mode. This is crucial because it optimizes telescope usage, scientific output, manpower and cost, overall in the weather devoid nights.

During the last meeting of the CAHA executive committee on Oct 2005, CALOP-II was scheduled at 1.23 m telescope as a long-term program.

This is the approximate observing scheme which CALOP-II is expected to follow. On one hand, binaries search program will operate the 5 nights of crescent Moon up to the night of full Moon, this excluded and only over disappearances. This scheduling will apply only for the period from September to March, when Moon is high. Moon sets early on the first 3 nights of every run, leaving enough time to do JHK photometry of sources which has been occulted in former runs. On the other

Table 7.10: Summary of speckle follow-up observations of LO binaries conducted so far.

Observer	Telescope	Date	SAO number	Telescope+Detector of LO detection
Horch	WIYN 3.5 m	19 Dec 2004	76131	T
		19 Dec 2004	76140	T
		19 Dec 2004	98427	F
		20 Dec 2004	110723	T
		20 Dec 2004	93083	T
		20 Dec 2004	93127	F
		20 Dec 2004	76131	
		20 Dec 2004	76140	T
		20 Dec 2004	98427	F
		21 Dec 2004	110325	T
		21 Dec 2004	110723	T
		21 Dec 2004	93083	T
		21 Dec 2004	93127	F
		21 Dec 2004	93777	T
		21 Dec 2004	93950	T,F
		21 Dec 2004	78514	T
		22 Dec 2004	80764	CB
Docobo	CAHA 3.5 m	Mar05	78174	T
		Jul05	160179	T
		Jul05	162001	Q
		Jul05	164323	T
		Jul05	164567	CA,T
		Jul05	165154	CB
		Jul05	183637	P
		Jul05	185691	CC
		Jul05	186497	Q

CA: OAN 1.5 m + CCD.
CB: OAN 1.5 m + IR MAGIC array.
CB: CAHA 2.2 m + IR MAGIC array.
T: TIRGO 1.5 m + near-IR photometer.
F: CAHA 1.2 m + near-IR photometer.
Q: CAHA 2.2 m + near-IR photometer.
P: WHT 4.2 m + near-IR photometer.

hand, follow-up occultations of special events as Galactic Center or rich T Tau stars regions passages will also be conducted on the specific nights mostly located on March, July and October. All in all, CALOP-II is estimated to employ a telescope
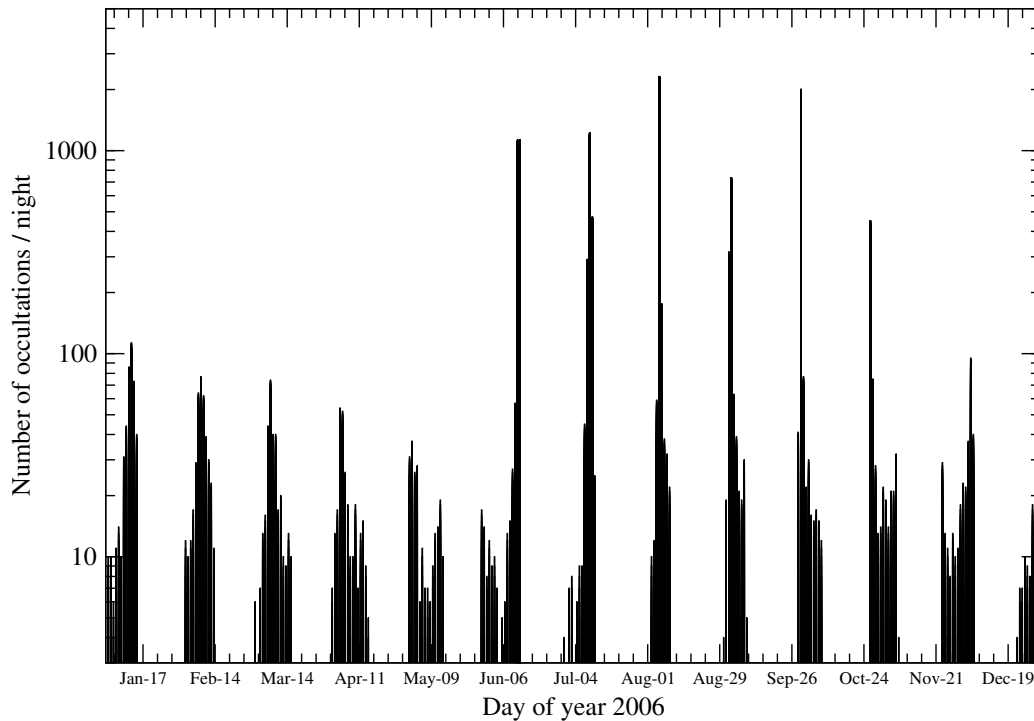
Figure 7.23: Day histogram of 14,289 potential occultations predicted for Calar Alto Observatory during the year 2006 with $K \leq 8.5$ mag. Only disappearances are considered.

time equivalent to about 40 nights/year, in comparison to the 17 nights/year used in CALOP.

In order to illustrate the outcome which CALOP-II is able to deliver, we below overview a few statistics of the potential objects to be occulted (disappearances only) during the year 2006 in Calar Alto Observatory. Fig. 7.23 helps in the understanding of the scheduling explained above. Note the larger number of global occultations in winter months, when Moon is high, but the richer single nights in summer when Moon scans Galactic Center region. These latter events will be further discussed in Sect. 7.9.4.

Fig. 7.24 includes the K magnitude histogram of the same sample of events. There is no particular magnitude distribution as, on average, the area scanned by the Moon during the whole year can be supposed to be uniform. No fainter sources have been considered as $K \sim 8.5$ is the limiting magnitude expected for the CA-1.23 m telescope.
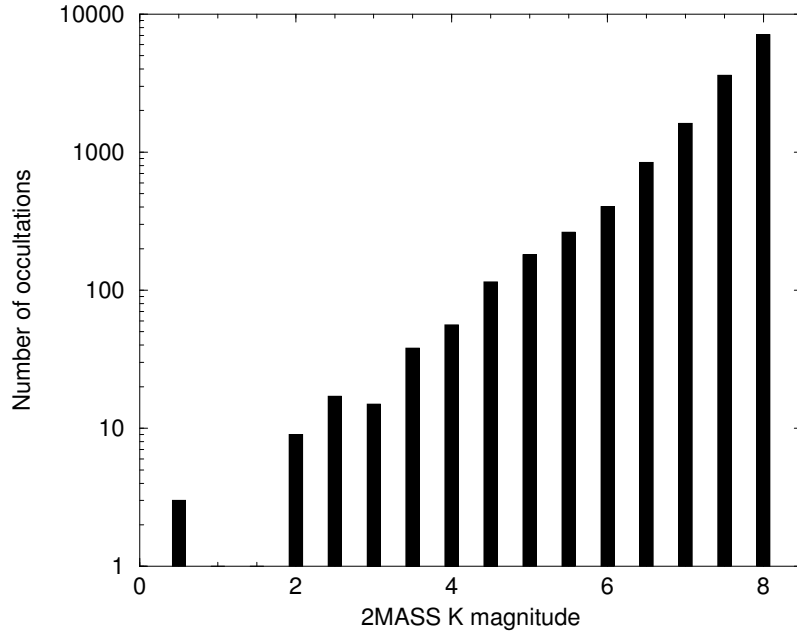
Figure 7.24: K magnitude histogram of the 14,289 potential sources to be occulted all along the year 2006 in Calar Alto observatory with $K \leq 8.5$ mag. Only disappearances are considered.

Fig. 7.25 provides a color-magnitude diagram for the sources being occulted. Note a number of very red objects ($[J - K] > 4$) is present, probably belonging to highly obscured regions as the Galactic Center. Excessive $[J - K]$ can be considered as a criteria for interesting occultations, since it can be taken as indication of additional circumstellar extinction.

Finally, we include Table 7.11 as an additional example of the great applicability of LO to diverse astrophysical areas. All the 14,289 occultations with $K \leq 8.5$ to be occured at Calar Alto Observatory during the year 2006 were predicted and automatically queried in the SIMBAD database. The object type information was extracted for every object, grouped accordingly and divided in two separate magnitude ranges. Despite only 19% of the objects are indeed classified in SIMBAD, the interest of LO is clear.

Finally, note the fact that CALOP scored a binarity probability of $\sim 5\%$ was because 2/3 of the runs were affected by thermal background resulting in lower SNR than expected. A more realistic probability of $\sim 10\%$ as the one achieved in TIRGO series (Richichi et al. 2000b) could be perfectly feasible for CALOP-II. Roughly, and taking into account the number of occultations disappearances during year 2006 and
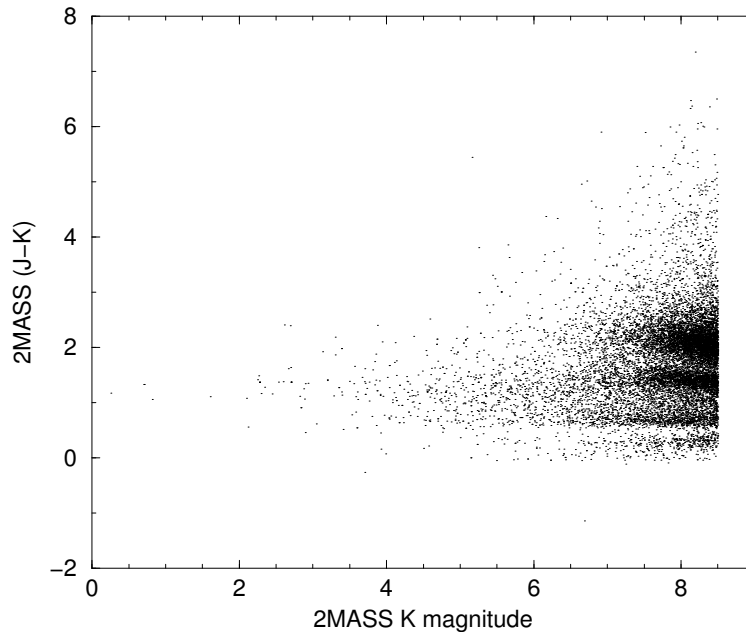
Figure 7.25: Color-magnitude diagram of the 14,289 potential sources to be occulted all along the year 2006 in Calar Alto observatory with $K \leq 8.5$ mag. Only disappearances are considered.

its day distribution from Table 7.23, a telescope and detector overhead of 75%, a weather success rate of 35%, we could tentatively expect a rate detection of $\sim$25 binaries/year. As a result, if CALOP-II could be maintained active during 2-3 years, could contribute very significantly in the field.

7.9.3   Special events

As stated in Table 7.4, a single-night observation (run K) was attempted at Calar Alto 3.5 m telescope in combination with OMEGA-CASS camera for obtaining high resolution information of Taurus star formation region. Unfortunately, this was devoid due to weather loss.

It is our aim to pursue in that kind of observations, where in a certain single night a 3-4 m class telescope can cover a number (10-15) of special events like these of T Tauri objects. The remaining time in between each T Tauri occultation will be filled to observe occultations of a large number field stars which will complement the ongoing program of detection of new binaries.

Table 7.11: Object type distribution as recorded in SIMBAD for the 14,289 potential occultations with $K \leq 8.5$ in Calar Alto Observatory during the year 2006. Only disappearances are considered.

Object type	Number of occultations	
	$K <= 6.0$	$6.0 < K < 8.5$
Semi-regular pulsating Star	5	3
Star in Cluster	2	28
Radio-source	0	1
Spectroscopic binary	0	1
Emission-line Star	1	4
Peculiar Star	1	0
Double or multiple star	10	46
Star	353	1459
Variable Star of Mira Cet type	3	9
Symbiotic Star	0	1
Variable Star of irregular type	3	0
Star in Nebula	1	0
Infra-Red source	50	56
Nebula of unknown nature	0	2
Variable Star of RR Lyr type	0	1
Carbon Star	6	2
X-ray source	1	3
(Micro)Lensing Event	0	1
Variable Star of Orion Type	0	2
T Tau-type Star	3	5
Pulsating variable Star	2	0
Star in double system	10	77
High proper-motion Star	9	23
Planetary Nebula	0	2
Variable Star of delta Sct type	0	2
Eclipsing binary	1	2
Variable Star	25	274
Reflection Nebula	1	0
S Star	2	0
Cluster of Stars	1	0
Variable of BY Dra type	0	1
Unclassified	260	11598

Other singular occultations can be worth to consider as potential LO targets. The object type distribution in Table 7.11 shows the large number of interesting

objects to be occulted for a 1.5 m telescope with a limiting magnitude $K = 8.5$ (the one estimated in basis of CALOP data). However, the number of potential occultations would increase if a larger telescope with a faster IR array were considered. For example, in the case of the 3.5 m telescope equipped with OMEGA-CASS at the same observatory, this would be able to detect detect up to K=10 binaries companions with 1:1 to 1:3 brightness ratio and measure diameters. Stellar diameters efficiency would be equally rewarded by the increase in SNR.

Finally, we point out several exciting occultations of extrasolar planets candidates in the near future (see Table 2 in Richichi (2003)). As was shown in that paper, LO at 8-10 m class telescopes can detect companions 5 to 11 mag fainter than the primary at separations of order $0.''01$. This enables LO as a simple technique for confirming hot-Jupiters candidates.

7.9.4   Galactic center passages at VLT

Special effort in this field was dedicated given during the semester before the completion of this thesis. The success of the pioneering Galactic Center passage conducted at CAHA 2.2 m (run J) motivated us to consider the appliance of same kind of events for larger telescopes.

Table 7.12 overviews the upcoming Galactic Center passages in Paranal and Calar Alto observatories. VLT-UT1 and Calar Alto 3.5 m telescopes were considered because they have IR arrays, ISAAC (Moorwood et al. 1999) and OMEGA-CASS (Lenzen et al. 1998), offering millisecond sampling in subarray mode. In the event at Paranal on Mar 21st 2006 Moon does not approach to GC at the level as the other four ones. However, it is scanning in the general GC direction and, as a result, will encounter a high stellar density region. The other events pass very close to the GC, specially the one in Paranal on Aug 5th 2006 approaching only $12'$. K_{lim} is accommodated according to telescope diameter and average stellar density (minimum GC-Moon approach) to provide a reasonable number of occultations. Note that in this regime LO efficiency is limited by telescope and detector overheads.

The lunar tracks for the five events of Table 7.12 are shown in Fig 7.26. Mar 21st 2006 passage is plotted separately in the top panel.

To date, only Mar 21st 2006 VLT proposals has been allocated. The expected

Table 7.12: Summary of upcoming Galactic Center passages for Paranal and Calar Alto Observatories during the year 2006. K_{lim} is accommodated according to telescope diameter and average stellar density (minimum GC-Moon approach) to provide a reasonable number of occultations. In this regime LO efficiency is limited by telescope and detector overheads.

Observing site	Instrument	Date	Start (UT)	End (UT)	Minimum GC-Moon angular approach (°)	K_{lim}	Number of occultations
Paranal	VLT-UT1	Mar 21st	04:05	10:46	13.11	11.0	802
Calar Alto	3.5 m	Jun 11th	21:01	02:46	1.95	8.5	2899
Calar Alto	3.5 m	Jul 9th	20:31	01:48	4.74	8.5	1586
Paranal	VLT-UT1	Aug 5th	22:27	06:15	0.20	7.5	1040
Calar Alto	3.5 m	Aug 5th	19:03	23:29	0.88	8.5	2315

limiting magnitude is $K \sim 11$ with a SNR sufficient to detect a 1:1 binary with 5 milliarcsecond separation, and to resolve angular sizes of 1 mas on sources of $K \sim 9$. This is more than 2.5 mags deeper than what was attained in run J with CA-2.2 m. We emphasize that this is the first time a LO run will be conducted in this fascinating area of the sky with such a outstanding telescope+instrumentation combination. This will allow us extract ~ 1 mas resolution information to a few hundreds number of sources with unprecedented level of SNR and accuracy. The variety of objects with astrophysical interest in both scans is astonishing. We just enumerate a few of them: cool giants and AGB stars, embedded IR sources, pulsating stars, Mira variables, flare stars, acreting X-ray binaries, planetary nebula, clusters of supermassive stars and even a supergiant VLTI calibrator.

7.9.5   Close binaries detection with wavelet analysis

In this subsection a brief report of the status of an ongoing project for using wavelet analysis in the detection of LO binaries. In particular, this effort is focused in those lightcurves with low SNR, where the standard analysis described in Sects. 7.5.1 and 7.5.2 is not able to yield positive companion detection. Despite no definitive results are available, a report of the procedure followed or intended to be followed is anticipated.
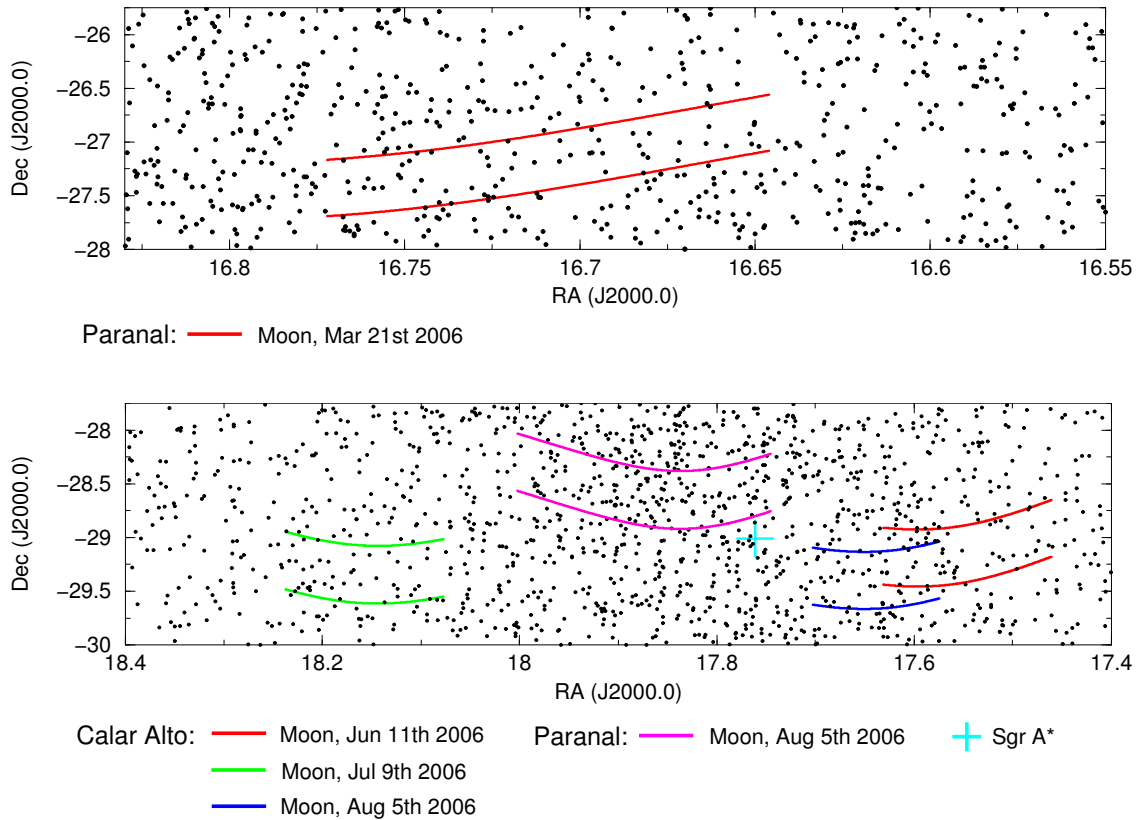
Figure 7.26: Lunar tracks for the upcoming Galactic Center (GC) passages during 2006 at Paranal and Calar Alto observatories. The event at Paranal on Mar 21st (top panel) is in the general direction of GC region with a high stellar density. The other four events (bottom panel) happen very close to the GC, specially the one in Paranal on Aug 5th (only a few arcmin ahead). Each pair of solid lines marks the edges of the path covered by the Moon. The dots mark the positions of 2MASS sources with $K \leq 8.5$ (top panel) and $K \leq 6$ (bottom panel). The position of the true Galactic Center (Sgr A*) is shown as a cross in cyan.

In Sect. 7.5.3 we employed wavelet decomposition for estimating the lightcurve parameters need for posterior fitting with ALOR. In brief, that was possible thanks to the good localization of t_0 in 7-th wavelet plane and the easy estimation of B_0 and F_0 in 5-th plane. It was shown that wavelet transform is very robust in finding these parameters, even in conditions of very low SNR (see Fig. 7.8).

One could wonder if other signatures of the lightcurves as for example the binarity could also be unveiled from the analysis of wavelet planes, and the noise robustness showed above could lead to a better detection of binaries in lightcurve with low SNR. Certainly, that is the situation of a large number of the lightcurves recorded

Table 7.13: Parameters of the three simulated noiseless and point-like lightcurves.

Identifier	Description	Separation (mas)	Brightness ratio
S	Single	-	-
B1	Wide and bright secondary	28.1	2.3
B2	Close and faint secondary	17.5	7.3

in CALOP.

To do this we have simulated with `ALOR` three lightcurves, one single and two binaries with the parameters shown in Table 7.13. All three are point-like, noiseless lightcurves with the same global intensity.

As seen in Fig. 7.27, the shape of the lightcurves differ considerably as a result of the interference of the diffraction fringes of each component. The `dwd` program has been applied to all three lightcurves in Fig. 7.27, for obtaining their discrete wavelet decomposition into $n_{wav} = 7$ planes of different scale. We show the results in Figs. 7.28, 7.29 7.30 for the S, B1 and B2 sources, respectively.

The following considerations from the comparison of these three figures can be stated:

- as derived from mathematical properties of wavelet decomposition based on *à trous* algorithm, the wavelet planes are null averaged, i.e., the total energy of every plane is zero.

- in general, appreciable differences between the wavelet planes of S and B1 and B2. In particular, 4th, 5th, 6th and 7th planes are the ones showing the most distinctive features in the binary cases.

- a large deviation in the original lightcurve shape from the single source case is translated into a larger number of distinctive wavelet planes. Note for example the notable difference between the 7th plane of B1 and the one from S, and on the contrary the little deviation from single source pattern of the one from B1.

As a possible analysis procedure over the lightcurves wavelet planes we propose the following approach. The binary i-th plane should be 1D deconvolved with the i-th plane of the single source lightcurve. This latter would be considered as the PSF
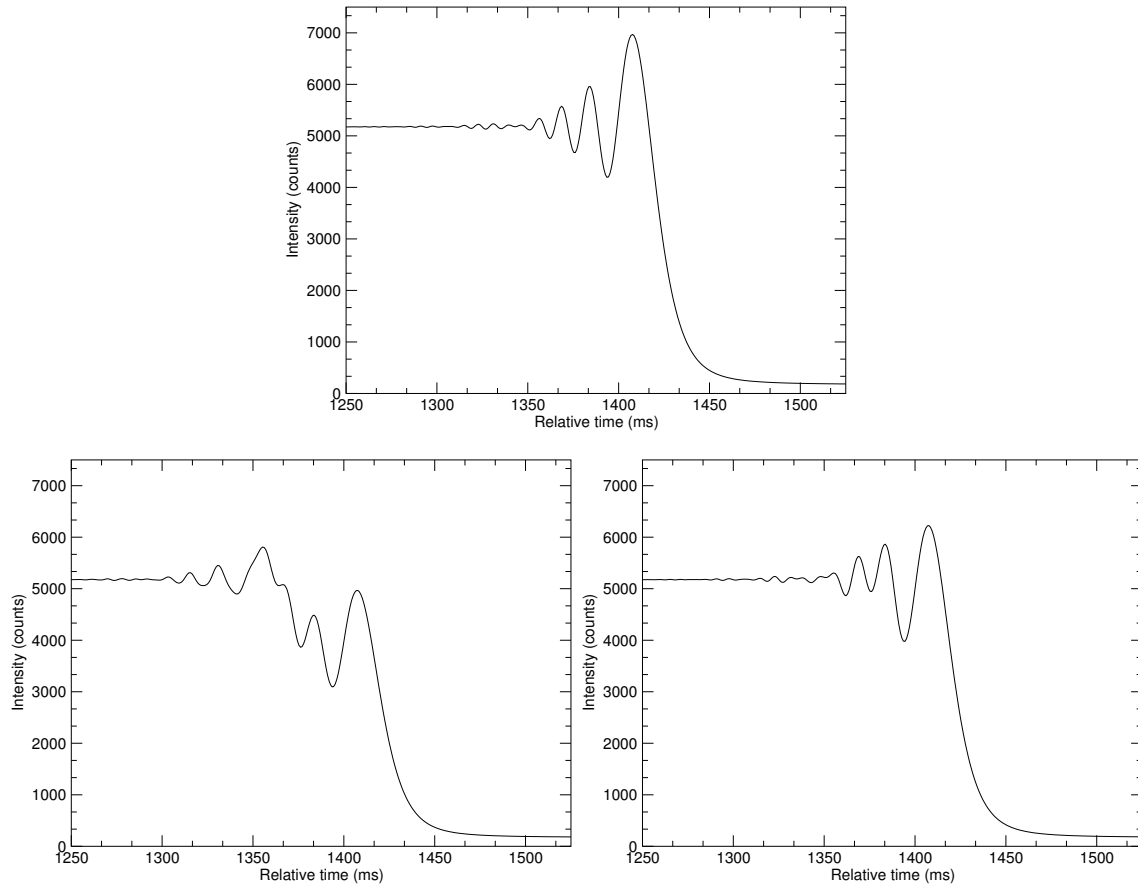
Figure 7.27: Simulated noiseless lightcurves of point-like sources. Top: single source. Left bottom: wide binary with bright secondary component. Right bottom: close binary with faint secondary component. The parameters of the simulation are shown in Table 7.13.

in this inverse problem. Ideally, the solution of this deconvolution process would be a set of δ-functions situated at the occultation time of each component. From there, the separation and brightness ratio could be extracted.

The CLEAN (Högbom 1974; Keel 1991) algorithm was chosen for this purpose because, to difference to other approaches as Richardson-Lucy or Maximum Entropy, can deal with non-positive images. Note also that wavelet planes are band-limited functions, which is a convenient regularization constraint in these deconvolution algorithms. Keel (2005) is in process of developing a new version of CLEAN for 1D data. Once this will become available the author will be able to further develop this study and evaluate the performance of this new analysis procedure under different situations of SNR, where wavelet transform is expected to show great robustness.

Note that no noisy lightcurves have been generated. However, it can be anticipated that, in presence of noise, the high frequencies due to this would be mainly isolated in the first wavelet plane. This is a well-known property of this transform, which was already evidenced Sect. 7.5.3and in Part I of this thesis. Lower frequency fluctuations caused by scintillation noise might be distributed along second and third plane. Therefore, the analysis situation would not majorly change with respect to the one we have in noiseless curves.
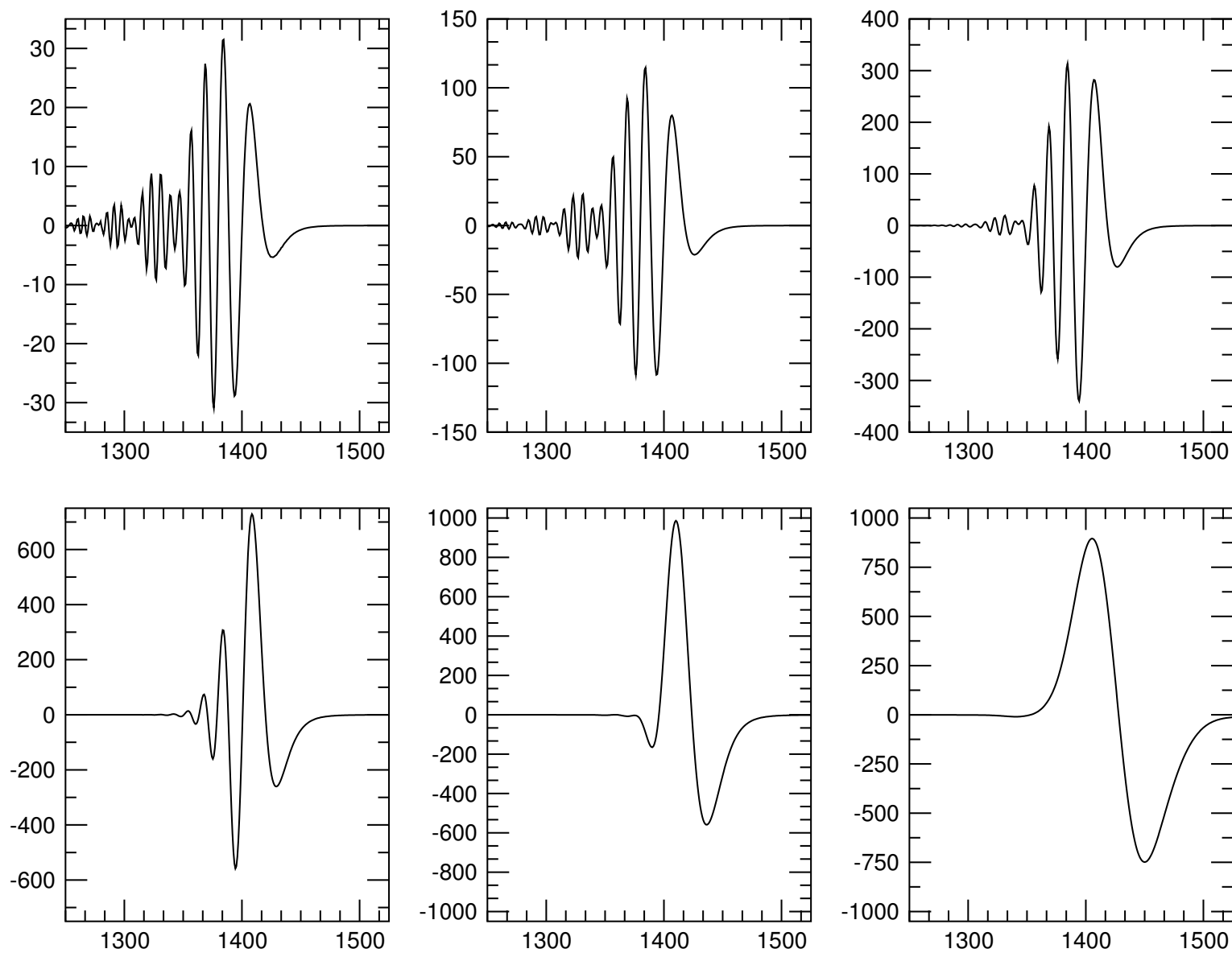
Figure 7.28: From top left to right bottom: Second to seventh wavelet planes of the lightcurve of a single source (see left panel in Fig. 7.27).
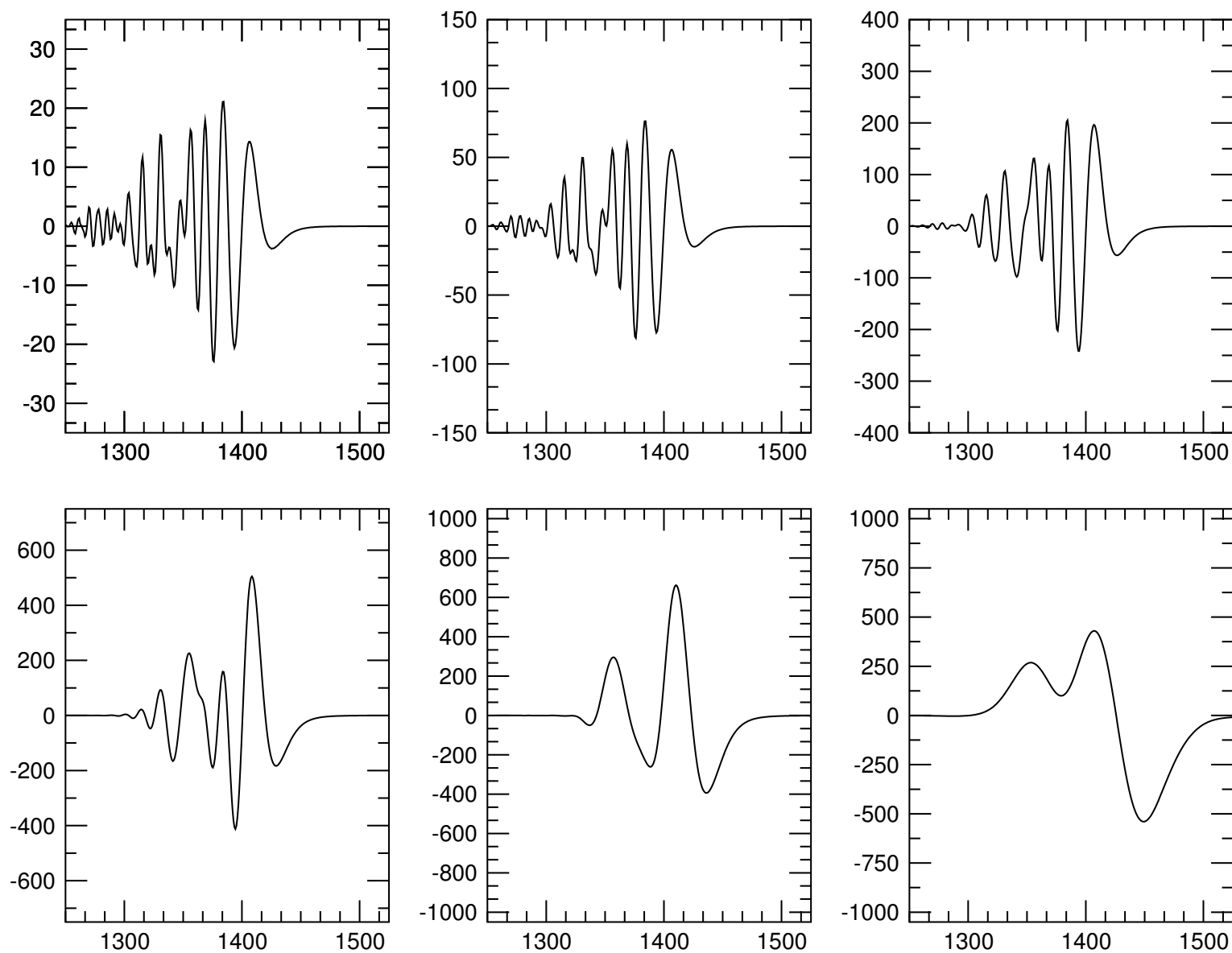
Figure 7.29: From top left to right bottom: Second to seventh wavelet planes of the lightcurve of a wide binary system (see central panel in Fig. 7.27).
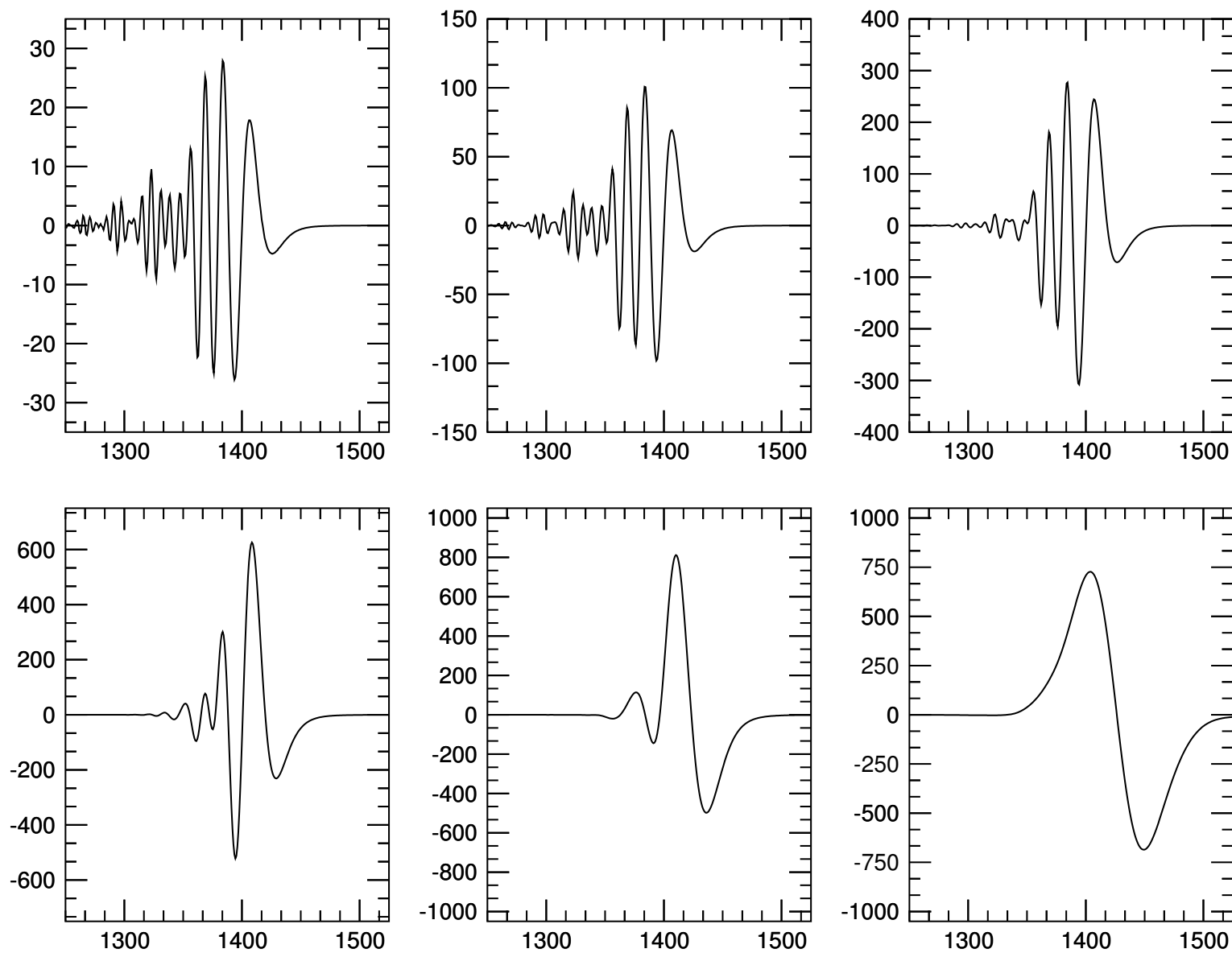
Figure 7.30: From top left to right bottom: Second to seventh wavelet planes of the lightcurve of a close binary system (see right panel in Fig. 7.27).

Chapter 8

Speckle interferometry

What is presented in this chapter has been partially published in Fors et al. (2004a) and presented in two symposiums (Fors & Núñez 2001; Núñez & Fors 2001).

In this chapter we will focus in the instrumental and analysis aspects of speckle interferometry technique. In particular, a new observing procedure and a new self-calibration method will be proposed.

8.1   Overview

Although a complete description of the physical phenomenon and a mathematical formalization of the problem would be desirable, this is beyond the scope of this study. Instead we refer the reader to Bates (1982); Horch (1995); Labeyrie (1978); McAlister (1985) for excellent review papers which discuss those and other aspects of this observational field. Instead, a brief descriptive overview of the speckle interferometry concept will be given.

Image resolution in large telescopes is limited by stochastic spatial and temporal variations in atmospheric refractive index. In the long exposure domain (> 1s), this turbulence leads to the appearance of the point-spread function (PSF), whose size is a number of times larger than the diffraction limit of the telescope. See Sect. 4.2 for a more detailed characterization of the PSF. However, in the short time domain ($<$ 0.1s) the situation is totally different: the refractive index inhomogeneities distribute

along the pupil image in a number of cells (*speckles*), which are on the order of 10 cm in size. The wavefront phase between speckles is different but not uncorrelated and it is approximately uniform within a single patch. Because of these two factors, the resolution content at the scale of the diffraction limit is not lost.

Labeyrie (1970) first established the basis of speckle interferometry for retrieving that limit-diffracted image information in the speckle pattern. If very short exposures frames (specklegrams) are recorded in a time scale of a few tens of milliseconds, the phase content in each specklegram can be considered stationary and time-independent. Therefore, if a large number of frames are recorded, the average image power spectrum $\langle|\hat{I}(\mathbf{u})|^2\rangle$ can be derived from the autocorrelation function of that series of specklegrams. When the observation sequence is repeated for an unresolved star, the same quantity gives us an estimation of the speckle transfer function $\langle|\hat{S}(\mathbf{u})|^2\rangle$. Taking into account the following expression derived from the convolution theorem:

$$\langle|\hat{I}(\mathbf{u})|^2\rangle = \langle|\hat{S}(\mathbf{u})|^2\rangle \cdot |\hat{O}(\mathbf{u})|^2 \tag{8.1}$$

the true binary power spectrum $|\hat{O}(\mathbf{u})|^2$ can be obtained by simple band-limited division. Consequently, binary stars parameters (separation, position angle and magnitude difference) can be directly retrieved from $|\hat{O}(\mathbf{u})|^2$.

Of course, speckle interferometry technique is not free of observational constraints. Smearing due to incoherence of polychromatic light and atmospheric color dispersion as a function of zenith angle are the most important ones for narrow field applications. Both can be minimized with the use of narrow-band filters and Risley prisms.

Note that Eq. 8.1 provides the object power spectrum $|\hat{O}(\mathbf{u})|^2$, but says nothing about its phase. Both components are needed if a reconstruction of the true diffraction–limited image is aimed. In view of this problem, a number of phase retrieval and image reconstruction methods were developed, extending the concept of speckle interferometry to the speckle imaging. These is a subset of these algorithms: closure phase (Rogstad 1968), speckle holography (Bates et al. 1973), phase unwrapping (Mertz 1979), Knox-Thompson algorithm (Knox & Thompson 1974) and directed vector autocorrelation (Bagnuolo et al. 1992) and bispectral analysis (Lohmann et al. 1983). This latter has been widely used in binary stars field and allows to obtain a phase map through the phase derivative information which bispectrum of the data contains. See further details on this in Sect. 8.4.

8.2 Data acquisition techniques

Apart from the above mentioned constraints, speckle interferometry technique requires the following specifications from the detector:

1. adequate time sampling interval. For visible wavelengths, this must be about a few tens of milliseconds.

2. high quantum efficiency. Under low light level conditions like these, a sufficient SNR in the fringes appearing in the spectrum is essential for obtaining accurate estimates of binary parameters.

3. low detector noise. Equally to the former item, read and dark noise should be minimized for keeping SNR within tolerable levels.

4. high dynamic range and linearity. The former assures that the same detector can be employed to study a number of objects spanning a wide range of magnitude. The latter is crucial for retrieving accurate Δm measurements in the case of binary systems.

Other features like an spatially and temporally uniform intra-pixel and inter-pixel response is equally important for disposing of homogeneous and astrometrically accurate data.

CCDs appears to be specially appealing for what concerns to 2. and 4. However, 1. and 3. are still to be completely met, at least attending to the standards of current professional and commercial CCD market available. Despite of this non-optimal panorama, several ingenious and successful approaches have been proposed for employing CCDs in speckle observations. In Sect. 8.2.1, two of these methods are presented. In addition, in Sect. 8.2.2 we propose a third acquisition technique which will serve us to conduct the observations and results presented in forthcoming sections.

8.2.1 Speckle in large format CCDs

Large format CCDs had been routinely used for speckle imaging in the context of two acquisition schemes:

The first one, called *fast subarray-readout mode* was developed by Horch et al. (1997) in the framework of their speckle campaigns in the Southern Hemisphere and Kitt Peak. In that approach, ten to twenty speckle frames were stored in a subarray strip of the KAF-4200 chip until it became filled as shown in Fig. 8.1. Afterwards, shutter was closed and the whole subarray was readout. Note that approach was possible thanks to the particular readout flexibility offered by the employed camera. This allowed to perform column charge shifting, which is typically fast ($\sim 1-10\mu$s) in CCDs, without being forced to readout through serial register and transfer to the computer, which is the real bottleneck of any CCD acquisition system. This last feature is not very common among conventional CCDs.
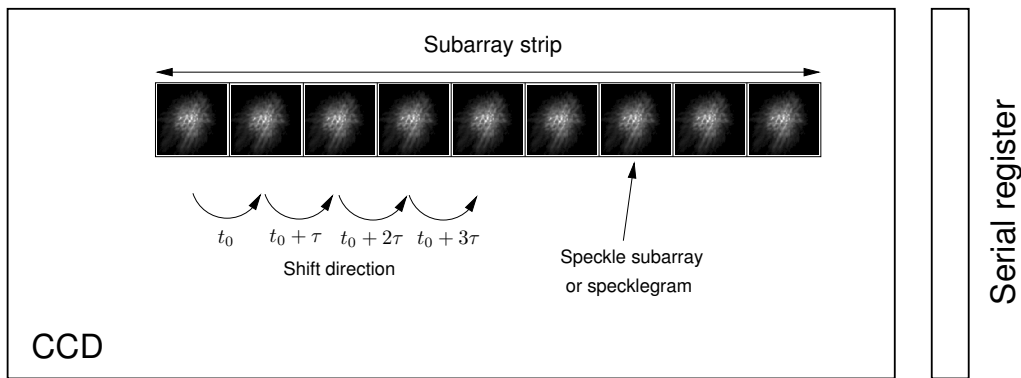
Figure 8.1: Schematic diagram of fast subarray-readout mode. Adapted from Horch et al. (1997).

The second approach, called RIT-Yale Tip-tilt Speckle Imager (RYTSI), has been recently conceived as an evolution of the former concept by the same authors (Horch et al. 2001). As illustrated in Fig. 8.2, the wise idea behind RYTSI is to use the CCD as a passive detector (no charge shift is performed in this case until the final readout) and to solve the problem of fast frame sampling by accurately moving a plano-parallel mirror at the desirable pattern. In either of the two possible methods, the result is that the entire CCD chip is filled by equally spaced specklegrams, which can be reduced after the sensor is readout in the conventional way.

Note that in RYTSI the maximum number of specklegrams per readout transfer is still limited by the size of the CCD chip. However, on the contrary to fast subarray-readout mode, this approach makes a more efficient use of this chip area. For example, with a large sensor as the 2×2K×4K Mini Mosaic at WIYN telescope, RYTSI can fit more than 900 specklegrams per readout sequence.
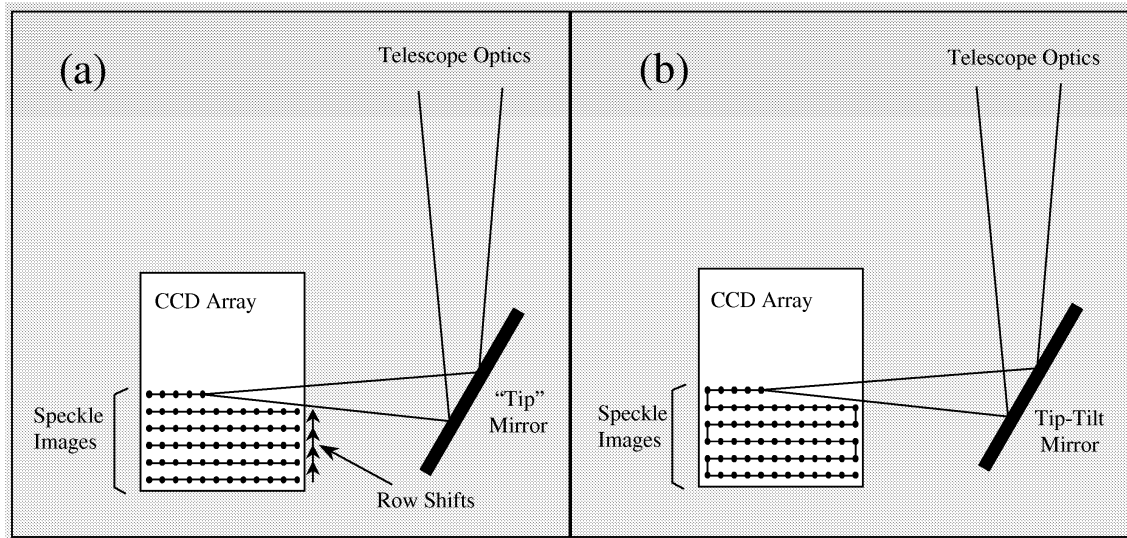
Figure 8.2: Schematic diagram of RYTSI operational mode in its two variants: (a) typewriter mode and (b) raster (or serpentine) mode. Adapted from Horch et al. (2001).

8.2.2 Fast drift scanning technique

As shown in Sect. 7.2.1, CCD fast drift scanning can be applied to obtain high-resolution measurements by means of lunar occultations (LO) observations. In that approach, the occultation lightcurve was recorded by reading out every millisecond the small fragment of the CCD column where the object was lying on. This procedure was continuously maintained until the occultation event took place and the user decided to stop the acquisition.

In this section we present a variation of the former acquisition technique applied to speckle imaging observations. As in LO approach, telescope tracking is turned on and the shutter remains open throughout the observation. As illustrated in Fig. 8.3, the continuous column readout is periodically interrupted by an amount of time Δt which matches approximately the atmospheric coherence interval. The resulting image of such process is an arbitrary long strip with a series of speckle frames.

Of course, the camera spends some measurable time while reading out all columns of each speckle frame. As a result of that unavoidable dead time between consecutive speckle frames, a low-level streaking appears between speckle images. In general, the importance of this effect will depend on the camera specifications, namely digitization and data transfer rates.
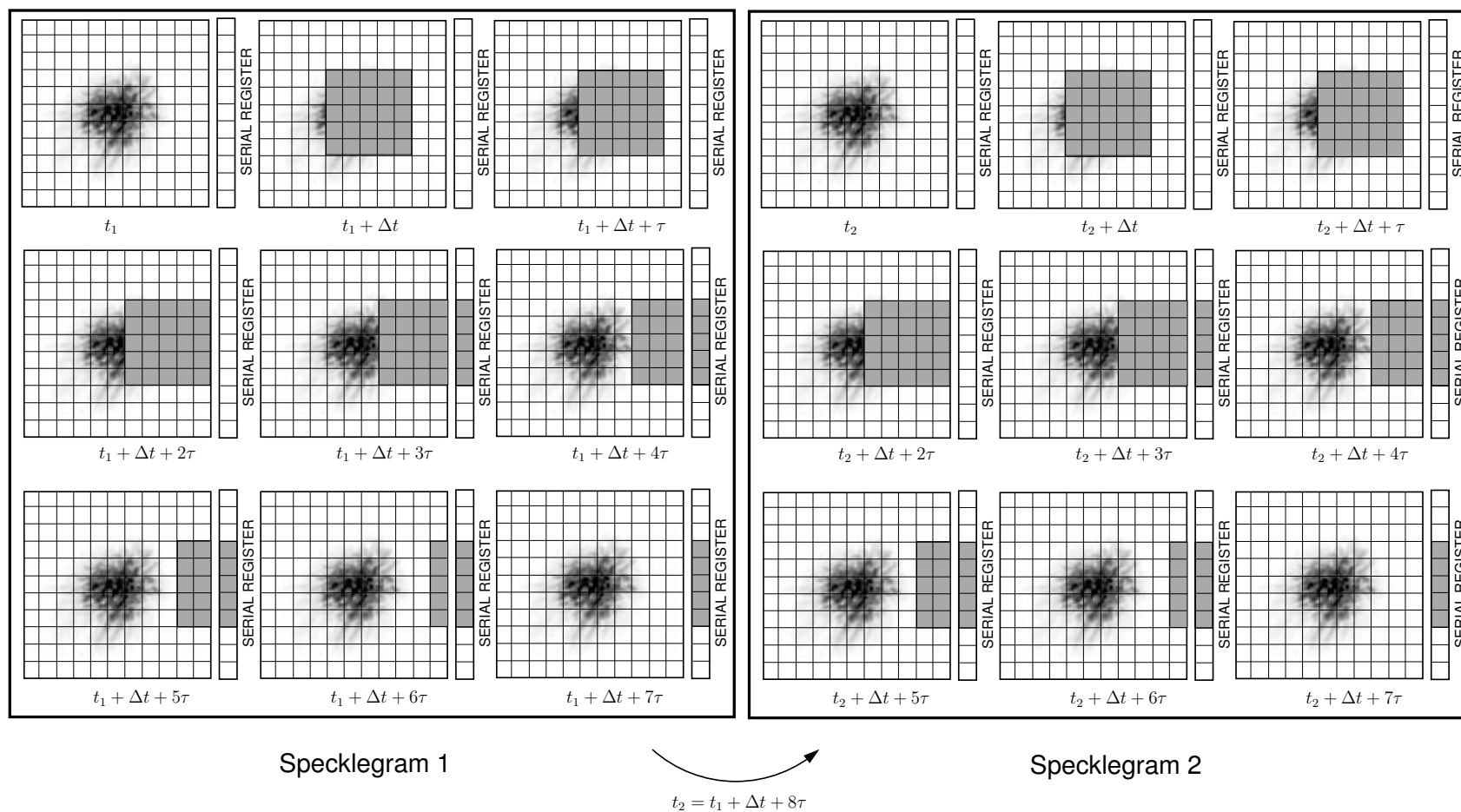
Figure 8.3: Sequence diagram of fast drift scanning acquisition mode applied to speckle imaging observations. Two consecutive specklegrams are included. First frame of each box corresponds to the periodic interruption by an amount of time which matches the atmospheric coherence interval, Δt. The other 8 frames correspond to dead time spent to shift and transfer the accumulated charge in column per column basis, τ. Speckle motion has been deliberately decreased for easing the figure comprehension. See text for further discussion.

Note that the proposed acquisition scheme is directly applicable to whatever full frame CCD camera which allows to set readout column rate and size by software means. No hardware or optical modification has to be made to the telescope for enabling this technique.

Fast drift scanning exhibits one advantage and one disadvantage with respect to fast subarray-readout described in Sect. 8.2.1. On one hand, now one can obtain as many speckle frames as desired without periodically closing the shutter: it is not limited by CCD chip size as in subarray-readout mode. On the other hand, the CCD is forced to readout all the columns between consecutive speckle frame exposures. As we commented, this restriction is the most common situation in commercial and also professional level CCDs. That yields larger dead time, which increases low-level light streaking. However, it is likely that dead time will be significantly reduced in very near future with new faster CCD cameras available on the professional and high-end amateur market (see Sect. 8.7 for further discussion on this topic).

In addition, we note that exhibits one advantage over the RYTSI approach. The source is approximately imaged over the same set of pixels and the spectral response is averaged along rows: again, drift scanning data naturally generates homogeneous images. On the contrary, RYTSI spreads the specklegrams across the chip and precise flatfield correction is required if accurate differential photometry is aimed. Of course, RYTSI benefits from the quasi-instantaneous mirror shift with its associated nearly zero dead time between specklegrams, which cannot be accomplished in fast drift scanning technique.

Note that the term *fast drift scanning* for both speckle imaging (and also lunar occultations) may seem somewhat ambiguous. In strict sense, drift scanning term should only be used when R.A. tracking drive is turned off and, as a result, the imaged scene *drifts* over the CCD chip at the same rate the column charge is clocked towards the serial register. However, in order to be consistent with Fors et al. (2001a), we will adopt the same designation.

8.3   Data description

Speckle observations were conducted at 1.5 m telescope of the Observatorio Astrónomico Nacional at Calar Alto in October, 2001. We used the same camera used for LO

observations in Fors et al. (2001a, 2004a), which was described in Sect. 7.4.

Four binary systems (ADS 755, ADS 2616, ADS 3711 and ADS 16836) were observed during 5 consecutive nights (see Cols. 1–6 in Table 8.1 in Sect. 8.5 for further details). Those were selected because they have well determined orbits which allow us to validate the acquisition technique described in Sect. 8.2.2. We obtained several speckle frame sequences for every object, containing each one several hundreds of frames.

All speckle observations were conducted with a Cousins R filter ($\lambda = 641 \pm 100$ nm). At this wavelength, the diffraction–limited spot size is equal to 108 mas for a 1.5 m telescope. On the other hand, the scale calibration was carried out by means of a standard plate solution of long exposure frames, and was found to be 9.375 mas mm^{-1}. Thus, our data is undersampled and this will be taken into account in the reduction process (see Sect 8.4).

In CCD-based speckle imaging there is a competition between readout noise and atmospheric correlation time. On the one hand, longer frame integration times give you more photons, which gives better contrast of the speckle pattern with the readout noise. On the other hand, you lose speckle contrast if a too long frame integration time is used. Therefore, it is not just an instrumental readout limitation that forces us to use a frame time longer than the correlation time, but it is desirable to minimize the effect of CCD read noise.

Data acquisition was performed using an implementation of the proposed technique into a DOS-based program called SCAN (Flohr 1999). This was already employed for LO observations with successful results in Sect. 7.4. Such program offers good enough relative timing accuracy when scheduling column readout at millisecond rate.

In Fig. 8.4 we show a subset of typical sequence of speckle frames obtained by means of such technique. For this particular case, a 20-pixel column is stored every 1.8 ms on average, yielding a dead time of 36 ms. That must be added to 39 ms. Note that this is significantly larger than the typical atmospheric coherence time for seeing of 1″3, which has been estimated at several observatories to be on the order of 4-8 ms. The choice of this longer exposure time and its consequences for data quality is justified and discussed in Sect. 8.4.
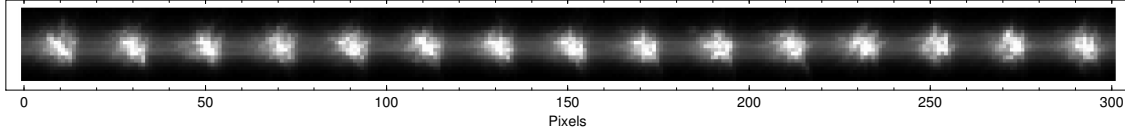
Figure 8.4: Raw strip image of ADS755 as observed when following the proposed technique. Specklegrams are 20x20 pixels size and exposure time is 39ms.

8.4 Data reduction and analysis

Once the raw data is read out of the camera, pixels around the object of interest are extracted and converted to FITS format. The FITS file is stored as an image stack where each image contains a 20×20 pixel speckle pattern. Approximately 500 of such images are contained in the stack of a single observation. These files are then analyzed in exactly the same way as described in Horch et al. (1997). Briefly, the method is to subtract the bias level and the streak between images caused by the readout scheme, and then to compute the autocorrelation and low-order bispectral subplanes needed for subsequent analysis.

In the case of reconstructed images, the relaxation technique of Meng et al. (1990) is used to generate a phase map of the object Fourier transform $\hat{O}(\mathbf{u})$, and this is combined with the object modulus obtained by taking the square root of the power spectrum $|\hat{O}(\mathbf{u})|^2$. By combining the modulus and the phase and inverse transforming, one arrives at the reconstructed image. An example of such an image is shown in Fig. 8.5.

In the case of deriving relative astrometry of binary stars, the weighted least squares approach of Horch et al. (1996) has been used. This method fits a power spectrum deconvolved by a point source calibrator to a trial fringe pattern and then attempts to minimize the reduced χ^2 of the function. As the data here are undersampled, the undersampling correction of Horch et al. (1997) was used.

8.4.1 Self-calibration scheme

For all data discussed here, an estimate for an unresolved point source power spectrum was constructed from the spectrum of a binary star. This has the advantage of allowing binary star observations to be taken without interruption for measurements

STF 73AB, Reconstructed Image
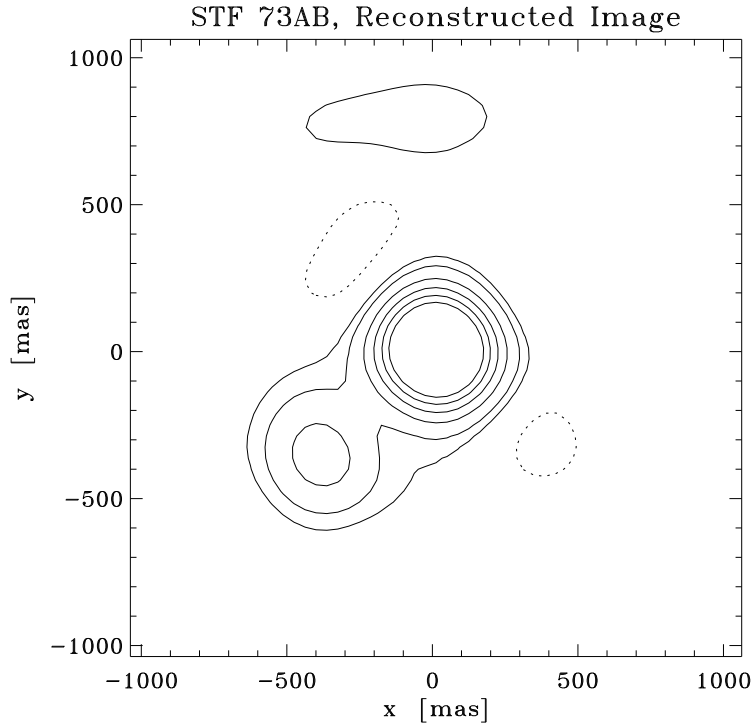
Figure 8.5: A reconstructed image of WDS 00550+2338 = ADS 755 = STF 73AB. North is down, East is to the right. Contours are drawn at -0.05, 0.05, 0.10, 0.20, 0.30, 0.40, and 0.50 of the maximum value in the array. The dotted contours indicate the value -0.05. The secondary star appears below and to the left of the primary, which is located in the center of the image. The feature in the upper part of the figure is not real and appears to be related to the mismatch between the seeing profile of the binary observation and the radially generated point source (see Sect. 8.4.1).

of the speckle transfer function. A synthetic point source estimate can be generated first by forming the power spectrum of any binary (see Fig. 8.6), and then extracting a trace from the image along the central fringe. Since the binary is not resolved along this direction, this is essentially a 1D estimate of an unresolved source. This one-dimensional function is then rotated about the origin of the frequency plane to fill a two-dimensional array. This generates a radially symmetric function, as indeed a true unresolved source should be under perfect conditions (see Fig. 8.7).

The method has limitations as we will discuss in Sect. 8.6 after the main body of results has been presented, but provides a way to make the deconvolution needed without recursing to point source observations.

As commented in Sect. 8.3, the speckle frame exposure time was chosen to be
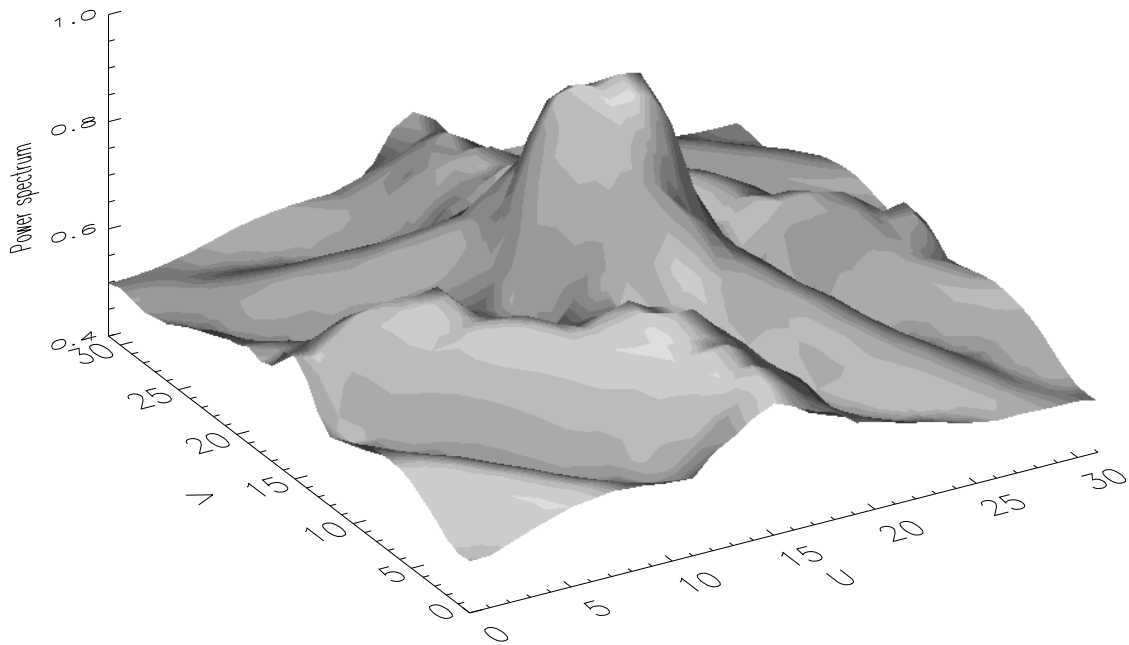
Figure 8.6: A surface plot of the power spectrum of one of the observing runs for ADS 755. Note fringe pattern due to duplicity of the object.
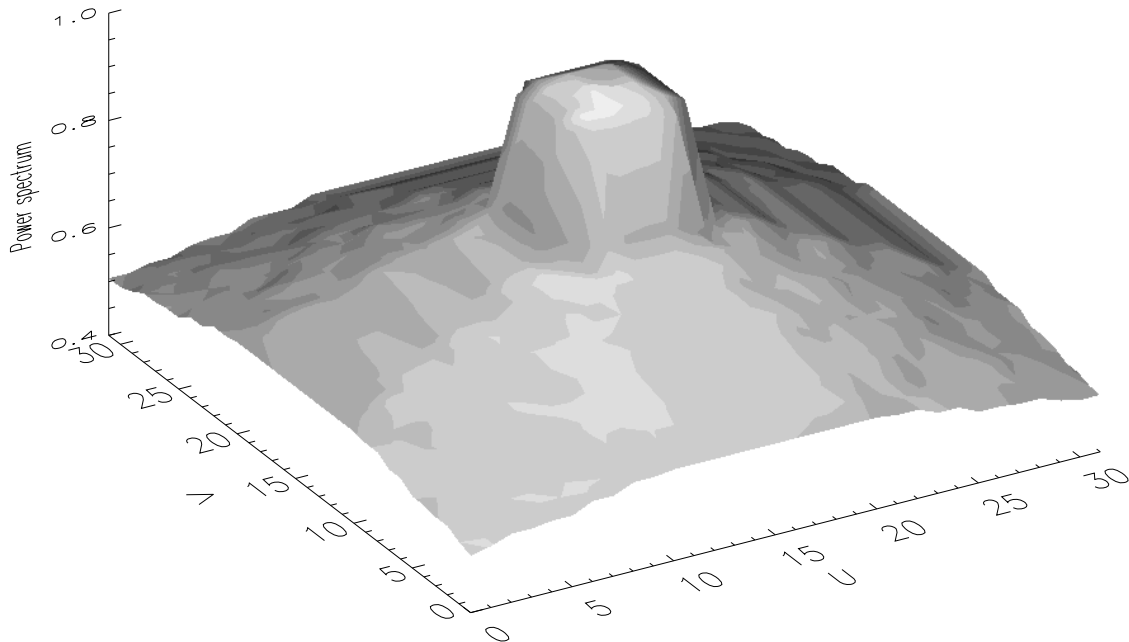
Figure 8.7: Power spectrum for calculated point source following self-calibration scheme. Compared to Fig. 8.6, central peak due to seeing remains approximately the same and fringes in speckle shoulder are not present, as expected.

larger than the coherence time. This choice is justified by the competition between readout noise and correlation time when performing CCD-based speckle imaging. On the one hand, speckle frames show the highest possible SNR when the integration time is in fact longer than the coherence time. Horch et al. (2002) has shown that 50 ms is the exposure time where the maximum in the SNR occurs at the WIYN telescope, which uses a CCD with a readout noise of 10 electrons. That probably implies a factor of 4 to 5 larger than the coherence time. On the other hand, in general speckle contrast decreases as longer exposure time are used. Therefore, it is not just an instrumental readout limitation that forces us to use a frame time longer than the correlation time, but it is desirable to minimize the effect of CCD read noise, while still preserving sufficient contrast on speckle patterns.

In addition, interframe dead time contributes to low-level streaking. However, note that light contributing to streaking is distributed far more uniformly and over more pixels than those forming the speckle pattern itself. As a result, the ratio between intensity peaks is much more favorable than the ratio between dead time and atmospheric coherence time.

All this introduces attenuation in the higher frequencies of our data. To illustrate how this affects resolution, a plot with four 1D power spectrum curves has been made. As shown in Fig. 8.8, one corresponds to an observed point source and the other three to the diffraction–limited spot one would obtain with the instrumental conditions of current study. The attenuation factor used for generating such simulated profiles is given by:

$$A = 0.435(r_0/D)^2, \tag{8.2}$$

where r_0 is the Fried parameter and D the telescope diameter. The 0.435 is a geometrical factor derived by Korff (1973) and Fried (1979).

Ideally, the high-frequency portion of the speckle transfer function should overlap to the simulated curve attenuated with the r_0 value which best matches the real seeing. However, due to the significant undersampling of our data, the observed power spectrum does not span up to the theoretical diffraction limit (close to ± 10 cycles arcsec^{-1}). It is worth mentioning that our reduction software does account for the aliasing effect of the undersampling and, in principle, is able to extract part of those frequencies which are aliased to lower frequencies. However, this last is somewhat limited by the low SNR which these high frequencies show. Thus, we see
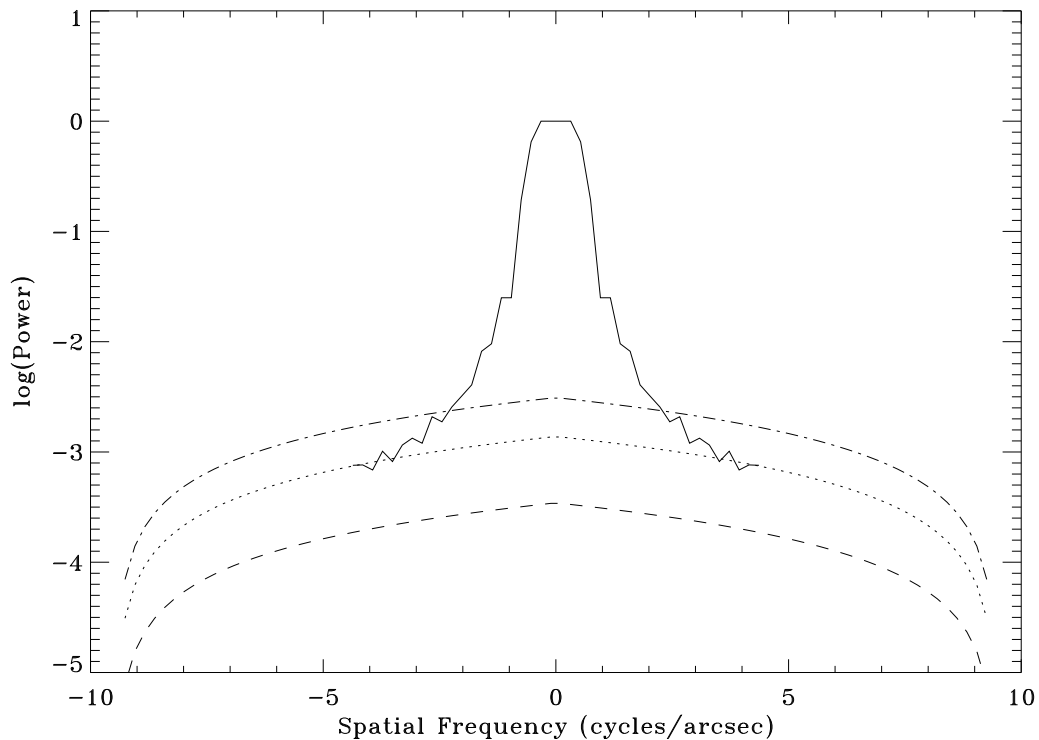
Figure 8.8: Comparison of cutoff frequencies of observed and simulated 1D speckle transfer functions. The former (solid line) was generated from the ADS 2616 point source. The latter represents the diffraction–limited power spectrum obtained at $641\,\text{nm}$ using a $1.5\,\text{m}$ aperture. Three different values of the Fried parameter r_0, $5\,\text{cm}$ (dashed), $10\,\text{cm}$ (dotted), and $15\,\text{cm}$ (dash-dotted), have been considered. Note that the better the seeing, the larger r_0 and so the higher the curve on the plot.

that the impact of longer exposure time is relatively small, and does not handicap our data quality.

Finally, note that we have not considered the systematic effect of intra-pixel sensitivity response and its implications to astrometry derived from speckle imaging. As was studied in Piterman & Ninkov (2002), this can introduce significant bias in the positions for the case of front-illuminated CCDs as the one we employed here. Unfortunately, no intra-pixel calibration map was available for our camera. However, at the pixel scale we are working with, we speculate this effect is not dominant over other error sources (readout noise, streaking, etc.).

8.5 Results

In Table 8.1 we show all speckle measures obtained during our five night observing run after applying the self-calibration analysis as explained in the previous section.

Table 8.1: Double star speckle measures.

ADS	Discoverer Designation	HD	HIP	WDS $(\alpha,\delta$ J2000.0$)$	Date (BY)	θ $(°)$	ρ $('')$	Δm
755	STF 73AB	5286	4288	$00550 + 2338$	2001.8127	311.5	0.935	1.17 [b]
					2001.8178	310.5	0.936	0.43
					2001.8207	311.0	0.936	0.53
2616	STF 412AB	22091	16664	$03344 + 2428$	2001.8208	175.8	0.651	0.35 [a]
					2001.8261	176.2	0.646	0.58 [a]
3711	STT 98	33054	23879	$05079 + 0830$	2001.8157	319.8	0.743	0.52
16836	BU 720	221673	116310	$23340 + 3120$	2001.8124	95.8	0.560	0.57 [b]
					2001.8208	97.2	0.585	0.36
					2001.8260	92.8	0.589	0.90 [b]

a. Position angle is inconsistent with previous observations.

b. Observation was taken at low elevation. That may introduce low quality result.

Column headings are as follows: (1) the Aitken Double Star number; (2) the discoverer designation as it appears in the Washington Double Star Catalog (WDS); (3) the Henry Draper Catalogue number; (4) the HIPPARCOS Catalogue number; (5) the Washington Double Star Catalogue number, which is the same as the position in 2000.0 coordinates; (6) the date in fraction of the Besselian year when the observation was made; (7) the position angle (θ) with North through East defining the positive sense of the angle; (8) the separation (ρ) in arc seconds; and (9) the magnitude difference as judged from the speckle observations. Position angles are not corrected for precession and therefore are only valid for the epoch of observation shown. Every (ρ,θ,Δ_m) triplet in the table is the result of averaging the analysis result of 5 frame sequences, which were exposed a few minutes one from each other. As indicated in the table, some observations were taken at low elevation. Note that position angle, separation, and magnitude differences for these measures appear discrepant with the rest of values. Therefore, self-calibration point source method should be used only at modest zenith angles (less than thirty degrees, if no

atmospheric dispersion compensation is performed). Further discussion about this limitation will be covered in Sect. 8.6.

In Fig. 8.9 we compare the obtained results with those from other observers and the predicted orbit for each object. In general, our measure-orbit offsets are within the global scatter of all other positions. Those that are farthest from the orbital ephemeris positions corresponds (again) to observations performed at low elevation. The point source calibrator in all cases was generated from a high SNR observation of ADS 755.

Assuming no major systematic errors, the total uncertainty for measures in Table 8.1 can be estimated by combining the uncertainty generated from night-to-night scatter when using the same point source and the variation in the result obtained by using different point source calibrators. Although the data set here does not permit definitive uncertainty estimates due to the small sample of objects observed, we can nonetheless make first order estimates of these quantities. Firstly, we obtain night-to-night scatter (σ^{nn}) by computing the standard deviations of two objects in Table 8.1 with the most observations, and averaging those two quantities. Secondly, we estimate point source error (σ^{ps}) by making use of values in Table 8.2, which can also be displayed in Fig. 8.10. Such table includes (ρ,θ,Δ_m) results obtained when using different point source calibrators for one single speckle sequence. The average of the two rows designated as σ represents an estimate of the point source error for one observation (σ_1^{ps}). Whereas, (ρ,θ,Δ_m) measures in Table 8.1 proceed from 5 consecutive speckle pattern sequences. As a result, in order to a get σ^{ps} fully comparable with σ^{nn}, σ_1^{ps} has been divided by $\sqrt{n-1}$, $n=5$. Finally, assuming statistical independence, we obtain the following expected uncertainties in each coordinate by adding σ^{ps} in quadrature with σ^{nn}:

Position angle: $\sigma_\theta = 1°\!.5$,
Separation: $\sigma_\rho = 0''\!.017$,
Magnitude difference: $\sigma_{\Delta m} = 0.34$ mag.

The separation error value is very similar to the result in Douglass et al. (1999) (U.S. Naval Observatory obtained speckle results with $\sigma_\rho = 0''\!.018$ using a 66-cm telescope). However, σ_θ is higher in our case (Douglass et al. (1999) obtained $0°\!.57$ for a $1''$ separation, although $1°$ is a typical uncertainty in well-calibrated speckle work). $\sigma_{\Delta m}$ is probably large because of the small window used and self-calibration technique limitations.
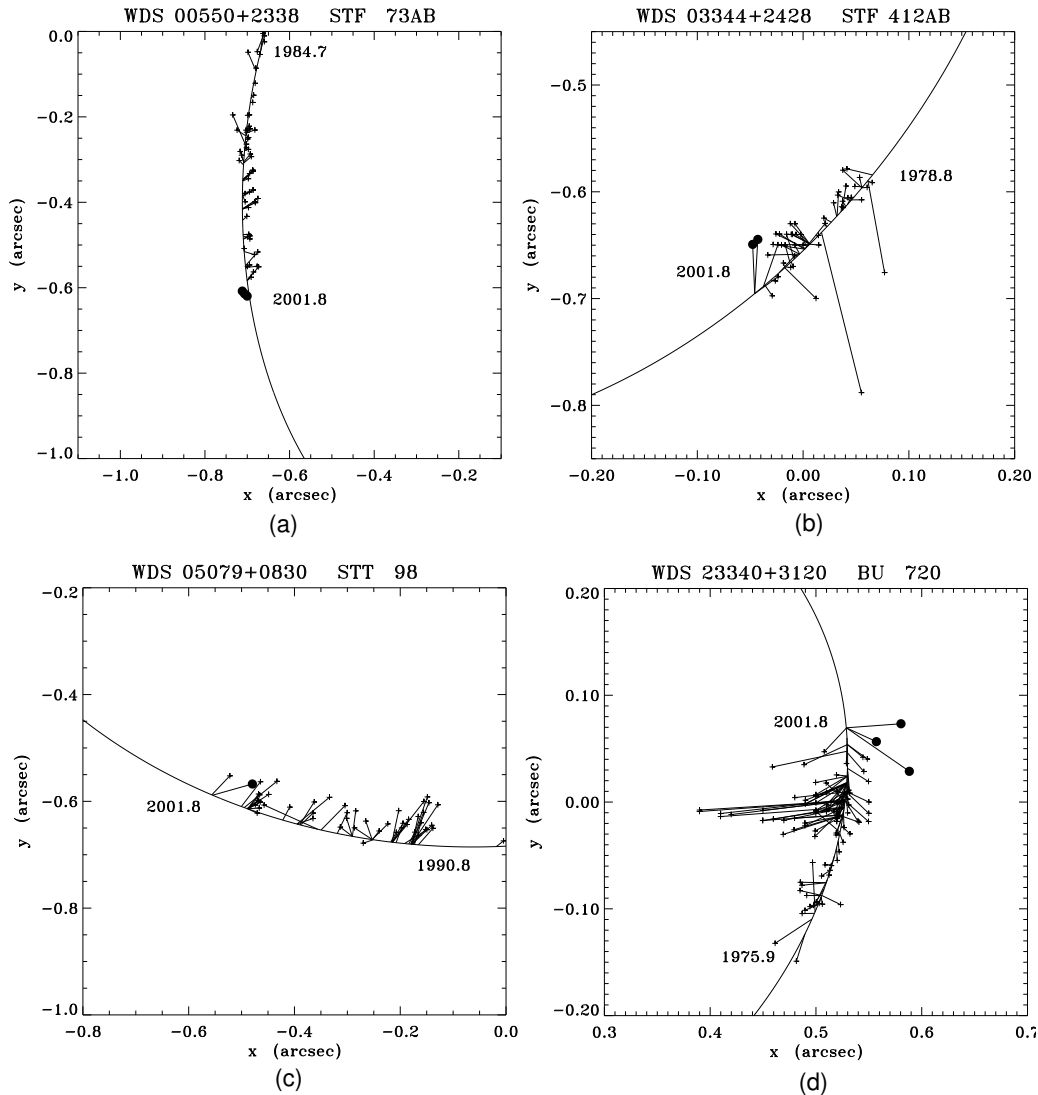
Figure 8.9: A comparison of the position angle and separation measures presented here with the work of other observers. In all plots, North is down and East is to the right. In all cases, the object has an orbit listed in the 6th Catalog of Orbits of Visual Binary Stars (Hartkopf & Mason 2003), and the orbital trajectory is plotted. Observations of previous observers, compiled by Hartkopf & Mason (2002), are marked with small plus symbols, with a line segment drawn from the point to the ephemeris prediction for that epoch. The observations presented here are marked with the solid dots, again with line segments joining the point to the predicted location given the orbital elements. (a) WDS 00550+2338 = STF 73AB = ADS 755. The orbit plotted is that of Docobo & Costa (1990), rated as a Grade 2 orbit in the Sixth Catalog. (b) WDS 03344+2428 = STF 412AB = ADS 2616. The orbit plotted is that of Scardia et al. (2002), rated as a Grade 3 orbit in the Sixth Catalog. (c) WDS 05079+0830 = STT 98 = ADS 3711. The orbit plotted is that of Baize (1969), rated as a Grade 3 orbit in the Sixth Catalog. (d) WDS 23340+3120 = BU 720 = ADS 16836. The orbit plotted is that of Starikova Starikova (1982), rated as a Grade 3 orbit in the Sixth Catalog.

Table 8.2: Comparison of results obtained with different point source power spectra. σ represents an estimate of the point source error for one observation.

ADS	Discoverer Designation	HD	HIP	WDS $(\alpha,\delta$ J2000.0$)$	Date (BY)	θ $(°)$	ρ $(\prime\prime)$	Δm
755	STF 73AB	5286	4288	$00550 + 2338$	2001.8207	311.7	0.939	0.76
					2001.8207	312.5	0.945	0.98
					2001.8207	311.7	0.936	0.73
					2001.8207	311.1	0.938	0.59
				σ		0.6	0.004	0.16
2616	STF 412AB	22091	16664	$03344 + 2428$	2001.8261	178.4	0.674	0.58
					2001.8261	174.5	0.642	0.31
					2001.8261	176.2	0.664	0.23
					2001.8261	173.5	0.634	0.35
					2001.8261	178.4	0.672	0.70
				σ		2.2	0.018	0.20
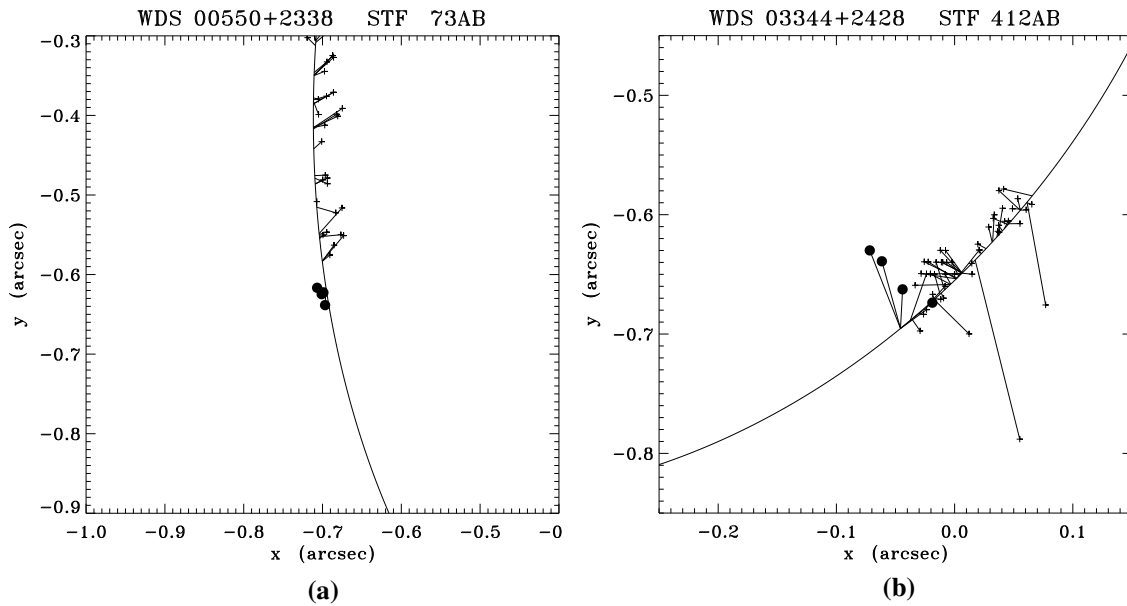
Figure 8.10: Comparison of astrometric results using different point source calibrations. Point sources generated from observations of ADS 3711 and ADS 755 were used in both cases. The plot symbols and orbital trajectories are the same as in Fig. 8.9. (a) WDS 00550+2338 = STF 73AB = ADS 755. (b) WDS 03344+2428 = STF 412AB = ADS 2616.

As stated above, the point source from ADS 755 was used for the analysis of all objects. To find the degree of validity of this assumption, and to determine how significant the change in atmospheric conditions is, we have divided the point source 1D power spectrum of ADS 755 by those from ADS 16836 and ADS 755, obtained on different nights. Ideally, the resulting curves should be constant and equal to unity for all frequencies. As shown in Fig. 8.11, the curves appear to be quite flat over the whole frequency domain. Only marginal residuals in the range of seeing wings are visible for the two upper plots. Those are due to region of the seeing peak not being considered when the power spectrum fits are performed. The information in Fig. 8.11 is complementary to what is shown in Table 8.2.
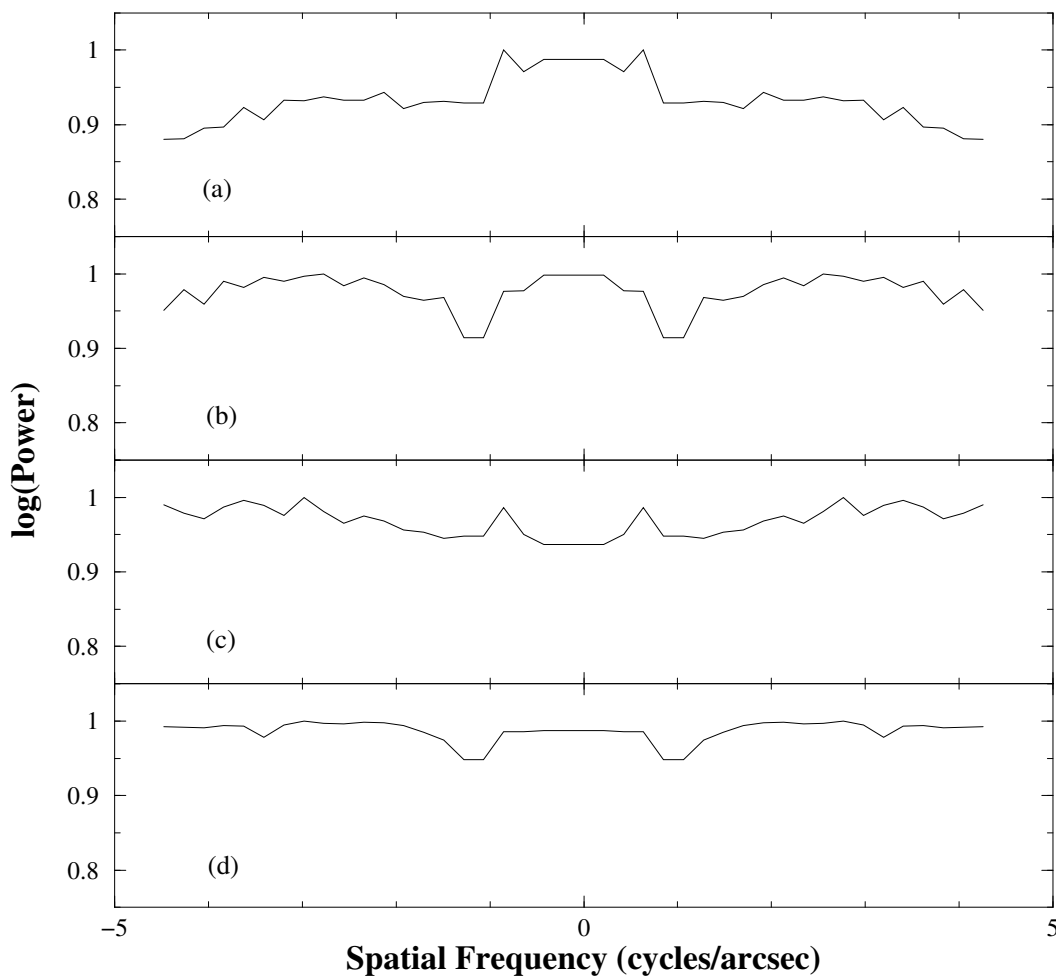
Figure 8.11: Comparison of 1D point source power spectrum of ADS 755 on the 5th night of observation with respect to: (a) ADS 16386 on 5th night, (b) ADS 16386 on 6th night, (c) ADS 755 on 2nd night and (d) ADS 755 on 4th night.

8.6 Limitations of self-calibration technique

The self-calibration method used here cannot be used in all situations. Indeed, the principal limitation is due to zenith angle. As the zenith angle increases, the dispersion of the atmosphere elongates speckles so that the speckle transfer function is no longer radially symmetric, and therefore, the point source estimate generated is not an appropriate representation for the speckle transfer function at high zenith angles. This in turn can affect the relative astrometry and photometry derived from such data.

In considering differential photometry, one would expect that this is more sensitive to calibration effects than the astrometric results, since the process of deriving the magnitude difference is equivalent to estimate the fringe depth in the Fourier plane. If one uses a symmetric PSF estimate to deconvolve an asymmetric binary power spectrum, the fringe depth can be severely affected while the fringe spacing and orientation would remain essentially the same.

It is also quite likely that in the case of a faint binary star, it is probably better to use a brighter binary to obtain the one-dimensional trace simply due to SNR considerations.

8.7 Upcoming CCD improvements

As commented in Sect 8.2, one of the justifications for disregarding CCD use in speckle field has been their not fast enough frame rate. In the case of the camera used in this study, its readout rate of 30 kpix s^{-1} can be considered as moderately low according CCDs currently in the market. The fact that it was controlled through parallel port interface fairly limited final readout rate. The use of drift scanning technique allow us to conduct the observation desired rate despite this adverse situation.

However, in the last few years, technologies directly related with CCD performance have experimented significant developments. Taking into account only those which have been applied to full-frame CCDs (i.e. the type used most in astronomy) we can consider the following advances:

1. readout noise has been continuously dropping in all kind of cameras. On the professional-edge market, the recently available L3Vision technology is offering sub-electron readout noise at Mpix s^{-1} rate (Basden et al. 2003; Jerram et al. 2001; Mackay et al. 2004). This has been a major step forward to low signal applications, as adaptive optics wavefront sensors (Downing 2005). This new technology has already been considered for speckle interferometry observations (Saha & Chinnappan 2002).

2. since the venue of old parallel port architecture, data transfer interfaces have dramatically increased their throughput (see Table 8.3).

   Accordingly, professional and commercial CCDs have incorporated USB 2.0 and Ethernet interfaces to CCDs, even in the high-end amateur market. Apogee (2003a) constitutes a recent example of this improvement. Some of its cameras can deliver frame rates typically 10 to 30 times faster than that offered by our port-parallel cameras.

Table 8.3: Data transfer rate for different port interfaces.

Type	Data transfer rate (Mbit s^{-1})
Serial	0.115
Parallel Port EPP/ECP	0.5-1
Firewire	200
USB 2.0	480
Ethernet	10/100/1000

3. parallely to the transfer interface developments, on-board SDRAM memory buffers have been implemented in commercial cameras (Apogee 2003b). This mode allows to store fast frame sequences without being limited by the data transfer interface throughput. Note that digitization-to-SDRAM memory rates can be as fast as 11 Mpix s^{-1}. Considering the typical size of a sequence of specklegrams, these could perfectly fit in one of those SDRAM buffer, which are several tens of Mb in size.

4. most important, drift scanning readout mode has been natively integrated in the electronics of some commercial cameras with an accurate 25Mhz time base (Apogee 2005). Thus, our CPU-interrupt based time tick control approach

would be no more needed. The manufacturer claims row shifts as fast as 5.12μs can be achieved.

5. multi output CCD also increases frame rate by dividing the data stream to be readout in several channels.

Therefore, the benefits that fast drift scanning technique take from all CCD improvements above are straightforward. On one hand, lower readout noise will increase SNR of the specklegrams. On the other hand, faster readout rate will certainly decrease dead time and, as a result, low-level streaking between speckle frames would be effectively reduced. Finally, integrated drift scanning mode opens the possibility of sampling specklegrams on the basis of real subframe mode ($\sim$10–30 pixels wide), as opposed to the drift scanning technique which only records the flux of a few pixels row.

8.8   Conclusions

A new acquisition approach based on fast drift scanning has been presented for performing CCD-based speckle imaging. Data obtained by those means bear enough quality to bring real scientific results, as shown in the objects observed in this chapter.

Results of separation, position angle and magnitude difference (ρ, θ, Δm) are in accordance with published measurements by other observers and predicted orbits. Error estimates for these have been found to be $\sigma_\rho = 0\rlap{.}{''}017$, $\sigma_\theta = 1\rlap{.}{°}5$, $\sigma_{\Delta m} = 0.34$ mag. These are in the order of other authors and can be considered as successful for a first trial of this technique.

In addition, a new method for calibrating power spectrum analysis has been introduced. It does not require point source observations, which yields to a more effective use of observation time. Some limitations have been observed for this method for zenith angles above $60°$ related to atmospheric dispersion. These conclusions can gain even more importance in the case of large telescopes. On one hand, as they have the highest observing time pressure, self-calibration technique would prevent from performing point sources observations. On the other hand, if conveniently equipped

with Risley prisms, they would be able to observe objects at low elevations without serious effects into the shape of speckles due to atmospheric dispersion. Thus, self-calibration would presumably not be limited by elevation.

CCDs, far from being specialized detectors, are very common among instrumentation available in most astronomical observatories. The fast drift scanning enables low budget professional and high-end amateur observatories, which routinely use full-frame CCDs for stare imaging, to perform CCD speckle imaging as well. The performance of such technique will be significantly higher with new faster and less noisy cameras which are becoming available in the CCD market.

Bibliography

Abell G.O., Morrison D., Wolff S.C., 1993, Exploration of the universe, New York: Saunders College Publishing, 1991, —c1993, 6th ed.

Africano J.L., Cobb C.L., Dunham D.W., et al., Sep. 1975, AJ, 80, 689

Apogee, 2003a, Alta USB2.0 and 100baset Interfaces, Tech. rep., Apogee Instruments Inc., available at
`http://www.ccd.com/alta_disc_interfaces.html`

Apogee, 2003b, Alta SDRAM memory buffer, Tech. rep., Apogee Instruments Inc., available at
`http://www.ccd.com/alta_disc_sdram.html`

Apogee, Jan. 2005, Precision TDI and Kinetics Readout Modes, Tech. rep., Apogee Instruments Inc., available at
`http://www.ccd.com/alta_disc_tdi.html`

Arnulf A., 1936, Compt. Rend. Acad. Sci. Paris, 202, 115

Ashok N.M., Chandrasekhar T., Ragland S., Bhatt H.C., 1994, Experimental Astronomy, 4, 177

Bagnuolo W.G., Mason B.D., Barry D.J., Hartkopf W.I., McAlister H.A., Apr. 1992, AJ, 103, 1399

Baize P., 1969, IAU Comm. 26 Inf. Circ., 48

Balega I., Balega Y.Y., Maksimov A.F., et al., Aug. 2004, A&A, 422, 627

Barnes T.G., Evans D.S., Mar. 1976, MNRAS, 174, 489

Barnes T.G., Evans D.S., Moffett T.J., May 1978, MNRAS, 183, 285

Basden A.G., Haniff C.A., Mackay C.D., Nov. 2003, MNRAS, 345, 985

Bates R.H.T., Oct. 1982, Physics Reports, 90, 203

Bates R.H.T., Gough P.T., Napier P.J., Jan. 1973, A&A, 22, 319

Batten A.H., Fletcher J.M., MacCarthy D.G., 1989, Publications of the Dominion Astrophysical Observatory Victoria, 17, 1

Beavers W.I., Eitter J.J., Cadmus R.R., Sep. 1981, AJ, 86, 1404

Bertin E., Arnouts S., Jun. 1996, A&ASS, 117, 393

Bizenberger P., 1993, MAGIC Homepage, Tech. rep., available at `http://www.mpia-hd.mpg.de/IRCAM/MAGIC/MAGIC.html`

Briceno C., Calvet N., Gomez M., et al., Jul. 1993, PASP, 105, 686

Codella C., Felli M., Natale V., Palagi F., Palla F., Jun. 1994, VizieR Online Data Catalog, 329, 10261

Couteau P., Jun. 1972, A&ASS, 6, 177

Couteau P., Jun. 1975, A&ASS, 20, 391

Couteau P., Apr. 1979, A&ASS, 36, 11

Couteau P., Aug. 1987, A&ASS, 70, 193

Couteau P., Sep. 1989, A&ASS, 79, 385

Cutri R.M., Skrutskie M.F., van Dyk S., et al., Jun. 2003, VizieR Online Data Catalog, 2246, 0

di Benedetto G.P., Mar. 1993, A&A, 270, 315

Diercks H., Hunger K., 1952, Zeitschrift fur Astrophysics, 31, 182

Docobo J.A., Mar. 1989, PASP, 101, 274

Docobo J.A., Costa J.M., Dec. 1990, PASP, 102, 1400

Docobo J.A., Andrade M., Ling J.F., et al., Feb. 2004, AJ, 127, 1181

Douglass G.G., Mason B.D., Germain M.E., Worley C.E., Sep. 1999, AJ, 118, 1395

Downing M., 2005, A Dedicated L3Vision CCD for Adaptive Optics Applications, Tech. rep., available at
`http://www.eso.org/projects/odt/documentations/paper_md_2005.pdf`

Duflot M., Figon P., Meyssonnier N., Dec. 1995, A&ASS, 114, 269

Dunham D., Sep. 2001, private communication

Dunham D., Bulder H., Sep. 2001, private communication

Dunham D., Herald D., 2004, private communication

Dunham D.W., Warren W.H., Feb. 1995, VizieR Online Data Catalog, 1201, 0

Dyck H.M., van Belle G.T., Thompson R.R., Aug. 1998, AJ, 116, 981

Epchtein N., Le Bertre T., Lepine J.R.D., et al., Oct. 1987, A&ASS, 71, 39

Evans D.S., Jun. 1970, AJ, 75, 589

Evans D.S., Sep. 1977, Sky Telesc., 54, 164

Evans D.S., Edwards D.A., Frueh M., McWilliam A., Sandmann W.H., Nov. 1985, AJ, 90, 2360

Evans D.S., McWilliam A., Sandmann W.H., Frueh M., Nov. 1986, AJ, 92, 1210

Fabricius C., Makarov V.V., Apr. 2000, A&A, 356, 141

Fabricius C., Høg E., Makarov V.V., et al., Mar. 2002, A&A, 384, 180

Flohr C., 1999, SCAN homepage, available at
`http://www.driftscan.com`

Fors O., Núñez J., Aug. 2000a, In: Proceedings of 19th European Symposium on Occultation Projects (ESOP XIX) - International Occultation Timing Association / European Section (IOTA/ES)

Fors O., Núñez J., Jun. 2000b, In: Proceedings of Minor Planet Amateur-Professional Worshop 2000, Comba Eds., New York

Fors O., Núñez J., 2001, In: Highlights of Spanish Astrophysics II, 293–+

Fors O., Núñez J., Richichi A., Nov. 2001a, A&A, 378, 1100

Fors O., Núñez J., Richichi A., Aug. 2001b, In: Proceedings of 20th European Symposium on Occultation Projects (ESOP XX) - International Occultation Timing Association / European Section (IOTA/ES)

Fors O., Horch E.P., Núñez J., Jun. 2004a, A&A, 420, 397

Fors O., Richichi A., Núñez J., Prades A., May 2004b, A&A, 419, 285

Fors O., Richichi A., Merino M., et al., 2006, In: Revista Mexicana de Astronomía y Astrofísica Conference Series (in press)

Fried D.L., 1979, Optica Acta, 26, 597

Ghedina A., Ragazzoni R., Baruffolo A., Jun. 1998, A&ASS, 130, 561

Gliese W., Jahreiss H., Nov. 1995, VizieR Online Data Catalog, 5070, 0

Hartkopf H.A. W. I.and McAlister, Mason B.D., 2002, Fourth Catalog of Interferometric Measurements of Binary Stars, United States Naval Observatory, Washington, USA, available at
http://ad.usno.navy.mil/wds/int4.html

Hartkopf W.I., Mason B.D., 2003, Sixth Catalog of Orbits of Visual Binary Stars, United States Naval Observatory, Washington, USA, available at
http://ad.usno.navy.mil/wds/orb6.html

Hartkopf W.I., McAlister H.A., Jan. 1984, PASP, 96, 105

Heckmann O., 1975, AGK 3. Star catalogue of positions and proper motions north of -2.5 deg. declination, Hamburg-Bergedorf: Hamburger Sternwarte, 1975, edited by Dieckvoss, W.

Heintz W.D., Oct. 1980, ApJSS, 44, 111

Henden A., Kaitchuck R.H., 1990, Astronomy, 18, 97

Herbst T.M., Beckwith S.V., Birk C., et al., Oct. 1993, In: Proc. SPIE Vol. 1946, Infrared Detectors and Instrumentation, Albert M. Fowler; Ed., 605–609

Hindsley R.B., Harrington R.S., Jan. 1994, AJ, 107, 280

Högbom J.A., Jun. 1974, A&ASS, 15, 417

Horch E.P., Dec. 1995, International Journal of Imaging Systems and Technology, 6, 401

Horch E.P., Dinescu D.I., Girard T.M., et al., Apr. 1996, AJ, 111, 1681

Horch E.P., Ninkov Z., Slawson R.W., Nov. 1997, AJ, 114, 2117

Horch E.P., Ninkov Z., Meyer R.D., van Altena W.F., May 2001, Bulletin of the American Astronomical Society, 33, 790

Horch E.P., Robinson S.E., Meyer R.D., et al., Jun. 2002, AJ, 123, 3442

Horch E.P., Meyer R.D., van Altena W.F., Mar. 2004, AJ, 127, 1727

Houk N., Smith-Moore M., 1988, In: Michigan Spectral Survey, Ann Arbor, Dept. of Astronomy, Univ. Michigan (Vol. 4) (1988), 0–+

Jerram P., Pool P.J., Bell R., et al., May 2001, In: Proc. SPIE Vol. 4306, Sensors and Camera Systems for Scientific, Industrial, and Digital Photography Applications II, Morley M. Blouke; John Canosa; Nitin Sampat; Eds., 178–186

Joint IRAS SWG, 1988, In: IRAS Point Source Catalog (1988), 0–+

Keel W.C., Jul. 1991, PASP, 103, 723

Keel W.C., Sep. 2005, private communication

Kenyon S.J., Hartmann L.W., Strom K.M., Strom S.E., Mar. 1990, AJ, 99, 869

Kervella P., Coudé du Foresto V., Perrin G., et al., Mar. 2001, A&A, 367, 876

Kholopov P.N., Samus N.N., Frolov M.S., et al., 1998, In: Combined General Catalogue of Variable Stars, 4.1 Ed (II/214A). (1998), 0–+

Knoechel G., von der Heide K., Jul. 1978, A&A, 67, 209

Knox K.T., Thompson B.J., Oct. 1974, ApJ Letter, 193, L45

Korff D., Aug. 1973, Journal of the Optical Society of America (1917-1983), 63, 971

Kukarkin B.V., Kholopov P.N., Pskovsky Y.P., et al., 1971, In: General Catalogue of Variable Stars, 3rd ed. (1971), 0–+

Labeyrie A., May 1970, A&A, 6, 85

Labeyrie A., 1978, ARA&A, 16, 77

Lane B.F., Kuchner M.J., Boden A.F., Creech-Eakman M., Kulkarni S.R., Sep. 2000, Nature, 407, 485

Lee O.J., Baldwin R.J., Hamlin D.W., Jan. 1997, VizieR Online Data Catalog, 2068, 0

Leinert C., 1991, private communication

Leinert C., 1992, private communication

Lenzen R., Bizenberger P., Salm N., Storz C., Aug. 1998, In: Proc. SPIE Vol. 3354, Infrared Astronomical Instrumentation, Albert M. Fowler; Ed., 493–499

Lohmann A.W., Weigelt G., Wirnitzer B., Dec. 1983, Appl. Optics, 22, 4028

Lucy L.B., Jun. 1974, AJ, 79, 745

Mackay C., Basden A., Bridgeland M., Sep. 2004, In: Z-Spec: a broadband millimeter-wave grating spectrometer: design, construction, and first cryogenic measurements. Edited by Bradford, C. Matt; Ade, Peter A. R.; Aguirre, James E.; Bock, James J.; Dragovan, Mark; Duband, Lionel; Earle, Lieko; Glenn, Jason; Matsuhara, Hideo; Naylor, Bret J.; Nguyen, Hien T.; Yun, Minhee; Zmuidzinas, Jonas. Proceedings of the SPIE, Volume 5499, 203–209

MacMahon P.A., Dec. 1908, MNRAS, 69, 126

Mason B.D., Jul. 1995, VizieR Online Data Catalog, 610, 70299

Mason B.D., Martin C., Hartkopf W.I., et al., Apr. 1999, AJ, 117, 1890

Mason B.D., Hartkopf W.I., Holdenried E.R., Rafferty T.J., Jun. 2001a, AJ, 121, 3224

Mason B.D., Wycoff G.L., Hartkopf W.I., Douglass G.G., Worley C.E., Dec. 2001b, AJ, 122, 3466

McAlister H.A., 1985, ARA&A, 23, 59

Meng J., Aitken G.J.M., Hege E.K., Morgan J.S., Jul. 1990, Optical Society of America Journal A, 7, 1243

Mertz L.N., Mar. 1979, Appl. Optics, 18, 611

Moore J.H., Paddock G.F., Jul. 1950, ApJ, 112, 48

Moorwood A., Cuby J.G., Ballester P., et al., 1999, The Messenger, 95, 1

Mozurkewich D., Johnston K.J., Simon R.S., et al., Jun. 1991, AJ, 101, 2207

Núñez J., Fors O., 2001, In: ASP Conf. Ser. 246: IAU Colloq. 183: Small Telescope Astronomy on Global Scales, 309–+

Núñez J., Codina J.M., Torras N., May 1992, AJ, 103, 1687

Neugebauer G., Leighton R.B., 1969, Two-micron sky survey. A preliminary catalogue, NASA SP, Washington: NASA, 1969

Neugebauer G., Leighton R.B., May 1997, VizieR Online Data Catalog, 2002, 0

Nordgren T.E., Armstrong J.T., Germain M.E., et al., Nov. 2000, ApJ, 543, 972

Otazu X., 2004, private communication

Palagi F., Cesaroni R., Comoretto G., Felli M., Natale V., Mar. 1993, VizieR Online Data Catalog, 410, 10153

Pasinetti Fracassini L.E., Pastori L., Covino S., Pozzi A., Feb. 2001, A&A, 367, 521

Paturel G., Petit C., Rousseau J., Vauglin I., Jul. 2003, A&A, 405, 1

Percy J.R., Hosick J., Aug. 2002, MNRAS, 334, 669

Piterman A., Ninkov Z., Jun. 2002, Optical Engineering, 41, 1192

Raharto M., Hamajima K., Ichikawa T., Ishida K., Hidayat B., 1984, Annals of the Tokyo Astronomical Observatory, 19, 469

Reynolds M., Povenmire H., Jan. 1975, IOTA Occultation Newsletter, 5, 45

Richichi A., Dec. 1989a, A&A, 226, 366

Richichi A., 1989b, Occultazioni Lunari di Sorgenti Stellari nel Vicino Infrarosso, Ph.D. thesis, Università degli Studi di Firenze

Richichi A., 1994, In: IAU Symp. 158: Very High Angular Resolution Imaging, 71–+

Richichi A., Jan. 2003, A&A, 397, 1123

Richichi A., Fors O., Dec. 2003, private communication

Richichi A., Percheron I., May 2002, A&A, 386, 492

Richichi A., Lisi F., di Giacomo A., Feb. 1992, A&A, 254, 149

Richichi A., Calamai G., Leinert C., Jun. 1994, A&A, 286, 829

Richichi A., Baffa C., Calamai G., Lisi F., Dec. 1996a, AJ, 112, 2786

Richichi A., Calamai G., Leinert C., Stecklum B., Trunkovsky E.M., May 1996b, A&A, 309, 163

Richichi A., Calamai G., Leinert C., Stecklum B., Jun. 1997, A&A, 322, 202

Richichi A., Ragland S., Calamai G., et al., Oct. 1999, A&A, 350, 491

Richichi A., Ragland S., Calamai G., Richter S., Stecklum B., Sep. 2000a, A&A, 361, 594

Richichi A., Ragland S., Calamai G., Richter S., Stecklum B., Sep. 2000b, A&A, 361, 594

Richichi A., Calamai G., Stecklum B., Jan. 2002, A&A, 382, 178

Richichi A., Percheron I., Khristoforova M., Feb. 2005, A&A, 431, 773

Richichi A., Fors O., Merino M., et al., Jan. 2006, A&A, 445, 1081

Ridgway S.T., Jacoby G.H., Joyce R.R., Wells D.C., Nov. 1980, AJ, 85, 1496

Ridgway S.T., Jacoby G.H., Joyce R.R., Siegel M.J., Wells D.C., Apr. 1982, AJ, 87, 680

Rogstad D.H., Apr. 1968, Appl. Optics, 7, 585

Saha S.K., Chinnappan V., 2002, Bulletin of the Astronomical Society of India, 30, 819

SAO Staff, Oct. 1995, VizieR Online Data Catalog, 1131, 0

Scardia M., Prieur J.L., Koechlin L., Aristidi E., Feb. 2002, In: IAU Commission on Double Stars, 1–3

Simon M., Ghez A.M., Leinert C., et al., Apr. 1995, ApJ, 443, 625

Sloan G.C., Price S.D., Dec. 1998, ApJSS, 119, 141

Speck A.K., Barlow M.J., Sylvester R.J., Hofmeister A.M., Nov. 2000, VizieR Online Data Catalog, 414, 60437

Starck J., Murtagh F., Aug. 1994, A&A, 288, 342

Starikova G.A., Jun. 1982, Pis ma Astronomicheskii Zhurnal, 8, 306

Stephenson C.B., 1976, Publications of the Warner & Swasey Observatory, 2, 21

Sturmann L., Dec. 1997, Ph.D. Thesis

The P.S., de Winter D., Perez M.R., Nov. 1993, VizieR Online Data Catalog, 410, 40315

van der Hucht K.A., Conti P.S., Lundstrom I., Stenholm B., Feb. 1997, VizieR Online Data Catalog, 3085, 0

VVAA, 1989, Publications of the Warner & Swasey Observatory, 3, 2

Walker H.J., Wolstencroft R.D., Dec. 1988, PASP, 100, 1509

Wichmann R., 1994, Ph.D. Thesis

Woolley R.v.d.R., 1970, Royal Observatory Annals, 5

Worley C.E., 1989, Publications of the U.S. Naval Observatory Second Series, 25, 1

Zhitetski A., Jan. 1977, IOTA Occultation Newsletter, 10, 110

Part III

General conclusions

Since each part contains its own conclusions, the general conclusions of the thesis are briefly listed.

Part I: Application of image deconvolution to wide field CCD surveys

1. A wavelet-based adaptive image deconvolution algorithm (AWMLE) has been applied to two sets of survey type CCD data: QUEST and NESS-T which were acquired in drift scanning and stare modes, respectively.

   Richardson-Lucy image deconvolution algorithm has been applied to survey type CCD drift scanning data (FASTT).

2. A complete methodology for applying deconvolution to CCD survey-type images has been proposed for the first time. This includes all the required steps providing homogeneity to the obtained results.

   We anticipate that could be of importance for survey programs which attempt to insert deconvolution in their pipeline reduction facilities.

3. The performance of AWMLE has been evaluated in terms of the gain in limiting magnitude. Values of $\Delta R_{\mathrm{lim}} \sim 0.64$ for QUEST and $\Delta R_{\mathrm{lim}} \sim 0.46$ for NESS-T were calculated. Note this magnitude gain is equivalent to an increase of 81% in the number of objects which can be measured in the deconvolved image and were not available in the original image.

   The asymptotic convergence of AWMLE has offered an outstanding detection efficiency with nearly zero false detection due to the algorithm itself. The outcome of AWMLE deconvolution in terms of new detected objects has been found to be independent of the number of iterations.

   Finally, the feasibility of this magnitude gain has been evaluated in the context of images which are routinely used for QSO lensing search (QUEST) or new NEOs discovery (NESS-T). As a by product of our study, the possible detection of a transient event in QUEST data set has been shown and tentative association with an new Halo X-ray Nova candidate has been discussed.

   In conclusion, AWMLE turns to be a powerful technique for increasing the number of useful science objects from the faint part of magnitude distribution. Note that the gained magnitude is equivalent to increasing in 80% the telescope collecting area (or a 32% its diameter), which would translate into multiplying its cost by 2.3. Therefore, this gain could be of interest for many projects.

4. The performance of AWMLE has been assessed in terms of the gain in limiting resolution. Identical values of $\Delta\phi_{\mathrm{lim}} \sim 1$ pixel are obtained for QUEST and NESS-T data, corresponding to $\Delta\phi_{\mathrm{lim}}^{\mathrm{QUEST}} \sim 1{''}\!\!.0$ and $\Delta\phi_{\mathrm{lim}}^{\mathrm{NESS-T}} \sim 3{''}\!\!.9$, respectively.

   Those resolution gains has been found to depend nearly exclusively on original sampling, and only slightly modulated by other factors as drift scanning systematics or limited PSF modeling.

   Finally, the feasibility of that resolution gain has been evaluated in the context of images which are used for QSO lensing search (QUEST) or new NEOs discovery (NESS-T). For example, after AWMLE deconvolution $\phi_{\mathrm{lim}}^{\mathrm{QUEST}} \sim 3{''}\!\!.9$, which is for the first time below the cutoff value of the separation distribution of the 82 gravitational lenses currently known.

   In conclusion, the deblending capabilities of AWMLE have been shown to be of interest for many projects.

5. The incidence of Richardson-Lucy deconvolution algorithm over original astrometry has been evaluated.

   A centering algorithm based on Levenberg-Marquardt Method-based specially indicated for undersampled data was employed for this astrometric evaluation. This method was found to be robust and was able to fit stellar profiles of FWHM up to 0.8 pixels (half the minimum value achieved by conventional algorithms).

   The astrometric bias present in the original FASTT images due to a defect of charge transfer efficiency in the CCD chip has been removed after deconvolution.

   Deconvolution practically has not modified the centering error with respect to the one for original FASTT images.

   No positional bias towards the centre of pixel has been observed for FASTT deconvolved positions, to the contrary of was shown in former studies of deconvolution applied to HST WF/PC 1 images.

Part II: New observational techniques and analysis tools for high resolution astrometry

Lunar Occultations

1. A new observational technique based on CCD fast drift scanning has been proposed for lunar occultations (LO) observations. It has been validated yielding positive detection of binaries up to 2.0 ± 0.1 mas of projected separation and stellar diameters measurements in $\phi \sim 7$ mas regime.

    The proposed technique implies no optical or mechanical additional adjustments and can be applied to nearly all available full frame CCDs. Thus, it enables all kind of professional and high-end amateur observatories for LO work. The recent advances in terms of speed and sensitivity in CCD technology can provide to our technique even better performance than the one accomplished in our results.

2. A four-year LO program at Calar Alto Observatory (named CALOP) spanning 71.5 nights of observation and 388 recorded events has been conducted by means of CCD and MAGIC IR array cameras at OAN 1.5 m and CAHA 2.2 m telescopes.

    The CALOP results include the detection of one triple system (IRC-30319) and 14 new and 1 known binaries in the near-IR, and one binary in the visible. Their projected separations range from $0''09$ to $0''002$, and brightness ratios reach up to 1:35 in the K band. Angular diameters of 30 Psc ($\phi_{\mathrm{UD}} = 6.78 \pm 0.07$ mas) in the visible and V349 Gem ($\phi_{\mathrm{UD}} = 5.10 \pm 0.08$ mas) and M6 RZ Ari ($\phi_{\mathrm{UD}} = 10.6 \pm 0.2$ mas) in the near-IR were also measured.

    We also calibrated the CALOP performance in terms of limiting magnitude and angular resolution yielding $K_{lim} \sim 8.0$ and ≈ 9.0, for the 1.5 m and the 2.2 m and ϕ_{lim} ranging 1-3 mas, respectively.

    Finally, CALOP binary detection probability was estimated to be $\approx 4\%$. This is significantly lower than other similar programs, and we attribute this discrepancy to that fact that the use of complete IR catalogues such as 2MASS has populated the faint magnitude end of the observable objects, where the detection efficiency is much smaller than for brighter stars.

3. a new series of special LO observations were initiated with the passage of the Moon over a crowded region close to the Galactic Center on July 28th,

2004. That resulted in 54 events observed in 1.5 effective hours, most of them IR sources without optical counterpart. This kind of events provide the opportunity to extract milliarcsecond resolution information in this obscured, crowded and relatively unstudied region. Future scheduled observations in this field with larger telescopes as VLT have also been described.

4. An innovative wavelet-based method for extracting and characterizing LO lightcurves in an automated fashion was proposed, implemented and applied to CALOP database. Typically, a few hundreds of lightcurves were reduced in matter of a few minutes. This pipeline addresses the need of disposing of preliminary results in short time basis for future programs at Calar Alto and VLT, which will provide large number of events.

Speckle Interferometry

1. A new observational technique based on CCD fast drift scanning has been proposed for speckle interferometry observations. It has been validated with the observation of four binary systems with well determined orbits.

   Results of separation, position angle and magnitude difference (ρ, θ, Δm) are in accordance with published measurements by other observers and predicted orbits. Error estimates for these have been found to be $\sigma_\rho = 0\rlap{.}{''}017$, $\sigma_\theta = 1\rlap{.}{°}5$, $\sigma_{\Delta m} = 0.34$ mag. These are in the order of other authors and can be considered as successful for a first trial of this technique.

2. CCD fast drift scanning is extensible to practically all full-frame CCDs in the market, both in professional and commercial market. Therefore, it enables low budget professional and high-end amateur observatories to conduct routine CCD speckle observations. This opens the possibility of a denser coverage of known binaries orbits still with adequate accuracy.

   The recent advances in terms of few Mpix s^{-1} frame rate and subelectron readout noise in CCD technology can lead to this new observational technique offer even better performance than the one showed in our results.

3. A new approach for calibrating the power spectrum analysis has been introduced. It does not require point source observations, which gives a more effective use of observation time. This advance is of more importance in the case of large telescopes.

This calibration method appears to be limited to zenith angles above 30°. However, we anticipate this is specific to our observation run, where Risley prisms were not used.

Appendix A

Project of automatization of a Baker-Nunn camera

In this chapter we introduce an ongoing project for the refurbishment and automatization of the Baker-Nunn camera[1] of the Real Instituto y Observatorio de la Armada en San Fernando[2]. This is a collaboration between the Fabra Observatory and the ROA. It aims to transform the Baker-Nunn camera at ROA, for robotic use with a large format CCD.

The inclusion of this appendix is fully justified and is indeed relevant in the context of this thesis for two reasons:

1. the data expected from the ROA BNC shares in common several characteristics with the surveys described and analysed all along Chapt. 3 and Chapt. 5, respectively.

   On one hand, the ROA BNC is in origin an almost twin instrument of the Canadian NESS-T BNC described in Sect. 3.2.3. In addition, as will be discussed along this chapter, the refurbishment and automatization project of the ROA BNC is very similar to the one which was executed for the NESS-T BNC. Therefore, the benefits brought by image deconvolution in the analysis carried out in Sects. 5.3.2 and 5.4.2 are also very likely to be applied to the modified ROA BNC.

---

[1]hereafter referred as modified BNC.
[2]hereafter referred as ROA.

On the other hand, the modified ROA BNC will be operated in TDI mode. This observational technique was already introduced in Sect. 3.1.3 and was shown that it shares many common features with drift scanning data. In Sects. 3.2.1 and 3.2.2 we already described two data sets from surveys operating in this mode (FASTT and QUEST), and in Sects. 5.3.1 and 5.4.1 we again showed that image deconvolution can yield successful results in terms of limiting magnitude increase and object deblending improvement.

2. this is one of the main projects which our group is currently running, in a collaboration between Fabra and San Fernando observatories. The author has dedicated a significant part of his time to develop this project.

Therefore, this project constitutes a good opportunity for applying and confirming those conclusions we reached in Part I.

What is included in this appendix has been presented and published in a summarized form in several international meetings and symposia (Núñez et al. 2003a,b,c).

A.1   Brief historical overview

The Baker-Nunn camera is an existing telescope, currently located at ROA. This instrument was one of the few units that the Smithsonian Astrophysical Observatory (Smithsonian Instituton, USA) constructed in late 50s and early 60s to carry out an observational program for photographic tracking of artificial satellites (González 2004; Henize 1957). In the particular case of the camera for current project, this was placed at ROA.

Once the technique of photographic observation of satellites was technically surpassed and replaced by program GEODSS at the beginning of the 80s (Beatty 1982), the telescope passed to property of the ROA, which has maintained it inactive although in excellent state of conservation until now.

In order to give an approximated idea of the scientific and instrumental value of the Baker-Nunn camera, an estimation of the reposition cost has been made. That amount gives an idea of the effort to construct again an instrument of similar characteristics. King-Hele (1966) estimated the cost of the instrument to be as
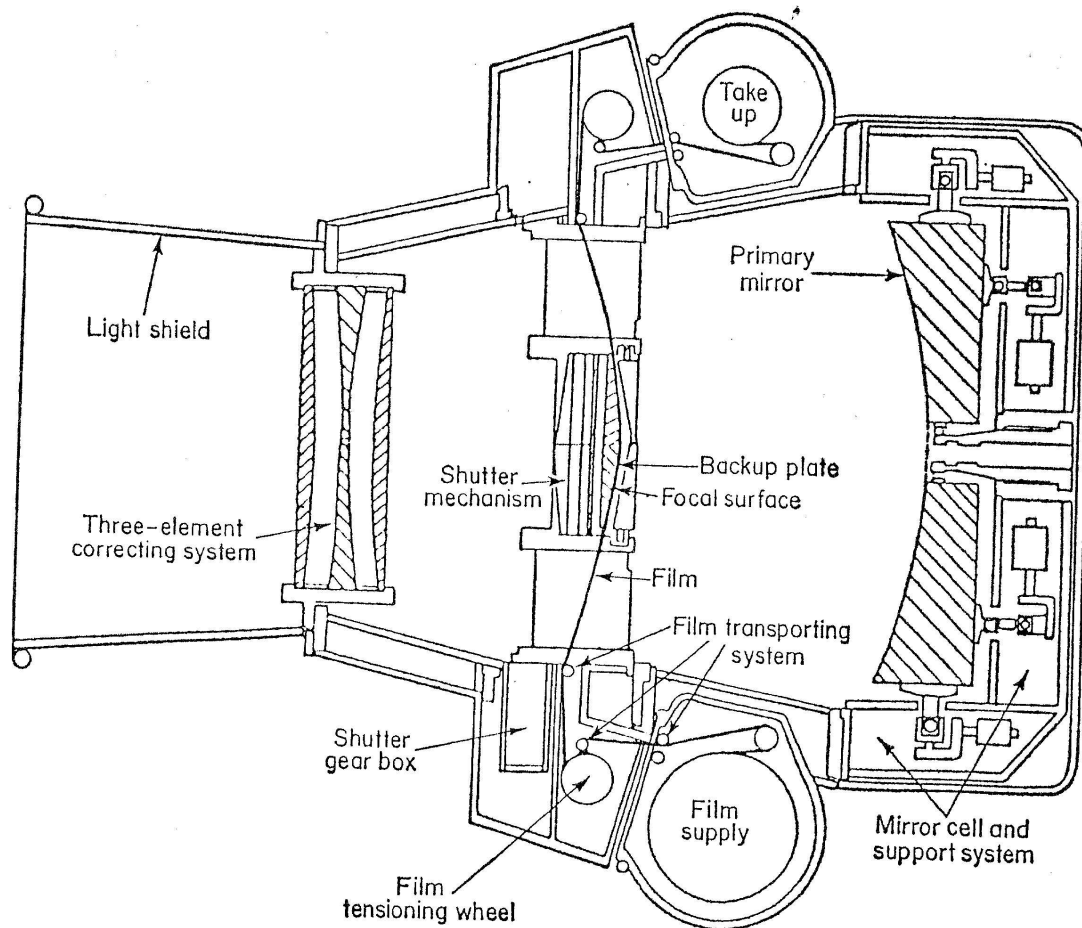
Figure A.1: Cross-section of the BNC, showing the corrector plate system, primary mirror and curved film support (Jeffrey & Jentsch 1967).

£100,000. Considering the ICP accumulated in United Kingdom from 1966, the current cost of reposition for the BNC would be about £1,180,000, i.e. 2,000,000 €.

A.2 Original instrument description

The ROA BNC is an f/1–50 cm aperture modified Super-Schmidt telescope designed for the photographic observation of artificial satellites. The superb optical characteristics of the camera confer to the instrument an extraordinary field of view (FOV) of 5°x30° with 80% incident light within a diameter less than 20μ throughout the FOV. As seen in Fig. A.1, this huge FOV is achieved both by placement of corrector plate triplet and by curving the film along the focal *plane*.

The specifications of the original design of the ROA BNC are included in Table A.1. Note that original BNC was on a three-axis mounting: azimuth, elevation and a third axis which matched the orbital plane of the satellite to be tracked. Only this last axis was motorized, as can be seen in Fig. A.2. The original optical design (Baker 1962) was considered innovative and optimized for such a short focal instrument, since it achieved to put 80% of the incident light within a 20 μm spot size and was applicable to all visible wavelengths. See Carter et al. (1992) for further details about original optical design.

Table A.1: Technical specifications of original ROA BNC.

Mechanics	
Mount Type	Alt-azimuthal
Motion	
Azimuth	Manual
Elevation	Manual
Orbital tracking	Synchronous drive
Optics	
Design	Original from James Baker
Aperture	50 cm
Focal ratio	f/1
Scale	410 $''$ mm^{-1}
Mirror diameter	0.78 m
Field of view	5 $°$ x 30 $°$
Spot size (80% energy)	$\leq 20~\mu m$
Detector	
Sensor	Curved Cinemascope film
Format	55 mm

A.3   Refurbishment project

In this section we detail all the steps needed to transform the original BNC into an automatic facility able to gather large amount of scientifically useful data. As will be seen, the adaptation of the camera for the use with CCDs can lead to a useful squared FOV of 5°x5° by means of a simple modification of the optical system. This opens the possibility, unique in its class, of performing precise systematic observations of huge sky areas in a reduced time and at a faint limiting magnitude regime.
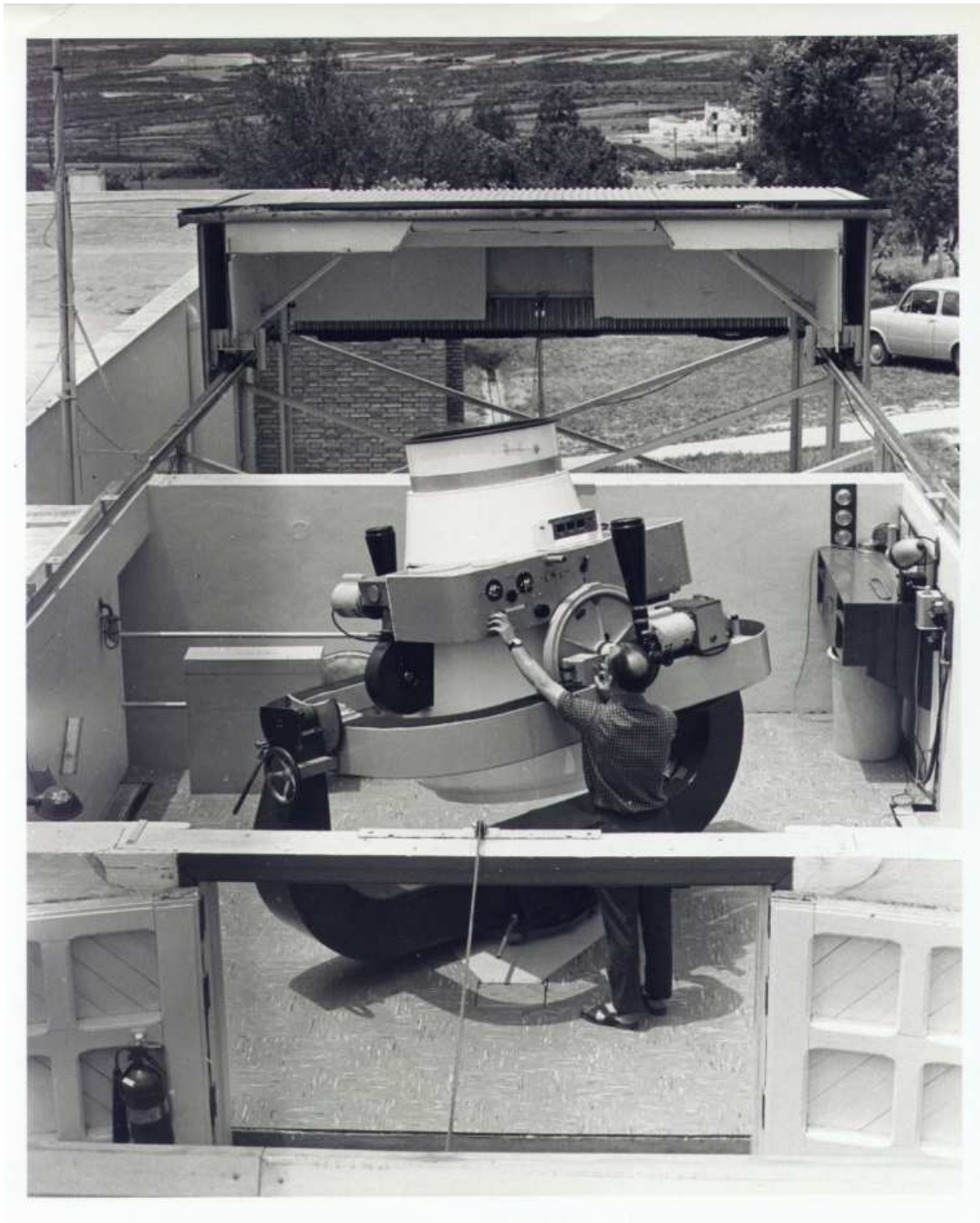
Figure A.2: Baker-Nunn camera in San Fernando when it was operating the follow-up program of artificial satellites, coordinated by the Smithsonian Astrophysical Observatory.

In Table A.2, we include a summary of the specifications for the ROA BNC once the refurbishment project will be completed. The various phases of the project are described below in order of execution:

Table A.2: Technical specifications for modified ROA BNC.

Mechanics	
Mount Type	Equatorial
Motion	
RA	Digital wide range servo drive
DEC	Digital wide range servo drive
RA maximum speed	5 deg s^{-1}
DEC maximum speed	5 deg s^{-1}
Pointing	
Tracking drift	< 1 sec h^{-1}
Absolute accuracy	RA:1.5 sec, DEC:20$''$
Optics	
Design	Baker design with field flattener
Aperture	50 cm
Focal ratio	f/1
Scale	410 $''$ mm^{-1}
Mirror diameter	0.78 m
Useful FOV for CCD	5 $^\circ$ x 5 $^\circ$
Spot size (80% energy)	$\leq 20\ \mu$m
Filters	Schott GG475 glass filter
Detector	
Sensor	Kodak KAF-168801E
Format	4Kx4K, 9 μm, 36.8 mm x 36.8 mm
QE	67% (peak)
Camera	Finger Lakes Instrumentation IMGX16801E
Cooling	Peltier (ΔT ~ 50 ℃) + intra-tube water heat pumping
Support CCD	Spider with low expansion material,
	tip-tilt orientation and
	$\pm 1\ \mu$m accurate remote focus

A.3.1   Optical refiguring

In order to maximize the useful FOV the projected image has to be disposed on a well-defined focal plane. On one hand, this will be partially achieved by modifying

certain parameters of the optical system as the focal length and the alignment and distance between the corrector lenses and the primary mirror. On the other hand, the inclusion of a new field flattener near the focal plane is mandatory.

The concept of this field flattener design has been adapted from the one adopted by the NESS-T BNC at Rothney Astrophysical Observatory, a project which was already introduced in Sect. 3.2.3, and further described in Mazur et al. (2005). Actually, both designs were performed by the same engineer Malcolm MacFarlane. For further details than those exposed in lines below, see MacFarlane (2004a). The Automated Patrol Telescope (APT), property of the Department of Astrophysics and Optics of the University of New South Wales (Australia) (Ashley 1992), has also been optically refigured by following a different approach which involves repolishing the exterior surface of the first lens of the 50 cm corrector triplet (Carter et al. 1992). Since this operation is potentially risky, we chose the approach followed by NESS-T BNC team, which does not imply the change of any of the original optical surfaces.

The field is flattened by means of a positive lens close to the CCD chip (actually inside camera housing) and a meniscus lens farther from the focus provides correction for the astigmatism introduced by the field flattener (see Fig. A.3). In order to keep the field flattener from introducing unacceptable aberrations, it is necessary to place it as close as possible to the focal plane array (see Fig. A.4).

The performance of the design is shown in Figs. A.5 and A.6. In the first, the spot sizes at different wavelengths and 5 different radial distances from the optical axis are shown. Note that the figure of merit is reasonably uniform across the $6°25$ diameter FOV. The second represents the polychromatic ensquared energy at these same five points and wavelengths. It is noteworthy that in more than five degrees of FOV 80% of the incident light is ensquared within a 20μm pixel, which meets the original design specification. Only at very extreme regions ($> 3°125$), the ensquared energy falls to just over 65%.

One remarkable difference exists between the chosen design and the one implement at the NESS-T BNC, and comes from the fact that the modifed BNC will be operated in a time delay integration mode (TDI). Two special considerations apply regarding this new requirement:

- the optical design should minimize the barrel distorsion which normally appears when correcting elements are included close to the focal plane. This has
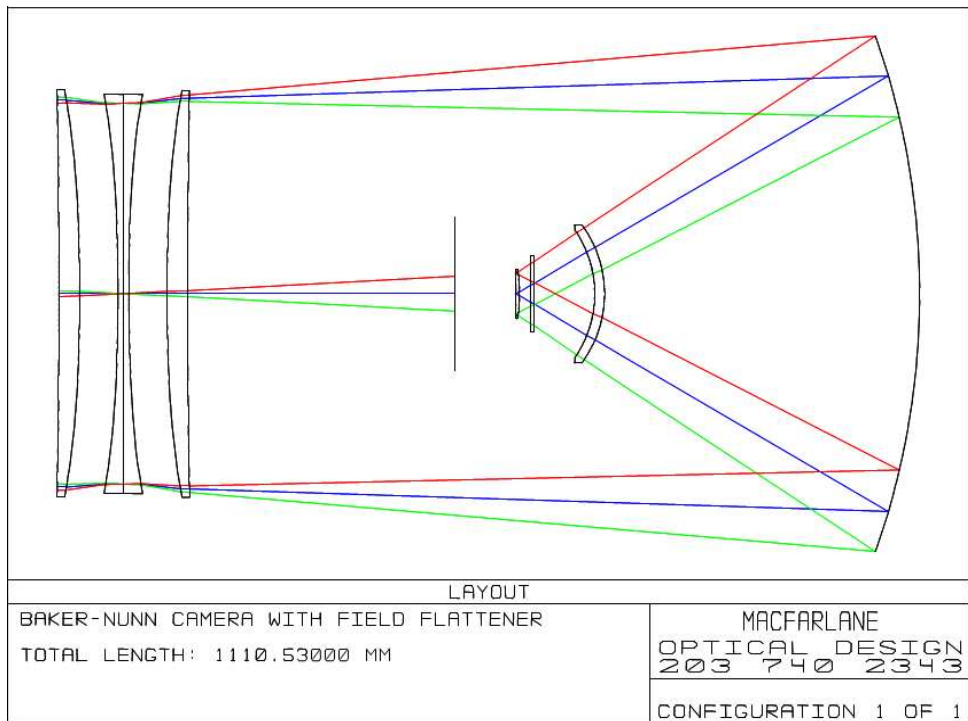
Figure A.3: Optical layout of modified ROA BNC.
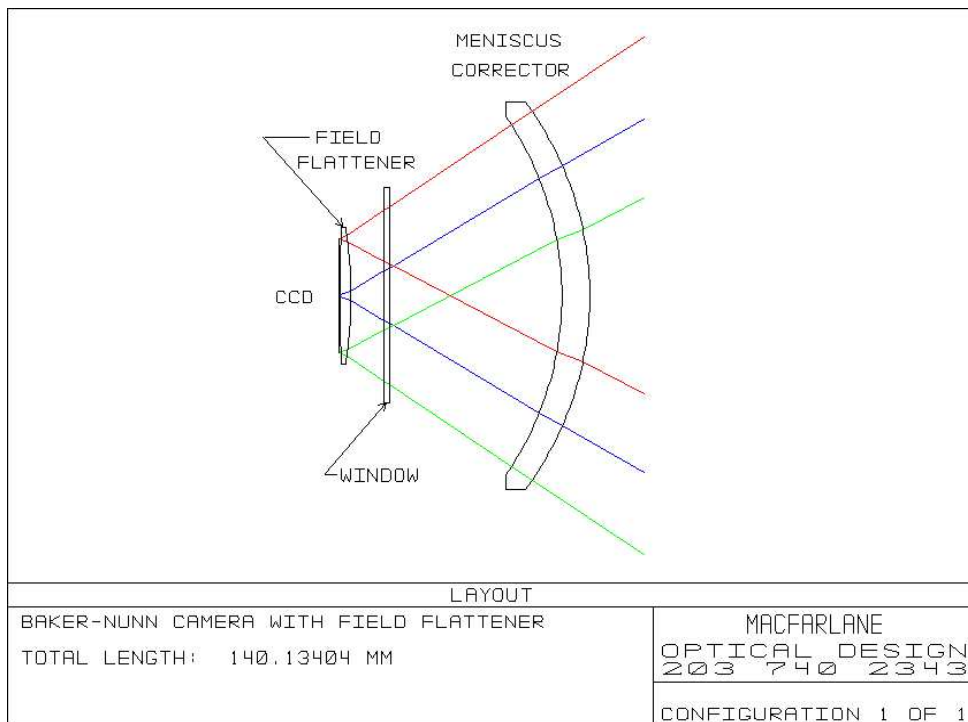
Figure A.4: Detail of the field flattener. The chosen GG475 glass filter will play as a CCD window.
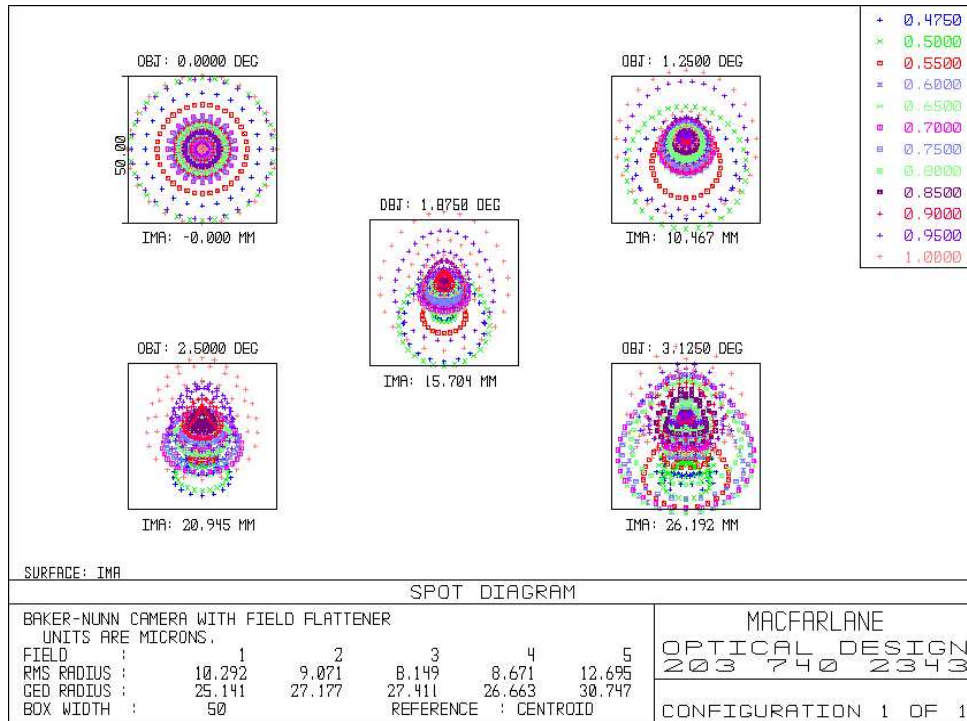
Figure A.5: Spot diagrams at 5 semi-field points in 12 wavelengths.
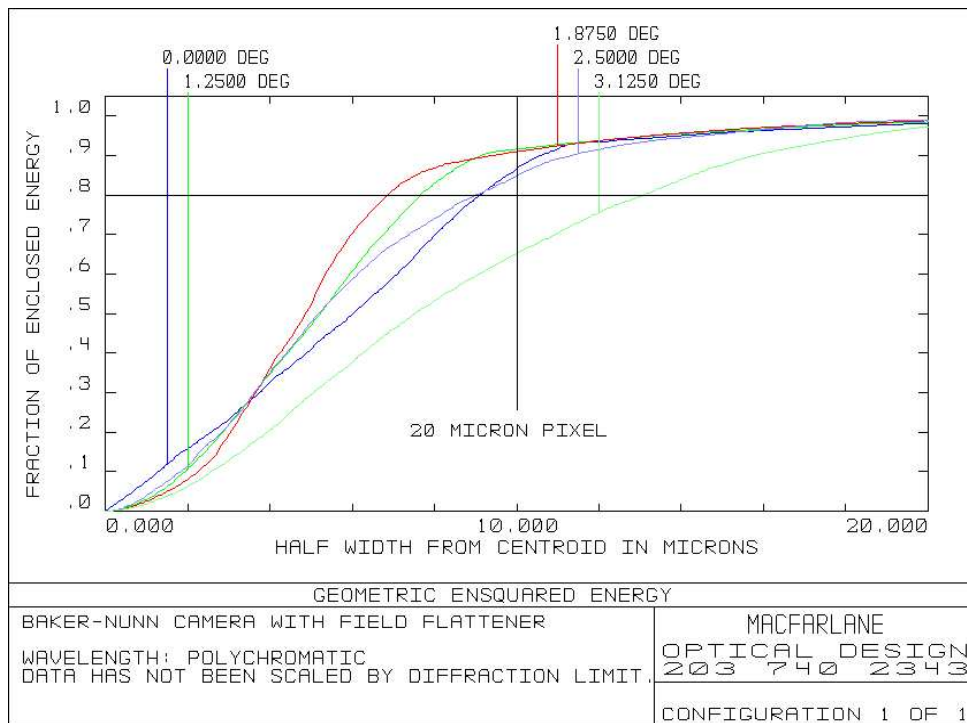
Figure A.6: Polychromatic ensquared energy plots at 5 semi-field points.

been already addressed in our case and, as seen in Fig. A.7, the distorsion at the edge of the FOV has been minimized.

- we recall that TDI observation inherently introduces distorsion in the stellar profiles due to curved stellar trails across the CCD (see Sect. 3.1.3). In the case of the modified ROA BNC with the specifications of Table A.2, the distorsion because of curvature effect is about 1.5 pixels in the extreme columns of the CCD FOV (Montojo 2004a,b).

Thus, the optical design should be conceived to compensate that distorsion, assuring that a star trail lies along a single column while shifting across the FOV. This could be achieved by introducing an inverse barrel distorsion with equal magnitude as trail curvature and only in the drift scanning direction. This approach has already been suggested and implemented by several authors in the past (Hickson & Richardson 1998; Vangeyte et al. 2002). We are currently considering the inclusion of that correction in the optical design (MacFarlane 2004b), keeping this as simplest as possible, and not introducing any additional element.

Further details of TDI operation with the modified ROA BNC will be commented in Sect. A.4.2.

At this point, a consideration about the chosen filter in the design (see Table A.2) is appropiate. GG475 is a short wave cutoff glass filter which blocks wavelenghts bluer than $\lambda = 475$ nm. The inclusion of Johnson filters was early discarded because they are incompatible with the compact 2-element flattenner design we chose. On one hand, this is greatly distorted (spherical aberration) due to the large incidence angle of the beam ($\sim 40°$) over the filter surface. On the other hand, the bandpass of the filter is being modified as a function of radial distance (Henden 2001). These two distortions are caused by the fact that Johnson filters are bandpass, resulting from the combination of short wave cutoff filters and, sometimes, interference edge filters. In contrast, GG475 is made of a single glass with far simpler structure and better behaved properties under high angle incident situations. Note that it is not surprising that Johnson filters do not perform well under an f/1 beam, because they were designed for the most common situation in astronomy where the focal ratio is much larger and incident angle far smaller.

In addition, it is noteworthy that Johnson filters could be used provided the f/1 beam were flatten before reaching the filter. This implies to repolish the first
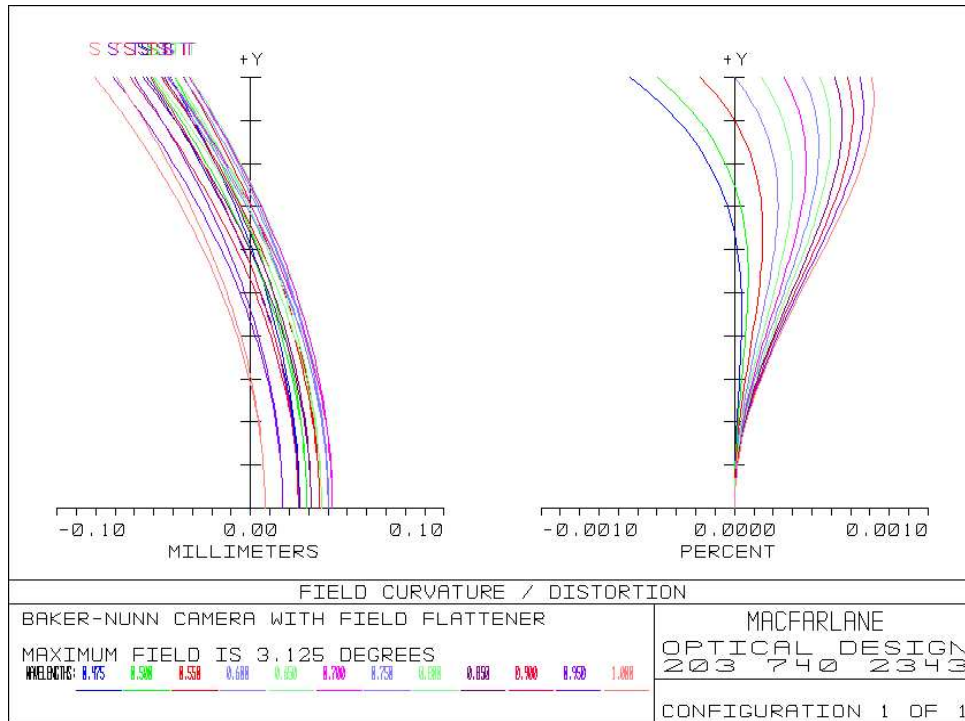
Figure A.7: Distortion vs. semi-field angle at 12 wavelengths showing <0.001% barrel distorsion.

element of the 50 cm triplet. That approach was already chosen by Carter et al. (1992), but we discarded it for being complex, expensive and risky.

Finally, in addition to the new field flattenner inclusion, a complete cleaning (internal and external) of the camera is planned. This will include an in-depth cleaning of the exterior side of the 50 cm corrector triplet lenses and its recoating with a anti-dew MgF_2 layer. The primary mirror will be also realuminized.

A.3.2 Mechanical modification

The complete automatization of the mount will take place in two different stages.

1. The original alt-azimuthal mount (see Fig. A.8) is being converted to equatorial. The choice of alt-azimuthal mount was early discarded, because the subsequent inclusion of a derotator would complicate the design of de detector support and focus accuracy. In this case, we followed the approach applied for the Australian BNC, since the azimuth axis was in both cases driven manually,
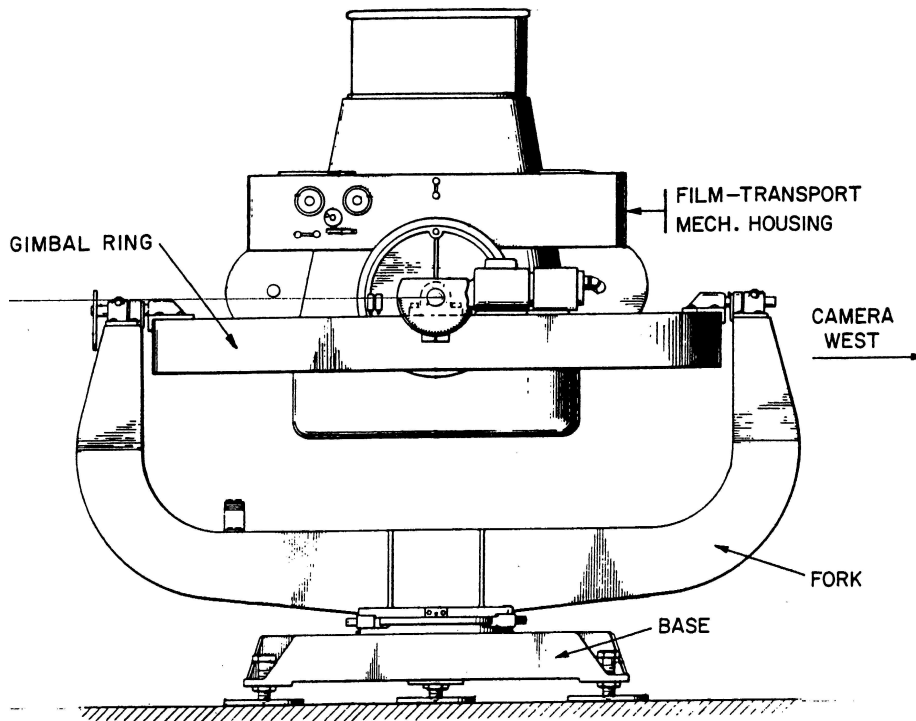
Figure A.8: North section of Baker-Nunn original camera, with its alt-azimuthal mount (adapted from BNC user manual (Jeffrey & Jentsch 1967)).
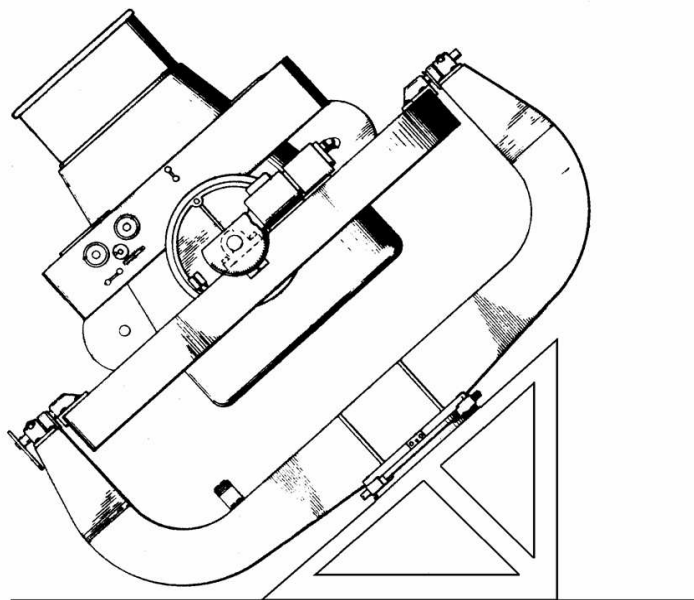
Figure A.9: North section of the modified ROA BNC equatorial mount (adapted from BNC user manual (Jeffrey & Jentsch 1967)).

in the contrary of NESS-T BNC which was originally motorized. The mount modification consists in removing the base and inclining the fork accordingly to the colatitude of the observing site. This will be achieved by inserting a new inclined base (see Fig A.9). As a result of this new mounting, the former elevation and orbital tracking axes turn to be the hour angle and declination axes, respectively.

The execution of this part of the modification is near completion. The manufacturance of the inclined base is being carried out at ROA. In addition, a new wheel has been manufactured and installed in the RA axis, as seen in Fig. A.10. Worm drive systems have been chosen in favour to friction drives due to the heavy optical tube assembly of the modified ROA BNC and that no extremely good pointing accuracy is required for our working scale. The likely to appear periodic error will be corrected by software means. In the same way, backlash will be compensated by the inclusion of a drive over the RA gear which guarantees constant pressure with the drive.

This mount transformation has one advantage and one disadvantage. On one hand, it allows to have an equatorial setting with very few changes in the original mount: except the suppression of the base, none of the other parts have to be modified in shape or length. On the other hand, the camera motion is somewhat limited in declination (regions with $|\delta| > 75$ ° are forbidden because of the gimbal ring occlusion) and in hour angle ($|\Delta H| < 4$ hours). Further details of this design can be seen in pictures included in Ashley (1992).

2. The next step is the motorization of both motion axes (right ascension and declination). There are two specific requirements in the modified ROA BNC which restrict the election of the axis drives solution. On one hand, TDI mode requires the declination axis to turn arbitrarily slow (see Sect. A.4.2 for further details). On the other hand, as pointed out in Sect. A.5.2, some specific observational programs as GRB detection, will require sub-minute fast slewing of the camera to location of the target. As a result, a motion system with wide dynamic range is required. A digital servo-controlled drive (Bearing Engineers 2002; Worldservo 1999), which offers position, velocity and torque closed-loop control, was chosen. Two additional interesting features of this election are worth mentioning. First, the drive can be easily controlled through an stepper controller card. Second, there is practically no dependence between the speed and the torque of the drive. This is very convenient for high inertia systems as the modified ROA BNC, which has a heavy optical tube assembly.

Figure A.10: Newly manufactured RA worm wheel drive installed at the RA axis.

3. Other devices which play a key role in the mount control are the absolute encoders (one per axis) and a GPS board plugged in the control computer. The first are necessary for feeding-back the actual position of the telescope to the servo drive. The second will be required for providing sub-millisecond accurate time stamps when operating the telescope in TDI mode. Those uniform time signals will be crucial for the proper astrometric reduction of resulting long TDI scans.

A.3.3   CCD support

Whereas the original design of the camera Baker-Nunn was intended for using photography film, the current project aims to use a large format CCD as a detector. As it is well known, this introduces a series of advantages (larger quantum efficiency, linearity, easier data processing and analysis, etc.).

Several considerations must be taken into account when addressing the design of the CCD support, namely:

1. since BNC is a Super-Schmidt system, the detector must be placed inside the tube. This introduces constraints in the specifications of the CCD camera to be installed. On one hand, it must be as much compact as possible to minimize the obscuration inherent in this kind of design. On the other hand, a heat evacuation system by water pumping is very recommended in order to minimize turbulence inside the tube. Finger Lakes Instrumentation IMGX16801E camera (FLI 2002) was found the one which best met both considerations.

2. as commented in Sect. A.3.1, the design for the field flattener turns to be very compact and, in the case of the second element, very close to the CCD chip. This introduces additional constraints in the design, as for example the inclusion of an anti-dew inert gas pumping system.

3. given the extremely short focal length of the instrument, the focus system becomes a crucial part of the overall telescope. An f/1 ratio implies that a minimum shift of whatever part of the optic system translates into a defocusing over the focal plane of exactly the same amount. Therefore a precise focus and tip-tilt stage is mandatory. In addition, the appropriate thermal low expansion material should be chosen for the CCD support.

With all this in mind, it is not surprising that CCD support is considered the most important part of the overall refiguring project. Note that it integrates the rest of new parts added to the original optical system, namely: a focus system and its housing, the CCD camera housing, an external large format shutter, the CCD camera and the two elements of the field flattener with their corresponding cells. As in the case of the design of the field flattener, we chose to follow the same approach as NESS-T BNC, which is the one we have briefly described in the lines above. This project was conceived and executed by DFM Engineering, Inc. See DFM (2003) and Mazur (2003) for further description of this part of the refiguring.

A.3.4 Observing site and operational modes

Once the refurbishment project will be completed, the modified ROA BNC will be moved to the definitve observing site. This is planned to be located at the newly created Observatori Astronòmic del Montsec, at the catalan pre-Pyrenees mountains (Fernández et al. 2004). This observatory already comprises a 80 cm

Figure A.11: Displaced spider vanes, focus and CCD housing of the NESS-T BNC while maintenance operations (courtesy of Rothney Astrophysical Observatory).

robotic telescope which, is operated by the Astronomy Department of the University of Barcelona among other institutions. From there the modified ROA BNC will be able to operate in three distinct modes:

1. **In situ** This is the basic mode which all the telescopes work. It is planned to allocate the modified ROA BNC in a glassfibre reinforced enclosure, in the same way other robotic projects as SUPERWASP in La Palma (Pollaco 2002) have done in the past.

2. **Remote** Recent advances in telecommunications have enabled the control in real time mode of remote devices: telescopes are not an exception. Thus, the installation of a high gain microwave antenna for fast internet communication and the mount upgrade and automatization described in Sect. A.3.2, will allow real time remote operation from any part of the world. Apart from routinary observations, this mode is crucial for checking the status of the whole system (telescope or control loop).

3. **Robotic** As will be explained in Sects. A.5.1 and A.5.2, most of the observational programs scheduled for the modified ROA BNC are conceived to be operated under unatended conditions, in other words, in robotic mode. This constitutes a new feature with respect to the other two modified BNCs, which are currently being operated only in situ and, in the Australian case, also in remote mode.

A robotic facility which is able to take decissions autonomously as a function of a number of well defined parameters (weather conditions, power network or internet failure, dome blockage, GRBs alarms), results to be a more effective and cheaper telescope, because actual hours of observation are increased, maintenance manpower is reduced and, of course, visitor expenses are minimized.

The team in ROA has accumulated extensive experience in this field leading since 1997 two fully operational robotic facilities: the Carlsberg Meridian Circle at La Palma (Belizón et al. 2003) and the San Fernando Automatic Meridian Circle at San Juan (argentina) (Muiños et al. 2003).

With this background in mind, we plan to implement that operational mode to the modified ROA BNC. Further details about this topic can be found at Muiños et al. (2004).

A.3.5 Observatory control system

For the proper development of the three operational modes enumerated above, an appropiate telescope control system (TCS) is required. The inclusion of remote and robotic modes, introduces higher complexity in the design of the TCS, because a higher number of devices must be controlled and centralized within a unique observing program. Robotic operation is actually the extreme case, due to it requires that ALL the instruments and sensors in the observatory have to be integrated in the TCS decision loop.

A short list of the devices to be controlled by TCS PC is shown in Fig. A.12. Note the PC-CCD line includes CCD camera command, image download and focus command. The PC-dome (or roll-roof) line includes dome motion control and global status webcam command. Finally, servo controllers-BNC line includes RA and DEC motor command and corresponding encoders feed-back.
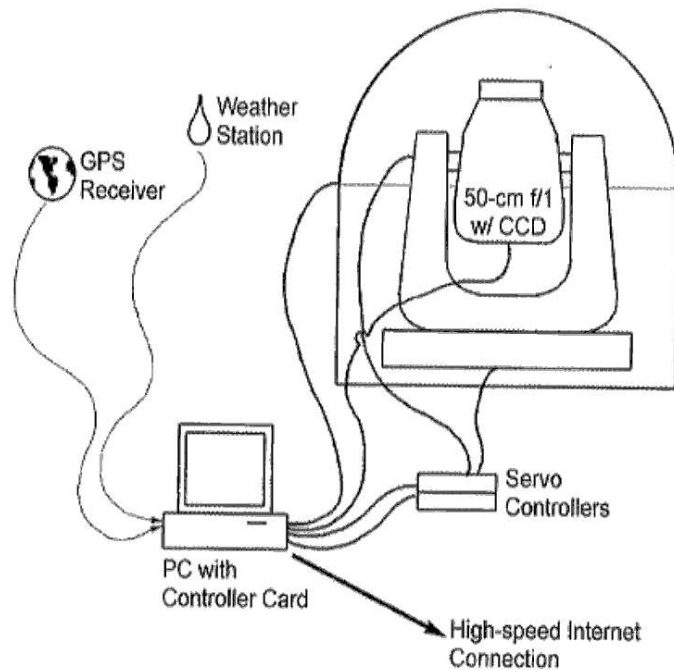
Figure A.12: Simplified scheme of some of the devices controlled by the TCS. See text for further details of devices not shown here. Courtesy from Mazur (2004).

We decided the TCS to be run under Linux, among other reasons, because this is the mainstream option in astronomic world, both in the TCS and data analysis and reduction sides. Consequently, some care was taken in the ellection of the devices and sensors giving preferences to those brands and models which do support Linux in their drivers and developer libraries.

A definitive TCS package has not been designed yet, since this highly depends on the final integration details of the hardware used. However, it seems to be clear that the ultimate TCS will result from an evolution of the package called Talon. This formidable TCS was created in 1999 by Elwood Downey under the name of OCAAS, which stands for Observatory Control and Astronomical Analysis System. This was sold to Torus Technologies, Inc. which renamed as Talon. Later they made it open source in Sourceforge (Steidler-Dennison 2003, 2004).

Talon supports insitu, remote (these two interactive and real-time) and robotic (unattended batch-scheduled use) operational modes. It controls a good number of devices present in an observatory: telescope mount, CCD camera, filter wheel, focuser, weather instrumentation, power supply, GPS receiver, internet line, dome

and shutter hardware, etc.

All the hardware chosen up to now for the control of the modified ROA BNC (multi-axis controller board, servo-drives, encoders, CCD camera, weather station, GPS board, etc.) do match with the drivers comprised inside Talon. So we expect to be fully operational with that package with little effort in adaptation process by our side.

In addition to Talon upgrade, the investigation of leading communication protocols are being considered. During the last few years, Downey & Mutlaq (2005) have been developing a parallel project for defining an XML-like communication protocol for interactive and automated remote control of telescopes. This is named INDI, which stands for Instrument-Neutral Distributed Interface. The main aim in INDI is in order to decouple GUI client from driver which resides in the observatory and talks to the device to be commanded. In a way, this allows to save time in migrating client-side software when a device has been changed or updated. As this is a client-server XML based protocol, INDI can be easily integrated into WWW browsers or other common query tools. In addition, INDI can be nested to other XML based protocols, such as Remote Telescope Markup Language (RTML) (Pennypacker et al. 2002, 2003), which are also under development.

Moreover, we also plan to incorporate part of the programs which ROA has been using for years to control the Carlsberg and the San Juan Meridians Circles. This code accumulates valuous and extensive experience in optimizing strategies when observing under robotic mode.

A.4 Data acquisition schemes

The modified ROA BNC will operate under both stare and TDI modes. This last was preferred instead of drift scanning, because of the large distorsion introduced by differential trailing effect in the case of a very large FOV instrument as the modified ROA BNC (see Eq. 3.6).

We refer the reader to Sect. 3.1.1 and 3.1.3 where the systematics for these two data acquisition schemes were introduced and discussed in a generic way. In the forthcoming lines, we discuss the impact of this effects and other data aspects of

those two observing modes in the particular case of modified ROA BNC.

A.4.1   Stare mode

This mode will be totally analogous to the one employed in NESS-T BNC. Therefore, in general we expect to obtain pretty similar data to the presented in Sect. 3.2.3 for the Canadian BNC. While there is no specific reason to suspect a significant change in the limiting resolution (see Sect. 5.4.2), the limiting magnitude is likely to increase due to the darker condition of our site with respect to NESS-T BNC:

On one hand, in Sect. 5.3.2 we obtained $R_{\mathrm{lim}} \sim 15.8$ for typical exposure times of 30 s, under waning crescent Moon and thin clouds conditions. Mazur (2004) reported $R_{\mathrm{lim}} \sim 19$ with 120 s exposure on a clear moonless night. That is in agreement with the range of zenithal $V_{\mathrm{sky}} \sim 20.1 - 19.1 \ \mathrm{mag}/\square''$ extracted from global light pollution maps (Cinzano et al. 2001a,b), which can be queried at Danko (2001) for the specific location of Rothney Astrophysical Observatory.

On the other hand, systematic light pollution study campaign has been conducted at Observatori Astronòmic del Montsec (Fernández et al. 2004; Torra & Fernández 2000). This yields to an estimate for zenithal V_{sky} which is around 22 $\mathrm{mag}/\square''$, which turns to be nearly natural darkness conditions.

Therefore, we estimate we could increase the limiting magnitude by a significant amount with respect to NESS-T BNC, given the exposure time would be less limited by the sky background brightness. All in all, a reasonable estimate for a exposure time of 120 s of the modified ROA BNC can be fixed as $R_{\mathrm{lim}}^{stare} \sim 20.5$.

Of course, under this stare mode, since all the key specifications of the modified ROA BNC (adopted optical design, CCD support and focus stage design and CCD camera) will be very similar (sometimes identical) to those followed in NESS-T BNC, we can savely expect that all conclusions extracted from the application of image deconvolution to the Canadian BNC data (see Sects. 5.3.2 and 5.4.2) will apply for our modified ROA BNC. In particular, two of those are worth remarking:

- increase in $\Delta R \sim 0.6$ in the limiting magnitude can be of great interest for improving the efficiency of those observational programs under stare mode which will described in Sect. A.5. In addition, we recall the relation between

$\Delta R \sim 0.6$ and the cost-effectiveness of a typical telescope building process, that we exposed in Chapt. 6. For the particular case of an f/1 high quality optics instrument as the BNC, it is likely that cost vs. diameter relation would become even more important, and therefore the limiting magnitude gain be even more advantatgeous.

- object deblending could help in the resolution and identification of close objects which otherwise would have been accounted as single detections.

A.4.2 TDI mode

The operation of the modified ROA BNC under TDI mode will be achieved by tracking the BNC in RA at sidereal rate (as it is normally done under stare mode), and simultaneously slewing the camera in DEC along great circles. In other words, during a single long DEC strip, the telescope follows a meridian of constant RA. The modified ROA BNC under this mode shares characteristics in common with the three data sets described at Sect. 3.2 and analyzed with image deconvolution in Chapt. 5.

On one hand, as already commented in Sect. A.4.1, the optical and the CCD specifications of both BNCs are very alike.

On the other hand, it will operate under TDI. This, as seen in Sects. 3.1.2 and 3.1.3, implies the introduction of several systematics, inherent to this adquisition mode. Below, we briefly discuss the impact of these effects in the particular case of modified ROA BNC under TDI:

1. recalling what is explained in Pags. 61 and 72, the discrete shifting effect depends only on the sampling of the data before being convolved with $\Lambda(x)$ function. In the case of the modified ROA BNC, we can safely assume this will be very similar to the value of $FWHM \sim 2.2$ pixels we obtained in Sect. 3.2.3 for the NESS-T BNC[3]. Thus, for a $\sigma = 2.2/2.354 = 0.93$ pixels we obtain, from Fig.3.4, that intensity peak decreases by a 12%. In comparison, note that the same instrument under stare mode will be affected by a 4%. As a

---

[3] We recall that the sampling for the modified ROA BNC and NESS-T BNC is slightly sensitive to seeing and dominated by spot size, because of their coarse pixel scale.

result, it is likely that the limiting magnitude of TDI data become slightly smaller than the one derived in previous Sect. under stare mode.

2. as explained in Sect. 3.1.3, the differential trailing effect is not present in TDI, in contrast to drift scanning projects, such as FASTT and QUEST projects (see Sects. 3.2.1 and 3.2.2, respectively), which does suffer from this effect.

3. although TDI does suffer from curvature effect (see Sect. 3.1.3), we aim that the inclusion in our design of the inverse barrel distorsion (see Sect· A.3.1), this effect will be greatly minimized.

Attending all these considerations, we can conclude that the systematics in the modified ROA BNC under TDI are likely to be less serious than those present in FASTT and QUEST.

Likewise, the modified ROA BNC turns to be a sure target for the applicability of the image deconvolution, in the sense that the expected results will be in the order of those exposed in Chapt. 5. Again, this conclusion is particularly interesting as regard as the reported limiting magnitude gain and the increase of resolution. In this way our group has been granted in a three-year project in order to develop image deconvolution and superresolution algorithms (AYA2005-08604).

Actually, such benefits are even more pertinent than in the stare mode case, since:

- object blending can be larger than in stare mode, due to the systematics explained above.

- under TDI the effective exposure time, although can be set arbitrarily long, in practice it is fixed to a given value which is a trade-off between limiting magnitude and surveying efficiency,

It is noteworthy that, if TDI succeeds, it will be the first modified ROA BNC, and one the few wide field facilities with moderate limiting magnitude, which will operate under this mode.

A.5 Scientific project

We can consider several observing programs to be developed with the modified ROA BNC. These can be grouped in the following two subsections.

A.5.1 QDSS: Quick Daily Sky Survey

This survey is the result of operating the modified ROA BNC in TDI mode. With the planned BNC FOV (4.2°x4.2° with the 4Kx4K CCD camera), up to 25% of the sky between $-30° < \delta < +70°$ up to $V \sim 19.5 - 20$ could be daily covered. Thus, we call this program Quick Daily Sky Survey (QDSS).

From a pratically view, the operation of this survey comprises the following steps:

1. one of the axis of the CCD chip must be aligned in the N-S direction, so that the serial register becomes perpendicular to that direction. This should be done only once and manually, but accurately.

2. the telescope tracking drive should be started, in order to the same RA of the sky is imaged during a whole single strip is imaged.

3. once we have park the telescope at the starting declination, we slowly slew declination drive at the same rate which CCD row charge is shifted towards serial register. In other words, we synchronize readout of every line with declination telescope drive. We plan to spend 30 ms for every line, resulting an effective exposure time of 120 s for a 4kx4k chip. Declination slew will tipycally last up to δ=80°, where strip overlapping starts to become significant.

   Note, however, that the readout line rate could be increased, if we see our dark sky allows us to go deeper, and this does not penalty the survey efficiency.

4. once a strip is finished, telescope is fastly slewed back to the starting declination while moving to its neighbour RA and it starts another strip in DEC.

This is the basic operational QDSS strategy, which greatly resembles other TDI surveys as the Sloan Digital Sky Survey (SDSS) (Gunn et al. 1998). Of course the strategy of QDSS can be optimized over a number of target functions, namely:

1. maximum covering area,

2. minimum employed time,

3. minimum overlapping in polar regions,

4. account special attention to specific zones of the sky (ecliptic, galactic plane, etc),

5. and several combinations of one of the above mentioned.

A significant effort in defining such strategies has been carried out by one member of our group (Montojo 2004a,b).

Below a brief discussion about the anticipated coverage efficiency figures is given:

Let assume a BNC with a useful FOV of 5°x5°. This could be covered up to 4.4°x4.4° with a 4kx4k 9μ pixel CCD, yielding an astrometric scale of $3.9''$ pixel^{-1}. Let us suppose, also, a TDI equivalent exposure time of 120 s. Therefore, we have a scanning speed of $v = 9.7$ □°/min= 581□°/h. Assume, finally, a 12h night (Δt=12h). We can estimate the daily coverage as:

$$S = v\Delta t = 6970\square°/\text{night} \tag{A.1}$$

which is more than the 25% of the overall visible sky from the Northern hemisphere.

Attending the considerations about limiting magnitude under TDI mode in Sect. A.4.2, we can estimate $R_{\text{lim}}^{QDSS} \sim 19.5 - 20$. In this magnitude range, there are many astronomical and astrophysical fields that could benefit from this survey.

One of the challenging aspects of the survey is the mining and analysis of the great volume of data produced. It is estimated that the QDSS will generate up to 25 Gb/night (4 Tb/year) of raw data. To face this, the group is participating in a COST-TIST Action, named Computational and Information Infrastructure in the Astronomical Datagrid (Murtagh 2001-2005), which is specifically devoted to this topic.

A.5.2 Specific observational programs

Apart from QDSS, BNC will be able to operate a good number of specific programs of diverse nature. See Kron (1995); Nemiroff & Rafert (1999) for an extensive review of the automated surveys operating similar observational programs. Below we mention a few of them:

1. Discovery and tracking of NEOs: A complete census of these objects is demanding for accurate calibration of Earth-collision probabilities. This is the main objective of NESS-T BNC under stare mode. A member of our group, M. Merino, has spent a research stay with that group, and the preliminary results obtained there have proven the feasibility of such program.

2. Observation and tracking of main belt asteroids and comets: This work has been developed at Fabra and San Fernado Observatories for more than a century. BNC technical specifications will be ideal to enforce this activity.

3. Discovery and tracking of transneptunian objects (TNOs) and Kuiper belt objects (KBOs). Although $R_{\lim}^{stare} \sim 20$, is a bit short for this field, this could be compensated with the extraordinarily large FOV of BNC, which will greatly increase the probability of discovering such slow motion objects. Actually, the Australian BNC (APT) has already succeed in this field (Sheppard et al. 2000).

4. Detection of extrasolar planets: again, photometric transit technique applied over a large FOV is likely to bring positive detections, since it greatly increases the number of measured stars per hour and, consequently, the probability of spoting a transit. A definitive proof of this is the University of New South Wales Extrasolar Planet Search which is succesfully being conducted at the Australian Baker-Nunn camera (APT) (Hidas et al. 2005). Other projects with similar specifications as WASP (Pollacco 2005) or XO (McCullough et al. 2004) are already active and obtaining promising results in this field of research.

5. Detection and monitoring of optical transient events such as gamma ray bursts (GRBs), supernovae (SNs) and novae. Again, the BNC large FOV combined with its planned fast slewing response will permit to point the GRB afterglow few tens of seconds after satellite alarm has been given.

6. Discovery and tracking of space debris (0.1m-1m). Curiously, this is what the original BNC was design for. A complete orbit catalogue of these objects

is demanding, and the modified ROA BNC could contribute to monitor and discover new objects of this kind.

Bibliography

Ashley M.C.B., 1992, The Automated Patrol Telescope, available at
  `http://www.phys.unsw.edu.au/~mcba/apt.html`

Baker J.G., 1962, U.S. Patent 3,022,708, where Baker-Nunn design is described

Bearing Engineers I., 2002, Avanced Vector Servo (AVS), available at
  `http://www.bearingengineers.com/avs.html`

Beatty J.K., 1982, Sky Telesc., 63, 469

Belizón F., Muiños J.L., Vallejo M., et al., Nov. 2003, In: Astronomy in Latin
  America, 61–68

Carter B.D., Ashley M.C.B., Sun Y.S., Storey J.W.V., 1992, Proc. Astron. Soc.
  Aust., 10, 74

Cinzano P., Falchi F., Elvidge C.D., Dec. 2001a, MNRAS, 328, 689

Cinzano P., Falchi F., Elvidge C.D., 2001b, The world atlas of the artificial night
  sky brightness, available at
  `http://www.lightpollution.it/dmsp`

Danko A., 2001, Rothney Astrophysical Observatory Light Pollution Map, available
  at
  `http://cleardarksky.com/lp/RothneyALlp.html`

DFM, Nov. 2003, Newsworthy Articles: University of Calgary Modernizes Baker-
  Nunn Camera, available at
  `http://www.dfmengineering.com/news_calgary.html`

Downey E.C., Mutlaq J., Apr. 2005, INDI: Instrument-Neutral Distributed Interface. Control Protocol Version 1.6, available at
`http://www.clearskyinstitute.com/INDI/INDI.pdf`

Fernández D., Isern J., Palau X., Torra J., 2004, Astronomische Nachrichten, 325, 657

FLI, 2002, IMGX16801E camera, available at
`http://www.fli-cam.com/pricing.htm`

González F., Jan. 2004, Jornadas Científicas 250 años de Astronomía en España: 1753-2003, 94–101

Gunn J.E., Carr M., Rockosi C., et al., Dec. 1998, AJ, 116, 3040

Henden A., 2001, private communication

Henize K.G., Jan. 1957, Sky Telesc., 16, 108

Hickson P., Richardson E.H., Sep. 1998, PASP, 110, 1081

Hidas M.G., Ashley M.C.B., Webb J.K., et al., Jun. 2005, MNRAS, 360, 703

Jeffrey E.A., Jentsch E.H., 1967, Baker-Nunn Camera Manual, Tech. Rep. 706-38, Smithsonian Institution, Astrophysical Observatory

King-Hele D., 1966, Observing Earth Satellites, London: MacMillan

Kron R.G., Aug. 1995, PASP, 107, 766

MacFarlane M., Feb. 2004a, Design of a Field Flattener for the Baker-Nunn Camera, internal technical report

MacFarlane M., Apr. 2004b, private communication

Mazur M., Mar. 2003, RothneyWeb - Rothney Astrophysical Observatory, available at
`http://www.geo.ucalgary.ca/~mazur`

Mazur M., 2004, private communication

Mazur M.J., Cardinal R., Hildebrand A.R., 2005, Final Report for Baker Nunn Telescope Retrofit, Tech. Rep. CR 2005-040, Defence Research and Development Canada

McCullough P.R., Stys J., Valenti J., et al., Dec. 2004, American Astronomical Society Meeting Abstracts, 205,

Montojo F.J., May 2004a, Boletín del Real Observatorio de la Armada, 5, 1

Montojo F.J., 2004b, Optimización de la estrategia observacional para el recubrimiento rápido del cielo por TDI, Master's thesis, Universitat de Barcelona

Muiños J.L., Belizón F., Vallejo M., Mallamaci C., Pérez J.A., 2003, In: Journées 2002 - systèmes de référence spatio-temporels. Astrometry from ground and from space, Bucharest, 25 - 28 September 2002, edited by N. Capitaine and M. Stavinschi, Bucharest: Astronomical Institute of the Romanian Academy, Paris: Observatoire de Paris, ISBN 2-901057-48-9, ISBN 973-558-108-6, 2003, p. 180 - 184, 180–184

Muiños J.L., Belizón F., Fors O., et al., May 2004, Estado actual de la robotización de la cámara Baker-Nunn del ROA, I Reunión de Astronomía Robótica, Mazagón (Huelva), 24 y 25 de Mayo de 2004

Murtagh F., 2001-2005, COST-TIST 283. Computational and Information Infrastructure in the Astronomical Datagrid, available at `http://cost.cordis.lu/src/action_detail.cfm?action=283`

Núñez J., Muiños J.L., Fors O., et al., Nov. 2003a, In: Astronomía Dinámica en Latino América, 9–14

Núñez J., Muiños J.L., Fors O., et al., 2003b, In: Proceedings de las Jornadas Científicas 250 años de Astronomía en España. San Fernando - España

Núñez J., Muiños J.L., Fors O., et al., 2003c, In: Highlights of Spanish Astrophysics III. Proceedings of the Fifth Scientific Meeting of the Spanish Astronomical Society (SEA) held in Toledo, Spain, September 9-13, 2002. By Jesús Gallego, Jaime Zamorano and Nicolás Cardiel Berlin: Springer, 2003, ISBN 1-4020-1388-4

Nemiroff R.J., Rafert J.B., Jul. 1999, PASP, 111, 886

Pennypacker C., Boer M., Denny R., et al., Nov. 2002, A&A, 395, 727

Pennypacker C., Aymon J., Gordon S., et al., Jun. 2003, Developing a Protocol and Implementing a Network for Ubiquitous Use of Telescopes Over the Internet: Remote Telescope Mark-up Language (RTML), 97–+, The Future of Small

Telescopes In The New Millennium. Volume I - Perceptions, Productivities, and Policies

Pollacco D., Feb. 2005, Astronomy and Geophysics, 46, 19

Pollaco D., 2002, SUPERWASP project - Wide Angle Search for Planets - Technical features, available at
`http://www.superwasp.org/technical.htm`

Sheppard S.S., Jewitt D.C., Trujillo C.A., Brown M.J.I., Ashley M.C.B., Nov. 2000, AJ, 120, 2687

Steidler-Dennison A., Apr. 2003, Project: Talon - Observatory Control Software, available at
`http://sourceforge.net/projects/observatory`

Steidler-Dennison A., Jan. 2004, Linux, Talon and Astronomy, available at
`http://www.linuxjournal.com/article/6673`

Torra J., Fernández D., 2000, Pla Pilot per a l'avaluació i reducció de la contaminació lumínica a Catalunya: Informe de les activitats dutes a terme durant l'any 2000 per l'equip del Departament d'Astronomia i Meteorologia

Vangeyte B., Manfroid J., Surdej J., Jun. 2002, A&A, 388, 712

Worldservo I., 1999, DSP Servo Drives for Brushless Motors, available at
`http://www.worldservo.com`

Appendix B

SNR performance of PEPs and CCDs in LO

Depending on the detector used and the temporal scale of the acquisition process, different noise sources appear in collected data. In the particular case of LO work, we should consider the following as dominant.

Firstly, in most astronomical situations, the detection process is Poisson distributed, i.e. the probability of obtaining a realization of intensity k coming from a source of mean flux μ is given by the Poisson probability:

$$\mathbf{P}(k|\mu) = e^{-\mu} \; \frac{(\mu)^k}{k!} \tag{B.1}$$

with an uncertainty over every realization $\sigma = \sqrt{\mu}$. Poisson noise, also known as shot noise, is inherent to light nature, and does not depend on the detector used.

Secondly, in some detectors, as CCDs, the realization k is read by the electronics of the detector, and a Gaussian readout noise of zero mean and standard deviation σ_{CCD} is introduced. The probability of obtaining a particular realization m from k is

$$\mathbf{P}(m|k) = \frac{1}{\sqrt{2\pi}\sigma_{\mathrm{CCD}}} \exp\left[-\frac{(m-k)^2}{2\sigma_{\mathrm{CCD}}^2}\right] \tag{B.2}$$

If, as in the case of CCDs, both processes in Eqs. B.1 and B.2 are part of the adquisition, the Poisson+Gaussian compound probability of obtaining a realization m given the mean μ and all its possible Poisson realizations k is (Núñez & Llacer

1993):

$$\mathbf{P}(m|\mu) = \sum_{k=0}^{\infty} \frac{1}{\sqrt{2\pi}\sigma_{\mathrm{CCD}}} \exp\left[-\frac{(m-k)^2}{2\sigma_{\mathrm{CCD}}^2}\right] e^{-\mu} \; \frac{(\mu)^k}{k!} \tag{B.3}$$

Thirdly, the light wavefront is distorted due to inhomogeneities in the index of refraction n. This random fluctuation in n makes recorded intensity vary temporally and spatially. This is normally referred to as scintillation noise. The intensity after scintillation can be approximated as a Log-normal distribution:

$$\mathbf{P}(m|k) = \frac{1}{\sqrt{2\pi}bm} \exp\left[-\frac{(\ln\frac{m}{k} - \frac{b^2}{2})^2}{2b^2}\right] \tag{B.4}$$

with $b = \sqrt{ln(\sigma_{\mathrm{sc}}^2 + 1)}$, where σ_{sc}^2 is the scintillation index, which characterizes the strength of the turbulence.

Likewise the former Poisson+Gaussian case in Eq. B.3, the Poisson+Log-normal compound probability of obtaining a realization m given the mean μ and all its possible Poisson realizations k is:

$$\mathbf{P}(m|\mu) = \sum_{k=0}^{\infty} \frac{1}{\sqrt{2\pi}bm} \exp\left[-\frac{(\ln\frac{m}{k} - \frac{b^2}{2})^2}{2b^2}\right] e^{-\mu} \; \frac{(\mu)^k}{k!} \; , \tag{B.5}$$

which, as derived in Sturmann (1997), yields an uncertainty

$$\sigma_{\mathrm{m}}^2 = \sigma_{sc}^2 \overline{m}^2 + \overline{m} + \sigma_{\mathrm{CCD}}^2 \tag{B.6}$$

where $\overline{m}$ is the mean number of photons detected in an integration time. We have included the Gaussian contribution from CCD readout noise accounted by σ_{CCD} in photons.

The right-hand terms in Eq. B.6 are scintillation, Poisson and Gauss noise contributions, respectively. For usual intensity ranges in LO, lightcurve SNR will be marginally affected by CCD readout noise σ_{CCD}. If, as usual, turbulence is not negligible ($\sigma_{\mathrm{sc}} \neq 0$), the scintillation factor must be taken into account, becoming dominant in the high intensity regime.

Now, Eq. B.6 should be the expression to use when evaluating SNR for a given detector. However, as the purpose of this section is to compare the SNR performance of PEPs and CCDs in LO observations, we will not include scintillation noise. This will not bias our conclusions, as atmospheric turbulence affects in the same way both detectors.

The SNR for a pure-Poisson detector like PEPs placed in the image plane can be expressed as:

$$SNR_{\mathrm{PEP}} = \frac{N_*}{(N_* + N_{\mathrm{b}})^{1/2}} \tag{B.7}$$

where N_* and N_{b} account for number of photon counts during integration time τ due to the star and sky background, respectively. Eq. B.7 can be reformulated as by Sturmann (1994):

$$SNR_{\mathrm{PEP}} = \frac{8.9\kappa^{1/2} F_* D^2 (D + v\tau)\tau^{1/2}}{(F_* D^2 + F_{\mathrm{b}} b^2)^{1/2}} \tag{B.8}$$

where $F_* = 1.10 \times 10^7 \times 10^{-0.4 m_{\mathrm{V}}}$ and $F_{\mathrm{b}} = 9.95 \times 10^6 \times 10^{-0.4 m_{\mathrm{V}}^{\mathrm{bg}}}$ are the extra-atmospheric average photon fluxes for a star of magnitude m_{V} and sky background of magnitude $m_{\mathrm{V}}^{\mathrm{bg}}$. Both correspond to a temperature $T = 6000\mathrm{K}$ and all expressed in [photons $\mathrm{m}^{-2}\mathrm{s}^{-1}\mathrm{\AA}^{-1}$] and [photons $\mathrm{s}^{-1}\mathrm{\AA}^{-1}\mathrm{arcsec}^{-2}$], respectively. The angular extension of the recorded scene projected over the image plane, measured in [arcsec^2], is given by b. Finally, κ stands for the product of detector quantum efficiency (QE) and a weighting function $g(\lambda)$ correcting flux for atmospheric extinction and optical system absorption. A typical value for g at $\lambda = 6500\mathrm{\AA}$ is 0.6.

Eq. B.8 for the case of CCD turns into:

$$SNR_{\mathrm{CCD}} = \frac{8.9\kappa^{1/2} F_* D^2 (D + v\tau)\tau^{1/2}}{(F_* D^2 + F_{\mathrm{b}} b^2 + \sigma_{\mathrm{CCD}}^2)^{1/2}} \tag{B.9}$$

where σ_{CCD} is expressed in [photons].

To assess of the theoretical SNR performance between PEPs and CCDs, we consider the following parameters to be input in Eqs. B.8 and B.9 for either case: $m_{\mathrm{V}} \sim 4$, $v \sim 0.5\mathrm{m\,ms}^{-1}$, $\tau \sim 1\,\mathrm{ms}$, $D = 0.36\,\mathrm{m}$, $\sigma_{\mathrm{CCD}} = 5\,\mathrm{counts}$, $b = 4\mathrm{arcsec}^2$ and $m_{\mathrm{V}}^{\mathrm{bg}} \sim 10$, which is typical during LO events just beside the Moon. This is close to the observational setting that we present in Sect. 7.4.1. As for the QE of both detector systems, we adopt from Kristian & Blouke (1982) typical values: $QE_{\mathrm{PEP}} \sim 0.15$ and $QE_{\mathrm{CCD}} \sim 0.70$.

Thus, the gain η obtained by the use of a CCD in moderately bright LO observations is:

$$\eta = \frac{SNR_{\mathrm{CCD}}}{SNR_{\mathrm{PEP}}} \sim 2.2 \tag{B.10}$$

Bibliography

Kristian J., Blouke M., Oct. 1982, Scientific American, 247, 66

Núñez J., Llacer J., Oct. 1993, PASP, 105, 1192

Sturmann L., Nov. 1994, PASP, 106, 1165

Sturmann L., Dec. 1997, Ph.D. Thesis

Appendix C

List of observed LO events in CALOP

In this appendix we include all the occultation events observed in the course of the Calar Alto Lunar Occultation program (CALOP).

The column format is as follows. Columns (1) through (3) list the source identification, the date of the event and the telescope+detector configuration used. Note that the 2MASS prefix in the longest identificators has been omitted. Column (4) lists the filter used. Column (5) lists the field of view set either by the diaphragm aperture or by the array subwindow. Columns (6) and (7) list the sampling time of the lightcurves and the integration time for each data point. Columns (8) and (9) list the total magnitude of the star in the V and K filters. In column (10) we report the spectral types, again extracted when available from the literature; in the case of multiple determinations, the most frequent or most recent was used. Finally, column (11) lists the distances based on Hipparcos parallaxes, when available. Those values affected by a large uncertainty ($> 10\%$) have been omitted.

Table C.1: List of the 388 occultation events recorded in CALOP and the circumstances of their observation.

(1) Source	(2) Date UT	(3) Telescope +detector	(4) Filter	(5) D (″)	(6) Δt (ms)	(7) τ (ms)	(8) V (mag)	(9) K (mag)	(10) Sp.	(11) Dist. (pc)
SAO 187645	22-10-01	CA	R	8	2.2	2.2	8.3		K1/K2III	
SAO 187660	22-10-01	CA	R	11	2.2	2.2	7.3		K2III	128
SAO 189746	24-10-01	CA	R	6	1.8	1.8	8.6		G8III	
SAO 189774	24-10-01	CA	R	8	5.0	5.0	9.5		K1/K2III	
SAO 164553	25-10-01	CA	R	7	5.0	5.0	8.5		F0III/IV	
SAO 164567	25-10-01	CA	R	8	1.8	1.8	7.4		K5III	
SAO 165121	26-10-01	CA	R	7	3.0	3.0	9.2		K1/K2III	
SAO 165128	26-10-01	CA	R	7	6.0	6.0	9.5		G2/G3V	
SAO 165136	26-10-01	CA	R	6	2.0	2.0	7.8		K0III	230
SAO 165578	27-10-01	CA	R	6	2.1	2.1	6.1		K5III	256
SAO 147033	28-10-01	CA	R	7	1.6	1.6	7.7		K0	238
SAO 147032	28-10-01	CA	R	7	1.5	1.5	7.8		F5	221
30 Psc	28-10-01	CA	R	6	1.5	1.5	4.4		M3III	127
SAO 78001	22-02-02	CB	K	7	8.5	3.0	9.1	7.7	F0	
SAO 78119	22-02-02	CB	K	7	8.7	3.0	8.1	4.9	K0	
SAO 78122	22-02-02	CB	K	7	8.4	3.0	7.9	5.7	G5	217
SAO 78168	22-02-02	CB	K	7	8.4	3.0	6.1	3.9	G8III	134
SAO 78176	22-02-02	CB	K	7	8.4	3.0	6.3	4.9	B3Ib	
SAO 78192	23-02-02	CB	K	7	8.4	3.0	8.4	3.6	M...	
SAO 78197	23-02-02	CB	K	7	8.6	3.0	8.2	5.3	K0	
DO 12097	23-02-02	CB	K	7	8.4	3.0	9.3	5.3		
SAO 78210	23-02-02	CB	K	7	8.5	3.0	6.6	4.5	G5	242
V349 Gem	23-02-02	CB	K	7	8.3	3.0	12.2	4.1		
SAO 78258	23-02-02	CB	K	7	8.5	3.0	8.2	6.9	G0	198
SAO 78272	23-02-02	CB	K	7	8.5	3.0	7.3	5.0	K0	
SAO 79133	23-02-02	CB	K	7	8.5	3.0	7.9	6.8	F5	72
AG+24 788	23-02-02	CB	K	7	8.4	3.0	10.3	6.4	K0	
SAO 79162	23-02-02	CB	K	7	8.5	3.0	5.9	4.8	F5III-IV	107
SAO 79176	23-02-02	CB	K	7	8.5	3.0	9.2	7.6	G5	
SAO 79194	23-02-02	CB	K	7	8.5	3.0	8.7	7.5	F5	
SAO 79214	23-02-02	CB	K	7	8.5	3.0	7.9	5.6	G5	236
SAO 79236	23-02-02	CB	K	7	8.5	3.0	8.1	7.0	F8	40
SAO 79251	23-02-02	CB	K	7	8.5	3.0	8.7	6.3	K0	
SAO 79257	23-02-02	CB	K	7	8.5	3.0	8.4	7.4	F5	167

CA: OAN 1.5 m + CCD.

CB: OAN 1.5 m + MAGIC.

CC: CAHA 2.2 m + MAGIC.

Table C.1: Complete list of occultation events and of the circumstances of their observation (continued)

(1)	(2)	(3)	(4)	(5)	(6)	(7)	(8)	(9)	(10)	(11)
Source	Date	Telescope	Filter	D	Δt	τ	V	K	Sp.	Dist.
	UT	+detector		″	ms	ms	mag	mag		pc
AG+24 824	23-02-02	CB	K	7	8.5	3.0	10.2	7.9	G0	
AG+23 808	24-02-02	CB	K	7	8.4	3.0	10.2	7.8	K0	
SAO 79302	24-02-02	CB	K	7	8.5	3.0	8.3	7.9	A2	280
SAO 79325	24-02-02	CB	K	7	8.5	3.0	9.5	7.0	K2	
SAO 79365	24-02-02	CB	K	7	8.5	3.0	9.3	6.2	K7	
IRAS 07231+2349	24-02-02	CB	K	7	8.4	3.0		4.0		
SAO 128864	05-11-03	CB	K	7	8.40	3.0	9.7	8.2	G0	
AG-00 73	05-11-03	CB	K	7	8.40	3.0	10.4	7.2	M0	
SAO 109803	06-11-03	CB	K	7	8.40	3.0	8.1	6.7	F8	
SAO 109820	06-11-03	CB	K	7	8.40	3.0	9.9	8.0	K0	
AG+04 167	06-11-03	CB	K	7	8.40	3.0	10.3	7.8	K0	
SAO 109832	06-11-03	CB	K	7	8.40	3.0	7.5	6.5	F0	102
AG+05 155	06-11-03	CB	K	7	8.40	3.0	10.2	7.7	K0	
SAO 109888	07-11-03	CB	K	7	8.33	3.0	9.3	6.9	K5	
SAO 109901	07-11-03	CB	K	7	8.40	3.0	8.7	7.8	F5	214
GSC 01902-00718	01-03-04	CB	K	7	8.48	3.0	9.3	6.2		
AG+26 730	01-03-04	CB	K	7	8.47	3.0	9.9	6.9	G5	
IRAS 06528+2641	02-03-04	CB	K	7	8.34	3.0		5.2		
06575655+2637589	02-03-04	CB	K	7	8.44	3.0		6.7		
SAO 78914	02-03-04	CB	K	7	8.46	3.0	8.6	5.9	K2	
GSC 01902-00833	02-03-04	CB	K	7	8.43	3.0	10.7	5.9		
AG+25 900	02-03-04	CB	K	7	8.34	3.0	10.5	8.1	G5	
SAO 79629	02-03-04	CB	K	7	8.37	3.0	9.4	7.5	G5	
AG+26 855	02-03-04	CB	K	7	8.35	3.0	10.5	7.5	K0	
76 Gem	02-03-04	CB	K	7	8.40	3.0	5.3	1.7	K5III	182
GSC 01916-01291	02-03-04	CB	K	7	8.47	3.0	10.2	7.9		
SAO 79672	02-03-04	CB	K	7	8.45	3.0	7.4	3.8	K5III	529
SAO 79684	02-03-04	CB	K	7	8.10	3.0	8.8	5.7	K7	
SAO 79685	02-03-04	CB	K	7	8.40	3.0	8.5	6.9	G5IV	53
AG+26 864	02-03-04	CB	K	7	8.49	3.0	10.0	6.2	K5	
SAO 79702	02-03-04	CB	K	7	8.38	3.0	9.3	6.7	K2	
07531704+2527173	03-03-04	CB	K	7	11.63	6.0		8.1		
GSC 01929-00425	03-03-04	CB	K	7	8.34	3.0	9.9	6.0		
GSC 01930-01242	03-03-04	CB	K	7	8.52	3.0	9.7	7.1		
08382433+2328215	03-03-04	CB	K	7	8.40	3.0		7.8		

CA: OAN 1.5 m + CCD.

CB: OAN 1.5 m + MAGIC.

CC: CAHA 2.2 m + MAGIC.

Table C.1: Complete list of occultation events and of the circumstances of their observation (continued)

(1) Source	(2) Date UT	(3) Telescope +detector	(4) Filter	(5) D "	(6) Δt ms	(7) τ ms	(8) V mag	(9) K mag	(10) Sp.	(11) Dist. pc
SAO 80310	03-03-04	CB	K	7	8.51	3.0	6.9	5.6	F8	35
GSC 01942-02645	03-03-04	CB	K	7	8.45	3.0	9.9	7.7		
SAO 80370	03-03-04	CB	K	7	8.36	3.0	9.7	7.3	K0	
GSC 01943-00150	04-03-04	CB	K	7	8.38	3.0	10.5	7.0		
08483998+2235329	04-03-04	CB	K	7	8.52	3.0		7.8		
SAO 80442	04-03-04	CB	K	7	8.45	3.0	9.3	6.8	K0	201
SAO 80456	04-03-04	CB	K	7	8.40	3.0	9.5	7.1	G5	
SAO 80469	04-03-04	CB	K	7	8.44	3.0	9.0	6.5	K0	202
SAO 80481	04-03-04	CB	K	7	8.46	3.0	9.5	7.3	K0	
SAO 80735	31-03-04	CB	K	7	8.40	3.0	8.7	5.9	K0	1282
SAO 80764	01-04-04	CB	K	7	8.40	3.0	7.8	4.0	K2	1429
SAO 80772	01-04-04	CB	K	7	8.36	3.0	8.7	5.0	K5	
[RHI84] 10- 333	28-07-04	CC	K	5	8.46	3.0		4.9	M6.5	
17411783-2816159	28-07-04	CC	K	5	8.42	3.0		7.0		
[RHI84] 10- 379	28-07-04	CC	K	5	8.43	3.0		6.4	M6.5:	
[RHI84] 10- 396	28-07-04	CC	K	5	8.54	3.0		5.1	M7	
17413954-2819536	28-07-04	CC	K	5	8.51	3.0		6.6		
IRAS 17396-2805	28-07-04	CC	K	5	8.45	3.0		5.6	M4	
[RHI84] 10- 421	28-07-04	CC	K	5	8.52	3.0		6.2	M5	
[RHI84] 10- 389	28-07-04	CC	K	5	8.40	3.0		6.4	M5	
SAO 185638	28-07-04	CC	K	5	8.40	3.0	8.3	3.8	G8Iab	
[RHI84] 10- 423	28-07-04	CC	K	5	8.77	3.0		4.4	M1	
IRAS 17399-2811	28-07-04	CC	K	5	8.50	3.0		4.0	M6.5:	
[RHI84] 10- 431	28-07-04	CC	K	5	8.35	3.0		5.2	M4	
17425620-2820370	28-07-04	CC	K	5	8.48	3.0		4.6		
17431472-2754338	28-07-04	CC	K	5	8.44	3.0		7.1		
17431415-2753091	28-07-04	CC	K	5	8.45	3.0		6.9		
[RHI84] 10- 456	28-07-04	CC	K	5	8.37	3.0		4.8	M4	
17432850-2754372	28-07-04	CC	K	5	8.37	3.0		6.7		
17433423-2755331	28-07-04	CC	K	5	8.34	3.0		7.2		
17435106-2801060	28-07-04	CC	K	5	8.36	3.0		6.6		
17434896-2758595	28-07-04	CC	K	5	8.47	3.0		6.7		
[RHI84] 10- 441	28-07-04	CC	K	5	8.31	3.0		3.7	M6	
17432189-2751590	28-07-04	CC	K	5	8.37	3.0		5.7		
17431718-2822397	28-07-04	CC	K	5	8.36	3.0		6.3		

CA: OAN 1.5 m + CCD.

CB: OAN 1.5 m + MAGIC.

CC: CAHA 2.2 m + MAGIC.

Table C.1: Complete list of occultation events and of the circumstances of their observation (continued)

(1)	(2)	(3)	(4)	(5)	(6)	(7)	(8)	(9)	(10)	(11)
Source	Date	Telescope	Filter	D	Δt	τ	V	K	Sp.	Dist.
	UT	+detector		$''$	ms	ms	mag	mag		pc
[RHI84] 10- 465	28-07-04	CC	K	5	8.34	3.0		5.5	M2	
17441302-2808449	28-07-04	CC	K	5	8.39	3.0		7.6		
[RHI84] 10- 482	28-07-04	CC	K	5	8.31	3.0		4.8	M5	
SAO 185661	28-07-04	CC	K	5	8.39	3.0	9.9	5.9	K5	
17443008-2758255	28-07-04	CC	K	5	8.32	3.0		6.7		
V744 Sgr	28-07-04	CC	K	5	8.38	3.0	13.0	2.9	M7	
[RHI84] 10- 518	28-07-04	CC	K	5	8.35	3.0		4.3	M6.5	
17450844-2810286	28-07-04	CC	K	5	8.35	3.0		6.8		
[RHI84] 10- 523	28-07-04	CC	K	5	8.35	3.0		3.7	M4	
IRC -30319	28-07-04	CC	K	5	8.39	3.0	8.8	1.8	K2	
17454657-2809090	28-07-04	CC	K	5	8.36	3.0		5.3		
17454891-2809333	28-07-04	CC	K	5	8.32	3.0		6.1		
IRAS 17428-2802	28-07-04	CC	K	5	8.38	3.0		5.2		
[RHI84] 10- 565	28-07-04	CC	K	5	8.40	3.0		3.4	M1	
[RHI84] 10- 564	28-07-04	CC	K	5	8.34	3.0		5.9	M8	
17455791-2821113	28-07-04	CC	K	5	8.55	3.0		7.8		
17454872-2823210	28-07-04	CC	K	5	8.46	3.0		6.8		
17464520-2809135	28-07-04	CC	K	5	8.43	3.0		7.3		
17463693-2820212	28-07-04	CC	K	5	8.30	3.0		6.7		
17470407-2811365	28-07-04	CC	K	5	8.44	3.0		5.9		
17471145-2810386	28-07-04	CC	K	5	8.38	3.0		6.2		
17471850-2812592	28-07-04	CC	K	5	8.50	3.0		4.7		
17472312-2810014	28-07-04	CC	K	5	8.39	3.0		7.3		
17472282-2813443	28-07-04	CC	K	5	8.30	3.0		6.3		
[RHI84] 10- 610	28-07-04	CC	K	5	8.32	3.0		7.5	M4:	
17464703-2753028	28-07-04	CC	K	5	8.37	3.0		5.5		
17473721-2812078	28-07-04	CC	K	5	8.31	3.0		7.6		
17473925-2803207	29-07-04	CC	K	5	8.36	3.0		6.9		
17473481-2759092	29-07-04	CC	K	5	8.33	3.0		6.7		
17473524-2818529	29-07-04	CC	K	5	8.45	3.0		6.6		
[RHI84] 10- 658	29-07-04	CC	K	5	8.44	3.0		5.1	M7	
21394110-1947036	18-11-04	CB	K	7	8.42	3.0		8.1		
HD 206048	18-11-04	CB	K	7	8.40	3.0	10.1	7.7	G8IV	
HD 206205	18-11-04	CB	K	7	8.40	3.0	10.3	8.0	G8/K0V	
HD 206232	18-11-04	CB	K	7	8.40	3.0	10.0	7.3	K1III:	

CA: OAN 1.5 m + CCD.

CB: OAN 1.5 m + MAGIC.

CC: CAHA 2.2 m + MAGIC.

Table C.1: Complete list of occultation events and of the circumstances of their observation (continued)

(1) Source	(2) Date UT	(3) Telescope +detector	(4) Filter	(5) D "	(6) Δt ms	(7) τ ms	(8) V mag	(9) K mag	(10) Sp.	(11) Dist. pc
SAO 190556	18-11-04	CB	K	7	8.53	3.0	7.0	4.3	K1III	173
HD 206339	18-11-04	CB	K	7	8.53	3.0	10.4	8.1	G6/G8III:	
HD 206355	18-11-04	CB	K	7	8.40	3.0	10.0	5.6	M0/M1	
SAO 164601	18-11-04	CB	K	7	8.58	3.0	6.2	5.7	A0m...	110
HD 206530	18-11-04	CB	K	7	8.40	3.0	9.9	8.2	G5/G6IV	
22313353-1507204	19-11-04	CB	K	7	8.40	3.0		4.9		
SAO 165154	19-11-04	CB	K	7	8.40	3.0	9.0	6.2	K1III	
PPM 723098	19-11-04	CB	K	7	8.53	3.0	9.8	7.5		
GSC 05817-01033	19-11-04	CB	K	7	8.40	3.0	10.9	8.4		
BD-15 6246	19-11-04	CB	K	7	8.40	3.0	10.5	7.8		
BD-14 6307	19-11-04	CB	K	7	8.40	3.0	9.6	7.5		
SAO 165182	19-11-04	CB	K	7	8.53	3.0	8.8	6.1	K1III	
BD-14 6314	19-11-04	CB	K	7	8.53	3.0	10.6	8.2		
SAO 165199	19-11-04	CB	K	7	8.40	3.0	8.3	5.7	K0III	223
BD-14 6322	19-11-04	CB	K	7	8.40	3.0	9.7	7.5		
HD 220142	20-11-04	CB	K	7	8.53	3.0	10.5	7.8	K2	
SAO 146681	20-11-04	CB	K	7	8.40	3.0	8.7	7.5	G0	77
HD 220374	20-11-04	CB	K	7	8.40	3.0	9.5	8.4	F8	
SAO 146683	20-11-04	CB	K	7	8.40	3.0	6.7	4.6	K0	160
SAO 146688	20-11-04	CB	K	7	8.40	3.0	8.9	6.5	K0	
SAO 146701	20-11-04	CB	K	7	8.53	3.0	9.4	6.4	K2	287
SAO 146718	20-11-04	CB	K	7	8.53	3.0	9.5	7.8	G5	
SAO 146726	20-11-04	CB	K	7	8.40	3.0	8.7	7.0	G5	166
AG+03 113	22-11-04	CB	K	7	8.53	3.0	10.5	7.5	K2	
SAO 109568	22-11-04	CB	K	7	8.53	3.0	7.6	6.4	F8	61
GSC 00015-01007	22-11-04	CB	K	7	8.40	3.0	10.8	8.0		
SAO 109599	22-11-04	CB	K	7	8.40	3.0	7.8	6.5	F5	88
GSC 00022-00601	22-11-04	CB	K	7	8.40	3.0	10.2	7.9		
SAO 109617	22-11-04	CB	K	7	8.40	3.0	8.2	5.5	K2	21
GSC 00622-01301	23-11-04	CB	K	7	8.53	3.0	9.6	7.5		
SAO 110089	23-11-04	CB	K	7	8.40	3.0	8.5	6.7	K0	47
SAO 110096	23-11-04	CB	K	7	8.40	3.0	8.4	7.7	F0	535
SAO 110099 (HIC 8110 inc)	23-11-04	CB	K	7	8.40	3.0	8.6	6.7	F5	
SAO 110100	23-11-04	CB	K	7	8.40	3.0	8.0	6.6	F2	70

CA: OAN 1.5 m + CCD.

CB: OAN 1.5 m + MAGIC.

CC: CAHA 2.2 m + MAGIC.

Table C.1: Complete list of occultation events and of the circumstances of their observation (continued)

(1)	(2)	(3)	(4)	(5)	(6)	(7)	(8)	(9)	(10)	(11)
Source	Date	Telescope	Filter	D	Δt	τ	V	K	Sp.	Dist.
	UT	+detector		$''$	ms	ms	mag	mag		pc
AG+09 168	23-11-04	CB	K	7	8.53	3.0	10.5	7.7	K0	
IRC +10022	23-11-04	CB	K	7	8.40	3.0	9.0	2.8	M...	
GSC 00625-01112	23-11-04	CB	K	7	8.53	3.0	10.1	7.0		
AG+10 200	23-11-04	CB	K	7	8.40	3.0	9.7	8.2	G5	
GSC 00625-00649	23-11-04	CB	K	7	8.40	3.0	10.0	7.0		
AG+10 202	23-11-04	CB	K	7	8.40	3.0	9.5	4.6	M0	
SAO 92659	23-11-04	CB	K	7	8.53	3.0	5.9	5.1	F2Vw	43
SAO 147041	18-12-04	CB	K	7	8.40	3.0	5.1	5.4	B7III-IV	125
HD 224959	18-12-04	CB	K	7	8.44	3.0	9.6	7.3	R...	513
SAO 128550	18-12-04	CB	K	7	8.53	3.0	8.7	7.9	A5	
SAO 110016	20-12-04	CB	K	7	8.40	3.0	8.5	5.5	K2	418
SAO 110020	20-12-04	CB	K	7	8.40	3.0	7.6	6.5	F5	170
AG+09 150	21-12-04	CB	K	7	8.53	3.0	9.3	4.9	K5	
SAO 110027	21-12-04	CB	K	7	8.40	3.0	8.8	7.7	G0	
G 3-38	17-01-05	CB	K	7	8.41	3.0	11.5	8.2	K7	46
GSC 00633-00057	17-01-05	CB	K	7	10.40	5.0	10.9	8.1		
GSC 00636-00646	17-01-05	CB	K	7	8.38	3.0	10.6	7.8		
AG+12 224	17-01-05	CB	K	7	8.42	3.0	9.5	8.1	G5	
AG+12 226	17-01-05	CB	K	7	8.48	3.0	9.3	4.8	M0	
SAO 92788	17-01-05	CB	K	7	8.38	3.0	9.1	7.6	K0	
SAO 92789	17-01-05	CB	K	7	8.46	3.0	7.9	6.7	F5	78
SAO 92795	17-01-05	CB	K	7	8.45	3.0	7.2	4.8	K0	141
SAO 92823	17-01-05	CB	K	7	8.49	3.0	8.9	6.6	G5	
GSC 01227-01287	18-01-05	CB	K	7	8.49	3.0	10.6	7.4		
GSC 01227-01318	18-01-05	CB	K	7	8.36	3.0	10.3	7.4		
RZ Ari	18-01-05	CB	NB	7	8.36	3.0	5.8	-0.9	M6III	124
GSC 01247-00517	19-01-05	CB	K	7	8.34	3.0	10.7	7.8		
03423832+2216449	19-01-05	CB	K	7	8.40	3.0		7.3		
CSS 80	19-01-05	CB	K	7	8.46	3.0	9.7	3.8		
03482003+2232543	19-01-05	CB	K	7	8.44	3.0		5.5		
SAO 76214	19-01-05	CB	K	7	8.47	3.0	8.2	5.4	K0	
LH 98-106	19-01-05	CB	K	7	8.47	3.0	7.3	6.0	F5	37
SAO 76283	20-01-05	CB	K	7	8.33	3.0	7.6	5.9	G0	27
03521570+2245296	20-01-05	CB	K	7	8.53	3.0		7.2		
04330652+2505165	20-01-05	CB	K	7	8.43	3.0		7.8		

CA: OAN 1.5 m + CCD.

CB: OAN 1.5 m + MAGIC.

CC: CAHA 2.2 m + MAGIC.

Table C.1: Complete list of occultation events and of the circumstances of their observation (continued)

(1)	(2)	(3)	(4)	(5)	(6)	(7)	(8)	(9)	(10)	(11)
Source	Date	Telescope	Filter	D	Δt	τ	V	K	Sp.	Dist.
	UT	+detector		"	ms	ms	mag	mag		pc
04330286+2511447	20-01-05	CB	K	7	10.44	5.0		8.4		
DL Tau	20-01-05	CB	K	7	8.44	3.0	13.6	8.0	GV:e...	
04343950+2513544	20-01-05	CB	K	7	8.50	3.0		7.4		
HD 283715	20-01-05	CB	K	7	8.53	3.0	10.6	6.5	K1III	
04345591+2521351	20-01-05	CB	K	7	8.59	3.0		6.4		
IRAS 04320+2519	20-01-05	CB	K	7	8.43	3.0		4.3		
04361037+2512529	20-01-05	CB	K	7	8.43	3.0		6.3		
04363513+2526425	20-01-05	CB	K	7	8.40	3.0		7.1		
04365667+2521061	20-01-05	CB	K	7	8.42	3.0		7.4		
Elias 3-29	20-01-05	CB	K	7	8.43	3.0		6.8	G9III	
04372451+2524318	20-01-05	CB	K	7	8.59	3.0		5.7		
IRAS 04349+2522	20-01-05	CB	K	7	8.56	3.0		5.2		
IRAS 04357+2528	20-01-05	CB	K	7	8.60	3.0		4.9		
GN Tau	20-01-05	CB	K	7	8.47	3.0	15.1	8.1	M2.5	
AG+25 438	20-01-05	CB	K	7	8.58	3.0	10.7	7.4	K5V	
Elias 3-18	20-01-05	CB	K	7	8.45	3.0		6.3	B5	
04405597+2531312	20-01-05	CB	K	7	8.54	3.0		7.2		
ITG 31	20-01-05	CB	K	7	8.48	3.0		5.2		
04413015+2527019	20-01-05	CB	K	7	8.39	3.0		7.6		
LkHA 332	21-01-05	CB	K	7	8.39	3.0	14.7	7.9	K5	
IRAS 04395+2521	21-01-05	CB	K	7	8.53	3.0		5.5		
[GKH94] 10	21-01-05	CB	K	7	8.41	3.0		7.1		
04440885+2540333	21-01-05	CB	K	7	8.59	3.0		6.9		
SAO 76732	21-01-05	CB	K	7	8.38	3.0	9.6	7.7	A0III	
Elias 3-19	21-01-05	CB	K	7	8.58	3.0		6.0	M4III	
HD 283878	21-01-05	CB	K	7	8.59	3.0	10.8	6.5	G5III	
IRC +30094	21-01-05	CB	K	7	8.55	3.0		2.3		
05265156+2659299	21-01-05	CB	K	7	8.58	3.0		7.5		
AG+26 492	21-01-05	CB	K	7	8.53	3.0	10.3	6.7	K0	
IRAS 05236+2646	21-01-05	CB	K	7	8.42	3.0		4.4		
05270549+2715022	21-01-05	CB	K	7	8.43	3.0		7.3		
05273859+2716477	21-01-05	CB	K	7	8.39	3.0		7.1		
05291081+2718030	21-01-05	CB	K	7	8.42	3.0		7.4		
GSC 01856-00734	21-01-05	CB	K	7	8.38	3.0	10.2	5.8		
05295303+2706414	21-01-05	CB	K	7	8.39	3.0		6.0		

CA: OAN 1.5 m + CCD.

CB: OAN 1.5 m + MAGIC.

CC: CAHA 2.2 m + MAGIC.

Table C.1: Complete list of occultation events and of the circumstances of their observation (continued)

(1)	(2)	(3)	(4)	(5)	(6)	(7)	(8)	(9)	(10)	(11)
Source	Date	Telescope	Filter	D	Δt	τ	V	K	Sp.	Dist.
	UT	+detector		$''$	ms	ms	mag	mag		pc
05300059+2727115	21-01-05	CB	K	7	8.56	3.0		6.9		
05303373+2708008	21-01-05	CB	K	7	8.77	3.0		7.8		
HD 244308	21-01-05	CB	K	7	8.77	3.0	9.8	4.6	K7	
05311866+2730551	21-01-05	CB	K	7	8.60	3.0		6.4		
05321151+2708449	21-01-05	CB	K	7	10.52	5.0		8.1		
05323754+2727475	21-01-05	CB	K	7	8.47	3.0		7.5		
05330539+2713357	21-01-05	CB	K	7	8.41	3.0		7.5		
05330852+2710533	21-01-05	CB	K	7	8.57	3.0		7.6		
05333882+2715046	21-01-05	CB	K	7	8.57	3.0		7.4		
05335555+2715363	21-01-05	CB	K	7	8.57	3.0		7.4		
SAO 77258	21-01-05	CB	K	7	8.77	3.0	7.9	4.3	K0	532
SAO 77266	21-01-05	CB	K	7	8.54	3.0	8.1	7.1	F0	116
05345840+2724187	21-01-05	CB	K	7	8.56	3.0		6.4		
GSC 01869-01803	22-01-05	CB	K	7	8.58	3.0	11.4	7.6		
GSC 01869-01378	22-01-05	CB	K	7	8.41	3.0	10.2	7.4		
SAO 77280	22-01-05	CB	K	7	8.40	3.0	8.8	4.1	M0	
GSC 01869-01288	22-01-05	CB	K	7	8.53	3.0	10.6	7.7		
GSC 01869-01804	22-01-05	CB	K	7	8.41	3.0	10.3	7.0		
GSC 01869-01778	22-01-05	CB	K	7	8.39	3.0	9.4	6.5		
GSC 01869-01436	22-01-05	CB	K	7	8.37	3.0	10.0	6.9		
05380288+2721511	22-01-05	CB	K	7	8.57	3.0		6.6		
05400930+2714478	22-01-05	CB	K	7	8.43	3.0		7.1		
05403514+2715388	22-01-05	CB	K	7	8.37	3.0		7.1		
05404432+2725221	22-01-05	CB	K	7	8.55	3.0		7.2		
05415664+2707323	22-01-05	CB	K	7	8.45	3.0		5.2		
SAO 78242	22-01-05	CB	K	7	8.77	3.0	8.8	6.6	K0	
AG+27 643	22-01-05	CB	K	7	8.51	3.0	9.9	7.5	K0	
AG+27 644	22-01-05	CB	K	7	8.54	3.0	9.9	6.9	K7	
SAO 78291	22-01-05	CB	K	7	8.47	3.0	7.7	4.5	K0Ib	735
06241536+2746220	22-01-05	CB	K	7	8.53	3.0		7.3		
06250582+2756209	22-01-05	CB	K	7	8.54	3.0		6.8		
06253942+2738004	22-01-05	CB	K	7	8.52	3.0		6.3		
AG+27 661	22-01-05	CB	K	7	10.61	5.0	10.3	7.8	K2	
AG+27 662	22-01-05	CB	K	7	8.53	3.0	8.9	6.7	K0	
SAO 78396	22-01-05	CB	K	7	8.59	3.0	9.8	7.2	K0	

CA: OAN 1.5 m + CCD.

CB: OAN 1.5 m + MAGIC.

CC: CAHA 2.2 m + MAGIC.

Table C.1: Complete list of occultation events and of the circumstances of their observation (continued)

(1)	(2)	(3)	(4)	(5)	(6)	(7)	(8)	(9)	(10)	(11)
Source	Date	Telescope	Filter	D	Δt	τ	V	K	Sp.	Dist.
	UT	+detector		"	ms	ms	mag	mag		pc
SAO 78410	22-01-05	CB	K	7	8.49	3.0	7.7	4.7	K1III	463
AG+27 677	23-01-05	CB	K	7	8.38	3.0	9.9	7.7	G0	342
SAO 78434	23-01-05	CB	K	7	8.56	3.0	8.6	5.4	A2	
06301773+2746270	23-01-05	CB	K	7	8.57	3.0		7.5		
06301839+2752010	23-01-05	CB	K	7	8.60	3.0		7.0		
IRAS 06277+2747	23-01-05	CB	K	7	8.54	3.0		5.0		
06322702+2739440	23-01-05	CB	K	7	8.43	3.0		7.7		
SAO 78486	23-01-05	CB	K	7	10.61	5.0	9.5	8.2	A7	
06335778+2728365	23-01-05	CB	K	7	8.41	3.0		7.5		
SAO 78509	23-01-05	CB	K	7	8.54	3.0	9.7	7.1	K2	
06345678+2732546	23-01-05	CB	K	7	8.41	3.0		6.6		
SAO 78527	23-01-05	CB	K	7	8.58	3.0	9.3	6.8	K0	
SAO 78540	23-01-05	CB	K	7	8.57	3.0	6.9	5.3	G0	36
GSC 01888-01733	23-01-05	CB	K	7	8.48	3.0	10.1	5.4		
04183702+2434105	16-02-05	CB	K	7	8.48	3.0		6.7		
HD 283610	16-02-05	CB	K	7	8.49	3.0	9.6	5.4	K5III	
Elias 3-3	16-02-05	CB	K	7	8.38	3.0		5.8	K2III	
SAO 76596	16-02-05	CB	K	7	8.38	3.0	9.3	6.0	G8III	
04255198+2503159	16-02-05	CB	K	7	8.40	3.0		6.3		
04264187+2500314	17-02-05	CB	K	7	8.44	3.0		6.7		
SAO 76615	17-02-05	CB	K	7	10.42	5.0	9.0	7.5	A1III	111
05095433+2648584	17-02-05	CB	K	7	10.36	5.0		6.9		
SAO 77000	17-02-05	CB	K	7	8.42	3.0	9.1	5.4	G5	244
IRAS 05087+2702	17-02-05	CB	K	7	8.36	3.0		4.8		
SAO 77040	17-02-05	CB	K	7	10.48	5.0	9.7	8.2	G0	115
SAO 77061	17-02-05	CB	K	7	10.45	5.0	10.0	8.2	G0	83
SAO 77070	17-02-05	CB	K	7	8.43	3.0	8.9	6.0	G5	164
05162746+2714049	17-02-05	CB	K	7	8.40	3.0		7.2		
05165224+2700265	17-02-05	CB	K	7	8.49	3.0		6.0		
05171636+2709420	17-02-05	CB	K	7	10.45	5.0		7.9		
05171881+2656220	17-02-05	CB	K	7	8.41	3.0		7.8		
05174804+2700307	17-02-05	CB	K	7	8.42	3.0		7.0		
05175703+2653281	17-02-05	CB	K	7	8.48	3.0		7.5		
IRAS 05156+2654	17-02-05	CB	K	7	8.42	3.0		4.5		
SAO 77108	18-02-05	CB	K	7	8.43	3.0	9.4	7.9	G5	112

CA: OAN 1.5 m + CCD.

CB: OAN 1.5 m + MAGIC.

CC: CAHA 2.2 m + MAGIC.

Table C.1: Complete list of occultation events and of the circumstances of their observation (continued)

(1) Source	(2) Date UT	(3) Telescope +detector	(4) Filter	(5) D $''$	(6) Δt ms	(7) τ ms	(8) V mag	(9) K mag	(10) Sp.	(11) Dist. pc
05201417+2654113	18-02-05	CB	K	7	8.48	3.0		7.5		
05212000+2652578	18-02-05	CB	K	7	10.37	5.0		7.2		
05220164+2659311	18-02-05	CB	K	7	8.41	3.0		5.7		
06051402+2809214	18-02-05	CB	K	7	8.35	3.0		6.1		
06055838+2751298	18-02-05	CB	K	7	8.42	3.0		7.3		
06064765+2805259	18-02-05	CB	K	7	10.43	5.0		8.1		
SAO 77969	18-02-05	CB	K	7	8.41	3.0	9.5	7.9	G0	
GSC 01872-01897	18-02-05	CB	K	7	8.44	3.0	9.8	7.0		
06073307+2809556	18-02-05	CB	K	7	8.46	3.0		7.1		
06075805+2751369	18-02-05	CB	K	7	8.37	3.0		7.0		
AG+28 611	18-02-05	CB	K	7	8.47	3.0	10.4	6.9	K0	
CSS 188	18-02-05	CB	K	7	8.45	3.0	13.9	5.5	S	
06085962+2755026	18-02-05	CB	K	7	8.40	3.0		5.6		
06093373+2759385	18-02-05	CB	K	7	10.48	5.0		7.8		
06093876+2801211	18-02-05	CB	K	7	10.49	5.0		7.6		
06100794+2800555	18-02-05	CB	K	7	8.37	3.0		6.9		
06103125+2757078	18-02-05	CB	K	7	8.46	3.0		7.1		
GSC 01885-00864	18-02-05	CB	K	7	8.37	3.0	9.5	5.5		
GSC 01885-01082	18-02-05	CB	K	7	8.39	3.0	10.3	7.3		
06113254+2751170	18-02-05	CB	K	7	8.42	3.0		7.7		
GSC 01885-00849	18-02-05	CB	K	7	8.48	3.0	10.0	7.2		
GSC 01885-01059	18-02-05	CB	K	7	8.41	3.0	10.3	7.5		
GSC 01885-01003	18-02-05	CB	K	7	8.44	3.0	10.2	7.6		
GSC 01885-01024	18-02-05	CB	K	7	8.39	3.0	9.6	5.6		
06132916+2758550	19-02-05	CB	K	7	8.40	3.0		7.2		
GSC 01885-01197	19-02-05	CB	K	7	8.45	3.0	10.2	6.4		
06143648+2756007	19-02-05	CB	K	7	8.47	3.0		6.3		
SAO 78128	19-02-05	CB	K	7	8.35	3.0	8.3	5.8	K2	178
06151320+2752458	19-02-05	CB	K	7	8.44	3.0		7.3		
06152640+2749330	19-02-05	CB	K	7	8.47	3.0		6.1		
SAO 78149	19-02-05	CB	K	7	8.52	3.0	8.0	4.4	K2	255
Kiso C2-125	19-02-05	CB	K	7	8.40	3.0	14.2	6.5		
06164415+2754332	19-02-05	CB	K	7	8.45	3.0		6.9		
06172566+2744429	19-02-05	CB	K	7	10.40	5.0		8.1		
GSC 01886-01909	19-02-05	CB	K	7	8.43	3.0	9.9	6.9		

CA: OAN 1.5 m + CCD.

CB: OAN 1.5 m + MAGIC.

CC: CAHA 2.2 m + MAGIC.

Table C.1: Complete list of occultation events and of the circumstances of their observation (continued)

(1) Source	(2) Date UT	(3) Telescope +detector	(4) Filter	(5) D "	(6) Δt ms	(7) τ ms	(8) V mag	(9) K mag	(10) Sp.	(11) Dist. pc
06173933+2731055	19-02-05	CB	K	7	8.44	3.0		7.9		
06174326+2752319	19-02-05	CB	K	7	8.45	3.0		7.0		
06181909+2732294	19-02-05	CB	K	7	8.43	3.0		6.3		
SAO 78917	19-02-05	CB	K	7	8.39	3.0	8.3	4.4	M0	
06584528+2747087	19-02-05	CB	K	7	10.47	5.0		8.1		
06595289+2744549	19-02-05	CB	K	7	8.42	3.0		7.4		
AG+27 746	19-02-05	CB	K	7	10.38	5.0	9.2	8.0	F8	429
GSC 01903-01226	19-02-05	CB	K	7	8.34	3.0	10.6	7.2		
SAO 78965	19-02-05	CB	K	7	8.42	3.0	9.0	6.4	K0	
SAO 78964	19-02-05	CB	K	7	8.40	3.0	8.9	4.1	M...	
AG+27 757	19-02-05	CB	K	7	10.48	5.0	10.3	7.3	K0	
SAO 78974	19-02-05	CB	K	7	8.40	3.0	9.1	6.6	K2	
GSC 01903-01256	19-02-05	CB	K	7	8.43	3.0	10.1	7.4		
GSC 01903-01683	19-02-05	CB	K	7	8.36	3.0	10.3	7.1		
GSC 01903-01680	19-02-05	CB	K	7	8.48	3.0	10.2	7.5		
GSC 01903-01497	19-02-05	CB	K	7	10.48	5.0	10.4	7.9		
07051697+2726124	19-02-05	CB	K	7	10.36	5.0		7.8		
GJ 265 A	19-02-05	CB	K	7	8.42	3.0	10.2	6.8	K5	24
GSC 01903-01419	19-02-05	CB	K	7	10.41	5.0	10.2	8.5		
07064204+2711078	19-02-05	CB	K	7	8.45	3.0		5.8		
GSC 01904-00825	20-02-05	CB	K	7	8.47	3.0	9.8	6.9		
07101734+2655104	20-02-05	CB	K	7	8.39	3.0		6.1		
FBS 0707+270	20-02-05	CB	K	7	8.48	3.0		5.4	C...	
SAO 79141	20-02-05	CB	K	7	8.43	3.0	5.8	5.4	A4IV	120
AG+26 773	20-02-05	CB	K	7	10.46	5.0	10.0	7.6	K0	
IRAS 07089+2711	20-02-05	CB	K	7	8.49	3.0		3.9		
GSC 01904-01000	20-02-05	CB	K	7	8.35	3.0	10.5	7.1		
07125078+2707059	20-02-05	CB	K	7	10.44	5.0		7.1		
GSC 01929-00326	20-02-05	CB	K	7	8.47	3.0	9.4	6.6		
GSC 01929-00388	20-02-05	CB	K	7	10.37	5.0	10.5	8.3		
SAO 79763	20-02-05	CB	K	7	8.43	3.0	8.6	6.1	K0	
GSC 01929-00556	20-02-05	CB	K	7	8.38	3.0	10.5	7.4		
SAO 79788	20-02-05	CB	K	7	8.38	3.0	9.5	6.0	K5	
GSC 01930-00682	21-02-05	CB	K	7	8.40	3.0	10.0	5.7		
SAO 79861	21-02-05	CB	K	7	8.43	3.0	5.9	3.9	G8III:	345

CA: OAN 1.5 m + CCD.

CB: OAN 1.5 m + MAGIC.

CC: CAHA 2.2 m + MAGIC.

Table C.1: Complete list of occultation events and of the circumstances of their observation (continued)

(1)	(2)	(3)	(4)	(5)	(6)	(7)	(8)	(9)	(10)	(11)
Source	Date	Telescope	Filter	D	Δt	τ	V	K	Sp.	Dist.
	UT	+detector		$''$	ms	ms	mag	mag		pc
SAO 79869	21-02-05	CB	K	7	8.49	3.0	6.3	6.2	A1V	183
SAO 79874	21-02-05	CB	K	7	8.42	3.0	8.6	4.2	K7	1370
SAO 79888	21-02-05	CB	K	7	8.39	3.0	8.2	5.0	K5	
08043031+2502030	21-02-05	CB	K	7	8.36	3.0		7.5		
SAO 79921	21-02-05	CB	K	7	8.41	3.0	9.6	7.4	K0	

CA: OAN 1.5 m + CCD.

CB: OAN 1.5 m + MAGIC.

CC: CAHA 2.2 m + MAGIC.